

VOLUME 82

MARCH 23, 1978

NUMBER 6

JPCHAx

---

THE JOURNAL OF

PHYSICAL

CHEMISTRY

---



PUBLISHED BIWEEKLY BY THE AMERICAN CHEMICAL SOCIETY

# THE JOURNAL OF PHYSICAL CHEMISTRY

**BRYCE CRAWFORD, Jr.**, *Editor*  
**STEPHEN PRAGER**, *Associate Editor*  
**ROBERT W. CARR, Jr.**, **C. ALDEN MEAD**, *Assistant Editors*

**EDITORIAL BOARD:** C. A. ANGELL (1978-1982), F. C. ANSON (1974-1978), V. A. BLOOMFIELD (1974-1978), J. R. BOLTON (1976-1980), L. M. DORFMAN (1974-1978), W. E. FALCONER (1977-1978), H. L. FRIEDMAN (1975-1979), H. L. FRISCH (1976-1980), W. A. GODDARD (1976-1980), E. J. HART (1975-1979), W. J. KAUFMANN (1974-1978), R. L. KAY (1977-1981), L. KEVAN (1978-1982), D. W. McCLURE (1974-1978), K. MYSELS (1977-1981), R. M. NOYES (1978-1982), R. G. PARR (1977-1979), J. PERI (1978-1982), W. B. PERSON (1976-1980), J. C. POLANYI (1976-1980), J. PRAUSNITZ (1978-1982), S. A. RICE (1976-1980), D. SETSER (1978-1980), W. A. STEELE (1976-1980), J. B. STOTHERS (1974-1978), F. A. VAN-CATLEDGE (1977-1981)

*Published by the*  
**AMERICAN CHEMICAL SOCIETY**  
**BOOKS AND JOURNALS DIVISION**  
D. H. Michael Bowen, Director; Marjorie Laflin, Assistant to the Director

Editorial Department: Charles R. Bertsch, Head; Marianne C. Brogan, Associate Head; Joseph E. Yurvati, Assistant Editor

Magazine and Production Department: Bacil Guiley, Head  
Research and Development Department: Seldon W. Terrant, Head

Advertising Office: Centcom, Ltd., 25 Sylvan Road South, Westport, Conn. 06880.

© Copyright, 1978, by the American Chemical Society. **Permission** of the American Chemical Society is granted for libraries and other users to make reprographic copies for use beyond that permitted by Sections 107 or 108 of the U.S. Copyright Law, provided that, for all articles bearing an article code, the copying organization pay the stated per-copy fee through the Copyright Clearance Center, Inc. For further information write to Office of the Director, Books and Journals Division at the ACS Washington address.

Published biweekly by the American Chemical Society at 20th and Northampton Sts., Easton, Pennsylvania 18042. Second class postage paid at Washington, D.C. and at additional mailing offices.

## Editorial Information

**Instructions for authors** are printed in the first issue of each volume. Please conform to these instructions when submitting manuscripts.

**Manuscripts for publication** should be submitted to *The Journal of Physical Chemistry*, Department of Chemistry, University of Minnesota, 207 Pleasant St. S.E., Minneapolis, Minn. 55455. Correspondence regarding **accepted papers and proofs** should be directed to the Editorial Department at the address below.

**Page charges** of \$60.00 per page may be paid for papers published in this journal. Payment does not affect acceptance or scheduling of papers.

**Bulk reprints or photocopies** of individual articles are available. For information write to Business Operations, Books, and Journals Division at the ACS Washington address.

The American Chemical Society and its Editors assume no responsibility for the statements and opinions advanced by contributors.

## Subscription and Business Information

**1978 subscription prices**, printed or microfiche, including postage. Microfiche by air mail; printed by surface mail. Printed edition air mail or air freight rates available from Membership & Subscription Services at the address below.

	U.S.	Foreign
Members	\$24.00	\$34.00
Nonmembers	96.00	106.00
Supplementary material (available in microfiche only)	20.00	36.00

**New and renewal subscriptions** should be sent with payment to the Office of the Controller at the ACS Washington address. **Changes of address** must include both old and new addresses with ZIP code and a recent mailing label. Send all address changes to Membership & Subscription Services. Please allow six weeks for change to become effective.

**Claims for missing numbers** will not be allowed if loss was due to failure of notice of change of address to be received in the time specified; if claim is dated (a) North America—more than 90 days beyond issue date, (b) all other foreign—more than 1 year beyond issue date; or if the reason given is "missing from files". Hard copy claims are handled by Membership & Subscription Services.

**Microfilm** editions of all ACS primary publications, by single volume or entire back issue collection, are available. For additional microfilm (and microfiche) information, contact Microforms Program at the ACS Washington address or call (202) 872-4554.

To order **single issues or back volumes**, printed or microfiche, contact Special Issues Sales at the ACS Washington address, or call (202) 872-4365. Current year single issue \$4.75. Prior year single issue \$5.00. Back volume \$126.00. Foreign postage additional.

**Supplementary material** mentioned in the journal appears in the microfilm edition. Papers containing supplementary material are noted in the Table of Contents with a ■. See Supplementary Material notice at end of article for number of pages. Orders over 20 pages are available only on 24× microfiche. Orders must state photocopy or microfiche. Full bibliographic citation including names of all authors and prepayment are required. Prices are subject to change.

	U.S.	Foreign
Microfiche	\$3.00	\$4.00
Photocopy		
1-8 pages	5.50	7.00
9-20 pages	6.50	8.00

Single microfiche or paper copies of Supplementary Material may be ordered from Business Operations, Books and Journals Division at the ACS Washington address, or call (202) 872-4559.

American Chemical Society  
1155 16th Street, N.W.  
Washington, D.C. 20036  
(202) 872-4600

Editorial Department  
American Chemical Society  
P.O. Box 3330  
Columbus, Ohio 43210  
(614) 421-6940 ext 3171

Membership & Subscription Services  
American Chemical Society  
P.O. Box 3337  
Columbus, Ohio 43210  
(614) 421-7230

THE JOURNAL OF  
PHYSICAL CHEMISTRY

---

Volume 82, Number 6 March 23, 1978

JPCA<sub>x</sub> 82(6) 627-752 (1978)

ISSN 0022-3654

Characterization of Hot Chlorine Atom Reactions with Hydrogen . . . Don J. Stevens and Leonard D. Spicer*	627
A Mass Spectrometric Study of the Fragmentation of the Lithium Fluoride Vapor System . . . R. T. Grimley,* J. A. Forsman, and Q. G. Grindstaff	632 ■
Thermal Ion-Molecule Reactions in Oxygen-Containing Molecules. Condensation-Elimination and Addition Reactions in Simple Aliphatic Ketones . . . Minoru Kumakura* and Toshio Sugiura	639
Application of RRKM Theory Using a Hindered Rotational Gorin Model Transition State to the Reaction $\text{HO}_2\text{NO}_2 + \text{N}_2 \rightleftharpoons \text{HO}_2 + \text{NO}_2 + \text{N}_2$ . . . . . A. C. Baldwin and D. M. Golden*	644
Kinetic Studies of Complexation of Divalent Strontium, Barium, Lead, and Mercury Cations by Aqueous 15-Crown-5 and 18-Crown-6 . . . . . Licesio J. Rodriguez, Gerard W. Liesegang, Michael M. Farrow, Neil Purdie, and Edward M. Eyring*	647 ■
Reactions of the Radical Cations of Methylated Benzene Derivatives in Aqueous Solution . . . K. Sehested* and J. Holcman	651
Irradiation of Benzene with $^{14}\text{CH}^+$ and $^{14}\text{CH}_3^+$ Ions . . . W. R. Erwin, B. E. Gordon, L. D. Spicer, and R. M. Lemmon*	654
Positron Lifetime Studies in $\gamma$ -Irradiated Organic Crystals . . . Yan-ching Jean and Hans J. Ache*	656
Mass Spectrometry of Solvated Ions Generated Directly from the Liquid Phase by Electrohydrodynamic Ionization . . . Brian P. Stimpson,* David S. Simons, and Charles A. Evans, Jr.	660
Ionization Constants and Heats of Ionization of the Bisulfate Ion from 5 to 55 °C . . . T. F. Young, C. R. Singleterry, and I. M. Klotz*	671
The Thermodynamics of Transfer of Phenol and Aniline between Nonpolar and Aqueous Environments . . . Kenneth J. Breslauer,* Lucia Witkowski, and Kristina Bulas	675
Hydrogenation of Dienes and the Selectivity for Partial Hydrogenation on a Molybdenum Disulfide Catalyst . . . Toshio Okuhara, Hiroyuki Itoh, Koshiro Miyahara, and Ken-ichi Tanaka*	678
The Influence of Cupric Ions on the Infrared Spectrum of Water . . . P. P. Sethna, Lary W. Pinkley, and Dudley Williams*	683
Polarizability, Proton Transfer, and Symmetry of Energy Surfaces of Phenol- <i>n</i> -Propylamine Hydrogen Bonds. Infrared Investigations . . . . . Georg Zundel* and Anton Nagyrevi	685
The Polarized Infrared Spectra and Structure of Crystalline Bromoacetic Acid . . . P. F. Krause, J. E. Katon,* and R. W. Mason	690
Electronic Absorption Spectra of Some Cation Radicals as Compared with Ultraviolet Photoelectron Spectra . . . . . Tadamasa Shida,* Yoshio Nosaka, and Tatsuhisa Kato	695
The Kerr Effect of Carbon Disulfide and Other Organic Liquids in the Ultraviolet . . . James W. Lewis and William H. Orttung*	698
Absolute Quantum Yield Determination by Thermal Blooming. Fluorescein . . . James H. Brannon and Douglas Magde*	705

Phosphate Radicals. Spectra, Acid-Base Equilibria, and Reactions with Inorganic Compounds . . . . . <b>P. Maruthamuthu and P. Neta*</b>	710
The Geometries of Some Small Dimers and Malonaldehyde by Approximate Molecular Orbital Theory . . . . . <b>Donna L. Breen</b>	714
Electron Paramagnetic Resonance Spectra of the Group 4 Hexafluoride Anion Radicals . . . . . <b>A. R. Boate, J. R. Morton,* and K. F. Preston</b>	718
Electron Paramagnetic Resonance Parameters of Copper(II) Y Zeolites . . . . . <b>Richard G. Herman* and Dennis R. Flentge</b>	720
Metal-Ammonia Solutions. 10. Electron Spin Resonance. A Blue Solid Containing a Crown Ether Complexing Agent . . . . . <b>R. L. Harris and J. J. Lagowski*</b>	729 ■
The Role of Defects in the Thermal Decomposition of Barium Azide . . . . . <b>V. R. Pai Verneker* and M. P. Kannan</b>	735 ■
Size and Geometric Effects in Copper and Palladium Metal Clusters . . . . . <b>R. C. Baetzold</b>	738
Vortical Flow as a Source of Optical Activity in J Aggregates of Cyanine Dyes? . . . . <b>Bengt Nordén</b>	744
Influence of Dynamic Quenching on the Thermal Dependence of Fluorescence in Solution. Study of Indole and Phenol in Water and Dioxane . . . . . <b>Gilbert Laustriat* and Dominique Gerard</b>	746

## COMMUNICATIONS TO THE EDITOR

Pulse Radiolysis and Electron Spin Resonance Studies Concerning the Reaction of $\text{SO}_4^{\cdot-}$ with Alcohols and Ethers in Aqueous Solution . . . . . <b>H. Eibenberger, S. Steenken,* P. O'Neill, and D. Schulte-Frohlinde</b>	749
Infrared Study of Hydrogen Sulfide and Carbon Monoxide Adsorption in the Presence of Hydrogen on Alumina-Supported Nickel Catalysts . . . . . <b>R. T. Rewick* and H. Wise</b>	751

■ Supplementary and/or miniprint material for this paper is available separately (consult the masthead page for ordering information); it will also appear following the paper in the microfilm edition of this journal.

\* In papers with more than one author, the asterisk indicates the name of the author to whom inquiries about the paper should be addressed.

## AUTHOR INDEX

Ache, H. J., 656	Grimley, R. T., 632	Liesegang, G. W., 647	Rodriguez, L. J., 647
Baetzold, R. C., 738	Grindstaff, Q. G., 632	Magde, D., 705	Schulte-Frohlinde, D., 749
Baldwin, A. C., 644	Harris, R. L., 729	Maruthamuthu, P., 710	Sehested, K., 651
Boate, A. R., 718	Herman, R. G., 720	Mason, R. W., 690	Sethna, P. P., 683
Brannon, J. H., 705	Holcman, J., 651	Miyahara, K., 678	Shida, T., 695
Breen, D. L., 714	Itoh, H., 678	Morton, J. R., 718	Simons, D. S., 660
Breslauer, K. J., 675	Jean, Y., 656	Nagyrevi, A., 685	Singleterry, C. R., 671
Bulas, K., 675	Kannan, M. P., 735	Neta, P., 710	Spicer, L. D., 627, 654
Eibenberger, H., 749	Kato, T., 695	Nordén, B., 744	Steenken, S., 749
Erwin, W. R., 654	Katon, J. E., 690	Nosaka, Y., 695	Stevens, D. J., 627
Evans, C. A., Jr., 660	Klotz, I. M., 671	Okuhara, T., 678	Stimpson, B. P., 660
Eyring, E. M., 647	Krause, P. F., 690	O'Neill, P., 749	Sugiura, T., 639
Farrow, M. M., 647	Kumakura, M., 639	Ortung, W. H., 698	Tanaka, K., 678
Flentge, D. R., 720	Lagowski, J. J., 729	Pai Verneker, V. R., 735	Williams, D., 683
Forsman, J. A., 632	Laustriat, G., 746	Pinkley, L. W., 683	Wise, H., 751
Gerard, D., 746	Lemmon, R. M., 654	Preston, K. F., 718	Witkowski, L., 675
Golden, D. M., 644	Lewis, J. W., 698	Purdie, N., 647	Young, T. F., 671
Gordon, B. E., 654		Rewick, R. T., 751	Zundel, G., 685

# THE JOURNAL OF PHYSICAL CHEMISTRY

Registered in U. S. Patent Office © Copyright, 1978, by the American Chemical Society

VOLUME 82, NUMBER 6 MARCH 23, 1978

## Characterization of Hot Chlorine Atom Reactions with Hydrogen

Don J. Stevens and Leonard D. Spicer\*<sup>†</sup>

Department of Chemistry, University of Utah, Salt Lake City, Utah 84112 (Received November 19, 1976; Revised Manuscript Received October 31, 1977)

Publication costs assisted by the United States Department of Energy

The reaction of nuclear recoil generated chlorine atoms with hydrogen to produce hydrogen chloride was studied in the presence of ethylene and iodine scavengers. The yield behavior is presented for this reaction over a relative average translational energy range extending from a lower limit of  $\sim 0.16$  eV determined by the thermal scavenging efficiency of the system to several tens of electron volts. The hydrogen isotope effect for  $H_2$  and  $D_2$  reactants is explored over this same energy range and found to exhibit a cross over from a normal value of 2.3 to an inverse effect of 0.8 as the average reaction energy is increased. The relative kinetic behavior of the isotopic systems is interpreted in terms of a steady state non-Boltzmann formalism and comparison is made with reported results for corresponding fluorine atom reactions.

### Introduction

Halogen atom reactions with hydrogen have been studied extensively in thermal and photochemical systems.<sup>1-4</sup> Recent investigations of these reactions have been extended to much higher energies via theoretical trajectory studies in the fluorine atom case and experimental nuclear recoil studies for both fluorine and chlorine atoms.<sup>5-8</sup> The quasiclassical trajectory calculations as well as the experimental results indicate that the reactive cross section for fluorine extends to several tens of electron volts center of mass translational energy. It is anticipated that other halogen atom reactions with hydrogen also occur efficiently at such high energies, and indeed experimental evidence for hot reaction of chlorine has been communicated by these authors.<sup>7</sup> These systems are particularly attractive for high energy kinetic studies because there are a limited number of reaction pathways available and the HX product molecule can carry away sizable amounts of translational, rotational, and vibrational energy. This allows stable product formation even at relatively high incident collision energy.

In hydrogen reactant, replacement and abstraction are indistinguishable processes with respect to the product HX formed. In hydrocarbon reactant systems, however, the

class of reactions which gives the same product is designated hydrogen abstraction. Such abstraction reactions by recoil fluorine atoms have been reported for a large number of saturated hydrocarbon and halogenated hydrocarbon reactants where the relative rates have been compared<sup>9-11</sup> and for olefinic reactants where abstraction is determined in competition with addition.<sup>12</sup>

In this report, the high energy reactions of recoil chlorine atoms with hydrogen and deuterium are examined as a function of added moderator concentration. Since a direct quantitative interpretation of the reaction kinetics in terms of the collisional and compositional properties of the medium is not possible, the non-Boltzmann kinetic technique recently reported by Keizer<sup>13</sup> is employed to explore dynamical features of the high energy reaction process and to verify empirical conclusions based on direct observation. This method has been successfully applied to experimental results for the recoil reaction of fluorine with hydrogen at high translational energies<sup>6</sup> and is informative in this system as well. In particular unlike the case of fluorine, the reaction of chlorine atoms with hydrogen and deuterium shows a definite cross over from a normal to an inverse isotope effect at high energies. Finally, the magnitude of the normal isotope effect extrapolated to an infinite moderator/hydrogen ratio in the presence of 5% ethylene scavenger suggests that the

\* Camille and Henry Dreyfus Teacher-Scholar 1971-1976.

scavenger present in this experimental system maintains an average effective low energy reaction temperature of  $\sim 1200$  K for chlorine reaction with hydrogen. This tends to limit the low energy results reported to the epithermal region.

### Experimental Section

Translationally hot  $^{38}\text{Cl}$  atoms were generated by the  $^{37}\text{Cl}(n,\gamma)^{38}\text{Cl}$  nuclear reaction. Sample vessels, filling and irradiation procedures, and sample analysis methods were identical with those described previously.<sup>14</sup> Samples contained  $\text{H}_2$  or  $\text{D}_2$  reactant,  $\text{CF}_2\text{Cl}_2$  moderator and source gas for the nuclear reaction, and an ethylene- $\text{I}_2$  competitive scavenger for low energy chlorine atoms. Matheson  $\text{H}_2$ ,  $\text{D}_2$ , and  $\text{CF}_2\text{Cl}_2$  and Phillips Research Grade  $\text{C}_2\text{H}_4$  were used directly from lecture bottles after gas chromatographic and mass spectroscopic analysis indicated purities of greater than 99.9%. Following irradiation, volatile hydrogen chloride product was separated from organic and other inorganic products using a carbonate stripper column described previously.<sup>14</sup> Involatile hydrogen chloride was removed from the reaction vessel walls with repeated rinses of 0.1 M aqueous  $\text{Na}_2\text{CO}_3$ , and the absolute yields of the hydrogen chloride as well as the summed absolute yields of all other products were determined in a  $3 \times 3$  in. NaI(Tl) scintillation detector.

The identity of the hydrogen chloride product on the reaction vessel wall and in the stripper apparatus was determined indirectly in an extensive series of investigations<sup>15</sup> which are described briefly below. The chlorine containing yield adsorbed on the reaction vessel wall following evacuation of other reactants demonstrated highest lability toward aqueous polar solvents. In order of decreasing efficiency, the solvents used included 0.1 M aqueous  $\text{Na}_2\text{CO}_3$ , 0.1 M aqueous  $\text{NaCl}$ ,  $\text{H}_2\text{O}$ , anhydrous  $\text{CH}_3\text{OH}$ , and anhydrous  $\text{C}_6\text{H}_6$ . Wall activity which was removed by either methanol or benzene solvent was quantitatively extractable into aqueous 0.1 M  $\text{Na}_2\text{CO}_3$ . Quantitative recovery of  $^{38}\text{Cl}$  activity as  $\text{Ag}^{38}\text{Cl}$  was also observed when an aqueous  $\text{NaCl}$  rinse was used followed by addition of 0.1 M  $\text{AgNO}_3$ . This behavior suggests that the wall yield is both polar and inorganic in nature and discounts the probability of significant contributions to the wall yield from chloroethyl radicals or from polymerized halocarbon products. Further, the wall yield was dependent on both the source and the quantity of abstractable hydrogen in the reactive system containing  $\text{H}_2$ ,  $\text{C}_2\text{H}_4$ , and  $\text{CF}_2\text{Cl}_2$  suggesting that the wall yield also contained hydrogen.

The identification of the wall yield as  $\text{H}^{38}\text{Cl}$  is further supported by addition of inorganic carrier gases to the reaction vessel following evacuation of other products into the cold trap.  $\text{HCl}$  carrier efficiently removed 98% of the wall activity after 2 min equilibration time, and that yield was quantitatively trapped on a carbonate stripper column.  $\text{ICl}$  carrier, by comparison, did not influence the wall yield and identical rinse yields were obtained whether or not  $\text{ICl}$  carrier was used.  $\text{ICl}$  passed through the carbonate stripper column and could be detected chromatographically, although no evidence of radioactive  $\text{I}^{38}\text{Cl}$  was seen in any experimental run. Chlorine gas added in carrier quantities removed  $\sim 80\%$  of the wall yield after 2 min equilibration time. The yield so removed, however, passed through the carbonate stripper and was collected quantitatively in the cold trap. The labeled chlorine product was also detected chromatographically despite the fact that no carrier free chlorine was ever detected. In view of this result and the fact that the  $\text{Cl}_2$  carrier was neither as effective as  $\text{HCl}$  in removing the wall activity nor was

retained in the carbonate stripper it is felt that the  $\text{Cl}_2$  exchanges chlorine atoms with labeled  $\text{H}^{38}\text{Cl}$  on the reaction vessel wall. This exchange process has been well documented<sup>16</sup> in thermal systems and depends critically on the dryness of the reaction vessel walls. It is concluded also that  $^{38}\text{ClF}$  is absent as a product since the wall and stripper yields showed no direct dependence on the quantity of source gas  $\text{CF}_2\text{Cl}_2$  present. It appears then that  $\text{H}^{38}\text{Cl}$  in carrier free quantities is largely adsorbed reversibly on the reaction vessel walls and can be removed by carrier addition or appropriate aqueous rinse.  $\text{H}^{38}\text{Cl}$  activity which remains in the gas phase is trapped on the carbonate stripper column.

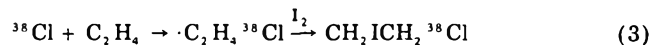
In the absence of added  $\text{Cl}_2$  no evidence of heterogeneous wall-catalyzed exchange was found. The wall yield results were independent of irradiation length or sample analysis time, and Pyrex wool placed in the reaction vessels to increase surface area gave identical results to samples without added surface area. The observed results were also independent of the severity of reaction vessel drying although in practice the vessels were routinely dried overnight at  $150^\circ\text{C}$  while a few were heated under vacuum immediately prior to sample preparation. The results suggest that the  $\text{H}^{38}\text{Cl}$  on the reaction vessel walls and on the carbonate stripper is a recoil reaction product.

### Results and Discussion

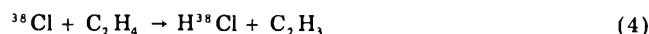
The reaction of recoil chlorine atoms with hydrogen and deuterium was monitored in the respective experimental systems by directly measuring the absolute product yields of  $\text{H}^{38}\text{Cl}$  and  $\text{D}^{38}\text{Cl}$  from the reactions



Thermalized chlorine atoms were scavenged by a combination ethylene- $\text{I}_2$  scavenger which resulted in the formation of chloriodoethane scavenger product:



The use of ethylene as a competitive scavenger for low energy chlorine atoms also presents a source of abstractable hydrogen which contributes to the hydrogen chloride yield through a direct abstraction mechanism as reported earlier.<sup>14</sup>



The yield of  $\text{H}^{38}\text{Cl}$  from this mechanism is directly proportional to the concentration of ethylene in the reactive system and changes by only 0.1% absolute yield per additional percent ethylene concentration. For the 5% scavenger concentration used, the ethylene produced  $\text{H}^{38}\text{Cl}$  yield can be accounted for on a quantitative basis. Hydrogen chloride can also be generated by unimolecular decomposition of the intermediate chloroethyl scavenger radical, but internal sample pressures of 1000 Torr in the present study suppress this reaction pathway to  $\leq 0.2\%$  of the absolute product yield.<sup>14</sup> Other sources of abstractable hydrogen or reaction pathways contributing to the  $\text{H}^{38}\text{Cl}$  yield were absent in the recoil system.

The energy dependence of the primary  $^{38}\text{Cl} + \text{H}_2(\text{D}_2)$  reaction was investigated experimentally by variation of the  $\text{CF}_2\text{Cl}_2$  moderator gas concentration. Freon-12 was found to be essentially inert to both hot and thermal chlorine reaction contributing less than 1% to the total yield of products in all systems studied. At high moderation, the recoil chlorine atom must, on the average, undergo numerous nonreactive energy degrading collisions with the inert collider prior to reaction with hydrogen, and the average reaction energy is expected to be near thermal.

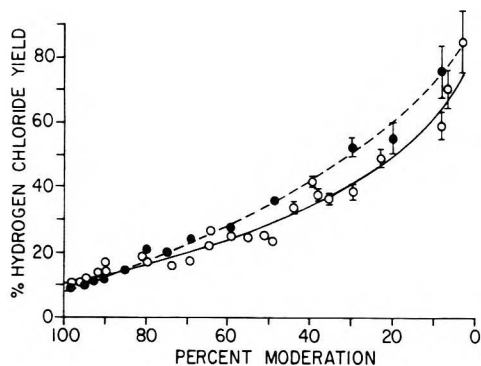


**Figure 1.** Dependence of the absolute yield of hydrogen chloride on  $\text{CF}_2\text{Cl}_2$  moderator concentration at 1000 Torr pressure for the reactions of  $^{38}\text{Cl}$  with  $\text{H}_2$  and  $\text{D}_2$  in the presence of ethylene-iodine scavenger: (O)  $\text{H}_2$  reactant; (●)  $\text{D}_2$  reactant.

At low moderator concentrations, however, the density of high energy collisions between the recoiling hot atom and  $\text{H}_2$  reactant increases and the average energy of reaction may increase accordingly if the reaction channel exhibits a significant cross section at high energies. The dependence of the  $\text{H}^{38}\text{Cl}$  yield on moderator concentration was monitored in a system of 2–95%  $\text{H}_2$ , ethylene- $\text{I}_2$  scavenger, and  $\text{CF}_2\text{Cl}_2$  moderator and source gas added to a total pressure of 1000 Torr. The ethylene scavenger concentration was maintained at 5% of the moderator concentration or 10 Torr pressure whichever was greater. The results of the moderation dependence for the  $^{38}\text{Cl} + \text{H}_2$  and  $^{38}\text{Cl} + \text{D}_2$  reactions are shown in Figure 1 and include the summed yields of hydrogen chloride generated by the primary reaction with  $\text{H}_2$  or  $\text{D}_2$ , as in (1) or (2), and by abstraction from ethylene as in (3). The error bars shown are representative and show one standard deviation in the data. These results indicate a definite hot contribution to the hydrogen chloride yield, and they show an inverse isotope effect arising at high energies in this recoil reaction system.<sup>7,15</sup>

The differences in zero point energies in the  $\text{H}_2$  and  $\text{D}_2$  systems are expected to give rise to sizable isotope effects at thermal energies. In thermally equilibrated systems at 300 K, normal isotope effects have been determined experimentally<sup>1</sup> to be  $k_{\text{H}_2}/k_{\text{D}_2} = 9.4$  for the  $\text{Cl} + \text{H}_2(\text{D}_2)$  abstraction reactions, and similar values have been calculated theoretically.<sup>17</sup> The measured isotope effect decreases rapidly at higher temperatures to a limiting minimum value predicted to be  $\sim 1.4$ . In the study reported here the high moderation yields were extrapolated to a moderator/hydrogen ratio of infinity and a scavenger concentration of 5%. The values for the  $\text{H}^{38}\text{Cl}$  and  $\text{D}^{38}\text{Cl}$  absolute yields determined in this way are  $\sim 10.6$  and  $\sim 8.3\%$ , respectively.<sup>7</sup> Subtraction of the 6.5%  $\text{H}^{38}\text{Cl}$  yield<sup>14,15</sup> from the ethylene reaction results in a measured low energy isotope effect of  $k_{\text{H}_2}/k_{\text{D}_2} = 2.3$ . Extrapolation of the published temperature dependence of the thermal isotope effect gives an effective minimum reaction temperature corresponding to  $\sim 1200$  K for these reactions at high moderation in the presence of 5% ethylene.

The high effective reaction temperature is thought to result from the increasing differential reactivity of the ethylene relative to hydrogen for low energy chlorine atoms as the moderator concentration is increased. Indeed it is expected that the average energy of reaction could be lowered further if the concentration of scavenger were reduced.

At low moderator concentrations, corresponding to high average energies of reaction, the  $\text{H}^{38}\text{Cl}$  and  $\text{D}^{38}\text{Cl}$  yields exhibit an inverse isotope effect where  $Y_{\text{DCl}} > Y_{\text{HCl}}$ .<sup>7</sup> The

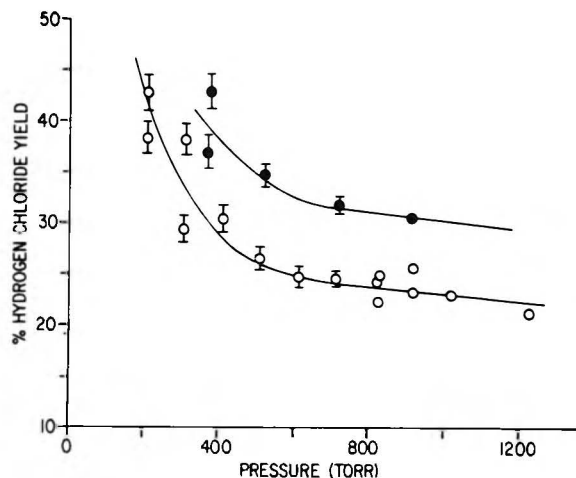


**Figure 2.** Pressure dependence of hydrogen chloride yield for gas mixtures containing 50%  $\text{H}_2(\text{D}_2)$  reactant, 45%  $\text{CF}_2\text{Cl}_2$  moderator, and 5% ethylene- $\text{I}_2$  scavenger: (O)  $\text{H}_2$  reactant; (●)  $\text{D}_2$  reactant. Error bars represent standard deviations in the yields.

crossover is thought to be the result of dynamical factors, involving either the primary reaction cross section or subsequent decomposition of the nascent product arising from the high energy reaction mechanism, which are independent of and which are substantially larger than the normal thermal kinetic isotope effect. The inverse isotope effect is also observed as a function of pressure at constant moderation in a system with 50%  $\text{H}_2(\text{D}_2)$  reactant, 45%  $\text{CF}_2\text{Cl}_2$  moderator and source gas, and 5% ethylene- $\text{I}_2$  scavenger. The  $\text{H}^{38}\text{Cl}$  ( $\text{D}^{38}\text{Cl}$ ) yields are shown in Figure 2 as a function of pressure. The increasing hydrogen chloride yield at low pressures results from the unimolecular decay of the  $^{38}\text{Cl} + \text{ethylene}$  reaction intermediate reported previously.<sup>14</sup> Subtraction of the ethylene-produced  $\text{H}^{38}\text{Cl}$  yield from the total hydrogen chloride yields at various pressures in the present system results in constant  $\text{H}^{38}\text{Cl}$  ( $\text{D}^{38}\text{Cl}$ ) yields from the  $^{38}\text{Cl} + \text{H}_2(\text{D}_2)$  reaction over the pressure range investigated experimentally in Figure 2. The net absolute yields from the chlorine atom reaction with  $\text{H}_2$  and  $\text{D}_2$  at 50% moderation are measured to be 16 and 26%, respectively, giving rise to an inverse isotope effect of 0.62. It is interesting to note that at lower moderator concentrations and higher average energies of reaction the inverse isotope effect reduces to  $\sim 0.8$ .

The kinetic behavior of the  $\text{Cl} + \text{H}_2(\text{D}_2)$  reaction has been well established in thermal systems with excellent agreement between experimental and theoretical results. Recently, a non-Boltzmann rate constant formalism has been proposed for recoil systems.<sup>6,13</sup> The  $^{38}\text{Cl} + \text{H}_2(\text{D}_2)$  reaction can be examined using this method in order to further explore the high energy isotope effect.

The formulation of the non-Boltzmann kinetic theory<sup>13</sup> postulates that the energy distribution function for hot atoms surviving after  $n$  collisions with surrounding bath gas can be characterized by a hot atom probability distribution  $W_n(E, E')$  which describes the probability of a recoil atom with initial energy  $E$  having energy  $E'$  after  $n$  collisions. In this approach the probability function  $W_n(E, E')$  is proposed to relax to a steady state distribution in the recoil system if the rate of reaction of hot atoms is significantly slower than the collision frequency, which allows the implicit time dependence of  $W_n(E, E')$  to be ignored. For this case, phenomenological rates for competitive reaction channels can be expressed in terms of energy dependent rate constants  $\kappa$  based on the non-Boltzmann steady state energy distribution function where

$$\kappa_j = \int dV_R \int dV_A (V_r) f_A(V_A) f_R(j, V_R) \sigma^*(j, V_r) \quad (5)$$

The term  $\sigma^*(j, V_r)$  is the reactive cross section for the  $j$ th internal state of the reactant,  $f_A(V_A)$  and  $f_R(j, V_R)$  are the velocity distribution functions for hot atoms A and reservoir molecules R, and  $V_r$  is the relative velocity of reactants.

The quantitative validity of the non-Boltzmann theory depends on the condition for attainment of the steady state energy distribution requiring the half-time for reaction to be longer than the half-time for momentum relaxation. In a nuclear recoil system the large reactivities of recoil species at high energies as evidenced, for example, by the calculated cross sections for the  $F + H_2(D_2)$  system suggest that the rate of reaction may approach the collision frequency.<sup>5</sup> For such highly reactive systems the steady state energy distribution may exist rigorously only at high moderator concentrations where the total probability of nonreactive collision is much larger than the probability of reactive collision. In principle, this problem can be eliminated through a direct utilization of a time dependent velocity distribution  $f_A(V_A, t)$  in (5), but such a treatment is necessarily complex. Root and co-workers have recently applied the time independent non-Boltzmann theory to experimental results from  $^{18}F$  to  $H_2(D_2)$  systems<sup>6b</sup> and have suggested in a preliminary report<sup>6a</sup> that their related calculations on time dependent rates support the qualitative significance of the rates obtained from the steady state approximation. The time independent non-Boltzmann theory thus appears to be a straight forward, approximate model for examining the experimental kinetic behavior of recoil systems.

For a steady state energy distribution, the non-Boltzmann rate constants  $\kappa_j$  can be handled in a manner similar to conventional chemical kinetics where the recoil system is approximated by an extremely small initial concentration of hot atoms. In the present study, competing reactions for recoil chlorine atoms include the direct reaction with hydrogen (1) or deuterium (2), the scavenging addition to ethylene (3), and the abstraction reaction with ethylene (4). Assigning the non-Boltzmann rate constants  $\kappa_H$ ,  $\kappa_D$ ,  $\kappa_S$ , and  $\kappa_A$  to these reactions, respectively, the rate of production of  $H^{38}Cl$  is given as

$$d[H^{38}Cl]/dt = \kappa_H [H_2] [^{38}Cl] + \kappa_A [^{38}Cl] [C_2H_4] \quad (6)$$

Combining eq 6 with the total rate of disappearance of  $^{38}Cl$  gives the yield of  $H^{38}Cl$  at  $t = \infty$  corresponding to the end of sample irradiation as

$$Y = \frac{[H^{38}Cl]}{[^{38}Cl]_0} = \frac{\kappa_H [H_2] + \kappa_A [C_2H_4]}{\kappa_H [H_2] + (\kappa_S + \kappa_A) [C_2H_4]} \quad (7)$$

Rearranging

$$\left( \frac{Y}{1-Y} \right) = \frac{\kappa_H}{\kappa_S} \frac{[H_2]}{[C_2H_4]} + \frac{\kappa_A}{\kappa_S} \quad (8)$$

Similar results will be obtained in terms of the overall hydrogen chloride yield  $Y = Y_{H^{38}Cl} + Y_{D^{38}Cl}$  if  $D_2$  is substituted for  $H_2$  as the primary reactant.

Since the energy dependencies of the reactions are implicitly contained in the rate constants, a plot of the concentration term in (8) vs. the yield term will be linear with a slope of  $\kappa_H/\kappa_S$  and an intercept of  $\kappa_A/\kappa_S$  provided the energy dependences of the individual constants  $\kappa_A$ ,  $\kappa_S$ ,  $\kappa_H$ , and  $\kappa_D$  are similar over the effective energy range explored by moderation. The plot of the ratio of the reactant concentrations vs. the measured yield term  $Y/(1-Y)$  calculated from the moderation dependence data for

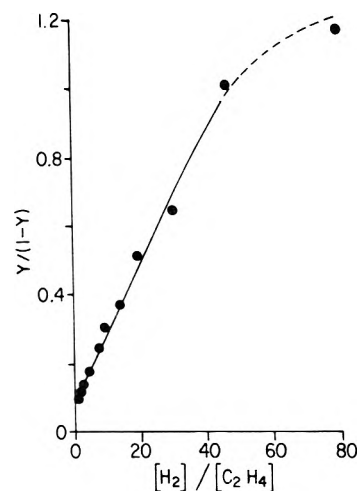


Figure 3. Absolute  $H^{38}Cl$  yield ratios  $Y/(1-Y)$  as a function of the sample composition ratio  $[H_2]/[C_2H_4]$  for the  $^{38}Cl + H_2$  reaction in the presence of ethylene-iodine scavenger.

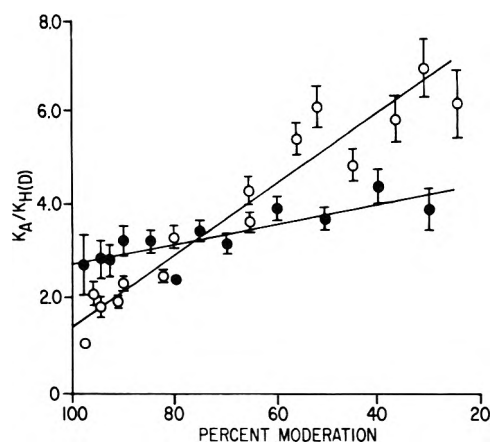


Figure 4. Calculated non-Boltzmann rate constants  $\kappa_A/\kappa_D$  and  $\kappa_A/\kappa_H$  as a function of moderation with  $CF_2Cl_2$ : (O)  $^{38}Cl + H_2$  reaction; (●)  $^{38}Cl + D_2$  reaction. Error bars represent the standard deviation.

the  $^{38}Cl + H_2$  reaction in Figure 1 is shown in Figure 3. The data in Figure 3 can be approximated by this linear relationship over the range of reactant concentrations from 0 to 66%. At lower moderation and correspondingly higher average energies of reaction there is significant curvature due both to the breakdown of the time independent steady state assumption in the highly reactive hydrogen system and to differences in the energy dependence of the individual reactions monitored. Extrapolating the linear region of Figure 3 to infinite moderation provides an intercept of  $\kappa_A/\kappa_S = 0.08$ . Thus  $\kappa_S = 12\kappa_A$ , and eq 7 or 8 can be further simplified to give

$$\frac{\kappa_A}{\kappa_H} = \frac{(1-Y)[H_2]}{(13Y-1)[C_2H_4]} \quad (9)$$

The ratios of the constants  $\kappa_A/\kappa_H$  can then be determined from eq 9 as a function of moderation in order to characterize the behavior of  $\kappa_H$  and  $\kappa_D$  in these reaction systems.

The ratios of  $\kappa_A/\kappa_H$  and  $\kappa_A/\kappa_D$  were calculated from eq 9 at various sample compositions using the experimental reactant concentrations and resultant hydrogen chloride yields from the  $H^{38}Cl$  moderation dependence study in Figure 1 and from similar data reported previously for the deuterium reaction.<sup>14,15</sup> Plots of the calculated ratios  $\kappa_A/\kappa_H$  and  $\kappa_A/\kappa_D$  vs. sample moderation are shown in Figure 4. Since the values of  $\kappa_H$  and  $\kappa_D$  are expected to rise at higher energies on the basis of their respective cross sections, the positive slopes of the lines in Figure 4 dictate that  $\kappa_A$  must



also be rising as an inverse function of moderator concentration. The magnitude of the increase in  $\kappa_A$ , however, appears to be greater than that expected on the basis of the direct moderator experiment with ethylene in the absence of hydrogen.<sup>14</sup> These results cast significant doubt on the quantitative interpretation of the values determined via this operational method. Nevertheless the technique is of considerable value in clearly illustrating the relative behavior of the high energy reactions with  $H_2$  and  $D_2$ .

The data also provide a direct comparison of the ratio  $\kappa_H/\kappa_D$  as a function of system composition. The isotope effect described by the non-Boltzmann rate constant ratios for the direct abstraction reactions with  $H_2$  and  $D_2$  is seen to exhibit a cross over from a normal to an inverse effect as a function of moderation. This directly reflects the behavior of the  $H^{38}Cl$  and  $D^{38}Cl$  yields vs. moderation.<sup>7</sup>

The rate ratios implicitly account for the energy dependence of the two reactions, and the observed behavior of  $\kappa_H/\kappa_D$  directly reflects changes in the energy distribution caused by moderation. Replacement of the  $CF_2Cl_2$  moderator with  $H_2$  or  $D_2$  reactant in these experiments, however, requires that the extent of any concurrent moderating isotope effect be carefully evaluated. Such effects can arise because  $H_2$  and  $D_2$  provide unequal, nonreactive collisional energy sinks for the recoil chlorine atoms, and thus the collisional energy distribution functions for the recoil species will, in general, be different at each moderation in the two systems. At infinite moderation the energy distribution of chlorine atoms in the respective hydrogen and deuterium systems must be identical because the moderator alone determines the distribution. At lower moderator concentrations, however, nonreactive collisions between hot chlorine atoms and  $H_2$  or  $D_2$  alter the energy distribution functions, and in particular deuterium, primarily because of its greater mass, is expected on an a priori basis to be a more efficient energy degradation agent than hydrogen.

The moderating isotope effect influences the non-Boltzmann rate constant ratio  $\kappa_H/\kappa_D$  either directly by altering  $\kappa_H$  with respect to  $\kappa_D$  or indirectly by altering the value of  $\kappa_A$  at each moderation in the respective  $H_2$  and  $D_2$  reactant systems. To anticipate the effect on  $\kappa_H$  and  $\kappa_D$  the average energy of hot reaction at fixed moderation must be considered. Because  $D_2$  is thought to be a better hot atom energy degrading agent than  $H_2$ , there should be a larger number of potentially reactive collisions with  $H_2$  than with  $D_2$  over any energy interval. This means that the average energy of potentially reactive collisions in the  $H_2$  case is higher than in the  $D_2$  case. To place the  $\kappa_H$  and  $\kappa_D$  values on a comparable energy scale then, the low moderation region of the abscissa in Figure 4 must be translated to higher effective moderation for  $H_2$  relative to  $D_2$ . This would have the net effect of emphasizing the magnitude of the inverse isotope effect at high energy and low moderation.

The moderating isotope effect also differentially influences  $\kappa_A$  in the two systems. At a particular moderation, as above, the abstraction reaction from ethylene would be less efficient in the  $D_2$  system than in the  $H_2$  system because there are fewer high energy collisions in  $D_2$  than in  $H_2$  bath. The value of the observed energy dependent constant  $\kappa_A$  would similarly be artificially low in the deuterium case. Since the same reactive cross section with ethylene is involved, the data can be corrected by adjusting the observed  $\kappa_{A(D)}$  upward relative to  $\kappa_{A(H)}$  in order to achieve an equal energy basis. This translation is also most pronounced in the low moderation region of Figure 4 and thus tends to reduce the magnitude of the high energy

isotope effect.

In the limiting case where there is no offsetting direct effect on  $\kappa_H$  or  $\kappa_D$ , the observed rate  $\kappa_A$  in Figure 4 must increase by a factor of at least 1.5 in going from  $D_2$  to  $H_2$  in order for the ratios  $\kappa_{A(H)}/\kappa_H$  and  $\kappa_{A(D)}/\kappa_D$  to coincide at 50% moderation and thus eliminate the isotope effect cross over. For  $\kappa_A$  to change by such a large extent, the average logarithmic energy loss per chlorine atom collision prior to ethylene reaction must be on the order of 1.5 times as large for deuterium as it is for hydrogen. This is inconsistent with experimental results in other recoil hot reaction systems where the relative difference in moderating efficiencies between hydrogen isotopes  $H_2$  and  $D_2$  has been shown to be small, and it is considered extremely unlikely in these studies. In addition, the moderating differences are expected to directly influence  $\kappa_H$  and  $\kappa_D$  as well as  $\kappa_A$ , and the compensating nature of the two influences will further reduce the importance of the moderating isotope effect. It is then concluded that the cross over in isotope effect reflected in the rate constant ratio  $\kappa_H/\kappa_D$  is kinetic in nature.

The cross over in the  $^{38}Cl + H_2(D_2)$  isotope effect has been discussed previously<sup>7</sup> in terms of dynamical features arising from a high energy reaction mechanism. It should be noted that no experimental evidence for a high energy inverse isotope effect was observed either directly in the data or in the non-Boltzmann rate constant evaluation of the recoil hot atom reactions of  $^{18}F$  with  $H_2(D_2)$ .<sup>6b</sup>

Semiclassical trajectory calculations have been used to evaluate the respective fluorine reaction cross sections as a function of translational energy in the center of mass, and results indicate that the  $H_2$  and  $D_2$  cross sections are nearly coincident over the entire reactive energy range with a maximum at about 2 eV.<sup>6a,18</sup> Likewise, it might be anticipated that the chlorine atom cross sections are also similar, although it is possible that the deuterium cross section is shifted to slightly higher energies, thus accounting for the observed yields. In any case, the hydrogen halide product of either reaction at high relative translational energies is expected to carry a significant fraction of the available energy away in vibrational and rotational excitation. In general, for these diatomics, energy transfer from rotation to vibration is rapid, and the total internal energy may well be sufficient to place the molecules in vibrational levels near the dissociation limit. The product molecules, which also possess significant translational energy due to momentum conservation, may be collisionally dissociated releasing the halogen atom at a low energy to be scavenged. If this mechanism is primarily responsible for the observed high energy isotopic effects, hydrogen chloride must be more easily dissociated on collision than hydrogen fluoride in recoil experiments, and HCl must either be formed with more vibrational energy than DCl or transfer of vibrational energy from DCl must be more efficient than from HCl on collision with  $D_2$  or  $H_2$ , respectively. Since there is no obvious dynamical feature in these reactions which could account for HCl being preferentially excited nearer its dissociation limit than DCl, the relative contribution of this factor to any collisional dissociation manifest in the observed yields cannot be assessed.

A second factor of importance is the relative effectiveness of the scavenger in competing with thermal abstraction from hydrogen. This is important because of the nature of recoil experiments in which low energy contributions to the reactive cross section are reflected more significantly in the product yields than higher energy contributions. In the recoil chlorine study described here,

the scavenger effectively terminates very low energy reaction processes as evidenced by the relatively high effective average temperature ( $\sim 1200$  K) observed for hydrogen chloride production at high moderation. Such effective elimination of very low energy abstraction reactions by fluorine is much more difficult to achieve due to the high intrinsic reactivity, and the competition provided by the scavenger may be slightly less favorable than in the chlorine studies. Due to the disproportionate impact of low energy processes and the fact that all near thermal reactions are expected to give a normal isotope effect, it might be anticipated that any small inverse effect at higher energies will be overshadowed in the total yields measured for hydrogen fluoride.

The combined effect of these factors and the degree to which the chlorine reactive cross sections are not superimposable cannot be evaluated quantitatively. The experimental data, however, provides clear evidence that the overall reactive process in the two recoil systems is different and that the stabilized product yields of the heavier halogen atom exhibit an inverse deuterium isotope effect at high energies which is absent from the yield data for the lighter halogen atom.

*Acknowledgment.* We thank Professors R. B. Bernstein, G. Pimentel, and H. K. Shin for valuable comments regarding the origin of the inverse isotope effect. This work was supported by the U.S. Department of Energy under Contract EY-76-S-02-2190. The cooperation of the staff at the University of Utah Nuclear Radiation Center is acknowledged. D.J.S. expresses appreciation for a NDEA Title IV Graduate Fellowship.

#### References and Notes

- (1) G. K. Rollefson, *J. Chem. Phys.*, **2**, 144 (1934); J. Bigeleisen, F. S. Klein, R. E. Weston, Jr., and M. Wolfsberg, *ibid.*, **30**, 1340 (1958);

- F. S. Klein and A. Persky, *ibid.*, **41**, 1799 (1964).  
 (2) A. Persky, *J. Chem. Phys.*, **59**, 3612, 5578 (1973); C. G. Fettes and J. H. Knox, *Prog. React. Kinet.*, **2**, 1 (1964); P. D. Mercer and H. O. Prichard, *J. Phys. Chem.*, **63**, 1468 (1959).  
 (3) A. Persky and A. Kuppermann, *J. Chem. Phys.*, **61**, 5035 (1974); D. Britton and R. M. Cole, *J. Phys. Chem.*, **65**, 1302 (1961); D. Britton and M. Davidson, *J. Chem. Phys.*, **25**, 810 (1956); M. Bodenstern and S. C. Lind, *Z. Phys. Chem.*, **57**, 168 (1906).  
 (4) J. H. Sullivan, *J. Chem. Phys.*, **46**, 73 (1967); J. H. Sullivan, *J. Phys. Chem.*, **65**, 722 (1961); S. W. Benson and R. Srinivasan, *J. Chem. Phys.*, **23**, 200 (1965).  
 (5) P. A. Whitlock and J. T. Muckerman, *J. Chem. Phys.*, **61**, 4618 (1974); J. T. Muckerman, *ibid.*, **57**, 3388 (1972); **56**, 2997 (1972); **54**, 1155 (1961).  
 (6) (a) D. F. Feng, E. R. Grant, and J. W. Root, *J. Chem. Phys.*, **64**, 3450 (1976); (b) E. R. Grant and J. W. Root, *ibid.*, **64**, 417 (1976).  
 (7) D. J. Stevens and L. D. Spicer, *J. Chem. Phys.*, **64**, 4798 (1976).  
 (8) E. R. Grant and J. W. Root, *J. Chem. Phys.*, **63**, 2970 (1975); *Chem. Phys. Lett.*, **27**, 484 (1974).  
 (9) R. G. Manning and J. W. Root, *J. Chem. Phys.*, **64**, 4926 (1976); *J. Phys. Chem.*, **79**, 1478 (1975); R. G. Manning, E. R. Grant, J. C. Merrill, N. J. Parks, and J. W. Root, *Int. J. Chem. Kinet.*, **7**, 39 (1975).  
 (10) K. A. Krohn, N. J. Parks, and J. W. Root, *J. Chem. Phys.*, **55**, 5771, 5785 (1971); N. J. Parks, K. A. Krohn, and J. W. Root, *ibid.*, **55**, 2690 (1971).  
 (11) T. Smail, R. S. Iyer, and F. S. Rowland, *J. Phys. Chem.*, **79**, 1478 (1975); J. P. Frank and F. S. Rowland, *ibid.*, **78**, 850 (1974); R. L. Williams and F. S. Rowland, *ibid.*, **77**, 301 (1973).  
 (12) R. L. Williams and F. S. Rowland, *J. Am. Chem. Soc.*, **94**, 1047 (1972); R. L. Williams and F. S. Rowland, *J. Phys. Chem.*, **76**, 3509 (1972); T. Smail, G. E. Miller, and F. S. Rowland, *ibid.*, **74**, 3464 (1970).  
 (13) J. Keizer, *J. Chem. Phys.*, **57**, 4524 (1973); **56**, 5959 (1972).  
 (14) D. J. Stevens and L. D. Spicer, *J. Phys. Chem.*, **81**, 1217 (1977).  
 (15) D. J. Stevens, Ph.D. Dissertation, University of Utah, 1976.  
 (16) W. H. Johnston and W. F. Libby, *J. Am. Chem. Soc.*, **73**, 854 (1951); J. R. Walton and W. H. Johnston, *ibid.*, **78**, 5991 (1956); J. E. Boggs, L. L. Ryan, and L. L. Peek, *J. Phys. Chem.*, **61**, 825 (1957).  
 (17) A. Persky and M. Baer, *J. Chem. Phys.*, **60**, 133 (1974); M. Baer, U. Halavee, and A. Persky, *ibid.*, **61**, 5122 (1974); A. Persky and F. S. Klein, *ibid.*, **44**, 3617 (1966).  
 (18) J. T. Muckerman and J. W. Root, unpublished results.

## A Mass Spectrometric Study of the Fragmentation of the Lithium Fluoride Vapor System

R. T. Grimley,\* J. A. Forsman, and Q. G. Grindstaff

Department of Chemistry, Purdue University, West Lafayette, Indiana 47907 (Received August 26, 1977)

The angular number distributions of species effusing through a cylindrical orifice have been used to investigate the fragmentation processes which occur in the ion source of a mass spectrometer. The lithium fluoride vapor system has been studied in the temperature range 785–825 °C. The monomer, dimer, and trimer have been identified as the neutral vapor species, and the fragmentation processes associated with the electron bombardment of each of these species have been identified. The approximate contribution of each of the neutral species to the fragment ions has been determined.

### Introduction

Although the LiF vapor phase system has been the subject of frequent investigation, there is substantial disagreement regarding the identity of the neutral precursor or precursors of the ions in the mass spectrum of the lithium fluoride vapor system. Mass spectrometric investigations of the fragmentation products of this system have been reported by Sidorov and Alikhanyan,<sup>1</sup> Berkowitz et al.,<sup>2,3</sup> Akishin et al.,<sup>4</sup> Porter and Schoonmaker,<sup>5</sup> Hildenbrand et al.,<sup>6</sup> and Searcy and Mohazzabi.<sup>7</sup> As a consequence of the fact that  $\text{Li}_3\text{F}_2^+$  is the ion of highest mass observed in the mass spectrum, it is generally assumed that  $\text{Li}_3\text{F}_2^+$  results from dissociative ionization of  $\text{Li}_3\text{F}_3$ . The source of  $\text{Li}_2\text{F}^+$  is most generally reported to

be  $\text{Li}_2\text{F}_2$ . However, both Akishin et al.<sup>4</sup> and Sidorov et al.<sup>1</sup> report  $\text{Li}_2\text{F}_2$  and  $\text{Li}_3\text{F}_3$  as the source of this ion. Only Hildenbrand et al.,<sup>6</sup> however, offered substantial experimental justification for the assignment of  $\text{Li}_2\text{F}_2$  as the only precursor molecule of  $\text{Li}_2\text{F}^+$ .

Berkowitz et al.<sup>2,3</sup> reported that  $\text{LiF}^+$  is formed predominantly from LiF as did Sidorov et al.<sup>1</sup> Both groups also claimed a small contribution to  $\text{LiF}^+$  from  $\text{Li}_2\text{F}_2$ , but they failed to agree on the extent of the  $\text{Li}_2\text{F}_2$  contribution. On the other hand, Hildenbrand et al.<sup>6</sup> found a substantial dimer contribution to  $\text{LiF}^+$  as well as a monomer contribution. Hildenbrand also found LiF to be the only neutral precursor of  $\text{Li}^+$ . The other studies<sup>1-5,7</sup> concluded that  $\text{Li}^+$  was formed from the dissociative ionization of

both  $\text{LiF}$  and  $\text{Li}_2\text{F}_2$ . However, there is no quantitative agreement regarding the extent of the dimer contribution.

It is apparent that the discrepancies concerning the identity of the neutral precursors of the ionic species produced by electron bombardment of the  $\text{LiF}$  vapor system have not been resolved by the existing high temperature mass spectrometric techniques. The angular distribution (AD) technique has proven particularly valuable in the determination of fragmentation patterns of complex polymeric vapor systems such as  $\text{AgCl}$ ,<sup>8</sup>  $\text{CuCl}$ ,<sup>9</sup> and  $\text{Bi}$ .<sup>10</sup> In this paper the AD method has been used as an additional tool in the investigation of the  $\text{LiF}$  system to provide some further answers to the fragmentation phenomena.

Additional data on this system have been obtained and these include vapor pressure measurements made by Evseev et al.,<sup>11</sup> Hildenbrand et al.,<sup>12</sup> and Scheffee and Margrave.<sup>13</sup> Thermodynamic data for the vapor species of lithium fluoride (monomer, dimer, and trimer) have been reported by Hildenbrand et al.,<sup>12</sup> Scheffee and Margrave,<sup>13</sup> Porter and Schoonmaker,<sup>5</sup> Akishin et al.,<sup>4</sup> Bauer and Porter,<sup>14</sup> and Berkowitz et al.<sup>2</sup> Data from infrared matrix isolation studies are consistent with a planar, rhomboid structure for the dimer.<sup>15-20</sup> In addition to the cyclic structure, Abramowitz et al.<sup>21</sup> have found evidence for a linear dimer.

### Experimental Section

Data were obtained with a  $60^\circ$  single focusing, 30.5-cm radius-of-curvature mass spectrometer. Two molecular beam sources were used in conjunction with the mass spectrometer: (1) a standard static Knudsen cell system, and (2) a rotary Knudsen cell system. The static unit allows one to determine atomic and molecular beam fluxes only at the normal to the orifice exit plane whereas the rotary assembly permits sampling of the fluxes at any off-axis angle between  $0$  and  $75^\circ$ . Details of the construction and operation of the rotary unit have been described.<sup>22</sup>

Radiant heating was used for the Knudsen cells in both the static and rotary units. Thermal energy was supplied by a bifilarly wound, platinum-10% rhodium helical filament surrounding the cell on  $\text{Al}_2\text{O}_3$  supports. Because of the reactivity of lithium fluoride vapor with  $\text{Al}_2\text{O}_3$ , the furnace assembly was covered by a shield made of 0.051-mm tantalum foil. The temperatures were determined by means of a calibrated chromel-alumel thermocouple peened into the base of the Knudsen cell. The thermocouple also provided the input signal to a specially designed temperature controller which was used in conjunction with a Hyperion Si 20-20 dc power supply to maintain the cell temperature constant to within  $\pm 0.02^\circ\text{C}$  of the nominal value.

The lid of the rotary cell had an orifice with an  $L/R = 4$  geometry and a 0.508-mm radius. The length to radius ratio of the static cell orifice was  $L/R = 0.10$ . In order to minimize the possibility of reaction between lithium fluoride and the cell, nickel was used in the construction of all cell components. No evidence of cell reactivity was found in the temperature range of this investigation. Specially designed jigs were used to align the orifice of these cells to within  $\pm 0.02$  mm in both the  $xy$  plane and the  $z$  direction thus ensuring mechanical reproducibility between runs. The cell was loaded with approximately 0.1 g of 3 N lithium fluoride (Electronic Space Products, Inc.) for each run.

Intensity data were collected using a 16-stage electron multiplier as the detector and a 640 Keithley vibrating capacitor electrometer in series with a 399 Keithley iso-

TABLE I: Relative Intensities, Appearance Potentials, and Heats of Sublimation<sup>a</sup> (Average Temperature  $805^\circ\text{C}$ )

Ion	Relative intensity	Appearance potential, eV $\pm 0.5$	Heat of sublimation, kcal/mol
$\text{Li}^+$	36.44	11.8	$61.9 \pm 0.4$
$\text{LiF}^+$	12.88	11.8	$62.0 \pm 0.5$
$\text{Li}_2\text{F}^+$	100.00	13.0	$68.1 \pm 0.4$
$\text{Li}_3\text{F}_2^+$	12.01	12.3	$73.6 \pm 0.3$

<sup>a</sup> Data taken at 18 eV.

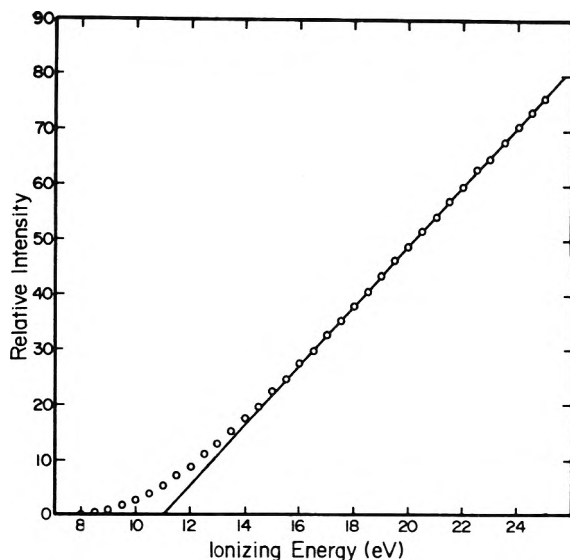


Figure 1. Ionization efficiency curve for  $\text{Li}^+$  at a cell temperature of  $825^\circ\text{C}$ .

lating amplifier. The output from the isolating amplifier was simultaneously fed to a strip chart recorder and a Hewlett-Packard Model 2212A voltage to frequency (V-to-F) converter whose output was measured with a Mech-Tronics Nuclear 715 dual scaler. The V-to-F converter and dual scaler functioned as a dc integrator with a variable-time base. By varying the integration times it is possible to maintain approximately the same average deviation for a wide range of peak intensities and signal-to-noise ratios.

### Results

Four ions were detected in the lithium fluoride mass spectrum, and they are as follows:  $\text{Li}^+$ ,  $\text{LiF}^+$ ,  $\text{Li}_2\text{F}^+$ , and  $\text{Li}_3\text{F}_2^+$ . Appearance potentials for all species except  $\text{Li}^+$  were determined by the linear extrapolation method, and values for the four ionic species observed are given in Table I. The spectroscopic ionization potential of mercury<sup>23</sup> (10.43 eV) was used as a reference for the energy scale. The ionization efficiency curve of  $\text{Li}^+$  is nonlinear as shown in Figure 1. Nonlinearity of this type may occur when an ionic species is formed from more than one neutral species.

The intensity of each of the ions was determined as a function of temperature over the range  $785$ – $825^\circ\text{C}$ . The equilibrium vapor pressure  $P$  of a neutral species in a Knudsen cell at a temperature  $T$  is related to the intensity  $I^+$  of the ionic species which results from electron bombardment of the neutral vapor species by the relation  $P = kI^+T$  where  $k$  is a constant.<sup>24</sup> If an ionic species results from ionization of only one neutral vapor species, then the heat of sublimation of the vapor species can be obtained from the slope of a plot of  $\log I^+T$  vs.  $1/T$ . However, if an ionic species is formed by the ionization of more than

one neutral species, then the observed heat of sublimation, assuming temperature independent cross sections for the ionization processes, will have a value which is between the heats of sublimation of the contributing neutral species. The exact value will depend on the relative contribution of each of the neutrals to the ionic species. Heats of sublimation are given in Table I for all species. Data were taken at an electron bombardment energy of 18 eV, and the data for each run were treated by the least-squares method. The tabulated heats of sublimation are the average of the least-squares data for at least five runs per ionic species. The uncertainties in these values are the standard deviations from these averages.

The angular distributions of species effusing from an orifice depend not only on the orifice geometry as predicted by Clausing, but also on the vapor species. Grimley et al.<sup>8,25</sup> have given a detailed description of the AD technique and its application to fragmentation studies. The information required to characterize each AD curve includes the cell angles  $\theta$ , the molecular beam intensities  $I(\theta)$  as a function of angle, and the temperature of the Knudsen cell. The beam intensities are normalized to the beam intensity at  $0^\circ$  by taking the ratio of the intensity at each angle  $\theta$  to the intensity at  $0^\circ$ . The relative intensities  $I(\theta)/I(0)$  are then plotted as a function of the angle  $\theta$ . The plot will hereafter be referred to as the AD curve. Initially distribution data were obtained for each species at an electron bombardment energy of 18 eV, and these data are given in Table II.<sup>26</sup> Additional angular distribution curves were obtained at several other ionizing electron energies and at two other temperatures. These curves will be considered in the discussion of the fragmentation process.

## Discussion

A preliminary analysis of the fragmentation behavior of the lithium fluoride system was attempted by use of the following standard techniques: stoichiometric constraints, appearance potentials, ionization efficiency curves, and heats of sublimation.

If the ionization potential of an atom or molecule has been determined previously, then appearance potential data can be used to assist in the identification of the neutral precursor of a given ion. The appearance potentials and heats of sublimation for the LiF system are given in Table I. The conclusion which may be surmised from the appearance potential data is that  $\text{Li}^+$  is a fragment ion.

Because of the low pressures present in the ion source, we have assumed that ion-molecule reactions may be neglected in the stoichiometric analysis. Based on the stoichiometric constraints,  $\text{Li}_3\text{F}_2^+$  could be formed from one or more of the neutrals  $\text{Li}_n\text{F}_n$ , where  $n \geq 3$ . However, the absence of breaks in the ionization efficiency curve would tend to indicate only one major contributor. The heat of sublimation data for  $\text{Li}_3\text{F}_2^+$  indicate at least one neutral contributor to  $\text{Li}_3\text{F}_2^+$  not common to the other ionic species. These data are consistent with the view that  $\text{Li}_3\text{F}_2^+$  arises primarily from one molecular source of the form  $\text{Li}_n\text{F}_n$ , where  $n \geq 3$ .

By a similar type analysis  $\text{Li}_2\text{F}^+$  is found to be formed from one species of the form  $\text{Li}_n\text{F}_n$ , where  $n \geq 2$ , and which is different from the precursors of the other ionic species. This type of analysis also indicates one primary molecular source for  $\text{LiF}^+$  which is different from the precursors of both  $\text{Li}_2\text{F}^+$  and  $\text{Li}_3\text{F}_2^+$ . Although these techniques indicate that  $\text{LiF}^+$ ,  $\text{Li}_2\text{F}^+$ , and  $\text{Li}_3\text{F}_2^+$  each results from ionization of a different molecular species, one may not eliminate the possibility of additional small contributions to these ions from other sources.

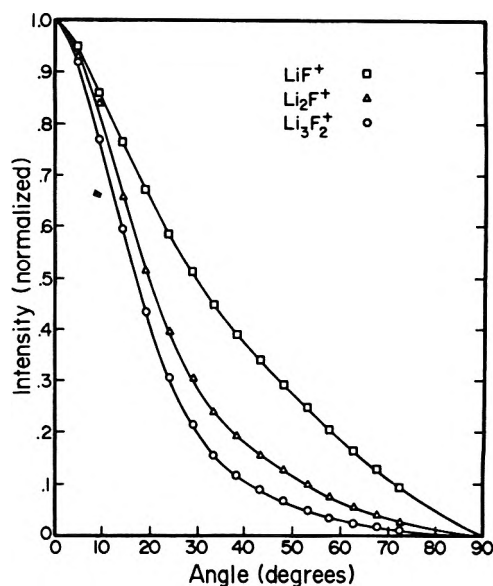
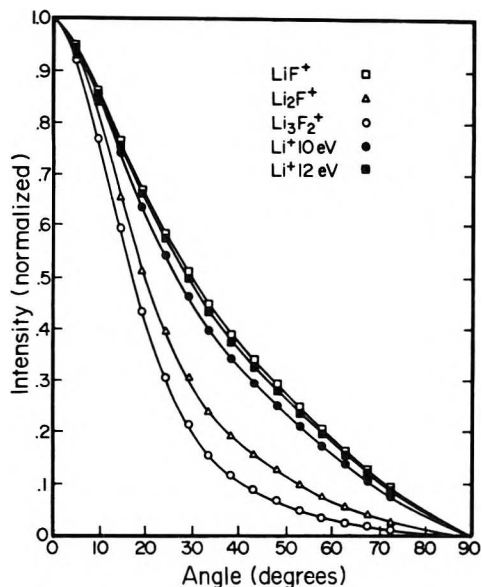


Figure 2. Angular distribution curves for  $\text{LiF}^+$ ,  $\text{Li}_2\text{F}^+$ , and  $\text{Li}_3\text{F}_2^+$  at a cell temperature of  $825^\circ\text{C}$  and 18 eV.

The elimination of atomic Li as a potential source of  $\text{Li}^+$  by virtue of the appearance potential measurement has already been noted. Stoichiometric constraints only limit the identity of the precursor to one or more of the species  $\text{Li}_n\text{F}_n$ , where  $n \geq 1$ . The ionization efficiency curve of  $\text{Li}^+$  shows appreciable curvature or tailing, and this behavior is sometimes indicative of two ionization processes. Thus there is the possibility that two sources of  $\text{Li}^+$  exist. The heat of sublimation data for  $\text{Li}^+$  and  $\text{LiF}^+$  at 18 eV are virtually identical. This result is normally interpreted to mean that  $\text{Li}^+$  and  $\text{LiF}^+$  are formed primarily from the same source or sources.

Since the standard techniques of identifying neutral species provide only limited information and the results of other research are inconclusive, the AD technique will be used almost exclusively to analyze the fragmentation pattern of lithium fluoride. The application of AD measurements to the analysis of fragmentation patterns depends on the assumption that each neutral vapor species will exhibit a unique AD pattern as it emerges from a Knudsen cell with a nonideal orifice. Thus the shape of the AD curve of an ion formed from a single neutral species is dependent only on the directional characteristics of that given atomic or molecular species as it leaves the orifice, and is independent of the ionizing electron energy. However, if an ion is formed by the electron bombardment of two or more neutral vapor species, then the shape of its AD curve will depend on the relative contribution from each of the neutral vapor species. In the case of two contributors the AD curve for the ion will be located between the AD curves of the two neutral species. The exact location will depend on the molecular fluxes and the ionization cross sections of the two neutral species. The flux can be varied by changing the equilibrium temperature of the system whereas the ionization cross section can be changed by varying the energy of the ionizing electrons. As a consequence the position and configuration of the angular distribution curve of the ion can be altered by changes in ionizing energy or temperature. The resulting shifts in the AD curves can then be used in the analysis of the fragmentation processes.

The AD curves for the  $\text{LiF}^+$ ,  $\text{Li}_2\text{F}^+$ , and  $\text{Li}_3\text{F}_2^+$  ions are shown in Figure 2. All data shown were taken at 18 eV and a cell temperature of  $825^\circ\text{C}$ . Three distinct curves may be seen, and these are associated with three different



**Figure 3.** Average angular distribution curves for  $\text{LiF}^+$ ,  $\text{Li}_2\text{F}^+$ , and  $\text{Li}_3\text{F}_2^+$  (18–75 eV) and  $\text{Li}^+$  at 10 and 12 eV and a cell temperature of 825 °C.

molecules. The simplest and generally the most sensitive means of determining if more than one precursor exists is to vary the energy of the ionizing electrons. This test was applied to the AD measurements of the four species  $\text{Li}^+$ ,  $\text{LiF}^+$ ,  $\text{Li}_2\text{F}^+$ , and  $\text{Li}_3\text{F}_2^+$ . The data for  $\text{LiF}^+$  exhibited no changes in the AD curves measured at 18, 25, 40, and 60 eV and a cell temperature of 825 °C as shown in Table III.<sup>26</sup> The independence of the AD curve with ionizing energy was also observed at cell temperatures of 805 and 785 °C. The shifting of the AD curve as a function of temperature has been explained by Voronin.<sup>27</sup> Within the sensitivity limitations of the AD technique (which is on the order of a few percent), only one precursor of  $\text{LiF}^+$  is observed. From the stoichiometry of the ion it is assumed that the neutral precursor is the  $\text{LiF}$  molecule.

The AD data measured at 18 eV for  $\text{Li}_2\text{F}^+$  and  $\text{Li}_3\text{F}_2^+$  showed that the AD curves for these species were different from each other and from  $\text{LiF}^+$ . However, energy dependence measurements are necessary to determine if one or more precursor molecules are present. The AD curves of the  $\text{Li}_2\text{F}^+$  ion were identical for energies of 18, 25, 40, and 60 eV; the data are given in Table III.<sup>26</sup> The AD curves for  $\text{Li}_3\text{F}_2^+$  were similarly independent of the energy of the ionizing electrons, and the resultant data are also contained in Table III.<sup>26</sup> From the stoichiometry of the ions it is assumed that the neutral precursors of  $\text{Li}_2\text{F}^+$  and  $\text{Li}_3\text{F}_2^+$  are  $\text{Li}_2\text{F}_2$  and  $\text{Li}_3\text{F}_3$ , respectively.

Since the data are energy independent, the representative AD curve at each temperature for the three species is taken as the arithmetic average of all energies studied, and these data are given in Table IV.<sup>26</sup>

In contrast to the other ionic species, the data for the  $\text{Li}^+$  ion exhibited shifting as a function of the ionizing energy. The AD curves for  $\text{Li}^+$  which demonstrate this effect are given in Figure 3.

The equations, from which the relative precursor contributions to the  $\text{Li}^+$  ion may be determined, are developed in a straightforward manner. The total ion intensity from all sources of each species is given by

$$I_k^+(T, \theta) = \sum_j I_{jk}^+(T, \theta) \quad (1)$$

The index  $k$  identifies the ion and index  $j$  serves to identify the neutral species which form species  $k$  upon ionization. In particular, for the  $\text{LiF}$  vapor system  $k = 0, 1, 2, 3$  refers

to the ions  $\text{Li}^+$ ,  $\text{LiF}^+$ ,  $\text{Li}_2\text{F}^+$ , and  $\text{Li}_3\text{F}_2^+$ , respectively. The index  $j = 1, 2, 3$  refer to the molecules  $\text{LiF}$ ,  $\text{Li}_2\text{F}_2$ , and  $\text{Li}_3\text{F}_3$ , respectively. The molecules  $\text{Li}_3\text{F}_3$ ,  $\text{Li}_2\text{F}_2$ , and  $\text{LiF}$  have been identified as the sole precursors, respectively, of the ions  $\text{Li}_3\text{F}_2^+$ ,  $\text{Li}_2\text{F}^+$ , and  $\text{LiF}^+$ . For the  $\text{LiF}$  system three ion intensity terms  $I_{jk}^+$  exist in which  $j = k$ . To identify these terms, the notation  $I_{jj}^+$  is used, where  $I_{11}^+$  is the intensity of  $\text{LiF}^+$ ,  $I_{22}^+$  the intensity of  $\text{Li}_2\text{F}^+$ , and  $I_{33}^+$  the intensity of  $\text{Li}_3\text{F}_2^+$ .

With a conventional Nier-type ion source, the partial ion intensity  $I_{jk}^+(T, \theta)$  may be expressed as

$$I_{jk}^+(T, \theta) = \frac{\kappa \nu_j(T, \theta) \sigma_{jk}(T)}{\bar{c}_j(T, \theta)} \quad (2)$$

where  $T$  is the temperature of the Knudsen cell,  $\theta$  is the cell rotation angle,  $\kappa$  is a constant related to the instrument geometry,  $\sigma_{jk}(T)$  is the ionization cross section in which ion  $k$  is produced from molecule  $j$ ,  $\nu_j(T, \theta)$  is the flux of molecule  $j$  at angle  $\theta$ , and  $\bar{c}_j(T, \theta)$  is the average speed of molecule  $j$ .

The ion intensity fraction  $F_{jk}(T, \theta)$  of the total intensity  $I_k^+(T, \theta)$  which results from the ionization of one species is defined as

$$F_{jk}(T, \theta) = I_{jk}^+(T, \theta) / I_k^+(T, \theta) \quad (3)$$

The intensity  $I_{jk}^+(T, \theta)$  cannot be measured directly. The term can be evaluated from the relationship

$$\frac{I_{jk}^+(T, \theta)}{I_{jj}^+(T, \theta)} = \frac{\kappa \nu_j(T, \theta) \sigma_{jk}(T)}{\bar{c}_j(T, \theta)} \frac{\bar{c}_j(T, \theta)}{\kappa \nu_j(T, \theta) \sigma_{jj}(T)} \quad (4)$$

$$\frac{I_{jk}^+(T, \theta)}{I_{jj}^+(T, \theta)} = \frac{\sigma_{jk}(T)}{\sigma_{jj}(T)} = a_{jk}(T)$$

where  $a_{jk}(T)$  is a constant at a given  $T$ . Therefore

$$I_{jk}^+(T, \theta) = a_{jk}(T) I_{jj}^+(T, \theta) \quad (5)$$

Using the result from eq 5 one may rewrite eq 1

$$I_k^+(T, \theta) = \sum_j a_{jk}(T) I_{jj}^+(T, \theta) \quad (6)$$

The normalized distribution  $D_j(T, \theta)$  of a precursor molecule  $j$  which is the sole source of an ionic species with intensity  $I_{jj}^+(T, \theta)$  is defined by the equation

$$D_j(T, \theta) = I_{jj}^+(T, \theta) / I_{jj}^+(T, 0) \quad (7)$$

Equation 6 may now be expressed in terms of  $D_j(T, \theta)$

$$I_k^+(T, \theta) = \sum_j a_{jk}(T) I_{jj}^+(T, 0) D_j(T, \theta) \quad (8)$$

The normalized angular distribution  $D_k(T, \theta)$  of an ion  $k$  which is formed by the ionization of more than one neutral precursor is defined by the equation  $D_k(T, \theta) = I_k^+(T, \theta) / I_k^+(T, 0)$ . By dividing eq 8 by  $I_k^+(T, 0)$  one obtains

$$D_k(T, \theta) = \sum_j a_{jk}(T) \frac{I_{jj}^+(T, 0)}{I_k^+(T, 0)} D_j(T, \theta) \quad (9)$$

We define  $f_{jk}(T)$  by the equation

$$f_{jk}(T) = \frac{a_{jk}(T) I_{jj}^+(T, 0)}{I_k^+(T, 0)} \quad (10)$$

Equation 9 may be rewritten in the form

$$D_k(T, \theta) = \sum_j f_{jk}(T) D_j(T, \theta) \quad (11)$$

The angular distribution term  $D_k(T, \theta)$  and the  $D_j(T, \theta)$

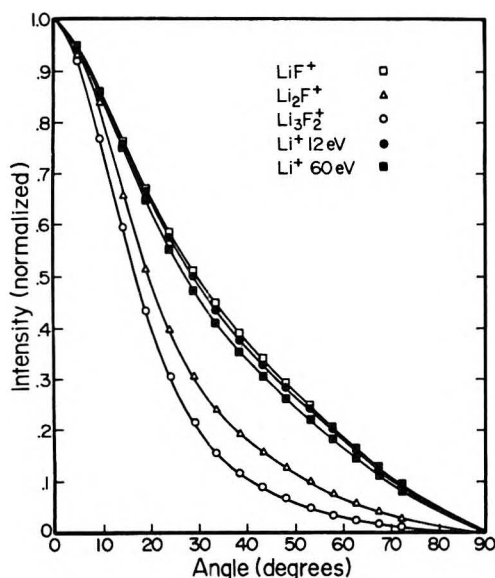


**Figure 4.** Average angular distribution curves for  $\text{LiF}^+$ ,  $\text{Li}_2\text{F}^+$ , and  $\text{Li}_3\text{F}_2^+$  (18–75 eV) and  $\text{Li}^+$  at 12 and 60 eV and a cell temperature of 825 °C.

terms are obtained from experimental data. The coefficients  $f_{jk}(T)$  may be determined by a least-squares procedure which will be discussed.

The coefficients  $f_{jk}(T)$  may be obtained from the experimental data; however, our primary interest is in the calculation of the ion intensity fractions,  $F_{jk}(T, \theta)$ . Therefore, it is necessary to develop a quantitative relationship between these quantities. We proceed by combining eq 3 and 5 to yield

$$F_{jk}(T, \theta) = a_{jk}(T) \frac{I_{jj}^+(T, \theta)}{I_k^+(T, \theta)} \quad (12)$$

The relationship between  $f_{jk}(T)$  and  $F_{jk}(T, \theta)$  can be obtained by taking the ratio  $f_{jk}(T)/F_{jk}(T, \theta)$  in conjunction with eq 10 and 12.

$$\frac{f_{jk}(T)}{F_{jk}(T, \theta)} = \frac{a_{jk}(T)I_{jj}^+(T, 0)}{I_k^+(T, 0)} \frac{I_k^+(T, \theta)}{a_{jk}(T)I_{jj}^+(T, \theta)} \quad (13)$$

Equation 13 may be simplified by use of eq 7.

$$F_{jk}(T, \theta) = \frac{D_j(T, \theta)}{D_k(T, \theta)} f_{jk}(T) \quad (14)$$

The definitions of  $D_j(T, \theta)$  and  $D_k(T, \theta)$  require that  $D_j(T, 0) = D_k(T, 0) = 1$ . Thus eq 14 reduced to

$$F_{jk}(T, 0) = f_{jk}(T) \quad (15)$$

at  $\theta = 0^\circ$ . This means that the experimental measurements of the coefficients  $f_{jk}(T)$  are equal to the ion intensity fractions  $F_{jk}(T, \theta)$  at a detector angle of  $0^\circ$ .

Substitution of the angular distribution data into eq 11 results in a set of overdetermined equations which is susceptible to least-squares analysis. A general least-squares program, GENLSQ, obtained from the Purdue University Computer Center was used to calculate the coefficients  $f_{jk}(T)$ . The program was modified slightly to give the maximum and average errors of the least-squares fit. The maximum error in all cases was less than the experimental error with the average error being of a considerably smaller magnitude.

In the analysis above it has been assumed that the ion intensities were measured with a point detector. A slit detector was used in these measurements, and it is possible

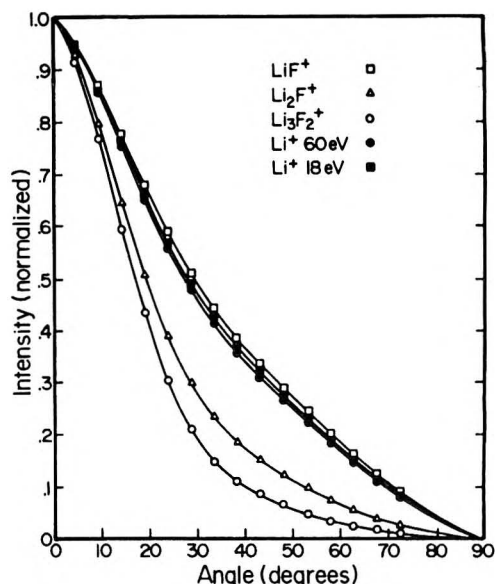


**Figure 5.** Average angular distribution curves for  $\text{LiF}^+$ ,  $\text{Li}_2\text{F}^+$ , and  $\text{Li}_3\text{F}_2^+$  (18–75 eV) and  $\text{Li}^+$  at 18 and 60 eV and a cell temperature of 805 °C.

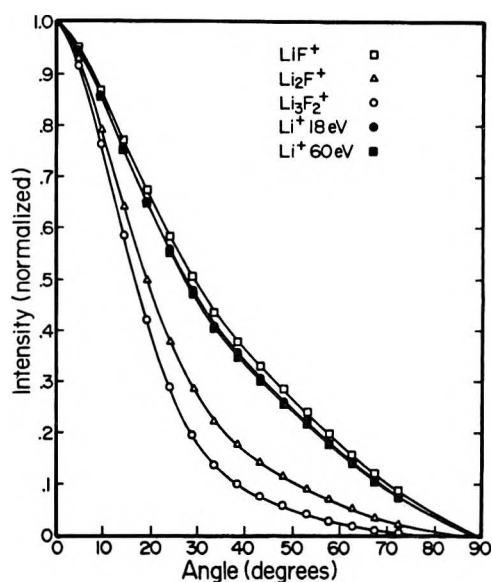


**Figure 6.** Average angular distribution curves for  $\text{LiF}^+$ ,  $\text{Li}_2\text{F}^+$ , and  $\text{Li}_3\text{F}_2^+$  (18–75 eV) and  $\text{Li}^+$  at 18 and 60 eV and a cell temperature of 785 °C.

to develop the necessary deconvolution mathematics to correct for the geometric effects of the detector if one assumes known behavior in the ionization region of the ion source. Unfortunately, the optical characteristics of the ion source are not well known, and preliminary measurements in this laboratory indicate a nonlinear response. Thus some inherent and nonquantized detector error exists. The quantitative treatment which we have employed, however, is sufficiently accurate to permit calculation of trends in the data.

The problem of the molecular contributions to the  $\text{Li}^+$  ion may now be examined. The curvature in the low energy portion of the IE curve of  $\text{Li}^+$  is indicative of the possibility of multiple precursor contributions. Accordingly the AD curves for  $\text{Li}^+$  were examined over a wide range of ionizing energies (10–60 eV) at each of several temperatures (785, 805, 825 °C). Examination of the AD curves in Figures 3 and 4 shows that the deviation of the AD curve for  $\text{Li}^+$  from the  $\text{LiF}$  AD curve is greatest at 10 eV, reaches a minimum at 12 eV, and then increases

TABLE VI: Ion Intensity Contributions (Arbitrary Units) to  $\text{Li}^+$  from  $\text{LiF}$  and  $\text{Li}_2\text{F}_2$ 

Ionizing energy, eV	$I_{10}^+(T, 0) \times 10^{-3}$			$I_{20}^+(T, 0) \times 10^{-3}$		
	785 °C	805 °C	825 °C	785 °C	805 °C	825 °C
10			6.48			1.92
10.5			9.84			2.13
11			14.67			1.71
12			25.17			1.23
13			36.24			1.74
14			49.98			2.46
15			62.91			3.30
16			77.52			4.50
18	36.90	64.83	106.38	4.37	6.42	6.84
25	72.35	126.33	204.09	8.93	14.01	24.09
40	129.79	225.60	356.40	19.17	34.41	68.73
60	174.42	301.68	477.45	26.10	50.40	103.38

continuously to 60 eV, the maximum energy for measurement. It is obvious that the most important contributor to  $\text{Li}^+$  is  $\text{LiF}$ . The selection of the polymeric contributor poses a more difficult problem. By a sufficient variation in the ionizing energies it has frequently been possible to cause a complete shifting of the AD curve between the contributing species. This was not possible with the  $\text{LiF}$  system. The least-squares procedure was employed assuming monomer, dimer, and trimer contributions. At a number of ionizing energies and temperatures, the coefficients  $f_{jk}(T)$  calculated for the dimer and trimer contributions were negative. Since these results are physically meaningless, the assumption of more than one polymer contributor is invalid. This method of analysis has been shown to be capable of providing an excellent fit in the case of the highly complex selenium vapor system.<sup>28</sup> Therefore it must be assumed that the  $\text{Li}^+$  ion results from the fragmentation of only two neutral species. Since the AD curve of  $\text{Li}^+$  is more diffuse than the dimer curve, the possible sources of  $\text{Li}^+$  are the monomer and dimer or the monomer and trimer. A quantitative solution is achieved assuming either case. With presently available techniques it is impossible to obtain a unique solution. The possibility exists that a double-cell distribution study might be able to resolve this problem. For the present, however, we are forced to assume that the polymeric species present in the greatest amount is the most likely source of the polymeric contributor to  $\text{Li}^+$ . Accordingly we have assumed that the monomer and dimer contribute to  $\text{Li}^+$ .

The fragmentation pattern of an ion which results from the ionization of more than one precursor molecule may be characterized by one or more of three arbitrarily defined parameters. These are (i) the ion intensity fraction  $F_{jk}(T, \theta)$ , (ii) the cross-section ratio  $\alpha_{jk}(T)$ , and (iii) the total intensity fraction  $Q_{jk}(T)$ .

(i) *Ion Intensity Fraction.* The ion intensity fraction has been defined according to the equation  $F_{jk}(T, \theta) = I_{jk}^+(T, \theta)/I_k^+(T, \theta)$ . The ion intensity fraction  $F_{jk}(T, \theta)$  is a measure of the ratio of the ion intensity contribution from a specific molecule  $j$  to the total intensity resulting from contributions to ion  $k$  from all sources. In high temperature studies the mass spectrometer is ordinarily located on the axis which is normal to the plane of the effusion orifice. Since the detector is located at  $\theta = 0$ , the ion intensity fraction of paramount importance is  $F_{jk}(T, 0)$ , and this quantity was shown by eq 15 to be equivalent to the superposition coefficients of eq 11. For the  $\text{Li}^+$  ion,  $f_{10}(T) = F_{10}(T, 0)$  and  $f_{20}(T) = F_{20}(T, 0)$ .

(ii) *Cross-Section Ratio.* The cross-section ratio has been defined by the equation  $\alpha_{jk}(T) = \sigma_{jk}(T)/\sigma_{jj}(T) = I_{jk}^+(T, \theta)/I_{jj}^+(T, \theta)$  where  $I_{jk}^+(T, \theta)$  is the ion intensity contribution of molecule  $j$  to ion  $k$ , and  $I_{jj}^+(T, \theta)$  is the intensity of ion  $j$  (not necessarily a parent ion) formed

solely from molecule  $j$ . The magnitude of  $\alpha_{jk}(T)$  provides a measure of the relative importance of the possible ionization paths for a given molecule.

(iii) *Total Intensity Fraction.* The total intensity fraction  $Q_{jk}(T)$  is defined by the equation

$$Q_{jk}(T) = \frac{I_{jk}^+(T, \theta)}{I_{jj}^+(T, \theta) + \sum_{k \neq j} I_{jk}^+(T, \theta)} \quad (16)$$

The total intensity fraction  $Q_{jk}(T)$  is a measure of the ratio of the intensity of ion  $k$  formed by molecule  $j$  to the total ion intensity resulting from all possible ionization modes of molecule  $j$ . Equation 16 may also be expressed in terms of cross sections.

$$Q_{jk}(T) = \frac{\sigma_{jk}(T)}{\sigma_{jj}(T) + \sum_{k \neq j} \sigma_{jk}(T)} \quad (17)$$

The denominator is equal to the total cross-section  $\sigma_j(T)$ , and

$$Q_{jk}(T) = \sigma_{jk}(T)/\sigma_j(T) \quad (18)$$

The quantity  $Q_{jk}(T)$ , therefore, is also a measure of the importance of one ionization path for molecule  $j$  relative to all possible ionization paths for this molecule.

The results of previous investigations have involved either (1) incomplete data on gas phase-condensed phase equilibria or (2) data on gas phase equilibria obtained by the double cell technique. Consequently, the data of other investigators cannot be used to determine ion intensity fractions comparable to those contained in this work. However, data on the ion intensity fractions are necessary to determine the individual ion intensity contributions  $I_{jk}^+(T, \theta)$ . The ion intensity contributions  $I_{jk}^+(T, \theta)$ , in turn, are used in thermochemical calculations.

The contributions of  $\text{Li}^+$  from  $\text{Li}_2\text{F}_2$  expressed in the form of  $f_{20}(T)$  are given as a function of temperature and the ionizing energy in Figure 7 and Table V.<sup>26</sup> The  $\text{Li}^+$  contributions from  $\text{LiF}$  are also listed in Table V.<sup>26</sup> It is evident that the dimer contribution  $f_{20}(T)$  exhibits a substantial energy dependence, particularly at the highest temperature of measurement. The limitations of machine sensitivity prevented measurements at lower energies and temperatures. The wide variation of the ion intensity fractions under differing measurement conditions provides evidence of the difficulties which may be encountered in comparing the data from different investigations. The relative ion intensity contributions to  $\text{Li}^+$  from  $\text{LiF}$ ,  $I_{10}^+(T, 0)$ , and  $\text{Li}_2\text{F}_2$ ,  $I_{20}^+(T, 0)$ , are given in Table VI for each of the ionizing energies and temperatures studied. It is apparent that the magnitude of the monomer term is always considerably larger than that of the dimer term.

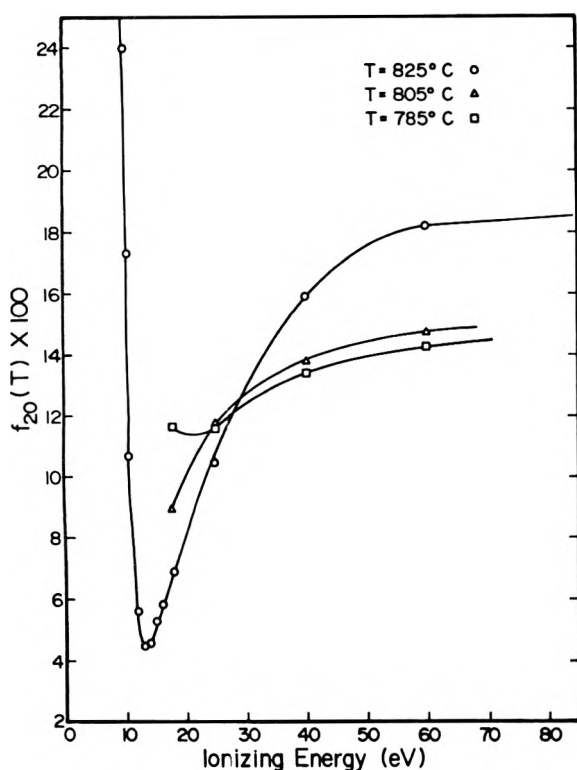


Figure 7. Plot of the percentage dimer contribution to  $\text{Li}^+$  as a function of ionizing energy at cell temperatures of 785, 805, and 825 °C.

TABLE VII: Cross-Section Ratios for the Formation of  $\text{Li}^+$  and  $\text{LiF}^+$  from  $\text{LiF}$  and the Formation of  $\text{Li}^+$  and  $\text{Li}_2\text{F}^+$  from  $\text{Li}_2\text{F}_2$

Ionizing energy, eV	$a_{10}(T) = \sigma_{10}(T)/\sigma_{11}(T)$			$a_{20}(T) = \sigma_{20}(T)/\sigma_{22}(T)$		
	785 °C	805 °C	825 °C	785 °C	805 °C	825 °C
10			1.83			0.261
10.5			1.98			0.132
11			2.04			0.068
12			2.12			0.027
13			2.25			0.019
14			2.34			0.020
15			2.47			0.021
16			2.55			0.024
18	2.72	2.67	2.88	0.051	0.036	0.025
25	2.86	2.77	3.07	0.046	0.044	0.036
40	3.03	2.96	3.35	0.052	0.050	0.054
60	3.11	3.23	3.50	0.055	0.054	0.063

The monomer, therefore, is the major contributor to the  $\text{Li}^+$  ion intensity under the conditions of this study.

In the range of ionizing energies from 12 to 10 eV a small maximum exists in the  $I_{20}^+(T, 0)$  data rather than the continuous decrease normally observed in ionization efficiency curves. The effect is seen in Figure 3 as a shift in the AD curve of the  $\text{Li}^+$  ion in the 10–12-eV range. The direction of the shift suggests that the effect is due to a polymeric contributor. Whether the enhanced ion intensity is due to ionization of the trimer or an alternate ionization process involving some other species cannot be determined.

The cross-section ratios  $a_{10}(T)$  and  $a_{20}(T)$  were determined by use of eq 10, and the resulting data are shown in Table VII. From the values of  $a_{10}(T)$  and  $a_{20}(T)$  it is evident that  $\text{Li}^+$  is the predominant ionic species formed from  $\text{LiF}$  and  $\text{Li}_2\text{F}^+$  is the principal ionic species formed from  $\text{Li}_2\text{F}_2$ .

While the cross-section ratios  $a_{jk}(T)$  and the total intensity fractions  $Q_{jk}(T)$  are functions of temperature and the ionization energy, they are independent of the com-

TABLE VIII: Comparative Cross-Section Ratio and Total Intensity Fraction Data

Author	$T, ^\circ\text{C}$	$\text{IE}, \text{eV}$	$a_{10}(T)$	$a_{20}(T)$	$Q_{10}(T)$	$Q_{20}(T)$
This work	785	60	3.11	0.055	0.757	0.052
This work	805	60	3.23	0.054	0.764	0.051
This work	825	60	3.50	0.063	0.778	0.059
This work <sup>c</sup>	777	75	3.16	0.057	0.760	0.054
Searcy et al. <sup>d</sup>	777	75	3.54	0.09	0.780	0.083
This work <sup>c</sup>	820	75	3.54	0.062	0.780	0.058
Berkowitz et al. <sup>e</sup>	820	75	4.02	0.141	0.801	0.123

<sup>a</sup> Nominal effusion cell temperature. <sup>b</sup> Electron ionizing energy. <sup>c</sup> Extrapolated values. <sup>d</sup> See ref 7. <sup>e</sup> See ref 2.

position of the  $\text{LiF}$  system. Therefore, it is possible to compare the values of  $a_{jk}(T)$  and  $Q_{jk}(T)$  obtained in this work with the results of other investigators. Each of the cross-section ratios reported in the existing literature were determined under different conditions of measurement. In order to compare the present work with that of other investigators, comparative data were obtained by interpolation of temperature data and extrapolation of the ionizing energy data reported in this work. These results were compared with the values of  $a_{10}(T)$ ,  $a_{20}(T)$ ,  $Q_{10}(T)$ , and  $Q_{20}(T)$  reported by Searcy<sup>7</sup> and Berkowitz.<sup>2</sup> The data comparisons are shown in Table VIII. Akishin<sup>4</sup> also reported a value for  $a_{20}(T)$  at 693 °C. However, the ionizing energy was not specified, and meaningful comparisons are not possible without this information. The  $a_{jk}(T)$  and  $Q_{jk}(T)$  values obtained by Searcy et al.<sup>7</sup> agree most closely with the results of this work. While there are differences between corresponding data, the agreement is quite good considering the measurement problems reported by various investigators.

**Supplementary Material Available:** Four tables containing AD data for  $\text{Li}^+$ ,  $\text{LiF}^+$ ,  $\text{Li}_2\text{F}^+$ , and  $\text{Li}_3\text{F}_2^+$  at 18 eV and 825 °C (Table II), AD data at 18, 25, 40, and 60 eV and 825 °C for  $\text{LiF}^+$ ,  $\text{Li}_2\text{F}^+$ , and  $\text{Li}_3\text{F}_2^+$  (Table III), average  $\text{LiF}^+$ ,  $\text{Li}_2\text{F}^+$ , and  $\text{Li}_3\text{F}_2^+$  AD data at 785, 805, and 825 °C (Table IV), and percentage contributions to  $\text{Li}^+$  from  $\text{LiF}$  and  $\text{Li}_2\text{F}_2$  (Table V) (4 pages). Ordering information is available on any current masthead page.

## References and Notes

- L. N. Sidorov and A. S. Alikhanyan, *Russ. J. Phys. Chem.*, **45**, 280 (1971).
- J. Berkowitz, H. A. Tasman, and W. A. Chupka, *J. Chem. Phys.*, **36**, 2170 (1962).
- J. Berkowitz and W. A. Chupka, *J. Chem. Phys.*, **29**, 653 (1958).
- P. A. Akishin, L. N. Gorokhov, and L. N. Sidorov, *Russ. J. Phys. Chem.*, **33**, 648 (1959).
- R. F. Porter and R. C. Schoonmaker, *J. Chem. Phys.*, **29**, 1070 (1958).
- M. H. Boyer, E. Murad, Y. H. Inami and D. L. Hildenbrand, *Rev. Sci. Instrum.*, **39**, 26 (1968).
- P. Mohazzabi and A. W. Searcy, *Int. J. Mass Spectrom. Ion Phys.*, **24**, 469 (1977).
- L. C. Wagner and R. T. Grimley, *J. Phys. Chem.*, **76**, 2819 (1972).
- L. C. Wagner, P. Robert, Q. Grindstaff, and R. T. Grimley, *Int. J. Mass. Spectrom. Ion Phys.*, **15**, 255 (1974).
- L. C. Wagner and R. T. Grimley, *Chem. Phys. Lett.*, **29**, 594 (1974).
- A. M. Evseev, G. V. Pozharskaya, An. N. Nesmeyanov, and Ya. I. Gerasimov, *Zh. Neorg. Khim.*, **4**, 2189 (1959).
- D. L. Hildenbrand, W. F. Hall, F. Ju, and N. D. Potter, *J. Chem. Phys.*, **40**, 2882 (1964).
- R. S. Scheffer and J. L. Margrave, *J. Chem. Phys.*, **31**, 1882 (1959).
- S. H. Bauer and R. F. Porter in "Molten Salt Chemistry", M. Blander, Ed., Wiley, New York, N.Y., 1964, p 627.
- M. J. Linevsky, *J. Chem. Phys.*, **34**, 587 (1961).
- M. J. Linevsky, *J. Chem. Phys.*, **38**, 658 (1963).
- A. Snelson and K. S. Pitzer, *J. Phys. Chem.*, **67**, 882 (1963).
- S. Schlick and O. J. Schnepf, *J. Chem. Phys.*, **41**, 463 (1964).
- R. L. Redington, *J. Chem. Phys.*, **44**, 1238 (1966).



- (20) A. Snelson, *J. Chem. Phys.*, **46**, 3652 (1967).  
(21) S. Abramowitz, N. Acquista, and I. W. Levin, *J. Res. Natl. Bur. Stand., Sect. A*, **72**, 487 (1968).  
(22) D. W. Muenow and R. T. Grimley, *Rev. Sci. Instrum.*, **42**, 455 (1971).  
(23) C. E. Moore, *Natl. Bur. Stand. (U.S.), Circ.*, No. 467, Vol. III (1958).  
(24) R. E. Honig, *J. Chem. Phys.*, **22**, 126 (1954).  
(25) R. T. Grimley, D. W. Muenow, and J. L. LaRue, *J. Chem. Phys.*, **56**, 490 (1972).  
(26) See paragraph at end of text regarding supplementary material.  
(27) G. F. Voronin, *Zh. Fiz. Khim.*, **41**, 1663 (1967).  
(28) R. T. Grimley, J. A. Forsman, and Q. G. Grindstaff, to be submitted for publication.

## Thermal Ion-Molecule Reactions in Oxygen-Containing Molecules. Condensation-Elimination and Addition Reactions in Simple Aliphatic Ketones

Minoru Kumakura\*

Takasaki Radiation Chemistry Research Establishment, Japan Atomic Energy Research Institute, Takasaki, Gunma, Japan

and Toshio Suglura

Japan Atomic Energy Research Institute, Shinbashi, Minato-ku, Tokyo, Japan (Received June 13, 1977; Revised Manuscript Received November 10, 1977)

Publication costs assisted by Engineering Information Service

Thermal ion-molecule reactions in simple aliphatic ketones have been studied with a time-of-flight mass spectrometer. The appearance potentials and ionization efficiency curves of fragment and product ions were measured by the RPD technique. Protonated, methylated, and acylated ions were formed by the reactions of molecular and acyl ions with ketones. The rate constants of condensation-elimination and addition reactions by molecular and acetyl ions increased with increasing carbon number of the alkyl group in the ketones ( $\text{CH}_3\text{COR}$ , with  $\text{R} = \text{CH}_3$ ,  $\text{C}_2\text{H}_5$ , and  $\text{C}_3\text{H}_7$ ). The increase of this rate constant could be explained by the polarizability of the molecules. Methylated ions ( $\text{CH}_3\text{CORCH}_3^+$ ) resulting from condensation-elimination reactions of the acetyl ions with ketones are due to the dissociation of the complexes ( $\text{CH}_3\text{CORCH}_3\text{CO}^{+*}$ ) from which carbon monoxide is eliminated. The rate constants of the methylation reactions by the acetyl ions decreased with increasing carbon number of the alkyl group, and the formation of the methylated ion was negligible in the case of 2-pentanone.

### Introduction

In this laboratory thermal ion-molecule reactions involving oxygen-containing ions have been studied with a time-of-flight mass spectrometer.<sup>1-5</sup> Consecutive association reactions by  $(\text{CH}_2\text{O})_n\text{H}^+$  to form cluster ions were observed in trioxane.<sup>1</sup> Condensation-elimination reactions involving  $\text{C}_2\text{H}_4\text{O}^+$  ions in ethylene oxide and acetaldehyde have been studied to obtain information for the behavior of structural isomer ions in gas phase ion chemistry.<sup>2</sup> In addition condensation-elimination reactions of  $\text{C}_2\text{H}_4\text{O}^+$ ,<sup>3,4</sup>  $\text{CH}_3\text{OCH}_3^+$ , and  $\text{CH}_3\text{OCH}_2^+$ <sup>5</sup> with cyclic ether molecule (trioxane) have been studied in binary mixtures. Ion-molecule reactions in acetone have been studied by several workers.<sup>6-12</sup> From these studies data on the mechanism and kinetics of several reactions were obtained. However other aliphatic ketones have not been studied in detail. In acetone<sup>7,8,11</sup> it is known that acetylated ions are formed by the reactions of  $\text{CH}_3\text{COCH}_3^+$  and  $\text{CH}_3\text{CO}^+$  with the neutral molecule. In general oxygen-containing ions such as  $\text{RCOR}^+$ ,  $\text{RCO}^+$ , and  $\text{R}'\text{CO}^+$  are generated from simple aliphatic ketones ( $\text{RCOR}'$ ) by electron impact. Therefore it is expected that condensation-elimination and addition reactions of these ions with ketones will occur. The  $\text{CH}_3\text{CO}^+$  ions are generated from both ethylene oxide and acetaldehyde by electron impact as abundant fragment ion, but addition reactions by these ions in both systems were not observed.<sup>2,8</sup> On the other hand, in *n*-propyl acetate,<sup>13</sup> condensation-elimination and addition reactions involving  $\text{CH}_3\text{COOH}_2^+$  and  $\text{CH}_3\text{CO}^+$  were observed to a significant

extent. As part of our program concerned with thermal ion-molecule reactions in oxygen-containing molecules, the present work was performed to clarify the mechanism and kinetics of condensation-elimination and addition reactions involving molecular and acyl ions in simple aliphatic ketones. The relationship between the carbon number of the alkyl group in ketone molecules and the rate constants of acylation reactions was systematically studied.

### Experimental Section

The instrument used was a Bendix Model 12-101 time-of-flight mass spectrometer, which has been modified by construction of a closed ion source and improvement of the rise times of the ionizing and ion withdrawal pulses as described elsewhere.<sup>14</sup> The ion source constructed permitted operation under elevated pressures and at long delay times. The pulse electronic circuits of the instrument were also modified and the variable delay time circuit permitted a variation of the time between the end of the ionizing pulse and the onset of the ion withdrawal pulse. During the delay time the entire ionization chamber is field free, so that ion-molecule reactions occurring in the time interval do so under purely thermal conditions. The retarding potential differential technique (RPD) was adopted for appearance potential and ionization efficiency curve measurements.<sup>15</sup> The electron energy scale was calibrated using the ionization efficiency curve of krypton. The measurement of the ionization efficiency curves of two ions was simultaneously performed by the two-channel ion

TABLE I: Thermal Ion-Molecule Reaction Rate Constants in Simple Aliphatic Ketones

Reactions	$k^a$	
	This work	Ref 7
(1a) $\text{CH}_3\text{COCH}_3^+ + \text{CH}_3\text{COCH}_3 \rightarrow \text{CH}_3\text{COCH}_3\text{H}^+ + \text{CH}_3\text{COCH}_2$ $\rightarrow \text{CH}_3\text{COCH}_2\text{CH}_3\text{CO}^+ + \text{CH}_3$	3.06 1.93	5.40
(1b) $\text{CH}_3\text{CO}^+ + \text{CH}_3\text{COCH}_3 \rightarrow \text{CH}_3\text{COCH}_3\text{H}^+ + \text{CH}_3\text{CO}$ $\rightarrow \text{CH}_3\text{COCH}_2\text{CH}_3^+ + \text{CO}$ $\rightarrow \text{CH}_3\text{COCH}_2\text{CH}_3\text{CO}^+$	2.13 0.56 1.26	
(2a) $\text{CH}_3\text{COC}_2\text{H}_5^+ + \text{CH}_3\text{COC}_2\text{H}_5 \rightarrow \text{CH}_3\text{COC}_2\text{H}_5\text{H}^+ + \text{C}_4\text{H}_7\text{O}$ $\rightarrow \text{CH}_3\text{COC}_2\text{H}_5\text{CH}_2\text{CO}^+ + \text{C}_2\text{H}_5$ $\rightarrow \text{CH}_3\text{COC}_2\text{H}_5\text{C}_2\text{H}_5\text{CO}^+ + \text{CH}_3$	5.56 3.62 0.07	
(2b) $\text{CH}_3\text{CO}^+ + \text{CH}_3\text{COC}_2\text{H}_5 \rightarrow \text{CH}_3\text{COC}_2\text{H}_5\text{H}^+ + \text{CH}_2\text{CO}$ $\rightarrow \text{CH}_3\text{COC}_2\text{H}_5\text{CH}_3^+ + \text{CO}$ $\rightarrow \text{CH}_3\text{COC}_2\text{H}_5\text{CH}_2\text{CO}^+$	3.31 0.08 2.82	
(3a) $\text{C}_2\text{H}_5\text{COC}_2\text{H}_5^+ + \text{C}_2\text{H}_5\text{COC}_2\text{H}_5 \rightarrow \text{C}_2\text{H}_5\text{COC}_2\text{H}_5\text{H}^+ + \text{C}_2\text{H}_5\text{COC}_2\text{H}_5$ $\rightarrow \text{C}_2\text{H}_5\text{COC}_2\text{H}_5\text{C}_2\text{H}_5\text{CO}^+ + \text{C}_2\text{H}_5$	5.31 2.43	
(3b) $\text{C}_2\text{H}_5\text{CO}^+ + \text{C}_2\text{H}_5\text{COC}_2\text{H}_5 \rightarrow \text{C}_2\text{H}_5\text{COC}_2\text{H}_5\text{H}^+ + \text{C}_2\text{H}_4\text{CO}$ $\rightarrow \text{C}_2\text{H}_5\text{COC}_2\text{H}_5\text{C}_2\text{H}_5\text{CO}^+$	2.56 2.25	
(4a) $\text{CH}_3\text{COC}_3\text{H}_7^+ + \text{CH}_3\text{COC}_3\text{H}_7 \rightarrow \text{CH}_3\text{COC}_3\text{H}_7\text{H}^+ + \text{CH}_3\text{COC}_3\text{H}_7$ $\rightarrow \text{CH}_3\text{COC}_3\text{H}_7\text{CH}_3\text{CO}^+ + \text{C}_3\text{H}_7$	6.28 4.27	
(4b) $\text{CH}_3\text{CO}^+ + \text{CH}_3\text{COC}_3\text{H}_7 \rightarrow \text{CH}_3\text{COC}_3\text{H}_7\text{H}^+ + \text{CH}_2\text{CO}$ $\rightarrow \text{CH}_3\text{COC}_3\text{H}_7\text{CH}_3\text{CO}^+$	3.86 3.24	

<sup>a</sup> All rate constants in units of  $10^{-10} \text{ cm}^3 \text{ molecule}^{-1} \text{ s}^{-1}$ .

detection technique. The sample pressure was measured with an MKS Baratron 90-X RP-2 capacitance manometer and was calibrated by the known rate constant ( $1.17 \pm 0.07 \times 10^{-9} \text{ cm}^3 \text{ molecule}^{-1} \text{ s}^{-1}$ )<sup>16</sup> for  $\text{CH}_5^+$  in methane. Studies of the variation of ion intensities of fragment and product ions with delay time were carried out at a number density of  $2.50 \times 10^{13} \text{ molecules cm}^{-3}$  and at an electron energy of 70 eV. The uncertainty of the rate constants obtained in this work is approximately 10%. Acetone, butanone, 3-pentanone, and 2-pentanone used were obtained from Tokyo Kasei Co. Ltd. and used after vacuum distillation at various temperatures.

## Results and Discussion

**Acetone.** The delay time dependence of fragment and product ions is shown in Figure 1. The ion intensities of the fragment ions  $\text{CH}_3\text{COCH}_3^+$ ,  $\text{CH}_3\text{CO}^+$ , and  $\text{CH}_3^+$  decreased with increasing delay time. As major product ions,  $\text{CH}_3\text{COCH}_3\text{H}^+$ ,  $\text{CH}_3\text{COCH}_2\text{CH}_3^+$ , and  $\text{CH}_3\text{COCH}_2\text{CH}_3\text{CO}^+$  were observed. In order to determine the precursors of these product ions the appearance potentials and ionization efficiency curves of the fragment and product ions were measured and are shown in Figure 2. The onsets of the ionization efficiency curves of  $\text{CH}_3\text{COCH}_3^+$ ,  $\text{CH}_3\text{CO}^+$ , and  $\text{CH}_3^+$  were obtained as  $9.71 \pm 0.05$ ,  $10.50 \pm 0.05$ , and  $14.28 \pm 0.05$  eV, respectively. The ionization potential of acetone obtained is in good agreement with the values reported by Watanabe ( $9.69 \pm 0.01$  eV),<sup>17</sup> Hurzeler et al. ( $9.65 \pm 0.1$  and  $9.75 \pm 0.03$  eV),<sup>18</sup> and Potapov and Sorokin ( $9.71 \pm 0.01$  eV).<sup>19</sup> The ionization potential obtained with photoionization will be the adiabatic ionization potential if the adiabatic lies in the Franck-Condon region. In general it will be a potential somewhere between the adiabatic and vertical potential. Thus the value obtained with electron impact in this work agreed with the vertical ionization potential ( $9.75 \pm 0.03$  eV) reported by Hurzeler et al.<sup>18</sup> The appearance potential of  $\text{CH}_3\text{CO}^+$  was determined as  $10.42 \pm 0.03$  eV by Potapov and Sorokin<sup>19</sup> and agreed with that obtained in this work. In Figure 2 the onsets of the ionization efficiency curves of  $\text{CH}_3\text{COCH}_3^+$  and  $\text{CH}_3\text{COCH}_2\text{CH}_3\text{CO}^+$  agreed with that of  $\text{CH}_3\text{COCH}_3^+$ . In addition the second appearance potentials of both  $\text{CH}_3\text{COCH}_3\text{H}^+$  and  $\text{CH}_3\text{COCH}_2\text{CH}_3\text{CO}^+$  agreed with the onset of the ionization efficiency curve of  $\text{CH}_3\text{CO}^+$ . Also an agreement of the onsets of the ionization efficiency curves of  $\text{CH}_3\text{COCH}_2\text{CH}_3\text{CH}_3^+$  and  $\text{CH}_3\text{CO}^+$  was

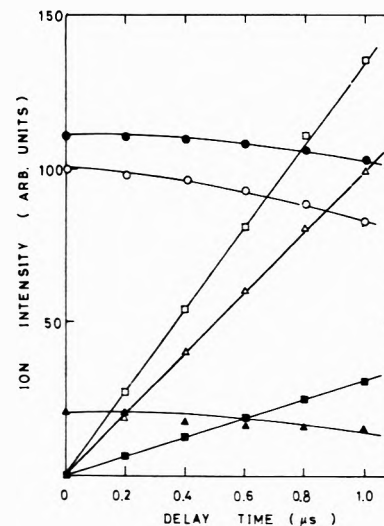


Figure 1. Delay time dependence of fragment and product ions in acetone: ( $\blacktriangle$ )  $\text{CH}_3^+$  ( $\times 1/10$ ); ( $\circ$ )  $\text{CH}_3\text{CO}^+$  ( $\times 1/10$ ); ( $\bullet$ )  $\text{CH}_3\text{COCH}_3^+$  ( $\times 1/2$ ); ( $\blacksquare$ )  $\text{CH}_3\text{COCH}_3\text{H}^+$ ; ( $\triangle$ )  $\text{CH}_3\text{COCH}_2\text{CH}_3^+$  ( $\times 100$ ); ( $\square$ )  $\text{CH}_3\text{COCH}_2\text{CH}_3\text{CO}^+$  ( $\times 100$ ).

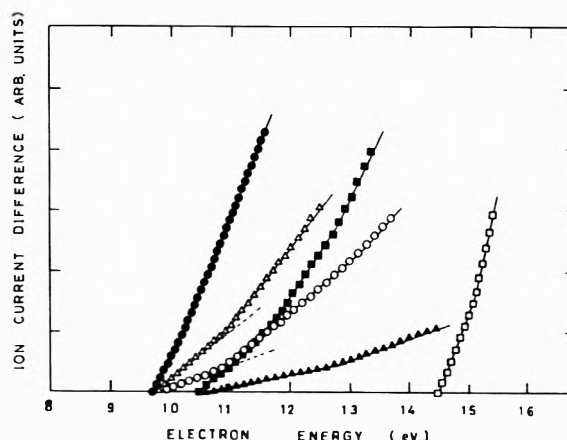
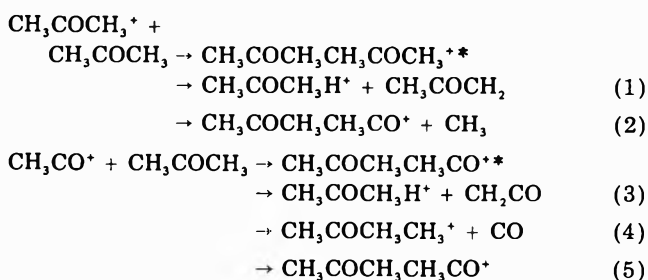


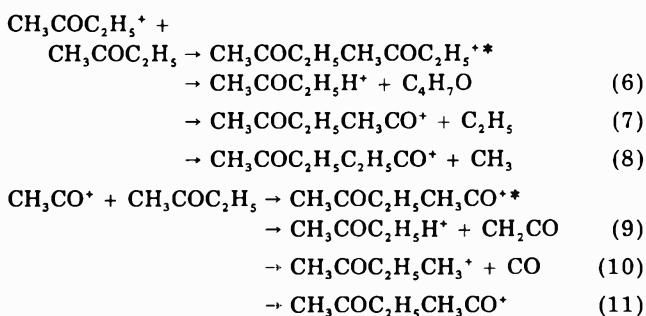
Figure 2. Ionization efficiency curves of major fragment and product ions in acetone: ( $\square$ )  $\text{CH}_3^+$ ; ( $\blacksquare$ )  $\text{CH}_3\text{CO}^+$ ; ( $\bullet$ )  $\text{CH}_3\text{COCH}_3^+$ ; ( $\triangle$ )  $\text{CH}_3\text{COCH}_3\text{H}^+$ ; ( $\blacktriangle$ )  $\text{CH}_3\text{COCH}_2\text{CH}_3^+$ ; ( $\circ$ )  $\text{CH}_3\text{COCH}_2\text{CH}_3\text{CO}^+$ .

observed. From these results it is concluded that  $\text{CH}_3\text{COCH}_3\text{H}^+$ ,  $\text{CH}_3\text{COCH}_2\text{CH}_3^+$ , and  $\text{CH}_3\text{COCH}_2\text{CH}_3\text{CO}^+$  are formed by the following condensation-elimination and addition reactions: The rate



constants of reactions 1-5 were obtained by the ratio plot technique and are summarized in Table I. The total rate constants for the reactions of  $\text{CH}_3\text{COCH}_3^+$  and  $\text{CH}_3\text{CO}^+$  with acetone agree with those of MacNeil and Futrell.<sup>7</sup> The relative rate constants of reactions 1 and 2 were  $k_1:k_2 = 0.65:0.35$ . This value agreed with the ratios 0.67:0.33 and 0.78:0.22 which have reported by MacNeil and Futrell<sup>7</sup> and Blair and Harrison.<sup>8</sup> The rate constant for the acetylation reaction by  $\text{CH}_3\text{COCH}_3^+$  was larger than that by  $\text{CH}_3\text{CO}^+$ .

**Butanone.** The delay time dependence of major fragment and product ions is shown in Figure 3. As product ions,  $\text{CH}_3\text{COC}_2\text{H}_5\text{H}^+$ ,  $\text{CH}_3\text{COC}_2\text{H}_5\text{CH}_3^+$ ,  $\text{CH}_3\text{COC}_2\text{H}_5\text{CH}_2\text{CO}^+$  and  $\text{CH}_3\text{COC}_2\text{H}_5\text{C}_2\text{H}_5\text{CO}^+$  were observed. The formation of  $\text{CH}_3\text{COC}_2\text{H}_5\text{CH}_2\text{CO}^+$  was remarkable as compared with that of  $\text{CH}_3\text{COC}_2\text{H}_5\text{C}_2\text{H}_5\text{CO}^+$ . The ionization efficiency curves of the fragment and product ions are shown in Figure 4. The onsets of the ionization efficiency curves of  $\text{CH}_3\text{COC}_2\text{H}_5^+$ ,  $\text{CH}_3\text{CO}^+$ , and  $\text{C}_2\text{H}_5^+$  were obtained as  $9.52 \pm 0.05$ ,  $10.36 \pm 0.05$ , and  $12.45 \pm 0.05$  eV, respectively. The ionization potential of butanone obtained in this work is in good agreement with the vertical ionization potential ( $9.55 \pm 0.03$  eV) reported by Hurzeler et al.<sup>18</sup> The onsets of the ionization efficiency curves of both  $\text{CH}_3\text{COC}_2\text{H}_5\text{H}^+$  and  $\text{CH}_3\text{COC}_2\text{H}_5\text{CH}_2\text{CO}^+$  agreed with that of  $\text{CH}_3\text{COC}_2\text{H}_5^+$ , and also the break points in the ionization efficiency curves of both product ions agreed with the onset of the curve of  $\text{CH}_3\text{CO}^+$ . The onsets of the ionization efficiency curves of  $\text{CH}_3\text{COC}_2\text{H}_5\text{C}_2\text{H}_5\text{CO}^+$  and  $\text{CH}_3\text{COC}_2\text{H}_5\text{CH}_3^+$  agreed with those of  $\text{CH}_3\text{COC}_2\text{H}_5^+$  and  $\text{CH}_3\text{CO}^+$ , respectively. From the results of these ionization efficiency curve measurements, the following reactions are derived:



The rate constants of these reactions are given in Table I and the rate constant of reaction 7 is larger considerably than that of reaction 8. The bond dissociation energy,  $D(\text{CH}_3\text{CO}-\text{C}_2\text{H}_5)$ , is somewhat smaller than that of  $D(\text{CH}_3-\text{COC}_2\text{H}_5)$ , that is,  $D(\text{CH}_3\text{CO}-\text{C}_2\text{H}_5) = 72.2 \text{ kcal mol}^{-1}$  and  $D(\text{CH}_3-\text{COC}_2\text{H}_5) = 72.6 \text{ kcal mol}^{-1}$ .<sup>20</sup> In the condensation-elimination reaction, it is presumed that the rate constant is affected by the bond dissociation energy. The rate constant of reaction 7 was comparable with that of addition reaction 11 of  $\text{CH}_3\text{CO}^+$  with the neutral molecule. Since  $\text{C}_2\text{H}_5\text{CO}^+$  from butanone was less abundant, the condensation-elimination and/or addition reaction was not observed. The methylation reaction (condensation-elimination reaction) by  $\text{CH}_3\text{CO}^+$  in butanone results in

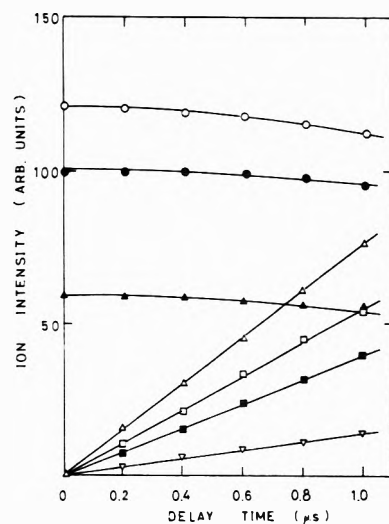


Figure 3. Delay time dependence of fragment and product ions in butanone: (O)  $\text{CH}_3\text{CO}^+$  ( $\times 1/10$ ); ( $\Delta$ )  $\text{C}_2\text{H}_5\text{CO}^+$ ; ( $\bullet$ )  $\text{CH}_3\text{COC}_2\text{H}_5^+$  ( $\times 1/2$ ); ( $\square$ )  $\text{CH}_3\text{COC}_2\text{H}_5\text{H}^+$ ; ( $\blacksquare$ )  $\text{CH}_3\text{COC}_2\text{H}_5\text{CH}_3^+$  ( $\times 200$ ); ( $\Delta$ )  $\text{CH}_3\text{COC}_2\text{H}_5\text{CH}_2\text{CO}^+$  ( $\times 20$ ); ( $\nabla$ )  $\text{CH}_3\text{COC}_2\text{H}_5\text{C}_2\text{H}_5\text{CO}^+$  ( $\times 200$ ).

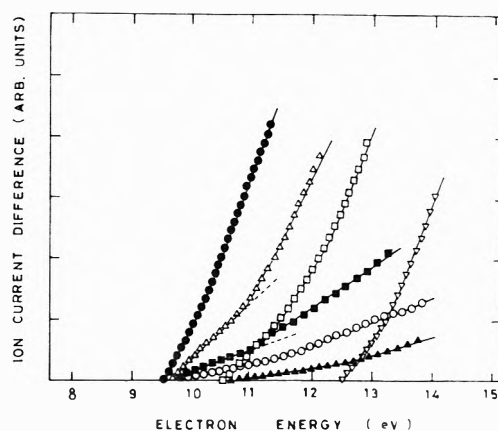
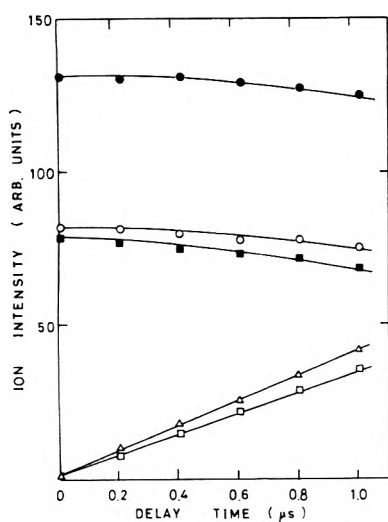


Figure 4. Ionization efficiency curves of major fragment and product ions in butanone: ( $\nabla$ )  $\text{C}_2\text{H}_5^+$ ; ( $\square$ )  $\text{CH}_3\text{CO}^+$ ; ( $\bullet$ )  $\text{CH}_3\text{COC}_2\text{H}_5^+$ ; ( $\Delta$ )  $\text{CH}_3\text{COC}_2\text{H}_5\text{H}^+$ ; ( $\blacktriangle$ )  $\text{CH}_3\text{COC}_2\text{H}_5\text{CH}_3^+$ ; ( $\blacksquare$ )  $\text{CH}_3\text{COC}_2\text{H}_5\text{CH}_2\text{CO}^+$ ; ( $\circ$ )  $\text{CH}_3\text{COC}_2\text{H}_5\text{C}_2\text{H}_5\text{CO}^+$ .

an elimination of carbon monoxide from intermediate complex ( $\text{CH}_3\text{COC}_2\text{H}_5\text{CH}_2\text{CO}^{+\bullet}$ ). The rate constant of methylation reaction 10 is smaller than that of the analogous reaction 4 in acetone. The rate constant ratios  $(k_3 + k_4)/k_5$  and  $(k_9 + k_{10})/k_{11}$  in acetone and butanone are 2.1 and 1.2. This difference in both systems indicates that the dissociation of  $\text{CH}_3\text{COCH}_2\text{CH}_2\text{CO}^{+\bullet}$  leading to the formation of protonated and methylated ions in acetone predominates as compared with that of  $\text{CH}_3\text{COC}_2\text{H}_5\text{CH}_2\text{CO}^{+\bullet}$  in butanone. The excess energy of  $\text{CH}_3\text{CO}^+$  will play an important role in the dissociation of the complex. In fact it is known that the excess translational energy of  $\text{CH}_3\text{CO}^+$  from acetone is higher than that from butanone.<sup>19,21</sup>

**3-Pentanone.** The major product ions formed in 3-pentanone were  $\text{C}_2\text{H}_5\text{COC}_2\text{H}_5\text{H}^+$  and  $\text{C}_2\text{H}_5\text{COC}_2\text{H}_5\text{C}_2\text{H}_5\text{CO}^+$  as can be seen in Figure 5. The ionization efficiency curves of the fragment and product ions are shown in Figure 6. The onsets of the ionization efficiency curves of  $\text{C}_2\text{H}_5\text{COC}_2\text{H}_5^+$  and  $\text{C}_2\text{H}_5\text{CO}^+$  were obtained as  $9.60 \pm 0.05$  and  $10.29 \pm 0.05$  eV, respectively. The onsets of the ionization efficiency curves of these product ions agreed with that of  $\text{C}_2\text{H}_5\text{COC}_2\text{H}_5^+$ , and also the break points in the curves of the product ions agreed with the onset of the curve of  $\text{C}_2\text{H}_5\text{CO}^+$ . The results of the ionization efficiency curve measurements confirm the



**Figure 5.** Delay time dependence of fragment and product ions in 3-pentanone: (■)  $C_2H_5^+$  ( $\times 1/10$ ); (○)  $C_2H_5CO^+$  ( $\times 1/10$ ); (●)  $C_2H_5COC_2H_5^+$ ; (Δ)  $C_2H_5COC_2H_5H^+$ ; (□)  $C_2H_5COC_2H_5C_2H_5CO^+$  ( $\times 20$ ).

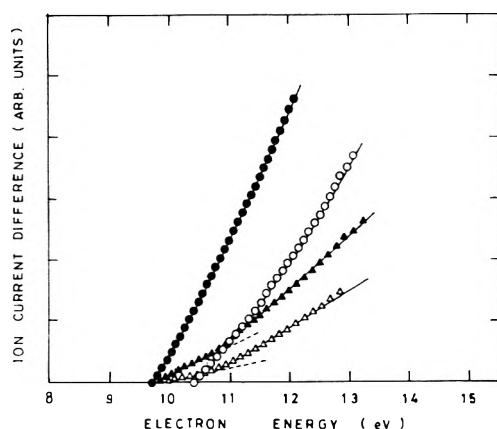
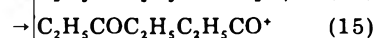
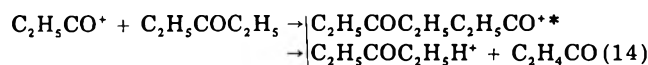
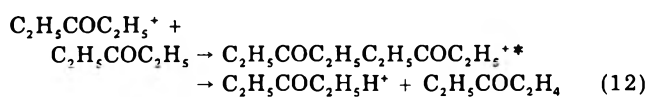


**Figure 6.** Ionization efficiency curves of major fragment and product ions in 3-pentanone: (○)  $C_2H_5CO^+$ ; (●)  $C_2H_5COC_2H_5^+$ ; (▲)  $C_2H_5COC_2H_5H^+$ ; (Δ)  $C_2H_5COC_2H_5C_2H_5CO^+$ .

view that  $C_2H_5COC_2H_5H^+$  and  $C_2H_5COC_2H_5C_2H_5CO^+$  are formed by the following reactions:



The rate constant of condensation-elimination reaction 13 was comparable with that of addition reaction 15 (Table I). The rate constant of the acylation reaction by  $C_2H_5COC_2H_5^+$  in 3-pentanone is larger than that by  $CH_3COC_2H_5^+$  in butanone.

**2-Pentanone.** The delay time dependence of major fragment and product ions is shown in Figure 7. The major product ions were  $CH_3COC_3H_7H^+$  and  $CH_3COC_3H_7CH_3CO^+$ , and the ionization efficiency curves of these ions are shown in Figure 8. The onsets of the ionization efficiency curves of  $CH_3COC_3H_7^+$  and  $CH_3CO^+$  were obtained as  $9.29 \pm 0.05$  and  $11.10 \pm 0.05$  eV, respectively. The onsets of the ionization efficiency curves of  $CH_3COC_3H_7H^+$  and  $CH_3COC_3H_7CH_3CO^+$  agreed with that of the curve of  $CH_3COC_3H_7^+$ , in addition, the break point in the curves of the product ions was in good agreement with the onset of the curve of  $CH_3CO^+$ . Ac-

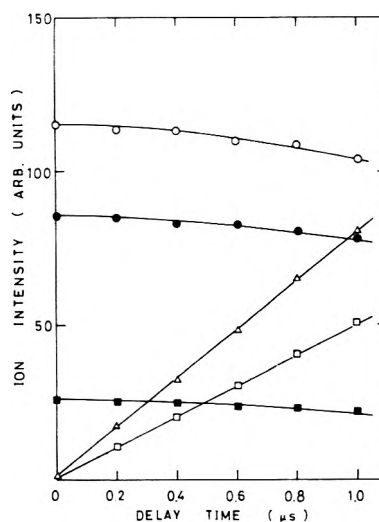


**Figure 7.** Delay time dependence of fragment and product ions in 2-pentanone: (○)  $CH_3CO^+$  ( $\times 1/10$ ); (■)  $CH_3COCOCH_2^+$  ( $\times 1/10$ ); (●)  $CH_3COC_3H_7^+$  ( $\times 1/2$ ); (□)  $CH_3COC_3H_7H^+$ ; (Δ)  $CH_3COC_3H_7CH_3CO^+$  ( $\times 20$ ).

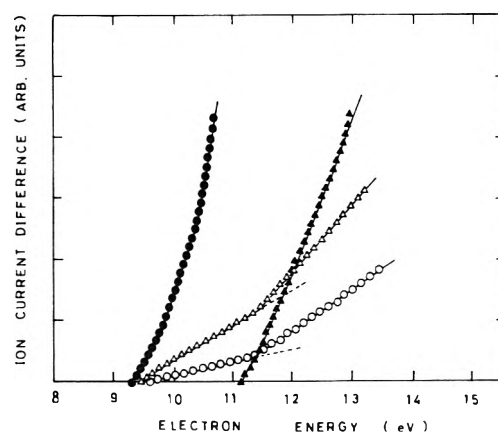
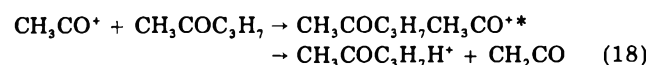
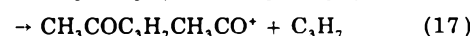
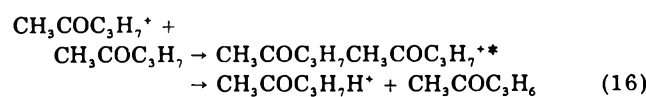


**Figure 8.** Ionization efficiency curves of major fragment and product ions in 2-pentanone: (▲)  $CH_3CO^+$ ; (●)  $CH_3COC_3H_7^+$ ; (Δ)  $CH_3COC_3H_7H^+$ ; (○)  $CH_3COC_3H_7CH_3CO^+$ .

cordingly it was found that  $CH_3COC_3H_7H^+$  and  $CH_3COC_3H_7CH_3CO^+$  result from the following reactions:



The rate constants of reactions 16–19 are summarized in Table I.

In simple aliphatic ketones, it is of interest to examine the relationship between the rate constants of acetylation reactions and the molecular structures of ketones. A plot showing the relation between the rate constants and the carbon number of the alkyl group in ketones,  $CH_3COR$  ( $R = CH_3, C_2H_5,$  and  $C_3H_7$ ), is shown in Figure 9. The rate constants for the acetylation reactions (condensation-elimination reactions) by the molecular ions ( $CH_3COR^+$ ) increase with increasing carbon number of the alkyl group in ketones. The acetylation reactions by  $CH_3COR^+$  occur via the cleavage of the C–R bond in the intermediate complexes ( $CH_3CORCH_3COR^+$ ). The dissociation energy of the C–C bonds ( $CH_3CO-R$ ) does not change with increasing carbon number of the alkyl group, that is  $D(CH_3CO-CH_3) = 72.6$ ,  $D(CH_3CO-C_2H_5) = 72.2$ , and  $D-$

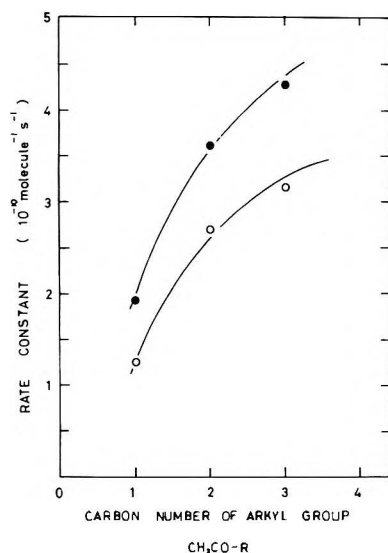


**Figure 9.** Rate constant vs. carbon number of the alkyl group in  $\text{CH}_3\text{COR}$  ( $\text{R} = \text{CH}_3, \text{C}_2\text{H}_5, \text{and } \text{C}_3\text{H}_7$ ): (●)  $\text{CH}_3\text{COR}^+ + \text{CH}_3\text{COR} \rightarrow \text{CH}_3\text{CORCH}_3\text{CO}^+ + \text{R}$ ; (○)  $\text{CH}_3\text{CO}^+ + \text{CH}_3\text{COR} \rightarrow \text{CH}_3\text{CORCH}_3\text{CO}^+$ .

$(\text{CH}_3\text{CO}-\text{C}_3\text{H}_7) = 72.5 \text{ kcal mol}^{-1}$ .<sup>20</sup> While, the polarizability of ketones increases with increasing carbon number of the alkyl group, that is,  $\text{CH}_3\text{COCH}_3 = 62.3 \times 10^{-25}$ ,  $\text{CH}_3\text{COC}_2\text{H}_5 = 82.3 \times 10^{-25}$ , and  $\text{CH}_3\text{COC}_3\text{H}_7 = 102.3 \times 10^{-25} \text{ cm}^3$ .<sup>22</sup> Also, the ionization potential of ketones becomes lower with increasing carbon number of the alkyl group as described above. It is known that the proton affinity of a molecule depends on its ionization potential.<sup>23</sup> Thus a relationship between the proton affinity and the rate constant for the acetylation reaction seems plausible. However the acetylation reactions would be dominated by the polarizability of the neutral molecules rather than the proton affinity. Furthermore the rate constants of the acetylation reactions (addition reactions) by the  $\text{CH}_3\text{CO}^+$  ions increase with increasing carbon number of the alkyl groups in the source molecules. The addition reactions of the  $\text{CH}_3\text{CO}^+$  ions with ketones would depend greatly on the translational energy of the  $\text{CH}_3\text{CO}^+$  ions and the polarizability of the neutral molecules. As can be seen in Figure 9, the rate constants of the acetylation reactions by the  $\text{CH}_3\text{CO}^+$  ions are smaller than those by the  $\text{CH}_3\text{COR}^+$  ions, and the differences in the rate constant between both reactions become large at the larger alkyl

groups. The  $\text{CH}_3\text{CO}^+$  ions play an important role in the formation of methylated ions as reactant ion. Methylated ions resulting from condensation-elimination reactions of  $\text{CH}_3\text{CO}^+$  ions with molecules are due to the dissociation of the intermediate complexes ( $\text{CH}_3\text{CORCH}_3\text{CO}^{**}$ ) from which carbon monoxide molecule is eliminated. The rate constants of the methylation reactions by the  $\text{CH}_3\text{CO}^+$  ions decreased with increasing carbon number of the alkyl group, and the formation of methylated ion was negligible in the case of 2-pentanone. Thus, as the carbon number of the alkyl group is increased, the dissociation channels leading to the formation of protonated and methylated ions become minor. The translational energies of the  $\text{CH}_3\text{CO}^+$  ions from ketones ( $\text{CH}_3\text{COR}$ ) become low with increasing carbon number of the alkyl group.<sup>19,21</sup> The dissociation of the complex would depend on the energy of  $\text{CH}_3\text{CO}^+$ . The correlation of rate constants with translational energies is feasible.

## References and Notes

- (1) M. Kumakura and T. Sugiura in "Recent Developments in Mass Spectroscopy", K. Ogata and T. Hayakawa, Ed., University Park Press, Baltimore, Md., 1970, p 988.
- (2) M. Kumakura, K. Arakawa, and T. Sugiura, *Int. J. Mass Spectrom. Ion Phys.*, in press.
- (3) M. Kumakura, K. Arakawa, and T. Sugiura, *Can. J. Chem.*, in press.
- (4) M. Kumakura, K. Arakawa, and T. Sugiura, *Bull. Chem. Soc. Jpn.*, in press.
- (5) M. Kumakura and T. Sugiura, *Z. Naturforsch.*, in press.
- (6) M. S. B. Munson, *J. Am. Chem. Soc.*, **87**, 5313 (1965).
- (7) K. A. G. MacNeil and J. H. Futrell, *J. Phys. Chem.*, **76**, 409 (1972).
- (8) A. S. Blair and A. G. Harrison, *Can. J. Chem.*, **51**, 703 (1973).
- (9) L. W. Sieck and P. Ausloos, *Radiat. Res.*, **52**, 47 (1972).
- (10) P. W. Tiedeman and J. M. Riveros, *J. Am. Chem. Soc.*, **95**, 3140 (1973).
- (11) W. J. Hart and H. A. Sprang, *J. Am. Chem. Soc.*, **99**, 32 (1977).
- (12) Z. Luczynski and H. Wincel, *Int. J. Mass Spectrom. Ion Phys.*, **23**, 37 (1977).
- (13) M. Kumakura, K. Arakawa, and T. Sugiura, *Int. J. Mass Spectrom. Ion Phys.*, in press.
- (14) M. Kumakura, A. Ito, and T. Sugiura, *Mass Spectrosc.*, **22**, 16 (1974).
- (15) M. Kumakura, T. Sugiura, and S. Okamura, *Mass Spectrosc.*, **16**, 16 (1968).
- (16) M. Henchman in "Ion-Molecule Reactions", J. L. Franklin, Ed., Plenum Press, New York, N.Y., 1972, p 101.
- (17) K. Watanabe, *J. Chem. Phys.*, **26**, 542 (1957).
- (18) H. Hurzeler, M. G. Inghram, and J. D. Harrison, *J. Chem. Phys.*, **28**, 76 (1958).
- (19) V. K. Potapov and V. V. Sorokin, *Khim. Vys. Energ.*, **6**, 387 (1972).
- (20) J. S. Roberts and H. A. Skinner, *Trans. Faraday Soc.*, **45**, 339 (1949).
- (21) I. Kanomata, *Bull. Chem. Soc. Jpn.*, **34**, 1864 (1961).
- (22) J. A. Beran and L. Kevan, *J. Phys. Chem.*, **73**, 3860 (1969).
- (23) D. H. Ave, H. M. Webb, and M. F. Bowers, *J. Am. Chem. Soc.*, **94**, 4726 (1972).

# Application of RRKM Theory Using a Hindered Rotational Gorin Model Transition State to the Reaction $\text{HO}_2\text{NO}_2 + \text{N}_2 \rightleftharpoons \text{HO}_2 + \text{NO}_2 + \text{N}_2^\ddagger$

A. C. Baldwin<sup>1</sup> and D. M. Golden\**Thermochemistry and Chemical Kinetics Group, SRI International, Menlo Park, California 94025 (Received November 7, 1977)*

We have calculated rate constants as a function of temperature and pressure for the title reaction, using RRKM theory in conjunction with a hindered rotational Gorin model for the transition state. This treatment is consistent with the direct experimental measurements on the forward and reverse reactions.

## Introduction

The recent identification and characterization by Fourier transform infrared spectroscopy of pernitric acid ( $\text{HO}_2\text{NO}_2$ ) in the gas phase by Niki et al.<sup>1</sup> has led to a great deal of interest in that compound. The formation of a long-lived complex between  $\text{HO}_2$  and  $\text{NO}_2$  was first suggested by Simonaitis and Heicklen,<sup>2</sup> who pointed out that this could have an effect on atmospheric chemistry.  $\text{HO}_2$  and  $\text{NO}_2$  both play a crucial role in the chemistry of the upper and lower atmosphere. Thus, reaction 1 and its reverse

$$\text{HO}_2 + \text{NO}_2 + \text{M} \rightleftharpoons \text{HO}_2\text{NO}_2 + \text{M} \quad (1,-1)$$

are potentially of great importance in the  $\text{HO}_x$  and  $\text{NO}_x$  cycles.

There have been two direct studies of the rate of reactions 1 and -1. Howard<sup>3</sup> measured the rate of reaction 1 ( $\text{M} = \text{He}, \text{N}_2, \text{O}_2, \text{NO}_2$ ) at low pressures (0.5–3 Torr) and 300 K, using laser magnetic resonance detection of  $\text{HO}_2$  in a discharge flow system. In the third-order, low-pressure limit, that process yielded  $k_1 = 2.09 \pm 0.52 \times 10^{-31} \text{ cm}^6 \text{ molecule}^{-2} \text{ s}^{-1}$  ( $\text{M} = \text{N}_2$ ). Graham, Winer, and Pitts<sup>4</sup> measured the rate of reaction -1 at 1 atm ( $\text{M} = \text{N}_2$ ) and temperatures 254–283 K, by direct observation of the decay of pernitric acid using Fourier transform infrared spectroscopy. Their experiment yielded  $k_{-1} = 1.3 \times 10^{14} \exp(-20700 \pm 500/RT) \text{ s}^{-1}$ , although, as the authors point out, the pressure at which they obtained their measurement is probably in the falloff region for the reaction.

Kinetic models of atmospheric chemistry require a knowledge of the rate of reactions 1 and -1 as a function of temperature and pressure. We have attempted to supply that information by the application of RRKM theory to reaction -1;  $k_1$  can then be deduced as  $k_1 = Kk_{-1}$ , where  $K$  is the equilibrium constant.

The application of RRKM theory requires a knowledge of the high-pressure limit Arrhenius parameters of reaction -1 and a model of the structure of the transition state. We have developed a hindered rotational Gorin model for the transition states of simple bond fission reactions<sup>5,6</sup> that should be applicable in this case. This reaction is therefore a suitable example with which to test further the validity of our model, and to see if the available data can be reconciled using reasonable model parameters. In this way we hope to generate a data base from which transition-state parameters for simple bond fissions may be selected a priori.

## Estimation of High-Pressure-Limit Arrhenius Parameters

Before any application of unimolecular rate theory is possible, it is necessary to know the high-pressure-limit

<sup>1</sup>This work was supported by Contract 68-02-2427 from the Environmental Protection Agency.

\* Postdoctoral Research Associate.

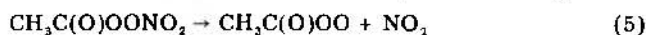
Arrhenius parameters for reaction -1. The very low values of the  $A$  factor measured by Graham et al., for instance, compared to that for nitric acid decomposition<sup>6,7</sup> of  $\sim 10^{16.5} \text{ s}^{-1}$ , provide reliable evidence that those measurements were not made in the high-pressure limit. Thus, the high-pressure parameters must be estimated, and the predicted rate at 1 atm may then be compared with the experimental value.

It is convenient to estimate  $A_1$ , and then calculate  $A_{-1}$  from the overall entropy change for the reaction, which is reasonably well known. Howard<sup>8</sup> has measured the rate of reaction 2 as  $10^{9.7 \pm 0.1} \text{ M}^{-1} \text{ s}^{-1}$ , and Batt et al.<sup>9</sup> have



calculated the rate of reaction 3 to be  $10^{9.7 \pm 0.6} \text{ M}^{-1} \text{ s}^{-1}$  based on their measured value of  $10^{10.1 \pm 0.6} \text{ M}^{-1} \text{ s}^{-1}$  for reaction 4, all assuming that there is no activation energy. Reaction 3 is precisely analogous to reaction 1 and isoelectronic with it, while the rate of reaction 1 is unlikely to be faster than reaction 2, although there is little evidence on the relative rates of combination and disproportionation for nonalkyl radicals. Thus, a reasonable value would seem to be  $A_1 = 10^{9.5} \text{ M}^{-1} \text{ s}^{-1}$  with no activation energy. The effects of errors in the estimate are discussed later.

The entropy of  $\text{HO}_2\text{NO}_2$  may be estimated with reasonable accuracy to be 71.6 eu, based on a measured value for  $\text{MeONO}_2$ ,<sup>10</sup> after correcting for the change of internal rotor from a methyl to an OH. That yields  $A_{-1} = 10^{16.4} \text{ s}^{-1}$  using standard values for the entropy of  $\text{HO}_2$  and  $\text{NO}_2$ .<sup>11</sup> It then remains to estimate the activation energy,  $E_{-1}$ . The only peroxyacetyl nitrate decomposition that has been studied is peroxyacetyl nitrate (PAN) by Hendry and Kenley<sup>12</sup> and Cox and Roffey (reaction 5).<sup>13</sup> They found that  $E_5 = 26.9$



$\pm 0.9$  and  $24.9 \pm 0.8 \text{ kcal mol}^{-1}$ , respectively.  $E_{-1}$  should be of similar magnitude. The effect of varying  $E_{-1}$  is discussed later.

## Application of RRKM Theory

RRKM is a statistical rate theory couched in transition state formulation, which assumes fast random access by allowed internal states to molecular energy,  $E^*$ . The unimolecular decomposition rate constant,  $k_{\text{uni}}$ , is given by

$$k_{\text{uni}} = \frac{Q_1^\ddagger e^{-E_0/kT}}{hQ_1Q_2} \int_0^\infty \frac{G(E^*)e^{-E^*/kT} dE^*}{1 + Q_1^\ddagger G(E^*)/hQ_1N(E^*)F\beta\omega} \quad (6)$$

where  $E_0$  is the critical energy,  $E^*$  is the total energy, and  $E^+ = E^* - E_0$  is the maximum energy of the critical

configuration;  $G(E^+)$  is the sum of the states of the complex below energy  $E^+$ , and  $N(E^*)$  is the density of molecular states;  $Q_1^+/Q_1$  is the partition function ratio of the inactive modes (moments of adiabatic rotors), and  $Q_2$  is the partition function for the active molecular modes;  $F$  is the Waage-Rabinovitch<sup>14</sup> centrifugal correction term for conservation of angular momentum among the adiabatic rotations,  $\omega$  is the (Lennard-Jones) collision frequency of excited substrate with bath gas at pressure  $P$ , and  $\beta$  is the collisional efficiency for stabilization (sufficient energy removal). Our calculations used the Stein-Rabinovitch<sup>15</sup> algorithm to compute  $G(E^+)$  and  $N(E^*)$ .

In order to evaluate eq 6 it is necessary to postulate a model for the critical configuration (transition state). A sometimes legitimate complaint about RRKM theory is that the parameters relating to the transition state are not a unique choice, and are often completely empirical. In simple bond fission reactions, which are the reverse of radical-radical combination reactions, a logical choice for the interfragment distance in the transition state is the top of the centrifugal barrier.<sup>11</sup> Using a Lennard-Jones potential, that gives

$$(r^*/r_0) = (6D_0/RT)^{1/6} \quad (7)$$

where  $r$  is the distance between the center of mass of the two fragments, and  $D_0 = E_0 +$  zero-point energy. We have used a hindered rotational Gorin model for the transition state, which provides a unique choice for the structure of the transition state while involving only one temperature-dependent parameter, the degree of hindrance,  $\eta$ . In the Gorin model, the internal modes of the transition state are simply the vibrations and rotations of the independent fragments. Thus, the six vibrations associated with the breaking bond in the molecule become the reaction coordinate, one one-dimensional and two two-dimensional rotations in the transition state.

At the interfragment distance of the critical configuration the fragment rotation generally will not be free, because of the presence of the other fragment. To account for that, we introduce the hindrance parameter,  $\eta$ , which decreases the entropy of internal rotation by reducing the effective moment of inertia of the rotor. We thus have a unique model for the transition state of any bond fission reaction involving only one empirical parameter. That parameter may be adjusted to give the desired entropy of the transition state, and hence the appropriate high-pressure-limit decomposition  $A$  factor. Determining the parameters for the properties of the transition state in this simple way should facilitate the comparison of data on similar types of reactions, and may even yield a useful predictive method.

A significant advantage of the hindered Gorin model is that it can reproduce the experimentally observed temperature dependence of the high-pressure  $A$  factors. As observed in studies over wide temperature ranges, the high-pressure  $A$  factors for bond fission and radical combination have a negative temperature dependence.<sup>7</sup> A vibrational model for the transition state would necessarily predict a positive temperature dependence. However, if  $\eta$  is allowed to increase with temperature, then the correct temperature dependence is achieved. That is physically reasonable, because the position of the centrifugal barrier means that the interfragment distance in the transition state decreases with temperature (see eq 7). Thus, it is to be expected that the rotation of the fragments should become more hindered as the temperature increases. The hindrance parameter,  $\eta$ , is therefore a simple representation of the "tightness" of the transition state.<sup>11</sup> The larger  $\eta$ , the lower the entropy of the transition state, and the

TABLE I: Frequency Assignment of HO<sub>2</sub>NO<sub>2</sub>

Frequency, cm <sup>-1</sup>	Type	Frequency, cm <sup>-1</sup>	Type
3540 <sup>a</sup>	OH stretch	633	NO stretch
1728 <sup>a</sup>	NO <sub>2</sub>	500	NO <sub>2</sub> rock
1304 <sup>a</sup>	NO <sub>2</sub>	735	NO <sub>2</sub> wag
803 <sup>a</sup>	NO <sub>2</sub>	125	O-NO <sub>2</sub> torsion
1396 <sup>a</sup>	OH bend	400	OOH bend
		880	OO stretch
		200	HO-O torsion

<sup>a</sup> From ref 1.

TABLE II: Temperature Dependent Parameters

T, K	Collisional efficiency $\beta$	% hindrance $\eta$
300	0.39	98 <sup>a</sup>
278	0.41	97 <sup>a</sup>
266	0.42	96 <sup>a</sup>
254	0.43	95 <sup>a</sup>
230	0.45	93 <sup>b</sup>
217	0.47	92 <sup>b</sup>

<sup>a</sup> Empirically derived to fit experimental data. <sup>b</sup> From linear extrapolation of high-temperature values.

lower the high-pressure  $A$  factor.

### Details of the Calculation

The frequency assignment for the molecule is given in Table I. The first five frequencies are those observed by Niki et al.; the remaining frequencies are based on those for FNO<sub>3</sub>, H<sub>2</sub>O<sub>2</sub>, and HNO<sub>3</sub>, with the low-frequency torsions adjusted to give the correct entropy for the molecule. The values used are compatible with the known torsion barriers for O-OH and O-NO<sub>2</sub>. The frequencies and moments of inertia for the transition state were those for isolated HO<sub>2</sub> and NO<sub>2</sub> taken from the JANAF<sup>16</sup> tables. The hindrance correction is applied to the two two-dimensional rotors, chosen to exclude rotation about the breaking bond axis. The one-dimensional rotor in the transition state is not hindered. That rotation which corresponds to external rotation about the breaking bond in the molecule is taken as active.<sup>17</sup>

The only other unknown parameter is  $\beta$ , the collisional efficiency. Troe<sup>18</sup> has developed a theory from which  $\beta$  as a function of temperature may be calculated using eq 8, where  $\langle \Delta E \rangle$  is the average energy transferred in all

$$\frac{\beta}{1 - \beta^{1/2}} = \frac{\langle \Delta E \rangle}{F_E RT} \quad (8)$$

collisions, and  $F_E$  is defined by eq 9. The values of  $\beta$  used

$$F_E = \sum_{\nu=0}^{s-1} \frac{(s-1)!}{(s-1-\nu)!} \left( \frac{kT}{E_0} \right)^\nu \quad (9)$$

in the calculations are tabulated in Table II. They were calculated using  $\langle \Delta E \rangle = 0.7$  kcal mol<sup>-1</sup>, a typical value for nitrogen as a collision partner.<sup>18</sup>

### Results and Discussion

Figure 1 shows the results of the calculation at 300 K for the pressure range 10<sup>-1</sup> to 10<sup>5</sup> Torr. The experimental points are the measurements of Graham et al., extrapolated 20° using the reported activation energy, and Howard's rate for the combination reaction converted to a decomposition rate using the equilibrium constant defined by the assumed high-pressure parameters. Figure 2 shows the results of the calculation at 1 atm over the temperature range 254-300 K. The experimental points are from Graham et al. The high-pressure Arrhenius parameters

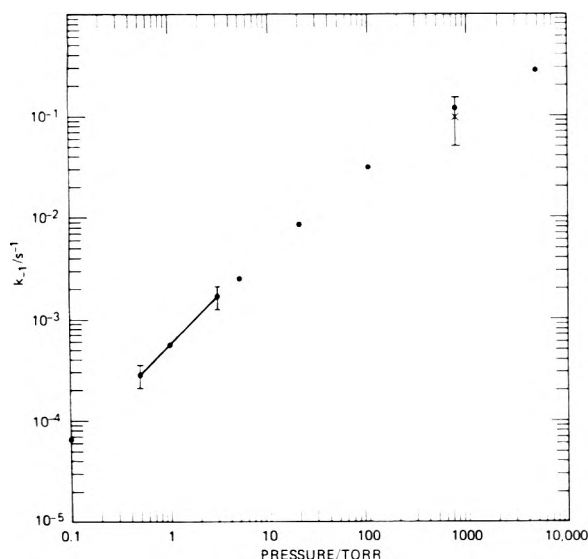


**Figure 1.**  $\text{HO}_2\text{NO}_2$  decomposition at 300 K. The rate constant for  $\text{HO}_2\text{NO}_2$  decomposition as a function of pressure at 300 K. Solid line is from Howard's low-pressure measurement, X is Graham et al., measurement, and ● calculated from RRKM theory.

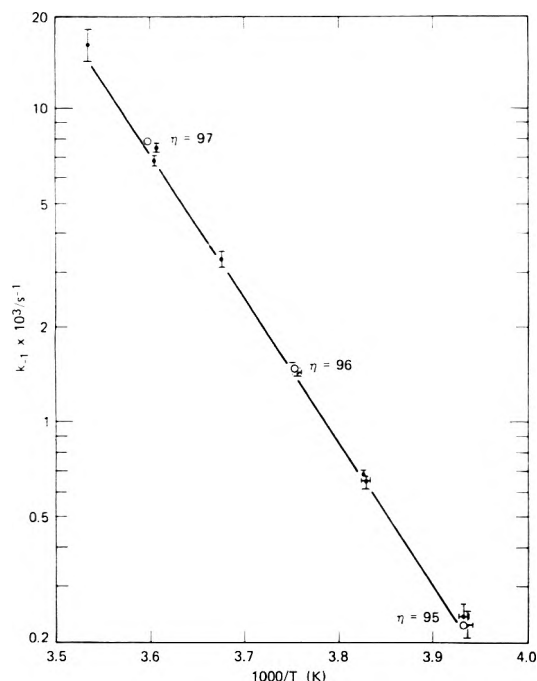


**Figure 2.** Arrhenius plot for the decomposition of  $\text{HO}_2\text{NO}_2$  at 1 atm. The Arrhenius plot reported by Graham et al.: ●, experimental points; O, calculated from RRKM theory using values of  $\eta$  shown.

used to produce these results are:  $A_{-1} = 10^{9.5} \text{ M}^{-1} \text{ s}^{-1}$ ,  $E_{-1} = 23.0 \text{ kcal mol}^{-1}$ ,  $S^\circ(\text{HO}_2\text{NO}_2) = 71.6 \text{ eu}$ , which yield  $A_{-1} = 10^{16.4} \text{ s}^{-1}$  at 300 K. The values of  $\eta$ , the hindrance parameter, are tabulated as a function of temperature in Table II.

As can be seen from the figures, the calculations reproduce the experimental results very well. However, the extent to which the assumed high-pressure Arrhenius parameters are a unique set remains in question. It is extremely unlikely that  $A_{-1}$  is less than  $10^{16.4} \text{ s}^{-1}$ . That value is already somewhat low compared to the  $A$  factor for nitric acid decomposition of  $\sim 10^{18.7} \text{ s}^{-1}$ , which should be the smaller.  $A_{-1}$  could be increased by increasing  $A_1$ ; however, that would then make  $A_1$  larger than the  $A$  factor for combination of OH and  $\text{NO}_2$  radicals, which is unlikely. It is possible that our entropy estimate for pernitric acid is too large, from the nature of the estimate it is most

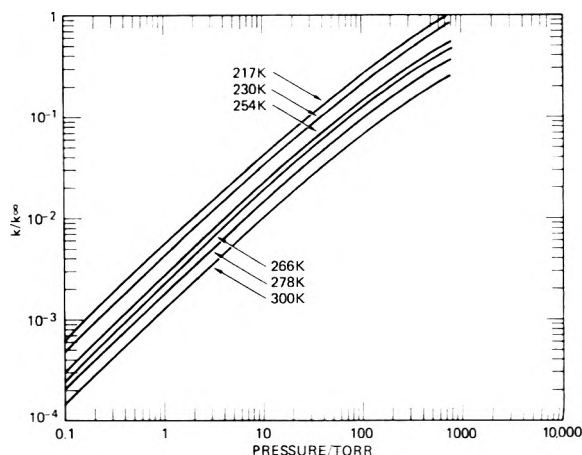


**Figure 3.**  $\text{HO}_2\text{NO}_2$  decomposition rate constants. The pressure and temperature dependence of the rate constants for the decomposition of  $\text{HO}_2\text{NO}_2$ :  $k_\infty = A_\infty(300) \exp(-E_\infty(300)/RT)$ ;  $k_\infty = 10^{16.43} \exp(-23.0/RT)$ .

unlikely to be too small; that would yield a larger value of  $A_{-1}$ . Taking a reasonable minimum value of  $S^\circ(\text{HO}_2\text{NO}_2)$  of 69.0 eu gives  $A_{-1} = 10^{17.0} \text{ s}^{-1}$  with  $A_1 = 10^{9.5} \text{ M}^{-1} \text{ s}^{-1}$ . To fit the low-pressure data, this requires  $E_{-1} = 27.0 \text{ kcal mol}^{-1}$ . However, the rate at 1 atm then differs from the measurement by at least a factor of 10. Therefore, those parameters seem to be a unique set, assuming that  $A_1$  cannot be any larger.

The values of the hindrance parameter used, from 98% at 300 K to 92% at 217 K, show the expected variation with temperature. However, the values are much larger at moderate temperatures than in our previous study of the decomposition of nitric acid. As yet, there are too few data to allow meaningful conclusions to be drawn from the size of the hindrance parameter. Further studies may be able to correlate the hindrance parameter with some physical properties of the system.

Figure 3 shows a plot of  $k/k_\infty$  for the decomposition reaction over the temperature and pressure range needed for atmospheric modeling. The hindrance parameters at temperatures for which no experimental data are available were estimated by linear extrapolation of the higher temperature values, which should be sufficiently accurate over the small ( $\sim 35^\circ$ ) temperature range. It should be noted that  $k_\infty$  in this case is calculated at any temperature using the high-pressure Arrhenius parameters at 300 K.

## Conclusions

Experimental data for the decomposition of pernitric acid, and the reverse radical combination reaction, are available only under widely disparate conditions. The application of RRKM theory has enabled us to arrive at a unique set of high-pressure Arrhenius parameters that are consistent with known thermochemistry and the experimental results. The theory has then been used to predict the pressure and temperature dependence of the reaction over a range of conditions appropriate to atmospheric modeling. That approach has demonstrated the utility of RRKM theory in comparing data on pressure sensitive reactions, and its ability to generalize the pressure, and temperature dependence from a limited set of data.

In applying RRKM theory, we have used a hindered rotational Gorin model for the transition state. That method offers several advantages over conventional vibrational models in that it can reproduce the observed temperature dependence of high pressure  $A$  factors, and that it offers a transition state involving only one empirical



parameter at each temperature. When further studies are available, it may be possible to make an a priori prediction of that parameter based on the physical properties of the system.

**Acknowledgment.** Discussions with Dr. D. G. Hendry (SRI International) concerning the pertinence of this work to atmospheric modeling were very helpful. We also thank C. J. Howard, R. A. Graham, A. M. Winer, and J. N. Pitts, Jr., for allowing us to quote their experimental results prior to publication.

## References and Notes

- (1) H. Niki, P. D. Maker, C. M. Savage, and L. P. Breitenbach, *Chem. Phys. Lett.*, **45**, 564 (1977).
- (2) R. Simonaitis and J. Heicklen, *J. Phys. Chem.*, **80**, 1 (1976).
- (3) C. J. Howard, *J. Chem. Phys.*, in press.
- (4) R. A. Graham, A. M. Winer, and J. N. Pitts, Jr., *Chem. Phys. Lett.*, **51**, 215 (1977).

- (5) S. W. Benson and D. M. Golden in "Physical Chemistry; An Advanced Treatise", Vol. VII, H. Eyring, D. Hendersen, and W. Jost, Ed., Academic Press, New York, N.Y., 1975.
- (6) D. M. Golden and G. P. Smith, *Int. J. Chem. Kinet.*, in press.
- (7) C. Anastasi and I. W. M. Smith, *J. Chem. Soc., Faraday Trans. 2*, **72**, 1459 (1976).
- (8) C. J. Howard and K. M. Evenson, *Geophys. Res. Lett.*, **4**, 437 (1977).
- (9) L. Batt, R. T. Milne, and R. D. McCullough, *Int. J. Chem. Kinet.*, **9**, 567 (1977).
- (10) D. R. Stull, E. F. Westrum, and G. C. Sinke, "The Chemical Thermodynamics of Organic Compounds", Wiley, New York, N.Y., 1969.
- (11) S. W. Benson, "Thermochemical Kinetics", Wiley, New York, N.Y., 1976.
- (12) D. G. Hendry and R. Kenley, *J. Am. Chem. Soc.*, **99**, 3198 (1977).
- (13) R. A. Cox and M. J. Roffey, *Environ. Sci. Technol.*, **11**, 900 (1977).
- (14) E. V. Waage and B. S. Rabinovitch, *Chem. Rev.*, **70**, 377 (1974).
- (15) S. E. Stein and B. S. Rabinovitch, *J. Chem. Phys.*, **58**, 2438 (1972).
- (16) "JANAF Thermochemical Tables", *Natl. Stand. Ref. Data Ser., Natl. Bur. Stand.*, No. 37 (1970).
- (17) This, in fact, violates the principal of conservation of angular momentum. Calculations in which the rotation was adiabatic change the final results by less than a factor of 2.
- (18) J. Troe, *J. Chem. Phys.*, **66**, 4745 (1977).

## Kinetic Studies of Complexation of Divalent Strontium, Barium, Lead, and Mercury Cations by Aqueous 15-Crown-5 and 18-Crown-6

Licesio J. Rodríguez,<sup>1a</sup> Gerard W. Liesegang,<sup>1b</sup> Michael M. Farrow,<sup>1b</sup> Neil Purdie,<sup>1c</sup> and Edward M. Eyring<sup>\* 1b</sup>

Department of Chemistry, University of Utah, Salt Lake City, Utah 84112 (Received June 24, 1977; Revised Manuscript Received October 27, 1977)

Publication costs assisted by the Office of Naval Research and the Air Force Office of Scientific Research

The rates of complexation-decomplexation of the 15-crown-5 [1,4,7,10,13-pentaoxacyclopentadecane] and 18-crown-6 [1,4,7,10,13,16-hexaoxacyclooctadecane] complexes of the aqueous cations  $\text{Sr}^{2+}$ ,  $\text{Ba}^{2+}$ ,  $\text{Pb}^{2+}$ , and  $\text{Hg}^{2+}$  have been determined from ultrasonic absorption measurements covering the 15–205-MHz frequency range at 25 °C. As in the case of previously reported studies of complexation of monovalent cations by these crown ethers, the data have been fitted to a two-step mechanism. Diffusion has been ruled out as the rate-limiting step in the complexation. Loss of the coordinated water from the ions is proposed as the rate-determining step.

## Introduction

Interest in the solution chemistry of the synthetic macrocyclic polyethers has increased greatly since their introduction by Pedersen,<sup>2</sup> stimulated by the many chemical and biological applications of these ligands as complexing and transport agents for metal ions.

In a previous kinetic investigation<sup>3</sup> of the complexation equilibria between monovalent metal ions and the crown ethers Chock proposed a mechanistic scheme involving a ligand conformational rearrangement followed by the stepwise substitution of the coordinated solvent molecules by the ligand. Kinetic studies in this laboratory<sup>4–6</sup> of aqueous monovalent metal ion and ammonium ion complexation by 18-crown-6 and 15-crown-5 have confirmed the existence of at least one conformational rearrangement equilibrium for each of the ligands. Furthermore, one conformer strongly predominates in each such conformational equilibrium; the predominant form is involved in the metal ion complexation equilibrium; and complexation is not diffusion controlled.

The kinetics of the complexation equilibria involving these same crown ethers with some divalent metal ions is considered here. If loss of coordinated water is rate limiting then complexation rates should be slower for

divalent ions compared to monovalent ions. In making our choice of divalent ions, two with inert gas configurations,  $\text{Sr}^{2+}$  and  $\text{Ba}^{2+}$ , and two ions with nonspherical coordinations,  $\text{Pb}^{2+}$  and  $\text{Hg}^{2+}$ , were selected. By analogy with the results for monovalent ions where faster complexation rates were observed for nonspherically coordinated  $\text{Ag}^+$  and  $\text{Tl}^+$  ions, the rates of complexation of  $\text{Pb}^{2+}$  and  $\text{Hg}^{2+}$  by the polyethers might be anticipated to be greater than those for  $\text{Sr}^{2+}$  and  $\text{Ba}^{2+}$ . If such were the case, we would have additional evidence for water loss as the rate-limiting step in the mechanism.

## Experimental Section

Ultrasonic absorption measurements were made at 25.0 ± 0.1 °C over an acoustic frequency range from 15 to 205 MHz, using a computer-controlled laser acoustooptic technique.<sup>7</sup> The argon ion laser was operated at the 514.5-nm green line and the piezoelectric acoustic transducer element was a gold-plated, 5-MHz frequency, X-cut quartz crystal which was driven at odd harmonics over the frequency range.

Additional low-frequency measurements were made on aqueous solutions of  $\text{BaCl}_2$  with 15-crown-5 using resonance ultrasonic absorption techniques.

TABLE I: Relaxation Parameters from Computer Analysis for Complexation by 15-Crown-5<sup>a</sup> Strontium

[SrCl <sub>2</sub> ] <sub>0</sub> , <sup>b</sup> M	[15-Crown-5] <sub>0</sub> , <sup>b</sup> M	f <sub>R,II</sub> , MHz	10 <sup>17</sup> A, Np cm <sup>-1</sup> s <sup>2</sup>	10 <sup>18</sup> rms <sup>c</sup>
1.00	0.0377	9.95	157.9	1.0
1.51	0.0377	14.09	82.37	1.3
1.82	0.0797	18.33	48.89	1.0

Barium<sup>d</sup>

[BaCl <sub>2</sub> ] <sub>0</sub> , M	[15-Crown-5] <sub>0</sub> , M	f <sub>R,II</sub> , MHz	10 <sup>17</sup> A, Np cm <sup>-1</sup> s <sup>2</sup>	10 <sup>18</sup> rms
0.756	0.0640	12.15	144	1.5
0.886	0.0364	15.92	126.7	2.5
1.01	0.0360	19.64	84.5	2.3

## Lead(II)

[Pb(ClO <sub>4</sub> ) <sub>2</sub> ] <sub>0</sub> , M	[15-Crown-5] <sub>0</sub> , M	f <sub>R,II</sub> , MHz	10 <sup>17</sup> A, Np cm <sup>-1</sup> s <sup>2</sup>	10 <sup>18</sup> rms
0.413	0.0783	19.72	69.17	1.2
0.516	0.130	20.80	83.87	1.8
0.688	0.0877	31.19	32.92	0.9

## Mercury(II)

[Hg(ClO <sub>4</sub> ) <sub>2</sub> ] <sub>0</sub> , M	[15-Crown-5] <sub>0</sub> , M	f <sub>R,II</sub> , MHz	10 <sup>17</sup> A, Np cm <sup>-1</sup> s <sup>2</sup>	10 <sup>18</sup> rms
0.590	0.114	14.97	759.3	2.3
0.871	0.111	18.91	572.1	2.3
1.15	0.107	26.20	287.1	1.9

<sup>a</sup> All symbols as defined in the text. <sup>b</sup> The subscript zero on concentration denotes total concentration. <sup>c</sup> Root mean square deviation. <sup>d</sup> Barium results based on resonance ultrasonic absorption measurements in the ~0.9- to ~4-MHz frequency range as well as on higher frequency acoustooptic data.

Solutions were prepared using deionized redistilled water. The 15-crown-5 and 18-crown-6 (Parish Chemical Co., Provo, Utah) were purified as described previously.<sup>4,6</sup> The inorganic ions were all analytical reagent grade. Strontium and barium ions were in the form of chloride salts and stock solutions were prepared by weight. The lead and mercury ions were introduced as perchlorates. These latter stock solutions were standardized either gravimetrically (PbSO<sub>4</sub>)<sup>8</sup> or titrimetrically (Hg(CNS)<sub>2</sub>).<sup>9</sup>

## Results

Total sound absorption data, expressed as  $(\alpha/f^2)_T$  Np cm<sup>-1</sup> s<sup>2</sup> (see paragraph at end of text regarding supplementary material), were analyzed in terms of relaxational and nonrelaxational contributions to the ultrasonic absorptions. In all cases only one relaxational process was detected. The best fit was obtained using the following one-relaxation equation:

$$(\alpha/f^2)_T = A[1 + (f/f_R)^2]^{-1} + B$$

where  $A$  is the relaxation amplitude,  $f$  and  $f_R$  are respectively the experimental ultrasonic and relaxational frequencies, and  $B$  is the solvent absorption, which was varied in the fitting process around the pure water value to take account of the structural changes in the solvent brought about by the added electrolyte. However, if the final best  $B$  value was in the range  $21.7 \pm 0.5 \times 10^{-17}$  Np cm<sup>-1</sup> s<sup>2</sup>, that of the pure water obtained on the present equipment, the central value  $21.7 \times 10^{-17}$  Np cm<sup>-1</sup> s<sup>2</sup> was used in the fit as a fixed parameter. Representative plots of experimental data for Ba<sup>2+</sup> and 15-crown-5 are shown

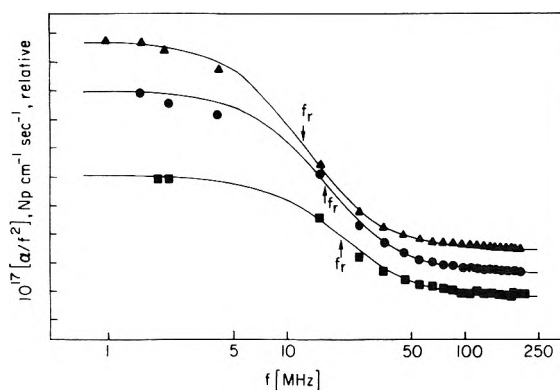


Figure 1. Plot of ultrasonic absorption, expressed as  $\alpha/f^2$ , vs. logarithm of the experimental frequency for aqueous solutions of BaCl<sub>2</sub> plus 15-crown-5. Experimental points are as follows:  $\blacktriangle$  for [Ba<sup>2+</sup>]<sub>0</sub> = 0.756 M, [15-crown-5]<sub>0</sub> = 0.064 M;  $\bullet$  for [Ba<sup>2+</sup>]<sub>0</sub> = 0.886 M, [15-crown-5]<sub>0</sub> = 0.0864 M;  $\blacksquare$  for [Ba<sup>2+</sup>]<sub>0</sub> = 1.01 M, [15-crown-5]<sub>0</sub> = 0.0860 M. The curves are computer calculated, nonlinear, least-squares fits of the experimental data. For clarity, the curves are arbitrarily displaced vertically; all have the same high-frequency asymptote of  $21.7 \times 10^{-17}$  Np cm<sup>-1</sup> s<sup>-1</sup>. The vertical amplitudes are as given in Table I. Data points at  $f < 10$  MHz were obtained by a resonance technique.

TABLE II: Relaxation Parameters from Computer Analysis for Complexation by 18-Crown-6<sup>a</sup> Strontium

[SrCl <sub>2</sub> ] <sub>0</sub> , M	[18-Crown-6] <sub>0</sub> , M	f <sub>R,II</sub> , MHz	10 <sup>17</sup> A, Np cm <sup>-1</sup> s <sup>2</sup>	10 <sup>18</sup> rms
1.00	0.100	10.82	89.00	2.1
1.40	0.100	17.12	64.70	1.4
1.89	0.0920	20.97	46.25	1.1

## Barium

[BaCl <sub>2</sub> ] <sub>0</sub> , M	[18-Crown-6] <sub>0</sub> , M	f <sub>R,II</sub> , MHz	10 <sup>17</sup> A, Np cm <sup>-1</sup> s <sup>2</sup>	10 <sup>18</sup> rms
1.00	0.100	19.19	39.48	1.7
1.30	0.100	24.76 (b)	25.14	1.2
1.50	0.100	28.10 (c)	21.99	1.1

## Lead(II)

[Pb(ClO <sub>4</sub> ) <sub>2</sub> ] <sub>0</sub> , M	[18-Crown-6] <sub>0</sub> , M	f <sub>R,II</sub> , MHz	10 <sup>17</sup> A, Np cm <sup>-1</sup> s <sup>2</sup>	10 <sup>18</sup> rms
0.242	0.0134	11.50 (d)	45.94	0.9
0.323	0.0179	16.37 (d)	30.92	0.5
0.430	0.0238	21.69 (e)	23.43	0.5

## Mercury (II)

[Hg(ClO <sub>4</sub> ) <sub>2</sub> ] <sub>0</sub> , M	[18-Crown-6] <sub>0</sub> , M	f <sub>R,II</sub> , MHz	10 <sup>17</sup> A, Np cm <sup>-1</sup> s <sup>2</sup>	10 <sup>18</sup> rms
0.354	0.0400	21.80	71.28	1.0
0.472	0.0450	28.51	58.39	1.1
0.590	0.0500	32.55	55.76	1.2

<sup>a</sup> A background of (b)  $23.0 \times 10^{-17}$ , (c)  $22.7 \times 10^{-17}$ , (d)  $20.6 \times 10^{-17}$ , (e)  $20.2 \times 10^{-17}$  Np cm<sup>-1</sup> s<sup>2</sup> give the best fit to the experimental data.

in Figure 1. For clarity the data sets have been displaced vertically relative to each other; all have the same  $\alpha/f^2$  in the limit of high frequencies ( $>250$  MHz).

Tables I and II show the parameters calculated at different concentrations of crowns and metal ions which give the best fit of the experimental data. The resulting values of the relaxation frequencies,  $f_R$ , are in some cases below the lower limit of the experimental frequency range scanned with the present equipment. For several of these sample solutions complementary measurements were made<sup>10</sup> on resonance ultrasonic spectrometers in the ~0.5-

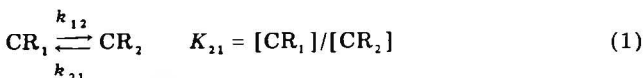
TABLE III: Rate Constants for Complexation by 15-Crown-5 and 18-Crown-6 in Aqueous Solution at 25 °C Calculated from Ultrasonic Absorption Data

Cation	15-Crown-5			18-Crown-6		
	$k_{23}, M^{-1} s^{-1}$	$k_{32}, s^{-1}$	$K_T, M^{-1}$	$k_{23}, M^{-1} s^{-1}$	$k_{32}, s^{-1}$	$K_T, M^{-1}$
Sr <sup>2+</sup>	$6.5 \times 10^7$	$7.3 \times 10^5$	89.1	$7.7 \times 10^7$	$1.5 \times 10^5$	$5.25 \times 10^2$
Ba <sup>2+</sup>	$1.2 \times 10^8$	$2.3 \times 10^6$	51.3	$1.3 \times 10^8$	$1.7 \times 10^4$	$7.41 \times 10^3$
Pb <sup>2+</sup>	$3.2 \times 10^8$	$4.6 \times 10^6$	70.8	$3.3 \times 10^8$	$1.8 \times 10^4$	$1.86 \times 10^4$
Hg <sup>2+</sup>	$1.6 \times 10^8$	$3.3 \times 10^6$	47.9	$4.0 \times 10^8$	$1.5 \times 10^6$	$2.63 \times 10^3$

<sup>a</sup> Izatt et al., ref 11.

to ~5-MHz frequency range. Discrepancies greater than a factor of 2 were noted in the absorption amplitudes for some of the strontium-15-crown-5 solutions. Other solutions gave generally better agreement between the two methods. Practically the same relaxation frequencies,  $f_R$ , were found from the composite ultrasonic data as were found originally in the laser acoustooptic measurements at Utah. By comparing the analysis of only the higher frequency acoustooptic data with the analysis of the composite data including the low frequency resonance results, an average maximum error of  $\pm 14\%$  in  $f_R$  was established for the three Ba<sup>2+</sup> and 15-crown-5 data sets (Figure 1). Since these three data sets show relaxation frequencies which might be considered to be at the lower analysis limit of the equipment in this laboratory, the value of ~14% error in  $f_R$  was used to estimate errors in the computed rate constants. This ~14% error in  $f_R$  gives rise to an uncertainty in the complexation rate constant  $k_{23}$  (determined graphically from a plot of eq 6) of the same magnitude. Since none of the calculations or conclusions in this paper are based on the ultrasonic absorption amplitudes, uncertainties in their magnitudes are irrelevant to the present discussion.

Earlier studies in this laboratory of the complexation kinetics of monovalent metal ions by 15-crown-5 and 18-crown-6 were interpreted<sup>4-6</sup> in terms of a two-step mechanism (eq 1 and 2) previously suggested by Chock<sup>3</sup>



for the case of metal ion complexation by dibenzo-30-crown-10 in methanol. Although the relaxation time of the conformational step was not measured in Chock's study, a concentration independent relaxation frequency for pure crown in aqueous solutions has been reported for both 15-crown-5<sup>6</sup> ( $f_{R,1} = 22.9$  MHz) and 18-crown-6<sup>4</sup> ( $f_{R,1} = 101$  MHz). Accordingly it seems reasonable to expect that a two relaxation process should be observed when complexing electrolytes are present. The above reaction scheme is mathematically described by the secular determinant in eq 3 where  $\lambda_i = 1/\tau_i$ , and the extent of

$$\begin{vmatrix} k_{12} + k_{21} - \lambda & -k_{21} \\ -k_{23}[M^{n+}] & k_{23}([M^{n+}] + [CR_2]) + k_{32} - \lambda \end{vmatrix} = 0 \quad (3)$$

coupling is determined by the terms  $-k_{21}$  and  $-k_{23}[M^{n+}]$ . In the case of complexation of monovalent cations by 15-crown-5, the analysis of the normal reactions and their amplitude factors showed that coupling does not exist since  $k_{21} \ll k_{12}$  and the amplitude of the conformational step is negligibly small compared to that of the complexing step. In the 18-crown-6 case,  $\tau_1^{-1}$  is sufficiently greater than  $\tau_{II}^{-1}$  that coupling between the steps is insignificant and only

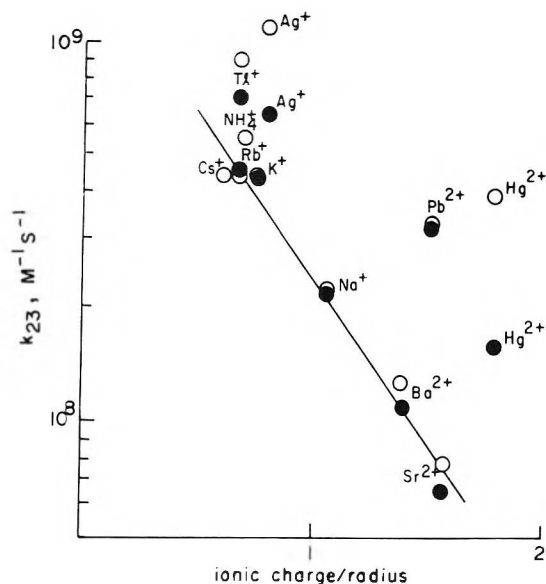


Figure 2. Plot of the logarithm of the rate constant for complexation,  $k_{23}$ , vs. the ratio of ionic charge to ionic radius (arbitrary units) for complexation by 18-crown-6, O, and by 15-crown-5, ●. The straight diagonal line is a least-squares fit of the alkali and alkaline earth metal data.

one relaxation is observed when electrolytes are present.<sup>5</sup> For the divalent ions, therefore, an analogous two-step mechanism is to be expected with the second step having the larger amplitude and thus giving rise to the detected relaxation. Consequently, the analysis of the kinetic data is made in terms of contributions from only this step, i.e.

$$\tau_{II}^{-1} = k_{23}([CR_2] + [M^{2+}]) + k_{32} \quad (4)$$

The experimental equilibrium concentrations can be calculated from the equilibrium constants for the overall complexation  $K_T$ , reported by Izatt et al.<sup>11</sup> in the form

$$K_T = [CR_2 M^{2+}]/([CR_1] + [CR_2])[M^{2+}] \quad (5)$$

Taking into account the fact that  $[CR_2] \gg [CR_1]$  since we have found<sup>12</sup> for both 15-crown-5 and 18-crown-6  $K_{21} \ll 1$ , then  $CR_2 \approx CR_T$  in eq 4 and so eq 4 can be arranged as

$$\tau_{II}^{-1} = k_{23}([CR_T] + [M^{2+}] + K_T^{-1}) \quad (6)$$

and  $k_{32}$  can subsequently be calculated from

$$k_{32} = k_{23}/K_T \quad (7)$$

In all cases the experimental kinetic data give an acceptable fit to eq 6. Table III shows the calculated  $k_{23}$  and  $k_{32}$  values obtained for the complexation of Sr<sup>2+</sup>, Ba<sup>2+</sup>, Pb<sup>2+</sup>, and Hg<sup>2+</sup> by 15-crown-5 and 18-crown-6 following this procedure.

## Discussion

To add perspective to the kinetic results from the current work, data from previous studies<sup>4-6</sup> on monovalent

ions have been added to Figure 2, which is a plot of the logarithm of  $k_{23}$  vs. the ratio of ion charge to ion size. There is an obvious separation between the ions with noble gas electronic configurations and the group of ions of the post transition elements. The observed linear dependence of  $\log k_{23}$  for the first group is consistent with the decrease in charge density with increasing ionic size, and the increasing relative ease with which coordinated water is lost.

The observed rate constants  $k_{23}$  for complexation, Table III, may be compared with the rate constants<sup>13</sup> for substitution of water molecules from the inner coordination sphere of metal ions,  $k_0$ . All that is required is an estimate of the stability constant for outer sphere complex formation,  $K_0$ , in the relation

$$k_{23} = K_0 k_{\text{ex}} \quad (8)$$

We estimate<sup>14</sup> a value of  $K_0 = 0.32 \text{ M}^{-1}$ . Thus for  $\text{Ba}^{2+}$  and 18-crown-6  $k_{23} = 1.3 \times 10^8 \text{ M}^{-1} \text{ s}^{-1}$  would correspond to a  $k_{\text{ex}} = 4 \times 10^8 \text{ s}^{-1}$  that is smaller than the solvent substitution rate constant  $k_0 \sim 2 \times 10^9 \text{ s}^{-1}$  reported by Winkler.<sup>13</sup> The other two cations,  $\text{Sr}^{2+}$  and  $\text{Hg}^{2+}$ , for which Winkler reports solvent substitution rate constants, follow the same trend although in the case of mercury and 18-crown-6  $k_{\text{ex}} = 1.3 \times 10^9 \text{ s}^{-1}$  is almost as large as  $k_0 \sim 2 \times 10^9 \text{ s}^{-1}$ .

Since we have not found a value of  $k_0$  for  $\text{Pb}^{2+}(\text{aq})$  in the recent literature, we are not able to make the same sort of comparison of  $k_{\text{ex}}$  and  $k_0$  for this ion. However, it may prove useful to others to assume that our  $k_{\text{ex}} = 1.0 \times 10^9 \text{ s}^{-1}$  is only slightly smaller than the solvent exchange rate constant,  $k_0$ , for this ion.

There is no apparent dependence of the rates of complexation on the "hole" dimensions of the ligands. Variations in overall stability constants have already been related to parallel variations in  $k_{32}$  for either ligand.<sup>4-6</sup> A dependence on ring dimensions is observed<sup>4-6</sup> for decomplexation rates for all ions. The smaller ring separates faster than the larger ring, which is indicative of a greater conformational strain on the 15-crown-5 when it complexes.

Complexation rates for the transition and post transition metal ions differ in two ways from the rates for the noble gas configuration ions. They are all larger in magnitude (Figure 2) and except for  $\text{Pb}^{2+}$  they show a distinct ligand dependence. A possible interpretation of the increased rate is that in the progressive substitution process fewer solvent molecules are lost. Also if the loss of coordinated water molecules other than the first is rate limiting, the rate of complexation could be enhanced by directional influences

through the hybridization network of these ions. Silver(I) and mercury(II) ions demonstrate the greatest dependence of  $k_{23}$  on the ligand. These ions commonly hybridize in sp geometry. A trans-directing influence, i.e., covalent bonding, of the coordinated ligand might enhance the rate of second substitution.<sup>15</sup> At the same time the ligand would undergo considerable conformational strain to accommodate itself to the linear geometry of the metal. Again the strain would be greater for the smaller and inherently more rigid 15-crown-5 polyether thus accounting for the slower complexation rate with this ligand.

*Acknowledgment.* This work was sponsored by a contract from the Office of Naval Research, by Grant No. AFOSR 77-3255 from the Directorate of Chemical Sciences, Air Force Office of Scientific Research, and by Biomedical Research Support Grant RR-07092 from the General Research Support Branch, National Institutes of Health. L.J.R., on leave from the University of Salamanca, was supported by a stipend from the Commission for Cultural Exchange between the U.S. and Spain. Roger K. Burnham assisted with the calculations.

*Supplementary Material Available:* Raw ultrasonic absorption data (8 pages). Ordering information is available on any current masthead page.

## References and Notes

- (1) (a) On leave from University of Salamanca, Salamanca, Spain, (b) University of Utah, (c) Oklahoma State University.
- (2) C. J. Pedersen, *J. Am. Chem. Soc.*, **89**, 707 (1967).
- (3) P. B. Chock, *Proc. Natl. Acad. Soc. U.S.A.*, **69**, 1939 (1972).
- (4) G. W. Liesegang, M. M. Farrow, N. Purdie, and E. M. Eyring, *J. Am. Chem. Soc.*, **98**, 6905 (1976).
- (5) G. W. Liesegang, M. M. Farrow, F. A. Vazquez, N. Purdie, and E. M. Eyring, *J. Am. Chem. Soc.*, **99**, 3240 (1977).
- (6) L. J. Rodriguez, G. W. Liesegang, R. D. White, M. M. Farrow, N. Purdie, and E. M. Eyring, *J. Phys. Chem.*, **81**, 2118 (1977).
- (7) M. M. Farrow, S. Olsen, N. Purdie, and E. M. Eyring, *Rev. Sci. Instrum.*, **47**, 657 (1976).
- (8) I. M. Kolthoff and P. J. Elving, Ed., "Treatise on Analytical Chemistry", Part II, Vol. 6, Interscience, New York, N.Y., 1964.
- (9) Reference 8, Part II, Vol. 3, 1961.
- (10) Dr. Raoul Zana in Strasbourg, France and Dr. Robert D. White in Moscow, Idaho graciously permitted E.M.E. to make these duplicate measurements on their equipment.
- (11) R. M. Izatt, R. E. Terry, B. L. Haymore, L. D. Hansen, N. K. Dalley, A. G. Avondet, and J. J. Christensen, *J. Am. Chem. Soc.*, **98**, 7620 (1976).
- (12) G. W. Liesegang, M. M. Farrow, L. J. Rodriguez, R. K. Burnham, E. M. Eyring, and N. Purdie, *Int. J. Chem. Kinet.*, in press.
- (13) R. Winkler, *Struct. Bonding*, **10**, 1 (1972).
- (14) R. M. Fuoss, *J. Am. Chem. Soc.*, **80**, 5059 (1958).
- (15) M. M. Farrow, N. Purdie, and E. M. Eyring, *Inorg. Chem.*, **14**, 1584 (1975).

## Reactions of the Radical Cations of Methylated Benzene Derivatives in Aqueous Solution

K. Sehested\* and J. Holcman

Accelerator Department, Risø National Laboratory, DK-4000 Roskilde, Denmark (Received August 8, 1977)

Publication cost assisted by Risø National Laboratory

The radical cations of methylated benzene decompose in acid solution into the corresponding methylbenzyl radical and a proton. The rate constant for this reaction decreases by three orders of magnitude as the number of methyl groups increases from one to five. The rate constants can be correlated with the ionization potential of the parent compound. In neutral solution the reverse reaction to the acid-catalyzed OH adduct conversion occurs and the radical cations react with water to form the OH adduct. In slightly alkaline solution the radical cations of the higher methylated benzenes ( $n \geq 3$ ) react with hydroxide ions forming the OH adduct.

In our previous paper<sup>1</sup> we reported on the OH-radical induced formation of radical cations of methylated benzenes in aqueous acidic and neutral solution. The precursor of the radical cation in acid media is the OH adduct, whereas the cation is formed directly in a reaction with  $\text{SO}_4^-$  radical anions in neutral solution. The dependency of ionic strength of some reactions of the radical cations demonstrated the unit positive charge of the species. The present report describes the proton loss reaction and the reactions with water and hydroxide ions. Some considerations of the reverse reactions are also included.

### Acid Solution

The radical cations decay in acid solution by first-order kinetics independent of solute and acid concentration up to 0.5 M acid. The product of the decay is exclusively the corresponding methylbenzyl radical (reaction 1). In acid



solution all the OH radicals yield methylbenzyl radicals, mainly through the conversion of the OH adduct via the radical cation, but with a small contribution from the direct attack on a methyl group.<sup>2</sup>

The rate constant for this conversion was previously determined by measuring the rate of the formation of the methylbenzyl radicals<sup>2</sup> as the existence of the radical cation as an intermediate species was not established yet. The formation of the radical cation from the OH adduct was demonstrated<sup>1</sup> to be a result of the reaction of the hydroxycyclohexadienyl radicals with hydrogen ions (reaction 2). The rate constant for this reaction is  $(1.5 \pm 0.5) \times 10^9$



$\text{M}^{-1}\text{s}^{-1}$  irrespective of the compound. The appearance of the radical cation in acid media, however, is governed by the rate of reaction, in which the radical cation reacts with water yielding the OH adduct (reverse of reaction 2).

The rate constants for the decay of the radical cations in reaction 1 were determined in  $10^{-3}$  to 1 M  $\text{HClO}_4$ , Ar or  $\text{O}_2$  saturated solution. These rate constants (Table I) agree with those measured for the buildup of the methylbenzyl radicals ( $k_2$  in ref 2) for compounds substituted with three or less methyl groups. For the higher methylated benzenes (four or five methyl groups) the rate of the decay of the cation is slower than the previously measured rate of buildup of the methylbenzyl radicals. This overestimation of the buildup rate may be due to the

low rate of reaction of the solute with the primary radicals because of the low solubility of the compounds together with a fairly high direct formation, up to 30%, of the corresponding methylbenzyl radicals. The rate constant for reaction 1 varies three orders of magnitude from one to five methyl substituents.

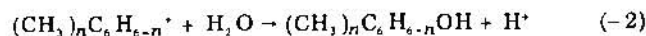
As the Hammett substituent constants for most of these compounds are not available, the rate constants,  $k_1$ , are correlated with the adiabatic ionization potential of the parent compound (Figure 1). The ionization potential is primarily determined by the energy of the highest occupied molecular orbital and Rao<sup>3</sup> has shown a linear relationship between the ionization potential and the Hammett substituent constants for disubstituted benzenes, where only little or no steric effects due to substituents are operative. No appreciable steric effect is expected from the methyl groups in the studied compounds thus the substituent effect is primarily of electronic nature.

At even higher acid concentrations, 1–8 M  $\text{HClO}_4$ , the  $k_1$ 's become successively lower, e.g., the rate for the *p*-xylene radical cation is lowered by an order of magnitude in going from 1 to 5 M acid. Accordingly we tried to detect the reverse reaction (-1), i.e., a protonation of the methylbenzyl radical. It was not possible to observe this reaction up to 5 M acid neither with methylbenzyl radicals produced by an H atom reaction with some methylbenzyl chloride compounds nor in the case where the direct formation of methylbenzyl radicals exceed 25% (high methylated compounds).

### Neutral Solution

As mentioned in our recent paper<sup>1</sup> the radical cations decay faster in neutral than in acid solution. Contrary to acid media, where the cations decay exclusively into the methylbenzyl radicals, the decay in neutral solution yields the OH adduct and the methylbenzyl radical. The rates of decay are independent of solute concentrations, which excludes a reaction with the parent hydrocarbon as is the case with anisole.<sup>4</sup> There is no indication of a radical-radical dimerization since the decay is strictly first order, independent of dose rate.

We ascribe these results to a reaction of radical cations with water in competition with reaction (1):



This reaction is analogous to that proposed for other aromatic radical cations.<sup>5</sup> Reaction -2 is the reverse of reaction 2. It was studied in electron irradiated Ar-sat-

TABLE I: Rate Constants for the Methylated Benzene Radical Cation Reactions in Aqueous Solution

	Proton loss reaction, $k_1$ , $s^{-1}$	Methylbenzyl radical, <sup>a</sup> %	Reaction with $H_2O$ , $k_{-2}$ , $M^{-1} s^{-1}$	Reaction with $OH^-$ , $k_3$ , $M^{-1} s^{-1}$
Toluene	$1.0 \pm 0.5 \times 10^7$	< 5	$> 2 \times 10^7$	
<i>o</i> -Xylene	$2.0 \pm 0.5 \times 10^6$	~ 10	$8 \pm 4 \times 10^5$	
<i>m</i> -Xylene	$2.0 \pm 0.5 \times 10^6$	~ 5	$1.5 \pm 0.5 \times 10^6$	
<i>p</i> -Xylene	$1.4 \pm 0.2 \times 10^6$	~ 10	$5.0 \pm 2.0 \times 10^5$	
Mesitylene	$1.5 \pm 0.2 \times 10^6$	~ 5	$1.0 \pm 0.5 \times 10^6$	
Hemimillitene	$1.5 \pm 0.3 \times 10^6$	40	$5.0 \pm 2.0 \times 10^4$	$\sim 1 \times 10^{10}$
Pseudocumene	$2.0 \pm 0.2 \times 10^5$	60	$3.0 \pm 1.0 \times 10^3$	$3.5 \pm 0.5 \times 10^9$
Isodurene	$1.0 \pm 0.2 \times 10^5$	65	$1.0 \pm 0.3 \times 10^3$	$1.2 \pm 0.2 \times 10^9$
Prehnitene	$2.5 \pm 0.2 \times 10^5$	~ 90	$4 \pm 2 \times 10^2$	$6.0 \pm 1.0 \times 10^8$
Durene	$2.7 \pm 0.5 \times 10^4$	> 95	$6 \pm 2$	$1.5 \pm 0.3 \times 10^8$
Pentamethylbenzene	$1.6 \pm 0.3 \times 10^4$	> 95	< 4	$1.0 \pm 0.2 \times 10^8$

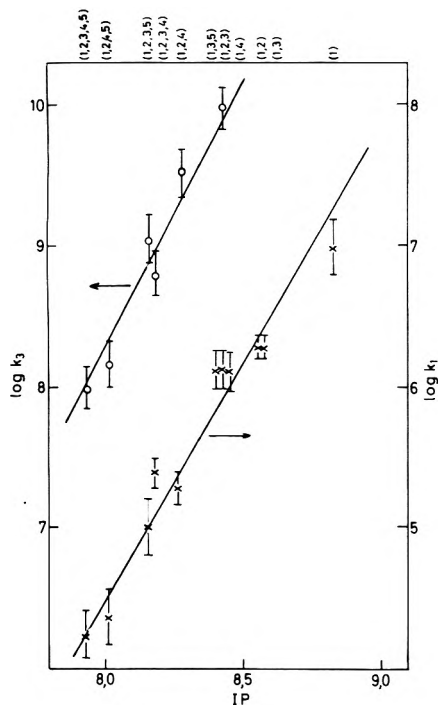
<sup>a</sup> See text.

Figure 1. Rate constants for the reactions 1 (X) and 3 (O) as a function of the adiabatic ionization potential of the parent compounds.

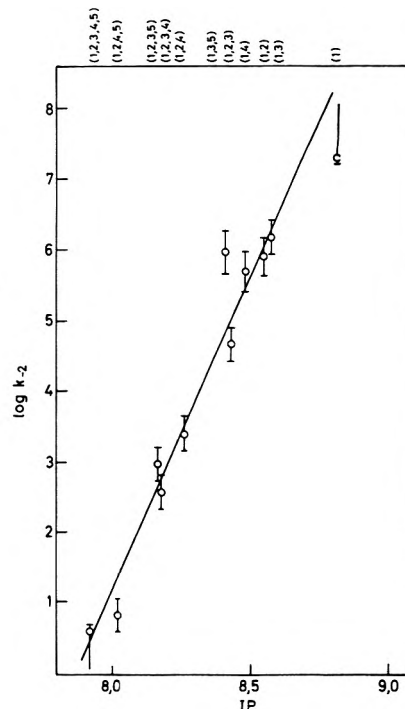


Figure 2. Rate constants of the reaction -2 as function of the adiabatic ionization potential of the parent compounds.

urated neutral solution containing persulfate by producing the radical cations in a reaction of  $SO_4^-$  radicals with the substrate. From the radical cation decay data we can derive  $k_{-2}$  under the assumption that  $k_1$  is the same in neutral as in moderate acid solution. Only the  $k_{-2}$ 's for the higher methylated compounds ( $n \geq 3$ ) can be determined in this way, as the decay of the lower methylated compounds ( $n = 1$  or 2) is either too fast to be measured (toluene and *m*-xylene) or the cation radical spectrum overlaps the original spectrum of the  $SO_4^-$  anion radical ( $\lambda_{max}$  450 nm), which prohibits a meaningful determination of the radical cation decay (*o*-xylene and mesitylene).

An independent way of determining the rate of reaction -2 is to measure the distribution of the OH adduct and the methylbenzyl radical formed from the radical cation. This was done by analyzing the spectrum from 240 to 340 nm in an Ar-saturated solution containing  $5 \times 10^{-3}$  M  $S_2O_8^{2-}$  and comparing this with the spectrum in  $N_2O$  saturated solutions. Using the extinction coefficients for the OH adduct (at 320–330 nm) and the methylbenzyl radical (at 250–270 and 320–330 nm) and taking into account the amount of directly formed methylbenzyl radicals,<sup>2</sup> the yields of the methylbenzyl radical produced from the decay of the radical cations were calculated. These yields are given as percentage of the total radical cation yields in Table I. From the distribution of the OH

adduct and the methylbenzyl radical and from the observed decay rate of the radical cation,  $k_1$  and  $k_{-2}$  can be calculated. The results confirm the assumption that the rate constants of reaction 1 are unchanged in acid and neutral solutions. Furthermore  $k_{-2}$  from the two sets of experiments agree. The mean values are shown in Table I. These rate constants decrease by seven orders of magnitude as the number of methyl groups increases from one to five. This trend is consistent with the high rate of this hydrolysis reaction reported for the benzene radical cation.<sup>6</sup>  $k_{-2}$  shows a good correlation with the ionization potential of the parent compound (Figure 2).

### Alkaline Solution

In alkaline solution the radical cation reacts with hydroxide ions forming the OH adduct (reaction 3). As a

$$(CH_3)_n C_6 H_{6-n}^+ + OH^- \rightarrow (CH_3)_n C_6 H_{6-n} OH \quad (3)$$

consequence of fast reaction -2 with water only the methylated benzenes with  $n \geq 3$  can be studied with respect to reaction 3. With compounds of  $n < 3$ ,  $k_{-2}$  is  $10^5$  or higher (Table I) and we are unable to establish a competition between reaction -2 and 3, because the decay of the radical cation is either too fast or mixed with the  $SO_4^-$  decay (see neutral solution), and the product in both cases is the OH adduct. Another limitation is that pro-

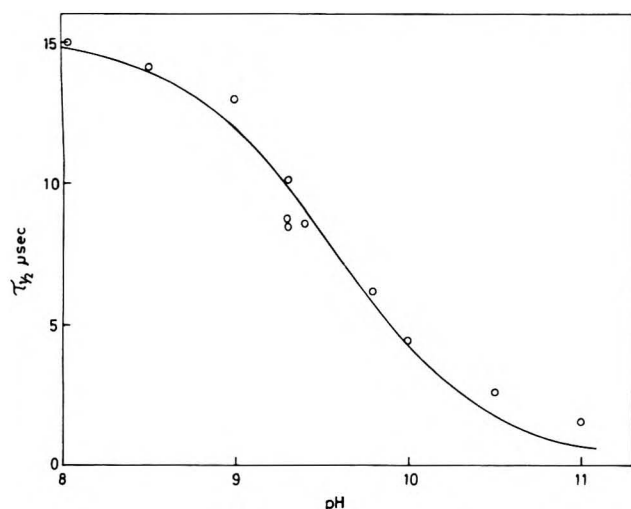


**Figure 3.** The half-life of the first-order decay of the radical cation of isodurene (1, 2, 3, 5) as function of pH. The solid line is calculated for  $k_3 = 1.2 \times 10^9 \text{ M}^{-1} \text{ s}^{-1}$ .

duction of the radical cation from  $\text{SO}_4^-$  is not feasible above  $\text{pH} \sim 12$ , as the rate constant for the reaction  $\text{SO}_4^- + \text{OH}^- \rightarrow \text{SO}_4^{2-} + \text{OH}$  is  $7.3 \times 10^7 \text{ M}^{-1} \text{ s}^{-1}$ .<sup>7</sup> On the other hand, if reactions 1 and 2 are competing, which means that an appreciable amount of methylbenzyl radicals are formed ( $n \geq 3$ ), we can establish a competition with reaction 3 in the pH region 8–12.

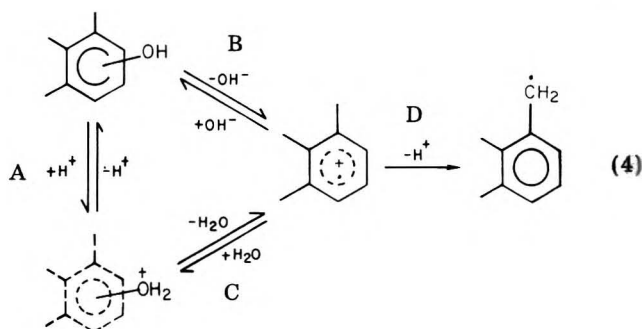
The radical cation was produced in an electron-irradiated Ar-saturated alkaline solution containing  $\text{S}_2\text{O}_8^{2-}$  and  $k_3$  was calculated from the decrease in the half-life of the radical cation over the pH range 8–12. As an example the half-life vs. pH for the isodurene radical cation is shown in Figure 3. The rate constants in Table I are determined by this method but checked by the method of determining the yield of methylbenzyl radicals formed. This is done by recording the resulting spectra as previously in neutral solution and from this yield,  $k_1$  and  $k_2$ , the rate of reaction 3 is derived. These rates agree with those measured from the kinetics. Also in case of reaction 3 the rate constants can be correlated with the ionization potential of the parent compound (Figure 1).

The reverse reaction of (3), a dissociation of the OH adduct, was not observed directly, but its existence for several of the compounds ( $n > 3$ ) is strongly suggested from our previous study on the formation of the methylated benzyl radicals in acid solution.<sup>2</sup> The flat portion of the growth curve at pHs 3–5 indicates the formation of the methylbenzyl radicals from an uncatalyzed reaction such as (–3) followed by reaction 1. This type of reaction, (–3), proceeds with DMA<sup>8</sup> and is discussed in more detail in a paper concerning uncatalyzed water elimination reactions.<sup>9</sup>  $k_{-3}$  for methylated benzenes are generally small ( $< 10^4$ ) and can be measured in only a few cases ( $n = 4$  or 5), but some upper limit estimates were made in our previous work ( $k_1$  in Table IV, ref 2). Reaction –2 must

be slow compared to reaction 1 in order to obtain reliable values.

### Summary

The reactions of the radical cations of methylated benzene can be summarized according to (4).



The appearance of the radical cation in aqueous solution is conjugated with the presence of the OH adduct via the pseudobasic equilibria A, B, and C. This is analogous to the reactions of quaternary heterocyclic cations.<sup>10,11</sup> The radical cations can thus be treated as an acid form of the OH adduct. The formation of the protonated OH adduct (formally identical with a monohydrated radical cation) is suggested by O'Neill et al.<sup>12</sup> in order to rationalize the acid catalyzed formation of the radical cation from the OH adduct of methoxylated benzene. The existence of the protonated OH adduct, however, has not been confirmed experimentally in any system. Step D is irreversible under our experimental conditions. The stability of the radical cation with respect to the reactions in (4) increases markedly with decreasing ionization potential of the parent compound.

**Acknowledgment.** We thank the operator staff of the accelerator and Hanne Corfitzen for technical assistance. We are grateful to Dr. E. J. Hart for valuable discussions during the work.

### References and Notes

- (1) K. Sehested, J. Holcman, and E. J. Hart, *J. Phys. Chem.*, **81**, 1363 (1977).
- (2) K. Sehested, H. Corfitzen, H. C. Christensen, and E. J. Hart, *J. Phys. Chem.*, **79**, 310 (1975).
- (3) C. N. R. Rao, *Tetrahedron*, **32**, 1561 (1976).
- (4) J. Holcman and K. Sehested, *J. Phys. Chem.*, **80**, 1642 (1976).
- (5) R. O. C. Norman, P. M. Storey, and P. R. West, *J. Chem. Soc. B*, 1087 (1970); C. Walling and D. M. Camaioni, *J. Am. Chem. Soc.*, **97**, 1603 (1975); S. Steenken, P. O'Neill, and D. Schulte-Frohlinde, *J. Phys. Chem.*, **81**, 26 (1977); M. K. Eberhardt, *J. Org. Chem.*, **42**, 832 (1977).
- (6) P. Neta, V. Madhavan, H. Zemel, and R. W. Fessenden, *J. Am. Chem. Soc.*, **99**, 163 (1977).
- (7) O. P. Chawla and R. W. Fessenden, *J. Phys. Chem.*, **79**, 2693 (1975).
- (8) J. Holcman and K. Sehested, *J. Phys. Chem.*, **81**, 1963 (1977).
- (9) J. Holcman and K. Sehested, to be submitted for publication.
- (10) O. S. Tee and M. Endo, *Can. J. Chem.*, **54**, 2681 (1976).
- (11) J. W. Bunting and D. J. Norris, *J. Am. Chem. Soc.*, **99**, 1189 (1977).
- (12) P. O'Neill, S. Steenken, and D. Schulte-Frohlinde, *J. Phys. Chem.*, **79**, 2773 (1975).

Irradiation of Benzene with  $^{14}\text{CH}^+$  and  $^{14}\text{CH}_3^+$  IonsW. R. Erwin, B. E. Gordon, L. D. Spicer,<sup>1</sup> and R. M. Lemmon\**Laboratory of Chemical Biodynamics, Lawrence Berkeley Laboratory, University of California, Berkeley, California 94720 (Received August 30, 1977)**Publication costs assisted by the U.S. Department of Energy*

Solid benzene at  $-196^\circ\text{C}$  was irradiated with  $^{14}\text{CH}^+$  and  $^{14}\text{CH}_3^+$  ions at 10-eV kinetic energy. Yields were determined for the labeled hydrocarbon products: benzene, toluene, cycloheptatriene, diphenylmethane, biphenyl, and phenylcycloheptatriene. The radioactivity distributions between the ring and the methyl group of the toluene product were also determined. These results have been compared to those previously obtained with  $^{14}\text{C}^+$  and  $^{14}\text{CH}_2^+$  ions. The comparisons have provided both insight into the reaction mechanisms and a tentative estimate of the distribution of the species ( $^{14}\text{CH}_x$ ) that react with the benzene.

In a recent report<sup>2</sup> we described the principal differences observed when *solid* benzene is irradiated with  $^{14}\text{CH}_2^+$  in place of  $^{14}\text{C}^+$  ions. This work was carried out to gain information on whether the  $^{14}\text{C}^+$  ion picks up hydrogen before the carbon-carbon bond forming interaction with benzene, or whether the initially formed  $\text{C}_7\text{H}_6$  intermediate then abstracts hydrogen from an adjacent benzene molecule. Although we irradiate with ions, the initial encounter with the benzene is thought to be charge exchange without significant loss of kinetic energy. Consequently, our work may be thought of as a study of the interactions of energetic, neutral species with benzene.

Our major observations and conclusions from the earlier work with accelerated  $^{14}\text{CH}_2^+$  were (a) labeled benzene yields appeared to be about the same as with  $^{14}\text{C}^+$ , this led us to surmise that methylenide (CH) radicals might be intermediates in a postulated bicyclo  $\text{C}_7$  intermediate in the mechanism leading to labeled benzene, (b) the high yields of toluene and cycloheptatriene pointed to similarities to known reactions of benzene with photolytically produced methylene, (c) in contrast to  $^{14}\text{C}$  results,  $^{14}\text{CH}_2$  produced high yields of labeled toluene and cycloheptatriene, and (d) also in contrast to the  $^{14}\text{C}$  results,  $^{14}\text{CH}_2$  produced toluene that had no measurable activity in the ring.

In the present report we describe extensions of our studies by irradiations of benzene with  $^{14}\text{CH}^+$  and  $^{14}\text{CH}_3^+$  ions.

### Experimental Section

Most of the experimental details have been described in a recent paper and in the literature cited therein.<sup>3</sup> All the irradiations reported in this paper were carried out at a kinetic energy of 10 eV. The accelerated ions were directed toward a continuously deposited solid benzene target, with the ratio of irradiating carbon ions to benzene molecules of about  $10^{-4}$ . The surface charge on the target was continuously neutralized by a spray of electrons from a nearby tungsten filament.

The ion source gas,  $^{14}\text{CH}_4$ , specific activity 62.7 mCi/mmol, was obtained from the New England Nuclear Co., Boston, Mass. Methane gives good beams of  $\text{C}^+$  and  $\text{CH}_3^+$  (about 1  $\mu\text{A}$ ) in our carbon-ion accelerator,<sup>4</sup> but poor beams of  $\text{CH}^+$  and  $\text{CH}_2^+$  (about 0.1  $\mu\text{A}$ ). The low intensities of the methylenide and methylene beams have been a major impediment in this work. The radioactivity in peaks emerging from the gas chromatograph were determined either by direct counting in a proportional tube connected to a multichannel analyzer, or by trapping and subsequent counting in a liquid scintillation solution.

TABLE I: Percent Yields of Products from Ions at 5 and 10 eV

Product	Irradiating Species and Energy					
	$\text{C}^+$		$\text{CH}^+$	$\text{CH}_2^+$		$\text{CH}_3^+$
	5 eV	10 eV	10 eV	5 eV	10 eV	10 eV
Benzene	4	4	7.6	1.5	3.3	1.5
Toluene	0.2	0.2	1.4	18	21	35
CHT <sup>a</sup>	0.5	0.5	4.2	51	36	5
$\text{PhC}\equiv\text{CH}$	0.3	0.5 <sup>b</sup>	<0.5	<0.5	<0.5	<0.1
PhCHO		14	19	5	10	2
$\text{Ph}_2$	1.5	1.5	5	1		<0.1
$\text{Ph}_2\text{CH}_2$	3	2	3	1	6	6
PhCHT	11	10	6	1		<0.1
Total yield <sup>c</sup>	20.5	18.7	27.2	73.5	66.3	47.5

<sup>a</sup> CHT = 1,3,5-cycloheptatriene. <sup>b</sup> At 15 eV. <sup>c</sup> Not including PhCHO, which is formed from residual oxygen-containing gases in the ion accelerator. <sup>d</sup> These three products were not adequately separated on the GLC column.

The toluene radioactivity distribution was determined by adding carrier toluene to the target benzene, isolating the toluene by gas-liquid chromatography (GLC) on Carbowax 20M, trapping the emerging peak in glacial acetic acid that contained additional carrier, and oxidizing the toluene to benzoic acid with  $\text{CrO}_3$  and sulfuric acid. The benzoic acid was converted to its silyl ester and the latter was rigorously purified by GLC on an SE-30 column. The ester's specific activity was determined by liquid scintillation counting, after which it was decarboxylated via the Schmidt reaction<sup>5</sup> to aniline (which contains the toluene's ring activity) and  $\text{CO}_2$  (which contains the methyl activity). The latter was trapped and analyzed for both mass and radioactivity after passage through a Poropak R GLC column. The residual sulfuric acid solution, which contained the aniline, was analyzed for radioactivity by liquid scintillation counting.

### Results

The yields, which we estimate to be reproducible to  $\pm 25\%$ , of the major labeled products obtained on irradiating benzene with  $^{14}\text{CH}^+$  and  $^{14}\text{CH}_3^+$  ions at 10 eV are shown in Table I. We repeat that these reactions should be thought of as between high-energy or collisionally thermalized neutral species ( $^{14}\text{CH}$ ,  $^{14}\text{CH}_3$ , etc.) and benzene. For comparison we include earlier data obtained with accelerated  $^{14}\text{C}^+$  and  $^{14}\text{CH}_2^+$  ions at 5 and 10 eV.

Toluene degradations were carried out on the target material from two irradiations with  $^{14}\text{CH}_3^+$  and two with  $^{14}\text{CH}^+$ , all at 10 eV. The  $^{14}\text{CH}_3^+$  results showed that no

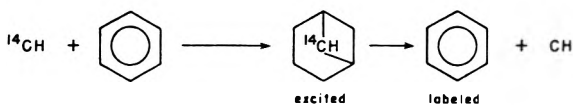
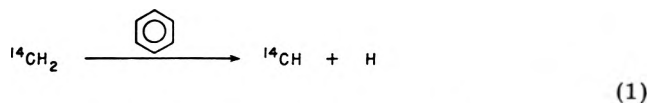


measurable radioactivity was incorporated into the ring of toluene. This result is the same as that previously found in the  $^{14}\text{CH}_2^+$  irradiations,<sup>2</sup> and is in contrast to the toluene product obtained on irradiation of benzene with  $^{14}\text{C}^+$  ions. With these ions, from 5000 down to 10 eV, we have always found about 85% of the toluene's activity in the methyl group, and the remaining approximately 15% in the ring. At 5 eV this ratio becomes about 60/40, and at 2 eV it is 94/6.<sup>6</sup> The  $^{14}\text{CH}^+$  irradiation gave a toluene product with about 10% of its radioactivity in the ring.

## Discussion

We have no data to indicate the electronic states of our reacting species. Since we expect deactivating collisions before the product-forming interactions with benzene, we presume that the bare carbon and the methylenes interact in the ground-state triplet form, and that the CH and  $\text{CH}_3$  radicals react as ground-state singlets.

In accord with a previously published mechanism<sup>2</sup> that we used to explain the production of labeled benzene from  $^{14}\text{CH}_2$ , we now find that our highest yields of the benzene come from  $^{14}\text{CH}$  irradiations. The mechanism is shown in (1). Evidence for a seven-membered intermediate has

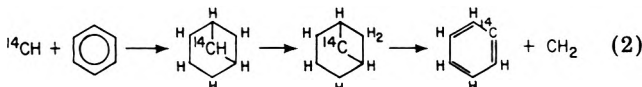


recently been reported in gas-phase mass spectral studies of  $\text{C}^+$  reactions with benzene;<sup>7</sup> in earlier work we found evidence for the specific bicyclo intermediate shown above.<sup>6</sup> In addition, this mechanism is in agreement with a higher yield of benzene from  $^{14}\text{CH}_2$  at 10 eV than from the same species at 5 eV. At the lower energy a lower probability of stripping off a hydrogen atom to produce methylenide radical is expected. This postulate is also useful in explaining the observation that, of the four accelerated species that we have used, methyl appears the least effective in producing labeled benzene.

The high yield of labeled biphenyl from the  $^{14}\text{CH}^+$  irradiations was not expected. If the excited intermediate in (1) ejects a CH, it becomes labeled benzene without generating a phenyl radical. In contrast, the intermediate from a  $^{14}\text{C}$  reaction (I) is expected to react with a



neighboring benzene molecule either to abstract hydrogen or to form labeled biphenyl. If  $^{14}\text{CH}$  is the primary reactant that produced biphenyl as the data suggest, hydrogen migration either before or during the secondary reaction most likely occurs with the expulsion of a methylene. This is shown in reaction 2 (nonbonding



electrons are omitted).

The yields of toluene rise with increased numbers of hydrogens on the irradiating carbon, that is, they are the highest of all with methyl. That methylene is an effective producer of toluene (by simple C-H bond insertion, as is indicated by the toluene's radioactivity distribution) is not

TABLE II: Estimated Distribution of Species Reacting with Benzene Derived from Initial Ion Beams of  $\text{C}^+$ ,  $\text{CH}^+$ ,  $\text{CH}_2^+$ , and  $\text{CH}_3^+$  at 10-eV Translational Energy

Ion beam	Reacting species, <sup>a</sup> %			
	C	CH	$\text{CH}_2$	$\text{CH}_3$
$\text{C}^+$	10	8	<1	
$\text{CH}^+$	<1	24	4	
$\text{CH}_2^+$		9	57	
$\text{CH}_3^+$		8	8	32

<sup>a</sup> Charge neutralization is expected to be the first result when these ions reach the benzene matrix; see ref 11 and 12.

surprising. That methyl is even more effective is surprising, although alkylation of arenes with methyl ions is strongly exothermic<sup>8</sup> and has been observed previously in the liquid phase.<sup>9</sup> Since it has been demonstrated that the attack of  $\text{C}^3\text{H}_3^+$  on benzene gives, among other products, labeled benzene,<sup>9</sup> it may be that in our work reported here we are observing the effects of methyl ion, rather than methyl radical, attack on benzene. This suggestion is reinforced by the ionization potentials of our four irradiating species. These are,<sup>8</sup> in eV, as follows: C, 11.26; CH, 11.13;  $\text{CH}_2$ , 10.40;  $\text{CH}_3$ , 9.83. We expect to be able to determine whether hydrogen is lost from the benzene or from the methyl ion by reacting accelerated  $\text{CD}_3^+$  with benzene, followed by a determination of the deuterium distribution in the toluene product.

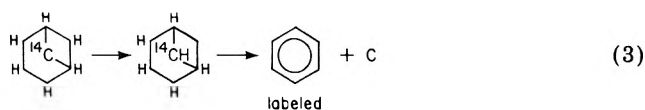
It is also noteworthy that, in contrast to toluene, cycloheptatriene yields are as expected, that is, they reach a maximum with methylene irradiations. This difference is probably explained on the basis that the main route to cycloheptatriene (CHT) is through C-C bond insertions, whereas toluene can be formed by both C-C and C-H bond insertions (ref 3, p 70).

The  $^{14}\text{C}$ , and to a lesser extent the  $^{14}\text{CH}$ , can give a toluene product that is partially ring labeled. Methylene and methyl, on the other hand, give toluene that is only methyl-group labeled. We interpret this to mean that the "bare carbon" ( $^{14}\text{C}$ ) gives ring-labeled toluene by insertion into a benzene C-C bond. We presume that  $^{14}\text{CH}$  leads to the ring labeled product through the CH-bridged bicyclo intermediate in reaction 2.

Based on the yields of Table I, a rough estimate can be made of the relative amounts of the four species,  $\text{CH}_{0-3}^+$  or their neutralized counterparts (see Table II, footnote a) that undergo a bond-forming (i.e., stable product forming) interaction with benzene when the initially accelerated species is  $\text{C}^+$ ,  $\text{CH}^+$ ,  $\text{CH}_2^+$ , or  $\text{CH}_3^+$ . Such estimates are presented in Table II. They follow directly from the following hypotheses: (1) that CHT comes primarily from  $\text{CH}_2$  and that the ratio of toluene to CHT found for  $\text{CH}_2$  represents the relative reactivities of  $\text{CH}_2$  to give these products; (2) that from the above assumption the amount of CHT formed from CH via a pick up of one hydrogen, and the amount of toluene formed from  $\text{CH}_3$  by loss of hydrogen, can be determined; (3) that for CH, the benzene, biphenyl, diphenylmethane, and phenylcycloheptatriene are formed directly via CH reaction; and (4) that from the above four yields, products derived from hydrogen pickup by C to form CH, and from hydrogen elimination from  $\text{CH}_2$  to form CH, can be determined. While the data provide evidence that diphenylmethane can also arise from a  $\text{CH}_2$  or  $\text{CH}_3$  intermediate, we are not able to suggest a reasonable mechanistic route for its formation from these species. Nevertheless, such a reaction would avoid the unfavorable consequence outlined below in which hydrogen atoms are lost from  $\text{CH}_2$  and would alter the figures reported in Table II in a minor way.

Although, as will be explained below, the above hypotheses are not firmly established, they lead to the rough approximations presented in Table II. These approximations indicate that at 10 eV (1) C picks up hydrogen almost as readily as it inserts in benzene. Such pick up reactions may occur via direct abstraction or by an insertion-decomposition reaction either into the ring, or as has been reported previously for recoil produced carbon atoms, into a C-H bond,<sup>10</sup> (2) CH reacts primarily by insertion, but prefers hydrogen pickup over elimination, (3) CH<sub>2</sub> also reacts primarily by insertion with only a small percentage of the methylene ions losing a hydrogen, and (4) CH<sub>3</sub> loses one or two hydrogens but also reacts readily to methylate benzene. It is also apparent both from Table I and Table II that the most reactive species in producing the insertion products observed at 10 eV is CH<sub>2</sub> followed, in order, by CH<sub>3</sub>, CH, and C.

The data of Table I leave no doubt that CH<sub>2</sub> is the most efficient species for forming CHT, and that CH is the most efficient species for forming benzene. However, this does not necessarily mean that the bare <sup>14</sup>C atom must pick up a hydrogen before the interaction that leads to the labeled benzene product. In fact, our previous studies<sup>6,13</sup> have shown that the yields of labeled benzene, toluene, and CHT from <sup>14</sup>C reactions are essentially constant through the translational energy range of 10–2 eV. Consequently, an alternative interpretation might postulate similar bicyclo-C<sub>7</sub> intermediates such as that in (1) arising from the initial reaction of C, CH, or CH<sub>2</sub> with benzene. In each case, labeled benzene and biphenyl would be produced following intramolecular hydrogen transfer when needed, as, for example, in reaction 2 or 3. How important the



suggested intramolecular hydrogen transfers are may be

determined by future experiments using <sup>14</sup>CH<sub>x</sub><sup>+</sup> beams at 5 eV, or lower, kinetic energy.

A problem with the intramolecular hydrogen shift mechanism lies in the experimental results which support the energetically unfavorable conclusion that C is more readily expelled than CH<sub>2</sub>. Such a mechanism yields labeled <sup>14</sup>CH fragments from C reactions and <sup>14</sup>CH<sub>2</sub> fragments from CH reactions, but in lower quantities than estimated in Table II. Here, as in the previous interpretation, there is no mechanistic explanation for the high yield of diphenylmethane in the methyl irradiations.

*Acknowledgment.* This research was supported by the Division of Biomedical and Environmental Research of the U.S. Energy Research and Development Administration.

## References and Notes

- (1) Present address: Department of Chemistry, University of Utah, Salt Lake City, Utah 84112.
- (2) W. R. Erwin, B. E. Gordon, and R. M. Lemmon, *J. Phys. Chem.*, **80**, 1852 (1976).
- (3) R. M. Lemmon, *Acc. Chem. Res.*, **6**, 65 (1973).
- (4) H. M. Pohlit, W. R. Erwin, F. L. Reynolds, R. M. Lemmon, and M. Calvin, *Rev. Sci. Instrum.*, **41**, 1012 (1970).
- (5) H. Wolff, "Organic Reactions", Vol. III, R. Adams, Ed., Wiley, New York, N.Y., 1946, p 307.
- (6) J. Lintermans, W. Erwin, and R. M. Lemmon, *J. Phys. Chem.*, **76**, 2521 (1972).
- (7) R. D. Smith and J. J. DeCorpo, *J. Phys. Chem.*, **80**, 2904 (1976).
- (8) (a) J. L. Franklin, J. G. Dillard, H. M. Rosenstock, J. T. Herron, K. Drazl, and F. H. Field, *Natl. Stand. Ref. Data Ser., Natl. Bur. Stand.*, **No. 26** (1969). (b) V. I. Vedeneyev, L. V. Gurvich, V. N. Kondrat'yev, V. A. Medvedev, and Y. L. Frankovich, "Bond Energies, Ionization Potentials, and Electron Affinities", St. Martin's Press, New York, N.Y., 1966. (c) R. Yamdazni and P. Kebarle, *J. Am. Chem. Soc.*, **98**, 1320 (1976). (d) "CRC Handbook", Chemical Rubber Co., Cleveland, Ohio, 51st ed, 1970–1971.
- (9) F. Cacace and P. Giacomello, *J. Am. Chem. Soc.*, **99**, 5477 (1977).
- (10) K. K. Taylor, H. J. Ache, and A. P. Wolf, *J. Am. Chem. Soc.*, **97**, 5970 (1975).
- (11) J. B. Hasted, *Proc. R. Soc. London, Ser. A*, **212**, 235 (1952).
- (12) H. B. Gilbody, *Proc. R. Soc. London, Ser. A*, **238**, 334 (1956).
- (13) H. M. Pohlit, W. Erwin, T. H. Lin, and R. M. Lemmon, *J. Phys. Chem.*, **75**, 2555 (1971).

## Positron Lifetime Studies in $\gamma$ -Irradiated Organic Crystals

Yan-ching Jean and Hans J. Ache\*

*Department of Chemistry, Virginia Polytechnic Institute and State University, Blacksburg, Virginia 24061 (Received October 25, 1977)*

Four organic solids, adamantane, guanosine, 2'-deoxyuridine, and 5-iodo-2'-deoxyuridine were  $\gamma$  irradiated in the dose range from 0 to 200 Mrad and their positron annihilation lifetimes and ESR signals measured, with and without subsequent thermal annealing. No consistent correlation between the positron lifetime data,  $\lambda_1$ ,  $\lambda_2$ , and  $I_2$  and free-radical concentration or absorbed radiation dose could be observed. On the basis of these results, it appears that the positron annihilation method is not a direct technique for the study of paramagnetic centers or radicals in irradiated solid organic materials because the interactions of positron or positronium with these species are frequently obscured by the response of the positron annihilation process to radiation-induced structural changes in these solid materials.

## Introduction

In previous papers several authors<sup>2-5</sup> studied the correlation between ESR or EPR and positron annihilation measurements<sup>6-12</sup> in  $\gamma$ -irradiated organic compounds.

In these investigations carried out by Eldrup et al.<sup>4</sup> and Hadley et al.<sup>3</sup> with  $\gamma$ -irradiated acetyl methionine, a reduction of  $I_2$ , the intensity of the long-lived component in

the positron lifetime spectra, with increasing radiation dose and EPR signal intensity was observed. Similar results were found by Hadley and Hsu<sup>2</sup> in  $\gamma$ -irradiated D,L-leucine, while more recently Ito and Tabata<sup>5</sup> investigated  $\gamma$ -irradiated eicosane and polyethylene where they observed an increase of the annihilation rate  $\lambda_2$  associated with the long-lived component and a simultaneous decrease of  $I_2$

with increasing radical concentration.

Although these authors could not establish a *simple* correlation between the EPR centers and the observed changes in the positron lifetimes, they prefer to associate their results with interactions of free radicals with orthopositronium (Ps) atoms.

However, since the  $\gamma$  irradiation of organic solids is known to cause in addition to the generation of free radicals macroscopic or structural changes in the solid, i.e., changes in free volume (swelling upon irradiation), vacancy formation, etc., to which the positron annihilation technique responds very strongly, we have studied the effect of  $\gamma$  irradiation in a variety of organic solids to further assess the origin of the observed changes in the annihilation parameters upon  $\gamma$  irradiation and to estimate the contribution made by the reaction of o-Ps with free radicals to the total effect observed. For this purpose we included in this study four organic solids such as adamantane, guanosine, 2'-deoxyuridine, and 5-iodo-2'-deoxyuridine. Adamantane was chosen because it is unusually stable toward radiation and even after applying massive radiation doses (at room temperature), only relatively small amounts of free radicals can be detected. The other three compounds were selected because they are components of important biological systems and it appeared interesting to investigate whether positron annihilation techniques could reveal details about their behavior upon  $\gamma$  irradiation, which could not be detected in ESR studies.

### Experimental Section

(A) *Purity of Compounds.* Adamantane was obtained from Aldrich and 2'-deoxyuridine, guanosine, and 5-iodo-2'-deoxyuridine were obtained from ICN Life Sciences Group. They were of the highest purity available (>99%), and no further purifications were made.

(B) *Preparation of Samples and Positron Lifetime Measurements.* The solids were degassed and sealed under vacuum in quartz tubes. The irradiations were carried out at room temperature with a  $^{137}\text{Cs}$   $\gamma$ -ray source at Brookhaven National Laboratory at a dose rate of 7.8 Mrad/h for guanosine samples and 1.6–1.9 Mrad/h for others. The irradiated samples were left under vacuum for 14 days, until the amount of free radicals had assumed an approximately constant value. Then, aliquots of the samples were transferred under vacuum into specially designed vials together with a positron source consisting of 3–5  $\mu\text{Ci}$   $^{22}\text{Na}$  deposited on a thin Al foil, which was placed in the center of the vial. The i.d. of the sample vial was 0.6 cm, which ensured that all of the positrons were annihilated in the sample before they reached the glass wall. All lifetime measurements were carried out at room temperature. The annealing of these samples was carried out under vacuum in an oil bath kept at 100 °C for a predetermined period of time. The positron lifetime measurements and their computational analysis were carried out by conventional methods as described previously.<sup>13</sup> The resolution of the fast-slow coincidence system was 0.4 ns as measured by the prompt spectrum of  $^{60}\text{Co}$ .

(C) *ESR Measurements.* A Varian E-12 spectrometer was employed to record the first-derivative spectra at a microwave frequency of approximately 9.08 GHz and 100 kHz magnetic modulation. The microwave powers were kept at 30 mW for all measurements. The standard DPPH spectra with known free-radical concentrations were recorded at exactly the same instrumental sensitivities for each sample measurement. The absolute free-radical concentrations were obtained in a standard way by comparing the ESR intensities of samples with DPPH standards. All ESR measurements were carried out at the

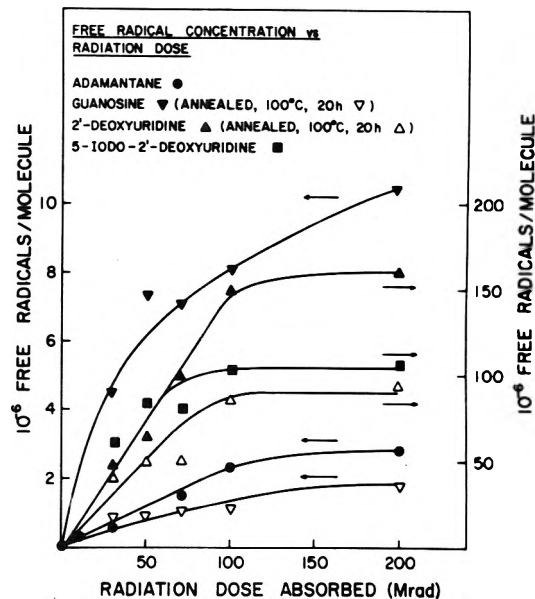


Figure 1. Free-radical concentration vs. radiation dose.

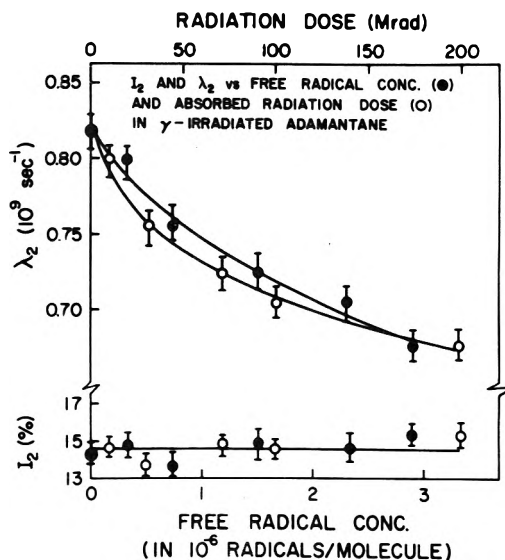


Figure 2.  $I_2$  and  $\lambda_2$  vs. free-radical concentration and absorbed radiation dose in  $\gamma$ -irradiated adamantane.

mean time of lifetime measurements at room temperature. For the identification of the ESR signals in the various compounds under investigation, see ref 14 and 15.

### Results and Discussion

Figure 1, where the radical concentration is plotted as a function of absorbed radiation dose, shows the expected smooth correlation between free-radical concentration and absorbed radiation dose. However, while in the case of adamantane and guanosine, a maximal concentration of about 2.7 and 10.5 radicals/molecule, respectively, is observed at 200 Mrad which, as shown for guanosine, can be almost completely annealed, the corresponding radical concentration in 2'-deoxyuridine and 5-iodo-2'-deoxyuridine is 170 and 100 radicals/molecule and can be, as shown for 2'-deoxyuridine, only partially annealed.

From Figures 1–5 it can clearly be seen that the changes in  $\lambda_2$  and  $I_2$  are relatively small, even after prolonged periods of  $\lambda$  irradiation, and do not follow in a consistent way the variation of the free-radical concentration.

The obvious divergence of the experimentally observed positron lifetime parameters,  $\lambda_2$  and  $I_2$ , in the four  $\gamma$ -irradiated systems as shown in Figures 2, 4, and 5 makes a unique interpretation in terms of the previously postulated

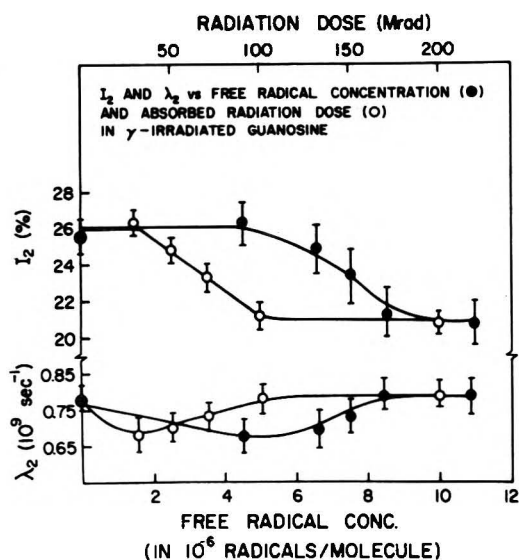


Figure 3.  $I_2$  and  $\lambda_2$  vs. free-radical concentration and absorbed radiation dose in  $\gamma$ -irradiated guanosine.

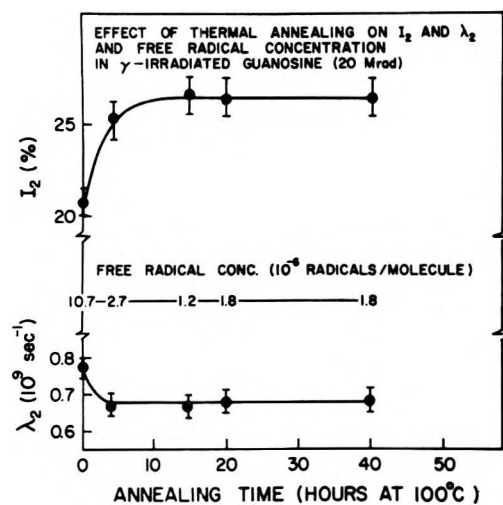


Figure 4. Effect of thermal annealing on  $I_2$  and  $\lambda_2$  and free-radical concentration in  $\gamma$ -irradiated guanosine. (Absorbed radiation dose 200 Mrad).

interactions of positrons or o-Ps with free radicals rather difficult. For example, in the adamantane system where the free radical concentration even after absorption of relatively high radiation doses is rather small, no change of  $I_2$  can be observed as a function of free-radical concentration (Figure 2). On the other hand  $\lambda_2$  shows a decrease with free-radical concentration, which is clearly the opposite of the effect one would expect from the most likely interaction between o-Ps and paramagnetic species, namely the ortho-para spin conversion of the Ps, which should lead to a shortening of the positron lifetime, i.e., an increase of  $\lambda_2$ .<sup>6-12</sup> Thus, the observed effect, i.e., the decrease of  $\lambda_2$ , cannot be associated with this process but may be most likely understood as the result of an increase of the free volume of the compound in which the o-Ps can reside and experience a longer lifetime.<sup>16</sup> This enlargement of the free volume, caused by the radiation-induced swelling of the solid, and its effect on the positron annihilation process clearly outweigh at these low radical concentrations the consequences of Ps reactions with the radicals present.

In  $\gamma$ -irradiated guanosine (Figure 3) the initial drop in  $\lambda_2$  at low radiation doses or free-radical concentrations may have the same origin as discussed above for adamantane, whereas the subsequent drop of  $I_2$  and increase of  $\lambda_2$  at

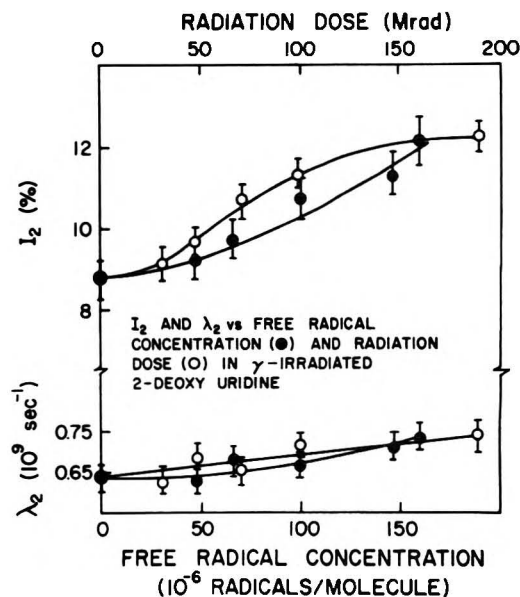


Figure 5.  $I_2$  and  $\lambda_2$  vs. free-radical concentration and absorbed radiation dose in  $\gamma$ -irradiated 2'-deoxyuridine.

higher free-radical concentrations may now be the result of the interaction of "hot"<sup>2-4,17,18</sup> and thermalized o-Ps, respectively, with the radicals present, which at these higher radical concentration overcompensate the free-volume effect. The decrease in  $I_2$  could, however, also be explained in terms of the simple spur reaction<sup>19</sup> or modified spur reaction model<sup>20</sup> by assuming a reduction in the number of available electrons for Ps formation due to fast reactions between radiation-produced species (radicals) and electrons in the positron spur, thus competing for available electrons with the Ps formation process.

The thermal annealing of a sample which had received 200 Mrad leads to an almost complete elimination of the paramagnetic centers, (Figure 4) from initially 10.7 to 1.2–1.8 radicals/molecule. This is accompanied by a change in the positron annihilation data, which assume values coinciding with those obtained at about 30 Mrad; i.e., where positronium-radical reactions seem to have no significant impact. Thus, it appears that while thermal annealing at 100 °C can eliminate most of the paramagnetic species produced, it cannot restore the initial structure of the organic solid.

It would be difficult to suggest such a simple interpretation for the 2'-deoxyuridine system, (Figure 5) where  $I_2$  and  $\lambda_2$ , both increase with free-radical concentration or absorbed radiation dose. This compound is very sensitive to radiation and the damage caused by the large radiation doses applied in this study has probably generated some profound structural changes in the compound and produced a considerable amount of stable radiolysis products whose interactions with Ps lead to the observed variations in the positron annihilation data. This is also supported by the fact that annealing of the compound (100 °C for 20 h) does not restore the initial  $I_2$  or  $\lambda_2$  values, nor does it lead to a complete elimination of the paramagnetic centers. An interpretation of the positron lifetime data in this system would require a much more detailed knowledge of the various species present after irradiation and is, because of lack of such data, presently not feasible.

The analysis of the positron lifetime spectra of 5-iodo-2'-deoxyuridine, is complicated by the fact, that the long-lived component has an intensity of only 1–2%, which introduces a large experimental error in the evaluation of  $\lambda_2$  and  $I_2$ . The measurements reveal only slight increases, even after large radiation doses have been absorbed, in  $I_2$

and  $\lambda_2$  (0 Mrad:  $I_2$  1.2%;  $\lambda_2$   $0.62 \times 10^9$  s<sup>-1</sup>; 100 Mrad:  $I_2$  2.7%,  $\lambda_2$   $0.72 \times 10^9$  s<sup>-1</sup>).

The explanations suggested above are essentially based on the model that the long-lived component in the lifetime spectra, with the decay rate  $\lambda_2$  and an intensity  $I_2$ , is the result of the thermalized o-Ps formed in the substance and its subsequent interactions with its environment.

These explanations may, however, have to be qualified if one considers the results of recent experiments by Hogg et al.<sup>21,22</sup> and Chuang and Tao,<sup>23</sup> which seem to indicate that the long lifetime component in positron annihilation lifetime spectra for organic solids may not be due to o-Ps.

These authors<sup>23</sup> prefer to associate this component with the annihilation of "free" positrons trapped in void-type defects of large size in the solid, in which case the size of the void would control the positron annihilation  $\lambda_2$  and a correlation should exist between the number of the positrons annihilating in these voids and  $I_2$ .

Since it can be assumed that the size and number of these voids depend on the radiation conditions, it is not surprising that  $\lambda_2$  and  $I_2$  are affected by the irradiation.

In summary, the experimental results obtained in this study seem to confirm the contention that values  $I_2$  and  $\lambda_2$  extracted from positron annihilation lifetime measurements in  $\gamma$ -irradiated substances cannot always be directly related to the presence of free radicals. It seems that whatever interaction between paramagnetic species and Ps or positrons in irradiated solid organic compounds occurs, it could be overshadowed by other parameters such as free volume and other structure changes introduced as a result of the irradiation, to which the positron annihilation process responds more directly. This appears to be especially true in cases where only a relatively small amount of radicals is formed as a result of massive radiation, as in the adamantane system, or where a rather complicated radiation chemistry results as a consequence of the irradiation as in 2'-deoxyuridine. Thus, one would have to conclude that the positron annihilation technique

cannot compete with ESR methods in the detection of paramagnetic species in irradiated solids because of its relative insensitivity, its susceptibility to interferences caused by structural changes in the substances, and its apparent failure to distinguish between different types of radicals. Its usefulness will, therefore, most likely be limited to the detection of paramagnetic centers in gaseous systems, where such interferences do not exist and where its sensitivity is dramatically increased, as recently shown by Brandt et al.<sup>24</sup>

## References and Notes

- (1) Work partially supported by the U.S. Energy Research and Development Administration.
- (2) J. H. Hadley, Jr. and F. H. Hsu, *Chem. Phys. Lett.*, **7**, 465 (1970).
- (3) J. H. Hadley, Jr. and F. H. Hsu, *Chem. Phys. Lett.*, **12**, 291 (1971).
- (4) M. Eldrup, E. Lund-Thomsen, and O. Mogensen, *J. Chem. Phys.*, **56**, 4902 (1972).
- (5) Y. Ito and Y. Tabata, *Bull. Chem. Soc. Jpn.*, **48** 808 (1975).
- (6) J. Green and J. Lee, "Positronium Chemistry", Academic Press, New York, N.Y., 1964.
- (7) V. I. Goldanskii, *At. Energy Rev.*, **6**, (1968).
- (8) J. D. McGervey in "Positron Annihilation", A. T. Stewart and L. O. Roellig, Ed., Academic Press, New York, N.Y., 1967, pp 143-154.
- (9) J. A. Merrigan, S. J. Tao, and J. H. Green in "Physical Methods of Chemistry", Vol. I, Part IIID, A. Weissberger and B. W. Rossiter, Ed., Wiley, New York, N.Y., 1972, pp 501-586.
- (10) H. J. Ache, *Angew. Chem., Int. Ed. Engl.*, **11**, 179 (1972).
- (11) J. H. Green, *MTP Int. Rev. Sci.*, **8**, 251-290 (1972).
- (12) V. I. Goldanskii and V. G. Firsov, *Annu. Rev. Phys. Chem.*, **22**, 209 (1971).
- (13) See, e.g., T. L. Williams and H. J. Ache, *J. Chem. Phys.*, **50**, 4493 (1969).
- (14) D. R. Gee, L. Fabes, and J. K. S. Wan, *Chem. Phys. Lett.*, **7**, 311 (1970).
- (15) A. Müller, *Prog. Biophys. Mol. Biol.*, **17**, 99 (1967).
- (16) W. Brandt and I. Spinn, *Phys. Rev.*, **142**, 231 (1966).
- (17) L. J. Bartal and H. J. Ache, *J. Phys. Chem.*, **76**, 1124 (1972).
- (18) L. J. Bartal and H. J. Ache, *Radiochim. Acta*, **19**, 49 (1973).
- (19) O. E. Mogensen, *J. Chem. Phys.*, **60**, 998 (1974).
- (20) S. J. Tao, *Appl. Phys.*, **10**, 67 (1976).
- (21) D. P. Kerr, S. Y. Chuang, and B. G. Hogg, *Mol. Phys.*, **10**, 13 (1965).
- (22) G. Deblonde, S. Y. Chuang, B. G. Hogg, D. P. Kerr, and D. M. Miller, *Can. J. Phys.*, **50**, 1619 (1972).
- (23) S. Y. Chuang and S. J. Tao, *Appl. Phys.*, **11**, 247 (1976).
- (24) W. Brandt and D. Spektor, *Phys. Rev. Lett.*, **38**, 595 (1977).

# Mass Spectrometry of Solvated Ions Generated Directly from the Liquid Phase by Electrohydrodynamic Ionization

Brian P. Stimpson,\* David S. Simons,<sup>†</sup> and Charles A. Evans, Jr.<sup>‡</sup>

Materials Research Laboratory, University of Illinois, Urbana, Illinois 61801 (Received July 26, 1977)

Publication costs assisted by the National Science Foundation

Electrohydrodynamic ionization is a technique whereby ions are generated directly from a liquid surface by application of an electric field. Organic liquids may be ionized if an electrolyte is dissolved to increase electrical conductivity. Emitted ions are formed by attachment of a cation or anion to polar solvent molecules. These cluster ions can decompose in the gas phase by the loss of one or more neutral solvent molecules. Positive ion mass spectra have been obtained for different electrolytes (NaI, KI, HCl, H<sub>2</sub>SO<sub>4</sub>, MgCl<sub>2</sub>, AlCl<sub>3</sub>, and SbCl<sub>3</sub>) dissolved in glycerol as well as NaI in diglycerol and ethylene glycol. Positive and negative ions from NaI in glycerol are analogous in composition. The average size of cluster ions and the probability of decomposition in the gas phase are determined predominantly by the size and electric charge of the cation or anion. The paper discusses the basic mechanisms of electrohydrodynamic ionization and this technique is compared with field desorption. Because solvated ions are sampled directly from the liquid phase, electrohydrodynamic ionization mass spectrometry can yield two types of complementary information regarding ion solvation: the distribution of cluster ions actually emitted reflects the degree of association in the liquid phase, whereas stability in the gas phase is a measure of ion-solvent bonding in the absence of the liquid phase. Implications for the mass spectrometric characterization of dissolved sample materials are considered.

## Introduction

An electric field applied across the surface of a liquid metal induces the formation of a stable liquid cone; sufficiently high fields cause ion emission from the tip of the cone.<sup>1-5</sup> This electrohydrodynamic ionization can take place under vacuum if the liquid has sufficiently low vapor pressure. The liquid is most conveniently supported by a hollow capillary needle connected to a suitable reservoir. A simple ion source<sup>6,7</sup> has been developed in this laboratory and used for the mass spectrometric analysis of metal alloys with low melting points.<sup>8-10</sup> Atomic, polyatomic, and multiply charged positive ions were all formed by electron abstraction.

Ions may be generated from nonvolatile organic liquids also but only if the applied electric field is high, the flow rate of liquid is sufficiently low, and electrical conductivity is adequately increased by dissolution of an ionic electrolyte.<sup>4,11,12</sup> If these conditions are not satisfied, then macroscopic droplets are emitted instead. Electrohydrodynamic ionization of doped organic liquids differs qualitatively from that of liquid metals. There is no single liquid cone; instead emission originates near the rim of the capillary needle, often from several sites simultaneously.<sup>4,13,14</sup> Emitted species are formed by attachment of a cation or anion to one or more polar solvent molecules. If an additional nonvolatile material (liquid or solid) is dissolved, then those molecules also may be incorporated within the emitted ion clusters.

We have used our ion source, in conjunction with a double-focusing mass spectrometer, to analyze a range of materials of biochemical interest (amino acids, sugars, nucleosides, peptides, and antibiotics) dissolved in glycerol with NaI as electrolyte.<sup>15,16</sup> These materials yielded quasimolecular positive ions resulting from cation (or proton) attachment to clusters of solvent and/or solute

molecules. It seems that electrohydrodynamic ionization can generate quasimolecular ions characteristic of any sample material which can be dissolved, together with an electrolyte, in a nonvolatile organic solvent and which then undergoes appreciable interaction with cations and anions in solution. There is no need for sample heating or volatilization, so electrohydrodynamic ionization mass spectrometry should be applicable to labile materials which cannot be ionized by other methods.

This paper will be concerned specifically with the interaction between organic solvent and dissolved electrolyte. We believe that the applied electric field sufficiently distorts the potential energy distribution at the liquid surface to permit direct emission of those solvated ions already present at the surface.<sup>17a,18,19a</sup> Such field-induced "evaporation" imparts virtually no additional vibrational or electronic energy to those ion species emitted into the gas phase.<sup>17b,20</sup> This absence of internal excitation is confirmed by the lack of molecular fragmentation as well as by the relative stability of large, weakly bound cluster ions.<sup>15,16</sup> As a result, the distribution of different cluster ions electrohydrodynamically emitted from the surface of a solution should reflect the nature and strength of ion-solvent and ion-ion association within the liquid phase. Furthermore, the subsequent stability of solvated cluster ions in the gas phase is a direct measure of ion-solvent bonding in the absence of the bulk liquid phase.

Thus electrohydrodynamic ionization mass spectrometry of electrolyte solutions can yield two types of complementary information regarding ion-solvent interaction. This paper reports our preliminary investigations and proposes how quantitative thermodynamic information could be derived from mass spectrometric measurements. We consider the implications of our results for the mass spectrometric characterization of dissolved sample materials.

## Experimental Section

The AEI MS902 double-focusing mass spectrometer was operated with a mass resolution of 800 (measured at 5% of peak height). The overall dynamic range within a single mass spectrum was such that ions with relative abundances

\* Author to whom inquiries about the paper should be addressed. Present address: Department of Chemistry, Harvard University, 12 Oxford Street, Cambridge, Mass. 02138.

<sup>†</sup> Present address: General Electric Company, Knolls Atomic Power Laboratory, Schenectady, N.Y. 12301.

<sup>‡</sup> Also School of Chemical Sciences, University of Illinois.

as low as 0.02–0.1% could be detected. Unless otherwise stated, mass spectra extended up to the maximum mass-to-charge ratio ( $m/z$  950 at 8-keV ion energy) accepted by the mass spectrometer. Our mass spectrometer has been modified so that the kinetic energy of ions transmitted by the electric sector may be adjusted manually to any value below the maximum of 8 keV; this predetermined ion energy is independent of the voltages applied to the ion source. The total energy bandwidth of the AEI MS902 mass spectrometer is 1.3% of the nominal ion energy. An electronic mass measurement system calculated mass-to-charge ratio as a combined function of magnetic field and transmitted ion energy.

The structure and operation of the electrohydrodynamic ion source have been described previously.<sup>15,16</sup> Unless otherwise stated, the voltage applied to the capillary needle emitter was approximately +8.6 kV; the exact value was selected during operation such that all ions which did not undergo any decomposition process would possess 8.0-keV energy within the mass spectrometer. The discrepancy between actual needle voltage and maximum ion energy represents a real voltage drop within the liquid solution at the tip of the capillary needle emitter. The corresponding energy dissipation results predominantly from electrical and hydrodynamic effects such as ohmic resistance and viscous liquid flow,<sup>14,21,22</sup> with small additional contributions resulting from electrode processes at the capillary needle and the energy required for ion emission into the gas phase.

Negative ion mass spectra (from NaI in glycerol) were obtained by reversing the polarity of all voltages applied to the ion source as well as the electric and magnetic fields of the mass spectrometer. Positive and negative ion currents were of the same magnitude, and there was no indication of electron emission in the latter case. However negative ion emission from the electrohydrodynamic ion source was appreciably less stable. It is probable that sodium, formed when the capillary needle is cathode, reacts with glycerol whereas molecular iodine, formed when the needle is anode, is readily soluble in glycerol.<sup>23</sup>

All solvents and electrolytes were of reagent grade except diglycerol, obtained from ICN Life Sciences Group (K&K), which was only 85–90% pure with glycerol and triglycerol as the major impurities. Both  $MgCl_2 \cdot 6H_2O$  and  $AlCl_3 \cdot 6H_2O$  were used in the hydrated, crystalline form.

HCl (aqueous solution),  $H_2SO_4$ , and  $MgCl_2 \cdot 6H_2O$  dissolved readily in pure glycerol at room temperature, as did NaI in ethylene glycol. Other solutions were prepared either by heating, with continuous stirring, or by using water as an intermediate solvent. Any water, whether used as intermediate solvent or introduced as water of hydration, was removed by preliminary pumping under vacuum. These procedures have been described elsewhere.<sup>16</sup> Of the electrolytes used, only HCl (introduced as concentrated aqueous solution) was appreciably volatile when dissolved in glycerol; removal of the water by preliminary pumping resulted in loss of most of the HCl initially added to the glycerol. Table I specifies the final concentration of HCl in glycerol. Chemical indicators demonstrated that the solutions of HCl,  $H_2SO_4$ ,  $AlCl_3$ , and  $SbCl_3$  in glycerol were strongly acidic; the other electrolytes gave neutral solutions.

We have previously suggested<sup>16</sup> that the most useful definition of molar concentration is the number of moles of electrolyte (or sample) dissolved relative to the number of moles of solvent set equal to 100%. This definition of molar concentration will continue to be used throughout this paper because it relates directly to the average

composition of cluster ions which will be emitted if electrolyte, sample, and solvent are removed from the liquid solution at the same rate.

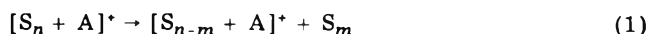
For each mass spectrum, relative abundances have been normalized to the peak height of the most abundant ion set equal to 100%. No correction has been made for the anomalous broadening of metastable peaks, so the true abundance of daughter ions is somewhat underestimated. The absolute ion currents specified in Figure 1 were calibrated by means of the auxiliary plate collector incorporated in the AEI MS902 mass spectrometer.

It will be convenient to define "ion energy ratio" as the ratio of the energy of the ions actually transmitted by the electric sector to the energy of ions emitted from the ion source (prior to any decomposition process).

## Results

*Decomposition of Solvated Ions in the Gas Phase.* The ions emitted electrohydrodynamically from a solution of a 1:1 electrolyte ( $A^+B^-$ ) in a solvent (S) are predominantly solvated cations and anions of the form  $[S_n + A]^+$  and  $[S_n + B]^-$ . Typically the value of  $n$  ranges from 0 to greater than 10, but for the most abundant ions  $n$  lies between 1 and 3.

In general, such cluster ions are not stable in the gas phase.<sup>22</sup> Decomposition of singly charged positive ions proceeds by the loss of one or more neutral solvent molecules, as follows



This may be expressed in more general terms



where  $[M]^+$  is the parent ion and  $[M - \Delta M]^+$  is the daughter ion. If such decomposition takes place while the parent ion is in transit within the mass spectrometer, then the daughter ion will not normally arrive at the collector or be recorded as part of the mass spectrum. However if the parent ion decomposes when located within one of three specific regions of the mass spectrometer, then the daughter ion may be detected and identified with a particular decomposition.

(1) An ion may decompose during acceleration within the ion source, between the capillary needle emitter and the grounded collector cup electrode. We consider a specific singly charged parent ion which decomposes, according to eq 2, at some position where it has already acquired a fraction  $c$  of the maximum possible kinetic energy  $E_0$ . This kinetic energy  $cE_0$  is then partitioned between the daughter ion and the neutral fragment such that velocity is unchanged and momentum is conserved. (Any release of internal energy is assumed negligible compared to the total kinetic energy.) The daughter ion is then accelerated through the remaining potential difference, so its final kinetic energy becomes

$$E = \left( \frac{M - \Delta M}{M} \right) cE_0 + (1 - c)E_0 \quad (3)$$

Because  $c$  can range from zero to unity, the daughter ions entering the electric sector of the mass spectrometer will possess a continuum of kinetic energies from the maximum  $E_0$  down to

$$E = \left( \frac{M - \Delta M}{M} \right) E_0 \quad (4)$$

(2) A parent ion which decomposes in the first field-free region (between the collector cup of the ion source and the entrance to the electric sector) has already acquired the maximum possible kinetic energy  $E_0$ . Therefore, wherever

a parent ion decomposes in this region, the daughter ion will subsequently have the kinetic energy given by eq 4. Because of the considerable length of this field-free region, a high proportion of all daughter ions entering the electric sector will possess this specific energy.

(3) If a parent ion decomposes in the second field-free region (between the electric and magnetic sectors), then it will already have passed through the electric sector set to accept ions with the full kinetic energy  $E_0$ . After decomposition, energy will again be partitioned according to eq 4; because the momentum of the charged species has been reduced, the daughter ion will then be transmitted by the magnetic sector at an apparent mass given by

$$M^* = (M - \Delta M)^2 / M \quad (5)$$

Equations 3–5 become more complex if parent and daughter ions are not both singly charged.<sup>24a</sup>

This behavior is identical with that of metastable molecular ions and similar experimental techniques may be used.<sup>24</sup> For convenience the term "metastable" will be applied to solvated cluster ions which decompose before arrival at the collector of the mass spectrometer.

This discussion shows that if daughter ions are formed during acceleration or within the first field-free region, then they will not pass through the mass spectrometer unless the electric sector is adjusted to accept ions of the energy given by eq 3 or 4. (Note that the characteristic parameter  $E/E_0$  specified by these equations has earlier been defined as the "ion energy ratio".) In particular, if the electric sector is set to accept ions with the full kinetic energy  $E_0$  (ion energy ratio equal to unity), then only parent ions which do not decompose will be recorded in the mass spectrum. A high proportion of all metastable ions decompose within the first field-free region. Consequently daughter ions resulting from a specific decomposition will be efficiently transmitted only if the electric sector is set to accept ions with the appropriate energy, given by eq 4; all other ions, whether stable parent ions or the products of other decompositions, will be rejected. A mass spectrum recorded under such conditions must necessarily be selective.

In order to demonstrate the feasibility of studying the decomposition of metastable ions in the first field-free region, successive mass spectra were recorded at different ion energy ratios. The voltage applied to the capillary needle emitter was maintained constant at +8.0 kV and consequently the total ion emission did not change. The absolute intensity of the ion currents due to specific daughter ions could then be determined as a function of ion energy ratio.

Figure 1 shows this variation for the two most abundant ions,  $[G_2 + Na]^+$  and  $[G_3 + Na]^+$ , observed from glycerol (G) with NaI as electrolyte. As the energy of the analyzed ions is reduced from 8 to 4 keV, definite structure is observed. No ions have an energy corresponding to the full needle voltage; as explained above, this is a consequence of the finite voltage drop (here 700 V) between the capillary needle and the liquid–vacuum interface at the emission sites. A maximum in ion current for each species at 7.3 keV corresponds to transmission of those parent ions which do not decompose within the mass spectrometer. Additional maxima at 5.1 keV for  $[G_2 + Na]^+$  and at 5.6 keV for  $[G_3 + Na]^+$  correspond to transmission of those species as daughter ions resulting from loss of one neutral glycerol molecule in the first field-free region. In other words, although  $[G_2 + Na]^+$  and  $[G_3 + Na]^+$  are observed in the mass spectra under these conditions, it is  $[G_3 + Na]^+$  and  $[G_4 + Na]^+$  respectively which are actually emitted from the liquid surface. A small maximum at 4.5 keV can

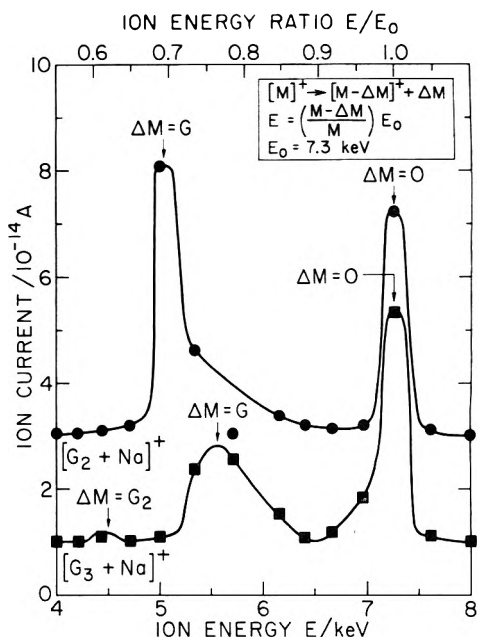


**Figure 1.** Ion current due to  $[G_2 + Na]^+$  and  $[G_3 + Na]^+$  (G = glycerol) transmitted as daughter ions by the mass spectrometer as a function of the ion energy transmitted by the electric sector. For clarity, the two curves are displaced vertically from the axis by different amounts ( $3 \times 10^{-14}$  and  $1 \times 10^{-14}$  A, respectively). The arrows show predicted ion energies for specific decompositions in the first field-free region. The voltage applied to the capillary needle emitter was 8.0 kV.

be attributed to loss of two neutral glycerol molecules from  $[G_5 + Na]^+$  with subsequent detection of  $[G_3 + Na]^+$ . Loss of two neutral glycerol molecules is always much less likely than loss of one. There is no evidence for decompositions involving the loss of species other than an integral number of neutral glycerol molecules.

If parent ions decomposed only within the first field-free region, then structure in the variation of ion current with ion energy would be sharp, limited in width only by the energy bandwidth of the electric sector (which is 100 eV at 8.0-keV ion energy and 50 eV at 4.0 keV). However, as explained above, decompositions also take place during acceleration of parent ions within the ion source; consequently each specific decomposition is associated with a continuum between the maximum ion energy  $E_0$  and the lower ion energy given by eq 4. Because of the nonlinear potential distribution within the ion source, the continuum varies in amplitude (as seen in Figure 1).

Information of the type illustrated in Figure 1 can be obtained for each positive ion in the mass spectrum. For each species, the maxima in transmitted ion current will occur at different ion energy ratios. In Figure 2, the ion energy corresponding to each of these maxima has been plotted as a function of the mass of the ion analyzed by the mass spectrometer. The individual data points compare well with the relationship predicted by eq 4, which is also illustrated. For these measurements, a composite solution of glucose, sucrose, and raffinose with NaI in glycerol was used; the mass spectrum obtained with this solution has been analytically interpreted elsewhere.<sup>16</sup>

Decomposition of metastable ions in the second field-free region can be detected in most mass spectra as anomalously broadened peaks (triangular in shape) at the apparent mass given by eq 5. Allocation of a specific decomposition to such peaks is straightforward and the relative abundances of these metastable peaks are included in Tables I and II, which are discussed below.

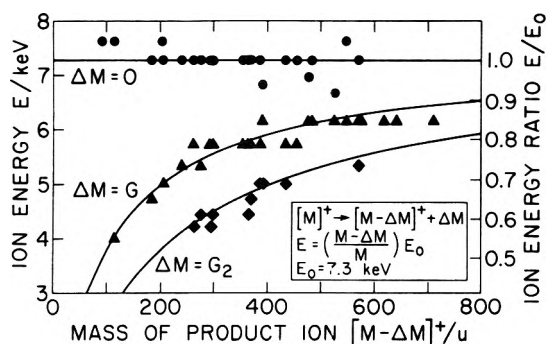
*Positive Ions from NaI–Glycerol.* Glycerol (G) with sodium iodide (NaI) as electrolyte was used exclusively for



TABLE I: Relative Abundances (%) of Positive Ions Characteristic of 1:1 Electrolytes<sup>a</sup> Dissolved in Glycerol (G)

	<i>n</i>	0	1	2	3	4	5	6	7	8	9	10
NaI Ion energy ratio = 1.00												
Positive ions <sup>b</sup>												
$[G_n + H]^+$			0.02	1.9	3.2	0.09						
$[G_n + Na]^+$	0.4	3.2	100	67	8.6	0.3	0.01		0.04	<0.01	<0.01	
$[G_n + Na + NaI]^+$				0.05	0.1	0.03	0.1	<0.01	<0.01			
Metastable ions												
$[G_n + H]^+ \rightarrow [G_{n-1} + H]^+$					0.05							
$[G_n + Na]^+ \rightarrow [G_{n-1} + Na]^+$				0.09	2.5	0.7	0.06				0.02	
$[G_n + Na + NaI]^+ \rightarrow [G_{n-1} + Na + NaI]^+$								0.01	0.01			
Negative ions												
$[G_n - H]^-$				0.5	1.8	0.08	0.04					
$[G_n + I]^-$	0.8	57	100	12	0.8	0.06						
$[G_n + I + NaI]^-$		0.3	0.9	0.4	0.2	0.08						
Metastable ions												
$[G_n + I]^- \rightarrow [G_{n-1} + I]^-$				1.2	0.6	0.1						
NaI Ion energy ratio = 0.75 <sup>c</sup>												
$[G_n + H]^+$		<0.1	1.4	1.3	0.2	<0.1						
$[G_n + Na]^+$	1.1	1.3	87	100	21	12	6.9	3.5	1.1			
$[G_n + Na + NaI]^+$		0.3	0.3	0.5	1.3	1.1	0.9					
Metastable ions												
$[G_n + Na]^+ \rightarrow [G_{n-1} + Na]^+$				<0.1	<0.1	<0.1	<0.1	<0.1	<0.1			
KI Ion energy ratio = 0.75 <sup>d</sup>												
$[G_n + H]^+$		0.9	26	6.9	0.6							
$[G_n + K]^+$		39	100	31	6.7	2.4	0.6					
Metastable ions												
$[G_n + K]^+ \rightarrow [G_{n-1} + K]^+$				0.1	0.5	0.2						
HCl Ion energy ratio = 1.00												
$[G_n + H]^+$		0.9	46	100	6.1	0.1			0.07	0.2	0.1	
Metastable ions												
$[G_n + H]^+ \rightarrow [G_{n-1} + H]^+$				0.09	5.4	0.6						

<sup>a</sup> NaI (molar concentration 6.1%), KI (4.8%), and HCl (1.4%). Relative abundances of negative ions characteristic of NaI in glycerol at ion energy ratio = 1.00 are also listed. <sup>b</sup> From ref 16. <sup>c</sup> From mass spectrum in ref 15; maximum *m/z* 800. <sup>d</sup> Maximum *m/z* 600.



**Figure 2.** Ion energy corresponding to each maximum in transmitted ion current due to specific singly charged positive ions as a function of the mass of the ion analyzed by the mass spectrometer. The solid symbols denote experimental measurements whereas the continuous curves show the predicted relationship for decompositions involving the loss of one or two neutral glycerol (G) molecules in the first field-free region. The voltage applied to the capillary needle emitter was 8.0 kV.

our earlier studies of electrohydrodynamic ionization.<sup>15,16</sup> We now compare the positive and negative ions emitted from this solution and then present positive ion mass spectra obtained by electrohydrodynamic ionization of other electrolytes and solvents.

Table I describes, in a matrix format, the cluster ions emitted from glycerol with NaI as electrolyte. The most abundant positive ions are of the form  $[G_n + Na]^+$ , representing varying degrees of solvation of the  $Na^+$  cations by glycerol molecules. At an ion energy ratio of unity, the most abundant positive ion is  $[G_2 + Na]^+$ . However the total ion current (measured at a monitor collector located between the electric and magnetic sectors) is greatest at an ion energy ratio of 0.75. With the latter operating

condition,  $[G_3 + Na]^+$  becomes the most abundant cluster ion in the mass spectrum; because the ion energy ratio has been reduced below unity,  $[G_4 + Na]^+$  is the ion actually emitted. The increase in relative abundance of larger cluster ions at the lower ion energy ratio confirms that the probability of decomposition in the gas phase increases rapidly with cluster size.

Two other species of solvated cluster ion are observed, but at much lower relative abundance. Solvation of free protons results in ion clusters of the form  $[G_n + H]^+$ . In general, such protonated clusters are two orders of magnitude less abundant than the corresponding  $[G_n + Na]^+$  clusters. Glycerol does not dissociate to an appreciable extent ( $pK = 14.1$ )<sup>25</sup> as an acid in water solution, and the very low electrical conductivity of the pure liquid<sup>26</sup> confirms that self-protolysis is an equally weak process. Consequently few free protons will be generated in the bulk liquid phase and the observed abundance of protonated clusters probably results from a greater concentration near the emission sites. It is probable that the high electric field at the liquid surface causes locally enhanced dissociation of the glycerol. Such field-enhanced dissociation<sup>27,28</sup> has also been suggested in connection with the electrohydrodynamic spraying of doped glycerol droplets.<sup>11,12</sup>

In addition, multiple incorporation of cations and anions results in clusters of the form  $[G_n + Na + NaI]^+$ . These ions are not very abundant but, as expected, the probability of incorporation of both sodium and iodine increases with the size of the cluster. These composite clusters may reflect the existence in solution of associated triple ions.<sup>29</sup> Certainly the molar concentration of NaI in glycerol is large enough (6.1%) to imply a considerable degree of association; however the variation of conductivity with concentration for this system<sup>14,26</sup> is sufficiently dominated by

the change in viscosity that any structure resulting from ion association<sup>29</sup> is obscured.

For all three types of ion-solvent cluster, metastable peaks are observed resulting from the loss of one neutral glycerol molecule. The probability of such decomposition in the second field-free region is seen to increase with cluster size although the measured abundance is, of course, determined by the probability of emission of the relevant parent ion. These metastable peaks are much more prominent at an ion energy ratio of unity than at an ion energy ratio of 0.75. Therefore a cluster ion of any specific size is less likely to decompose if it is a daughter ion resulting from an earlier decomposition than if it is the parent ion directly emitted from the liquid. This observation implies that daughter ions have significantly less internal energy than parent ions of the same composition. On decomposition, some internal energy is required to overcome the force binding the neutral fragment to the parent cluster. (We discuss later how the activation energy for decomposition might be measured.) In addition an appreciable amount of kinetic energy may be imparted to the charged and neutral decomposition products. The anomalous broadening of metastable peaks is directly related to the kinetic energy released during decomposition, which can be calculated from the width and shape of the metastable peak.<sup>24b</sup> For the dominant  $[G_3 + Na]^+ \rightarrow [G_2 + Na]^+$  transition at apparent  $m/z$  143.3, the total width of the major isotopic component of the metastable peak is 1.1 u (with a parent ion energy of 8 keV and an ion energy ratio of unity). The corresponding maximum energy release is 0.066 eV, which is certainly comparable with the thermal energy of the trimolecular parent cluster.

*Negative Ions from NaI-Glycerol.* Two series of cluster ions dominate the negative ion mass spectrum from glycerol with NaI as electrolyte (Table I). These correspond to  $I^-$  anion attachment to solvent molecules and to proton loss from glycerol clusters to the solution, giving  $[G_n + I]^-$  and  $[G_n - H]^-$ , respectively. Both series of negative ions are analogous in composition to positively charged species. Electrohydrodynamic ionization proceeds similarly for both polarities of applied electric field because electron transfer is not involved. Triple ion clusters  $[G_n + I + Na]^-$  with net negative charge are detected; the smallest cluster ions of this type incorporate only one glycerol molecule.

At an ion energy ratio of unity,  $[G_2 + I]^-$  is the most abundant negative ion. Table I definitely suggests that the average number of glycerol molecules in clusters incorporating the  $I^-$  anion is lower than the average number in clusters incorporating the  $Na^+$  cation. In particular,  $[G + I]^-$  is more abundant than  $[G_3 + I]^-$  whereas the relative abundance of the analogous positive ions is reversed. For any particular cluster size, the transition  $[G_n + I]^- \rightarrow [G_{n-1} + I]^-$  is more probable (relative to the abundance of the intact parent ion) than the corresponding positive ion decomposition,  $[G_n + Na]^+ \rightarrow [G_{n-1} + Na]^+$ . All of these observations suggest that the strength of the bond between glycerol molecules and the large  $I^-$  ion decreases rapidly as the number of solvent molecules in the cluster increases; comparison with the other halide anions might permit a direct correlation with ion radius.

*Other 1:1 Electrolytes.* Potassium iodide (KI) was dissolved as electrolyte in glycerol in order to change only the cation available in solution. Comparison with the positive ion mass spectrum from NaI-glycerol at the same ion energy ratio of 0.75 reveals two significant differences (Table I). First the degree of proton attachment is higher; the series of  $[G_n + H]^+$  ions is an order of magnitude more

abundant than when NaI is the electrolyte. In addition to the field-induced dissociation of glycerol described above, the high electric field may induce specific chemical reactions between electrolyte and solvent resulting in enhanced proton transfer. Alternatively the local electric field required for electrohydrodynamic ionization may not be the same for different electrolytes in the same solvent; the degree of field-induced dissociation would not then be identical. Second the  $K^+$  cation is associated with a smaller average number of glycerol molecules than is the  $Na^+$  cation; at an ion energy ratio of 0.75, the ratio of the abundances of the ions  $[G_n + K]^+/[G_n + Na]^+$  decreases rapidly from 30 at  $n = 1$  to 0.09 at  $n = 6$ . This smaller average cluster size is accompanied by larger metastable peaks (and since the ion energy ratio is less than unity, the daughter ions which are actually detected have undergone two decompositions, one before and one after the electric sector). It seems therefore that the  $K^+$  cation, like the  $I^-$  anion, is not able to maintain a solvation shell as large as the smaller  $Na^+$  cation.

The inverse correlation of cluster size with ion radius is further supported by the positive ion mass spectrum obtained with hydrochloric acid (HCl) as electrolyte in glycerol. (As explained above, the volatility of this electrolyte necessitated a low molar concentration.) As shown in Table I, the most abundant ion at an ion energy ratio of unity is  $[G_3 + H]^+$  although decompositions with this species as parent ion are also probable. Emission of unsolvated protons could not be observed above the minimum detectable relative abundance of 0.02%. Ion emission current and source pressure were both rather unstable for this solution (and for other solutions with  $Cl^-$  anions), probably resulting from evolution of HCl from the solution or  $Cl_2$  gas at the capillary needle as anode. The main features of this mass spectrum were reproducible, however, and it is evident that an acidic electrolyte can induce strong protonation of clusters of solvent molecules.

Sulfuric acid ( $H_2SO_4$ ) was also investigated as an acidic electrolyte because it is one of the few strong mineral acids which has low volatility (extrapolation of published data<sup>30</sup> gives a vapor pressure of  $1.2 \times 10^{-2}$  Pa,  $9 \times 10^{-5}$  Torr at 20 °C). From glycerol including  $H_2SO_4$  at a molar concentration of 9.3%, large but unstable positive ion currents were obtained; the most abundant species was  $[G_2 + H]^+$ . A small amount of glycerol monosulfuric acid ester,  $HOCH_2CHOHCH_2(SO_4H)$  was formed as a reaction product<sup>31a</sup> and incorporated in a minor series of solvated cluster ions.

*2:1 and 3:1 Electrolytes.* We have previously observed<sup>15</sup> doubly charged clusters of the form  $[G_n + Fe]^{2+}$  for  $5 \leq n \leq 8$  where the  $Fe^{2+}$  ions were generated by electrochemical attack of a stainless steel capillary needle emitter. This interference has subsequently been avoided by the use of platinum capillary needles. We now report a study of the solvation of multiply charged cations generated from solutions of 2:1 and 3:1 electrolytes in glycerol.

Table II lists relative abundances of the characteristic ions emitted electrohydrodynamically from a solution of magnesium chloride ( $MgCl_2$ ) in glycerol. Mass spectra were obtained at ion energy ratios of 1.00 and 0.75; the latter value corresponds to maximum total ion current at the monitor collector located after the electric sector. The spectra obtained at these two values of ion energy ratio are completely different in character.

At an ion energy ratio of unity, the dominant ion species are of the form  $[G_n + H]^+$ . Two other series of ions, neither of which is very abundant, can be directly attributed to the  $MgCl_2$  electrolyte: the doubly charged cluster ion  $[G_n$

TABLE II: Relative Abundances (%) of Positive Ions Characteristic of 2:1 and 3:1 Electrolytes<sup>a</sup> Dissolved in Glycerol (G)

	n 0	1	2	3	4	5	6	7	8	9	10	11	12	13	14	15	16	
MgCl <sub>2</sub> , Ion energy ratio = 1.00																		
[G <sub>n</sub> + H] <sup>+</sup>		1.6	100	11	0.3													
[G <sub>n</sub> + Mg] <sup>2+</sup>			0.4		0.9	3.5	3.3	1.3	0.4									
[G <sub>n</sub> + MgCl] <sup>+</sup>			1.3	1.5	1.2	0.2	0.3											
Metastable ions																		
[G <sub>n</sub> + H] <sup>+</sup> → [G <sub>n-1</sub> + H] <sup>+</sup>			0.5	0.4		0.5	0.8	0.4	0.5									
[G <sub>n</sub> + Mg] <sup>2+</sup> → [G <sub>n-1</sub> + Mg] <sup>2+</sup>																		
[G <sub>n</sub> + MgCl] <sup>+</sup> → [G <sub>n-1</sub> + MgCl] <sup>+</sup>				0.3	0.3													
MgCl <sub>2</sub> , Ion energy ratio = 0.75																		
[G <sub>n</sub> + H] <sup>+</sup>		1.9		4.3														
[G <sub>n</sub> + Mg] <sup>2+</sup>				7.0	11	100	60	40	18	9.0	0.7	1.9	1.0	2.0	0.7			
[G <sub>n</sub> + MgCl] <sup>+</sup>				95	31	2.8	7.0	1.9										
Metastable ions																		
[G <sub>n</sub> + Mg] <sup>2+</sup> → [G <sub>n-1</sub> + Mg] <sup>2+</sup>						0.3	1.8	2.3	0.8		1.2							
[G <sub>n</sub> + MgCl] <sup>+</sup> → [G <sub>n-1</sub> + MgCl] <sup>+</sup>					0.9													
AlCl <sub>3</sub> , Ion energy ratio = 1.00																		
[G <sub>n</sub> + H] <sup>+</sup>	0.03	2.0	100	14	0.09													
Metastable ions																		
[G <sub>n</sub> + H] <sup>+</sup> → [G <sub>n-1</sub> + H] <sup>+</sup>				0.2	0.3													
AlCl <sub>3</sub> , Ion energy ratio = 0.70																		
[G <sub>n</sub> + H] <sup>+</sup>	0.7	100	87	29		6.7	2.7											
[G <sub>n</sub> + AlCl] <sup>2+</sup>				3.6	6.0	21	5.3	30	40	26	47	19	18	8.0	12	6.7	3.3	3.3
[G <sub>n</sub> + AlCl <sub>2</sub> ] <sup>+</sup>				1.3	11													
Metastable ions																		
[G <sub>n</sub> + AlCl] <sup>2+</sup> → [G <sub>n-1</sub> + AlCl] <sup>2+</sup>										1.3	0.7	2.0	1.3	1.3	1.3	1.3		

<sup>a</sup> MgCl<sub>2</sub> (molar concentration 4.5%) and AlCl<sub>3</sub> (3.5%).

+ Mg]<sup>2+</sup>, easily identified by the halved mass difference between isotope peaks and between successive clusters of the series, and the solvated ion pair [G<sub>n</sub> + MgCl]<sup>+</sup>, for which the chlorine atom contributes a characteristic isotope pattern. There is some interference between isotope peaks because the two ions [G<sub>2n+1</sub> + Mg]<sup>2+</sup> and [G<sub>n</sub> + MgCl]<sup>+</sup> differ in mass-to-charge ratio by only one atomic mass unit. Metastable peaks are detected corresponding to decomposition of all three types of ion. The ratio of the amplitude of each metastable peak to that of the corresponding stable parent ion is high enough to suggest that both ions incorporating magnesium are relatively unstable in the gas phase.

This hypothesis is reinforced by the much larger abundance of the same ions at an ion energy ratio of 0.75; ions analyzed by the mass spectrometer are now the products of an earlier decomposition. In a mass spectrum recorded under this condition, the [G<sub>n</sub> + Mg]<sup>2+</sup> ions are dominant, with [G<sub>5</sub> + Mg]<sup>2+</sup> the most probable species. Very large doubly charged clusters, up to [G<sub>14</sub> + Mg]<sup>2+</sup> at *m/z* 656, can be detected. Singly charged ions of the form [G<sub>n</sub> + MgCl]<sup>+</sup> for 3 ≤ *n* ≤ 7 are of somewhat lower abundance, which may reflect the degree of association of cations and anions in glycerol solution. At this lower ion energy ratio, metastable peaks are smaller relative to the abundance of the corresponding stable parent ions; as discussed above, it seems that decomposition of a cluster ion in the second field-free region is less likely if that ion is itself the product of a previous decomposition. Because of the larger electrostatic forces acting within the liquid, the effective solvation shell for multiply charged cations will involve, on average, more solvent molecules than in the case of singly charged cations. Consequently electrohydrodynamic ionization generates larger cluster ions. However, after they have been emitted into the gas phase, the stabilizing effect of the bulk liquid phase is absent; the large multiply charged cluster ions are then sufficiently unstable that most clusters undergo at least one decomposition before arrival at the collector of the mass spectrometer.

This model is compatible also with electrohydrodynamic ionization mass spectra obtained from a solution of aluminum chloride (AlCl<sub>3</sub>) in glycerol. At an ion energy ratio of unity, only the series of ions of the form [G<sub>n</sub> + H]<sup>+</sup> and the associated metastable peaks are observed; this was the only solution from which a small signal due to unsolvated protons could be detected. AlCl<sub>3</sub> hydrolyzes in water to give aluminum oxychlorides and hydrochloric acid;<sup>32a</sup> HCl must be formed in glycerol also because the solution was strongly acidic.

At an ion energy ratio of 0.70, corresponding to maximum total ion current at the monitor collector, the same series of protonated [G<sub>n</sub> + H]<sup>+</sup> ions remains most abundant; as for other electrolytes, the distribution is shifted to larger cluster sizes at ion energy ratios less than unity. Additional ions observed only at the lower ion energy ratio are [G<sub>n</sub> + AlCl]<sup>2+</sup> and [G<sub>n</sub> + AlCl<sub>2</sub>]<sup>+</sup>. Both of these species result from solvation of associated ions. Since AlCl<sub>3</sub> is a relatively weak electrolyte, it will not dissociate totally at the high molar concentration of 3.5%. No ions of the form [G<sub>n</sub> + Al]<sup>3+</sup> or any other triply charged ions are detected. The doubly charged [G<sub>n</sub> + AlCl]<sup>2+</sup> ions are associated with very large numbers of glycerol molecules: the largest cluster detected is [G<sub>16</sub> + AlCl]<sup>2+</sup> at *m/z* 767. A series of singly charged ions of the form [G<sub>n</sub> + Al - 2H]<sup>+</sup> for 2 ≤ *n* ≤ 7 is not included in Table II but the maximum relative abundance is 12% at *n* = 5; analogous ions from SbCl<sub>3</sub> as electrolyte are discussed below. The

composition of another minor series of ions is explained as [G<sub>n</sub> + AlCl + (C<sub>3</sub>H<sub>7</sub>O<sub>2</sub>Cl)<sub>*m*</sub>]<sup>2+</sup> where *m* equals 1 or 2; glycerol monochlorohydrin, HOCH<sub>2</sub>CHOHCH<sub>2</sub>Cl, is a reaction product of hydrochloric acid and glycerol<sup>31b,33a</sup> and can be incorporated in cluster ions.

Although it is a covalent compound, antimony trichloride (SbCl<sub>3</sub>) can be used as an electrolyte in glycerol for electrohydrodynamic ionization<sup>34</sup> because it decomposes<sup>32b</sup> to give HCl which then provides ions in solution and thereby increases electrical conductivity. Cohen<sup>35</sup> states that ions containing antimony are also formed in glycerol solution.

Two solutions of SbCl<sub>3</sub> at molar concentrations of 2.8 and 4.0% in glycerol were employed but the mass spectra were similar. At an ion energy ratio of unity, the principal peaks result from solvated protons, with [G<sub>2</sub> + H]<sup>+</sup> the most abundant ion; the associated metastable peaks are also seen. At an ion energy ratio of 0.75, [G<sub>3</sub> + H]<sup>+</sup> becomes the most abundant ion. Two additional ions have relative abundances of 83 and 50% and can be explained as [G<sub>n</sub> + SbCl - H]<sup>+</sup> with *n* = 3 and 4, respectively. Another ion with a relative abundance of 7.0% has the similar composition [G<sub>3</sub> + Sb - 2H]<sup>+</sup>. Incorporation of Sb and Cl can be confirmed from their characteristic isotope pattern. Ions of these types are seen, but with much lower abundance, at an ion energy ratio of unity. These species are formed by replacement of exchangeable hydrogen atoms of the glycerol molecule. Both (HOCH<sub>2</sub>CHOHCH<sub>2</sub>O)SbCl<sub>2</sub> and (HOCH<sub>2</sub>CHOHCH<sub>2</sub>O)<sub>2</sub>SbCl are likely products of solvolysis reactions between SbCl<sub>3</sub> and glycerol;<sup>35</sup> ionic dissociation of these two products would generate Cl<sup>-</sup> anions and solvated cations with the composition described above. In addition to these unexpected species, ions of the form [G<sub>n</sub> + SbCl<sub>2</sub>]<sup>+</sup> are observed for 2 ≤ *n* ≤ 4 with low relative abundance (<3%) at both ion energy ratios. There was no evidence for the emission of [G<sub>n</sub> + SbCl]<sup>2+</sup> or any other multiply charged ions.

*Other Solvents.* There are few solvents which are suitable for direct electrohydrodynamic ionization under vacuum. The principal requirements are low vapor pressure and ability to dissolve ionic electrolytes dissociatively; in general, the latter requirement is satisfied only by solvents with high dielectric constant. For experimental convenience, the solvent should be liquid at room temperature. Glycerol<sup>31c,33b</sup> (HOCH<sub>2</sub>CHOHCH<sub>2</sub>OH, molecular weight 92) satisfies all requirements and is also able to dissolve and thereby permit electrohydrodynamic ionization of many organic materials of analytical interest. Interpretation of mass spectra is facilitated because few interfering impurities are found in commercially available glycerol. Although glycerol has a relatively low molecular weight, the three hydroxyl groups of the glycerol molecule cause considerable hydrogen bonding within the liquid, which results in abnormally high viscosity and low volatility (extrapolation of published data<sup>30</sup> suggests a vapor pressure of 4 × 10<sup>-2</sup> Pa, 3 × 10<sup>-4</sup> Torr at 20 °C). We have now investigated some other solvents which are chemically and physically similar.

Diglycerol<sup>31c,33b</sup> (HOCH<sub>2</sub>CHOHCH<sub>2</sub>OCH<sub>2</sub>CHOHCH<sub>2</sub>OH, molecular weight 166) is an ether formed from two molecules of glycerol with removal of H<sub>2</sub>O; it has a lower vapor pressure and higher viscosity than glycerol. The electrohydrodynamic ionization mass spectrum obtained from a solution of NaI in diglycerol includes a large number of positive ions, all of which can be explained in terms of Na<sup>+</sup> cation or proton attachment to various combinations of diglycerol with the glycerol and triglycerol impurities. Table III lists only those species with relative

TABLE III: Positive Ions with Relative Abundances Greater Than 10% Characteristic of NaI (Molar Concentration 13.0%) Dissolved in Diglycerol (Dg) with Appreciable Glycerol (G) and Triglycerol (Tg) Impurities<sup>a</sup>

<i>m/z</i>	Ion	Rel abundance, %
189	[Dg + Na] <sup>+</sup>	40
207	[G <sub>2</sub> + Na] <sup>+</sup>	64
263	[Tg + Na] <sup>+</sup>	23
281	[G + Dg + Na] <sup>+</sup>	100
355	[Dg <sub>2</sub> + Na] <sup>+</sup> and [G + Tg + Na] <sup>+</sup>	69
429	[Dg + Tg + Na] <sup>+</sup>	34
447	[G + Dg <sub>2</sub> + Na] <sup>+</sup> and [G <sub>2</sub> + Tg + Na] <sup>+</sup>	11
521	[Dg <sub>3</sub> + Na] <sup>+</sup> and [G + Dg + Tg + Na] <sup>+</sup>	21

<sup>a</sup> Ion energy ratio = 0.75.

abundances greater than 10%; where two alternative ion species are listed, that given first will be the dominant component because diglycerol comprises 85–90% of the solvent. It can be seen that the most abundant clusters incorporate one or two solvent molecules regardless of their mass.

Because of the high viscosity of glycerol and diglycerol, electrolytes and nonionic solutes do not dissolve easily. In addition the low mobility of ions in solution limits electrical conductivity. An appreciably less viscous solvent might require a lower electrolyte concentration for ion emission (as opposed to the macroscopic droplets which are formed from liquids of lower conductivity).

For this reason, a solution of NaI at a molar concentration of 4.1% in ethylene glycol<sup>33c,36</sup> (HOCH<sub>2</sub>CH<sub>2</sub>OH, molecular weight 62) was investigated. Although this solvent has a much lower viscosity than glycerol, it has a relatively high vapor pressure (12 Pa,  $9 \times 10^{-2}$  Torr at 20 °C).<sup>30</sup> During electrohydrodynamic ionization the pressure in the ion source rises to 0.4 Pa,  $3 \times 10^{-3}$  Torr, which results in a mean free path for ions sufficiently low that collision with neutral gas molecules is significant. Furthermore the high rate of evaporation from the capillary needle emitter causes rapid depletion of liquid at the ionization sites; once initiated, stable ion emission can be maintained for only a few tens of seconds. Efficient electrohydrodynamic ionization is achieved for a potential difference between capillary needle emitter and the two counterelectrodes (extractor, collector cup) as low as 4 kV; ionization at lower electric fields may result directly from an increase in electrical conductivity of the solution. With ion energy ratios near unity, virtually no ions are detected. High volatility in the liquid phase is probably associated with greater instability of clusters in the gas phase. At an ion energy ratio of 0.70, the major ions characteristic of ethylene glycol (Eg) are [Eg<sub>*n*</sub> + Na]<sup>+</sup> for  $1 \leq n \leq 4$ .

The difficulties experienced with ethylene glycol suggest that electrohydrodynamic ionization under vacuum of even more volatile solvents will not easily be achieved. Brief experiments with NaI as electrolyte in water revealed two additional problems. First, excessively high pressure near the capillary needle induces electrical discharge between emitter and counterelectrodes. Second, evaporation of solvent causes cooling of the remaining solution which results in freezing of water at the tip of the emitter.

## Discussion

*Electrohydrodynamic Ionization and Relationship to Field Desorption.* Holland, Soltmann, and Sweeley<sup>37</sup> have recently suggested a model for field desorption in which quasimolecular ions are formed within a thin fluidized

layer by chemical attachment reactions which are predominantly thermally dependent; the electric field then extracts these ions from the emitter surface. Anbar and St. John<sup>38</sup> have developed a variant of conventional field desorption in which the organic sample is dissolved into a matrix consisting of water, NaCl, polyvinyl alcohol, and sucrose; a similar composite solution is used for inorganic materials.<sup>38–40</sup> Mass spectra obtained with this technique demonstrate interaction between ions and polar molecules; it is possible that the polyvinyl alcohol inhibits complete evaporation of water. These workers<sup>38</sup> suggest that "the polar polymer matrix is a viscous medium in which the ionic species may migrate in the applied field to the points of highest field strength whence they are desorbed with minimum decomposition".

The types of ion seen in field desorption mass spectra are compatible with these ideas. Often the dominant quasimolecular ions result from protonation,<sup>20,41</sup> which generally requires less energy than direct molecular ionization.<sup>42,43</sup> Cation attachment can be induced by adding a suitable salt to the emitter surface;<sup>44–48</sup> multiple cation attachment, or attachment of both cations and anions, can occur at high salt concentrations.<sup>47,48</sup> Multimolecular cluster ions, formed by attachment of protons<sup>41,49,50</sup> or cations,<sup>45, 48,50</sup> are generated under certain operating conditions. Only low electric fields are required<sup>51</sup> for field desorption of inorganic or organic salts, which results in emission of cations or anions as well as various cation–anion complexes with net positive<sup>38,40,51–54</sup> or negative<sup>39</sup> charge.

Multimolecular cluster ions incorporating volatile solvent molecules can be generated by field ionization because the high electric field at the emitter surface enhances condensation of vapor from the gas phase.<sup>17c,19b,55,56</sup> Water forms multimolecular layers from which protonated clusters of the form [(H<sub>2</sub>O)<sub>*n*</sub> + H]<sup>+</sup> are desorbed.<sup>19c,43,55–60</sup> Protonated clusters incorporating other polar molecules such as alcohols, acids and ketones have also been observed.<sup>19c,19d,43,56,61–64</sup> Because increased dissociation of adsorbed molecules is induced by the electric field,<sup>19c,19e,56–58,61,62</sup> the relative abundances of the various molecular and cluster ions are influenced by applied voltage.<sup>19e,55,58,61,62</sup> Decomposition of cluster ions in the gas phase by loss of one or more neutral molecules has occasionally been reported.<sup>13c,59,61</sup>

It is clear that field desorption and electrohydrodynamic ionization are closely related. Both processes generate electrically charged clusters involving weak bonding between polar molecules and an ion. However electrohydrodynamic ionization is distinguished by two specific characteristics.

(1) Both techniques require surfaces with high curvature so that the applied electric field is sufficiently large to induce ion emission. In electrohydrodynamic ionization, these high curvature surfaces are not solid but are formed from the liquid solution by interaction between the electric field and the liquid. Consequently, so long as liquid solution continues to be available, the ionization process is inherently self-sustaining. Nevertheless variations in emission are observed; these may be caused by the finite rate of consumption of solution (due to emission of ions and evaporation of neutrals), electrode processes<sup>14,23,35,65</sup> (such as chemical reaction and gas evolution) at the liquid–solid interface, and fundamental electrohydrodynamic instabilities<sup>1,65–68</sup> (perhaps resulting in mobility and finite lifetime of individual emission sites). The ion currents from field ionization<sup>19f,56,64,69</sup> and field desorption<sup>50</sup> sources also suffer from essentially statistical fluctuations.

(2) Neutral molecules and ion-molecule clusters are transported to emission sites within the bulk of the liquid phase and not along a two-dimensional surface. Consequently efficient electrohydrodynamic ionization occurs at room temperature. In contrast, field desorption emitters must usually be heated<sup>20,37</sup> in order to enable surface diffusion of sample to the tip of the solid emitter.

Of these ionization techniques, only electrohydrodynamic ionization involves sampling of solvated ions actually from the liquid phase. This unique property enables direct mass spectrometric investigation of ion-solvent interactions in solution. As a result, this new technique can provide information complementary to that obtained by studies of gas-phase solvation in high-pressure ion sources.<sup>70-72</sup>

*Mass Spectrometry of Solvated Ions.* These preliminary results confirm that electrohydrodynamic ionization mass spectrometry can yield two types of basic information regarding ion-solvent interaction: the relative abundance of the different cluster ions emitted from the liquid surface and the subsequent stability of each of these solvated species in the gas phase. However recorded mass spectra represent a convolution of these two sets of quantitative information. The composition and relative abundance of the various ions analyzed by the mass spectrometer are not identical with those of the emitted species; instead they are related by the rate constant for each possible decomposition process in the gas phase. Consequently the distribution of cluster ions actually emitted from the liquid surface can be calculated only after all significant decomposition reactions have been quantitatively characterized. We discuss below how such fundamental information might be derived and applied toward a better understanding of ion-molecule interaction in liquid solution and in the gas phase.

If the distribution of cluster ions actually emitted from the liquid surface does reflect the extent of ion-solvent association in solution, then the most abundant cluster represents the preferred size of solvation shell. Furthermore any discontinuity in the distribution of emitted cluster sizes indicates certain preferred or improbable solvation structures. However, for several basic reasons, the composition and relative intensity of emitted cluster ions may not exactly reflect normal solvation processes in the bulk of the liquid phase. The high electric field at the emission sites may enhance or inhibit certain types of ion-ion, ion-solvent, and solvent-solvent interaction, especially when solvent molecules are themselves strongly polar. In addition dissociation equilibria may be modified, as discussed above for self-protolysis of glycerol. The electric field may even facilitate chemical reactions between solvent and electrolyte which are otherwise unimportant. (We have shown that mass spectra can indicate the presence of reaction products.) Electrohydrodynamic ionization is obviously a "soft" process with little excess energy imparted to electrically charged species as they pass from the liquid phase into vacuum; the fact that large, weakly bound cluster ions are emitted at all is evidence for this, as is the absence of molecular fragmentation during ionization of complex organic materials.<sup>15,16</sup> Nevertheless those solvent molecules which are most weakly bound to a dissolved cation or anion may be unable to accompany that ion across the liquid-vacuum interface; therefore the distribution of cluster sizes probably reflects only the number of solvent molecules bound to each ion with an energy, at the moment of emission, in excess of some minimum value. The fundamental requirement that emission take place from a liquid surface may result in

modification of behavior characteristic of the bulk. An ion in a dielectric liquid with finite electrical conductivity can experience an appreciable electrostatic force only if it lies within some critical distance from the surface. This proximity to the surface may cause the solvation shells of such ions to be asymmetric and smaller than those in the bulk of the solution.

Electrohydrodynamic ionization mass spectrometry is also able to study stability in the gas phase of the various cluster ions. The results presented earlier demonstrate that the rate of decomposition increases rapidly with the number of solvent molecules incorporated in a cluster. It is for this reason that mass spectra, recording only those ions stable for the entire transit time within the mass spectrometer, are inevitably biased toward smaller cluster sizes. However a complete knowledge of the rate of each possible decomposition would permit reconstruction of the spectrum of species actually emitted. In addition, thermodynamic information regarding gas-phase decomposition would indicate the relative stability of different cluster ions in a nonequilibrium situation, where exchange of solvent molecules with the bulk liquid phase is not possible. If a certain size of cluster ion is particularly stable or unstable in the gas phase, then this will be reflected in an abnormal rate of decomposition. On the other hand, if solvated cluster ions have no distinct structure then decomposition rates will increase monotonically with cluster size. For parent ions with the same internal energy, decompositions (at least those involving loss of only one neutral solvent molecule) should follow first-order kinetics. Variation of rate constant with temperature will then yield the activation energy for each specific decomposition. Emitted cluster ions should have a characteristic temperature which is essentially the same as that of the bulk liquid solution near the emission sites. However that liquid may become heated above ambient temperature by the electrohydrodynamic ionization process. The ion current must flow across the potential difference between the capillary needle and the emission sites; the majority of this energy loss must be dissipated as heat, predominantly by thermal conduction through the liquid and along the capillary needle.<sup>14,21,73</sup>

With a conventional double-focusing magnetic mass spectrometer, the parent and daughter ions involved in a specific decomposition can be monitored by several different measurements. The normal ion peak in a mass spectrum obtained at an ion energy ratio of unity gives the number of parent ions which have not decomposed within the time required for ions of that mass and energy to travel through the mass spectrometer. In the same mass spectrum, the area within the broadened metastable peak at the apparent mass given by eq 5 yields the number of daughter ions formed in the second field-free region. The normal ion peak due to daughter ions in a mass spectrum obtained at the ion energy ratio given by eq 4 is a measure of the number of decompositions occurring within the first field-free region. Finally, the extent of decomposition while parent ions are being accelerated within the ion source is reflected in the variation of ion current due to daughter ions for ion energy ratios between unity and the value given by eq 4. Since electrostatic potential and thereby ion energy and transit time can be evaluated as functions of position, the shape of the continuum can be converted into a direct relationship between decomposition rate and time. Such measurements have already been used for the study of fast reactions in field ionization sources.<sup>19g,24c,56,74</sup>

Development of these techniques will enable quantitative investigation of electrohydrodynamic emission and

the kinetics of cluster ion decomposition in the gas phase. A range of experiments is possible since, for most polar solvents, suitable electrolytes can be chosen to donate or accept protons or supply any of the positive alkali or negative halide ions; many polyatomic or multiply charged ions can be similarly studied. The change in cluster ion composition as a function of electrolyte concentration has not yet been investigated systematically. Increased concentration, especially in less polar solvents, will probably encourage ionic association, thereby enhancing the emission of triple ion clusters and other species formed by multiple ion attachment. Complex cluster ions of this type may decompose other than by the loss of an integral number of solvent molecules; for example, both products might be electrically charged.

If the distribution of cluster sizes actually emitted from the liquid surface can be derived, then it becomes possible to determine whether an overall balance is achieved between the molar concentrations of solvent, electrolyte, and solute in the liquid solution and the concentrations emitted into the gas phase. If balance is not achieved, then preferential enhancement or elimination of certain species in the remaining solution must result. Such imbalance would reflect the relative degree of ion-solvent, ion-solute, and solvent-solute interaction; there would be considerable implications with regard to the quantitative analysis of dissolved sample materials and the long-term stability of the emission process.

*Mass Spectrometry of Dissolved Sample Materials.* It is evident from this work that electrohydrodynamically generated cluster ions entering the mass spectrometer have acquired a wide range of kinetic energies because of decomposition processes which take place during ion acceleration or within the first field-free region. In order to enable routine characterization of dissolved sample materials, therefore, ions with only a narrow range of energies should be selected for mass analysis; any magnetic mass spectrometer must have a double-focusing geometry. We have argued before<sup>16</sup> that representative mass spectra of dissolved sample materials can, in general, only be obtained at an ion energy ratio of unity.

There is strong evidence that electrohydrodynamic ionization emits into the gas phase only those solvated ions which are already present at the liquid surface. Dissolved sample molecules may be included within the effective solvation shell, but only if there is some degree of attractive interaction between either cation or anion and the sample molecule. As in field desorption, unfavorable stereochemistry may inhibit such ion attachment.<sup>48</sup> If no appreciable ion-molecule interaction occurs within the liquid phase, then quasimolecular ions incorporating the sample will not be seen in the mass spectrum under any operating conditions.

The actual composition and abundance of such quasimolecular ions must depend on the nature of the various ion-molecule interactions, the equilibrium between the competitive solvation of ions by solvent and sample molecules, and the availability of protons, cations, and anions in solution. We have already shown<sup>16</sup> that the apparent efficiencies of ionization of different sample molecules (measured at an ion energy ratio of unity) can vary over more than one order of magnitude. The chemical properties of the solvent and the molar concentration of sample and electrolyte may have to be selected carefully if quasimolecular ions incorporating a dissolved sample are to be generated efficiently.

Proton affinities of polar molecules are relatively high and quasimolecular ions resulting from protonation are

often more abundant than those formed by cation attachment, even when few free protons are available in solution.<sup>16</sup> Protonation of sample molecules may be possible even when attachment of larger cations is sterically hindered. Quasimolecular species formed by protonation can be enhanced by the use of acidic electrolytes or solvents. In contrast, basic electrolytes or solvents can be expected to enhance those negative quasimolecular ions resulting from proton abstraction. Variation of the hydrogen ion concentration (pH) of the solution may be equally valuable as a means of increasing the solubility of difficult sample materials. However field desorption experiments<sup>45-48</sup> suggest that cationized molecular ions are often better stabilized against molecular fragmentation than the corresponding protonated species. Polar molecules generally have higher affinities for lithium than for other alkali cations,<sup>45-47</sup> so lithium salts may be useful electrolytes for electrohydrodynamic ionization.

An important potential application of electrohydrodynamic ionization mass spectrometry is determination of the molecular weight of complex, nonvolatile materials. The positive quasimolecular ions in the mass spectrum may not unambiguously identify the molecular weight of the sample because the number of incorporated solvent molecules is not known. Furthermore, either a proton or a cation may be attached to any specific quasimolecular species. Incorporation of any cation or anion with a characteristic isotope pattern can be easily recognized. In addition, the difference between the mass-to-charge ratios of positive and negative quasimolecular ions will distinguish between proton and cation attachment for positive species and between proton abstraction and anion attachment for negative species. Instead a second mass spectrum can be obtained from a similar solution in which an alternative electrolyte with different cation and/or anion has been substituted; the mass-to-charge ratios of any quasimolecular ions resulting from cation and/or anion attachment will be altered, whereas those resulting from proton attachment or abstraction will not change. In order to establish the number of solvent molecules incorporated in a quasimolecular ion, it will generally be necessary to use two solvents of different molecular weight, either as a mixture or in two separate solutions; solvation behavior will be unchanged if isotopically labeled and unlabeled versions of the same solvent are used.

Often different combinations of solvent, electrolyte, and sample molecules will give rise to more than one possible ion species at a specific nominal value of mass-to-charge ratio.<sup>16</sup> Although the interference can usually be resolved by the use of high mass resolution, the resulting loss in transmission may not be acceptable. For any given sample, however, the interference can nearly always be eliminated by an appropriate change in either solvent or electrolyte.

Incorporation of a multiply charged cation or anion within a cluster ion can be employed as a means of extending the effective mass range of a mass spectrometer for any given ion accelerating voltage. Multiple attachment of singly charged ions to large molecules has been observed<sup>16</sup> and can be used similarly to analyze species whose mass exceeds the normal upper limit of the mass spectrometer. An additional problem is that the gain of electron multipliers can be impractically low for such heavy ions; however multiply charged quasimolecular ions will undergo a more efficient ion-to-electron conversion at the first dynode than singly charged ions of the same mass.

This discussion demonstrates that an understanding of electrohydrodynamic ionization and the associated solution chemistry is not only of fundamental interest. The same

knowledge will also be needed to develop and apply this new technique for the mass spectrometric analysis of dissolved sample materials.

*Acknowledgment.* This work was supported by research grants from the National Institutes of Health (HEW-PHS-GM-19749) and the National Science Foundation (NSF-DMR-76-01058).

## References and Notes

- (1) D. S. Swatik, Ph.D. Thesis, University of Illinois, 1969.
- (2) D. S. Swatik and C. D. Hendricks, *AIAA J.*, **6**, 1596 (1968).
- (3) C. D. Hendricks and C. S. Swatik, *Astronaut. Acta*, **18**, 295 (1973).
- (4) B. W. Weinstein, Ph.D. Thesis, University of Illinois, 1975.
- (5) J. F. Mahoney, A. Y. Yahiku, H. L. Daley, R. D. Moore, and J. Perel, *J. Appl. Phys.*, **40**, 5101 (1969).
- (6) C. A. Evans, Jr., and C. D. Hendricks, *Rev. Sci. Instrum.*, **43**, 1527 (1972).
- (7) C. D. Hendricks and C. A. Evans, Jr. in "Proceedings of the Second International Conference on Ion Sources", Vienna, 1972, F. Viehböck, H. Winter, and M. Bruck, Ed., p 831.
- (8) B. N. Colby and C. A. Evans, Jr. in "Proceedings of the Second International Conference on Ion Sources", Vienna, 1972, F. Viehböck, H. Winter, and M. Bruck, Ed., p 837.
- (9) B. N. Colby and C. A. Evans, Jr., *Anal. Chem.*, **45**, 1884 (1973).
- (10) B. N. Colby and C. A. Evans, Jr., *Adv. Mass Spectrom.*, **6**, 565 (1974).
- (11) R. J. Pfeifer, Ph.D. Thesis, University of Illinois, 1965.
- (12) R. J. Pfeifer and C. D. Hendricks, Jr., *AIAA J.*, **8**, 496 (1968).
- (13) A. G. Bailey, *J. Phys. D.*, **6**, 276 (1973).
- (14) M. N. Huberman and E. Cohen, "Research on Charged Particle Electrostatic Thrusters", AFAPL-TR-67-115, TRW Systems, 1967.
- (15) D. S. Simons, B. N. Colby, and C. A. Evans, Jr., *Int. J. Mass Spectrom. Ion Phys.*, **15**, 291 (1974).
- (16) B. P. Stimpson and C. A. Evans, Jr., *Biomed. Mass Spectrom.*, **5**, 52 (1978).
- (17) R. Gomer, "Field Emission and Field Ionization", Harvard University Press, Cambridge, Mass., 1961: (a) pp 91-93; (b) pp 100-102; (c) pp 80-83.
- (18) E. W. Müller and T. T. Tsong, "Field Ion Microscopy. Principles and Applications", Elsevier, New York, N.Y., 1969, pp 60-63.
- (19) H.-D. Beckey, "Field Ionization Mass Spectrometry", Pergamon, Oxford, 1971: (a) pp 210-211; (b) pp 190-195; (c) pp 198-203; (d) pp 218-222; (e) pp 203-207; (f) pp 24-28; (g) pp 143-180.
- (20) H. D. Beckey and H.-R. Schulten, *Angew. Chem., Int. Ed. Engl.*, **14**, 403 (1975).
- (21) J. Perel et al., "Electroless Particle Thruster", AFAPL-TR-67-106, Electro-Optical Systems, Inc., 1967.
- (22) M. N. Huberman, *J. Appl. Phys.*, **41**, 578 (1970).
- (23) D. W. Horning, M. S. Thesis, University of Illinois, 1967.
- (24) R. G. Cooks, J. H. Beynon, R. M. Caprioli, and G. R. Lester, "Metastable Ions", Elsevier, Amsterdam, 1973: (a) pp 50-51, 267; (b) pp 57-70; (c) pp 85-88.
- (25) E. M. Woolley, J. Tomkins, and L. G. Hepler, *J. Solution Chem.*, **1**, 341 (1972).
- (26) J. D. Hepburn, F. E. Vermeulen, and F. S. Chute, *AIAA J.*, **9**, 2270 (1971).
- (27) M. Wien and I. Schiele, *Phys. Z.*, **32**, 545 (1931).
- (28) L. Onsager, *J. Chem. Phys.*, **2**, 599 (1934).
- (29) R. M. Fuoss and C. A. Kraus, *J. Am. Chem. Soc.*, **55**, 2387 (1933).
- (30) D. R. Stull, *Ind. Eng. Chem.*, **39**, 517, 1684 (1947); **40**, 496 (1948).
- (31) C. S. Miner and N. N. Dalton, Ed., "Glycerol", Reinhold, New York, N.Y., 1953: (a) pp 358-360; (b) pp 352-356; (c) pp 366-369.
- (32) J. C. Bailar, Jr., H. J. Emeléus, R. Nyholm, and A. F. Trotman-Dickenson, "Comprehensive Inorganic Chemistry", Pergamon, Oxford, 1973: (a) Vol. 1, pp 1019-1022; (b) Vol. 2, pp 599-600.
- (33) J. W. Lawrie, "Glycerol and the Glycols: Production, Properties and Analyses", Chemical Catalog Company, New York, N.Y., 1928: (a) pp 216-217; (b) pp 303-307; (c) pp 361-395.
- (34) V. E. Krohn, Jr., *Prog. Astronaut. Aeronaut.*, **9**, 435 (1963).
- (35) E. Cohen, "Research on Charged Colloid Generation", APL TDR 64-75, TRW Space Technology Laboratories, 1964.
- (36) G. O. Curme, Jr., and F. Johnston, Ed., "Glycols", Reinhold, New York, N.Y., 1952.
- (37) J. F. Holland, B. Soltmann, and C. C. Sweeley, *Biomed. Mass Spectrom.*, **3**, 340 (1976).
- (38) M. Anbar and G. A. St. John, *Anal. Chem.*, **48**, 198 (1976).
- (39) M. Anbar and G. A. St. John, *J. Am. Chem. Soc.*, **97**, 7195 (1975).
- (40) M. Anbar and G. A. St. John, *Inorg. Chem.*, **15**, 727 (1976).
- (41) H.-R. Schulten and H. D. Beckey, *Org. Mass Spectrom.*, **9**, 1154 (1974).
- (42) H. J. Heinen, H. H. Gierlich, and H. D. Beckey, *J. Phys. E*, **8**, 877 (1975).
- (43) H. J. Heinen, F. W. Röllgen, and H. D. Beckey, *Z. Naturforsch. A*, **29**, 773 (1974).
- (44) H.-R. Schulten and H. D. Beckey, *Org. Mass Spectrom.*, **6**, 885 (1972).
- (45) F. W. Röllgen and H.-R. Schulten, *Z. Naturforsch. A*, **30**, 1685 (1975).
- (46) F. W. Röllgen and H.-R. Schulten, *Org. Mass Spectrom.*, **10**, 660 (1975).
- (47) U. Giessmann and F. W. Röllgen, *Org. Mass Spectrom.*, **11**, 1094 (1976).
- (48) J.-C. Prome and G. Puzo, *Org. Mass Spectrom.*, **12**, 28 (1977).
- (49) H.-R. Schulten, *Biomed. Mass Spectrom.*, **1**, 223 (1974).
- (50) H. Budzikiewicz and M. Linscheid, *Biomed. Mass Spectrom.*, **4**, 103 (1977).
- (51) F. W. Röllgen, U. Giessmann, H. J. Heinen, and S. J. Reddy, *Int. J. Mass Spectrom. Ion Phys.*, **24**, 235 (1977).
- (52) H.-R. Schulten and F. W. Röllgen, *Org. Mass Spectrom.*, **10**, 649 (1975).
- (53) H.-R. Schulten and F. W. Röllgen, *Angew. Chem., Int. Ed. Engl.*, **14**, 561 (1975).
- (54) H. J. Veith, *Org. Mass Spectrom.*, **11**, 629 (1976).
- (55) H. D. Beckey, *Z. Naturforsch. A*, **14**, 712 (1959).
- (56) H. D. Beckey, *Adv. Mass Spectrom.*, **2**, 1 (1963).
- (57) H. D. Beckey, *Z. Naturforsch. A*, **15**, 822 (1960).
- (58) W. A. Schmidt, *Z. Naturforsch. A*, **19**, 318 (1964).
- (59) I. V. Gol'denfeld, V. A. Nazarenko, and V. A. Pokrovskii, *Dokl. Phys. Chem.*, **161**, 276 (1965).
- (60) A. R. Anway, *J. Chem. Phys.*, **50**, 2012 (1969).
- (61) J. Block, *Z. Naturforsch. A*, **18**, 952 (1963).
- (62) J. Block and P. L. Moentack, *Z. Naturforsch. A*, **22**, 711 (1967).
- (63) H. D. Beckey and P. Schulze, *Z. Naturforsch. A*, **21**, 214 (1966).
- (64) J. H. Beynon, A. E. Fontaine, and B. E. Job, *Z. Naturforsch. A*, **21**, 776 (1966).
- (65) D. J. Lines, B. Makin, and A. W. Bright in "Static Electrification, 1975. Conference Series No. 27", A. R. Blythe, Ed., Institute of Physics, London, 1975, p 44.
- (66) R. S. Carson, Ph.D. Thesis, University of Illinois, 1964.
- (67) R. S. Carson and C. D. Hendricks, *AIAA J.*, **3**, 1072 (1965).
- (68) C. D. Hendricks, Jr., R. S. Carson, J. J. Hogan, and J. M. Schneider, *AIAA J.*, **2**, 733 (1964).
- (69) H. D. Beckey and D. Schütte, *Z. Instrum.*, **68**, 302 (1960).
- (70) P. Kebarle in "Ions and Ion Pairs in Organic Reactions", Vol. 1, M. Szwarc, Ed., Wiley, New York, N.Y., 1972, p 27.
- (71) P. Kebarle in "Ion-Molecule Reactions", Vol. 1, J. L. Franklin, Ed., Plenum Press, New York, N.Y., 1972, p 315.
- (72) P. Kebarle, *Mod. Aspects Electrochem.*, **9**, 1 (1974).
- (73) J. M. Crowley, *J. Appl. Phys.*, **48**, 145 (1977).
- (74) A. M. Falick, P. J. Derrick, and A. L. Burlingame, *Int. J. Mass Spectrom. Ion Phys.*, **12**, 101 (1973).



# Ionization Constants and Heats of Ionization of the Bisulfate Ion from 5 to 55 °C<sup>1</sup>

T. F. Young, C. R. Singleterry, and I. M. Klotz\*<sup>2</sup>

Department of Chemistry, University of Chicago, Chicago, Illinois 60637 (Received May 11, 1977; Revised Manuscript Received January 9, 1978)

By the use of a novel precision indicator method the ionization constants of the  $\text{HSO}_4^-$  ion have been determined at 10 °C intervals from 5 to 55 °C with an error that is probably less than 2%. Because of specific salt effects, these constants may be in error by as much as 6%, but any larger value seems highly improbable. The value obtained from these data for the heat of ionization at 25 °C is in good agreement with calorimetric measurements. Both the ionization constants and the related heats of ionization reported here are in sharp disagreement with those obtained from electromotive force measurements. For each of the temperatures studied, the thermodynamic quantities  $\Delta G^\circ$ ,  $\Delta H^\circ$ , and  $\Delta S^\circ$  have been calculated from the change of the ionization constant with temperature. At 25 °C they have the following values:  $K = 0.01015$ ,  $\Delta H^\circ = -5188$  cal/mol,  $\Delta G^\circ = 2721$  cal/mol, and  $\Delta S^\circ = -26.52$  cal/mol/deg.

When this investigation was started, there existed a substantial discrepancy between calorimetric values for the heat of ionization of the  $\text{HSO}_4^-$  ion and that derived from electromotive force measurements. From the early measurements and calculations of Noyes et al.<sup>3</sup> to the then contemporary direct calorimetric experiments of Pitzer<sup>4</sup> it was apparent that  $\Delta H^\circ$  of ionization of the bisulfate ion is near  $-5$  kcal mol<sup>-1</sup>. In contrast electromotive force measurements of cells containing bisulfate-sulfate solutions<sup>5</sup> led to a value near  $-2.2$  kcal mol<sup>-1</sup>.

An experimental resolution of this conflict should be based on a method which is different in principle from previous calorimetric or electrical techniques. If direct calorimetric methods are disallowed, the enthalpy change must be obtained from the temperature dependence of the ionization constant,  $K_{\text{HSO}_4^-}$ . Determination of an ionization constant of the order of  $10^{-2}$  is generally difficult, however, because in solutions dilute enough to allow precise estimates of activity coefficients the extent of dissociation of the acid is very high.

The novel method devised is based on some observations made previously by Mullane<sup>6</sup> on the effects of neutral salts on indicators in dilute unbuffered solutions. The essential principle of the procedure is to determine the relative effect on the absorption of an acid-base indicator of (1) a set of neutral salts, and (2) the monobasic salt of the acid under consideration. From the first set of measurements it is possible to correct for salt effects, the apparent changes in hydrogen ion concentration observed in the second set. In contrast to other indicator methods, this one dispenses completely with any necessity of knowing the ionization constant of the indicator, and uses the actual hydrogen ion concentration only as a second-order correction in the calculations.

The thermodynamic constants for the ionization of  $\text{HSO}_4^-$  measured by this novel technique are probably still the most precise ones available, and they have been cited, without documentation, in several authoritative monographs.<sup>7,8</sup> However, there is no published description of the methods used to obtain the original data or of the treatments that extracted the thermodynamic quantities. These details need to be made available so that the reliability of our procedures and accuracy of our results can be judged independently. Despite the long lapse of time since the conclusion of this study, the subject of the ionization of  $\text{HSO}_4^-$  is still drawing attention.<sup>9</sup>

## Principle of the Method

For an indicator of the type used, methyl orange, the equilibrium may be represented by the equation



The corresponding equilibrium constant,  $K$ , expressed in logarithmic form, is related to concentrations and activity coefficients,  $\gamma$ , by the equation

$$-\log (\text{H}^+) = -\log K + \log \left[ \frac{(\text{I}^-)/({}^+\text{HI}^-)}{\log \left[ \frac{(\gamma_{\text{H}^+} \cdot \gamma_{\text{I}^-})}{(\gamma_{{}^+\text{HI}^-})} \right]} \right] \quad (2)$$

For a given reference solution we may write a similar equation

$$-\log (\text{H}^+)_0 = -\log K + \log \left[ \frac{(\text{I}^-)/({}^+\text{HI}^-)}_0 + \log \left[ \frac{(\gamma_{\text{H}^+} \cdot \gamma_{\text{I}^-})}{(\gamma_{{}^+\text{HI}^-})}_0 \right] \right] \quad (3)$$

Subtracting eq 2 from 3, we obtain

$$\log \left[ \frac{(\text{H}^+)}{(\text{H}^+)_0} \right] + \log (f/f_0) = \left[ \log \left[ \frac{(\text{I}^-)/({}^+\text{HI}^-)}_0 - \log \left[ \frac{(\text{I}^-)/({}^+\text{HI}^-)} \right] \right] \right] \quad (4)$$

where

$$\left[ \frac{(\gamma_{\text{H}^+} \cdot \gamma_{\text{I}^-})}{\gamma_{{}^+\text{HI}^-}} \right] \equiv f \quad (5)$$

The effect of the addition of neutral salts is merely to change the activity coefficients of the indicator and of the hydrogen ion. Any change in hydrogen ion concentration due to increased dissociation of the indicator is negligible, since the original acid concentration is made about  $10^2$  times the indicator concentration. Therefore, for the addition of neutral salts

$$\log (f/f_0) = \log \left[ \frac{(\text{I}^-)/({}^+\text{HI}^-)}_0 - \log \left[ \frac{(\text{I}^-)/({}^+\text{HI}^-)} \right] \right] \quad (6)$$

When the salt of a "weak" acid and strong base (such as  $\text{Na}_2\text{SO}_4$ ) is added, however, the removal of hydrogen ion has a pronounced effect on  $\log (\text{H}^+)$  so that we must retain the full equation (primes used to distinguish the equation from that given for neutral salts)

$$\log \left[ \frac{(\text{H}^+)'}{(\text{H}^+)_0} \right] + \log (f'/f_0) = \left[ \log \left[ \frac{(\text{I}^-)/({}^+\text{HI}^-)}_0 - \log \left[ \frac{(\text{I}^-)/({}^+\text{HI}^-)'} \right] \right] \right] \quad (7)$$

It is necessary, then to obtain  $\log [(I^-)/({}^+\text{HI}^-)]$  for the indicator solution containing no salt, and containing

various amounts and kinds of salts, respectively. To do this we make use of Beer's law. When we have the indicator of total concentration,  $c$ , in basic solution

$$\log (I_0/I)_b = k_b cd \quad (8)$$

where  $I_0$  is the intensity of incident light,  $I$  the intensity of transmitted light,  $k$  the extinction coefficient of the absorbing substance,  $c$  the concentration of the absorbing substance, and  $d$  the optical path length of the absorption cell. In strong acid solution in which the indicator is completely in the acid form

$$\log (I_0/I)_a = k_a cd \quad (9)$$

In any solution of intermediate acidity where the degree of dissociation of the indicator is  $\alpha$

$$\log (I_0/I)_x = \alpha ck_b d + (1 - \alpha)ck_a d \quad (10)$$

Since  $(I^-)/(^+HI^-)$  is equal to  $\alpha/(1 - \alpha)$

$$\frac{(I^-)}{(^+HI^-)} = \frac{\log (I_0/I)_x - \log (I_0/I)_a}{\log (I_0/I)_x - \log (I_0/I)_b} \quad (11)$$

Since we use a reference indicator solution instead of pure solvent

$$\frac{(I^-)}{(^+HI^-)} = - \frac{\log (I_r/I)_x - \log (I_r/I)_a}{\log (I_r/I)_x - \log (I_r/I)_b} \equiv R \quad (12)$$

Substituting into eq 6 and 7, we obtain for the addition of neutral salt

$$\log (f/f_0) = \log R_0 - \log R \quad (13)$$

and for the salt of a weak acid and a strong base

$$\log (H^+)'/(H^+)_0 + \log (f'/f_0) = \log R_0 - \log R' \quad (14)$$

Three experimental quantities,  $(I_r/I)_x$ ,  $(I_r/I)_b$ , and  $(I_r/I)_a$  are necessary for the evaluation of  $R$ . No difficulties are encountered in the determination of the first two, but because the indicator, methyl orange, has a relatively large ionization constant ( $4 \times 10^{-4}$ ), an extrapolation procedure was used to evaluate  $(I_r/I)_a$ . Small quantities of concentrated HCl were added successively to the working cell and the respective transmissions measured. These, after conversion to absorbancies and correction for dilution of the solution by added acid, were plotted against the reciprocal of the acid concentration and extrapolated to infinite  $H^+$  concentration. The intercept was taken as  $\log (I_r/I)_a$ .

We have to calculate yet the ionization constant of the weak acid HA from the change in  $H^+$  concentration due to the addition of the salt NaA or KA to the indicator solution. In actual practice it has proved to be convenient to distinguish between the following two situations:  $A^- + H^+ = HA$ , and  $A^{2-} + H^+ = HA^-$ . The following equations which are developed for the specific case of  $SO_4^{2-}$  are also valid for an ion of the charge type  $A^-$ .

If we subtract eq 13 from 14 we obtain

$$\log [(H^+)'/(H^+)_0] + \log (f'/f_0) - \log (f/f_0) = \log R - \log R' \quad (15)$$

We shall assume that

$$\log (f'/f_0) = \log (f/f_0) \quad (16)$$

for a given ionic strength. This is certainly not true for any finite concentration. However, as we go to more and more dilute solutions, eq 16 becomes a better and better approximation, and for various chlorides is valid within

experimental error for concentrations below 0.01 M. Equations 15 and 16 reduce to

$$\log [(H^+)'/(H^+)_0] = \log R - \log R' \equiv \log S \quad (17)$$

$$(H^+) = (H^+)_0 S \quad (18)$$

The equilibrium constant for the bisulfate ionization is

$$\frac{(H^+)'(SO_4^{2-})}{(HSO_4^-)} \frac{\gamma_{H^+}\gamma_{SO_4^{2-}}}{\gamma_{HSO_4^-}} = K \quad (19)$$

Conservation of mass requires that the following relations also be true:

$$(HSO_4^-) = (H^+)_0 - (H^+) = (H^+)_0(1 - S) \quad (20)$$

$$(SO_4^{2-}) = m_{Na_2SO_4} - m_{HSO_4^-} = m - (H^+)_0(1 - S) \quad (21)$$

where  $m_{Na_2SO_4}$  refers to the total of this salt added to the solution. Substituting eq 18, 20, and 21 into eq 19 we obtain

$$\frac{S[m - (H^+)_0(1 - S)]}{(1 - S)} \frac{\gamma_{H^+}\gamma_{SO_4^{2-}}}{\gamma_{HSO_4^-}} = K \quad (22)$$

Thus we see that our final expression does not contain the indicator constant, and contains  $(H^+)_0$  only as part of a small correction in the sulfate ion concentration. Test calculations show that the error in  $K$  will not, even in the most unfavorable case, exceed 0.3% for an error of 0.1 unit in the pH of the stock solution. To obtain  $K$ , we compute values for  $\gamma_{H^+}\gamma_{SO_4^{2-}}/\gamma_{HSO_4^-}$  by means of the completed form of the Debye-Hückel equation

$$\log \frac{\gamma_{H^+}\gamma_{SO_4^{2-}}}{\gamma_{HSO_4^-}} = \frac{-4A\mu^{1/2}}{1 + a\mu^{1/2}} \quad (23)$$

where  $A$  is a constant for a given temperature and solvent and  $a$  is a parameter which is a function of the respective distances of closest approach of the ions. For this work  $a$  was determined empirically by successive substitutions until a straight, practically horizontal line was obtained in a plot of  $K$  against  $\mu$ . (A similar procedure has been used by Naidich and Ricci.<sup>10</sup>) This line is then extrapolated to  $\mu = 0$ .

### Experimental Methods and Materials

A photoelectric spectrophotometer was constructed<sup>1</sup> capable of measuring absorbances with a precision better than 0.001 unit. A Steinheil spectrograph was used for monochromation. Since commercial instruments currently available are equivalent in capabilities, the actual instrument used will not be described.

The absorption cells were 5 cm in optical path. The sample cell had a 200 cm<sup>3</sup> flask, connected to a port near the midpoint of the long axis of the optical cell, to provide a large volume to which salts could be added.

Successive portions of the pure salt to be studied were added to the indicator solution in the reference cell. The indicator solutions used in this study contained approximately  $4 \times 10^{-6}$  mol of methyl orange and  $3-6 \times 10^{-4}$  mol of hydrochloric acid per liter. All of the observations were made with light of about 520 nm wavelength. At each temperature, a separate series of measurements was made of the effects of NaCl, BaCl<sub>2</sub>, and Na<sub>2</sub>SO<sub>4</sub> upon the relative absorption of this light by the indicator solution. At 25 °C similar measurements were also made with KCl, K<sub>2</sub>SO<sub>4</sub>, KNO<sub>3</sub>, and NaNO<sub>3</sub>.

NaCl (Baker's Analyzed, Fused) was recrystallized once from a clear, distilled water solution by addition of 95%

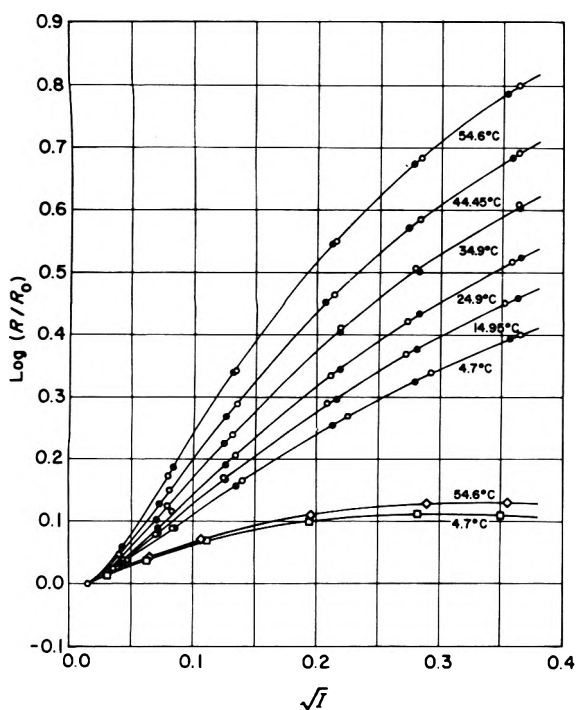


Figure 1.  $\log R_0/R$  vs. square root of ionic strength,  $I^{1/2}$ , for sodium sulfate and sodium chloride with methyl orange: (O ●) sodium sulfate (two observers); (◇) sodium chloride at 54.6 °C; (□) sodium chloride at 4.7 °C.

alcohol, and was then dried in an oven at 120 °C. KCl (Mallinckrodt's Analytical Reagent) was recrystallized once from distilled water and dried at 120 °C.  $\text{BaCl}_2 \cdot 2\text{H}_2\text{O}$  (Mallinckrodt's Analytical Reagent) was recrystallized once from distilled water, and was dehydrated and dried at 120 °C.  $\text{Na}_2\text{SO}_4$  (Kahlbaum's, Fused) was recrystallized twice from distilled water as the decahydrate and allowed to remain in a desiccator until needed. Several months later the white crystalline powder was heated in an oven at 120 °C.  $\text{K}_2\text{SO}_4$  (De Haen's) was recrystallized once from distilled water and dried at 120 °C.

HCl was prepared by distillation of a mixture of commercial HCl and water in an all glass still. Commercial HCl was used in the early part of the work (some of the measurements at 15 and 25 °C) but was found to cause destruction of the indicator at higher temperatures.

Methyl orange (Grubler and Co.) was recrystallized once from water and dried over  $\text{CaCl}_2$ . Stock solutions were made by the addition of approximately 5 mg of indicator to 4 L of distilled water. The solution was acidified with 5 or 6 drops of distilled HCl.

## Results

The ionization constant of the bisulfate ion was determined at intervals of approximately 10 °C from 5 to 55 °C. Both barium chloride and sodium chloride were used as standards to correct for the neutral salt effect. At each temperature, two series of measurements of the effect of sodium sulfate on the relative light absorption of the indicator solution were made by different observers. Some of the data are presented graphically in Figure 1. In Figure 1,  $\log(I^-/{}^+\text{HI}^-)_0 - \log(I^-/{}^+\text{HI}^-)$  for the sodium sulfate series is plotted against the square root of the ionic strength. The quantities plotted have been corrected by extrapolation so that  $\log(I^-/{}^+\text{HI}^-)_0$  refers to a common ionic strength,  $\mu^{1/2} = 0.0150$ , for all the measurements. (The quantity to be added to  $\log(I^-/{}^+\text{HI}^-)_0 - \log(I^-/{}^+\text{HI}^-)$  for a particular series was obtained by graphical extrapolation of the neutral salt curve through the original

TABLE I: Ionization Constants of the  $\text{HSO}_4^-$  Ion at 5–55 °C

Temp, °C	$K(\text{obsd})$ series 1	$K(\text{obsd})$ series 2	$K(\text{obsd})$ average	$K(\text{calcd})$
NaCl as Reference Salt; $K$ Calculated from Eq 25				
4.7	0.01800	0.01825	0.01813	0.01818
14.95	0.01345	0.01370	0.01358	0.01359
24.9	0.01018	0.01018	0.01018	0.01018
34.9	0.00756	0.00783	0.00770	0.00757
44.45	0.00570	0.00566	0.00568	0.00568
54.6	0.00418	0.00416	0.00417	0.00417
BaCl <sub>2</sub> as Reference Salt; $K$ Calculated from Eq 26				
4.7	0.01905	0.01945	0.01925	0.01909
14.95	0.01385	0.01425	0.01405	0.01433
24.9	0.01078	0.01078	0.01078	0.01069
34.9	0.00777	0.00807	0.00792	0.00787
44.45	0.00588	0.00585	0.00587	0.00582
54.6	0.00415	0.00413	0.00414	0.00419

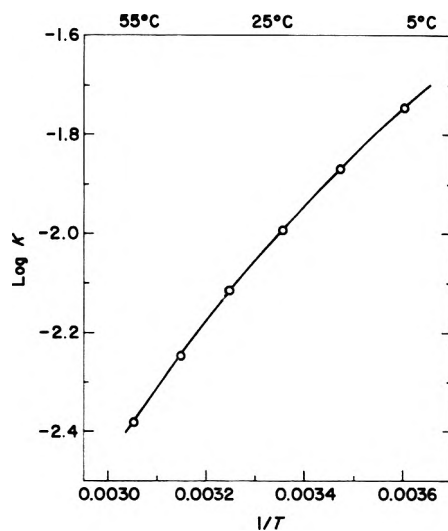


Figure 2.  $\log K_{\text{HSO}_4^-}$  (average) vs.  $1/T$  with sodium chloride as the reference salt.

reference point to  $\mu^{1/2} = 0.0150$ . The corresponding increment in  $\log(I^-/{}^+\text{HI}^-)_0 - \log(I^-/{}^+\text{HI}^-)$  was the appropriate correction.) The corresponding values for the measurements with sodium chloride at 5 and 55 °C appear for purposes of comparison. Complete tables of data for neutral salt effects of NaCl, KCl,  $\text{KNO}_3$ , and  $\text{BaCl}_2$  are available in the original theses,<sup>1</sup> as are data comparing the effects of  $\text{K}_2\text{SO}_4$  with  $\text{Na}_2\text{SO}_4$ .

The values of  $K_{\text{HSO}_4^-}$  computed by the methods described above are listed in Table I and summarized in Figure 2.

## Discussion

The largest source of uncertainty affecting the values of the  $K$ 's reported is that there are specific salt effects upon the indicator equilibrium at the lowest concentrations for which reliable values of  $K$  can be calculated. We have so far no way of determining which neutral salt most nearly duplicates the effect of sulfate ions (and of the minute amounts of hydrogen and of bisulfate ions present) upon the methyl orange equilibrium. Experiments at 25 °C showed<sup>1</sup> that the use of NaCl,  $\text{BaCl}_2$ , and KCl as reference neutral salts for the calculation of  $K$  from experiments made with  $\text{Na}_2\text{SO}_4$  led to different values of  $K$ . The  $K$  from  $\text{BaCl}_2$ , with its doubly charged positive ion, exceeded that obtained with NaCl by 6%, whereas the constant from KCl was only 3.5% larger than that from NaCl.

On the other hand,  $K$ 's calculated from the salt pairs  $\text{Na}_2\text{SO}_4$ -NaCl,  $\text{Na}_2\text{SO}_4$ - $\text{NaNO}_3$ , and  $\text{K}_2\text{SO}_4$ -KCl agree

within the experimental uncertainty of about 1%; this suggests that specific effects on the indicator equilibrium may be less pronounced from negative than from positive ions. It is still possible that the sulfate ion, with its double negative charge, may have an effect on the indicator equilibrium different from that of the anions of uni-univalent neutral salts. However, we would expect for theoretical reasons that the large negative indicator ion would be more susceptible than the hydrogen or the zwitterion to specific salt effects, so that the change from chloride ion to sulfate ion should produce less uncertainty in  $K$  than the change from sodium to barium ion described above. At present we conclude that while the error in the  $K$ 's calculated from  $\text{Na}_2\text{SO}_4$ -NaCl is probably less than 2%, it is not impossible that the values of  $K$  tabulated for 25 °C and below are in error by as much as 6%. The uncertainty should become less as we go to higher temperatures. Such a systematic error in  $K$  need not introduce a correspondingly large error in  $\Delta H^\circ$ , which depends only upon the differences in  $K$  at different temperatures.  $\Delta H^\circ$  would be affected only 3% by a uniform trend from a correct  $K$  at one end of the temperature range to one in error by 6% at the other end. The heats of ionization calculated from the two series of constants agree within 100 cal at 25 °C; they show their largest difference, 464 cal, at 55 °C.

The uncertainty resulting from specific salt effects is large enough, when compared with the precision of the experimental procedure, that we may reasonably hope that the reliability of the constants could be improved by measurements with some other indicator which shows smaller specific salt effects than methyl orange. Methyl orange was chosen for this work because of its stability, and because its behavior in neutral salt solutions had already been investigated by several workers.

Measurements are not reported for higher temperatures because a test at 65 °C revealed a small but definite fading of the indicator solution during a period of 1 h. Further work is needed to determine whether suitable procedures, or possibly another indicator, will permit measurements at 65 °C or higher.

The values of  $K$  obtained from the extrapolations described appear in Table I. It was found that the experimental results could be closely represented by empirical equations of the form

$$\log K = A - B/T - C \log T \quad (24)$$

Such an equation, which implies a constant  $\Delta C_p^\circ$  for the ionization process, is thermodynamically plausible; it is also convenient in that  $\Delta H^\circ$  and  $\Delta C_p^\circ$  may be obtained simply from the constants  $B$  and  $C$ . The equation adopted for the ionization constants derived from investigation of sodium chloride and sodium sulfate was

$$\log K = 61.378 - 1857.1/T - 23.093 \log T \quad (25)$$

That for the series employing barium chloride as a standard neutral salt was

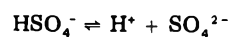
$$\log K = 77.5486 - 2551.8/T - 28.6778 \log T \quad (26)$$

TABLE II: Thermodynamic Properties of the Reaction  $\text{HSO}_4^- = \text{H}^+ + \text{SO}_4^{2-}$

Temp, °C	$K(\text{calcd})$	$\Delta H^\circ$ , cal/mol	$\Delta G^\circ$ , cal/mol	$\Delta S^\circ$ , cal/mol/deg
NaCl as Reference Salt				
5	0.01797	-4270	2222	-23.34
15	0.01357	-4729	2463	-24.96
25	0.01015	-5188	2721	-26.52
35	0.00755	-5647	2993	-28.03
45	0.00558	-6106	3281	-29.50
55	0.00412	-6565	3583	-30.92
BaCl <sub>2</sub> as Reference Salt				
5	0.01894	-4179	2193	-22.90
15	0.01432	-4749	2432	-24.92
25	0.01065	-5319	2692	-26.86
35	0.00785	-5889	2969	-28.74
45	0.00572	-6459	3266	-30.56
55	0.00413	-7029	3581	-32.32

The coefficients of  $\log T$  given above correspond to  $\Delta C_p^\circ = -45.9$  cal for the NaCl series, and  $\Delta C_p^\circ = -57$  cal for the BaCl<sub>2</sub> standard. Values of  $K$  computed from these equations appear in Table I, which presents the separate values of  $K$  obtained by extrapolation from measurements by two observers, and the mean of the individual values. The NaCl data are presented graphically in Figure 2, in which the plotted points represent averaged experimental values, and the smooth curve eq 25.

In Table II are presented the values calculated from these equations at rounded 10 °C intervals for  $K$ ,  $\Delta H^\circ$ ,  $\Delta G^\circ$ , and  $\Delta S^\circ$  of the reaction



The value obtained from these data for the  $\Delta H^\circ$  of ionization at 25 °C,  $-5188$  cal mol<sup>-1</sup>, is in good agreement with earlier calorimetric measurements.<sup>1,4</sup> Furthermore, the ionization constants over the temperature range of 5-55 °C are in excellent accord with those determined by other methods<sup>11</sup> during the 3 decades since the completion of this study. Thus this particular spectrophotometric method is still an appropriate precise technique for determining ionization constants in the range of 10<sup>-1</sup> to 10<sup>-3</sup>.

## References and Notes

- (1) Publication of this paper was delayed by personal circumstances of the authors. The investigations comprised the Ph.D. Dissertations of C. R. Singleterry and I. M. Klotz, University of Chicago, 1940.
- (2) To whom correspondence should be addressed at Department of Chemistry, Northwestern University, Evanston, Ill. 60201.
- (3) A. A. Noyes et al., "The Electrical Conductivity of Aqueous Solutions", Carnegie Institution, Washington, D.C., 1907, pp 239-281.
- (4) K. S. Pitzer, *J. Am. Chem. Soc.*, **59**, 2365 (1937).
- (5) W. J. Hamer, *J. Am. Chem. Soc.*, **56**, 860 (1934).
- (6) J. J. Mullane, Ph.D. Dissertation, University of Chicago, 1940.
- (7) H. S. Harned and B. B. Owen, "The Physical Chemistry of Electrolytic Solutions", Reinhold, New York, N.Y., 1st ed, 1943; 3rd ed, 1958, p 755.
- (8) R. A. Robinson and R. H. Stokes, "Electrolyte Solutions", Butterworths, London, 1959, pp 385-387.
- (9) See, for example, K. S. Pitzer, R. N. Roy, and L. F. Silvester, *J. Am. Chem. Soc.*, **99**, 4930 (1977).
- (10) S. I. Naidich and J. E. Ricci, *J. Am. Chem. Soc.*, **61**, 3268 (1939).
- (11) W. L. Marshall and E. V. Jones, *J. Phys. Chem.*, **70**, 4028 (1966), and references cited therein.

# The Thermodynamics of Transfer of Phenol and Aniline between Nonpolar and Aqueous Environments<sup>†</sup>

Kenneth J. Breslauer,\* Lucia Witkowski, and Kristina Bulas

Department of Chemistry, Douglass College, Rutgers, The State University, New Brunswick, New Jersey 08903 (Received November 9, 1977)

Publication costs assisted The Rutgers Research Council

A recently developed calorimetric technique is employed to directly determine the enthalpy change accompanying the transfer of phenol and aniline from nonpolar to aqueous environments. In conjunction with equilibrium studies, complete thermodynamic profiles are obtained for the transfer of phenol from octane, toluene, and octanol to water and for the transfer of aniline from toluene to water. The data are interpreted in terms of solute-organic solvent and solute-water interactions. These results are discussed in the light of currently accepted views concerning the nature of hydrophobic and hydrophilic forces.

## Introduction

Several years ago we described the development of a new calorimetric technique that allows the direct determination of the enthalpy change accompanying the transfer of a molecule from a nonpolar to an aqueous environment.<sup>1</sup>

Our work in this area was stimulated by the fact that many investigators were reporting thermochemical data on complex biochemical systems that they were unable to explain in terms of currently recognized molecular interactions. At the same time, several laboratories were suggesting that important contributions to the energetics of many biochemical processes arose from the transfer of groups from nonpolar to aqueous environments, or the reverse.<sup>2-4</sup> For example, in the denaturation of a globular protein those amino acid side chains originally embedded in the relatively nonpolar interior of the macromolecule, upon unfolding, become exposed to the highly polar, aqueous environment of the solvent. In contrast, the binding of an inhibitor or substrate to a macromolecule was frequently envisioned as involving a change in the environment of the binding species from a purely polar, aqueous environment to the relatively nonpolar surroundings of the binding site.<sup>5</sup>

In general, it was becoming clear that if one was to explain the molecular origins of the thermochemical data obtained on complex biochemical systems, one had to be able to define the thermodynamic contribution arising from such polar-nonpolar environmental changes. Unfortunately, these data are quite difficult to obtain by studying the biological systems themselves since these environmental changes invariably occur concurrently with charge-charge interactions as well as conformational changes.

In order to isolate the thermodynamic changes associated purely with the transfer of a macromolecular component from one environment to another, one can study the thermodynamics accompanying environmental changes for small molecules that can serve as models for the individual groups that make up these biopolymers. In this connection, the free energy change associated with the transfer of a small molecule from a nonpolar to an aqueous medium would be of interest. Such determinations can and have been carried out by studying the equilibrium distribution of various compounds between water and some

relatively nonpolar organic solvent.<sup>6</sup> Alternatively, some workers have used solubility measurements to calculate partition coefficients.<sup>4</sup> The results of such experiments have been used to construct free energy tables (hydrophobicity scales) which reflect the relative affinity of various compounds and molecular groups for the organic and the aqueous phases.

However, to begin to understand on a microscopic level what constitutes a hydrophobic or hydrophilic interaction as well as to explain much of the accumulated thermochemical data, one must dissect the free energy term into its constituent parts. That is to say, one must expand the model to include the determination of values for the enthalpy, entropy, and heat capacity changes accompanying these distribution experiments. Unfortunately, very few data exist for the enthalpy change accompanying the transfer of a molecule from a nonpolar to an aqueous environment. This probably has been due to the fact that no accurate and convenient method for measuring this parameter has in the past been available.

In an attempt to alleviate this situation, we initiated a program that has resulted in the development of a direct and accurate calorimetric technique for measuring the enthalpy change accompanying the transfer of a molecule from a nonpolar to an aqueous medium. In this paper we present the results obtained by application of this technique to several molecules of general and biological interest.

## Experimental Section

**Chemicals.** Phenol and Aniline were obtained from Fisher Scientific Co., Fair Lawn, N.J. and were used without further purification.

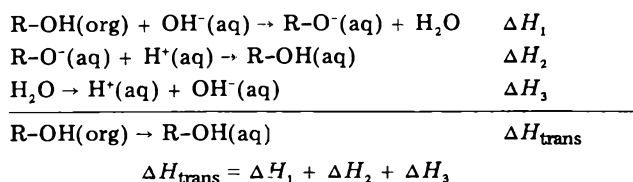
Chromatography quality toluene and octane were purchased from Matheson Coleman and Bell. Grade 1 99% pure octanol was obtained from Sigma Chemical Co., St. Louis, Mo.

## Method

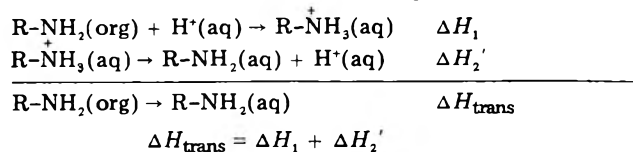
**The Calorimeter.** The experimental technique makes use of an extremely sensitive flow microcalorimeter developed by Sturtevant in collaboration with Beckman Instruments, Palo Alto, Calif.<sup>7</sup> The main components of the instrument are a precision fluid delivery system and a 10 000 junction thermopile which is enclosed within a massive aluminum heat sink. The fluid delivery system consists of two glass syringes equipped with gas-tight Teflon-tipped plungers which are independently driven by

<sup>†</sup>This work was supported by grants from the Rutgers Research Council, the Charles and Johanna Busch Memorial Fund, and the Research Corporation.

## Scheme I: Determination of Enthalpies of Transfer



## Scheme II: Determination of Enthalpies of Transfer



two variable speed 10 rpm synchronous motors.

The two fluids are separately delivered to the calorimeter system by passage through Teflon tubes. At the entrance to the heat sink, the Teflon tubing is changed to platinum tubing (1.0 mm i.d.) which is in good thermal contact with the heat sink. This ensures proper equilibration of the liquids prior to their entering the thermopile. Upon reaching the thermopile the two platinum tubes are brought together by means of a Y junction which serves to initiate the mixing process. The mixed liquids then pass through the platinum tubing which is pressed tightly against the inside surface of a 10000 junction thermopile. Thus, any heat evolved or absorbed upon mixing the two solutions is quantitatively conducted through the thermopile to the massive aluminum heat sink. The resulting electrical output (which is proportional to the heat evolved or absorbed) is amplified and recorded.

*Enthalpies of Transfer.* The technique employed involves the extraction of a compound of interest from an organic to an aqueous phase in the flow calorimeter described above. To avoid excessive heats of solvent mixing it is essential to use immiscible phases. The extraction is readily accomplished by flowing a dilute alkaline (or acidic) aqueous solution against an organic solution of the compound to be transferred. Obviously, such a compound must possess a site for facile protonation or deprotonation so that either an acidic or alkaline aqueous solution can be used to ensure complete extraction during the calorimetric residence time. Previous work has shown that the extraction is in fact complete before the solution exits from the calorimeter.<sup>1</sup>

The overall extraction process results in an enthalpy change which not only includes the heat associated with the transfer of the molecule between the two phases, but also the heat of ionization (or protonation) of the compound transferred. In addition, one must correct for the heat of formation of water whenever an alkaline extracting solution is used. This latter enthalpy is well known and thus can be subtracted from the overall heat of the process. On the other hand, a separate experiment must be performed in order to determine the heat of protonation (or deprotonation) for each compound transferred.

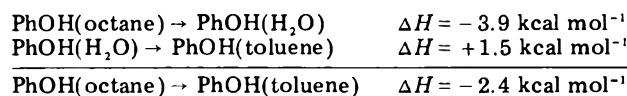
For the case of a molecule possessing an "active" hydrogen, the overall transfer process can be summarized as outlined in Scheme I. On the other hand, when dealing with compounds such as amines that are transferred (extracted) by means of aqueous acid, the overall set of reactions reduces to those shown in Scheme II. Thus, simply by adding the three processes illustrated in Scheme I or the two processes illustrated in Scheme II one obtains a value for the enthalpy change associated with transferring the uncharged molecule from a nonpolar to an aqueous environment.

TABLE I: Enthalpy of Transfer of Phenol and Aniline from Toluene to Water at 25 °C<sup>a, b</sup>

Compd	$\Delta H_1$ , kcal mol <sup>-1</sup>	$\Delta H_2$ , kcal mol <sup>-1</sup>	$\Delta H_3$ , kcal mol <sup>-1</sup>	$\Delta H_{\text{trans}}$ , kcal mol <sup>-1</sup>
Phenol	-9.19	-5.65	+13.34	-1.50 ± 0.13
Aniline	-8.48	-7.28		-1.20 ± 0.15

<sup>a</sup> See Schemes I and II for meaning of symbols. <sup>b</sup> All enthalpies are averages of at least four determinations. The mean calculated enthalpies of transfer are listed in the last column along with the standard errors of the mean.

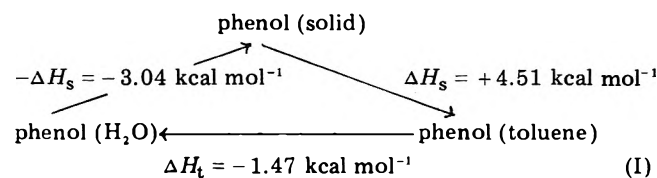
## Scheme III: Enthalpy of Transfer of Phenol (PhOH) between Two Organic Solvents



## Results and Discussion

Table I summarizes the enthalpy data obtained for the transfer of phenol and aniline from toluene to water. As described below, these data can be used to test the new calorimetric technique employed in this work.

The enthalpy of transfer of phenol from toluene to water is exothermic by 1.5 kcal mol<sup>-1</sup> (note: 1 cal<sub>Th</sub> = 4.184 J). This value should be compared with the corresponding enthalpy of transfer that can be derived from previously published heats of solution. Parsons and co-workers found the heat of solution (25 °C) of solid phenol in water to be +3.04 kcal mol<sup>-1</sup>.<sup>8</sup> Arnett and co-workers determined the heat of solution (at 25 °C) of solid phenol in toluene to be +4.51 kcal mol<sup>-1</sup>.<sup>9</sup> From these data, one can derive a value for the enthalpy of transfer of phenol from toluene to water as shown in I.



The derived value of -1.47 kcal mol<sup>-1</sup> for the toluene to water transfer is in very good agreement with the 1.5 kcal mol<sup>-1</sup> determined by means of our direct calorimetric technique. This exothermicity probably reflects favorable hydrogen bonding between the phenolic hydroxyl group and water.

The enthalpy of transfer of aniline from toluene to water was found to be -1.2 kcal mol<sup>-1</sup> at 25 °C (see Table I). Whetsel and Lady determined the enthalpy of complex formation between aniline and benzene to be -1.64 kcal mol<sup>-1</sup>.<sup>10</sup> By combining these two sets of data, one can derive a lower limit of -2.84 kcal mol<sup>-1</sup> for the enthalpy of formation of a hydrogen bond between water and the aromatic amino group of aniline.

*Influence of the Organic Solvent.* Clearly, different organic solvents will provide different "nonpolar environments" so that the enthalpy data reported above should not be interpreted exclusively in terms of solute-water interactions. To determine the degree to which solute-organic solvent interactions contribute to the observed enthalpies of transfer, phenol was transferred to water from several different organic solvents. The results of these studies are summarized in Table II.

These data clearly indicate that the  $\Delta H_t^\circ$  values are strongly dependent upon the specific organic solvent selected. Furthermore, by combining the data of Table II one can derive enthalpy values for the transfer of phenol

TABLE II: Enthalpies of Transfer of Phenol from Various Organic Solvents to Water at 25 °C.<sup>a,b</sup>

Transfer process	$\Delta H_1$ , kcal mol <sup>-1</sup>	$\Delta H_2$ , kcal mol <sup>-1</sup>	$\Delta H_3$ , kcal mol <sup>-1</sup>	$\Delta H_{\text{trans}}$ , kcal mol <sup>-1</sup>
Octane → H <sub>2</sub> O	-11.60	-5.65	+13.34	-3.91 ± 0.11
Toluene → H <sub>2</sub> O	-9.19	-5.65	+13.34	-1.50 ± 0.13
Octanol → H <sub>2</sub> O	-5.04	-5.65	+13.34	+2.65 ± 0.18

<sup>a</sup> See Schemes I and II for meaning of symbols. <sup>b</sup> All enthalpies are averages of at least four determinations. The mean calculated enthalpies of transfer are listed in the last column along with the standard errors of the mean.

TABLE III: Enthalpies of Transfer of Phenol between Two Organic Solvents at 25 °C

Transfer process	$\Delta H_{\text{trans}}$ , kcal mol <sup>-1</sup>
Octane → toluene	-2.4
Octane → octanol	-6.5
Toluene → octanol	-4.1

between two organic solvents as illustrated in Scheme III. These data, which are summarized in Table III, provide considerable, new insights into the nature of solute-organic solvent interactions and deserve further comment.

We have suggested earlier that the 1.5 kcal mol<sup>-1</sup> exothermicity observed for the transfer of phenol from toluene to water reflects favorable hydrogen bonding between the phenolic hydroxyl group and water. We now see that for the octane-water solvent system phenol has a heat of transfer of -3.9 kcal mol<sup>-1</sup> (see Table II). By combining these data we can conclude that phenol has an energetically favorable interaction with toluene (relative to octane) of 2.4 kcal mol<sup>-1</sup> (see Table III).

This result is in excellent agreement with a spectroscopic study carried out by Pimentel and co-workers.<sup>11</sup> These investigators found a favorable interaction of some -2.3 kcal mol<sup>-1</sup> between phenol and benzene. Thus the derived value of -2.4 kcal mol<sup>-1</sup> for the transfer of phenol from octane to toluene (see Table III) is in very good agreement with their findings. In connection with these studies, it is interesting to note that Arnett and co-workers<sup>9</sup> found no free hydroxyl frequency in the infrared spectrum of phenol in a base as weak as benzene.

It should be emphasized that compilations such as Table III are useful in that they clearly demonstrate that the enthalpy changes determined for these transfer processes are not all simply a result of interactions with water. In addition, as illustrated above for phenol, we are able to glean further useful information concerning molecular interactions by looking at the derived enthalpies of transfer between two organic solvents.

The data in Table II also indicate that the transfer of phenol from octanol to water is accompanied by an enthalpy change of +2.65 kcal mol<sup>-1</sup>. This endothermicity is probably due to the formation of a hydrogen bond between the hydroxyl group of the solute and that of the organic solvent. Such a value for this sort of interaction can be compared with that derived from heats of solution reported in the literature. Parsons and co-workers found the heats of solution for phenol in methanol and water to be +0.88 and +3.04 kcal mol<sup>-1</sup>, respectively. From these data one can derive a value of +2.16 kcal mol<sup>-1</sup> for the enthalpy of transfer of phenol from methanol to water. Considering the differences in the solvent systems, this number agrees rather well with the +2.65 kcal mol<sup>-1</sup> determined for the octanol to water transfer.

By combining this result with the data from the octane-water system, one can derive the  $\Delta H_t$  for the transfer

TABLE IV: Thermodynamics of Transfer of Phenol and Aniline between Various Organic Solvents and Water at 25 °C

Transfer process	$\Delta G_t^\circ$ , kcal mol <sup>-1</sup>	$\Delta H_t^\circ$ , kcal mol <sup>-1</sup>	$\Delta S_t^\circ$ , cal deg <sup>-1</sup> mol <sup>-1</sup>
Phenol			
Octane → H <sub>2</sub> O	-1.14	-3.9	-9.2
Toluene → H <sub>2</sub> O	+0.27	-1.5	-5.9
Octanol → H <sub>2</sub> O	+1.80	+2.6	+2.8
Aniline			
Toluene → H <sub>2</sub> O	+1.32	-1.2	-8.7

of phenol from octane to octanol. As seen in Table III, a value of -6.5 kcal mol<sup>-1</sup> is obtained for the hydrogen bond assumed to be formed between phenol and octanol. Such a result is not unreasonable in light of the work of Nagakura<sup>12</sup> and Arnett.<sup>9</sup> These investigators studied hydrogen bond formations between phenol and a number of different proton acceptors (ether, dioxane, ethyl acetate, *N*-methylformamide, *N,N*-dimethylformamide) and found  $\Delta H$  values ranging from -4 to -6.8 kcal mol<sup>-1</sup>.

*Free Energies of Transfer.* Free energies of transfer were calculated as previously described by determining partition coefficients of the compounds between water and various organic solvents.<sup>1</sup> These partition coefficients were found to be independent of solute concentration over the range of 10<sup>-1</sup> to 10<sup>-4</sup> M. This allows us to conclude that our data are not influenced by aggregation of the solute molecules.

The free energies of transfer, along with the calorimetrically determined enthalpies of transfer, allow the calculation of the entropy of transfer. As discussed below, knowledge of the sign and magnitude of this entropy change leads to further insights into the nature of the molecular interactions involved in a given transfer process.

Table IV provides complete thermodynamic profiles for the transfer of phenol from several organic solvents to water and for the transfer of aniline from toluene to water. Significantly, the transfer of phenol from either octane or toluene to water is strongly entropy inhibited as is the transfer of aniline from toluene to water.

Frank and Evans<sup>13</sup> and Kauzmann<sup>2</sup> have described models in which the transfer of nonpolar groups from organic to aqueous medium should result in a decrease in entropy due to the ordering of water molecules around the hydrophobic groups. The observed entropic inhibition to the transfer of phenol and aniline to water is consistent with their predictions.

In contrast, the transfer of phenol from octanol to water is accompanied by an increase in entropy. This may well reflect a high degree of order required for the formation of a phenol-octanol hydrogen bond. Clearly, in this solvent system octanol does not provide an "inert" nonpolar environment.

## Conclusion

We believe that we have demonstrated that a great deal of new, fundamentally important information concerning the nature of solute-solvent interactions can be obtained by investigating the thermodynamic changes accompanying the transfer of molecules between organic solvents and water.

In the past, such studies were limited to the calculation of free energies of transfer from partition coefficients. The calorimetric technique described here provides a convenient method for determining enthalpies of transfer which in turn allows the calculation of entropies of transfer.

We strongly believe that further application of this general technique to additional compounds will lead to the recognition of the molecular forces responsible for the thermodynamic changes observed in many biochemical reactions.

### References and Notes

- (1) K. J. Breslauer, B. Terrin, and J. M. Sturtevant, *J. Phys. Chem.*, **78**, 2363 (1974).
- (2) W. Kauzmann, *Adv. Protein Chem.*, **14**, 1 (1959).
- (3) C. Tanford, *J. Am. Chem. Soc.*, **84**, 4240 (1962).
- (4) C. Tanford and Y. Nozaki, *J. Biol. Chem.*, **246**, 2211 (1971).
- (5) I. V. Berezin, A. V. Lerashov, and K. Martinek, *FEBS Lett.*, **7**, 20 (1970).
- (6) C. Hansch and T. Fujita, *J. Am. Chem. Soc.*, **86**, 1616 (1964).
- (7) J. M. Sturtevant and P. A. Lyons, *J. Chem. Thermodyn.*, **1**, 201 (1969).
- (8) G. H. Parsons, C. H. Rochester, and C. E. C. Wood, *J. Chem. Soc. B*, 533 (1971).
- (9) E. M. Arnett, L. Joris, E. Mitchell, T. S. S. F. Marty, T. M. Gorrie, and P. v. R. Schleyer, *J. Am. Chem. Soc.*, **92**, 2365 (1970).
- (10) K. B. Whetsel and J. H. Lady, *J. Phys. Chem.*, **69**, 1596 (1965).
- (11) G. C. Pimentel and C. M. Huggins, *J. Phys. Chem.*, **60**, 1615 (1956).
- (12) S. Nagakura, *J. Am. Chem. Soc.*, **76**, 3070 (1954).
- (13) H. S. Frank and M. W. Evans, *J. Chem. Phys.*, **13**, 507 (1945).

## Hydrogenation of Dienes and the Selectivity for Partial Hydrogenation on a Molybdenum Disulfide Catalyst

Toshio Okuhara, Hiroyuki Itoh, Koshiro Miyahara, and Ken-ichi Tanaka\*

Research Institute for Catalysis, Hokkaido University, Sapporo, Japan (Received July 18, 1977)

Publication costs assisted by the Research Institute for Catalysis

The hydrogenation reactions of conjugated and nonconjugated dienes on MoS<sub>2</sub> catalyst are brought about by the 1,2 addition of hydrogen, and the reaction with a mixture of H<sub>2</sub> and D<sub>2</sub> yields selectively *d*<sub>0</sub> and *d*<sub>2</sub> adducts. It has been found that the hydrogenation of isoprene on heterogeneous catalysts such as MoS<sub>2</sub>, ZnO, Cr<sub>2</sub>O<sub>3</sub>, Pt black, Pd black, and Raney Ni yields more 2-methyl-1-butene than 3-methyl-1-butene, while homogeneous catalysts give the opposite selectivity. Upon deuteration of isoprene on MoS<sub>2</sub>, the deuterium molecular identity is maintained more strictly in 3-methyl-1-butene than in 2-methyl-1-butene, which may suggest a repulsive effect of the methyl group of isoprene on its adsorption. An extended Hückel MO calculation for the Mo atom or its ions as well as for a cluster of the Mo ions surrounded by four sulfur ions supports the repulsive effect of the methyl group on adsorption.

### Introduction

The hydrogenation of conjugated dienes on a heterogeneous catalyst may be brought about by either 1,2 addition<sup>1,14</sup> or 1,4 addition.<sup>2</sup> In a previous paper,<sup>3</sup> it has been shown that the hydrogenation of butadiene on a MoS<sub>2</sub> catalyst occurs only through the *sec*-butenyl intermediate ( $\sigma$ -allylic species) and that the  $\sigma$ -allylic intermediate does not bring about interconversion to the  $\pi$ -allylic species. In the case of the hydrogenation of butadiene on ZnO catalyst, both 1,2 addition and 1,4 addition occur simultaneously through different intermediates,<sup>4</sup> and the two intermediates do not undergo mutual interconversion on ZnO during the hydrogenation reaction.

In contrast to the hydrogenation of butadiene on MoS<sub>2</sub> and ZnO, it is well known that the  $\sigma$ -allylic complex converts easily to the  $\pi$ -allylic form in Co(CN)<sub>5</sub><sup>3-</sup> and PdCl(2-methylallyl)PPh<sub>3</sub> as a function of the concentration of ligands, CN<sup>-</sup> and PPh<sub>3</sub>,<sup>5,6,10</sup> and the prevalence of the  $\sigma$ -allylic form yields 1,2 addition while the  $\pi$ -allylic form prefers 1,4 addition. In conformity with these facts, the hydrogenation of a series of dienes on MoS<sub>2</sub> catalyst has been performed, and the selectivity for the hydrogenation of dienes by 1,2 addition will be discussed.

### Experimental Section

A commercial MoS<sub>2</sub> powder (Kanto Chemicals Co.) was purified by boiling in a HCl solution for several hours and also in a NaOH solution for several hours, followed by washing with distilled water as well as with hot distilled water as described in the previous paper.<sup>7</sup> The impurity metals analyzed by atomic absorption were as follows (in

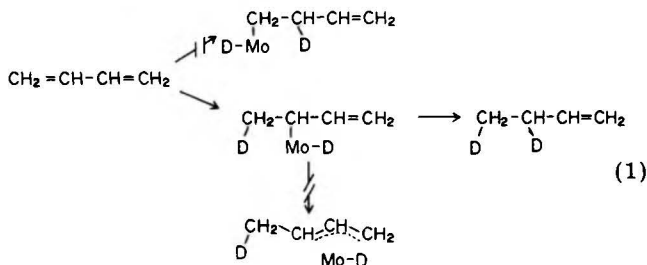
percentage): Fe, 0.02; Mg, 0.0015; Ca, 0.0077; Na, 0.012; Mn, 0.0003; Cr < 0.0001; K < 0.1. Auger spectroscopic analysis of the evacuated MoS<sub>2</sub> at 450 °C for 4 h is shown in Figure 1, which indicates no appreciable segregation of impurity metals.

X-ray diffraction of the MoS<sub>2</sub> powder showed that MoS<sub>2</sub> has a typical 2-H (hexagonal) layer structure, and the surface area of the sample evacuated at ca. 450 °C for several hours was 15 m<sup>2</sup>/g by the BET method with nitrogen adsorbent. The reaction was carried out in a closed circulating system with a total volume of about 300 mL. Analysis of dienes and/or olefins was carried out by on-line gas chromatography. The deuterioolefins were preliminarily separated by gas chromatography and were subjected to mass spectrometric analysis with 11 eV ionization voltage to obtain parent ions, from which the deuterium distribution was computed. The purification of dienes was performed by passing over a trap containing molecular sieve at room temperature. Hydrogen was purified by diffusing through a silver-palladium thimble, and deuterium from a commercial cylinder was used after passage through a liquid nitrogen temperature trap. Pretreatment of the catalyst consisted of evacuation at about 450 °C for 4–5 h, and the reactions were run at room temperature.

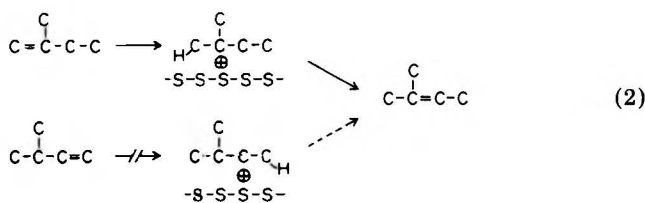
### Results and Discussion

The hydrogenation of butadiene on MoS<sub>2</sub> catalyst occurs through the *sec*-butenyl intermediate ( $\sigma$ -allylic form), which does not bring about interconversion to the  $\pi$ -allylic intermediate (reaction 1).<sup>3</sup> As a result, the deuteration of butadiene on MoS<sub>2</sub> catalyst gives 1-butene-3,4-*d*<sub>2</sub> se-





lectively. In fact, it was found that hydrogenation of butadiene with a mixture of H<sub>2</sub> and D<sub>2</sub> gives only 1-butene-3,4-*d*<sub>2</sub> and 1-butene-*d*<sub>0</sub>,<sup>9</sup> and the reaction with HD gives 1-butene-3-*d*<sub>1</sub> and 1-butene-4-*d*<sub>1</sub> in the ratio of 3-*d*<sub>1</sub>/4-*d*<sub>1</sub> = 1.45.<sup>19</sup> The deuteration of butadiene and olefins on MoS<sub>2</sub> catalyst is divided into three groups by the fraction of *d*<sub>2</sub> adducts: butadiene (100%), olefins (85%), and ethylene (55%), where the values in parentheses are the percent of *d*<sub>2</sub> adducts extrapolated to zero conversion. In contrast with the butadiene molecule, the conjugated double bonds in the isoprene molecule are not equivalent, consequently, the selectivity for the hydrogenation of the two double bonds and the conservation of the deuterium molecular identity in the deuteration of the two double bonds should be interesting. A typical time course for the hydrogenation of isoprene on MoS<sub>2</sub> catalyst is shown in Figure 2, where 2-methyl-1-butene formation occurs about a factor of 4 faster than 3-methyl-1-butene formation. When isoprene is almost consumed, the isomerization of 2-methyl-1-butene to 2-methyl-2-butene occurs but that of 3-methyl-1-butene does not take place appreciably. Recently, we have confirmed that the isomerization of 2-methyl-1-butene occurs via the carbonium ion mechanism on the basal plane of a MoS<sub>2</sub> crystal constructed with a sulfur layer.<sup>8</sup> That is, the sulfur layer of the MoS<sub>2</sub> crystal has sufficient proton activity to make carbonium ions from 2-methyl-1-butene but the proton activity is not sufficient for 3-methyl-1-butene, so that the selective isomerization of 2-methyl-1-butene can proceed without hydrogen on the MoS<sub>2</sub> catalyst via the carbonium ion mechanism as described in reaction 2.



Reference data for the selectivity for the hydrogenation of isoprene by various catalysts are summarized in Table I. From this table, it may be recognized that 2-methyl-1-butene formation is preferred over 3-methyl-1-butene formation on either heterogeneous catalysts, metals, oxides, or MoS<sub>2</sub>, however, the trend is completely opposite for the hydrogenation by homogeneous catalysts. Such contrast of heterogeneous and homogeneous catalysts in the hydrogenation of isoprene may be caused by the steric effect of the methyl group on the adsorption of the isoprene molecule on the heterogeneous catalysts. This supposition is also inferred from the difference in the conservation of the deuterium molecular identity in the addition to the two nonequivalent double bonds.

If the deuteration of isoprene is performed on MoS<sub>2</sub> catalyst, 2-methyl-1-butene-*d*<sub>2</sub> and 3-methyl-1-butene-*d*<sub>2</sub> are selectively formed as shown in Table II and in Figure 3. From these results, it may be concluded that the deuterium molecular conservation in 2-methyl-1-butene is undoubtedly different from that in 3-methyl-1-butene,

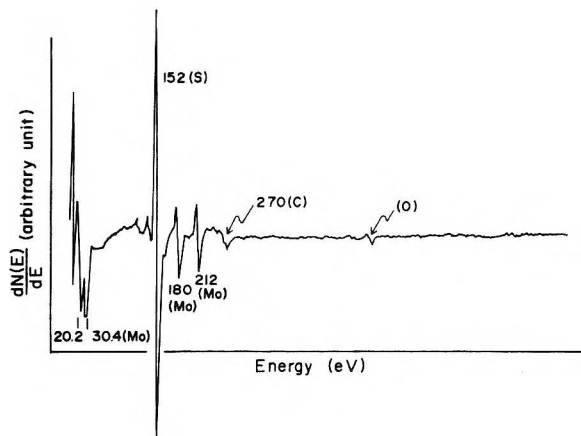


Figure 1. Auger spectroscopic analysis of a MoS<sub>2</sub> catalyst evacuated at 450 °C for 4 h.

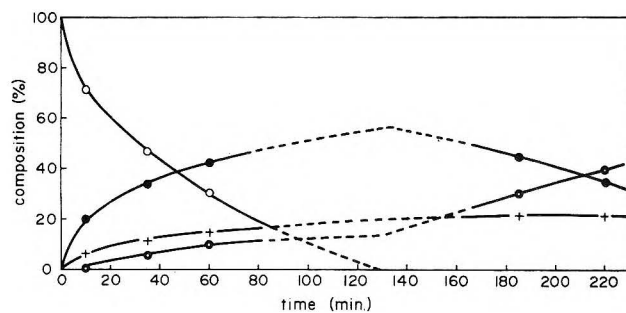


Figure 2. Hydrogenation of isoprene on MoS<sub>2</sub> at room temperature. The initial pressures were as follows: isoprene, 16 mmHg; hydrogen, 32 mmHg; (O) isoprene; (●) 2-methyl-1-butene; (+) 3-methyl-1-butene; (⊙) 2-methyl-2-butene.

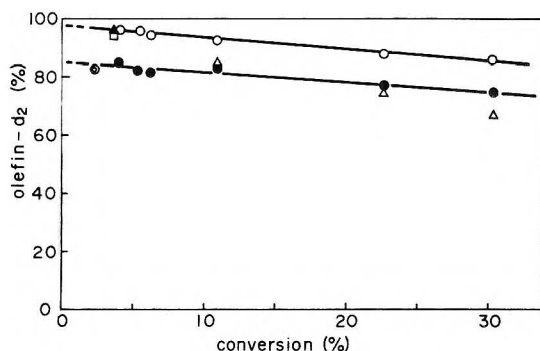


Figure 3. *d*<sub>2</sub> adduct formation in the deuteration of isoprene, 1,3-pentadiene, and 1,4-pentadiene on MoS<sub>2</sub> at room temperature. The upper line shows the formation of 1-butene-*d*<sub>2</sub> from butadiene and lower line alkane-*d*<sub>2</sub> from olefins: (O) 3-methyl-1-butene; (●) 2-methyl-1-butene; (Δ) 2-methyl-2-butene; (▲) 2-pentene from *cis*-1,3-pentadiene; (□) 1-pentene from *cis*-1,3-pentadiene; (⊙) 1-pentene from 1,4-pentadiene.

that is, the values for 3-methyl-1-butene-*d*<sub>2</sub> are on the same line with 1-butene-*d*<sub>2</sub> from butadiene, while those of 2-methyl-1-butene are compatible with the conservation in the deuteration of olefins. Furthermore, it is known that 2-methyl-1-butene formed by the deuteration of isoprene contains a rather large amount of the *d*<sub>3</sub> and *d*<sub>4</sub> species in comparison with the *d*<sub>1</sub> species, while the amounts of these multiply exchanged species are not as large in 3-methyl-1-butene. These facts lead us to the conclusion that the adsorption of isoprene molecules with the double bond adjacent to the methyl group may be loose compared with the adsorption to the other side of the double bond. That is, if *K*<sub>3</sub> > *K*<sub>1</sub>, in reaction Scheme I the lifetime of adsorbed isoprene-*d*<sub>1</sub> (III) may be longer than that of adsorbed isoprene-*d*<sub>1</sub> (IV). As a result, adsorbed isoprene-*d*<sub>1</sub> (III) has more chance for multiple exchange with

TABLE I: Selectivity (%) in the Hydrogenation of Isoprene by Various Catalysts

Catalysts	$\begin{array}{c} \text{C} \\   \\ \text{C}=\text{C}-\text{C} \\   \\ \text{C} \end{array}$	$\begin{array}{c} \text{C} \\   \\ \text{C}-\text{C}=\text{C} \\   \\ \text{C} \end{array}$	$\begin{array}{c} \text{C} \\   \\ \text{C}-\text{C}=\text{C} \\   \\ \text{C} \end{array}$	Ref
MoS <sub>2</sub>	77.0	20.6	2.4	This work
ZnO	68	18	14	15
Cr <sub>2</sub> O <sub>3</sub>	86.6	8.7	4.8	15
Pt black	54	15	31	13
Pd black	32	25	43	13
Raney Ni	42	16	42	13
HCo(CN) <sub>5</sub> <sup>3-</sup> <sup>a</sup>	23	64	12	10
BrCo(PPh <sub>3</sub> ) <sub>3</sub> <sup>b</sup>	4.5	86	9.1	11
+ BF <sub>3</sub>				
PyCo(dm <sub>g</sub> ) <sub>2</sub> <sup>b</sup>	23.4	67.8	8.8	12
Equilibrium (25 °C)	10.7	0.2	89.1	

<sup>a</sup> In solution of CN<sup>-</sup>/Co(II) = 6. <sup>b</sup> dm<sub>g</sub>, dimethyl glyoxime; py, pyridine; PPh<sub>3</sub>, triphenyl phosphine.

TABLE II: Deuteration of Isoprene on a MoS<sub>2</sub> Catalyst

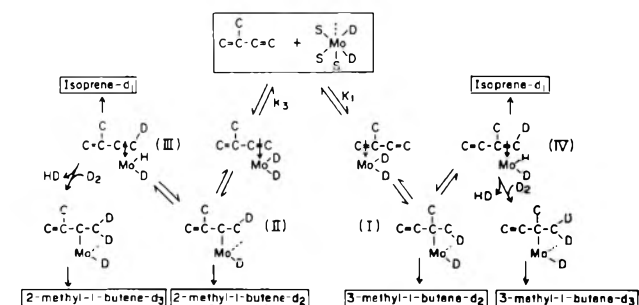
Conversion, %	$\begin{array}{c} \text{C} \\   \\ \text{C}=\text{C}-\text{C} \\   \\ \text{C} \end{array}$					$\begin{array}{c} \text{C} \\   \\ \text{C}-\text{C}=\text{C} \\   \\ \text{C} \end{array}$					$\begin{array}{c} \text{C} \\   \\ \text{C}-\text{C}=\text{C}-\text{C} \\   \\ \text{C} \end{array}$				
	d <sub>0</sub>	d <sub>1</sub>	d <sub>2</sub>	d <sub>3</sub>	d <sub>4</sub>	d <sub>0</sub>	d <sub>1</sub>	d <sub>2</sub>	d <sub>3</sub>	d <sub>4</sub>	d <sub>0</sub>	d <sub>1</sub>	d <sub>2</sub>	d <sub>3</sub>	d <sub>4</sub>
	4.3 <sup>a</sup>		1.1	95.0	3.9		1.0	84.0	9.1	5.8					
5.8 <sup>a</sup>		1.9	95.2	2.8		2.0	81.0	9.9	7.1						
6.2 <sup>a</sup>		2.0	93.4	3.4	1.3	2.0	79.8	11.3	7.0						
11.2		1.7	91.6	5.3	1.3	2.4	82.2	8.6	6.7		4.5	84.2	8.3	3.0	
22.7		4.7	86.4	7.6	1.2	3.7	75.8	12.6	7.9		7.9	73.9	10.0	3.7	
30.3		5.0	84.8	8.6	1.5	4.4	74.1	13.6	7.8		15.9	65.5	14.5	4.0	

<sup>a</sup> Different experimental runs.

TABLE III: Deuteration of *cis*-1,3-Pentadiene and 1,4-Pentadiene on a MoS<sub>2</sub> Catalyst at Room Temperature

Reactant	Products	Compn, %	Compn, %				
			d <sub>0</sub>	d <sub>1</sub>	d <sub>2</sub>	d <sub>3</sub>	d <sub>4</sub>
<i>cis</i> -1,3-Pentadiene		77.4	96.6	3.4	0	0	0
	1-Pentene	1.3	0	1.5	93.6	4.6	0
	2-Pentene	2.5	0	2.3	94.2	3.5	0
	<i>trans</i> -1,3-Pentadiene	18.8	94.4	5.6	0	0	0
1,4-Pentadiene		88.9	95.2	4.8	0	0	0
	1-Pentene	2.6	2.0	9.0	80.6	8.1	0.3
	2-Pentene	0.2					
	<i>trans</i> -1,3-Pentadiene	8.3	83.0	17.0	0	0	0

Scheme I:



D<sub>2</sub> before desorption compared with adsorbed isoprene-d<sub>1</sub> (IV). This expectation is quite well established in the deuteration of isoprene on MoS<sub>2</sub> catalyst as shown in Table II. Furthermore, provided that K<sub>3</sub> is larger than K<sub>1</sub>, predominant 2-methyl-1-butene formation in the hydrogenation of isoprene on heterogeneous catalysts is quite comprehensible. In conformity with the strict 1,2 addition of hydrogen in the hydrogenation of olefins as well as of dienes on MoS<sub>2</sub> catalyst, the selectivity for hydrogenation of the inner double bond relative to the outer double bond of polyolefins should be an interesting problem. In this sense, the hydrogenation of pentadiene was carried out on

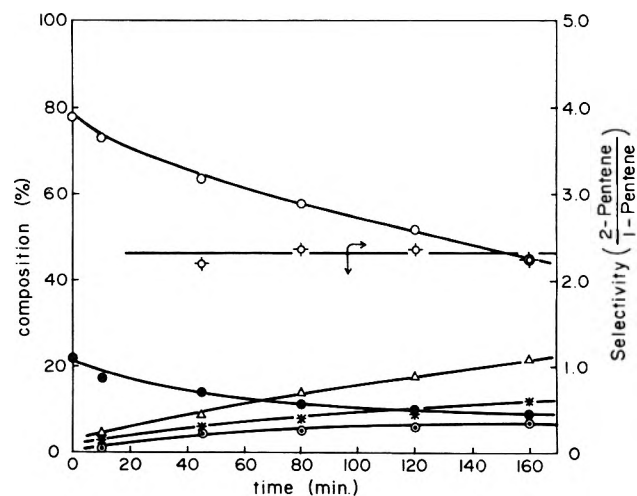


Figure 4. Hydrogenation of the equilibrated 1,3-pentadiene on MoS<sub>2</sub> at room temperature. The initial pressures were as follows: 1,3-pentadiene, 20 mmHg; hydrogen, 40 mmHg; (O) *trans*-1,3-pentadiene; (●) *cis*-1,3-pentadiene; (○) 1-pentene; (Δ) *trans*-2-pentene; (⊙) *cis*-2-pentene.

MoS<sub>2</sub> catalysts at room temperature. The selectivity for the hydrogenation of the outer double bond given by the

TABLE IV: Parameters Used for EHMO Calculation of the Mo(d<sup>n</sup>)(S<sup>2-</sup>)<sub>4</sub> Cluster<sup>a</sup>

	Orbitals	VSIP, eV	$\zeta$
Mo	4d	8.56	2.85
	5s	7.10	1.22
	5p	3.92	1.10
S	3s	20.7	2.122
	3p	11.6	1.827

<sup>a</sup> Reference 16.

ratio of 2-pentene/1-pentene was about 2.3, and the selectivity was independent of the hydrogenation conversion as shown in Figure 4.

The conservation of the deuterium molecular identity in the deuteration of pentadiene was found to be identical for both inner and outer double bond deuteration as shown in Table III, and the percentage of 1-pentene-*d*<sub>2</sub> and/or 2-pentene-*d*<sub>2</sub> is in quite close agreement with that of 1-butene-*d*<sub>2</sub> from the deuteration of butadiene on MoS<sub>2</sub> as shown in Figure 3.

Accordingly, it may be concluded that the alkyl branch, such as methyl in isoprene, being adjacent to the double bond might weaken the adsorption by that double bond, and that the selectivity for the hydrogenation of isoprene on heterogeneous catalysts may be caused by the steric effects dominating the reaction intermediates have been observed in the hydrogenation of allene and methylacetylene on MoS<sub>2</sub> catalyst.<sup>14</sup>

In order to estimate the steric effect of the methyl group on the adsorption of the isoprene molecule, an extended Hückel molecular orbital calculation (EHMO) was performed for a cluster model. A MoS<sub>2</sub> crystal is constructed from the trigonal prismatic coordination units such as shown in Figure 5b, and half-hydrogenated species are formed on the surface of the side of the layered crystal on which molybdenum ions are exposed.<sup>18,20</sup> The cluster model used for the calculation is shown in Figure 5c, and may correspond to a section of the layered crystal cut along the dotted line in Figure 5a, in which the lattice parameters are written.

The parameters of the molybdenum atom and sulfur used for the EHMO calculation of the cluster described in Figure 5c are listed in Table IV, where VSIP is the valence state ionization potential and  $\zeta$  is the orbital exponent for Slater type orbitals.<sup>16</sup> The calculated energy levels for a cluster, Mo(d<sup>n</sup>)(S<sup>2-</sup>)<sub>4</sub>, are shown in Figure 6, in which the x-ray photoelectron spectra of 2H-MoS<sub>2</sub> obtained by Wertheim et al.<sup>17</sup> is compared with the calculated result. For a comparison of the calculated energy levels with the photoelectron spectra, the peak corresponding to sulfur s band matches the calculated energy levels. The surprisingly good agreement of the calculated energy levels with the observed spectra may imply that the simple

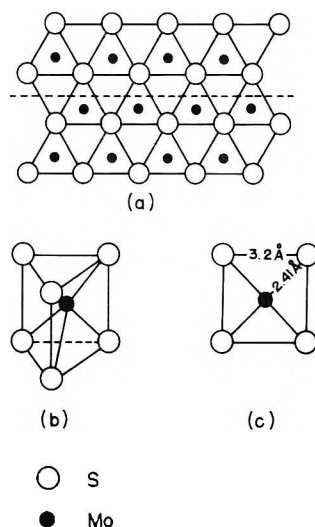


Figure 5. Crystallographic structure of MoS<sub>2</sub>. (a) Top view of MoS<sub>2</sub> crystal. (b) Trigonal prismatic coordination unit. (c) Mo(d<sup>n</sup>)(S<sup>2-</sup>)<sub>4</sub> cluster formed by removing two sulfur atoms from the trigonal prismatic unit (b).

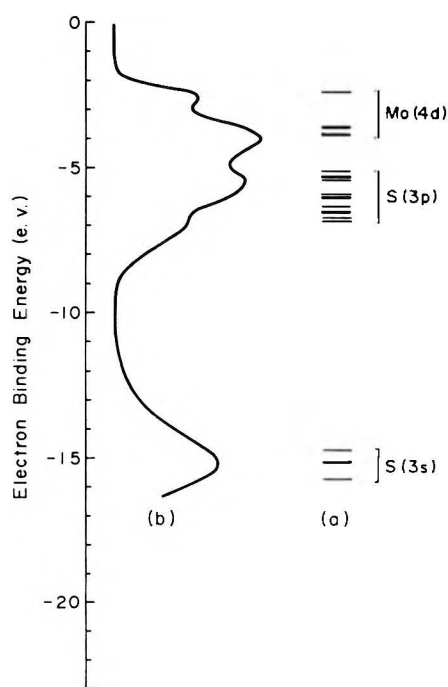


Figure 6. (a) Calculated energy levels of the Mo(d<sup>n</sup>)(S<sup>2-</sup>)<sub>4</sub> cluster. (b) X-ray photoelectron spectra of 2H-MoS<sub>2</sub> obtained by Wertheim et al.<sup>17</sup>

cluster model shown in Figure 5c seems to characterize the side surface of the layered crystal of MoS<sub>2</sub>.

As has been discussed in this paper, the prevalent 2-methyl-1-butene formation in the hydrogenation of

TABLE V: Total Energy Calculation for Isoprene-Mo(d<sup>n</sup>) and Isoprene-[Mo(d<sup>n</sup>)(S<sup>2-</sup>)<sub>4</sub>]<sup>a</sup>

d <sup>n</sup>	Mo valence	Total energy, eV				
		I	II	III	IV	V
(a) Isoprene-Mo(d <sup>n</sup> )						
0	+6	-495.799	-495.153	-495.291	-494.775	-493.948
2	+4	<u>-516.349</u>	-515.285	-514.431	-514.643	-514.123
4	+2	<u>-533.916</u>	-533.115	-531.908	-531.750	-531.221
6	0	<u>-550.824</u>	-550.209	-549.000	-548.836	-548.305
(b) Isoprene-[Mo(d <sup>n</sup> )(S <sup>2-</sup> ) <sub>4</sub> ]						
2	+4	-954.240	-956.884	-956.049	-954.754	<u>-957.403</u>
4	+2	-970.688	-973.878	-972.915	-971.853	<u>-974.173</u>
6	0	-986.707	<u>-990.641</u>	-989.346	-988.934	-990.432

<sup>a</sup> The underline indicates the lowest total energy.

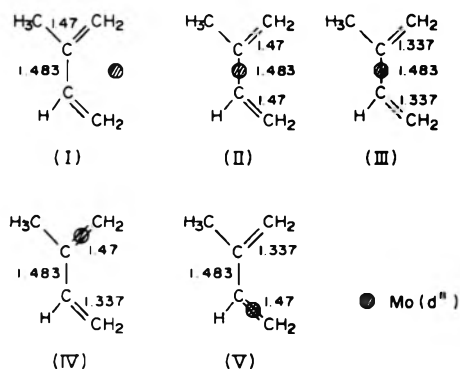


**Figure 7.** Arrangements of the isoprene molecule for the total energy calculation. The distance between isoprene and molybdenum ion is fixed at 2 Å.

isoprene on MoS<sub>2</sub> and the different conservation of the deuterium molecular identity in 2-methyl-1-butene and 3-methyl-1-butene from the deuteration of isoprene seem to be dominated by the steric effect of the methyl group in the isoprene molecule on adsorption.

Assuming that the catalytic reaction takes place on the side surface of the MoS<sub>2</sub> crystal, a total energy calculation has been attempted for the models arranged as described in Figure 7, where the molybdenum atom is arranged 2 Å below the molecular plane of isoprene for both the Mo(d<sup>n</sup>) and Mo(d<sup>n</sup>)(S<sup>2-</sup>)<sub>4</sub> cluster, and the molybdenum atom in conformation I is arranged to be equal distance from the four carbon atoms. The calculations have been done by assuming the double bond length interacting with the molybdenum ion or atom is 1.337 or 1.47 Å, where the value of 1.47 was postulated to be equal to the bond length of ethylene coordinated to the platinum complex. The total energy calculation for each conformation is summarized in Table V, where the d electrons are changed from d<sup>6</sup> to d<sup>2</sup> depending on the valence state of molybdenum, Mo atom to Mo<sup>4+</sup> ion. From this calculation, it may be concluded that conformation I is the most profitable arrangement for an isoprene molecule interacting with a single molybdenum atom or ion. In contrast with this, the arrangement of the cluster alienated from the methyl group, conformation V, becomes the most stable conformation as has been inferred above. The calculation on the transoid form of the isoprene molecule (the two double bonds in a trans conformation) gives quite similar results, that is, an arrangement like conformation II gives

the lowest total energy for the interaction with the Mo atom or its ions, while the arrangement corresponding to conformation V is the most profitable coordination for the cluster. The results of these calculations, accordingly, seem to support the postulate that the steric effect of the methyl group may dominate the selectivity for the hydrogenation of isoprene on heterogeneous catalysts, and may reveal the possibility for selective hydrogenation of the inner double bond by sheltering the outer double bond with steric effects from attached groups. The opposite selectivity for the hydrogenation of isoprene by homogeneous catalysts giving 3-methyl-1-butene predominantly might be caused by the different electrophilic reactivity of the two unequal double bonds with the hydrogen coordinated to the complex.

## References and Notes

- (1) R. L. Burwell, Jr., A. B. Littlewood, M. Cardew, G. Pass, and C. T. H. Stoddart, *J. Am. Chem. Soc.*, **82**, 6272 (1960); W. C. Conner, R. A. Innes, and R. J. Kokes, *ibid.*, **90**, 6858 (1968); K. Tanaka, H. Nihira, and A. Ozaki, *J. Phys. Chem.*, **74**, 4510 (1970); S. Naito, Y. Sakurai, H. Shimizu, T. Onishi, and K. Tamaru, *Bull. Chem. Soc. Jpn.*, **43**, 2274 (1970); *Trans. Faraday Soc.*, **67**, 1529 (1971); T. Okuhara, K. Tanaka, and K. Miyahara, *J. Chem. Soc., Chem. Commun.*, 42 (1976).
- (2) H. Hattori, Y. Tanaka, and K. Tanabe, *J. Am. Chem. Soc.*, **98**, 4652 (1976).
- (3) T. Okuhara, T. Kondo, and K. Tanaka, *Chem. Lett.*, 717 (1976).
- (4) T. Okuhara, T. Kondo, and K. Tanaka, *J. Phys. Chem.*, **81**, 808 (1977).
- (5) J. Kwiatek, I. L. Mador, and J. K. Seyler, *Adv. Chem. Ser.*, **No. 37**, 201 (1963); J. Kwiatek and J. K. Seyler, *J. Organometal. Chem.*, **3**, 421 (1965).
- (6) F. A. Cotton, J. W. Faller, and A. Musco, *Inorg. Chem.*, **6**, 179 (1967).
- (7) T. Okuhara, K. Tanaka, and K. Miyahara, *J. Catal.*, **48**, 229 (1977).
- (8) T. Okuhara, K. Tanaka, and K. Tanabe, *J. Chem. Soc., Chem. Commun.*, 180 (1977).
- (9) T. Okuhara, K. Tanaka, and K. Miyahara, *J. Chem. Soc., Chem. Commun.*, 42 (1976).
- (10) T. Suzuki and T. Kwan, *J. Chem. Soc. Jpn.*, **88**, 1341 (1965).
- (11) K. Kawakami, T. Mizoroki, and A. Ozaki, *Chem. Lett.*, 847 (1976).
- (12) T. Mizuta and T. Kwan, *J. Chem. Soc. Jpn.*, **88**, 471 (1967).
- (13) G. C. Bond, "Catalysis by Metals", Academic Press, London, 1962, p 307.
- (14) T. Okuhara, T. Kondo, and K. Tanaka, *Chem. Lett.*, 119 (1977).
- (15) Unpublished data.
- (16) L. J. Guggenberger and A. W. Sleight, *Inorg. Chem.*, **8**, 2041 (1969); H. Basch, A. Viste, and H. B. Gray, *Theor. Chim. Acta (Berl.)*, **3**, 458 (1965); E. Clementi and D. L. Raimondi, *J. Chem. Phys.*, **38**, 2686 (1963).
- (17) G. K. Wertheim, F. Di-Salvo, and D. N. E. Buchanan, *Solid State Commun.*, **13**, 1225 (1973).
- (18) T. Okuhara and K. Tanaka, Japanese Chemical Society Annual Meeting at Osaka, April, 1977.
- (19) T. Okuhara and K. Tanaka, *J. Chem. Soc., Chem. Commun.*, 199 (1976).
- (20) K. Tanaka and T. Okuhara, *Catal. Rev.*, **15**, 242 (1977).

# The Influence of Cupric Ions on the Infrared Spectrum of Water

P. P. Sethna, Lary W. Pinkley,<sup>†</sup> and Dudley Williams\*

Department of Physics, Kansas State University, Manhattan, Kansas 66506 (Received October 20, 1977)

Publication costs assisted by the Office of Naval Research

We have measured the spectral reflectance of aqueous solutions of several cupric salts under conditions of near-normal incidence. Values of the refractive index  $n(\nu)$  and absorption index  $k(\nu)$  have been determined from measured spectral reflectance by Kramers-Kronig phase-shift analysis. The influence of the  $\text{Cu}^{2+}$  ions on the water spectrum is markedly different from the influences of other monovalent and divalent metallic ions studied earlier. In addition to the familiar liquid water bands, we have evidence for additional bands near 3080, 1660, and 930  $\text{cm}^{-1}$ , which we tentatively attribute to water molecules in quasi-stable association with the  $\text{Cu}^{2+}$  ions.

## Introduction

In an earlier study<sup>1</sup> of cupric sulfate we found that certain bands associated with the water of crystallization in a single  $\text{CuSO}_4 \cdot 5\text{H}_2\text{O}$  crystal also appeared in the spectra of aqueous solutions of cupric sulfate. In another study<sup>2</sup> we investigated the influence of dissolved divalent ions on the gross features of the water spectrum; the results indicated that the influence of  $\text{CuCl}_2$  on the water spectrum was markedly different from the influence of  $\text{MgCl}_2$ , although the sizes of the  $\text{Cu}^{2+}$  and  $\text{Mg}^{2+}$  ions are nearly the same. Although the early theoretical work of Bernal and Fowler<sup>3</sup> as well as subsequent theoretical work had indicated that the influence of dissolved ions on the liquid water structure depends chiefly on the ratio of charge to ionic radius, we have found<sup>4</sup> that in the case of the alkali and alkaline-earth halides the influence of negative ions is considerably greater than that of positive ions. Thus, the marked differences in the water spectrum produced by  $\text{Cu}^{2+}$  and  $\text{Mg}^{2+}$  constitutes something of an anomaly, which is the subject of the present study.

## Experimental Section

The method involved in the present work makes use of quantitative measurement of spectral reflectance  $R(\nu)$  at near-normal incidence. The spectral reflectance  $R(\nu)_s$  of solutions of cupric salts was determined by direct comparison with the spectral reflectance  $R(\nu)_w$  of water at 27 °C. With  $r$  as the measured reflectance of the ratio of solution reflectance to water reflectance, the absolute value of  $R(\nu)_s = rR(\nu)_w$ . The values of  $R(\nu)_w$  are based on the values of  $R(\nu)_w$  obtained from tabulated values of the refractive index  $n(\nu)$  and the absorption index  $k(\nu)$  for water given in the recent summary article by Downing and Williams.<sup>5</sup> The tabulated values of these optical constants of water are based on extensive measurements of absolute spectral reflectance along with independent quantitative measurements of spectral absorption.

## Data Analysis

Kramers-Kronig (KK) phase-shift analysis can be employed to obtain values of the refractive index  $n(\nu)$  and the absorption index  $k(\nu)$  in terms of the phase shift

$$\phi(\nu) = \frac{2\nu}{\pi} P \int_0^\infty \frac{\eta \rho(\nu') d\nu'}{\nu'^2 - \nu^2} \quad (1)$$

where  $\rho(\nu') = [R(\nu')]^{1/2}$ . The resulting values of  $k(\nu)$  for a 4.3 M solution of  $\text{CuCl}_2 \cdot 2\text{H}_2\text{O}$  are plotted as a function

of wavenumber  $\nu$  in Figure 1. The maximum value of  $k(\nu)$  in the vicinity of the  $\nu_1, \nu_3$  water band is smaller than for the corresponding band in pure water; the absorption peak occurs at a lower wavenumber than in pure water and the shape of the low-frequency wing of the band is different from that of the water band. Less obvious differences between the solution spectrum and the water spectrum occur near the  $\nu_2$  band near 1650  $\text{cm}^{-1}$  and in the high-wavenumber wing of the librational band  $\nu_L$  near 500  $\text{cm}^{-1}$ . In the present study, we used a somewhat different procedure for comparing the solution spectra with that of water.

The KK relationship expressed in eq 1 is based on quite general relationships and there is no reason to doubt its validity. However, the limits of the integral include *all* frequencies and experimental investigations cover finite frequency ranges; in our case, the range covered is from 6800 to 350  $\text{cm}^{-1}$ . Outside the range in which we have actually made measurements (M), it is necessary to make a high-frequency extrapolation (HFE) and a low frequency extrapolation (LFE). Thus, for any solution the value of the phase shift  $\phi(\nu)_s$  in eq 1 can be written

$$\phi(\nu)_s = \phi(\nu)_{s\text{LFE}} + \phi(\nu)_{s\text{M}} + \phi(\nu)_{s\text{HFE}} \quad (2)$$

where the subscripts indicate the contribution to  $\phi(\nu)_s$  from the LFE, the HFE, and the actual range of measurement M for the solutions.

Similarly, for water we may write the corresponding phase shift  $\phi(\nu)_w$  in the form

$$\phi(\nu)_w = \phi(\nu)_{w\text{LFE}} + \phi(\nu)_{w\text{M}} + \phi(\nu)_{w\text{HFE}} \quad (3)$$

By working with relatively dilute solutions, it is possible in good approximation to set  $\phi(\nu)_{s\text{LFE}} = \phi(\nu)_{w\text{LFE}}$  and  $\phi(\nu)_{s\text{HFE}} = \phi(\nu)_{w\text{HFE}}$ . Under these conditions, we can subtract eq 3 from eq 2 and write

$$\Delta(\nu) = \phi(\nu)_s - \phi(\nu)_w = \phi(\nu)_{s\text{M}} - \phi(\nu)_{w\text{M}} \quad (4)$$

or

$$\phi(\nu)_s = \phi(\nu)_w + \Delta(\nu)$$

In this expression  $\phi(\nu)_w$  at 27 °C is well known from measurements of both reflection and absorption and  $\Delta(\nu)$  is simply the difference between  $\phi(\nu)_s$  and  $\phi(\nu)_w$  as determined by eq 1 with identical LFE and HFE and therefore involves only the differences between  $\phi(\nu)_{s\text{M}}$  and  $\phi(\nu)_{w\text{M}}$  based on the spectral range in which measurements were made.

In terms of  $\phi(\nu)_s$  the optical constants are obtained by the familiar relations  $n(\nu)_s = [1 - R(\nu)]/[1 + R(\nu) - 2R^{1/2}(\nu) \cos \phi(\nu)]$  and  $k(\nu)_s = [-2R^{1/2}(\nu) \sin \phi(\nu)]/[1 + R(\nu) - 2R^{1/2}(\nu)$

<sup>†</sup> Present address: Lockheed Space and Missiles Co., Huntsville, Ala.

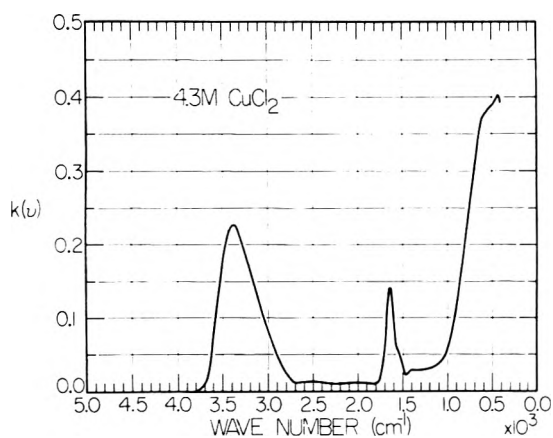


**Figure 1.** The spectral absorption index of a 4.3 M solution of cupric chloride as determined from a Kramers-Kronig phase-shift analysis of measured spectral reflectance.

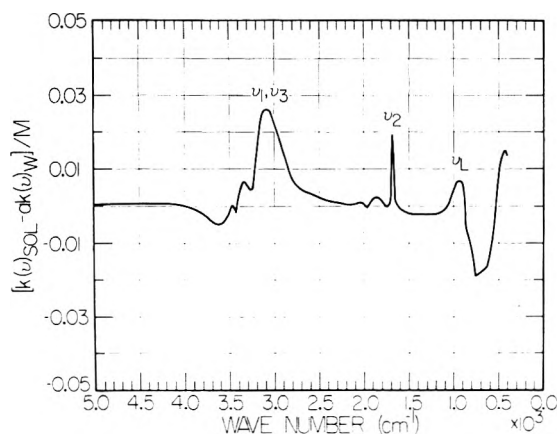


**Figure 2.** The spectral absorption index of cupric chloride solutions as compared with the spectral absorption index of water.

cos  $\phi(\nu)$ ]. The value of  $k(\nu)$  for any absorber is directly proportional to the number of absorbers per unit volume and thus to the molar concentration of the absorber.

In the present study we have determined  $k(\nu)_s$  for 0.5 and 1.0 M solutions of  $\text{CuCl}_2$  and  $\text{CuBr}_2$ . In order to determine the effects of these solutes on the water spectrum, we can take the difference between  $k(\nu)_s$  for the solution and  $ak(\nu)_w$  where  $a$  is the ratio of the molar concentration of water in the solution to the molar concentration of water in normal liquid water; thus,  $a$  is simply the ratio of the number density of water molecules in the solution to the number density of water molecules in normal water. In order to summarize our work, we have computed the ratio of the difference  $k(\nu)_s - ak(\nu)_w$  to the molar concentration  $M$  of the solute. Plots of this quantity  $[k(\nu)_s - ak(\nu)_w]/M$  are given in Figures 2 and 3 for  $\text{CuCl}_2$  and  $\text{CuBr}_2$ , respectively.

In the plots in these figures the ordinate values are negative in regions where the solution is more transparent than water and positive in regions where the solution is more absorbing than water. The regions in which the solutions are more transparent usually involve shifts in the major bands of bulk water caused by the solute. The curves in the figures represent the mean values of the curves obtained with 0.5 and 1.0 M solutions of the salts. Throughout most of the spectrum the ordinates of the curves have an estimated uncertainty of approximately  $\pm 0.003$ .

## Results

In the relative absorption curve shown in Figure 2 for the  $\text{CuCl}_2$  solutions we note a small negative excursion near

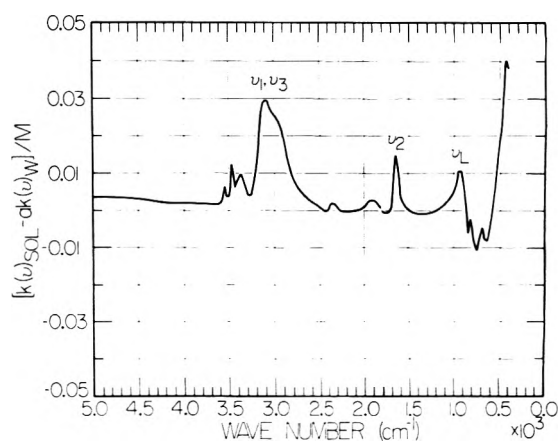


**Figure 3.** The spectral absorption index of cupric bromide solutions as compared with the spectral absorption index of water.

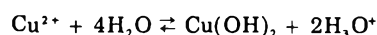
$3600 \text{ cm}^{-1}$  followed by a positive excursion near  $3300 \text{ cm}^{-1}$  which we tentatively attribute to a shift of the  $\nu_1, \nu_3$  fundamental band of bulk water. Similarly, there is a larger negative excursion near  $700 \text{ cm}^{-1}$  followed by a large rise near  $450 \text{ cm}^{-1}$ , which we similarly attribute to a shift of the librational band of bulk water. In addition to these excursions, there are three fairly well-defined absorption maxima in the curves. These maxima occur at  $3080, 1680,$  and  $930 \text{ cm}^{-1}$ ; the relative strength  $\int k(\nu)_s d\nu$  of these bands are proportional to the  $\text{CuCl}_2$  concentration in the  $0.5\text{--}1.0 \text{ M}$  range.

Similar well-defined maxima appear in the curves shown in Figure 3 for the  $\text{CuBr}_2$  solutions at  $3080, 1635,$  and  $940 \text{ cm}^{-1}$ . In the relative absorption curve in Figure 3, there is a large negative excursion near  $600 \text{ cm}^{-1}$  along with a large positive excursion near  $450 \text{ cm}^{-1}$ , which we tentatively attribute to a shift of the librational band of bulk water in the solution. There are no clearly defined excursions in the vicinity of the  $\nu_1, \nu_3$  band appearing near  $3400 \text{ cm}^{-1}$  in the spectrum of pure water.

Smaller absorption maxima appear in the curves of Figures 2 and 3 between  $3600$  and  $3200 \text{ cm}^{-1}$ . Other peaks appearing in the curves are so small that they fall within the  $\pm 0.003$  uncertainty mentioned earlier.

## Discussion of Results

In our earlier studies of acids<sup>6</sup> we found that well-defined positive peaks in a relative absorption curve similar to the ones in Figures 2 and 3 could be attributed to the  $\text{H}_3\text{O}^+$  ion, which is a well-defined entity in acid solutions. It is well known that the cupric compounds of present interest are regarded as hydrolyzing salts. In aqueous solution reactions of the type



are to be expected. However, the absorption bands in Figures 2 and 3 differ in both frequency and general contour from bands that have been attributed to the  $\text{H}_3\text{O}^+$  ion. On the basis of the known dissociation constants and measured pH values for the solutions, we find that only one out of every 200  $\text{Cu}^{2+}$  ions is in the form  $\text{Cu}(\text{OH})^+$  or  $\text{Cu}(\text{OH})_2$ . In view of this extremely low concentration, it is not surprising that the  $\text{H}_3\text{O}^+$  bands are not observable in Figures 2 and 3.

We suggest that the strong absorption peaks in the curves in Figures 2 and 3 can be attributed to water molecules associated with the  $\text{Cu}^{2+}$  ions in quasi-stable groups. In certain crystals the  $\text{Cu}^{2+}$  ion is connected by ligands to neighboring oxygen atoms<sup>7</sup> including those in the water of crystallization. In a study of the nuclear

TABLE I: Band Frequencies ( $\text{cm}^{-1}$ ) of  $\text{H}_2\text{O}$  Molecules

	$\nu_1, \nu_3$	$\nu_2$	$\nu_L$
Bulk water at 27 °C	3390	1640	570
Ice at -7 °C	3260	1640	810
$\text{CuCl}_2$ solution	3080	1680	930
$\text{CuBr}_2$ solution	3080	1635	940
$\text{CuSO}_4$ solution	3090	~1680	910 <sup>a</sup>
		~1600	
$\text{CuSO}_4 \cdot 5\text{H}_2\text{O}$ crystal	3160	~1650	910 <sup>a</sup>

<sup>a</sup> Overlapped by the  $\nu_1$  fundamental of  $\text{SO}_4^{2-}$  at 870  $\text{cm}^{-1}$ .

magnetic resonance of  $^{17}\text{O}$ , Swift and Connick<sup>8</sup> have suggested that the ion  $\text{Cu}(\text{H}_2\text{O})_6^{2+}$  exists in aqueous solutions of cupric salts and has a lifetime of the order of  $10^{-8}$  to  $10^{-9}$  s. In analogy to ligand bonds between  $\text{Cu}^{2+}$  and neighboring O atoms in crystals, the bonded O atoms form a distorted octahedron with four O atoms in the equatorial plane at a distance of approximately 2 Å from the  $\text{Cu}^{2+}$  ion and with two axial O atoms at a greater distance.

We suggest that the peaks in Figures 2 and 3 are associated with water molecules bound to  $\text{Cu}^{2+}$  ions in quasi-stable groups. The broad bands near 3080  $\text{cm}^{-1}$  can be attributed to the overlapping  $\nu_1$ , and  $\nu_3$  fundamentals of bound water molecules and the narrower bands near 1650  $\text{cm}^{-1}$  can be attributed to the  $\nu_2$  fundamental of such molecules. The  $\nu_2$  band in bulk water is itself quite narrow as compared with the other water bands. Although there is clear evidence for the presence of the  $\nu_2$  bands in Figures 2 and 3, the exact frequencies of the  $\nu_2$  bands may be somewhat in error as a result of the subtraction process involving two narrow bands. Similarly, we propose that the bands near 930  $\text{cm}^{-1}$  can be attributed to the librational motion  $\nu_L$  of bound water molecules in the local lattice.

In Table I, we list the frequencies of these bands as they appear in water, in ice, and in solutions containing cupric ions. We also include the frequencies of the bands ob-

served in a  $\text{CuSO}_4 \cdot 5\text{H}_2\text{O}$  crystal. The  $\nu_1$ ,  $\nu_3$ , and  $\nu_L$  bands of  $\text{H}_2\text{O}$  molecules associated with  $\text{Cu}^{2+}$  ions are significantly shifted from their positions in the bulk water and ice spectra. The frequencies of the weaker  $\nu_2$  band of  $\text{H}_2\text{O}$  in various materials do not differ greatly from one another; further careful study of this band by transmission methods might be useful.

It is tempting to suggest that the small absorption maxima in the 3600–3200- $\text{cm}^{-1}$  regions in Figures 2 and 3 and in the spectrum of  $\text{CuSO}_4$  solutions<sup>1</sup> may be attributed to  $\text{H}_2\text{O}$  molecules at the axial positions in the  $\text{Cu}(\text{H}_2\text{O})_6^{2+}$  octahedron. However, because the observed absorption maxima are scarcely greater than our estimated uncertainty of  $\pm 0.003$ , such a suggestion is probably not justified.

If our suggestions regarding the bands in cupric solutions are correct, it is probably possible to subject the  $\text{Cu}(\text{H}_2\text{O})_6^{2+}$  ion or other complex to a normal coordinate analysis. Other modes of vibration of the groups involved would probably result in absorption bands in the far infrared. If our suggestions are correct, it is to be expected that ions of the other transition elements form similar types of association with water in aqueous solutions.

*Acknowledgment.* We express our appreciation to the Office of Naval Research for its generous support of this work. Our thanks also go to Professors J. D. Petersen and H. C. Moser for helpful discussions.

## References and Notes

- (1) P. P. Sethna, L. W. Pinkley, and D. Williams, *J. Opt. Soc. Am.*, **67**, 499 (1977).
- (2) H. D. Downing and D. Williams, *J. Phys. Chem.*, **80**, 1950 (1976).
- (3) J. D. Bernal and R. H. Fowler, *J. Chem. Phys.*, **1**, 515 (1933).
- (4) P. Rhine, D. Williams, G. M. Hale, and M. R. Query, *J. Phys. Chem.*, **78**, 238 (1974).
- (5) H. D. Downing and D. Williams, *J. Geophys. Res.*, **80**, 1656 (1975).
- (6) H. D. Downing and D. Williams, *J. Phys. Chem.*, **80**, 1640 (1976).
- (7) L. E. Orgel, "Transition-Metal Chemistry: Ligand Field Theory", Methuen, London, 1960, Chapter 4.
- (8) T. J. Swift and R. E. Connick, *J. Chem. Phys.*, **37**, 307 (1962).

## Polarizability, Proton Transfer, and Symmetry of Energy Surfaces of Phenol-*n*-Propylamine Hydrogen Bonds. Infrared Investigations

Georg Zundel\* and Anton Nagyvrevl†

Physikalisch-Chemisches Institut der Universität, Theresienstrasse 41, D-8 München 2, West Germany (Received August 5, 1977)

Chlorophenol + *n*-propylamine systems (ratio 1:1) are studied in deuterioacetonitrile, pure and with the addition of water. The proton transfer equilibria in the  $\text{OH}\cdots\text{N}=\text{O}\cdots\text{H}^+\text{N}$  hydrogen bonds are determined from bands of chlorophenol and *n*-propylamine molecules. Furthermore, an IR continuum indicates when these hydrogen bonds are easily polarizable. 50% proton transfer is observed with the water-free systems for  $\Delta\text{p}K_a = 3.25$ , i.e., when the  $\text{p}K_a$  of the phenol is 3.25 values smaller than that of *n*-propylamine. Hence for  $\Delta\text{p}K_a = 3.25$  the  $\text{OH}\cdots\text{N}=\text{O}\cdots\text{H}^+\text{N}$  hydrogen bonds are largely symmetrical. An IR continuum indicates that these hydrogen bonds are easily polarizable in a relatively large  $\Delta\text{p}K_a$  region around  $\Delta\text{p}K_a = 3.25$ . In these polarizable hydrogen bonds double minimum energy surfaces are present. Water molecules shift the proton transfer equilibrium in favor of the polar  $\text{O}\cdots\text{H}^+\text{N}$  proton boundary structure.

### I. Introduction

Transfer of the proton in  $\text{B}_1\text{H}\cdots\text{B}_2 \rightleftharpoons \text{B}_1^-\cdots\text{H}^+\text{B}_2$  hydrogen bonds has been studied earlier with various methods.<sup>1-26a</sup> Dielectric studies have shown<sup>7,20</sup> that sigmoid

curves are found when the dipole moment change  $\Delta\mu$  is plotted vs.  $\Delta\text{p}K_a$ , i.e.,  $\text{p}K_{a\text{B}_2\text{H}^+} - \text{p}K_{a\text{B}_1\text{H}}$ . With phenol-triethylamine systems the dipole moment changes are very large with complete transfer. Ratajczak and Sobczyk,<sup>7</sup> for instance, observed nearly 10 D. Similar sigmoid curves are observed when the absorbance of UV<sup>3</sup> or IR bands of the acceptor or donor groups are plotted vs.  $\Delta\text{p}K_a$ , i.e., the

\* Present address: Département de Chimie, Université de Montréal, Montréal, Québec, Canada.

TABLE I: Results with Phenol-*n*-Propylamine Systems

Substance	Letters in Figure 3	$pK_a$	$\Delta pK_a$	Proton transfer, %	$K_T$	$\log K_T$
Pure <i>n</i> -propylamine in methanol		10.708 (33)				
<i>n</i> -Propylamine with the following hydrogen bond donor:						
Phenol	a	9.89 (33)	0.82	0	0	$-\infty$
4-Chlorophenol	b	9.18 (33)	1.53	1	0.01	-2.0
3-Chlorophenol	c	8.85 (33)	1.86	3	0.031	-1.5
2-Chlorophenol	d	8.49 (33)	2.22	6	0.064	-1.2
3,5-Dichlorophenol	e	7.92 (34)	2.79	15	0.176	-0.75
2,4-Dichlorophenol	f	7.75 (34)	2.96	23	0.30	-0.53
2,3-Dichlorophenol	g	7.44 (33)	3.27	84	5.25	+0.72
2,4,5-Trichlorophenol	h	6.00 (33)	4.71	99	99	+2.0
Pentachlorophenol	i	5.26 (33)	5.45	100	$\infty$	$\infty$

proton transfer equilibria can be determined from these bands.<sup>6,14,22-26</sup> The position of the proton transfer equilibria depends not only on the nature of acceptors B, but also on the environment in which the  $B_1H \cdots B_2 \rightleftharpoons B_1 \cdots H^+B_2$  bonds are present, as was shown by Jadzin and Mafeki.<sup>13</sup> Especially water molecules in the neighborhood of these hydrogen bonds shift these equilibria in favor of the polar proton boundary structure.<sup>22</sup> A quantitative formulation regarding these equilibria was already given in 1964 by Huyskens and Zeegers-Huyskens:<sup>4</sup>

$$\log K_{pT} = \xi \Delta pK_a + C'$$

whereby the solvation influence is taken into account by  $C'$  and the interdependence of the two proton boundary structures by  $\xi$ .

When  $B_1 = B_2$  in hydrogen bonds of the types  $(B_1H \cdots B_2)^+ \rightleftharpoons (B_1 \cdots HB_2)^+$ , double minimum energy surfaces or very broad flat wells are present, and the polarizability of these bonds is 1-2 orders of magnitude larger than usual polarizabilities of electron systems. This polarizability decreases with increasing splitting of the two lowest levels, i.e., with decreasing barrier in the energy surface.<sup>27-31</sup> As a result of this polarizability, various strong interactions of these hydrogen bonds with their environment occur, by which the energy surfaces become strongly deformed and the energy levels shifted. In the IR spectra, continua are observed, when, as in the case for solutions, the strength of these interaction effects shows a broad distribution. These continua indicate the presence of such easily polarizable hydrogen bonds.<sup>27-32</sup>

The question was whether  $B_1H \cdots B_2 \rightleftharpoons B_1 \cdots H^+B_2$  bonds may also be easily polarizable when  $B_1 \neq B_2$  and how sensitively polarizability and the occurrence of IR continua depend on the degree of asymmetry of the energy surfaces. Various authors have already studied these problems with  $H_2PO_4-N$  base systems,<sup>23</sup> with carboxylic acid- $N$  base systems,<sup>22</sup> with polyhistidine-carboxylic acid systems,<sup>24</sup> and with phosphin oxide-HCl systems.<sup>26a</sup> The investigations have shown that these proton transfer hydrogen bonds are easily polarizable over a relatively large  $\Delta pK_a$  region around the symmetrical system. This paper studies whether and under what conditions hydrogen bonds between chlorophenols and *n*-propylamine become easily polarizable proton transfer hydrogen bonds.

## II. Results and Discussion

Trideuterioacetonitrile solutions of chlorophenols and *n*-propylamine (ratio 1:1) are studied. Typical IR spectra are shown in Figure 1. Furthermore, 2-chlorophenol-*n*-propylamine, 3-chlorophenol-*n*-propylamine, and 3,5-dichlorophenol-*n*-propylamine systems are investigated in trideuterioacetonitrile solutions as a function of the

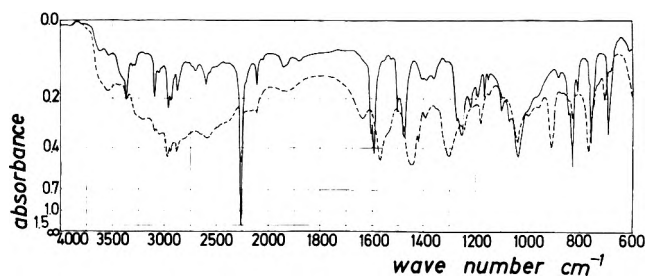


Figure 1. IR spectra of trideuterioacetonitrile solutions of 1:1 phenol + *n*-propylamine mixtures, layer thickness 19.18  $\mu\text{m}$ , temperature  $25.0 \pm 0.3$  °C: (—) phenol + *n*-propylamine; (---) 2,3-dichlorophenol + *n*-propylamine.

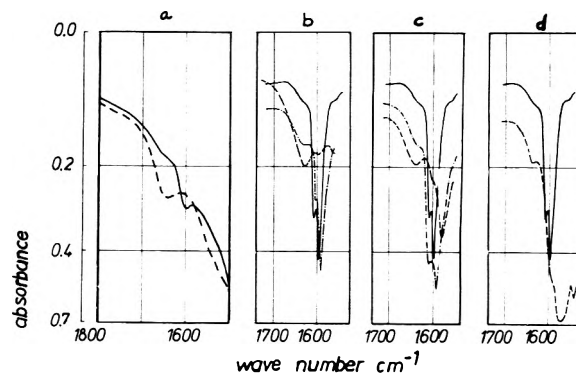


Figure 2. IR spectra of solutions in methanol (a) and trideuterioacetonitrile (b) layer thickness 24.16  $\mu\text{m}$ , temperature  $25.0 \pm 0.3$  °C. (a) Solutions in methanol: (—) *n*-propylamine 0.83 M, (---) *n*-propylamine chloride 0.76 M. Solutions in trideuterioacetonitrile: (b) (—) phenol + *n*-propylamine, (----) 2-chlorophenol + *n*-propylamine, (---) pentachlorophenol + *n*-propylamine; (c) (—) phenol + *n*-propylamine, (----) 3-chlorophenol + *n*-propylamine, (---) 2,4-dichlorophenol + *n*-propylamine; (d) (—) phenol + *n*-propylamine, (----) 3,5-dichlorophenol + *n*-propylamine.

addition of water molecules.

II.1. 1:1 Systems without Water. In Table I, all results with water-free 1:1 systems are summarized.

*Degree of Proton Transfer.* To find out which bands can be used to determine the position of the proton transfer equilibria, we first plotted spectra of *n*-propylamine and *n*-propylamine chloride in methanol (*n*-propylamine chloride is not soluble in deuterioacetonitrile). The characteristic change of an amine band with addition of the proton is shown in Figure 2a. The  $-\text{NH}_2$  bending vibration at  $1596 \text{ cm}^{-1}$  vanishes and the antisymmetrical bending vibration of the  $-\text{NH}_3^+$  groups arises at  $1631 \text{ cm}^{-1}$ . Another amine band vanishes with proton addition at  $1376 \text{ cm}^{-1}$ . Similar changes are observed with phenol bands, as shown in Figure 4. In the series *n*-propylamine with various phenols, the *n*-propylamine chloride band at  $1631$



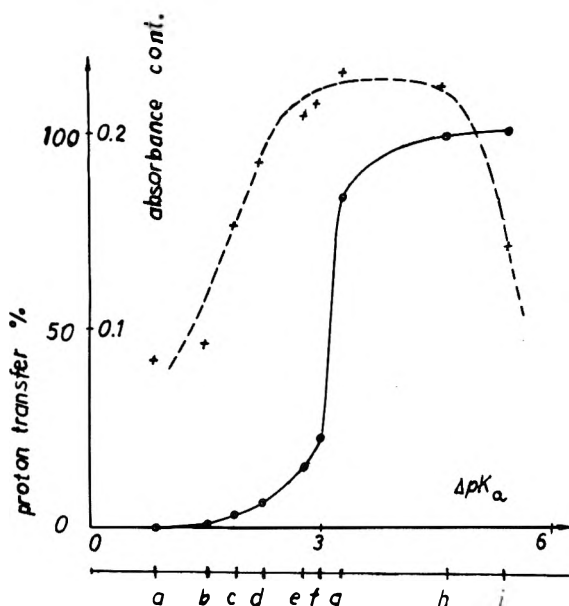


**Figure 3.** Phenol + *n*-propylamine, ratio 1:1, in water-free trideuterioacetonitrile: (a) phenol +, (b) 4-chlorophenol +, (c) 3-chlorophenol +, (d) 2-chlorophenol +, (e) 3,5-dichlorophenol +, (f) 2,4-dichlorophenol +, (g) 2,3-dichlorophenol +, (h) 2,3,5-trichlorophenol +, and (i) pentachlorophenol + *n*-propylamine system. (—) Percent proton transfer; (---) absorbance of the continuum at about 1750  $\text{cm}^{-1}$  dependent on  $\Delta pK_a$ .

$\text{cm}^{-1}$  is used to determine the proton transfer equilibria, since different phenol or phenolate bands are present in the various systems.

In Figure 2b-d selected examples show how the band of the  $-\text{NH}_3^+$  bending vibration increases in the series phenol- to pentachlorophenol-*n*-propylamine systems. The percentage of proton transfer is obtained by comparing the integral absorbance of this band in the various systems with the same band in the pentachlorophenol system, in which the transfer of the proton to the amine molecules is complete. The latter is demonstrated by the fact that no bands of nonprotonated *n*-propylamine are present. This is especially true with regard to the *n*-propylamine band at 1376  $\text{cm}^{-1}$ .

The degree of proton transfer dependent on the  $\Delta pK_a$  value of the various systems ( $\Delta pK_a = pK_{a\text{NH}_3^+} - pK_{a\text{OH}}$ ) is plotted in Figure 3 as solid line. The  $K_T$  and  $\log K_T$  values calculated from the percent proton transfer are given in Table I.

**Proton Transfer Dependent on  $\Delta pK_a$ .** The degree of proton transfer, solid line in Figure 3, demonstrates the following: In the case of the water-free trideuterioacetonitrile solutions of chlorophenols and *n*-propylamine in the ratio 1:1, 50% proton transfer occurs at  $\Delta pK_a = 3.25$ , i.e., when the  $pK_a$  of the phenols is 3.25 values smaller than that of the protonated *n*-propylamine.

Recently Beier and Schuster<sup>26b</sup> determined the position of the proton transfer equilibrium in the case of the 4-nitrophenol-piperidine system in acetonitrile by UV spectroscopy. They found 91% proton transfer. The  $\Delta pK_a$  of this system amounts to 3.95. Hence, this value fits very well in our proton transfer curve.

Studying substituted phenol-*n*-propylamine systems in benzene, Zeegers-Huyskens<sup>6</sup> found 50% proton transfer at  $\Delta pK_a = 1.5$ . Studying substituted phenol-triethylamine systems in nonpolar solvents, Ratajczak and Sobczyk<sup>7</sup> found 50% proton transfer at  $\Delta pK_a = 5.0$ . The comparison of all these results shows that the proton transfer equilibria in the  $\text{OH}\cdots\text{N} \rightleftharpoons \text{O}^-\cdots\text{H}^+\text{N}$  bonds strongly depend on the solvent, i.e., the environment in which these bonds are present.

**Polarizability and Symmetry of Energy Surfaces.** Are these  $\text{OH}\cdots\text{N} \rightleftharpoons \text{O}^-\cdots\text{H}^+\text{N}$  bonds easily polarizable? In Figure 1 the spectra of the phenol + *n*-propylamine system and the 2,3-dichlorophenol + *n*-propylamine system are plotted. With the 2,3-dichlorophenol + *n*-propylamine system, a background absorbance, i.e., a continuous absorbance, is observed which begins at about 3000  $\text{cm}^{-1}$  and extends toward smaller wave numbers. The proton transfer curve in Figure 3 shows that the phenol system is largely asymmetrical, whereas the 2,3-dichlorophenol + *n*-propylamine system is present in the region in which both proton boundary structures of the  $\text{OH}\cdots\text{N} \rightleftharpoons \text{O}^-\cdots\text{H}^+\text{N}$  bonds are of considerable weight, i.e., where these hydrogen bonds are more or less symmetrical. When both proton boundary structures have the same weight, both structures have the same free energy. Thus the continuum demonstrates that, as expected, the  $\text{OH}\cdots\text{N} \rightleftharpoons \text{O}^-\cdots\text{H}^+\text{N}$  bonds with the largely symmetrical 2,3-chlorophenol + *n*-propylamine system are easily polarizable.

The absorbance of these continua evaluated as described in the Experimental Section is plotted as a dashed line in Figure 3. Consideration of this absorbance and of the proton transfer curve (solid line in this figure) indicates that the absorbance of the continuum (at about 1750  $\text{cm}^{-1}$ ) shows a plateau in a relatively large  $\Delta pK_a$  region in which both proton boundary structures of the  $\text{OH}\cdots\text{N} \rightleftharpoons \text{O}^-\cdots\text{H}^+\text{N}$  bonds have appreciable weight. This demonstrates that these bonds are easily polarizable in a relatively large  $\Delta pK_a$  region.

Hydrogen bonds with double minima or a very broad flat well are easily polarizable. This polarizability is larger the smaller the distance of the two lowest levels, i.e., the higher the barrier in the energy surface is.<sup>27-31</sup> With carboxylic acid + N base systems it was already shown that double minima are present in the hydrogen bonds when these bonds are easily polarizable.<sup>22</sup> The same is true for the phenol + *n*-propylamine systems. When instead of double minima broad flat wells were present, bands of acceptors should be in a position in between the positions in which these bands are observed with protonated and nonprotonated species. With carboxylic acid-carboxylate hydrogen bonds this was demonstrated by Hadzi and Nowak.<sup>35</sup> Thus, if broad flat single minima were present in the  $\text{OH}\cdots\text{N} \rightleftharpoons \text{O}^-\cdots\text{H}^+\text{N}$  bonds in the transition region, a band in a position between the  $\text{NH}_3$  and  $\text{NH}_2$  bending vibrations should be observed instead of the  $\text{NH}_3$  bending vibration. This is not the case. Thus double minima are present in the  $\text{OH}\cdots\text{N} \rightleftharpoons \text{O}^-\cdots\text{H}^+\text{N}$  bonds in the transition region.

Comparison of proton transfer curve and absorbance of the continuum in Figure 3 shows the following: When the proton is already largely located on one side of the hydrogen bond, the absorbance of the continuum is weaker, but does not completely vanish. This demonstrates, in good agreement with theory,<sup>36-38</sup> that the increase in residence time in the lower well is much more rapid than is the decrease in the fluctuation frequency of the proton, i.e., even if the residence time of the proton in the higher well is short, the polarizability is smaller, but still appreciable.

**II.2. Influence of Water on the Proton Transfer Equilibrium.** In the series of measurements in which the influence of water on the proton transfer equilibria is studied, phenol and phenolate bands as well as the *n*-propylamine band at 1376  $\text{cm}^{-1}$  are evaluated to determine the degree of proton transfer. To find out which bands can be used, we first plotted spectra of the phenols and phenolates. Figure 4 shows bands which appear or dis-

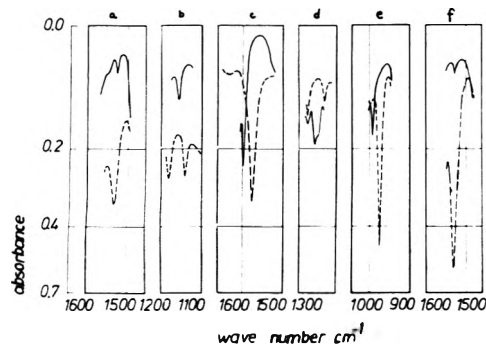


**Figure 4.** IR bands of phenol and phenolate solutions in trideuterioacetonitrile, layer thickness 19.18  $\mu\text{m}$ , temperature  $25 \pm 0.3$   $^{\circ}\text{C}$ , (—) phenol, (---) phenolate: (a, b) 3-chlorophenol and sodium 3-chlorophenolate; (c, d) 2-chlorophenol and sodium 2-chlorophenolate; (e, f) 3,5-dichlorophenol and sodium 3,5-dichlorophenolate.

appear with proton removal from the phenol molecules.

The absorbance of some bands of these substances already changes, however, when water is added to solutions of the pure substances. Therefore, we studied first the influence of water on the bands in the deuterioacetonitrile solutions of the pure substances. To determine the degree of proton transfer only those bands are used which do not show any changes dependent on water addition under these conditions. All bands shown in Figure 4 are within experimental error completely independent of the addition of water to the solutions of pure substances. Therefore these bands were used to determine the degree of proton transfer.

The percentage of proton transfer is obtained by comparing the integral absorbance of these bands with the phenol + *n*-propylamine systems with the corresponding bands in the spectra of the deuterioacetonitrile solutions of the pure phenols, phenolates, and pure *n*-propylamine solutions.

In Figure 5 the degree of proton transfer is plotted vs. the addition of water molecules for the systems 3-chlorophenol + *n*-propylamine, 2-chlorophenol + *n*-propylamine, and 3,5-dichlorophenol + *n*-propylamine. It is shown that with all three systems the percent proton transfer obtained from the phenol, phenolate, and *n*-propylamine bands agree within experimental and evaluation errors.

With all systems the percent proton transfer increases with the addition of water molecules. Hence, as with carboxylic acid + N base<sup>22</sup> and polyhistidine + carboxylic acid systems<sup>24</sup> water molecules shift the proton transfer equilibria  $\text{OH}\cdots\text{N} \rightleftharpoons \text{O}^-\cdots\text{H}^+\text{N}$  in favor of the polar proton boundary structure. Increasing weight of the polar structure favors dissociation of the hydrogen bonds in aqueous solutions, as earlier demonstrated with electrochemical methods by Vinogradov et al.<sup>39</sup>

The shift of the proton transfer equilibria toward the polar structure due to addition of water molecules increases from the 3-chlorophenol + *n*-propylamine system to the 3,5-dichlorophenol + *n*-propylamine system. This can easily be understood, since in this series the degree of asymmetry of the  $\text{OH}\cdots\text{N} \rightleftharpoons \text{O}^-\cdots\text{H}^+\text{N}$  bonds decreases, i.e., the polarizability of the hydrogen bonds increases. When the polarizability is larger the induced dipole interaction of the hydrogen bonds with the water molecules is stronger and therefore a larger shift in the proton transfer equilibria is observed.

### III. Conclusions

Hydrogen bonds of the types  $(\text{BH}\cdots\text{B})^+ \rightleftharpoons (\text{B}\cdots\text{HB})^+$  or  $(\text{BH}\cdots\text{B})^- \rightleftharpoons (\text{B}\cdots\text{HB})^-$ , i.e., bonds having the same donor

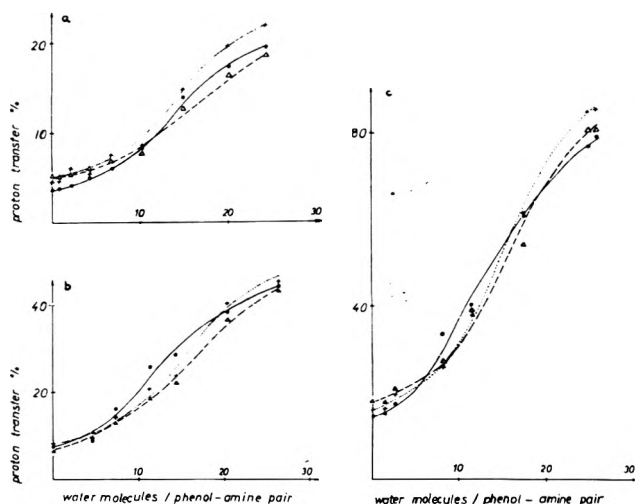


**Figure 5.** Proton transfer in percent as function of the number of water molecules per phenol + amine pair. (a) 3-Chlorophenol + *n*-propylamine: (—●) from the chlorophenolate band at 1539  $\text{cm}^{-1}$ ; (---Δ) from the chlorophenol band at 1155  $\text{cm}^{-1}$ ; (···+) from the *n*-propylamine band at 1376  $\text{cm}^{-1}$ . (b) 2-Chlorophenol + *n*-propylamine: (—●) from the chlorophenolate band at 1572  $\text{cm}^{-1}$ ; (---Δ) from the chlorophenol band at 1246  $\text{cm}^{-1}$ ; (···+) from the *n*-propylamine band at 1376  $\text{cm}^{-1}$ . (c) 3,5-Dichlorophenol + *n*-propylamine: (—●) from the chlorophenolate band at 1533  $\text{cm}^{-1}$ ; (---Δ) from the chlorophenolate band at 970  $\text{cm}^{-1}$ ; (···+) from the *n*-propylamine band at 1376  $\text{cm}^{-1}$ .

and acceptor groups, are easily polarizable. This was demonstrated earlier by IR continua found with a large number of systems (Table I in ref 31). The reasons for these polarizabilities are double minimum energy surfaces or energy surfaces with a very broad flat well.<sup>27-31</sup>

In ref 31 p 740 ff, it has been discussed whether  $\text{B}_1\text{H}\cdots\text{B}_2 \rightleftharpoons \text{B}_1\cdots\text{H}^+\text{B}_2$  bonds may be easily polarizable, too, when  $\text{B}_1 \neq \text{B}_2$ . This question could not be answered, since the experimental evidence available at that time was not sufficient.

In the meantime investigations of phosphin oxide-HCl,<sup>26a</sup> carboxylic acid-N base,<sup>22</sup>  $\text{H}_2\text{PO}_4\text{-N}$  base,<sup>23</sup> and polyhistidine-carboxylic acid<sup>24</sup> systems have shown that  $\text{B}_1\text{H}\cdots\text{B}_2 \rightleftharpoons \text{B}_1\cdots\text{H}^+\text{B}_2$  bonds have largely symmetrical energy surfaces over a considerable region of  $\Delta\text{p}K_a$  values. These  $\Delta\text{p}K_a$  values, at which the systems are largely symmetrical, are different for the various types of systems. With all types of systems, however, IR continua indicate that the  $\text{B}_1\text{H}\cdots\text{B}_2 \rightleftharpoons \text{B}_1\cdots\text{H}^+\text{B}_2$  bonds are easily polarizable with systems over a relatively large  $\Delta\text{p}K_a$  region around the  $\Delta\text{p}K_a$  for 50% proton transfer.

This result is confirmed by the investigations of the chlorophenol + *n*-propylamine systems presented here. The  $\text{OH}\cdots\text{N} \rightleftharpoons \text{O}^-\cdots\text{H}^+\text{N}$  bonds formed between phenol and *n*-propylamine molecules are easily polarizable in relatively large  $\Delta\text{p}K_a$  regions around  $\Delta\text{p}K_a = 3.25$ . Double minimum energy surfaces are present in these hydrogen bonds.

### IV. Experimental Section

**Material.** The substances, purity, and sources were as follows: phenol, purissimum, Merck-Schuchardt AG; 2-chlorophenol and 3-chlorophenol, purum, Fluka AG, Buchs; 4-chlorophenol, purissimum, Fluka AG, Buchs; 2,3-dichlorophenol, 98%, EGA Chemie KG, Steinheim; 2,4-dichlorophenol and 3,5-dichlorophenol, purum, Merck-Schuchardt AG; 2,4,5-trichlorophenol and pentachlorophenol, purissimum, Fluka AG, Buchs; *n*-propylamine for synthesis, Merck-Schuchardt AG; trideuterioacetonitrile for spectroscopy, E. Merck, Darmstadt. The phenolates were prepared from the phenols.

With the IR investigations, cells with Ge windows were used. Because of the high reflectivity of these windows, considerable interferences superpose the spectrum when these windows are arranged parallel, therefore, wedge-shaped layers were used.<sup>40</sup> The mean layer thicknesses were determined as described in ref 22. The reproducibility of this mean-layer thickness was  $\pm 0.1 \mu\text{m}$ .

The spectra were plotted with a spectrophotometer Model 325, supplied by Bodenseewerk Perkin-Elmer, Überlingen, West Germany. Registration data were as follows: slit program 6.5; gain 1.2–1.9; time constant 2; recording speed 0.5–1.5 wavenumbers/s. The spectrophotometer was flushed with dry and CO<sub>2</sub> free air. All spectra were taken at  $25 \pm 0.3^\circ\text{C}$ .

The absorbance taken from the spectra had to be corrected taking into account the following: First, in the case of a wedge-shaped layer the Lambert-Beer law is no longer valid. The necessary corrections were made as described in ref 22a. Secondly, the absorbance must be related to the same number of phenol + *n*-propylamine pairs in the beam. This was performed as described in ref 14.

The percent proton transfer was determined from the integral absorbance of the bands given above. The integral absorbance was related either to that of the same band in a system with no or with complete proton transfer, respectively. The absorbance of the continuum was evaluated at about  $1750 \text{ cm}^{-1}$ . With this, from the background absorbance of the phenol + amine solutions, the background absorbance of the solutions containing only the phenol is subtracted and the difference related to the same number of phenol amine pairs in the beam, as described in ref 14.

**Acknowledgment.** We thank the Deutsche Forschungsgemeinschaft and the Fonds der Chemischen Industrie for providing the facilities for this work.

## References and Notes

- (1) G. M. Barrow and E. Anne Yerger, *J. Am. Chem. Soc.*, **77**, 4474 (1955).
- (2) G. M. Barrow, *J. Am. Chem. Soc.*, **78**, 5802 (1956).
- (3) J. Nasielski and E. V. Donckt, *Spectrochim. Acta*, **19**, 1989 (1963).
- (4) P. Huyskens and Th. Zeegers-Huyskens, *J. Chim. Phys.*, **61**, 81 (1964).
- (5) S. L. Johnson and K. A. Rumon, *J. Phys. Chem.*, **69**, 74 (1965).
- (6) Th. Zeegers-Huyskens, *Spectrochim. Acta*, **21**, 221 (1965).
- (7) H. Ratajczak and L. Sobczyk, *J. Chem. Phys.*, **50**, 556 (1969).
- (8) H. Ratajczak and L. Sobczyk, *Bull. Acad. Pol. Sci. Sec. Sci. Chim.*, **18**, 93 (1970).
- (9) G. V. Gusakova, G. S. Denisov, A. L. Smolyanskii, and V. A. Schreiber, *Dokl. Akad. Nauk SSSR*, **193**, 1065 (1970).
- (10) G. Debecker and P. Huyskens, *J. Chim. Phys.*, **68**, 287, 295 (1971).
- (11) G. V. Gusakova, G. S. Denisov, and A. L. Smolyanskii, *Zh. Prikl. Spektrosk.*, **14**, 860 (1971).
- (12) H. Chihara and N. Nakamura, *Bull. Chem. Soc. Jpn.*, **7**, 1980 (1971).
- (13) J. Jazdzin and J. Mateki, *Acta Phys. Polon. A*, **41**, 599 (1972).
- (14) R. Lindemann and G. Zundel, *J. Chem. Soc., Faraday Trans. 2*, **68**, 979 (1972).
- (15) L. Sobczyk and Z. Pawelka, *Rocz. Chem.*, **47**, 1523 (1973).
- (16) R. Nouwen and P. Huyskens, *J. Mol. Strukt.*, **16**, 459 (1973).
- (17) L. Sobczyk and Z. Pawelka, *J. Chem. Soc., Faraday Trans. 1*, **70**, 832 (1974).
- (18) Z. Dega-Szlaran, E. Grech, M. Z. Naskret-Barcizweska, and M. Szafrań, *J. Chem. Soc., Perkin Trans. 2*, 251 (1975).
- (19) E. Jakusek, M. Pajdowska, and L. Sobczyk, *Chem. Phys.*, **9**, 205 (1975).
- (20) L. Sobczyk in "The Hydrogen Bond. Recent Developments in Theory and Experiments", Vol. III, P. Schuster, G. Zundel, and C. Sandorfy, Ed., North Holland Publishing Co., Amsterdam, 1976, p 937 ff.
- (21) J. Mateki, *J. Chem. Soc., Faraday Trans. 2*, **72**, 1214 (1976).
- (22) (a) R. Lindemann and G. Zundel, *J. Chem. Soc., Faraday Trans. 2*, **73**, 788 (1977); (b) *Biopolymers*, **16**, 2407 (1977).
- (23) M. Matthies and G. Zundel, *Biophys. Biochem. Res. Commun.*, **74**, 831 (1977).
- (24) R. Lindemann and G. Zundel, *Biopolymers*, in press.
- (25) N. S. Golubev, G. S. Denisov, and A. I. Koltzow, *Dokl. Akad. Nauk SSSR*, **232**, 841 (1977).
- (26) (a) M. Rospenk, A. Koll, and L. Sobczyk, *Adv. Relaxation Processes*, in press. (b) G. Beier, Thesis, Institute of P. Schuster, Vienna, 1975.
- (27) E. G. Weidemann and G. Zundel, *Z. Naturforsch. A*, **25**, 627 (1970).
- (28) G. Zundel, *Allg. Prakt. Chem. (Wien)*, **21**, 329 (1970).
- (29) R. Janoschek, E. G. Weidemann, H. Pfeiffer, and G. Zundel, *J. Am. Chem. Soc.*, **94**, 2387 (1972).
- (30) R. Janoschek, E. G. Weidemann, and G. Zundel, *J. Chem. Soc., Faraday Trans. 2*, **69**, 505 (1973).
- (31) G. Zundel in "The Hydrogen Bond. Recent Developments in Theory and Experiments", Vol. II, P. Schuster, G. Zundel, and C. Sandorfy, Ed., North Holland Publishing Co., Amsterdam, 1976, p 683 ff.
- (32) G. Zundel, "Hydration and Intermolecular Interaction", Academic Press, New York, N.Y., 1969, and Mir Moscow, 1972.
- (33) "Handbook of Chemistry and Physics", 49th ed., Chemical Rubber Co., Cleveland, Ohio, 1969.
- (34) Landolt-Börnstein, Zahlenwerte und Funktionen, Vol. II, part 7, 1960, p 878.
- (35) D. Hadži and A. Novak, "Infrared Spectra of, and Hydrogen Bonding in, Some Acid Salts of Carboxylic Acids", University of Ljubljana, 1960.
- (36) E. G. Weidemann and G. Zundel, *Z. Naturforsch. A*, **28**, 236 (1973).
- (37) E. G. Weidemann in "The Hydrogen Bond. Recent Developments in Theory and Experiments", Vol. I, P. Schuster, G. Zundel, and C. Sandorfy, Ed., North Holland Publishing Co., Amsterdam, 1976, p 245 ff.
- (38) H. Pfeiffer, E. G. Weidemann, and G. Zundel, manuscript in preparation.
- (39) S. N. Vinogradov, R. A. Hudson, and R. M. Scott, *Biochim. Biophys. Acta*, **216**, 6 (1970).
- (40) K. P. Hofmann and G. Zundel, *Z. Naturforsch. C*, **29**, 19 (1974).

# The Polarized Infrared Spectra and Structure of Crystalline Bromoacetic Acid<sup>†</sup>

P. F. Krause,

*Department of Chemistry, University of Central Arkansas, Conway, Arkansas 72032*

J. E. Katon,\* and R. W. Mason<sup>‡</sup>

*Department of Chemistry, Miami University, Oxford, Ohio 45056 (Received September 23, 1977)*

*Publication costs assisted by the U.S. Air Force*

The polarized infrared spectra of oriented polycrystalline films of one polymorph of bromoacetic acid have been recorded. The observed factor group splittings are consistent with a hydrogen-bonded polymeric structure. The enhanced resolution afforded by the infrared polarization studies along with appropriate factor group analyses has allowed approximation of both site and factor group symmetries. These are discussed in relation to recent x-ray crystallographic data.

## Introduction

It is firmly established that carboxylic acids in the solid state may form more than one hydrogen-bonded structure, since a number of crystalline acids have been studied by x-ray diffraction. These compounds often exist in polymorphic modifications, however, many of which have not been studied structurally.

Recent studies on a variety of compounds have shown that structures may be predicted through the polarized infrared spectra of oriented polycrystalline films.<sup>1-4</sup> Single-crystal and oriented polycrystal polarized mid-infrared spectra for  $\alpha$ -chloroacetic acid<sup>5</sup> are consistent with a hydrogen-bonded polymer structure or the hydrogen-bonded tetramer structure more recently found by x-ray diffraction studies.<sup>6</sup> Polarized mid-infrared spectra of oriented polycrystalline films of  $\gamma$ -chloroacetic acid<sup>7</sup> are consistent with a polymer structure, while  $\beta$ -chloroacetic acid single-crystal polarized infrared spectra are consistent with a hydrogen-bonded dimer<sup>7</sup> in agreement with recent x-ray studies.<sup>8</sup> Vibrational analyses on polycrystalline but nonoriented samples of both bromoacetic<sup>9</sup> and iodoacetic<sup>10</sup> acids have supported dimeric structures.

The vibrational spectra of dimeric carboxylic acids are complicated by the fact that the fundamental modes occur as phase-related pairs. The monomeric units are weakly coupled and the selection rules derived from group-theoretical arguments are not rigorous. In an attempt to solidly establish the solid-state structure of bromoacetic acid via vibrational spectroscopy, the infrared spectrum of crystalline bromoacetic acid has been reinvestigated using the polarized infrared technique. As the room-temperature and low-temperature spectra of solid but nonoriented bromoacetic acid are similar to the melt, the structure of the polymorph of bromoacetic acid under investigation was thought to remain unchanged. For this reason, the dimeric structure was chosen as a starting point for the analysis of the polarized infrared data.

Three polymorphs of bromoacetic acid have been reported<sup>11</sup> of which two are stable only at elevated pressures. However, a recent x-ray diffraction study<sup>12</sup> reported crystal-structure data for two polymorphs of bromoacetic acid. These were prepared by evaporation from different solvents. The results of the vibrational study of crystalline bromoacetic acid presented in this

study will be discussed in relationship to the x-ray diffraction results. Since the crystal structures of two polymorphs are known, this investigation further serves to indicate the usefulness of recording polarized infrared spectra of polycrystalline compounds in terms of the structural arguments that can be forwarded.

## Experimental Section

Reagent grade bromoacetic acid purchased from Matheson Coleman and Bell was purified by vacuum distillation. The fraction used in all experiments was collected at 74 °C under a vacuum of less than 1 Torr. The samples were stored in vacuo and redistilled frequently.

Oriented polycrystals of organic liquids have been grown by simply cooling the sample between alkali halide plates.<sup>13,14</sup> In the present cases, oriented polycrystalline films of bromoacetic acid were prepared by warming the sample to just above its melting point (48 °C) and then pressing the sample between KBr windows. The sample was then placed in a desiccator where crystallization was allowed to occur. A qualitative indication as to the degree of orientation was provided by observing the degree of light extinction produced by the sample between crossed Polaroids. If the sample was sufficiently oriented, the cell was transferred to a conventional liquid-nitrogen Dewar or to the sample compartment of a Cryogenic Technology, Inc., Model 20 Cryostat. The sample was allowed to cool to the desired temperature before recording of the spectra.

Spectra were recorded on a Perkin-Elmer Model 180 infrared spectrophotometer. The estimated accuracy of the frequencies is at worst  $\pm 1 \text{ cm}^{-1}$  for measurements on different samples. For different polarizer settings for a particular sample, the precision, which is more significant than the accuracy, is estimated to be at least  $\pm 0.2 \text{ cm}^{-1}$ .

## Results

Typical mid-infrared spectra of oriented polycrystalline bromoacetic acid at 77 K are shown in the two traces in Figure 1. The differences between the top and bottom spectra are due to a 90° rotation of the wire-grid polarizer. The sample chosen shows excellent orientation and no vibrational modes yielded maximum or minimum intensities at polarizer settings other than 90° apart. The corresponding infrared data are given in Table I. Comparison of spectra at temperatures as low as 20 K with room-temperature spectra show little variation. Changes in the spectra that were observed are those due to typical band sharpening upon cooling and also the observation of

<sup>†</sup>Supported in part by the U. S. Air Force under contract No. F33615-77-C-5013.

<sup>‡</sup>Present Address: Olin Corporation, Lake Charles, La. 70605.

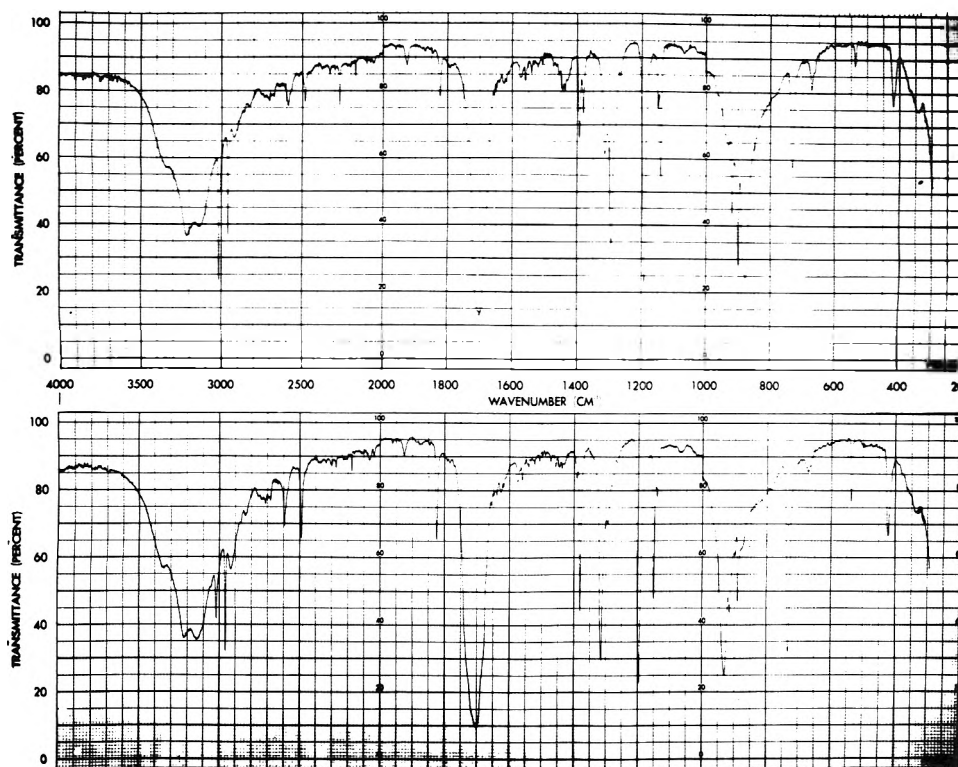


Figure 1. Polarized infrared spectrum of crystalline bromoacetic acid. Top trace:  $\theta + 90^\circ$  spectrum. Bottom trace:  $\theta$  spectrum (see text and Table I).

a few additional bands at lower temperatures. These new bands were observed only when the polarized infrared technique was utilized and are readily attributed to resolution of factor group components. It is important to note that the spectra recorded at a given temperature for all crystal films was independent of sample preparation. This indicates that the same polymorph is being investigated in all cases. Except for frequency shifts with the OH vibrational modes as the temperature was lowered, the experimentally observed frequencies were also essentially temperature independent.

Three crystallographic modifications of bromoacetic acid were proposed in 1961<sup>11</sup> with no information reported concerning their molecular or crystallographic symmetry. Leiserowitz and vor der Brück<sup>12</sup> have recently reported two crystallographic forms of bromoacetic acid as indicated by x-ray diffraction studies. Form I was grown by slow evaporation from carbon tetrachloride while form II was prepared by slow evaporation from methylcyclohexane. The x-ray diffraction results are summarized in Table II.

It is of real interest to determine whether our crystal-film structure is the same as one of those reported. Crystals of bromoacetic acid were grown from both carbon tetrachloride and methylcyclohexane and mid-infrared survey spectra (Nujol mulls) of these samples were compared with mid-infrared survey spectra of crystal films of bromoacetic acid. Differences are noted in the spectra of the samples recrystallized from the two different solvents but they are fairly minor; striking differences are observed between these spectra and spectra obtained from crystal films. Figure 2 shows a portion of the mid-infrared spectrum (1400–600  $\text{cm}^{-1}$ ) comparing bromoacetic acid recrystallized from carbon tetrachloride (upper trace) with a nonpolarized crystal-film spectrum of bromoacetic acid (lower trace). Both spectra were recorded at room temperature. The two spectra show many differences. Three of these differences are as follows: (1) A very strong band at about 1200  $\text{cm}^{-1}$  exists in the crystal-film spectrum, which has been assigned to the  $\text{CH}_2$  wag. This mode is apparently

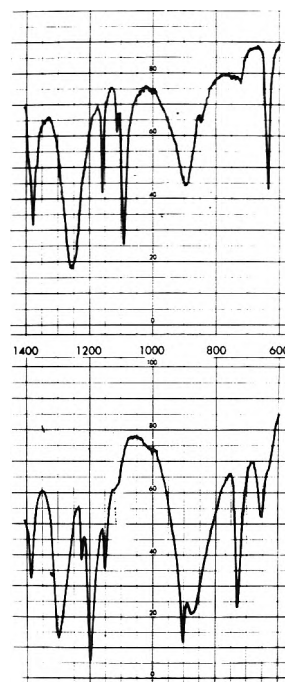


Figure 2. Upper trace: Nujol-mull infrared spectrum (1400–600  $\text{cm}^{-1}$ ) of bromoacetic acid recrystallized from  $\text{CCl}_4$  recorded at room temperature. Lower trace: mid-infrared spectrum (1400–600  $\text{cm}^{-1}$ ) of a crystal film of bromoacetic acid recorded at room temperature.

greatly shifted in the Nujol-mull spectrum of bromoacetic acid recrystallized from  $\text{CCl}_4$ , since it is not clearly visible. (2) The OH out-of-plane deformation at about 900  $\text{cm}^{-1}$  in the Nujol-mull spectrum is shifted to about 870  $\text{cm}^{-1}$  in the crystal-film spectrum. (3) The CBr stretching mode shows a shift from about 630  $\text{cm}^{-1}$  in the Nujol-mull spectrum to 729  $\text{cm}^{-1}$  in the crystal-film spectrum. These observations are certainly convincing evidence that the oriented polycrystals grown from the melt between alkali halide windows are of a different structural modification

TABLE I: Infrared Spectral Data<sup>a</sup> for Crystalline Bromoacetic Acid

Nonoriented crystal		Oriented crystal 77 K		Assign
298 K <sup>b</sup>	77 K <sup>c</sup>	$\theta$ <sup>c,d</sup>	$\theta + 90$ <sup>c,d</sup>	
			3213.4	
2900-3200	3223.8		3212.8	} $\nu_a(\text{OH})$
	~3153		3141.9	
			3132.7	} $\nu_s(\text{CH}_2)$
3009	3009.4		3018.9	
			3018.0	} $\nu(\text{CH}_2)$
2954	2955		2962.6	
			2960.6	} $\nu(\text{CH}_2)$
			2594.0	
2580	2594.4		2591.9	} $\nu(\text{CH}_2)$
			2487.7	
2481	2490.7		2486.7	} $\nu(\text{C}=\text{O})$
			2269.2	
			2282.9	} $\delta(\text{OH})$
			2268.5	
1814	1822.6	1823.9	1824.1	} $\delta(\text{OH})$
1720	1720		1703.4	
			1700.2	} $\nu(\text{C}=\text{O})$
			1446.0	
			1445.6	} $\delta(\text{OH})$
	~1433		1397.4	
			1392.8	} $\delta(\text{CH}_2)$ (scissors)
1385	1385.7		1380.6	
			1380.3	} $\delta(\text{CH}_2)$ (scissors)
			1316.0	
			1315.1	} $\nu(\text{C}-\text{O})$
1296	1313.1		1296.5	
			1294.4	} $\nu(\text{C}-\text{O})$
			1197.3	
1197	1200.3		1193.3	} $\delta(\text{CH}_2)$ (wag)
			1150.8	
			1150.3	} $\delta(\text{CH}_2)$ (twist)
1151	1153.3		1141.1	
			930.0	} $\delta(\text{OH})$
			926.9	
871	886.2		915.3	} $\delta(\text{OH})$
			913.2	
900	902.3		895.7	} $\delta(\text{CH}_2)$ (rock)
			895.1	
			887.4	} $\nu(\text{C}-\text{C})$
			874.8	
			731.3	} $\nu(\text{C}-\text{Br})$
729	730.1		730.8	
			670.3	} $\delta(\text{CO}_2)$ (scissors)
			669.1	
656	668.4		538.7	} $\delta(\text{CO}_2)$ (wag)
539	541.9	538.7	538.5	
			420.5	} $\delta(\text{CO}_2)$ (rock)
			418.9	
410				

<sup>a</sup> All frequencies in  $\text{cm}^{-1}$ . <sup>b</sup> Reference 8. <sup>c</sup> This work.  
<sup>d</sup> Relative polarizer angle.

than the polymorphs reported by Leiserowitz and vor der Bruck.<sup>12</sup> This apparent third modification will be indicated as form III. The relatively high frequency ( $729 \text{ cm}^{-1}$ ) for the carbon-bromine stretching vibration is consistent

TABLE II: X-Ray Diffraction Results for Two Polymorphs of Bromoacetic Acid<sup>a</sup>

I (Dimer) (from $\text{CCl}_4$ )	II (Dimer) (from methylcyclohexane)
Monoclinic	Orthorhombic
$P2_1/c$ ( $C_{2h}^5$ )	$Pccn$ ( $D_{2h}^{10}$ )
$Z = 4$	$Z = 8$
Monomer site $C_1$	Monomer site $C_1$
Dimer site $C_i$	Dimer site $C_i$
Conformation angle $9^\circ$	Conformation angle $22^\circ$

<sup>a</sup> L. Leiserowitz and D. vor der Brück, *Cryst. Struct. Commun.*, 4, 647 (1975).

with a conformational angle of about  $0^\circ$  in other carbonyl compounds.<sup>15</sup> This can be compared with the conformational angles of  $9^\circ$  for form I and  $22^\circ$  for form II. The form III polymorph can be obtained from the bromoacetic acid recrystallized from  $\text{CCl}_4$  by simply melting the sample, pressing the melt between alkali halide windows, and allowing the sample to cool. The conclusion that we are studying a third crystalline modification, whose structure is unknown, makes the analysis of the polarized spectra somewhat more complex and speculative.

It should be noted that form III has been prepared by cooling a liquid film between two alkali halide windows under pressure. This polymorph is presumably metastable at ambient conditions and if disturbed by scratching or scraping will convert to one of the more stable polymorphs. Such behavior has been noticed previously with chloroacetic acid. The  $\gamma$  polymorph is formed when liquid chloroacetic acid is cooled between alkali halide windows and is readily converted to the  $\alpha$  polymorph upon mechanical disturbance.<sup>7</sup> It cannot, therefore, be removed from the windows and studied in other ways.

## Discussion

The analysis of the polarized infrared spectra of bromoacetic acid begins with the following pertinent observations. (1) For any molecular vibrational mode of the cyclic dimer, only two bands are observed in the crystal. It appears that there are two components for all bands. (2) There are a number of relatively strong infrared bands observed in the polarized spectra that appear at frequency separations greater than one would expect for factor group components but which are not resolved in the nonpolarized spectra. The C-O stretching region illustrates this behavior (see Table I). The single medium-strong band at  $1296 \text{ cm}^{-1}$  in the crystal-film spectrum of a nonoriented sample of bromoacetic acid yields bands at  $1316.0 \text{ cm}^{-1}$  (strong) and  $1296.5 \text{ cm}^{-1}$  at one polarizer setting in the polarized spectra. With a  $90^\circ$  rotation of the polarizer, bands at  $1315.1 \text{ cm}^{-1}$  and  $1294.4 \text{ cm}^{-1}$  (strong) are observed. The bottom trace of Figure 3 illustrates the former behavior while the top trace shows the latter.

The  $\text{CH}_2$  scissoring mode ( $1385.7 \text{ cm}^{-1}$  in the nonpolarized spectrum) also illustrates this behavior. At the setting of the polarizer shown in the top trace of Figure 3, two bands at  $1397.4 \text{ cm}^{-1}$  and  $1380.6 \text{ cm}^{-1}$  are observed. With a  $90^\circ$  rotation of the polarizer (bottom trace) two other bands with frequencies  $1392.8 \text{ cm}^{-1}$  and  $1380.3 \text{ cm}^{-1}$  are observed.

A previous analysis of polycrystalline, nonoriented bromoacetic acid<sup>9</sup> indicated that there were bands at  $1385$  and  $1296 \text{ cm}^{-1}$  in the infrared (non-Raman observable) and bands at  $1395$  and  $1306 \text{ cm}^{-1}$  in the Raman spectrum (non-infrared observable). This indicates the presence of a center of symmetry and, by implication, a hydrogen-bonded dimer structure. The very large splittings observed in the polarized spectra,  $20 \text{ cm}^{-1}$  for the C-O stretch and

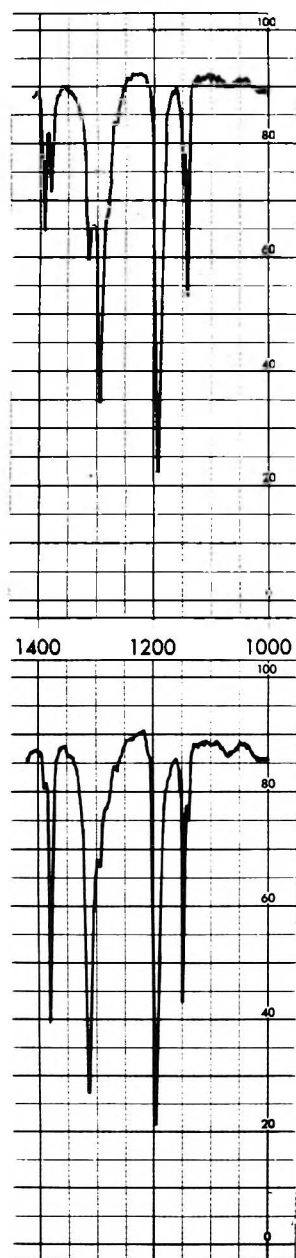


Figure 3. A portion ( $1400\text{--}1000\text{ cm}^{-1}$ ) of the polarized infrared spectrum of crystalline bromoacetic acid at 77 K. The upper trace is of the  $\theta + 90^\circ$  spectrum while the bottom trace is of the  $\theta$  spectrum.

$12\text{ cm}^{-1}$  for the  $\text{CH}_2$  scissors, suggest that the bands at  $1392$  and  $1306\text{ cm}^{-1}$  correspond to the Raman bands observed in the dimer structure. This indicates that the polymorph under investigation does not have a center of symmetry and is, therefore, a hydrogen-bonded polymer.

Other portions of the polarized spectra show similar behavior, notably the OH stretching region. In the infrared spectrum of a nonoriented sample of crystalline bromoacetic acid, a strong, broad, unresolved band ( $3200\text{--}2900\text{ cm}^{-1}$ ) was observed at room temperature. Nonoriented sample spectra have clearly indicated two bands at  $3223.8$  and  $\sim 3153\text{ cm}^{-1}$  at 77 K, however. The enhanced resolution afforded by the polarized infrared technique yields further splittings;  $3212.8$  and  $3132.7\text{ cm}^{-1}$  at one polarizer setting and  $3213.4$  and  $3141.9\text{ cm}^{-1}$  at a polarizer setting rotated by  $90^\circ$ . The most plausible explanation follows the same reasoning as employed above; that is, the bands at  $3213$  and  $3135\text{ cm}^{-1}$  are assigned to the infrared-active and Raman-active "dimeric" OH stretching modes which are now both infrared active because of the structural change, while the smaller splittings observed are due to

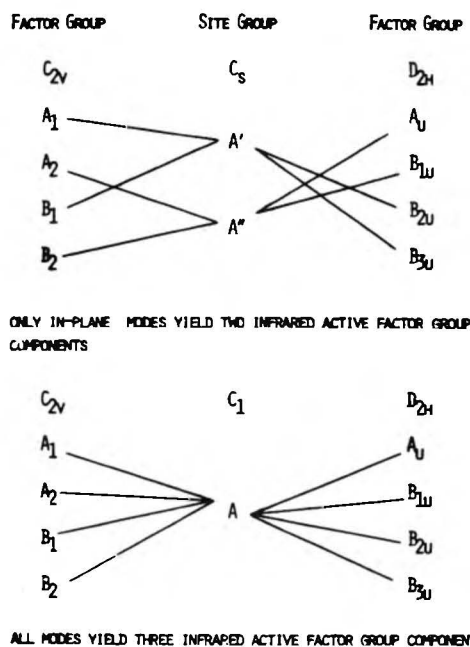
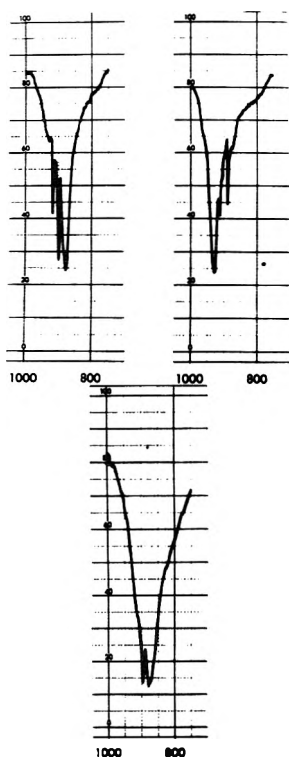


Figure 4. Correlations between possible site and factor groups for bromoacetic acid.

the resolution of two factor group components for each band.

In terms of gross structural features of the particular polymorph investigated, the data seem most consistent with monomer molecules which are hydrogen-bonded in a polymeric or tetrameric framework. Analogous structures to these have been reported for chloroacetic acid ( $\gamma$  and  $\alpha$ , respectively).<sup>6,7</sup> Some aspects of the crystal structure can be derived from the polarized infrared results and relationships with the molecular structure of this particular polymorph can be postulated. As stated above, each fundamental vibrational mode apparently splits into four infrared-active factor group components. These occur in pairs. One pair corresponds to the Raman-active modes of the cyclic dimer and the other pair corresponds to the infrared-active modes of the cyclic dimer. Clearly, the polymer structure still shows the strong coupling of adjacent molecules through the hydrogen bonding since these pairs are split by a fairly large amount ( $10\text{--}20\text{ cm}^{-1}$ ). The two components of each pair are split by much smaller amounts ( $<5\text{ cm}^{-1}$ ). These splittings must reflect inter-chain interactions while the former reflect intrachain interactions. Each component of every pair behaves differently upon rotation of the polarizer. As one component maximizes the other component minimizes, and all maxima and minima occur at the same polarizer settings— $90^\circ$  apart.

The observed results are consistent with either orthorhombic or monoclinic crystal systems but, in each case, are consistent only with certain orientations. If the crystal is orthorhombic, the factor group symmetry for this polymorph must be  $D_2$ ,  $C_{2v}$ , or  $D_{2h}$ . Correlation diagrams between  $C_s$  and  $C_1$  site groups with  $C_{2v}$  and  $D_{2h}$  factor groups are shown in Figure 4. If  $C_s$  were the appropriate site symmetry,  $C_{2v}$  or  $D_{2h}$  factor groups would be the only choices for the unit-cell symmetry since  $C_s$  is not a subgroup of  $D_2$ . However, the predictions concerning polarization properties and splittings for factor group components for a  $C_s$  site symmetry are not consistent with the experimental observations. From the top diagram in Figure 4 one sees that the out-of-plane modes ( $A''$ ) yield only a single factor group component in both the  $C_{2v}$  and  $D_{2h}$  factor group symmetries. (Only the ungerade modes



**Figure 5.** Upper traces: A portion of the polarized infrared spectra of an oriented sample of crystalline bromoacetic acid at 77 K. Lower trace: A portion of the nonpolarized infrared spectrum of a nonoriented sample of polycrystalline bromoacetic acid at 77 K.

are shown for  $D_{2h}$ ). The observation of two such components for all bands restricts the bromoacetic acid site symmetry to  $C_1$ , which is the only other possible symmetry for the bromoacetic acid monomer. Hence, the conformational angle cannot be  $0^\circ$  (see above).

The bottom diagram of Figure 4 shows the correlation between a  $C_1$  site and  $C_{2v}$  and  $D_{2h}$  factor groups. A similar correlation exists between  $C_1$  and  $D_2$ . Note that three infrared-active factor group components are predicted for each molecular mode. This is the prediction for a general crystal orientation. We have found that carboxylic acids, which crystallize in the orthorhombic system, crystallize with one of the crystallographic axes perpendicular to the alkali halide windows under these conditions.<sup>13,14</sup> When this occurs, only two factor group components are observed. These predictions lead us to the conclusion that the proper crystal system could be orthorhombic if there were eight molecules per unit cell. In such a crystal system we would expect, if our experimental observations were made parallel to one crystal axis, four factor group components for each fundamental. Two of the four should be polarized in one way while the other two should be polarized in the opposite way. It should be noted that eight molecules per unit cell requires, in the case of a  $C_{2v}$  factor group, that two different sets of  $C_1$  sites be occupied. For the  $D_{2h}$  factor group only one set of sites is required for the eight molecules.

A tetrameric structure similar to that of  $\alpha$ -chloroacetic acid<sup>6</sup> is possible for a  $D_{2h}$  factor group, but seems unlikely. Such a structure would require a  $C_i$  site symmetry for the tetramer which implies a Bravais cell containing 16 monomer units—an unusually large Bravais cell.

If the crystal is monoclinic the factor group symmetry must be  $C_2$ ,  $C_s$ , or  $C_{2h}$ . The observed number of factor

group components (four) are inconsistent with a  $C_s$  site in any of these factor groups. Hence, we again reach the conclusion that the conformational angle cannot be  $0^\circ$ .

If we consider the situation in which the crystal face which is being observed is one containing the unique  $b$  axis of a monoclinic crystal, however, we find the observed results are consistent with the following possibilities: a  $C_2$  or  $C_s$  factor group containing four molecules per Bravais cell and occupying two sets of  $C_1$  sites; a  $C_{2h}$  factor group containing eight molecules per unit cell and occupying two sets of  $C_1$  sites. Finally, the monoclinic system does provide a more likely possibility for a hydrogen-bonded tetramer structure. The space groups  $C_{2h}^2$ ,  $C_{2h}^4$ , and  $C_{2h}^6$  all have  $C_i$  sites with two molecules per site. This would lead to eight monomer units per Bravais cell, again with predicted factor group splittings and polarizations consistent with observations.

We may conclude from our experimental results that form III is either a hydrogen-bonded polymer or tetramer and that the conformation angle is not  $0^\circ$ . The number of possible space groups is rather large, however, since the crystal may be either orthorhombic or monoclinic.

The importance of obtaining as complete a spectrum as possible is indicated in Figure 5. The traces at the top show the 1000–750  $\text{cm}^{-1}$  region of the polarized infrared spectrum of an oriented sample of crystalline bromoacetic acid at 77 K. The bottom trace shows the same region at the same temperature but the sample is nonoriented and obviously the spectrum is a nonpolarized one. The upper traces differ by a  $90^\circ$  rotation of the polarizer. In this region, three fundamentals should be observed—an OH deformation, a  $\text{CH}_2$  rock, and a carbon-carbon stretching mode. As can be seen from the nonoriented sample spectrum, only two bands are observed and it would be difficult to draw structural conclusions. In the polarized spectrum eight bands are observed and, even making allowance for factor group splittings, twice as many bands are observed in the polarized spectrum. The new assignments are included in Table I. We feel this is striking evidence for the advantage of using polarized spectra with oriented samples.

## References and Notes

- (1) P. F. Krause, B. G. Glagola, and J. E. Katon, *J. Chem. Phys.*, **61**, 5331 (1974).
- (2) M. P. Marzocchi and P. Manzelli, *J. Chem. Phys.*, **52**, 2630 (1970).
- (3) M. P. Marzocchi, H. Bonadao, and G. Taddei, *J. Chem. Phys.*, **53**, 867 (1970).
- (4) E. A. D'Alessio, E. Doderio, and C. Pomposiello, *J. Chem. Phys.*, **57**, 4136 (1972).
- (5) D. Sinha, J. E. Katon, and R. J. Jakobsen, *J. Mol. Struct.*, **20**, 381 (1974).
- (6) J. A. Kanters and G. Roelofsen, *Acta Crystallogr., Sect. B*, **32**, 3228 (1976).
- (7) D. Sinha, J. E. Katon, and R. J. Jakobsen, *J. Mol. Struct.*, **24**, 279 (1975).
- (8) J. A. Kanters, G. Roelofsen, and T. Feenstra, *Acta Crystallogr., Sect. B*, **32**, 3331 (1976).
- (9) J. E. Katon and R. L. Kleinlein, *Spectrochim. Acta, Part A*, **29**, 791 (1973).
- (10) J. E. Katon and T. P. Carll, *J. Mol. Struct.*, **7**, 391 (1971).
- (11) A. R. Glasgow and J. Timmermans, *Bull. Soc. Chim. Belg.*, **70**, 623 (1961).
- (12) L. Leiserowitz and D. von der Brück, *Cryst. Struct. Commun.*, **4**, 647 (1975).
- (13) P. F. Krause, J. E. Katon, and K. K. Smith, *Spectrochim. Acta, Part A*, **32**, 957 (1976).
- (14) P. F. Krause, J. E. Katon, J. M. Rogers, and D. B. Phillips, *Appl. Spectrosc.*, **31**, 110 (1977).
- (15) S. Mizushima, "Structure of Molecules and Internal Rotation", Academic Press, New York, N.Y., 1954.



# Electronic Absorption Spectra of Some Cation Radicals as Compared with Ultraviolet Photoelectron Spectra

Tadamasa Shida,\* Yoshio Nosaka, and Tatsuhiro Kato

Department of Chemistry, Faculty of Science, Kyoto University, Kyoto 606, Japan (Received November 9, 1977)

Cation radicals of some aromatic hydrocarbons, aliphatic amines, and aromatic amines are produced by  $\gamma$  irradiation of frozen glassy solutions using organic halides as the solvent. The electronic absorption spectra of the cation radicals are compared with the photoelectron spectra of the parent molecules in order to find correlations between the two spectra. Complementary aspects of the two types of spectroscopy are discussed.

## Introduction

Alkyl halides such as *sec*-butyl chloride and a Freon mixture have been shown to produce cation radicals of solutes dissolved in the halides when the solution is frozen and  $\gamma$  irradiated.<sup>1,2</sup> The assignment of cation radicals is, in most cases, made on the basis of systematic consistency among the observed spectra and of the agreement with appropriate MO calculations for the cations. However, it is desirable to ascertain the assignment by a comparison with an independent experiment. The purpose of the present paper is twofold; the confirmation of the reliability of the irradiation method by comparison with available photoelectron spectra and the presentation of new absorption spectra for some cation radicals. Consistent agreements between the two kinds of spectrum for all the cases studied are taken as additional evidence for the credibility of the irradiation method.

## Experimental Section

All the compounds studied were obtained commercially and were dissolved to a concentration of 20–30 mM in deaerated *sec*-butyl chloride or a Freon mixture (CCl<sub>3</sub>F + CF<sub>2</sub>BrCF<sub>2</sub>Br, equimolar mixture). The solutions were frozen to a glassy solid at 77 K and  $\gamma$  irradiated whereupon the solute molecules were oxidized by migrating positive holes generated in the matrix molecules. Optical and ESR spectra of the cations were measured as described before.<sup>1,2</sup>

Perhaps a few explanations for the use of the rather unusual Freon mixture<sup>22</sup> solvent may be appropriate. The mixture forms transparent glasses at 77 K, scavenges electrons produced on irradiation very efficiently, and both components possess relatively high ionization potentials (IP<sub>vert</sub>(CCl<sub>3</sub>F) = 11.78 eV and IP<sub>v</sub>(CF<sub>2</sub>BrCF<sub>2</sub>Br) = 11.40 eV as measured by Dr. T. Kobayashi, The Institute of Physical and Chemical Research, Wako. The authors acknowledge Dr. Kobayashi). All these properties are prerequisite for a matrix yielding solute cations.<sup>1,2</sup>

## Results and Discussion

An obvious relation holds between the UV photoelectron spectra (PES) of molecules and the electronic absorption spectra of cation radicals; the energy difference of the *n*th peak of PES relative to the first peak corresponds to a transition energy of a cation radical from its ground doublet state to the (*n* - 1)th excited doublet state provided that the nuclear arrangements at equilibrium do not change appreciably upon ionization.<sup>3,4</sup> Therefore, the newly observed spectra that are to be assigned to cation radicals can be checked by the comparison with PES of the parent molecules. It will be shown that the comparison

of the two types of spectroscopy is useful in the identification of the spectrum and that the limitations and virtues of the two are complementary in some respects.

(i) *Benzo*[*c*]phenanthrene. As representative of aromatic hydrocarbons the spectrum of the cation radical of benzo[*c*]phenanthrene which has not been reported is shown in Figure 1b. The PES of the hydrocarbon is reproduced from the literature in Figure 1a together with the stick diagram derived from the PES.<sup>5</sup> The diagram gives the difference of vertical ionization potentials as well as the transition symmetry expected for the cation. The symmetry assignment is based on the HMO calculation performed by Schmidt.<sup>5</sup>

The stick spectrum below the optical spectrum (Figure 1c) was drawn after a Longuet-Higgins-Pople type calculation of the cation taking into account 40 configurations<sup>2</sup> and referring to the known nonplanar structure of the molecule.<sup>6</sup> The intercombination between the ground state <sup>2</sup>B [0.991 × (··φ<sub>7</sub><sup>2</sup>φ<sub>8</sub><sup>2</sup>φ<sub>9</sub><sup>1</sup>) + ··] with the excited states yields the symmetry of transition moments as denoted in the spectrum. The major configurations in the first six excited states along with the transition energies and oscillator strengths are as follows: (1) <sup>2</sup>A [0.979 × (φ<sub>8</sub> → φ<sub>9</sub>)], 0.381 eV, 0.0051; (2) <sup>2</sup>A [0.962 × (φ<sub>7</sub> → φ<sub>9</sub>)], 1.233 eV, 0.1850; (3) <sup>2</sup>B [0.973 × (φ<sub>6</sub> → φ<sub>9</sub>)], 1.402 eV, 0.0073; (4) <sup>2</sup>B [0.960 × (φ<sub>5</sub> → φ<sub>9</sub>)], 2.350 eV, 0.0515; (5) <sup>2</sup>A [0.929 × (φ<sub>4</sub> → φ<sub>9</sub>)], 2.424 eV, 0.0238; (6) <sup>2</sup>B [0.614 × (φ<sub>9</sub> → φ<sub>10</sub>) - 0.651 × (φ<sub>3</sub> → φ<sub>9</sub>)], 3.074 eV, 0.0155. It is only in the sixth state that configuration mixing becomes appreciable.

The correspondence between Figure 1a and 1b is obvious. Similarly, all the hydrocarbon spectra assigned in a previous paper<sup>2</sup> were analyzed in reference to the abundant PES data.<sup>5,7-9</sup> The HMO assignment by Schmidt was consulted first and optically allowed transitions of cation radicals were derived therefrom. The observed optical spectra were then compared with the derived transitions referring also to the result of SCF-MO calculations for the cations.

The correlation between the difference in ionization potentials derived from PES and the optical transition energies of the cation radicals is shown in Figure 2. The least-squares fit of the data yielded the following regression equation with 95% confidence limits and 46 degrees of freedom:  $E_{\text{obsd}} = (0.952 \pm 0.047) \Delta IP + (0.036 \pm 0.091)$

$$E_{\text{obsd}} = (0.952 \pm 0.047) \Delta IP + (0.036 \pm 0.091)$$

The less-than-unity slope may be grossly paraphrased by saying that the optical spectra are slightly red shifted owing to the matrix effect. However, such a red shift may not be general in other types of cation radicals discussed below.

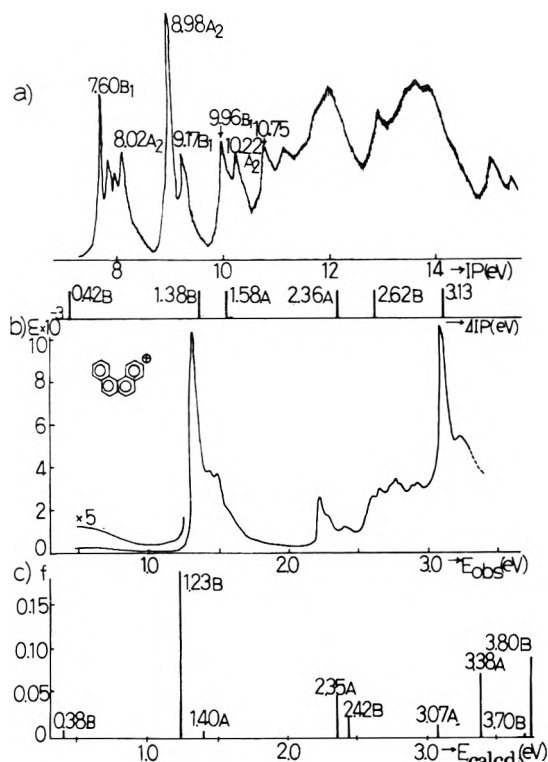


**Figure 1.** Photoelectron spectrum of benzo[*c*]phenanthrene and electronic absorption spectrum of its cation radical. (a) Photoelectron spectrum and  $\Delta IP$  diagram. (b) Electronic spectrum. (c) Calculated spectrum for the cation.

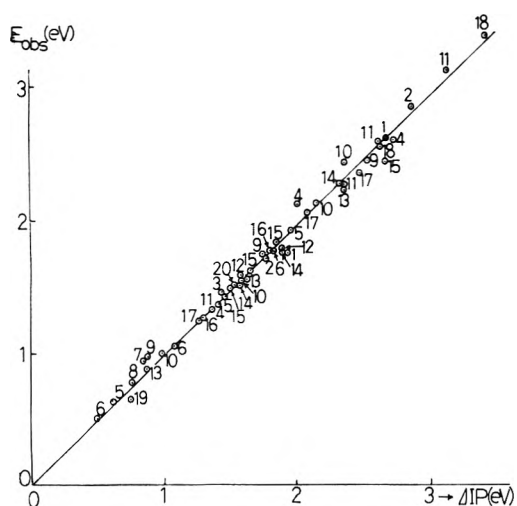


**Figure 2.** Correlation between the difference in ionization potentials ( $\Delta IP$ ) and the transition energy estimated from the optical spectra:<sup>2</sup> (1) naphthalene, (2) anthracene, (3) tetracene, (4) phenanthrene, (5) 1,2-benzanthracene, (6) chrysene, (7) picene, (8) triphenylene, (9) 1,2,3,4-dibenzanthracene, (10) 1,2,7,8-dibenzochrysene, (11) 3,4-benzophenanthrene, (12) pyrene, (13) 1,2-benzopyrene, (14) perylene, (15) 1,12-benzperylene, (16) coronene, (17) biphenylene, (18) azulene, (19) acenaphthylene, (20) fluoranthene.

The fair correlation in Figure 2 indicates that the molecular structure changes little upon ionization which is already apparent by the sharp line profile of PES with most intensities concentrated on the 0-0 bands.<sup>5,7-9</sup>

(ii) *Triethylenediamine and Triethylamine.* Triethylenediamine (TED) is an interesting aliphatic amine giving rise to two bands in the photoelectron spectrum at 7.52 and 9.65 eV which are ascribed to the ionization of electrons in the  $a_1'(n_+)$  and  $a_2''(n_-)$  orbitals, respectively.<sup>10,11</sup> Vibrational analysis of the bands led to the conclusion that the first and the second ionic states were dominantly excited in the C-C stretching ( $\nu_4$ ) and the N-C-C bending

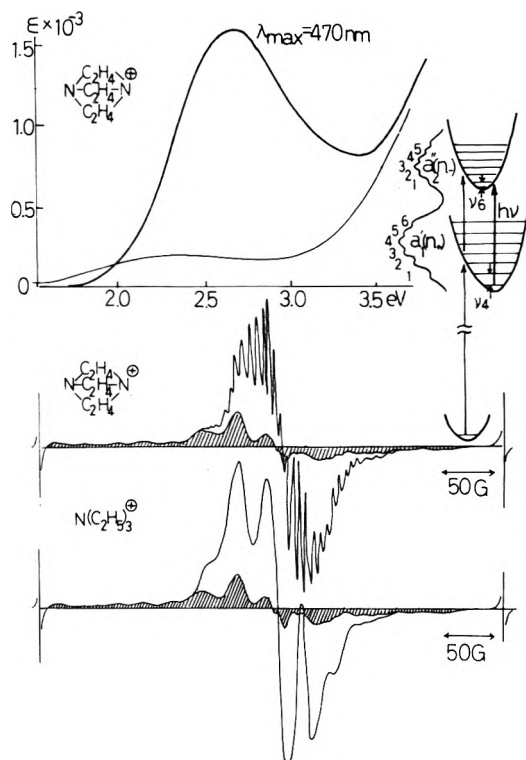


**Figure 3.** Electronic absorption and ESR spectra of TED and TEA cation radical. The fine curve in the optical spectrum represents the absorption of triethylamine cation radical. The inset shows schematic diagram of photoelectron spectrum of TED. The shaded area in the ESR spectra represents the accompanying unwanted signal due to the concomitantly produced matrix radicals. The sharp doublet at the extremities in the ESR spectrum is the signal due to hydrogen atoms concomitantly produced in the sample cell upon irradiation.

( $\nu_6$ ) modes as schematically shown in the insert of Figure 3.<sup>11</sup> These PES data immediately predict that the cation radical of TED should absorb fairly strongly at about 2 eV ( $= 9.65-7.52$  eV).

The optical and ESR spectra of TED in the Freon mixture after  $\gamma$  irradiation are shown in Figure 3. The ESR spectrum agrees with the known spectrum of the cation in fluids<sup>12</sup> and in viscous solutions<sup>13</sup> except for the accompanying unwanted signal due to the concomitantly produced matrix radicals which are shaded in Figure 3. Since the optical band with  $\lambda_{\max}$  at 470 nm behaved in parallel with the ESR signal, it is most assuredly corresponding to the predicted transition at about 2 eV. A CNDO/S calculation for the TED cation also predicts the transition of  $a_1'(n_+) \rightarrow a_2''(n_-)$  at about 1.4 eV with an oscillator strength of 0.08. The latter compares favorably with the experimentally determined  $f = 0.106$  (see  $\epsilon$  of Figure 3).

In contrast to the diamine triethylamine (TEA) yielded an undetermined absorption extending over the whole visible region with the intensity one order of magnitude smaller than that of the band at  $\lambda_{\max}$  470 nm of the TED cation (see Figure 3). The assignment of the diffuse absorption is not immediately known (probably it is related to various  $\sigma-n$  excitations as judged from PES of TEA<sup>14</sup>), but the accompanying triplet ESR spectrum shown in Figure 3 clearly indicates that the monoamine also has become its cation radical in the irradiated Freon mixture solution. The splitting constant of about 25 G of the triplet is fairly close to  $a_N \approx 21$  G calculated for the planar  $NH_3^+$  cation radical.<sup>15</sup>

(iii) *Aniline and Its N-Methyl Derivatives.* The photoelectron spectra of anilines have been studied by a number of workers.<sup>14,16</sup> The first three bands appearing

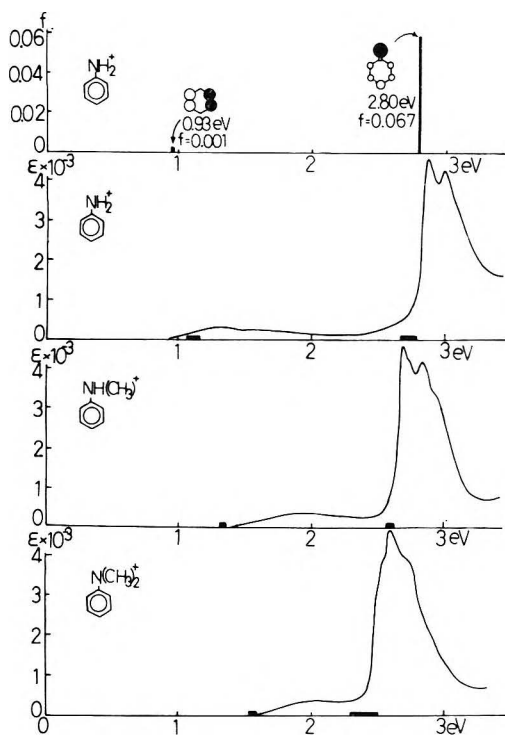


**Figure 4.** Electronic absorption spectra of cation radicals of anilines. The stick spectrum is for the cation radical of aniline. Numbers denote the transition energy (in eV) and the oscillator strength. The small horizontal bars in the spectra indicate the transition energies expected from PES. The molecular orbital patterns represent major half-occupied orbitals.

in 7–11-eV region are assigned to ionization of  $\pi$  electrons in  $b_1$ ,  $a_2$ , and  $b_1$  orbitals in the order of increasing ionization potential. The first ionization potential is suppressed as the amino hydrogen atoms are replaced by the methyl group while the second ionization potential remains nearly constant. As a result the energy separation between the first and second ionization potentials becomes larger upon methylation. Similarly, a systematic trend in the third ionization potential is clearly seen. Such changes in the ionization potential have been thoroughly discussed in terms of the character of the  $\pi$  orbitals involved.<sup>17,18</sup>

The  $\Delta$ IP PES spectra are shown as small horizontal bars in Figure 4 (the width of the bars indicates the variance of PES data from several sources). The spectra in Figure 4 show the absorption due to  $\gamma$ -irradiated anilines in the Freon mixture matrices. Although part of the spectrum was reported previously,<sup>19</sup> the weak absorption band in the region of 450–1000 nm was missing and the intensities of the absorption were not given. In this respect the spectra in Figure 4 may be regarded as the first complete spectra of the cations in the visible region. Use of *sec*-butyl chloride instead of the freon mixture caused a slight shift of some  $\lambda_{\max}$ , e.g., for aniline 430 and 413 nm in the freon whereas 436 and 415 nm in *sec*-butyl chloride. The blue shift of the first absorption and the red shift of the second absorption band agree well with the  $\Delta$ IP spectra. Here, the agreement of an SCF-MO calculation for the  $\pi$  electron system of the aniline cation with the observed optical spectrum is remarkably good (see Figure 4).

(iv) *Diphenylamine and Its Related Compounds.* Haink et al. reported PES of diphenylamine, acridan, and carbazole among others.<sup>20</sup> For the first two they observed four distinguishable PES bands in the 7–11-eV region and attributed them to  $\pi_7(b_1)$ ,  $\pi_6(b_1)$ ,  $\pi_4(a_2)$ , and  $\pi_3(b_1)$ , the missing  $\pi_5(a_2)$  being obscured by the close-lying bands of  $\pi_4$  and  $\pi_6$ . The energy separations between the first and the subsequent ionization potentials are 1.60, 1.81, and 3.20

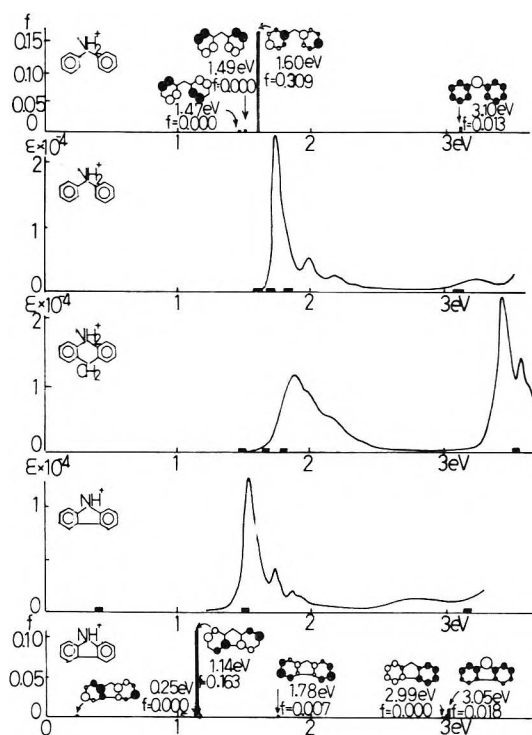


**Figure 5.** Electronic absorption spectra of cation radicals of diphenylamine, acridan, and carbazole. See the caption for Figure 4.

eV for diphenylamine and 1.50, 1.80, and 3.53 eV for acridan. For carbazole near degenerate  $\pi_6$ ,  $\pi_5$ , and  $\pi_4$  are widely split and all five  $\pi$  bands are identified as  $\pi_7$  (7.68 eV),  $\pi_6$  (8.08 eV),  $\pi_5$  (9.09 eV),  $\pi_4$  (9.78 eV), and  $\pi_3$  (10.82 eV).

The optical spectra of cation radicals and the calculated results are shown in Figure 5 which are again consistent with the transition energies deduced from PES data. The failure of optical detection of the first absorption band of the carbazole cation may be excused because it lies in the infrared region with an extremely weak intensity.

### General Discussion

It may be worthwhile to compare the strong and weak aspects of the two kinds of spectroscopy under consideration. In photoelectron spectroscopy definite assignment of such processes as ionization accompanying simultaneous excitation of another electron to a bound excited orbital is difficult because of its diminished intensity and of overlapping transitions due to ionization of  $\sigma$  electrons.<sup>21</sup> However, optical excitation corresponding to such a two-electron process may be strongly allowed depending on the symmetry of molecule. For example, the absorption band at 3.2 eV in Figure 1b, which is probably associated with the excitation with configuration of ( $\phi_3 \rightarrow \phi_9$ ) plus ( $\phi_9 \rightarrow \phi_{10}$ ), may correspond to the weak but fairly sharp peak at 10.75 eV in PES ( $\Delta$ IP = 10.75–7.60 eV, see Figure 1a). The peak has not been assigned in Schmidt's paper but the proximity of the difference in ionization potentials to the observed optical transition at 3.2 eV suggests the correspondence.

If the transition energy of the first excited state of cation radicals is so small that the absorption band appears in the infrared region, it may elude detection in the optical measurement. However, in photoelectron spectroscopy it is much easier to identify the first excited state of the cations. For example, it is by referring to PES that the weak IR band in Figure 1b was revealed. Likewise, photoelectron spectroscopy is capable of detecting optically forbidden transitions as clearly as allowed ones provided

that the ionization is a one-electron process.

In summary, all the optical spectra obtained by the irradiation method are endorsed by PES which guarantees the assignment of the spectra to the cation radicals of solute molecules. Since there seems to be no other systematic method of producing cation radicals, the method described above should be exploited to accumulate optical data of cation radicals to remedy the paucity of information on the electronic states of this important group of molecules.

## References and Notes

- (1) T. Shida, T. Kato, and Y. Nosaka, *J. Phys. Chem.*, **81**, 1095 (1977).
- (2) T. Shida and S. Iwata, *J. Am. Chem. Soc.*, **95**, 3473 (1973).
- (3) R. Zahradnik, P. Carsky, and Z. Slanina, *Collect. Czech. Chem. Commun.*, **38** 1886 (1973).
- (4) R. Egdell, J. C. Green, and C. N. R. Rao, *Chem. Phys. Lett.*, **33**, 600 (1975).
- (5) S. Oberland and W. Schmidt, *J. Am. Chem. Soc.*, **97**, 6633 (1975) (microfilm edition).
- (6) F. L. Hirshfeld, S. Sandler, and G. M. J. Schmidt, *J. Chem. Soc.*, 2108 (1963).
- (7) W. Schmidt, *J. Chem. Phys.*, **66**, 828 (1977).
- (8) R. Boschi, E. Clar, and W. Schmidt, *J. Chem. Phys.*, **60**, 4406 (1974).
- (9) R. Boschi and W. Schmidt, *Tetrahedron Lett.*, **25**, 2577 (1972).
- (10) P. Bischof, J. A. Hashmall, E. Heilbronner, and V. Hornung, *Tetrahedron*, **46**, 4025 (1969).
- (11) E. Heilbronner and K. A. Muskat, *J. Am. Chem. Soc.*, **92**, 3818 (1970).
- (12) T. M. McKinney and D. H. Geske, *J. Am. Chem. Soc.*, **87**, 3013 (1965).
- (13) G. W. Esastland and M. C. R. Symons, *Chem. Phys. Lett.*, **45**, 422 (1977).
- (14) K. Siegbahn, "Handbook of Spectroscopy", Vol. 1, J. W. Robinson, Ed., C.R.C. Press, Cleveland, Ohio, 1974, p 255.
- (15) G. Giacometti and P. L. Nordio, *Mol. Phys.*, **6**, 301 (1963).
- (16) T. P. Debies and J. W. Rabalais, *J. Electron Spectrosc.*, **1**, 355 (1972/1973).
- (17) A. D. Baker, D. P. May, and D. W. Turner, *J. Chem. Soc. B*, 22 (1968).
- (18) J. W. Rabalais, "Principles of Ultraviolet Photoelectron Spectroscopy", Wiley-Interscience, New York, N.Y., 1977, p 301.
- (19) T. Shida and W. H. Hamill, *J. Chem. Phys.*, **44**, 2369 (1966).
- (20) H. J. Haink, J. E. Adams, and J. R. Huber, *Ber. Bunsenges. Phys. Chem.*, **78**, 436 (1974).
- (21) J. W. Rabalais, "Principles of Ultraviolet Photoelectron Spectroscopy", Wiley-Interscience, New York, N.Y., 1977, p 67.
- (22) A. Grimison and G. A. Simpson, *J. Phys. Chem.*, **72**, 1776 (1968).

## The Kerr Effect of Carbon Disulfide and Other Organic Liquids in the Ultraviolet<sup>1-3</sup>

James W. Lewis<sup>4</sup> and William H. Orttung\*

Department of Chemistry, University of California, Riverside, California 92521 (Received September 20, 1977)

A short-path Kerr cell of novel design was used to measure Kerr constant ratios,  $B(\lambda)/B(400 \text{ nm})$ , for liquid carbon disulfide, benzene, and five substituted benzenes in the ultraviolet. For carbon disulfide, the ratio was  $+3.59 \pm 0.05$  at 272 nm, the sign being determined by two methods. Earlier workers reported negative ratios in this wavelength region. The dispersion of the molecular optical anisotropy of carbon disulfide was estimated by the Born-Langevin theory, which proved inadequate, and by an extension of the Scholte theory for nonspherical molecules. The latter theory gave results in agreement with estimates from light scattering depolarization data on the vapor. Hyperpolarizability contributions to the optical anisotropy were not observed in the dispersion data.

### Introduction

The wavelength dependence of the Kerr effect provides information about dispersion of the molecular polarizability anisotropy. This information in turn can be related to the absorption spectrum and, in favorable cases, can be used to determine the polarization of transitions and other molecular properties.<sup>5,6</sup> The Kerr constant is also sensitive to the optical local field. Since the local field function should change with the wavelength of the light, the dispersion of the Kerr effect can be used to test local field models.

Previous experimental work had been done primarily in the visible part of the spectrum.<sup>7-9</sup> For the study of electronic transitions and for the purpose of analyzing local field effects over the largest range it was important that measurements be made in the ultraviolet. Only two such studies had been made in the past.<sup>10,11</sup> For carbon disulfide, it was reported that in the transmitting region between the weak absorption at 323 nm and the strong absorption centered at 210 nm, the Kerr constant was negative and had a magnitude 8-10 times larger than that of the positive Kerr constant at 400 nm.<sup>11</sup> This is a surprising result since in the vapor the first allowed transition is known to be polarized parallel to the long molecular axis.<sup>12,13</sup>

Data on carbon disulfide are also of interest from the standpoint of local field theories since the molecule has a large polarizability anisotropy and is poorly represented by a spherical shape. These characteristics are often neglected in the application of local field theories. In this work, however, a theory of the Kerr effect of nonpolar liquids is derived which uses the Scholte<sup>14</sup> local field. This theory is appropriate for spheroidal molecules with large anisotropies.

The Kerr constant of carbon disulfide between the two absorbing regions was measured in the present work by two different methods and the sign was found to be positive. The magnitude was analyzed using both the Born-Langevin theory and the theory based on the Scholte local field. The latter theory did not need to assume that the relative importance of hyperpolarizability greatly increases in the ultraviolet. Measurements are also reported for several liquids not previously studied outside the visible part of the spectrum.

### Experimental Section

*Method.* The light incident on the Kerr cell was linearly polarized at an angle of 45° to the field in the cell. (All angles are measured counterclockwise looking toward the light source.) The optical electric field can be decomposed

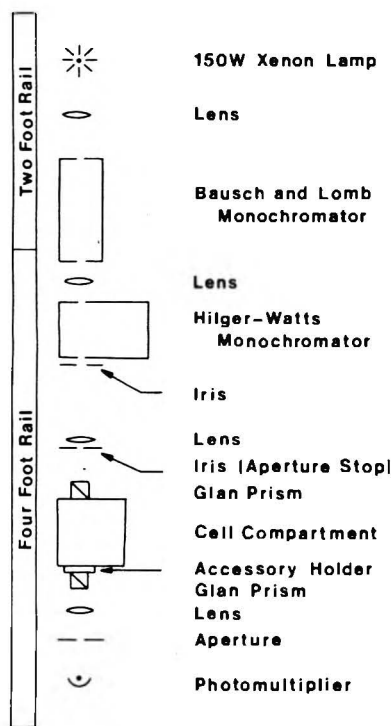


Figure 1. The optical arrangement of the Kerr effect apparatus. Two monochromators were required for measurements in absorbing regions.

into components polarized parallel and perpendicular to the static field in the cell. The total retardation,  $\delta$ , is the additional phase angle executed by the component polarized parallel to the static field relative to the perpendicular component. The total retardation is the sum of  $\delta_0$ , a field independent part due primarily to the cell windows, and  $\delta_1$ , the usual field dependent part given by,

$$\delta_1 = 2\pi l(n_{\parallel} - n_{\perp})/\lambda \quad (1)$$

Here  $l$  is the effective length of the sample in a uniform field,  $n_{\parallel}$  and  $n_{\perp}$  are the refractive indices of the sample parallel and perpendicular to the applied field, and  $\lambda$  is the vacuum wavelength of the light. The Kerr constant used for pure liquids is defined by

$$B = (n_{\parallel} - n_{\perp})/\lambda E^2 = \delta_1/2\pi l E^2 \quad (2)$$

Here  $E$  is the static electric field strength in the cell.

The light intensity,  $I_r$ , transmitted by the analyzer when  $\delta = 0$  is  $I_0 \sin^2 r + I_{r=0}$ , where  $r$  is the angle by which the analyzer deviates from being crossed with respect to the polarizer, and  $I_0$  is the change in transmitted intensity when  $r$  goes from 0 to  $\pi/2$  radians. By measuring the transmitted intensity with the analyzer rotated by a known angle,  $I_0$  can be determined. When retardation  $\delta$  is added between crossed polarizer and analyzer the transmitted intensity,  $I_{\delta}$ , is given by

$$I_{\delta} = I_0(1 - \cos \delta)/2 \cong I_0 \delta^2/4 \quad (3)$$

with the last equality true for small  $\delta$ 's.

A quarter wave plate between the cell and analyzer with its fast axis along the original polarization direction can be used to determine the sign of  $\delta$ . If  $0 < \delta < \pi$ , the axis of the linearly polarized light reaching the analyzer from the quarter wave plate will be rotated counterclockwise from the original polarization axis. For  $-\pi < \delta < 0$  a clockwise rotation will result.

**Apparatus.** The apparatus is shown in Figure 1. The optical components were mounted on two CENCO optical rails. The first rail was 66 cm long and carried the lamp housing, a lens, and the first monochromator. The second

rail, clamped to the end of the first, was 132 cm long and carried the rest of the optical components.

The light source was a 150-W xenon short arc lamp mounted in a Schoeffel LH 151 N lamp housing. The condenser lens in the housing was used to focus the image of the arc on the entrance slit of the Bausch & Lomb 33-86-01 grating monochromator. The image of the first monochromator's exit slit was focused on the entrance slit of a Hilger-Watts D292 grating monochromator using a 5-cm focal length lens. This lens, like all others used in the optical system, was made of fused silica. An iris diaphragm following the monochromator served as a field stop (diameter 0.5 cm). The image of the exit slit was focused beyond the electrodes in the Kerr cell using a 9.8 cm focal length lens. An iris diaphragm following this lens served as an aperture stop (diameter 0.85 cm). The polarizer mounted at the front of the cell compartment polarized the light reaching the Kerr cell at an angle of  $45^\circ$  from the horizontal plane. The Kerr cell was held in a pair of "V" shaped cradles and was positioned so that for green light the image of the second monochromator's exit slit was focused 2.5 cm beyond the ends of the electrodes. The electric field in the Kerr cell was horizontal. An accessory holder and the analyzer were mounted at the back of the cell compartment. The accessory holder could be used for either the quarter wave plate or the strain compensator. The analyzer could be rotated around the optical axis by means of a micrometer drive. This drive allowed the transmission axis of the analyzer to be adjusted over a  $13^\circ$  range accurate to  $0.01^\circ$ . At approximately the center of this range the analyzer was crossed with respect to the polarizer. Both polarizer and analyzer were Karl Lambrecht 20-mm Glan prisms. The extinction ratio,  $I_{r=0}/I_{r=\pi/2}$ , obtained with cell removed was  $2 \times 10^{-6}$  at 546 nm and  $5 \times 10^{-6}$  at 272 nm. After passing through the analyzer the light was focused by a 4.4 cm focal length lens through a 0.25 cm circular aperture and then diverged to create a diffuse spot on the photocathode of the EMI 9558QB photomultiplier. A  $10^6$ -ohm anode resistor was used, and the photomultiplier dynode string was powered by a Fluke 412 B dc power supply set at  $-1.5$  kV. The voltage across the anode resistor was measured using a Leeds and Northrop K-3 potentiometer and electronic null detector. Saturation was never observed for signals below 0.5 V and all Kerr measurements involved signals considerably smaller.

Originally the apparatus was used with only the Hilger-Watts monochromator. This proved satisfactory for Kerr measurements outside absorbing regions. The second monochromator was added so that accurate measurements could be made in absorbing regions where stray light was a source of error. The Hilger-Watts monochromator covered the range 200–1030 nm, but the later measurements were further limited by the long wavelength limit (400 nm) of the Bausch & Lomb monochromator. The slit widths used were 3 mm on the Bausch & Lomb and 0.5 mm on the Hilger-Watts. The monochromators were calibrated using an Orion Optics low pressure mercury lamp.

The Kerr cell is shown in Figure 2. The body of the cell was borosilicate glass with two female, standard taper 29/26 ground glass joints for window inserts. The window inserts were made by fusing a  $7/8$  in. diameter,  $1/16$  in. thick window to the end of a male, standard taper 29/42 ground joint. Both window and joint were fused silica requiring a final annealing step in an oven at  $1050^\circ\text{C}$ . The top for the cell was a borosilicate glass flange made by grinding away the grooved portion of an O-ring joint. It rested on

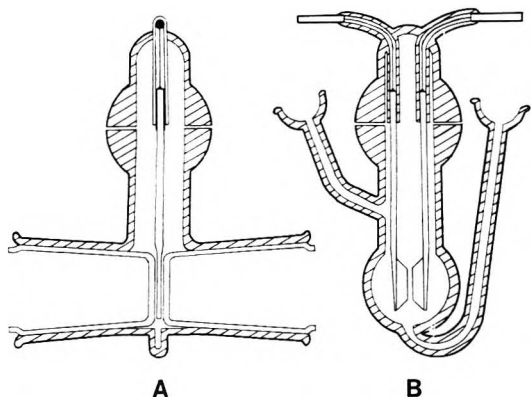


**Figure 2.** The Kerr cell. (A) Side section through the cell with slit assembly removed. The overall length of the cell was 10 cm. (B) End section through the electrodes.

a similar flange on the cell body. Glass tubes fused to the top of the cell carried the copper supports for the electrodes. Soft copper bushings and a chemically resistant, heat cure epoxy (Shell Epon 828, Curing Agent CL) were used to fasten the supports inside the glass tubes. Wires soldered to the supports passed through the tubes to glass to metal seals used for electrical connection to the electrodes. The nickel electrodes soldered to the supports were trapezoidal in cross section and were 1.05 mm thick. Their separation was 1.0 mm. The top was attached to the cell body using quartz type sticky wax around the outside edges of the flange joint. A slit assembly 0.5 mm by 5 mm was positioned approximately 1 mm from the front window of the cell. This assembly was friction fitted inside the front window insert. The small tubes on the cell body were for filling. The liquid level remained below the vent tube when the cell was full. The path length of the cell depended on the inserts used and was approximately 2.5 mm.

The dc high voltage for the cell was provided by a Condenser Products Co. PST10-1M60 high voltage module. The output was continuously variable from 0 to 10 kV by means of a variable transformer connected to the input of the module. A meter gave an approximate measure of the output voltage. Accurate measurement of the output was made using a 10000:1 voltage divider constructed by placing a  $1.1 \times 10^3$  ohm resistor across the output of a Tektronix P6013 high voltage probe. The K-3 potentiometer was used to measure the output of the divider.

The quartz quarter wave retarder zero order, at 272 nm, was provided by Optics for Research.<sup>15</sup> It was important that the manufacturer align the two plates of the retarder while viewing it between crossed polarizers. The plates were aligned so that best minimum in the transmitted intensity was obtained when the axes of the retarder were aligned with the axes of the polarizers. The strain compensator, shown in Figure 3, was a 1 in. square piece of fused silica microscope slide held in a disk of phenolic composite material. The edges of the slide were protected by strips cut from Tygon tubing. Pressure was applied to the edge of the slide by means of an aluminum bar which rested against two set screws used to adjust the retardation of the compensator. The retardation used in these experiments was approximately  $1^\circ$  at 400 nm. The fact that the strain was uniform was verified by measuring the retardation of the compensator with the strain axis aligned with the axis of incident polarized light. The retardation obtained was less than 5% of the value obtained with the strain axis at  $45^\circ$  to the incident polarized light. All measurements were made at room temperature, which was  $23 \pm 1^\circ\text{C}$ .

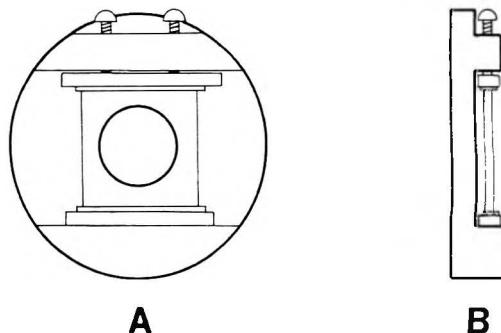


**Figure 3.** The strain compensator. (A) Front view. Pressure applied by the screws provided a uniform optical retardation of approximately  $1^\circ$  over the 15 mm aperture of the device. (B) Side view. Height 6 cm.

**Magnitude of the Kerr Constant.** After filling the Kerr cell the photomultiplier signal was measured with the analyzer in the crossed position. The reading on the K-3 was  $R_c$ . The analyzer was then rotated away from the crossed position by an angle,  $r$ , between 1 and  $5^\circ$ . The photomultiplier signal was measured and the reading was  $R_r$ . The analyzer was returned to the crossed position and the electric field was turned on in the cell. The photomultiplier signal was measured and the K-3 reading was  $R_s$ . The output of the high voltage divider was measured on the K-3 and the reading was  $R_f$ . The field in the cell was then set to a new value and the last two measurements were repeated. On the average, measurements were made at eight field points between 3 and 8 kV. Often, in between field points,  $R_c$  was remeasured. This was especially important for systems with small Kerr constants.

**Sign of the Kerr Constant.** For the first method the quarter wave plate was placed in the holder between the cell and analyzer with its fast axis along the original polarization direction. The crossed position of the analyzer was then determined by adjusting the analyzer until a minimum in the photomultiplier signal was obtained. The analyzer was rotated  $5^\circ$  from the new crossed position. The photomultiplier signal,  $R_r'$ , was measured on the K-3. The field in the cell was then turned on and the photomultiplier signal,  $R_r''$ , and the output of the voltage divider,  $R_f$ , were measured using the K-3.

For the second method of determining the sign of the Kerr constant, the strain compensator was placed in the holder between the cell and the analyzer with its strain axis perpendicular to the field in the cell. Measurements then proceeded as for the magnitude of the Kerr constant.

**Treatment of Data.** The photomultiplier signal minus the dark signal was proportional to the transmitted light intensity, since saturation was avoided. The hypothetical photomultiplier signal,  $R_0$ , corresponding to  $I_0$  was calculated,  $R_0 = (R_r - R_c)/r^2$ , where  $r$  is in radians and the approximation  $\sin^2 r = r^2$  has been made. The difference  $R_s - R_c$  was related to the retardations, using eq 3 for small  $\delta$  and  $\delta_0$ :

$$4(R_s - R_c)/R_0 = (\delta_0 + \delta_1)^2 - \delta_0^2 \quad (4)$$

Combining eq 2 and eq 4

$$(R_s - R_c)/R_0 \pi l E^2 = B^2 \pi l E^2 + \delta_0 B \quad (5)$$

A plot of the left-hand side of this equation against  $\pi l E^2$  should be a straight line with slope  $B^2$  and intercept  $\delta_0 B$ .

A typical plot of eq 5 is shown in Figure 4. The electric field strength was calculated by multiplying  $R_f$  by the voltage divider ratio and dividing by the electrode spacing. The value of  $l$  used in these calculations was 0.13 cm. This value was only approximate since it was not possible to

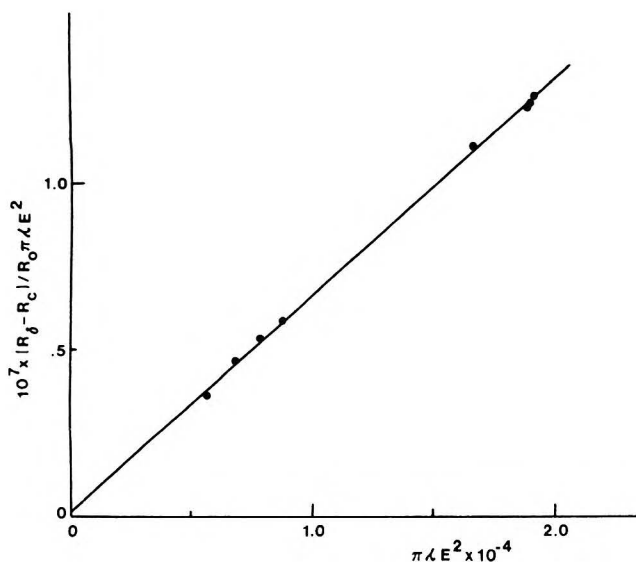


Figure 4. Plot of the experimental data for one run on carbon disulfide at 272 nm. The axes are in cgs units. The y intercept for this run was  $1.5 \times 10^{-9}$ .

quantitatively correct for field spreading at the electrode ends. Quadrupole orientation by the small transverse field gradients within the light beam at the electrode ends is not likely to be of importance. In order to minimize end effects, the reported results are ratios of the Kerr constant to that of carbon disulfide at 400 nm. The absolute Kerr constant of carbon disulfide at 400 nm was determined by measuring the ratio of the Kerr constant at 400 and 546 nm. Using Otterbein's<sup>16</sup> result for the Kerr constant at 546 nm,  $3.55 \times 10^{-7}$  (in electrostatic cgs units), this gave, for the Kerr constant of carbon disulfide at 400 nm,  $6.13 \times 10^{-7}$ .

The average of the  $\delta_0$ 's obtained for all the runs was  $1.6 \times 10^{-3}$  at 400 nm and  $3.2 \times 10^{-3}$  at 272 nm. The origin of  $\delta_0$  seemed to be primarily the cell windows since  $I_c/I_0$  increased from  $5 \times 10^{-6}$  at 400 nm with the cell compartment empty, to  $1 \times 10^{-5}$  when the cell with the electrodes removed was placed in the optical path. No noticeable further deterioration in  $I_c/I_0$  was observed when the electrodes were added.

**Materials.** The carbon disulfide, toluene, and benzene were spectroscopic grade and were used without further purification. Identical results were obtained using carbon disulfide from three different manufacturers. The mesitylene was 99+ % pure. The other liquids were reagent grade from new bottles. To determine the effects of particles in the liquids, several runs were made using samples from a syringe with a 0.22- $\mu$ m Millipore filter. Identical results were obtained using filtered and unfiltered samples.

## Results

**The Magnitude of the Kerr Constant.** The Kerr constant ratios that were measured are given in Table I. The reported values are the ratio of the Kerr constant of the substance to that of carbon disulfide at 400 nm. The slope and intercept of eq 5 were determined by the least-squares method. The number of runs and the variance is given where appropriate. For all liquids, measurements were made at the shortest wavelength permitted by the absorption of the sample. The data for carbon disulfide, shown in Figure 5, are in agreement with the results of Blackwell<sup>17</sup> and McComb<sup>7</sup> over the wavelength range where comparison is possible. Similar agreement was obtained with the results of Szivessy and

TABLE I: Kerr Constant Ratios

Sample	$\lambda$ , nm	No. of runs	$B/B_{CS_2}$ (400 nm)	Variance
CS <sub>2</sub>	268	1	3.90	
	272	8	3.59	0.05
	276	1	3.20	
	366	1	1.19	
	400	6	1.00	0.015
	450	1	0.791	
Benzene	550	2	0.556	0.025
	280	3	0.239	0.009
	300	3	0.187	0.007
Toluene	400	5	0.116	0.002
	285	1	0.431	
o-Xylene	400	1	0.210	
	285	1	0.690	
	340	1	0.462	
m-Xylene	400	1	0.356	
	300	1	0.347	
	400	1	0.191	
p-Xylene	300	2	0.357	0.007
	400	1	0.195	
Mesitylene	320	3	0.284	0.016
	400	3	0.180	0.002

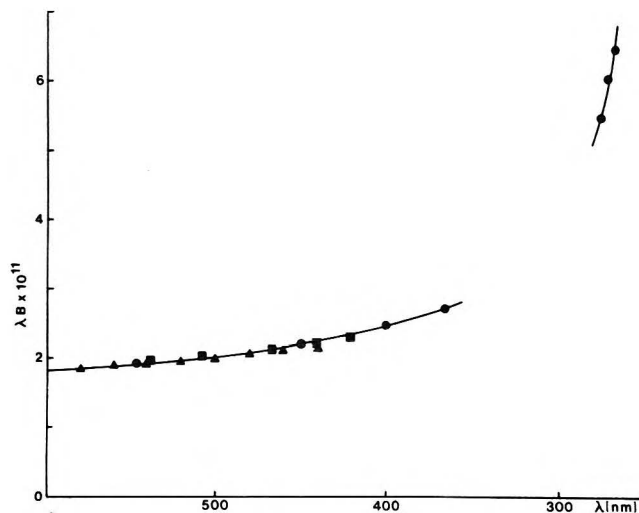


Figure 5. Plot of  $\lambda B$  vs. wavelength for carbon disulfide. Points denote Blackwell's<sup>17</sup> data (■), McComb's<sup>7</sup> data (▲), and present results (●). The break in the curve is due to the absorption at 323 nm. The product  $\lambda B$  is in cgs units.

Dierkesmann<sup>10</sup> for toluene and *m*-xylene. One run was made for hexane to assure that the close proximity of the cell windows to the electrodes did not lead to field dependent birefringence in the windows. The result was that no observable increase in signal was detected when a voltage of 5 kV was applied to the cell. This was as expected since hexane's Kerr constant is too small to be measured with this apparatus.

**The Sign of the Kerr Constant.** For all of the liquids except carbon disulfide, measurement of the Kerr constant can be made continuously from the visible region of the spectrum to the shortest wavelengths measured here. Based on the known sign of  $B$  in the visible, extrapolation to the present measurements in the ultraviolet indicates that for these liquids the Kerr constant remains positive well into the edge of the first absorption. For carbon disulfide, however, such continuous measurements are made impossible by the absorption in the liquid centered at 323 nm. The sign of the Kerr constant on the other side of this absorption had to be measured independently.

The experiments using the quarter wave plate gave clear evidence that the sign of  $B$  for carbon disulfide was positive at the center of the transmitting region, 272 nm. With the

fast axis of the plate parallel to the original polarization direction and the analyzer rotated  $5^\circ$  from the crossed position,  $R_r''$  became noticeably larger than  $R_r'$  for cell voltages as small as 2 kV. Progressively larger differences were obtained for larger voltages. For a cell voltage of 6 kV,  $R_r'' - R_r'$  was approximately equal to  $R_r' - R_c$ . This gave clear evidence that  $B$  was positive at 272 nm. A similar run at 364 nm also found  $R_r'' - R_r'$  increasing as the field in the cell increased, consistent with the known positive sign of  $B$  at the wavelength. Since previous workers<sup>11</sup> using a similar method had reached the opposite conclusion about the sign of  $B$  at 272 nm, the measurements with the strain compensator were made.

Keeping the orientation of the strain compensator fixed, runs were made at 400 and 272 nm. The presence of the compensator made  $\delta_0$  approximately 20 times larger than that found with the cell alone. The increase in  $\delta_0$  made it possible to determine the sign of  $B$  from the intercept of eq 5. The intercept of both the 400- and 272-nm runs was positive. A series of measurements of  $R_c/R_0$  for the compensator alone at 30-nm intervals between 400 and 270 nm showed that  $R_c - R_0$  was a smoothly increasing function over this range. These measurements confirmed that  $B$  was positive for carbon disulfide at 272 nm.

### Theoretical Development

The earliest theory of the Kerr constant, which used the Scholte<sup>14</sup> local field, was that of Klages.<sup>18</sup> Approximations in the theory, however, make it unsuitable for strongly anisotropic molecules such as  $\text{CS}_2$ . The extension of the theory given here corrects the deficiencies for spheroidal nonpolar molecules.

In the following derivations, Greek subscript will be used to denote vectors and tensors. Thus  $x_\alpha$  represents the three components of a vector. If a Greek subscript appears twice in the same symbol or in a product of symbols, summation over that index is implied. The initial subscript l or 0 will be used to denote optical or static frequency, respectively.

The electric field  $E_{l\alpha}$ , displacement  $D_{l\alpha}$ , and polarization  $P_{l\alpha}$ , due to a light wave propagating through a continuous medium, are related by

$$D_{l\alpha} = \epsilon_{l\alpha\beta} E_{l\beta} = E_{l\alpha} + 4\pi P_{l\alpha} \quad (6)$$

where  $\epsilon_{l\alpha\beta}$  is the dielectric tensor at the optical frequency. For the Kerr effect, the medium is axially symmetric around the static electric field  $E_{0\alpha}$ , and  $\epsilon_{l\alpha\beta}$  is diagonal. Let  $\epsilon_{li}$  represent the  $i$ th principal value of  $\epsilon_{l\alpha\beta}$ . In particular, let  $i = p$  or  $s$  refer to the values parallel or perpendicular to  $E_{0\alpha}$ . The two independent components of eq 6 may then be written

$$\epsilon_{lp} - 1 = 4\pi P_{lp} / E_{lp} \quad (7)$$

$$\epsilon_{ls} - 1 = 4\pi P_{ls} / E_{ls} \quad (8)$$

If  $\epsilon_{li}$  is replaced by  $n_i^2$ , the square of the refractive index, and if  $P_{li}$  is replaced by  $N \langle m_{l\alpha} e_{i\alpha} \rangle$ , where  $N$  is the number of molecules per  $\text{cm}^3$ ,  $m_{l\alpha}$  is the induced moment, and  $e_{i\alpha}$  is a unit vector for  $i = p$  or  $s$ ; then eq 7 and 8 may be written:

$$n_p^2 - 1 = 4\pi N \langle m_{l\alpha} e_{p\alpha} \rangle / E_{lp} \quad (9)$$

$$n_s^2 - 1 = 4\pi N \langle m_{l\alpha} e_{s\alpha} \rangle / E_{ls} \quad (10)$$

Our objective is to express the Kerr constant  $B$ , as defined in eq 2, in terms of the molecular averages appearing on the right of eq 9 and 10. Thus, if  $i = p$  or  $s$

$$\langle m_{l\alpha} e_{i\alpha} \rangle = \frac{\int (m_{l\alpha} e_{i\alpha}) e^{-U(\tau, E_0) / kT} d\tau}{\int e^{-U(\tau, E_0) / kT} d\tau} \quad (11)$$

where  $\tau$  specifies the orientation of the molecule, and  $U(\tau, E_0)$  is its field-dependent potential energy. Equation 11 assumes that classical statistical mechanics is valid, and treats the molecule as though it is in a cavity in a continuous dielectric medium.

The moment  $m_{l\alpha}$  may be expressed in terms of an optical polarizability  $\pi_{l\alpha\beta}$  and an optical local field  $F_{l\alpha}$  as follows:

$$m_{l\alpha} = \pi_{l\alpha\beta} F_{l\beta} \quad (12)$$

where  $\pi_{l\alpha\beta}$  is a property of the molecule in vacuo. It may include hyperpolarizability effects due to the large static local field  $F_{0\alpha}$ :

$$\pi_{l\alpha\beta} = \alpha_{l\alpha\beta} + {}^1/2 \gamma_{l\alpha\beta\gamma\delta} F_{0\gamma} F_{0\delta} \quad (13)$$

where  $\alpha_{l\alpha\beta}$  is the polarizability tensor in small fields and a nonpolar molecule is assumed. Note that  $\gamma_{l\alpha\beta\gamma\delta}$  is defined in terms of both optical and static fields.

Consider the static or optical local field  $F_\alpha$  to be the sum of a cavity field  $G_\alpha$ , and a reaction field  $R_\alpha$ , and express the linear relationship of these vectors to  $E_\alpha$  the average field in the medium, or to  $m_\alpha$  as follows:

$$F_\alpha = l_{\alpha\beta} E_\beta; G_\alpha = g_{\alpha\beta} E_\beta; R_\alpha = f_{\alpha\beta} m_\beta \quad (14)$$

Then, from eq 12 and 13 (neglecting hyperpolarizabilities) and the above definition of  $F_\alpha$ , in cases where  $\alpha_{\alpha\beta}$ ,  $l_{\alpha\beta}$ ,  $g_{\alpha\beta}$ , and  $f_{\alpha\beta}$  are diagonal with principal values  $\alpha_m$ ,  $l_m$ ,  $g_m$ , and  $f_m$  ( $m = 1, 2, 3$  or  $x, y, z$  will be used for the coordinate component subscript), we have:

$$l_m = g_m / (1 - \alpha_m f_m) \quad (15)$$

for nonpolar molecules.

For the model of an ellipsoidal cavity with semi-axes  $a$ ,  $b$ , and  $c$  in a medium of dielectric constant  $\epsilon$ , the cavity field factors are<sup>14</sup>

$$g_m = \frac{\epsilon}{\epsilon + (1 - \epsilon)A_m} \quad (16)$$

where the  $A_m$ 's are the so-called demagnetizing factors.<sup>20</sup> If the molecule is considered to be a dielectric ellipsoid which exactly fills the cavity, and has principal dielectric constants  $\epsilon_m'$  along the ellipsoid axes, then the polarizability components are<sup>14</sup>

$$\alpha_m = \frac{abc}{3} \frac{\epsilon_m' - 1}{1 + (\epsilon_m' - 1)A_m} \quad (17)$$

and the reaction field factors are<sup>14</sup>

$$f_m = \frac{3}{abc} \frac{A_m(1 - A_m)(\epsilon - 1)}{\epsilon + (1 - \epsilon)A_m} \quad (18)$$

For optical fields,  $\epsilon$  and the  $\epsilon_m'$  values are replaced by  $n^2$  and  $n_m'^2$ .

The potential energy of the ellipsoid in the static field (required for eq 11) is<sup>18,21</sup>

$$U = -{}^1/2 m_{0\alpha}^* E_{0\alpha} \quad (19)$$

where  $m_{0\alpha}^*$  is the external moment with components<sup>18</sup>

$$m_{0m}^* = \frac{\epsilon_m' - \epsilon}{\epsilon_m' - 1} \alpha_{0m} l_{0m} E_{0m} \quad (20)$$

At this point it is convenient to introduce two auxiliary symbols:

$$\tilde{\alpha}_{0m} = \frac{\epsilon_m' - \epsilon}{\epsilon_m' - 1} \alpha_{0m} \quad (21)$$

and an "external polarizability"

$$\tilde{\alpha}_{0m}^* = \tilde{\alpha}_{0m} l_{0m} \quad (22)$$



TABLE II: Summary of Estimates of the Optical Parameters of CS<sub>2</sub>

Theory	$\lambda$ , nm	$n_{\text{liq}}$	$\bar{\alpha}_1$	$\Delta\alpha_1$	$\alpha_{11}$	$\alpha_{12}$
Born-Langevin and Lorentz-Lorentz	546	1.656 <sup>a</sup>	8.8 <sup>c</sup>	10.1 <sup>a,b</sup>	15.5 <sup>d</sup>	5.4 <sup>d</sup>
	272	2.033 <sup>a</sup>	12.2 <sup>c</sup>	23.3 <sup>c</sup>	27.7 <sup>d</sup>	4.4 <sup>d</sup>
Extended Klages and Scholte	546	1.678 <sup>c</sup>	8.9 <sup>a</sup>	10.1 <sup>a,b</sup>	15.6 <sup>a</sup>	5.5 <sup>a</sup>
	272	1.989 <sup>c</sup>	11.4 <sup>d</sup>	17.8 <sup>c</sup>	23.3 <sup>c</sup>	5.5 <sup>b</sup>
	272	2.033 <sup>a</sup>				6.1 <sup>c,d</sup>

<sup>a</sup> Data, or closely related to data. <sup>b</sup> Invokes an assumption. <sup>c</sup> Calculated. <sup>d</sup> Deduced from calculated results.

that interacts with the average field in the medium. Analogous definitions will be used for the optical parameters, with  $n_m^2$  and  $n^2$  replacing  $\epsilon_m'$  and  $\epsilon$ . The potential energy in the static field may then be concisely written as

$$U = -1/2 \sum_{m=1}^3 \tilde{\alpha}_{0m}^* E_{0m}^2 \quad (23)$$

The moment of eq 11 can then be written as

$$m_{1\alpha} = \alpha_{1\alpha\beta} l_{1\beta\epsilon} E_{1\epsilon} + 1/2 \gamma_{1\alpha\beta\gamma\delta} l_{1\beta\epsilon} E_{1\epsilon} F_{0\gamma} F_{0\delta} \quad (24)$$

Assuming that  $U \ll kT$ , the exponentials in eq 11 can be expanded in powers of  $E_0$  about  $E_0 = 0$  to give for  $i = p$  or  $s$ :

$$\begin{aligned} \langle m_{1\alpha} e_{i\alpha} \rangle = & l_{1i\beta\epsilon} E_{1i} \{ \alpha_{1\alpha\beta} \langle E_{i\alpha} e_{i\epsilon} \rangle_0 + \\ & \frac{1}{2kT} \alpha_{0\gamma\delta}^* E_0^2 \langle e_{i\alpha} e_{i\epsilon} e_{p\gamma} e_{p\delta} \rangle_0 - \\ & \langle e_{i\alpha} e_{i\epsilon} \rangle_0 \langle e_{p\gamma} e_{p\delta} \rangle_0 \} + \\ & 1/2 \gamma_{1\alpha\beta\gamma\delta} l_{0\gamma\kappa} l_{0\delta\zeta} E_0^2 \langle e_{i\alpha} e_{i\epsilon} e_{p\kappa} e_{p\zeta} \rangle_0 \end{aligned} \quad (25)$$

where  $E_{1i}$ ,  $E_0$ , and  $F_0$  are vector magnitudes; the subscript  $i$  on the local field factor  $l_{1i\beta\epsilon}$  indicates that  $n_i$  ( $i = p$  or  $s$ ) is used to evaluate the factor; and the notation  $\langle \rangle_0$  means an average carried out in the absence of the external field. The term containing the product of two averages is from the denominator of eq 11. The averages may be evaluated by the method of Buckingham and Pople<sup>22</sup> to give

$$\langle m_{1\alpha} e_{i\alpha} \rangle = [\bar{\alpha}_{1i}^* + (\theta^* + \frac{1}{20kT} \gamma_{1\alpha\alpha\beta\beta}^* E_0^2)] E_{1i} \quad (26)$$

where

$$\bar{\alpha}_{1i}^* = 1/3 \sum_{m=1}^3 \alpha_{1im} l_{1im} = 1/3 \sum_{m=1}^3 \alpha_{1im}^* \quad (27)$$

$$\gamma_{1\alpha\beta\gamma\delta}^* = \gamma_{1\alpha\epsilon\kappa\zeta} l_{1\epsilon\beta} l_{0\kappa\gamma} l_{0\delta\zeta} \quad (28)$$

and, for spheroidal molecules

$$\theta^* = \frac{2}{45kT} (\alpha_{11}^* - \alpha_{12}^*) (\tilde{\alpha}_{01}^* - \tilde{\alpha}_{02}^*) \quad (29)$$

From eq 27 and the  $l_{im}$  given by eq 15-18, we see that  $\bar{\alpha}_{1p}^* \neq \bar{\alpha}_{1s}^*$ . This lack of equality also occurs in the Born-Langevin theory, in which Lorentz local field factors are used, and in the Onsager spherical model. However, in both of these cases,  $l_{ijm}$  (and  $l_{0im}$ ) are independent of  $m$  and may be factored from the right-hand sides of eq 27 and 26. For the ellipsoidal model, we cannot factor the local field quantities, and must proceed with the remainder

of the derivation in the following manner.

If eq 27 is evaluated by substituting eq 15-18, we obtain

$$\bar{\alpha}_{1p}^* - \bar{\alpha}_{1s}^* = (n_p^2 - n_s^2) C \quad (30)$$

where

$$\begin{aligned} C = 1/3 \sum_{m=1}^3 \{ \alpha_{1m} A_m [1 + (3\alpha_{1m}/ab^2)(1 - \\ A_m)] / [n^2 + (1 - n^2)A_m - (3\alpha_{1m}/ab^2)A_m(1 - \\ A_m)(n^2 - 1)]^4 \} \end{aligned} \quad (31)$$

Now, if eq 26 is substituted into eq 9 and 10, and if eq 10 is subtracted from eq 9, we obtain

$$n_p^2 - n_s^2 = \frac{2\pi N E_0^2}{1 - 4\pi N C} [3\theta^* + \frac{1}{15} \gamma_{1\alpha\alpha\beta\beta}^*] \quad (32)$$

Using the approximation,  $n_p^2 - n_s^2 \approx 2n(n_p - n_s)$ , and substituting eq 32 in eq 2, we obtain

$$\begin{aligned} B = \frac{\pi N}{15(1 - 4\pi N C)\lambda n} \left[ \frac{2}{kT} (\alpha_{11}^* - \alpha_{12}^*) (\tilde{\alpha}_{01}^* - \right. \\ \left. \tilde{\alpha}_{02}^*) + \gamma_{1\alpha\alpha\beta\beta}^* \right] \end{aligned} \quad (33)$$

## Calculations

**Born-Langevin Theory.** It is interesting to compare the result of analyzing the data for carbon disulfide using the Born-Langevin<sup>23,24</sup> theory with the result obtained using the extended version of Klages' theory derived in the preceding section. The results of the following calculations are summarized in Table II. The Born-Langevin theory of the Kerr effect uses the Lorentz local field for both optical and static fields. For a nonpolar molecule with cylindrical symmetry, this leads to the result

$$B = \frac{2\pi N(n^2 + 2)^2(\epsilon + 2)^2}{1215n\lambda kT} (\alpha_{11} - \alpha_{12})(\alpha_{01} - \alpha_{02}) \quad (34)$$

A value of  $\Delta\alpha_1 = \alpha_{11} - \alpha_{12}$  for the liquid at 272 nm can be calculated from the following data: (1) the ratio of Kerr constants at 272 and 546 nm (6.29); (2) the values of  $n$  of the liquid at these wavelengths (2.033 and 1.656, respectively<sup>25</sup>); (3) the vapor value of  $\Delta\alpha_1$  at 546 nm (10.1 Å<sup>3</sup>), determined by interpolating the results of Alms et al.<sup>26</sup> and (4) the assumption that  $\Delta\alpha_1$  is the same for the liquid and the vapor. The calculated value of  $\Delta\alpha_1$  from eq 34 is then 23.3 Å<sup>3</sup> at 272 nm.

The consistency of this result can be checked by using the Lorentz-Lorentz equation

$$\bar{\alpha}_1 = \frac{3}{4\pi N} \frac{n^2 - 1}{n^2 + 2} \quad (35)$$

in combination with the relations,  $\alpha_{11} = \bar{\alpha}_1 + 2/3\Delta\alpha_1$  and  $\alpha_{12} = \bar{\alpha}_1 - 1/3\Delta\alpha_1$ , to calculate the individual values,  $\alpha_{11}$  and  $\alpha_{12}$ . The results using the Lorentz local field are that  $\alpha_{11}$

goes from 15.5 Å at 546 nm to 27.7 Å<sup>3</sup> at 272 nm. Over the same range  $\alpha_{12}$  goes from 5.4 to 4.4 Å<sup>3</sup>. The decrease in  $\alpha_{12}$  found using this theory is unexpected since the polarizability would be expected to increase as the strong absorptions in the ultraviolet are approached. The absorption at 323 nm is too weak to have a noticeable effect.

**Extended Klages Theory.** To use eq 33 to calculate  $\Delta\alpha_1$  at 272 nm, separate values of  $\alpha_{11}$  and  $\alpha_{12}$  at 546 nm were taken from an analysis of vapor phase refractive index and light scattering measurements.<sup>26</sup> By interpolation of the results of Alms et al.,  $\alpha_{11}$  is 15.6 Å<sup>3</sup> and  $\alpha_{12}$  is 5.5 Å<sup>3</sup>.<sup>26</sup> The static polarizabilities were estimated using Gans<sup>27</sup> method, that is, by adding 5% to the values of the optical polarizabilities extrapolated to infinite wavelength.<sup>26</sup> This gives  $\alpha_{01} = 14.7 \text{ Å}^3$  and  $\alpha_{02} = 5.58 \text{ Å}^3$ .

The value chosen for  $ab^2$  was 18.0 Å<sup>3</sup>. This value was obtained by assuming the molecular volume to be the same as that of two sulfur atoms of van der Waals radius 1.85 Å. The mean radius,  $r$ , of such a molecule is 2.32 Å. The value of  $ab^2$  chosen was equal to  $(2.32 + 0.3)^3$ . The addition of 0.3 Å to the radius determined from molecular dimensions has been shown to be reasonable for amino acids.<sup>28</sup> For carbon disulfide this method gives for the cavity used in the model a volume midway between that determined from van der Waals radii and that determined from assuming that the molecules occupy the entire liquid volume. The demagnetizing factor  $A_1$  was determined by calculating  $B$  at 546 nm for various values of  $A_1$  using eq 33 and neglecting hyperpolarizability.<sup>29</sup> Agreement with the experimental value of  $B$  at this wavelength was obtained for  $A_1 = 0.19$ . Only  $A_1$  is independent since  $A_1 + 2A_2 = 1$ . This value corresponds to a spheroid with axial ratio 1.82:1,<sup>20</sup> which is close to the geometric expectation.

Using these values of  $ab^2$  and  $A_1$ , and assuming that the dispersion of  $\alpha_{12}$  may be neglected, the Kerr constant at 272 nm can be calculated for a range of values of  $\alpha_{11}$  using eq 33. Agreement is obtained with the experimental value,  $B = 2.20 \times 10^{-6}$ , for  $\alpha_{11} = 23.3 \text{ Å}^3$ . The change in  $\Delta\alpha_1$  in going from 546 to 272 nm is 7.65 Å<sup>3</sup>. This may be contrasted to the change in  $\Delta\alpha_1$  of 13.2 Å<sup>3</sup> over the same range calculated using the Born-Langevin equation.

A check on the consistency of this result is obtained by calculating the refractive index using the Scholte theory. The expression for refractive index is

$$n^2 - 1 = 4\pi N\overline{\alpha_1^*} \quad (36)$$

Using this equation  $n$  may be calculated at 546 and 272 nm for the values of  $\alpha_{11}$  used above for the Kerr constant. This gives  $n = 1.678$  at 546 nm and  $n = 1.989$  at 272 nm. Since the calculated value at 546 nm is slightly larger than the observed value, the values of the  $\alpha_{11}$ 's used above are sufficiently large. The fact that a smaller value is calculated at 272 nm than is observed indicates that  $\alpha_{12}$  increased over the wavelength range studied. In order to account for the observed index of refraction,  $\alpha_{12}$  must increase by at least 0.6 Å<sup>3</sup> over the range 546–272 nm. This increase is in better agreement with the expected behavior of  $\alpha_{12}$  than is the 1 Å<sup>3</sup> decrease calculated using eq 34 and 35.

The values of  $\Delta\alpha_1$  at 272 nm calculated using eq 33 and 34 can be compared to the value of  $\Delta\alpha_1$  obtained by extrapolation of the results of depolarized Rayleigh scattering<sup>26</sup> to 272 nm, which gives  $\Delta\alpha_1 = 14.5 \text{ Å}^3$ . Use of the nonlinear curve<sup>26</sup> would produce a somewhat larger value of  $\Delta\alpha_1$  in better agreement with the value, 17.8 Å<sup>3</sup>, determined using eq 33 and neglecting hyperpolarizability. It is reasonable to conclude, therefore, that the light scattering data support the use of the extended Klages

theory over the Born-Langevin theory for liquid Kerr data.

## Discussion

The positive sign of the Kerr constant of carbon disulfide at 272 nm reported here is in agreement with the assignment of the first fully allowed absorption in the spectrum of the liquid to a transition polarized parallel to the long axis of the molecule. The rapid increase in  $B$  around 272 nm indicates that the allowed perpendicular transition on the long wavelength side of the first allowed parallel transition found recently in solid samples<sup>30</sup> is not in that position in the liquid. As a perpendicular transition is approached the Kerr constant would be expected to decrease.

Bogaard et al.<sup>31</sup> measured the temperature dependence of the Kerr constant of carbon disulfide vapor, at 632.8 nm, and found that the hyperpolarizability term accounted for approximately 10% of the Kerr effect at room temperature. The agreement obtained in the present work between  $\Delta\alpha_1$  at 272 nm calculated neglecting hyperpolarizability and the  $\Delta\alpha_1$  estimated by extrapolating light scattering data indicates that the relative importance of the hyperpolarizability term to  $B$  does not greatly increase in going from 546 to 272 nm. Further separation of polarizability anisotropy and hyperpolarizability contributions requires the measurement of the oscillator strengths of the nearby absorptions in the liquid. This would allow the dispersion of  $\Delta\alpha_1$  to be calculated independently.

The cause of the larger optical anisotropy,  $\Delta\alpha_1$  at 272 nm calculated with the Born-Langevin theory, is the Lorentz optical local field used in that theory. Even the Onsager-Böttcher local field (which is more suitable for spherical molecules with small polarizability anisotropies than the Lorentz local field) is not appropriate for liquid carbon disulfide.<sup>29</sup> The Scholte local field used in the extended version of Klages' theory increases more rapidly with decreasing wavelength and thus requires a smaller increase in  $\Delta\alpha_1$  to explain the wavelength dependence of the Kerr effect.

## References and Notes

- (1) This investigation was supported in part by Public Health Service Research Grant GM 11683, and by Intramural Research Grants from the Committee on Research, University of California, Riverside.
- (2) Presented in part at the 13th Western Regional Meeting of the American Chemical Society, Anaheim, Calif., Oct 12–14, 1977.
- (3) Based on a thesis submitted by J. W. Lewis in partial fulfillment of the requirements for the Ph.D. Degree, Aug 1977.
- (4) Present address: Chemistry Board of Studies, Natural Sciences II, University of California, Santa Cruz, Calif. 95064.
- (5) A. D. Buckingham, *Proc. R. Soc. London, Ser. A*, **267**, 271 (1962).
- (6) S. H. Lin, C. Y. Lin, and H. Eyring, *J. Phys. Chem.*, **70**, 1756 (1966).
- (7) H. E. McComb, *Phys. Rev.*, **29**, 525 (1909).
- (8) G. Becker, *Ann. Phys.*, (4) **76**, 849 (1925).
- (9) M. Schwob, *C. R. Acad. Sci. (Paris)*, **198**, 2232 (1934).
- (10) G. Szivessy and A. Dierkesmann, *Ann. Phys.*, (5) **3**, 507 (1929).
- (11) G. Bruhat and G. Raoult, *J. Phys. Radium*, **6**, 6 (1945).
- (12) A. D. Walsh, *J. Chem. Soc.*, 202 (1953).
- (13) J. W. Rabalais, J. M. McDonald, V. Scherr, and S. P. McGlynn, *Chem. Rev.*, **71**, 73 (1971).
- (14) T. G. Scholte, *Physica*, **15**, 437 (1949).
- (15) Box 82, Caldwell, N.J. 07006.
- (16) G. Otterbein, *Phys. Z.*, **35**, 257 (1934).
- (17) H. L. Blackwell, *Proc. Am. Acad. Arts Sci.*, **41**, 650 (1906).
- (18) G. Klages, *Naturforsch. A*, **9**, 602 (1954).
- (19) S. Kielich, "Dielectric and Related Molecular Processes", Vol. 1, Chemical Society, London, 1972.
- (20) J. A. Osborn, *Phys. Rev.*, **67**, 351 (1945).
- (21) W. F. Brown, Jr., "Handbuch der Physik", Vol. 17, Springer-Verlag, Berlin, 1956, p. 1.
- (22) A. D. Buckingham and J. A. Pople, *Proc. Phys. Soc., Ser. A*, **68**, 905 (1955).
- (23) P. Langevin, *C. R. Acad. Sci. (Paris)*, **151**, 475 (1910).
- (24) M. Born, *Ann. Phys.*, **55**, 177 (1918).
- (25) G. Bruhat and M. Pauthenier, *J. Phys. (Paris)*, **6**, 287 (1925).
- (26) G. R. Alms, A. K. Burnham, and W. H. Flygare, *J. Chem. Phys.*, **63**, 3321 (1975).

- (27) R. Gans, *Z. Phys.*, **17**, 353 (1923).  
 (28) W. H. Orttung and J. A. Meyer, *J. Phys. Chem.*, **67**, 1911 (1963).  
 (29) J. W. Lewis, "The Kerr Effect of Organic Liquids in the Ultraviolet", Ph.D. Dissertation, University of California, Riverside, Aug 1977.  
 (30) K. M. Monahan, R. L. Russell, and W. C. Walker, *J. Chem. Phys.*, **65**, 2112 (1976).  
 (31) M. P. Bogaard, A. D. Buckingham, and G. L. D. Ritchie, *Mol. Phys.*, **18**, 575 (1970).

## Absolute Quantum Yield Determination by Thermal Blooming. Fluorescein

James H. Brannon and Douglas Magde\*

Department of Chemistry, University of California, San Diego, La Jolla, California 92093 (Received August 5, 1977; Revised Manuscript Received October 27, 1977)

Publication costs assisted by the Petroleum Research Fund

We report a refinement of the thermal blooming method which makes possible simple and precise measurements of absolute luminescence quantum yields for dilute liquid solutions. Our technique, which compares an unknown to a nonluminescent reference, offers advantages over conventional photometric measurements by requiring a minimum of calibration and being immune to most systematic errors. It appears to be much simpler and more versatile than other calorimetric schemes. We measured the absolute quantum yield of the fluorescence standard sodium fluorescein in 0.1 N aqueous sodium hydroxide at concentrations below  $10^{-6}$  mol  $\text{dm}^{-3}$ . The yield was  $0.95 \pm 0.03$ . Thermal blooming seems to be a powerful and widely applicable technique well suited to the determination of new luminescence standards.

### I. Introduction

A thermal blooming measurement is, in essence, a calorimetric determination of the very small temperature gradients induced by the absorption of light energy. The technique can be extremely sensitive and allows one to measure exceptionally weak absorption.<sup>1-3</sup>

Hu and Whinnery,<sup>1</sup> in their landmark contribution, pointed out a second application. They suggested that when combined with conventional transmission data, a thermal blooming measurement permits calculation of a luminescence quantum yield. They reported success in demonstrating the method, but presented no details. Nor has any quantitative test appeared since. We will argue here that the thermal blooming method is not merely an alternative approach for measuring luminescence quantum yields, but rather one which offers very significant advantages.

Conventional luminescence yield measurements involve two steps.<sup>4</sup> First, a luminescence standard must be measured. This is so difficult<sup>4,5</sup> that it has been attempted only a few times. Values from different laboratories have not infrequently disagreed. At present, only quinine sulfate and, perhaps, fluorescein, at specified standard conditions, have been characterized to a precision of 5%. Second, a particular measurement requires comparison of an unknown with a standard. Careful attention must be given to corrections for differences in solvent, temperature, wavelength response of monochromators and detectors, polarization effects, and so on. Such a comparison should be possible to within 5% precision. Random scatter in the data is the least of the problems; what is more serious is the uncertainty of systematic effects when the sample differs considerably from the standard.

We believe that the thermal blooming technique can significantly reduce the uncertainties in both parts of the quantum yield "problem". We have found, in addition, that it is simple to carry out and, in some cases, inexpensive as well.

As a demonstration of the thermal blooming approach, we report here our measurement of the absolute

fluorescence yield of the present standard sodium fluorescein. At concentrations below  $10^{-6}$  mol  $\text{dm}^{-3}$ , in the usual buffer, 0.1 N sodium hydroxide, we find  $\phi_f = 0.95 \pm 0.03$ .

We discuss briefly the features of the thermal blooming method which make it an attractive choice for absolute luminescence yield determinations and suggest that it would be particularly useful in generating a new standard in the red portion of the spectrum.

### II. Principle of the Measurement

The essential idea is very simple. The energy (power) conservation involved is illustrated in Figure 1. The laser power incident on any sample  $P_L$  must be equal to the sum of the power transmitted  $P_t$  plus the power emitted as luminescence  $P_f$  plus the power degraded to heat  $P_{th}$ :

$$P_L = P_t + P_f + P_{th} \quad (1)$$

We assume that reflection and scattering losses are correctly accounted for as usual.

An ordinary transmission measurement determines the ratio

$$T = P_t/P_L \quad (2a)$$

We define the fractional absorption

$$A = 1 - T \quad (2b)$$

Then, we may write

$$P_f = AP_L - P_{th} \quad (2c)$$

The emission quantum yield is by definition

$$\phi_f = \frac{P_f/\langle\nu_f\rangle}{(P_L - P_t)/\nu_L} \quad (3)$$

Here,  $\nu_L$  is the laser frequency and  $\langle\nu_f\rangle$  is the mean luminescence emission frequency, evaluated as

$$\langle\nu_f\rangle = \int \nu_f dn(\nu_f) / \int dn(\nu_f) \quad (4)$$

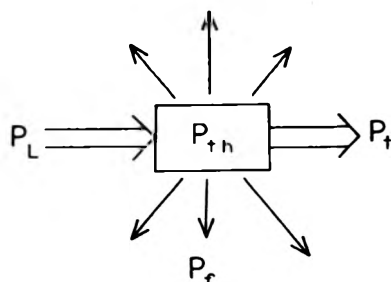


Figure 1. Power conservation for luminescence:  $P_L$ , incident excitation laser power;  $P_t$ , transmitted power;  $P_f$ , fluorescence or phosphorescence emission power;  $P_h$ , thermal power deposited as heat.

The quantity  $dn(\nu_f)$  in photons  $s^{-1}$  is the number of photons emitted in an incremental bandwidth centered at  $\nu_f$ . We may rewrite (3) in the form

$$\phi_f = \frac{\nu_L}{\langle \nu_f \rangle} \left[ 1 - \frac{P_{th}}{AP_L} \right] \quad (5)$$

The ratio  $\nu_L/\langle \nu_f \rangle$  takes account of the Stokes shift, which entails some deposition of heat in the sample even for a 100% luminescence quantum yield. The absorption  $A$  may be measured with an ordinary spectrophotometer. The thermal blooming technique<sup>1</sup> offers a novel means of measuring  $P_{th}$ .

One arrangement for the thermal blooming measurements is shown in Figure 2. A laser beam of appropriate frequency to excite the luminescence is brought to a focus with a lens and then allowed to expand. The sample is located one Rayleigh length past the focal plane. Recall that the Rayleigh length  $Z_R$  is a measure of the depth of focus. It is given by  $Z_R = \pi w_0^2/\lambda_L$  where  $\lambda_L$  is the laser wavelength and  $w_0$  is the characteristic parameter of the intensity distribution in the focal plane, which for a TEM<sub>00</sub> Gaussian beam is proportional to  $\exp[-2r^2/w_0^2]$ , where  $r$  is the radial distance from the axis of the beam.

Heat generated in the region of the absorption increases the local temperature, modifies the refractive index, and induces what is, in fact, an optical lens. For most liquids it is a negative lens. A measurement is performed by opening rapidly a shutter located at the focal plane. The thermal lens develops over a period of a few tenths of second. During that time, the laser beam may be observed as a spot on a plane located a few meters past the sample. The spot "blooms" or increases in size. It is not actually necessary to measure the size of the spot; a tiny photodiode detector positioned carefully at the center of the spot produces a photocurrent which is proportional to the laser intensity on axis and thus inversely proportional to the beam area. As the area blooms, the photocurrent diminishes according to the expression<sup>1</sup>

$$I(t) = I_0 [1 - \theta(1 + t_c/2t)^{-1} + 1/2\theta^2(1 + t_c/2t)^{-2}]^{-1} \quad (6)$$

Here  $\theta$  is directly proportional to  $P_{th}$

$$\theta = P_{th}(dn/dT)/\lambda_L k \quad (7)$$

where  $(dn/dT)$  is the temperature dependence of the refractive index and  $k$  is the thermal conductivity. The parameter  $t_c$  is a characteristic time for thermal diffusion.

This time dependent photosignal (6) may be displayed on an oscilloscope. A typical example is shown in Figure 3. The important parameter  $\theta$  can be obtained by detailed curve fitting, by examining the initial slope, or by measuring the initial photocurrent before the lens develops  $I_0$  and the final photocurrent at long times  $I_\infty$ . The last

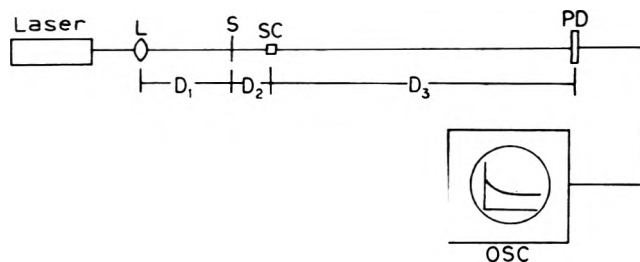


Figure 2. Experimental configuration for a thermal blooming experiment: L, lens; S, shutter; SC, sample cell; PD, photodiode detector; OSC, oscilloscope;  $D_1$ , focal length;  $D_2$ , Rayleigh length;  $D_3$ , arbitrary but large.

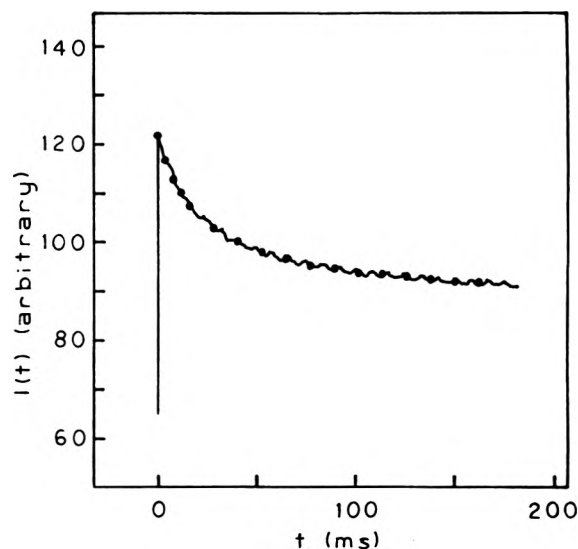


Figure 3. Typical photocurrent signal for thermal blooming. The continuous line is experimental. At  $t = 0$ , a shutter is opened and the photocurrent increases instantly to a maximum and then falls. The filled circles are individual points on a theoretical curve which obeys (6) with parameter values  $I_0 = 121.8$ ;  $t_c = 56.8$  ms;  $\theta = -0.337$ .

method is most practical for manual computation. One calculates

$$I = (I_0 - I_\infty)/I_\infty \quad (8a)$$

and obtains  $\theta$  as

$$\theta = 1 - (1 + 2I)^{1/2} \quad (8b)$$

Note that according to (7),  $\theta$  will be negative for most liquids.

Almost as convenient is an examination of the initial slope of  $I(t)$ . For small  $t$ , we expand (6) to generate

$$I(t) = I_0 [1 + 2\theta t/t_c + (2\theta^2 - 4\theta)(t/t_c)^2 + O(t^4)] \quad (9)$$

The initial slope  $m$  is

$$m = 2\theta/I_0 t_c \quad (10)$$

For the dilute solutions used in quantum yield determinations, one assumes that the thermo-optic properties are solely determined by the solvent, while the optical properties are dominated by the solute. Consequently, one might measure  $\theta$  as just described and evaluate  $P_{th}$  according to (7) using tabulated data for the solvent. Then  $P_{th}$  may be used in (5) to obtain the quantum yield. This apparently was the approach chosen by Hu and Whinery.<sup>1</sup> We verified that such a procedure "works" for the present study. However, the precision with which we know thermo-optic coefficients is inadequate for careful measurements. Furthermore, the direct approach places a very strong burden on the experiment to match the many assumptions involved in deriving (6), (7), and (8). Con-

sequently, we have developed a comparison method.

In addition to measuring the sample, now designated by a superscript *s*, we measure in the same solvent a nonluminescent reference compound, denoted *r*. It is not necessary for the reference to be *strictly* nonfluorescent. A quantum yield below, e.g., 0.5% is adequate. This can be verified *a posteriori*. For the reference, we have therefore

$$AP_L^r = P_{th}^r \quad (11)$$

We multiply by unity in (5) to obtain

$$\phi_f = \frac{\nu_L}{\langle \nu_f \rangle} \left[ 1 - \frac{A^r P_L^r P_{th}^s}{A^s P_L^s P_{th}^r} \right] \quad (12)$$

Since the same solvent is used for sample and reference, as well as the same excitation wavelength, we can express  $P_{th}$  in terms of  $\theta$  to obtain

$$\phi_f = \frac{\nu_L}{\langle \nu_f \rangle} \left[ 1 - \frac{A^r P_L^r}{A^s P_L^s} \frac{\theta^s}{\theta^r} \right] \quad (13)$$

Now we require only that the experiment be able to measure the ratio  $\theta^s/\theta^r$ .

If only the initial slope  $m$  is measured,  $\theta$  will be inaccessible because  $t_c$  remains unknown. Even so, if the geometry is identical for sample and reference  $t_c$  will be the same for sample and reference and an alternate expression for  $\phi_f$  is convenient:

$$\phi_f = \frac{\nu_L}{\langle \nu_f \rangle} \left[ 1 - \frac{A^r P_L^r}{A^s P_L^s} \frac{m^s}{m^r} \right] \quad (14)$$

One important precaution is required. Although the solute will usually dominate, dilute solutions in some solvents may require a blank correction. Since  $P_{th}$  is additive, we have for both sample and reference

$$\theta = \theta(\text{solution}) - \theta(\text{solvent}) \quad (15)$$

The thermal blooming measurement in the configuration just described presupposes<sup>1</sup> that five conditions are satisfied: (1) The excitation beam must have a TEM<sub>00</sub> Gaussian profile for its transverse mode structure. (2) The absorbed power must be low enough to avoid spherical aberrations and convection currents. The upper limit to avoid aberrations is<sup>1</sup>

$$P_{th} < 2.2\lambda_L k / (dn/dT) \text{ or } \theta < 2.2 \quad (16)$$

where I have retained a factor of  $2^{1/2}$  which was dropped previously.<sup>1</sup> The upper limit to avoid convection has an inverse cubic dependence on the vertical dimension of the heated region. For focused beams, with submillimeter dimensions, convection will not be a problem if (16) is satisfied. For larger beams it would have to be considered. (3) The cell should be accurately positioned at one Rayleigh length past the focal plane and be short enough so that the beam has a constant area throughout the cell. (4) The cell must be long compared to the beam radius so that end effects on thermal diffusion may be neglected.<sup>6</sup> (5) The detector must be small, far from the sample, and accurately centered so that it measures the intensity at the center of the expanding laser beam in the far field limit.

These conditions are easily met. The comparison method introduced here is less sensitive to the assumptions than are direct calculations which use (7). In a variety of preliminary tests, we found it difficult to violate these conditions sufficiently to introduce bias into the mea-

surements. However, we suspect that if the present ~5% precision is to be reduced to <1%, these conditions will require additional scrutiny.

### III. Experimental Section

Sodium fluorescein was obtained from Aldrich Chemical Co. and purified by the method of Orndorff and Hemmer<sup>7</sup> as recommended by Demas and Crosby.<sup>4</sup> Its peak absorptivity, absorption spectrum, and emission spectrum were similar to those reported recently by Heller and co-workers.<sup>5</sup> From the latter's spectrum, we calculate a mean emission frequency  $\langle \nu_f \rangle = 18.83 \text{ kKaysers} = (531.3 \text{ nm})^{-1}$ . (In more detail, our corrected emission spectrum peaked closer to that of Crosby as quoted by Heller,<sup>5</sup> but is shaped more like that of Heller,<sup>5</sup> with somewhat less intensity in the red tail than either. These minor differences do not affect our final result here. What is most significant is the close agreement of all three independent results.) The solvent was 0.1 N sodium hydroxide. Solutions were freshly prepared and were not degassed. The temperature was 22 °C.

The reference absorber was the dye basic fuchsin used as received from Eastman. The solvent was deionized water.

The laser was a Spectra Physics Model 166 argon ion laser operating at 496.5 nm attenuated to about 100 mW. We verified that the profile was predominately TEM<sub>00</sub>. The lens had a focal length of 500 mm. The sample cell was located about 600 mm from the lens. The exact position was optimized by seeking the location which maximized the thermal blooming effect. This has been shown<sup>1</sup> to occur at the Rayleigh distance past the focus. The detector was a silicon photodiode (RCA C30808) located 2.5 m past the sample, at which distance the laser beam had expanded to a diameter of several centimeters. The output current was dropped across a load resistor of 10 kΩ and dc coupled to a Biomation 805 transient recorder. The output of this digital recorder was displayed on a Houston Omniscribe chart recorder. Both instruments have a linearity of 0.25%.

The photometric absorption measurements were made with a Beckman ACTA spectrophotometer. Solutions were contained in 1-cm fused silica cells and the same cells were used for both photometric and thermal blooming measurements.

We have carried out a large variety of tests on these solutions as well as on other fluorescent molecules, other nonluminescent references, and other solvents than water. We have used lenses with focal lengths from 150 to 1000 mm, sample cell lengths varying from 1 to 50 mm, concentrations varying by a factor of 200 for a given absorber, and a wide range of laser power levels. Systematic effects have remained elusive. Consequently, we conclude that by choosing conditions conservatively consistent with the general assumptions of the method, as outlined briefly above and detailed more fully elsewhere,<sup>1</sup> and by utilizing our comparison method, systematic errors should be smaller than random errors. Random errors stem from several sources. The total laser output may fluctuate over periods of milliseconds by a fraction of a percent. The direction of the laser beam propagation may be unstable so that the beam shifts relative to the detector. Defects in cell windows may lead to incorrect  $I_0$  values or may modulate  $I(t)$  if vibration is present. And so on. If  $I(t)$  is uncertain by even 1%, then  $\theta$  will be uncertain by typically several percent (proportional to  $\theta^{-1}$  for small  $\theta$ ), whether  $\theta$  is determined from (8) or from the initial slope of  $I(t)$ . This implies that fewer than a dozen repetitions may suffice to reach a 5–10% precision with 95% confi-

TABLE I: Thermal Blooming Data for Fluorescein

Molecule	Concn, mol dm <sup>-3</sup>	Absorption, A	Slope, <i>m</i> (arbitrary)
Fluorescein	5.34 × 10 <sup>-6</sup>	0.63	4.9 ± 1
Fluorescein	2.60 × 10 <sup>-6</sup>	0.38	5.0 ± 0.5
Basic fuchsin		0.25	43.6 ± 5
Basic fuchsin		0.102	46.5 ± 3

dence, but that improvement to the 1–2% level would benefit from automated signal averaging.

Water, because of its large thermal conductivity and small  $dn/dT$ , is among the “least sensitive” solvents for thermal blooming. In fact,  $P_{th}$  must be from 10 to 30 times larger than in typical organic solvents to induce the same  $\theta$ . Using values from the International Critical Tables,<sup>8</sup> ( $dn/dT = 5.3 \times 10^{-6} \text{ K}^{-1}$ ,  $k = 5.9 \times 10^{-3} \text{ W cm}^{-1} \text{ K}^{-1}$ , in (7), we find  $\theta = 18P_{th}$  where  $P_{th}$  is in watts. Similarly, the aberration limit in (15) becomes  $P_{th} < 0.12 \text{ W}$ . While  $\theta$  need not be as large as unity, measurement precision improves if it can be kept larger than, e.g., one-tenth. At such high power levels, we observed a dark photodecomposition product for the sodium fluorescein solutions after irradiation of several tens of seconds. We chose, therefore, to employ an initial slope analysis and opened the shutter only for 1–2 s at intervals of about 4 min. Since the initial change should also be free from optical aberration effects which accumulate only as the phase retardation becomes too large, we concentrated on rather strongly absorbing solutions, for which  $A$  could be measured directly and precisely and for which a large change in  $I(t)$  occurs during the initial linear period.

#### IV. Results

In Table I are the data for the thermal blooming measurements on fluorescein and the reference at two different concentrations each. Error estimates are 95% confidence limits assuming Student's *t* distribution for four to six recorded traces for each condition. The laser was operated with feedback control to keep the output constant, so we have  $P_L^r = P_L^s$ .

Using these data in (14), together with the Stokes factor 1.07 calculated from parameters discussed above, we find  $\phi_f = 0.95 \pm 0.03$ .

Finally, we measured the relative yield for the reference absorber, fuchsin, using the currently preferred<sup>4</sup> “optically dilute” method with fluorescein as the standard. We found that the quantum yield was safely below 1%. Since the basic fuchsin was of indeterminate purity, no quantitative value was assigned.

#### V. Discussion

Sodium fluorescein is probably the second best characterized luminescence standard after quinine sulfate. Methods for purification and conditions for reproducibility of the yield have been documented<sup>4,5</sup> and were employed in the present study. When the procedures are followed, the yield is not very sensitive to small variations in such parameters as temperature, concentration, or oxygen tension. Significant overlap of the absorption and emission spectra which can lead to reabsorption–reemission problems is the major concern. It is considered<sup>4,5</sup> good practice, when using standard methods, to keep the concentration below  $10^{-6} \text{ mol dm}^{-3}$  even though the intrinsic yield does not vary until much higher concentrations are reached.<sup>9</sup> Thermal blooming is much less restricted in this regard, since it is only necessary that luminescence escape from a region of submillimeter dimension. No harm occurs if absorption takes place elsewhere in the solutions. Even so, our thermal blooming

data refer to concentrations only a few times  $10^{-6} \text{ mol dm}^{-3}$ . Our result, therefore, is to be compared directly with conventional values for  $\phi_f$ .

Demas and Crosby<sup>4</sup> critically reviewed the literature and suggested that  $\phi_f = 0.90$  for fluorescein should be adopted as a compromise interim value, which should be “accurate within 10% and probably within 5%”. Our result agrees with this. It agrees even better with those values they regarded as most reliable, which were near 0.92 and 0.93. More recently, Heller and co-workers<sup>5</sup> found values ranging from 0.91 to 0.94, under various conditions of purification and excitation, relative to the standard quinine sulfate taken to have  $\phi_f = 0.55$  in 1 N H<sub>2</sub>SO<sub>4</sub>. This latter number, in turn, is considered<sup>4</sup> secure to within  $\pm 0.03$ . However two recent redeterminations suggest that this number might, in fact, be about 2% low. Adams and co-workers<sup>10</sup> used a photoacoustic method. (Their values are for 0.1 N H<sub>2</sub>SO<sub>4</sub> as solvent and must be corrected<sup>4,5</sup> before comparison with 1 N data.) Gelernt and co-workers<sup>11</sup> used refined conventional calorimetry. This small change would bring Heller's relative value into coincidence with our absolute determination. This entire discussion involves refinements within the claimed error limits of each individual measurement, which have never been less than 5% of absolute value. For a primary standard no one has really improved on Melhuish's now classic contribution.<sup>12</sup> It is necessary to add, furthermore, that Ware and Rothman<sup>13</sup> recently carried our precision relative measurements, which on the internal evidence appear as reliable as any, which lead to a quantum yield greater than unity for diphenylanthracene in cyclohexane unless the value for the quinine standard is reduced slightly below 0.55. (Again the discrepancy does not exceed expected errors.) On the present balance of evidence, however, it appears that the quantum yield for purified fluorescein at standard conditions is more likely to lie between 0.90 and 0.95 than in the range 0.90–0.85.

This review of the fluorescein question reveals that what slow progress is being made in refining luminescence yield standards comes from statistical averaging over independent determinations. There has been little progress in basic methodology in two decades, although now correct procedure is better documented and instruments are more convenient and widespread. We believe that the thermal blooming offers excellent prospects for significant reduction in the experimental uncertainty with which selected standards are measured.

The conventional approach for absolute yield determinations, which we take to be the substitution method using some well characterized scatterer, is most susceptible to the criticism that it has a long history and new breakthroughs are unlikely. It is not only tedious to carry out fully all the calibrations, but just as important it is difficult and tedious to document. Even if exceptionally accurate measurements were made, they might prove difficult to recognize.

Calorimetric methods have always been popular in principle,<sup>14,15</sup> but have not produced superior precision in practice. Perhaps few photophysical laboratories have wished to face also the challenges of precision calorimetry by conventional methods. It is premature to speculate on the ultimate prospects for photoacoustic methods.

An approach<sup>16</sup> grounded in chemical actinometry appears capable of high precision, but has not yet been fully implemented. It does require assumptions about the actinometer, for example with regard to its constancy over wavelength, which are plausible but perhaps hard to prove to accuracies approaching or below 1%.

In contrast, we see no reason why the thermal blooming approach should not be capable of refinement to better than the 1% level for highly luminescent molecules. The preferred procedure, we suggest, will be to use the thermal blooming in a comparison mode and adjust concentrations so that  $P_{th}^s = P_{th}^r$ . This reduces the importance of systematic errors and makes the measurement less dependent on assumptions in the theory of lens formation. The laser may be stabilized to keep  $P_L^s = P_L^r$ . The method lends itself to statistical averaging with each repetition taking about 1 min. The absorption measurements  $A^s$  and  $A^r$  can be made to better than 1% with care. Ultimately, the limiting factor should be Stokes' correction. This makes the absolute determination at least as accurate as the best relative determinations.

All calorimetric methods become useless at low yields. Even at  $\phi_f = 0.25$ , a good relative or substitution measurement will be preferred. Relative methods, however, are most accurate when the solvent, wavelength, temperature, and so on of unknown and standard are similar. It may be reasonable to generate standards "to order", to measure a highly luminescent sample by the thermal blooming method and then to make an immediate comparison with the unknown of current interest. In any case, it would be most desirable to enlarge the present catalog of standards. Thermal blooming would be particularly useful in generating a red or near-infrared standard. Several candidates exist which have molar absorptivities exceeding  $10^4$  at helium, neon, or krypton wavelengths. Methylene blue has been proposed more than once.<sup>4,17</sup> We have confirmed Oster's<sup>18</sup> measurement of a low yield, ~1%, which renders it unsuitable for checking by any calorimetric method. We think it is a poor candidate. Chloroaluminum phthalocyanine has a very high yield, comparable to fluorescein, and is quite stable, but has solubility problems. An oxazine dye, such as cresyl violet or Nile blue, will have a yield greater than 50% (Drexhage<sup>19</sup> gives 70% without detail) and has only the drawbacks characteristic of all dyes, spectral overlap and possible purification troubles. Inorganic complexes of ruthenium, osmium, and iridium have been warmly endorsed<sup>14</sup> but no species has yet emerged which is sufficiently luminescent in the red for calorimetric calibration.<sup>20</sup>

If less than optimal precision will suffice, thermal blooming is inexpensive to implement, as long as an appropriate laser is available. An ordinary oscilloscope, a spectacle lens, and a simple silicon photodiode are all that is needed. The need for an appropriate laser wavelength for excitation is restrictive. However in the visible region

there are enough common lines to match the broadband absorbers considered here. Except for the "difficult" solvent water, only about 1 mW of power is needed.

## VI. Conclusion

We have described the procedure for a new approach to the determination of absolute luminescence quantum yields. We have measured  $\phi_f = 0.95 \pm 0.03$  for sodium fluorescein. This is an absolute measurement, independent of any previous quantum yield determination. We believe that the method will permit precision measurement of select standards and the generation of new standards which are more accurate and, equally important, more reliably documented. The result for fluorescein given here compares already with the present state of the art and does not reflect fully the best reproducibility we have achieved.

Efforts to generate a red standard are in progress. The fluorescein value can be improved further. However also desirable will be tests on some other of the current primary or secondary standards.

*Acknowledgment.* We thank Professor S. Lee and Mr. B. Bartholomew for the loan of the argon laser. The work was supported by the donors of the Petroleum Research Fund, administered by the American Chemical Society.

## References and Notes

- (1) C. Hu and J. R. Whinnery, *Appl. Opt.*, **12**, 72 (1973).
- (2) M. E. Long, R. L. Swofford, and A. C. Albrecht, *Science*, **191**, 183 (1976).
- (3) A. J. Twarowski and D. S. Kilger, *Chem. Phys.*, **20**, 259 (1977).
- (4) J. N. Demas and G. A. Crosby, *J. Phys. Chem.*, **75**, 991 (1971).
- (5) C. A. Heller, R. A. Henry, B. A. McLaughlin, and D. E. Bliss, *J. Chem. Eng. Data*, **19**, 214 (1974).
- (6) F. W. Dabby, R. W. Boyko, C. V. Shank, and J. R. Whinnery, *IEEE J. Quantum Electron.*, **QE-5**, 516 (1969).
- (7) W. R. Orndorff and A. J. Hemmer, *J. Am. Chem. Soc.*, **49**, 1271 (1927).
- (8) National Research Council (USA), "International Critical Tables" McGraw-Hill, New York, N.Y., 1926.
- (9) A. Budo, J. Dombi, and L. Szollosy, *Acta, Univ. Szeged., Acta Phys. Chem.*, **2**, 18 (1956).
- (10) M. J. Adams, J. G. Highfield, and G. F. Kirkbright, *Anal. Chem.*, **49**, 1850 (1977).
- (11) B. Gelernt, A. Findeisen, A. Stein, and J. A. Poole, *J. Chem. Soc., Faraday Trans. 2*, **70**, 939 (1974).
- (12) W. H. Melhuish, *J. Phys. Chem.*, **65**, 229 (1961).
- (13) W. R. Ware and W. Rothman, *Chem. Phys. Lett.*, **39**, 449 (1976).
- (14) G. A. Crosby, J. N. Demas, and J. B. Callis, *J. Res. Natl. Bur. Stand., Sect. A*, **76**, 561 (1972).
- (15) J. B. Callis, *J. Res. Natl. Bur. Stand., Sect. A*, **80**, 413 (1976).
- (16) J. N. Demas and B. H. Blumenthal, *J. Res. Natl. Bur. Stand., Sect. A*, **80**, 409 (1976).
- (17) W. H. Melhuish, *J. Res. Natl. Bur. Stand., Sect. A*, **76**, 547 (1972).
- (18) N. Wotherspoon and G. Oster, *J. Am. Chem. Soc.*, **79**, 3992 (1957).
- (19) K. H. Drexhage, *Laser Focus*, **9**, No. 3, 35 (March, 1973).
- (20) J. N. Demas, personnel communication.

# Phosphate Radicals. Spectra, Acid-Base Equilibria, and Reactions with Inorganic Compounds<sup>1</sup>

P. Maruthamuthu and P. Neta\*

Radiation Laboratory, University of Notre Dame, Notre Dame, Indiana 46556 (Received October 3, 1977)

Publication costs assisted by the Division of Basic Energy Sciences, U.S. Department of Energy

The phosphate radicals were produced by the reaction of  $e_{aq}^-$  with peroxodiphosphate ions and their spectra and acid-base equilibria were determined:  $H_2\dot{P}O_4$  ( $\lambda_{max}$  520 nm,  $\epsilon_{max}$  1850 M<sup>-1</sup> cm<sup>-1</sup>)  $\xrightleftharpoons{(pK_1, 5.7)}$   $HP\dot{O}_4$  ( $\lambda_{max}$  510 nm,  $\epsilon_{max}$  1550 M<sup>-1</sup> cm<sup>-1</sup>)  $\xrightleftharpoons{(pK_2, 8.9)}$   $P\dot{O}_4^{2-}$  ( $\lambda_{max}$  530 nm,  $\epsilon_{max}$  2150 M<sup>-1</sup> cm<sup>-1</sup>). The reaction of OH with phosphate ions was also examined and discrepancies in the literature are discussed. The rate constants for the reactions of the acid-base forms of the phosphate radical, as well as those of the sulfate radical, with several inorganic compounds were determined. These reactions involve either hydrogen abstraction or one-electron oxidation. The radicals formed by H abstraction from  $H_2O_2$ ,  $HPO_3^{2-}$ , and  $H_2PO_2^-$  can reduce peroxodisulfate and peroxodiphosphate efficiently and thus propagate a chain reaction. The rate constants for the abstraction reactions are similar for  $S\dot{O}_4^-$  and  $H_2\dot{P}O_4$  but slower for  $HP\dot{O}_4^-$  and  $P\dot{O}_4^{2-}$ . The rate constants for oxidation differ considerably for the different radicals and substrates. From these rates it is concluded that the oxidation capabilities decrease in the order  $S\dot{O}_4^- > H_2\dot{P}O_4 > HP\dot{O}_4^- > P\dot{O}_4^{2-}$ .

## Introduction

The reactions of sulfate ( $S\dot{O}_4^-$ ) and phosphate ( $H_2\dot{P}O_4$ ,  $HP\dot{O}_4^-$ ,  $P\dot{O}_4^{2-}$ ) radicals with organic compounds in aqueous solutions have been recently studied by various techniques. Spectrophotometric pulse radiolysis experiments were used to measure the rate constants for these reactions<sup>2-12</sup> while ESR spectroscopy was used to identify many of the radicals produced by these reactions.<sup>10-16</sup> Differences between the reactivities of the various radicals were noticed and were found to cause changes in the mode of reactions with certain compounds, for example, when hydrogen abstraction and one-electron oxidation are competing processes (compare, e.g., ref 12 and 16). In the present study the reactions of sulfate and phosphate radicals with inorganic compounds were examined in order to compare their relative oxidizing capabilities. In general, two types of reaction were found to take place, i.e., hydrogen abstraction and electron transfer. The differences observed among the electron transfer rate constants suggest that the oxidizing capabilities decrease in the order  $S\dot{O}_4^-$ ,  $H_2\dot{P}O_4$ ,  $HP\dot{O}_4^-$ ,  $P\dot{O}_4^{2-}$ . A comparison of these radicals with OH led to reexamination of the reaction of OH with phosphate ions and of the spectra and dissociation constants of the phosphate radical.

## Experimental Section

The formation of the sulfate and phosphate radicals from the corresponding peroxy dianions in irradiated aqueous solutions and the determination of their rate constants by spectrophotometric pulse radiolysis were described previously.<sup>9</sup>

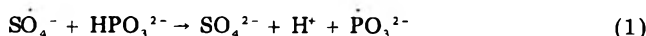
Peroxodiphosphate was prepared electrochemically and purified by the method described previously.<sup>17</sup> Peroxodisulfate was obtained from Sigma Chemical Co. as a sodium salt. Most inorganic compounds used were Baker Analyzed Reagents, except hydrazine and hydroxylamine which were from Fisher and sodium hypophosphite from Heico.

All details of the experiments were similar to those used in our previous work.<sup>9</sup>

## Results and Discussion

*Hydrogen Abstraction by Sulfate and Phosphate Radicals.* The sulfate and phosphate radicals can react

with inorganic compounds either by an electron transfer oxidation or by hydrogen abstraction. Abstraction can occur from N-H or P-H bonds as observed, for example, with  $NH_2OH$ ,  $N_2H_4$ ,  $H_2PO_2^-$ , and  $HPO_3^{2-}$ . The reaction can be described, e.g., by



The radicals resulting from the above mentioned and several other compounds were directly observed by ESR.<sup>12,16</sup> Some of these radicals may reduce peroxodisulfate and peroxodiphosphate ions, e.g.



and thus propagate a chain reaction, similar to that observed with certain alcohols.<sup>9,18</sup> This mechanism was tested for several inorganic compounds by measuring the *G* values for decomposition of peroxodisulfate and peroxodiphosphate. The results are summarized in Table I.

It is seen from Table I that both peroxy dianions studied develop chain reaction with  $HPO_3^{2-}$ ,  $H_2PO_2^-$ , and  $H_2O_2$ , but not with  $NH_2OH$  or  $SO_3^{2-}$ . Apparently  $NH_2\dot{O}$  and  $SO_3^-$  radicals do not reduce the peroxy dianions efficiently. The length of the chain is influenced more strongly by the concentration of the peroxy dianion than by that of the other solute. This finding indicates that the reduction of the peroxy dianion such as reaction 2 has a lower rate constant than the other step involved in the propagation. A similar conclusion was previously drawn from experiments with organic substrates.<sup>9</sup>

The length of the chain reaction involving peroxodiphosphate is strongly dependent upon the pH of the solution. When the pH increases  $H_2P_2O_8^{2-}$  dissociates into  $HP_2O_8^{3-}$  and then  $P_2O_8^{4-}$ . Reduction of these anions becomes more difficult as the charge increases<sup>18</sup> and, therefore, propagation step 2 becomes less efficient and the *G* value decreases sharply. Another effect of pH on reaction 2 can be caused by acid-base equilibria of the reducing radical, such as  $\dot{P}O_3H \rightleftharpoons \dot{P}O_3^{2-}$  for which  $pK = 5.9$  was determined.<sup>12</sup> This equilibrium must be the main cause of the decrease in the chain reaction with peroxodisulfate. This decrease, however, is found to be much less pronounced than that observed in the peroxodiphosphate system. The reaction of  $S\dot{O}_4^-$  with  $OH^-$  at high pH<sup>7,12</sup> should not affect the chain length because the OH radical



TABLE I: Radiolytic Decomposition of Peroxodisulfate and Peroxodiphosphate in the Presence of Inorganic Additives

Additive	[Additive], M	[PDP or PDS], M	pH	G(-PDS)	G(-PDP)	
H <sub>2</sub> PO <sub>4</sub> <sup>-</sup>	0.005	0.01	3.0	33	74	
	0.01	0.01	3.0	55	87	
	0.03	0.01	3.0	55	87	
	0.10	0.01	3.0	63	90	
	0.30	0.01	3.0	110	210	
	0.01	0.015	3.0	69	115	
HPO <sub>4</sub> <sup>2-</sup>	0.01	0.01	6.5	44	25	
	0.01	0.01	9.0	36	6.1	
	0.01	0.01	10.6	37	7.3	
	0.01	0.01	11.3		5.4	
H <sub>2</sub> PO <sub>3</sub> <sup>-</sup>	0.005	0.01	3.0	74	52	
	0.01	0.01	3.0	110	71	
	0.03	0.01	3.0	110	75	
	0.15	0.01	3.0	129	93	
	0.3	0.01	3.0	159	189	
	0.005	0.015	3.0		91	
	0.005	0.02	3.0		132	
	0.01	0.015	3.0	210		
	0.01	0.01	6.5	82	8.0	
	0.01	0.01	9.0	71	3.0	
	0.01	0.01	10.6	69	2.9	
	H <sub>2</sub> O <sub>2</sub>	0.001	0.02	3.0	36	44
		0.002	0.02	3.0	41	50
0.003		0.02	3.0	47	56	
0.001		0.02	6.5	33	18	
0.003		0.02	6.5	46	21	
0.001		0.02	9.0	30	12	
*NH <sub>2</sub> OH	0.001	0.02	10.4	29	12	
	0.02	0.01	3.0	3.1	4.4	
	NH <sub>2</sub> OH	0.02	0.01	7.1	3.0	5.1
	SO <sub>3</sub> <sup>2-</sup>	0.0005	0.015	3.0	4.3	3.1
	0.0005	0.015	6.5	4.2	3.0	
	0.0005	0.015	9.0	4.2	3.4	

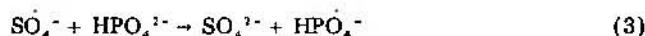
produced will react with the inorganic compound in the same manner as SO<sub>4</sub><sup>-</sup>.

The rate constants for the reactions of sulfate and phosphate radicals with various inorganic compounds are

summarized in Table II along with the rates determined previously for OH radical reactions. For compounds which may undergo hydrogen abstraction (top portion of Table II) the rate constants of SO<sub>4</sub><sup>-</sup> and H<sub>2</sub>PO<sub>4</sub><sup>-</sup> are found to be somewhat similar while those of HPO<sub>4</sub><sup>-</sup> and PO<sub>4</sub><sup>2-</sup> are lower. The same trend was noted for abstraction from organic compounds.<sup>9</sup> A logarithmic plot of the rate constants of SO<sub>4</sub><sup>-</sup> vs. those of HPO<sub>4</sub><sup>-</sup> gives a reasonably straight line with a slope that indicates a slightly higher selectivity in the reactions of HPO<sub>4</sub><sup>-</sup> as compared with those of SO<sub>4</sub><sup>-</sup>. Rate constants for the ions that undergo oxidation do not fit on the same line, apparently because they are governed by different factors. For hydrazine and hydroxylamine the rate constants are found to be higher for the neutral than for the protonated forms, similar to the previous findings for reactions of OH radicals.<sup>19</sup>

**Oxidation by Sulfate and Phosphate Radicals.** The lower part of Table II lists the rate constants for oxidation of various anions. The values in these cases strongly depend on the redox potentials of both the radicals and the substrates. The strongly reducing anions, such as sulfite, azide, and iodide, react rapidly with all the radicals under study. However, the weaker reductants reveal the differences in the potentials between the various radicals. While SO<sub>4</sub><sup>-</sup> can oxidize Cl<sup>-</sup> and Br<sup>-</sup> readily, H<sub>2</sub>PO<sub>4</sub><sup>-</sup> oxidizes Br<sup>-</sup> rapidly but Cl<sup>-</sup> very slowly, and HPO<sub>4</sub><sup>-</sup> oxidizes Br<sup>-</sup> very slowly while no reaction could be detected with Cl<sup>-</sup>. The results suggest that the oxidation potentials of the radicals decrease in the order SO<sub>4</sub><sup>-</sup> > H<sub>2</sub>PO<sub>4</sub><sup>-</sup> > HPO<sub>4</sub><sup>-</sup> > PO<sub>4</sub><sup>2-</sup>.

To further confirm this order, oxidation of phosphate ions by sulfate radicals was examined. The observations were made at 560 nm where the phosphate radical has more intense absorption than SO<sub>4</sub><sup>-</sup>. The buildup of absorption by the reaction



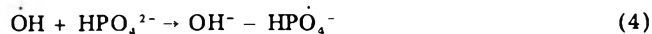
was monitored using solutions of S<sub>2</sub>O<sub>8</sub><sup>2-</sup> and HPO<sub>4</sub><sup>2-</sup> and a rate constant of  $(1.2 \pm 0.3) \times 10^6 \text{ M}^{-1} \text{ s}^{-1}$  was determined.

TABLE II: Rate Constants for Reaction of Sulfate and Phosphate Radicals with Inorganic Compounds

Compd	Rate constants, M <sup>-1</sup> s <sup>-1</sup>				
	OH <sup>a</sup>	SO <sub>4</sub> <sup>-</sup> (pH 7) <sup>b</sup>	H <sub>2</sub> PO <sub>4</sub> <sup>-</sup> (pH 4) <sup>b</sup>	HPO <sub>4</sub> <sup>-</sup> (pH 7) <sup>b</sup>	PO <sub>4</sub> <sup>2-</sup> (pH 12) <sup>b</sup>
*NH <sub>2</sub> OH	≤ 5 × 10 <sup>9</sup>	1.5 × 10 <sup>7</sup> (4.1)	1.2 × 10 <sup>7</sup>		
H <sub>2</sub> PO <sub>4</sub> <sup>-</sup>		1.6 × 10 <sup>7</sup> (4)	4 × 10 <sup>7</sup>		
HPO <sub>4</sub> <sup>2-</sup>	3.5 × 10 <sup>9</sup>	6.2 × 10 <sup>7</sup> (8.3)		5.9 × 10 <sup>6</sup> (9)	5.5 × 10 <sup>6</sup>
H <sub>2</sub> O <sub>2</sub>		1.2 × 10 <sup>7</sup>	5.5 × 10 <sup>7</sup> <sup>c</sup>	2.7 × 10 <sup>7</sup> (9) <sup>c</sup>	
H <sub>2</sub> PO <sub>3</sub> <sup>-</sup>	1.7 × 10 <sup>9</sup>	1.8 × 10 <sup>8</sup>	3.9 × 10 <sup>8</sup>	5.9 × 10 <sup>7</sup>	7.9 × 10 <sup>7</sup>
*N <sub>2</sub> H <sub>4</sub>	1 × 10 <sup>9</sup>	2.1 × 10 <sup>8</sup> (4)	1.9 × 10 <sup>8</sup>	1.4 × 10 <sup>8</sup>	
N <sub>2</sub> H <sub>4</sub>	1.4 × 10 <sup>10</sup>	8.1 × 10 <sup>8</sup> (9.5)		4.9 × 10 <sup>8</sup> (9.4)	<i>d</i>
NH <sub>2</sub> OH	9.5 × 10 <sup>9</sup>	8.5 × 10 <sup>8</sup> (8.2)		4.9 × 10 <sup>8</sup> (9)	<i>d</i>
H <sub>2</sub> PO <sub>3</sub> <sup>-</sup>	~ 2 × 10 <sup>4</sup> <sup>e</sup>	≤ 7 × 10 <sup>4</sup>			
HPO <sub>4</sub> <sup>2-</sup>	(1.5 ± 0.3) × 10 <sup>5</sup> <sup>e</sup>	(1.2 ± 0.3) × 10 <sup>6</sup> (9)			
HCO <sub>3</sub> <sup>-</sup>		9 × 10 <sup>6</sup> <sup>f</sup>			
OH <sup>-</sup>		8 × 10 <sup>7</sup> (> 10) <sup>g,h</sup>			(5 ± 1) × 10 <sup>5</sup>
Cl <sup>-</sup>		3 × 10 <sup>8</sup> <sup>h</sup>	2.2 × 10 <sup>6</sup>	≤ 10 <sup>4</sup>	≤ 10 <sup>4</sup>
Br <sup>-</sup>	~ 1 × 10 <sup>9</sup>	3.5 × 10 <sup>9</sup> <sup>g</sup>	8 × 10 <sup>8</sup>	6.5 × 10 <sup>6</sup> (9)	<i>i</i>
NO <sub>2</sub> <sup>-</sup>	8 × 10 <sup>9</sup>	8.8 × 10 <sup>8</sup>		1.4 × 10 <sup>7</sup>	
SO <sub>3</sub> <sup>2-</sup>	5.5 × 10 <sup>9</sup>	≥ 5 × 10 <sup>8</sup> <sup>j</sup>		2.7 × 10 <sup>7</sup> (9)	4.1 × 10 <sup>7</sup>
HSO <sub>3</sub> <sup>-</sup>	9.5 × 10 <sup>9</sup>	≥ 1 × 10 <sup>9</sup> <sup>j</sup>	2.7 × 10 <sup>8</sup>		
S <sub>2</sub> O <sub>3</sub> <sup>2-</sup>	8 × 10 <sup>9</sup>			1.0 × 10 <sup>8</sup>	
N <sub>3</sub> <sup>-</sup>	1.1 × 10 <sup>10</sup>	~ 3 × 10 <sup>9</sup>		1.1 × 10 <sup>8</sup>	<i>d</i>
S <sub>2</sub> O <sub>5</sub> <sup>2-</sup>				1.9 × 10 <sup>8</sup>	
I <sup>-</sup>	2 × 10 <sup>10</sup>	<i>d</i>		<i>d</i>	3 × 10 <sup>8</sup>

<sup>a</sup> Taken from the literature as summarized in ref 19, except as noted. <sup>b</sup> Measured at this pH unless different value is given in parentheses next to the rate constant. Measurements at pH 9 actually represent a mixture of HPO<sub>4</sub><sup>-</sup> and PO<sub>4</sub><sup>2-</sup>. Accurate to ± 15% unless otherwise indicated. <sup>c</sup> From ref 6. <sup>d</sup> Thermal reaction was sufficiently fast to prevent accurate measurement. <sup>e</sup> Determined in the present work. <sup>f</sup> From ref 3. <sup>g</sup> From ref 7. <sup>h</sup> From ref 12. <sup>i</sup> Results complicated probably by production of BrO<sup>-</sup> from decay of Br<sub>2</sub><sup>-</sup> at this pH. <sup>j</sup> From E. Hayon, A. Treinin, and J. Wilf, *J. Am. Chem. Soc.*, 94, 47 (1972).

However, in these solutions the reaction



may also contribute to the buildup of absorption. We measured the rate constant for the latter reaction in  $\text{N}_2\text{O}$  saturated solutions of  $\text{Na}_2\text{HPO}_4$  by monitoring the buildup of absorption at 560 nm and found a value of  $1.5 \times 10^5 \text{ M}^{-1} \text{ s}^{-1}$ . This value is lower than that ( $7.9 \times 10^5$ ) reported previously.<sup>20</sup> The difference may result from the fact that with our computer controlled apparatus we were able to use very low doses and average over 50 pulses to obtain a good signal-to-noise ratio, while minimizing the effect of the second-order reactions such as  $\text{OH} + \text{OH}$ . With  $k_4$  being only  $1.5 \times 10^5 \text{ M}^{-1} \text{ s}^{-1}$  the value of  $(1.2 \pm 0.3) \times 10^6 \text{ M}^{-1} \text{ s}^{-1}$  measured in the  $\text{S}_2\text{O}_8^{2-}$  system can be assigned to  $k_3$  without any correction.

The reaction of  $\text{SO}_4^{\cdot -}$  with  $\text{H}_2\text{PO}_4^-$  was found to be immeasurably slow ( $\leq 7 \times 10^4 \text{ M}^{-1} \text{ s}^{-1}$ ) and so was the opposite reaction of  $\text{H}_2\text{PO}_4^-$  with  $\text{SO}_4^{2-}$ . Apparently the redox potentials of these two radicals are somewhat similar. The reaction of  $\text{OH}$  with  $\text{H}_2\text{PO}_4^-$  was also examined and found to be slower than reported previously (see below).

**Spectra and Dissociation Constants of the Phosphate Radical.** The results presented above indicate that  $\text{OH}^-$  can be oxidized by all the acid-base forms of the phosphate radical. Oxidation by  $\text{PO}_4^{2-}$  was measured to have a rate constant of  $5 \times 10^5 \text{ M}^{-1} \text{ s}^{-1}$  (Table II). Oxidation by  $\text{HPO}_4^{2-}$  and  $\text{H}_2\text{PO}_4^-$  cannot be experimentally measured because these species exist only in neutral or acidic solutions. However, based on their behavior in oxidizing other anions, it can be concluded that they should oxidize  $\text{OH}^-$  more rapidly than  $\text{PO}_4^{2-}$  does. These arguments can be reversed to suggest that oxidation of the phosphate anions by  $\text{OH}$  radicals should become more rapid in going from  $\text{H}_2\text{PO}_4^-$  to  $\text{HPO}_4^{2-}$ , to  $\text{PO}_4^{2-}$ . Previous measurements<sup>20</sup> indicated a higher rate constant for  $\text{H}_2\text{PO}_4^-$  than for  $\text{HPO}_4^{2-}$ , contrary to this suggestion. However, since our measurement of the rate constant for  $\text{OH} + \text{HPO}_4^{2-}$  showed a lower value than that previously reported,<sup>20</sup> we decided to reexamine the  $\text{OH} + \text{H}_2\text{PO}_4^-$  reaction as well.

Using 1 M solutions of  $\text{NaH}_2\text{PO}_4$  and observing the transient absorption of the phosphate radical in the 500–550-nm region, it was found that the absorption produced in this system is very much lower than that observed from the reaction of  $e_{\text{aq}}^-$  with peroxodiphosphate at the same pH. A discrepancy also exists when the results of Black and Hayon<sup>21</sup> are compared with those of Levey and Hart.<sup>18</sup> The former authors oxidized phosphate ions and found an increasing absorption as the pH increased, while the latter reduced peroxodiphosphate ions and observed *decreasing* absorption as the pH increased. This apparent disagreement can be explained if the reaction of  $\text{H}_2\text{PO}_4^-$  with  $\text{OH}$  is very slow and does not take place efficiently even at 1 M phosphate. The small absorption produced in 1 M  $\text{H}_2\text{PO}_4^-$  solutions, as observed previously<sup>20,21</sup> and in the present work, can be rationalized by a direct effect of radiation on the solute to produce a small yield of phosphate radicals.

In our experiments with  $\text{N}_2\text{O}$  saturated 1 M  $\text{H}_2\text{PO}_4^-$  we observe an absorption immediately after the pulse which corresponds to a phosphate radical yield of  $G \approx 0.4$ . This was followed by an increase of absorption with time up to a level approximately twice as high, i.e., only a small portion of the  $\text{OH}$  radicals oxidize  $\text{H}_2\text{PO}_4^-$ . The rate constant derived from the buildup of adsorption is  $\sim (3 \pm 1) \times 10^4 \text{ M}^{-1} \text{ s}^{-1}$ , which, because of incomplete scavenging, suggests a rate constant for  $\text{OH} + \text{H}_2\text{PO}_4^-$  lower than this value. Furthermore, the addition of methanol

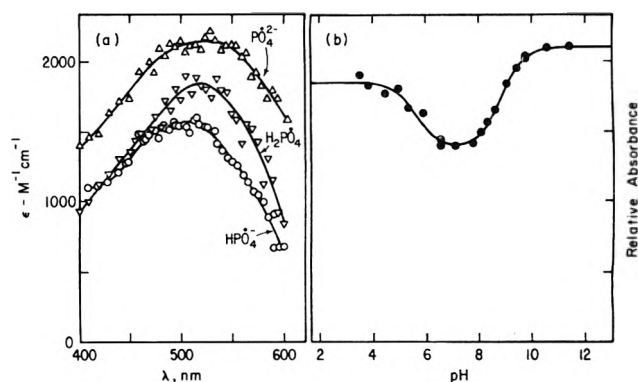


**Figure 1.** Absorption spectra and dissociation constants of the phosphate radicals. (a) Spectra of the three acid-base forms of the phosphate radical. Recorded using aqueous solutions of  $2.5 \times 10^{-2} \text{ M}$  peroxodiphosphate ions at pH 4 ( $\nabla$ ), pH 7 (O), and pH 11 ( $\Delta$ ). The transient absorption was monitored 2–10  $\mu\text{s}$  after the pulse, after the formation was complete, and in the case of pH 4 it was extrapolated to time zero because some decay was observable. (b) Effect of pH on the absorbance at 540 nm. The curve was calculated from the plateau values using  $\text{p}K_1 = 5.7$  and  $\text{p}K_2 = 8.9$ .

( $1 \times 10^{-5}$  to  $1 \times 10^{-4} \text{ M}$ ) did not affect the initial “direct action” portion of the absorbance but decreased that portion which is formed more slowly, because of competition for  $\text{OH}$  radicals. The decrease indicates a value for  $k(\text{OH} + \text{H}_2\text{PO}_4^-)$  of only  $\sim 1\text{--}2 \times 10^4 \text{ M}^{-1} \text{ s}^{-1}$ . These measurements are not very accurate, but nevertheless they show that  $\text{OH}$  reacts with  $\text{H}_2\text{PO}_4^-$  much more slowly than with  $\text{HPO}_4^{2-}$  and than reported previously.<sup>20</sup>

The increased absorbance with pH, observed in the pulse radiolysis of phosphate ions,<sup>20,21</sup> may result from the increased reactivity of  $\text{OH}$  with phosphate and not necessarily represent the dissociation of the phosphate radical. It is, therefore, necessary to determine the  $\text{p}K$  values using the peroxodiphosphate system. Experiments were carried out with  $2.5 \times 10^{-2} \text{ M}$  solutions of peroxodiphosphate and the results presented in Figure 1a show that the absorption maximum of the phosphate radical clearly shifts with pH. Although the peaks are broad, detailed monitoring of the absorption shows shifts from 520 nm at pH 4 to 510 nm at pH 7 and up to 530 nm at pH 11. The extinction coefficients, however, differ by less than 40%, contrary to the large differences reported previously.<sup>18,20,21</sup> The error in the experiments<sup>20,21</sup> using phosphate ion oxidation by  $\text{OH}$  radicals results, as mentioned above, from the very limited extent of scavenging of  $\text{OH}$  by the phosphate, especially at low pH. The low value observed<sup>18</sup> at high pH using peroxodiphosphate may also result from incomplete scavenging of the  $e_{\text{aq}}^-$  since the rate constant decreases by over an order of magnitude upon dissociation of the peroxodiphosphate into  $\text{P}_2\text{O}_8^{4-}$ .

The shifts in the spectra shown in Figure 1a allow the determination of the  $\text{p}K$  values as shown in Figure 1b. The calculated best-fit curve gives  $\text{p}K_1 = 5.7 \pm 0.2$  and  $\text{p}K_2 = 8.9 \pm 0.1$ . The first  $\text{p}K$  happens to be very similar to that reported previously, while the second  $\text{p}K$  is lower than the previous values (10.1, 10.7)<sup>20,21</sup> measured using solutions of phosphate ions. Those higher values were probably affected by the acid-base equilibria of the parent phosphate ions which change the extent of  $\text{OH}$  scavenging by the phosphate.

**Comparison with Reactions of Hydroxyl Radicals.** In comparing the reactions of  $\text{OH}$  with those of  $\text{SO}_4^{\cdot -}$  and  $\text{H}_2\text{PO}_4^-$  it can be seen that in hydrogen abstraction reactions  $\text{OH}$  radicals exhibit a higher reactivity. Their rate constants are about an order of magnitude higher than those of  $\text{SO}_4^{\cdot -}$  and  $\text{H}_2\text{PO}_4^-$ , whether H abstraction from inorganic

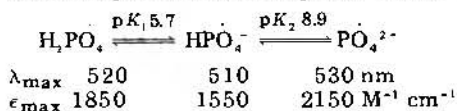
(Table II) or organic<sup>9</sup> compounds is considered. This difference may reflect a stronger HO-H bond compared with SO-H and PO-H. However, when electron transfer reactions are considered the OH radical is a weaker oxidant than  $\text{SO}_4^-$  and  $\text{H}_2\text{PO}_4^-$ . The OH<sup>-</sup> can be, in fact, oxidized by the latter radicals while oxidation of sulfate and phosphate ions by OH radicals is very slow.

The conclusion that OH is a weaker oxidant can be also drawn from a comparison of the reactions of these various radicals with carboxylic acids. The reaction of  $\text{SO}_4^-$  leads predominantly to decarboxylation<sup>12-15,22</sup> and that of  $\text{H}_2\text{PO}_4^-$  leads to partial decarboxylation,<sup>16,22</sup> while only  $\leq 10\%$  of the OH react by this mechanism.<sup>23</sup> The overall rate constants of OH are higher than those of  $\text{SO}_4^-$  and  $\text{H}_2\text{PO}_4^-$  because the reaction of OH takes place mainly via addition or hydrogen abstraction which are more rapid with OH than with  $\text{SO}_4^-$  or  $\text{H}_2\text{PO}_4^-$ . If the contribution of the different mechanisms is taken into account the partial rate constant for decarboxylation by OH can be estimated. The estimates for malonic and benzoic acids show that decarboxylation by OH is slower than that by  $\text{SO}_4^-$ .

If OH is indeed a weaker oxidant than  $\text{SO}_4^-$ , it may be further suggested that the oxidation of inorganic anions, such as  $\text{NO}_2^-$  and  $\text{SO}_3^{2-}$  (Table II), usually formulated as an electron transfer process, actually involves addition of OH. This mechanism would explain why the rate constants of OH with such anions are higher than those of  $\text{SO}_4^-$  despite the fact that  $\text{SO}_4^-$  is the stronger oxidant. The initial addition of OH can be, of course, followed by a rapid loss of OH<sup>-</sup>. In fact, this mechanism was shown to operate in the reactions of OH with halides and pseudohalides<sup>24</sup> and may be operative in many other reactions as well.

### Summary and Conclusions

The reaction of hydrated electrons with peroxodiphosphate ions was used to produce the phosphate radical in order to examine its properties. The absorption spectrum of this radical was found to change with pH. Changes in extinction coefficient amount to  $\sim 40\%$  and are easily observed. However, because the spectrum is very broad and the changes in  $\lambda_{\text{max}}$  are relatively small, these changes become observable only after extensive monitoring of the absorption in the 400–600-nm region. The peak was found to shift from 520 nm in acid solution to 510 nm in neutral and 530 nm in alkaline solutions. The dissociation constants of the phosphate radical, determined from the effect of pH on the absorption, are 5.7 and 8.9:



These radicals may be also produced by the reaction of OH with phosphate ions. This latter reaction was reexamined and found to be slower than reported previously. In fact, the reaction with  $\text{H}_2\text{PO}_4^-$  has a rate constant of only  $\sim 10^4$  M<sup>-1</sup> s<sup>-1</sup> so that under the pulse radiolysis conditions it takes place only to a very limited extent even in 1 M  $\text{H}_2\text{PO}_4^-$ . The previous report on the pK of the phosphate radical

produced by this reaction has to be reinterpreted in terms of direct action of radiation on the phosphate and changes with pH in the extent of OH scavenging. Disagreements in the literature concerning the spectra of the acid-base forms of the phosphate radical were thus explained (see text).

The rate constants for the reactions of the acid-base forms of the phosphate radical, as well as those of the sulfate radical, with inorganic compounds were determined and intercompared. The rate constants for reaction with  $\text{H}_2\text{O}_2$ ,  $\text{HPO}_3^{2-}$ ,  $\text{H}_2\text{PO}_2^-$ ,  $\text{N}_2\text{H}_4$ , and  $\text{NH}_2\text{OH}$  in their various acid-base forms are generally similar for  $\text{SO}_4^-$  and  $\text{H}_2\text{PO}_4^-$  but somewhat slower for  $\text{HPO}_4^{\cdot-}$  and  $\text{PO}_4^{2-}$ . Since this behavior parallels that observed for reactions with alcohols it is suggested that the mechanism in these cases involves hydrogen abstraction.

The rate constants for the oxidation of OH<sup>-</sup>, Cl<sup>-</sup>, Br<sup>-</sup>,  $\text{NO}_2^-$ , and several other anions show large differences in the reactivity of the various radicals which suggest that the oxidation capabilities decrease in the order  $\text{SO}_4^-$ ,  $\text{H}_2\text{PO}_4^-$ ,  $\text{HPO}_4^{\cdot-}$ ,  $\text{PO}_4^{2-}$ .

A comparison of the rate constants of these radicals with those of OH indicates that the OH radical is more reactive in hydrogen abstraction reactions. It is also suggested that OH is a weaker oxidant which may react with many inorganic ions by addition rather than by direct electron transfer.

### References and Notes

- (1) The research described herein was supported by the Division of Basic Energy Sciences of the U.S. Department of Energy. This is Document No. NDRL-1809 from the Notre Dame Radiation Laboratory.
- (2) E. Heckel, A. Henglein, and G. Beck, *Ber. Bunsenges. Phys. Chem.*, **70**, 149 (1966).
- (3) L. Dogliotti and E. Hayon, *J. Phys. Chem.*, **71**, 2511 (1967).
- (4) L. Dogliotti and E. Hayon, *J. Phys. Chem.*, **71**, 3802 (1967).
- (5) W. Roebke, M. Renz, and A. Henglein, *Int. J. Radiat. Phys. Chem.*, **1**, 39 (1969).
- (6) M. Nakashima and E. Hayon, *J. Phys. Chem.*, **74**, 3290 (1970).
- (7) J. L. Redpath and R. L. Wilson, *Int. J. Radiat. Biol.*, **27**, 389 (1975).
- (8) P. Neta, V. Madhavan, H. Zemel, and R. W. Fessenden, *J. Am. Chem. Soc.*, **99**, 163 (1977).
- (9) P. Maruthamuthu and P. Neta, *J. Phys. Chem.*, **81**, 1622 (1977).
- (10) P. O'Neill, S. Steenken, and D. Schulte-Frohlinde, *J. Phys. Chem.*, **79**, 2773 (1975).
- (11) S. Steenken, P. O'Neill, and D. Schulte-Frohlinde, *J. Phys. Chem.*, **81**, 26 (1977).
- (12) O. P. Chawla and R. W. Fessenden, *J. Phys. Chem.*, **79**, 2693 (1975).
- (13) R. O. C. Norman, P. M. Storey, and P. R. West, *J. Chem. Soc. B*, 1087 (1970).
- (14) B. C. Gilbert, J. P. Larkin, and R. O. C. Norman, *J. Chem. Soc., Perkin Trans. 2*, 1272 (1972).
- (15) H. Zemel and R. W. Fessenden, *J. Phys. Chem.*, **79**, 1419 (1975).
- (16) P. Maruthamuthu and H. Taniguchi, *J. Phys. Chem.*, **81**, 1944 (1977).
- (17) I. I. Creaser and J. O. Edwards, *Top. Phosphorus Chem.*, **7**, 379 (1972).
- (18) G. Levey and E. J. Hart, *J. Phys. Chem.*, **79**, 1642 (1975).
- (19) See compilation by Farhataziz and A. Ross, *Natl. Stand. Ref. Data Ser., Natl. Bur. Stand.*, No. 59.
- (20) G. Grabner, N. Getoff, and F. Schwörer, *Int. J. Radiat. Phys. Chem.*, **5**, 393, 405 (1973).
- (21) E. D. Black and E. Hayon, *J. Phys. Chem.*, **74**, 3199 (1970).
- (22) V. Madhavan, H. Levanon, and P. Neta, to be submitted for publication.
- (23) D. Behar, A. Samuni, and R. W. Fessenden, *J. Phys. Chem.*, **77**, 2055 (1973).
- (24) See, e.g., D. Behar, *J. Phys. Chem.*, **76**, 1815 (1972), and references therein.

## The Geometries of Some Small Dimers and Malonaldehyde by Approximate Molecular Orbital Theory

Donna L. Breen

Department of Chemistry, Auburn University, Auburn, Alabama 36830 (Received May 9, 1977)

Publication costs assisted by Auburn University

A CNDO type semiempirical molecular orbital method has been applied to the prediction of intermolecular geometries and relative binding energies of some small hydrogen-bonded dimers containing nitrogen and fluoride intermolecular hydrogen bonds, and the molecule malonaldehyde which exhibits an intramolecular O–H bond. The predominant part of the attraction of these complexes comes from the electrostatic interaction energy. The calculation of good monomer ionization potentials is suggested to be an important part of the ability of a semiempirical MO method to predict dimerization energies. The molecule malonaldehyde is shown to slightly favor  $C_s$  symmetry with a hydrogen bond distance in good agreement with experiment and the results of nonempirical calculations.

### Introduction

The prediction of the geometries of hydrogen-bonded molecular complexes is an area that lends itself to treatment by theoretical methods. These interactions between molecules play a decisive role in biological processes. The most satisfactory procedures whereby such calculations are attempted are those using a nonempirical or ab initio formalism. Despite the number of quantum mechanical calculations of a semiempirical or approximate nature, relatively few have dealt with predicting the orientation of molecules in dimers or molecular complexes. Foretelling an energy minimum is a demanding undertaking basically due to the kinds of contributions present. There are electrostatic contributions which may range from simple dipole–dipole to H bonding. There also may be polarization, charge transfer, exchange repulsion, and dispersion terms.

The Hartree–Fock SCF–MO or “supermolecule” approach normally does not treat dispersion forces.<sup>1</sup> Most approximate MO methods would neglect exchange as well. Perturbation theory calculations using multipole expansions of the interaction operator as suggested by London<sup>2,3</sup> are useful but do not account for intermolecular exchange. At long range these forces are mostly attractive; the exchange repulsion needs to be included to obtain a minimum. However, recent work on polar and nonpolar complexes has shown that the predominant term responsible for distinguishing the most stable orientation of a complex is the difference in the electrostatic interactions.<sup>4–6</sup> It may then be worthwhile to consider approximate MO methods which neglect exchange repulsion and dispersion but give fairly good estimates of electrostatic interaction energies. In this way, a general picture of the most stable geometry of the complex may be produced. We report here the use of such an approach to investigate hydrogen bonding interactions in several molecules.

In this work we have applied a modified CNDO method developed recently by Hojer and Meza.<sup>7</sup> This method has previously been applied to water dimers and trimers.<sup>8</sup> The binding energies of these complexes were found to be in good agreement with ab initio calculations. The method had been parametrized to yield good ionization potentials, heats of atomization, and dipole moments for molecules. The stabilization energy of a donor–acceptor complex has been shown to be proportional to the ionization potential of the donor.<sup>9,10</sup> Although charge transfer could be thought to be responsible for this effect, the main contributions

to the van der Waals interactions for such complexes are not from charge-transfer forces.<sup>11</sup>

The purpose of this work is to study the results of applying this approximate MO method which gives good ionization potentials on molecules, to some small H-bonded dimers and ions, and an intramolecular H-bonded molecule which might form a symmetric structure. The systems were chosen because there were ab initio calculations and experimental data available for them. Our goal is to show that the method has promise of being applicable to the calculation of intermolecular interactions on much larger H-bonded systems. Ab initio methods are, of course, the preferred ones for such small systems as they are more reliable. However, we wish to establish that this parametrized method will be viable on small H-bonded molecules and could then be extended to treat larger systems on which ab initio calculations are impractical. It is especially important to develop a method which can treat biomolecular H bonding.

### Method

The CNDO-structured equations of Hojer and Meza<sup>7</sup> were used along with their suggested parameters and orbital exponents by rewriting a CNDO program and inserting the new equations. The main features such as the ZDO approximation and the calculations of the Coulomb integrals over 2s functions are retained by the method. Optimized orbital exponents from minimal basis set ab initio atomic calculations are used.<sup>12</sup> The number of one- and two-center repulsion integrals calculated is increased because different radial exponents are employed for each type of orbital. Thus, the repulsion integral between an s electron in orbital  $\mu$  on A and a p electron in orbital  $\gamma$  on B is given by

$$\gamma_{\mu\nu}^{sp} = \gamma_{AB}^{sp} = \langle 2s_A^S(1)2s_B^P(2) | 1/r_{12} | 2s_A^S(1)2s_B^P(2) \rangle$$

In this way, the proper radial dependence of the orbital is retained as well as rotational invariance through the use of s orbitals.

The one-center core integrals,  $U_{\mu\mu}$ , are calculated from the ionization potential of an orbital with s radial dependence by

$$I_{\mu}^s = -U_{\mu\mu}^s - \sum_{l \in A} (n_A^l - \delta_{sl}) \gamma_{AA}^{sl}$$

where  $n_A^l$  is the occupation number of orbital  $l$  on atom A in the ground state electronic configuration. The ionization potential used for the first and second row atoms

were those of Pople and Segal.<sup>13</sup> Third row atom ionization potentials were calculated empirically by fitting the results to observed data.

The two-center core terms  $V_{AB}^s$  are evaluated by

$$V_{AB}^s = \sum_{i \in B} n_B^i \gamma_{AB}^{si}$$

The off-diagonal core integrals are calculated as in the CNDO/2 approximation

$$H_{\mu\nu}^{si} = 1/2 S_{\mu\nu}^{si} (\beta_A + \beta_B)$$

The bonding parameter  $\beta$ , however, is chosen as that which gives the optimum reproduction of binding energies, ionization potentials, and dipole moments on small molecules. The problems associated with the adjustment of  $\beta$ s are explained in detail by Wadt and Goddard.<sup>14</sup>

The closed shell Hartree-Fock matrix elements are then, for orbital  $\mu$  with radial dependence  $s$

$$F_{\mu\mu}^s = -I_{\mu\mu}^s + (1 - 1/2 P_{\mu\mu}) \gamma_{AA}^{ss} - \sum_{i \in A} n_A^i \gamma_{AA}^{si} - \sum_{B \neq A} \sum_i n_B^i \gamma_{AB}^{si} + \sum_{\lambda \in A} P_{\lambda\lambda}^i \gamma_{AA}^{s\lambda} + \sum_{\lambda \in B} P_{\lambda\lambda}^i \gamma_{AB}^{s\lambda}$$

$$F_{\mu\nu}^{si} = 1/2 S_{\mu\nu}^{si} (\beta_A + \beta_B) - 1/2 P_{\mu\nu} \gamma_{AB}^{si}$$

A subroutine to perform a geometry optimization was added to provide intermolecular angle and distance minimization of the total energy. SCF convergence was met when the energy was consistent to four decimal eV's.

## Results and Discussion

Recent ab initio multistructure valence bond (VB) calculations on  $\pi$  systems by Wormer and van der Avoird<sup>4</sup> investigated two relative orientations of the ethylene dimer: the stacked or parallel dimer which is prototype of charge transfer complexes of the  $\pi$ - $\pi^*$  type, and the perpendicular dimer which has a quadrupole-quadrupole interaction. The latter was found to possess an energy minimum at 4.7 Å. The stacked dimer was found to have no van der Waals attraction, a result consistent with orbital symmetry rules.<sup>15</sup> The most important contribution to the energetics was the electrostatic interaction. Calculations using an ab initio MO approach yielded the same results as the valence bond. Both CNDO/2 and MINDO/3 calculations differed from the ab initio results. Application of the CNDO/2 method to the two geometries resulted in minima for both orientations, stacked and perpendicular.<sup>4</sup> The MINDO/3 calculations performed by us yielded a repulsive ground state for both structures.

When our modified CNDO procedure was used on the ethylene dimers, the perpendicular geometry was predicted by the more stable arrangement. The parallel dimer exhibited an entirely repulsive ground state in agreement with ab initio VB and MO calculations<sup>4</sup> and the results of extended Huckel procedures.<sup>16,17</sup> This encouraged us to extend the application of this method to cases of hydrogen-bonded molecular systems. The specific kinds of H bonds to be tested were selected to be those involving N-H, halogen-H, and intramolecular O-H.

**The HCN Dimer.** The hydrogen cyanide dimer in the gas phase has been reported as linear and to have a dimerization enthalpy of -3.28 kcal.<sup>18</sup> Two geometric isomers considered previously for the structure of the dimer were the cyclic and linear orientations. Rae<sup>20</sup> has computed the

linear  $H-C \equiv N \cdots H-C \equiv N$

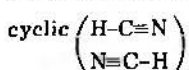
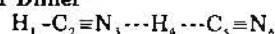


TABLE I: Intermolecular Distances and Energies for the HCN Linear Dimer



Method	$N_3 \cdots C_5$ distance, Å	Dimerization energy, kcal	Amount of charge transferred
Rae <sup>2</sup>	3.3	4.7	
STO-3G <sup>21</sup>	3.2	3.7	0.015 e
This work	2.9	4.5	0.02 e
Experiment <sup>18</sup>	3.3	3.28	

minimum energy geometry of  $(HCN)_2$  using polarizabilities and perturbation theory. Johansson and co-workers,<sup>21</sup> using an ab initio STO-3G procedure, found the linear dimer to be more stable than the cyclic by about 2 kcal. The latter was very little stabilized compared to the monomers. The monomer geometry used in the calculations was the experimental one. Table I lists the distances and dimerization energies of the linear structure that have been calculated.

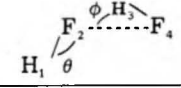
Previous CNDO/2 calculations on  $(HCN)_2$  had predicted the cyclic structure by a large amount over the linear.<sup>19</sup> We performed CNDO/2 calculations on the two structures using the optimized monomer geometry, (C-H) 1.09 Å and (C≡N) 1.18 Å, and found the difference in the stabilization energies of the cyclic and linear forms to be 48 kcal. However, our method yields much better ionization potentials than CNDO/2. The ionization potential of the molecule may play an important role in determining the stability of dimers.<sup>9-11,39</sup> This method predicts 13.66 eV for HCN; the ab initio value is 13.91 eV. Therefore, we might fare better than the CNDO/2 results. The dimerization energies of the cyclic and linear forms were 8 and 4.5 kcal, respectively. The difference in stability between these two structures is much smaller than that predicted by CNDO/2. However, we are still neglecting certain terms which may be reversing the order of stability. Examining the experimental results, we find that four HCN infrared bending modes were reported in  $N_2$  and CO matrices.<sup>18</sup> This was attributed to site symmetry lowering and not to a cyclic structure. A linear structure should exhibit no such vibrations.

In Table I are the results of our calculations on linear  $(HCN)_2$  along with the ab initio results. The linear dimer had a  $\Delta E_{stab}$  of 4.5 kcal. This is rather close to Rae's value but 36% greater than the experimental value. Since Rae's calculation includes dispersion forces and ours does not, it might be concluded that dispersion plays a minor role in the stabilization of this structure and that the electrostatic energy is the predominant controlling factor. The phenomena was proposed by Hanna<sup>22,23</sup> several years ago for benzene and halogen complexes and by Kolos<sup>24</sup> for interactions between polar substances.

The intermolecular distance is somewhat shorter but not too far from the ab initio results. The amount of charge transferred, 0.02 e<sup>-</sup>, is in good agreement with Johansson's estimate 0.015 e<sup>-</sup>. The dimer was calculated in both cyclic and linear arrangements using the optimized monomer geometry. In the linear case, the N-H distance was varied as well as the H-C bond. The latter did not show a great change from the optimized monomer value (about +0.01 Å).

**The HF Dimer and the Bifluoride Ion,  $HF_2^-$ .** Since much work, both experimental and theoretical, has been done on the  $(HF)_2$  dimer, we decided to investigate its structure using this approximate technique. The results of the calculations are given in Table II.

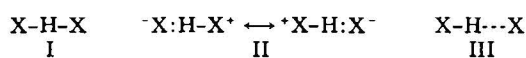
TABLE II: Electronic and Molecular Structure of  $(\text{HF})_2$  from Nonempirical and Semiempirical Methods

			
Method	F-F distance, Å	H-F distance, Å	
STO-4G <sup>26</sup>	2.55	0.92	
This work	2.50	1.02	
Experiment <sup>27</sup>	2.79	0.92	
Method	$\theta$ , deg	$\phi$ , deg	Dimerization energy, kcal
STO-4G <sup>26</sup>	111	4	5.2
This work	137	1.6	8.3
Experiment <sup>27</sup>	110-120	~0	4.8
Atomic charges			
	This work	ab initio	
H <sub>1</sub>	+0.23	+0.26	
F <sub>2</sub>	-0.19	-0.21	
H <sub>3</sub>	+0.23	+0.24	
F <sub>4</sub>	-0.27	-0.28	

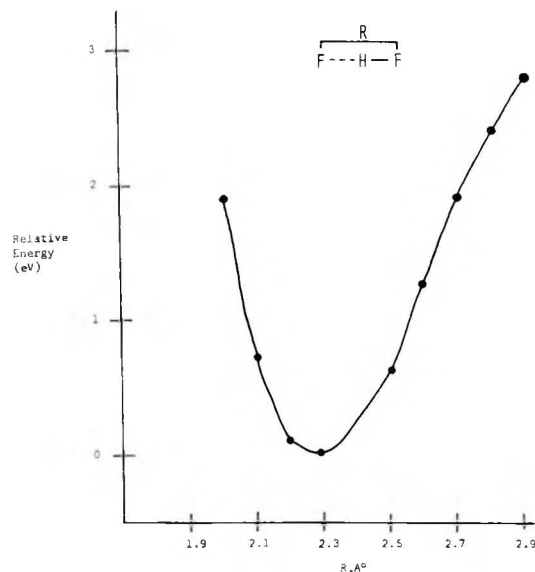
Pople and del Bene<sup>26</sup> used a STO-4G basis set for their *ab initio* calculations on this system and found a 2.55-Å F-F distance. The experimental work was done by Dyke, Howard, and Klemperer<sup>27</sup> who found a 2.79-Å distance between fluorine atoms. After a complete geometry optimization, the dimer is here predicted to have a 2.50-Å F-F distance which is again smaller than the experimental value but as good as the *ab initio* results. The  $\text{H}_1\text{F}_2\text{F}_4$  angle of 137° is predicted to be greater than both the reported values of 111°<sup>26</sup> and 110-120°.<sup>27</sup> We do predict an almost linear structure whose dimerization energy is in fair agreement with experiment. The intramolecular bond distances are overestimated but this is a typical feature of CNDO-type methods. The atomic charges are essentially the same as the *ab initio* values, therefore, the amount of charge transferred is consistent between these two methods. This should result in approximately the same electrostatic energy and, if this energy is the main "steering" factor, then roughly the same binding energy of the complex. This apparently is the case. Our value is 8.3 kcal compared to the *ab initio* value of 5.2 kcal for the binding energy.

In this hydrogen-bonded complex we find the hydrogen distinctly belongs to one monomer. However, there are examples in which such favoritism does not occur and the hydrogen is located midway between the two electronegative atoms. In these cases the bond distance between the two atoms is quite short, less than 2.5 Å, and the species is charged.

An example of a charged, symmetric H-bonded system is the bifluoride ion  $\text{HF}_2^-$ . It has a F-F distance of 2.27 Å with the hydrogen located halfway between the two fluorines.<sup>29</sup> In hydrogen bonding between two identical halogen atoms, canonical structures I-III can contribute



to the stability.<sup>30</sup> For bonding of the anion  $\text{X}^-$  to H-X, the charge delocalization presented by structure II would confer added stability, becoming important in the resonance hybrid and resulting in a symmetrical geometry. Structure I has high energy requirements. When X-H-X is neutral, resonance delocalization would not be significant (about 4%) and only structure III need be considered.<sup>30</sup> The manner in which the halogen atom approaches H-X

Figure 1. Potential energy of  $\text{HF}_2^-$  as function of F-F distance from this work.

should then influence the outcome of the symmetry. If the proton views the X atom as an atomic dipole with charge concentrated along the direction of newly forming atomic hybrid orbitals then asymmetrical bonds might result. This is apparently the case with the neutral radical  $\text{HX}_2$  since it shows asymmetry.<sup>31a</sup> The hydrogen bond, then, arises from dipole-type electrostatic contributions to the resonance hybrid due to the polarizability of the approaching atom.

Figure 1 gives the result of applying our CNDO method to the potential energy curve of  $\text{HF}_2^-$ . We optimized the position of the hydrogen at every point. The minimum is found at a F-F distance of 2.28 Å, in excellent agreement with the experimental value of 2.27 Å. The H-F distance is 1.14 Å or midway between the fluorines. We found this to be the case at every F-F distance smaller than 2.6 Å. For larger distances than this, the hydrogen is asymmetrically located, favoring one fluorine atom. Kollman and Allen<sup>31b</sup> found a double well potential for F-F distances larger than 2.4 Å from these *ab initio* calculations. Previous *ab initio* calculations have reported F-F distances of 2.25,<sup>31a</sup> 2.28,<sup>31b</sup> and 2.46 Å (corrected to 2.28 Å upon considering vibrational stretching states in a Boltzmann distribution).<sup>31c</sup> The ion was found to be symmetrical. The experimental hydrogen bond energy has been given as  $58 \pm 5$ <sup>29a</sup> and  $37 \pm 2$  kcal/mol.<sup>29b</sup> Nonempirical calculations found 51<sup>31b</sup> and 40 kcal/mol,<sup>31a</sup> in agreement with either experimental result. This work gives a bonding energy of 94 kcal which is greatly overestimated. However, the linear geometry is well-predicted within the approximate framework of this method.

*The Malonaldehyde Controversy.* We shall now turn attention to an intramolecular hydrogen bond which has been in the limelight lately, namely, that present in the enol tautomer of the molecule malonaldehyde (MA). This tautomer is sketched in Figure 2. Two recent *ab initio* calculations have predicted  $C_s$  symmetry with an asymmetrical H bond.<sup>32,33</sup> A third *ab initio* calculation<sup>34</sup> found  $C_{2v}$  symmetry in which the hydrogen is located equidistant from the two oxygens with a single minimum potential curve. Del Bene and Kochenour<sup>33</sup> and Isaacson and Morokuma<sup>34</sup> in their calculations on malonaldehyde employed the same basis set (STO-3G) and scaling factors. The first group<sup>33</sup> allowed all degrees of freedom to change, whereas the other<sup>34</sup> constrained the C-C and C-O bond lengths to fixed values which were the average of a single

TABLE III: Comparison of Symmetries and the O-O Distances Predicted for Malonaldehyde

Method	O-O distance, Å		Symmetry predicted	Barrier, kcal	Ref
	$C_s$ form	$C_{2v}$ form			
ab initio	2.63	2.29	$C_s$	11.5	32
ab initio	2.56	2.29	$C_s$	6.6	33
ab initio	(2.38) <sup>a</sup>	(2.28) <sup>a</sup>	$C_{2v}$	1.1	34
CNDO/2	2.38	2.32	$C_s$	1.7	32
	(2.416) <sup>a</sup>	(2.28) <sup>a</sup>	$C_{2v}$	2.5	34
INDO		2.28	$C_{2v}$		34
This work	2.50	2.41	$C_s$	1.4	
Microwave spectrum	2.55		$C_s$		36

<sup>a</sup> Values in parentheses are from an incomplete geometry optimization of CC and CO bonds, see ref 34.

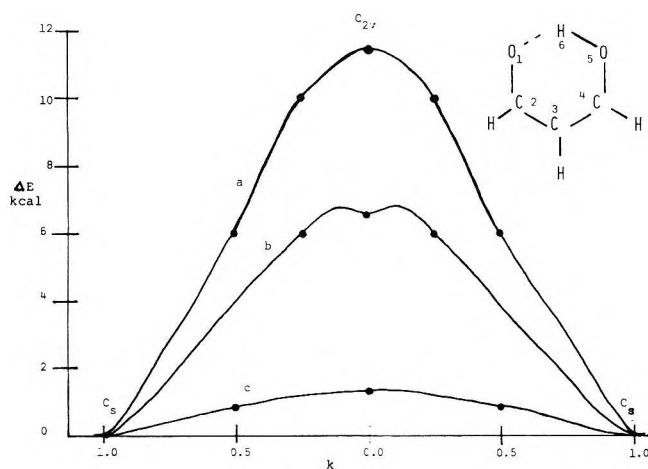


**Figure 2.** Potential energy curve for malonaldehyde as function of geometry coordinate  $k$ . The equation  $r = kr_{C_s} + (1-k)r_{C_{2v}}$  at each  $k$  value is used to find the intermediate geometry between the  $C_s$  and  $C_{2v}$  forms;  $r$  is either a bond distance or angle: (a) ab initio calculation, ref 32; (b) ab initio calculation, ref 33; (c) this method.

and double bond and varied only the interior angles in a  $C_{2v}$  framework. If the molecule has  $C_{2v}$  symmetry, then it is unique since it has no charge and would be expected to exhibit asymmetrical H bonding. In the study which predicted  $C_{2v}$  symmetry,<sup>34</sup> the O-O distance was singled out as being crucial to the predicted O-H distance.

We decided to test the ability of the present method to predict the symmetry of the molecule and the consequent O-O distance since electrostatic interactions presumably play an important role in both. We found that the hydrogen prefers to be equidistant from each oxygen if the rest of the molecule is constrained to  $C_{2v}$  symmetry. However, we did not pursue the cutoff O-O distance for this symmetry as was done in ref 34.

To obtain the  $C_s$  energy, we varied all the bond lengths and angles subject to only two restraints: the C-H bonds were fixed at 1.1 Å and were assumed to bisect the CCC and CCO angles of their respective carbons. Next we performed another geometry optimization on the molecule subject to  $C_{2v}$  symmetry and the previous two restraints and obtained the  $C_{2v}$  lowest energy structure. The C-C and C-O bond lengths were found to be single and double bond averages. The initial geometries were taken from the ab initio results.<sup>32</sup>

Table III compares the results of our calculations with those of the ab initio methods, CNDO/2 and INDO. The O-O distance predicted for the  $C_s$  form, 2.50 Å, is in good agreement with the experimental value of 2.55 Å. The O-O distance found for the  $C_{2v}$  symmetry is much larger than those of other calculations 2.41 Å, but compares favorably with systems which are known to exhibit equidistant hydrogen bond structures: for example, the hydrogen maleate anion and  $H_5O_2^+$  have O-O distances of 2.44 and

2.45 Å, respectively.<sup>35</sup> The rest of the optimized geometry is presented in Table IV along with some comparisons from nonempirical procedures.

In Figure 2, some simple potential curves from ab initio results are compared to this work. Double minima were obtained with a  $C_{2v}$  maximum at 1.4 kcal above the  $C_s$  form. The  $C_s$  form is predicted to be slightly more stable than the  $C_{2v}$  in agreement with the microwave results by Rowe, Duerst, and Wilson<sup>36</sup> and an x-ray diffraction study<sup>37</sup> on a similar system. The present method predicts a smaller energy difference between  $C_{2v}$  and  $C_s$  geometries than the ab initio.

## Conclusions

The application of this semiempirical procedure to the systems discussed indicates that this method, which yields good ionization energies for the monomers, has a real potential for producing fair estimates of the geometries of H-bonded molecular systems. In applications to other molecules, parameters may have to be adjusted to give correct ionization energies for monomers. The electrostatic energy influences the geometric orientation of these complexes and much of the depth of the potential energy well. A qualitative picture of the arrangement of some large biological complexes might well be achieved by such methods.

## References and Notes

- (1) H. Margenau and N. R. Kestner, "Theory of Intermolecular Forces", Pergamon Press, Oxford, 1969.
- (2) F. London, *Z. Phys.*, **63**, 245 (1930).
- (3) F. London, *J. Phys. Chem.*, **46**, 305 (1942).
- (4) P. E. S. Wormer and A. van der Avoird, *J. Chem. Phys.*, **62**, 3326 (1975).
- (5) K. Morokuma, S. Iwata, and W. A. Lathan in "The World of Quantum Chemistry", R. Daudel and B. Pullman, Ed., Reidel, Dordrecht, Holland, 1974.
- (6) S. Iwata and K. Morokuma, *J. Am. Chem. Soc.*, **95**, 7563 (1973).
- (7) G. Hojer and S. Meza, *Acta Chem. Scand.*, **26**, 3723 (1972).
- (8) G. Hojer and J. Keller, *J. Am. Chem. Soc.*, **96**, 3746 (1974).
- (9) R. L. Flurry, Jr., *J. Phys. Chem.*, **69**, 1927 (1965).
- (10) R. L. Flurry, Jr., and P. Politzer, *J. Phys. Chem.*, **73**, 2787 (1969).
- (11) M. J. S. Dewar and C. C. Thompson, Jr., *Tetrahedron, Suppl.* **No. 7**, 97 (1966).
- (12) The one- and two-center repulsion integrals are still calculated over 1s and 2s orbitals retaining rotational invariance; orbital exponents are those of E. Clementi and D. L. Raimondi, *J. Chem. Phys.*, **38**, 2686 (1936).
- (13) J. A. Pople and G. A. Segal, *J. Chem. Phys.*, **33**, 5136 (1965).
- (14) W. R. Wadt and W. A. Goddard, *J. Am. Chem. Soc.*, **96**, 5996 (1974).
- (15) R. B. Woodward and R. Hoffman, "The Conservation of Orbital Symmetry", Academic Press, New York, N.Y., 1970.
- (16) R. Polak and J. Paldus, *Theor. Chem. Acta*, **4**, 37 (1966).
- (17) There is experimental evidence that the van der Waals ethylene dimer is nonpolar based on refocusing properties in quadrupole electric fields from molecular beam experiments. S. Novick, J. M. Lehn, and W. Klemperer, *J. Am. Chem. Soc.*, **95**, 8189 (1973).
- (18) C. M. King and E. R. Nixon, *J. Chem. Phys.*, **48**, 1685 (1968).
- (19) J. R. Hoyland and L. B. Kier, *Theor. Chim. Acta*, **15**, 1 (1969).
- (20) A. I. M. Rae, *Mol. Phys.*, **16**, 257 (1969).
- (21) A. Johansson, P. Kollman, and S. Rothenberg, *Theor. Chim. Acta*, **26**, 97 (1972).
- (22) M. W. Hanna, *J. Am. Chem. Soc.*, **90**, 285 (1968).
- (23) M. W. Hanna and D. E. Williams, *J. Am. Chem. Soc.*, **90**, 5358 (1968).

- (24) W. Kolos in "The World of Quantum Chemistry", R. Daudel and B. Pullman, Ed., Riedel, Dordrecht, Holland, 1974.
- (25) J. D. Morrison and J. A. C. Nicholson, *J. Chem. Phys.*, **20**, 1021 (1952).
- (26) J. A. Pople and J. E. del Bene, *J. Chem. Phys.*, **56**, 2442 (1972).
- (27) T. Dyke, B. J. Howard, and W. Klemperer, *J. Chem. Phys.*, **56**, 2442 (1972).
- (28) W. C. Hamilton and J. A. Ibers, "Hydrogen Bonding in Solids", W. A. Benjamin, New York, N.Y., 1968.
- (29) (a) J. A. Ibers, *J. Chem. Phys.*, **41**, 25 (1964); (b) S. A. Harrell and D. H. McDaniel, *J. Am. Chem. Soc.*, **86**, 4497 (1964).
- (30) F. A. Cotton and G. Wilkinson, "Advanced Inorganic Chemistry", 3rd ed, Interscience, New York, N.Y., 1972, Chapter 5.
- (31) (a) P. N. Noble and R. N. Kortzeborn, *J. Chem. Phys.*, **52**, 5375 (1970); (b) P. A. Kollman and L. C. Allen, *J. Am. Chem. Soc.*, **92**, 6101 (1970); (c) J. Almlöf, *Chem. Phys. Lett.*, **17**, 49 (1972).
- (32) G. Karlström, H. Wennerström, B. Jonsson, S. Forsen, J. Almlöf, and B. Roos, *J. Am. Chem. Soc.*, **97**, 4188 (1975).
- (33) J. E. del Bene and W. L. Kochenour, *J. Am. Chem. Soc.*, **98**, 2041 (1976).
- (34) A. D. Isaacson and K. Morokuma, *J. Am. Chem. Soc.*, **97**, 4453 (1975).
- (35) (a) S. F. Darlow and W. Cochran, *Acta Crystallogr.*, **14**, 1250 (1961); (b) A. F. Beecham, A. C. Hurley, M. F. Mackey, V. M. Maslen, and A. Mathieson, *J. Chem. Phys.*, **49**, 3312 (1968).
- (36) W. F. Rowe, Jr., F. W. Duerst, and E. B. Wilson, *J. Am. Chem. Soc.*, **98**, 4021 (1976).
- (37) D. E. Williams, *Acta Crystallogr.*, **21**, 340 (1966).
- (38) From A. H. Lowrey, C. George, P. D. Antonio, and J. Karle, *J. Am. Chem. Soc.*, **93**, 6399 (1971).
- (39) O. Mo, M. Yanez, and J. I. Fernandez-Alonso, *J. Phys. Chem.*, **79**, 137 (1975).

## Electron Paramagnetic Resonance Spectra of the Group 4 Hexafluoride Anion Radicals<sup>1</sup>

A. R. Boate,<sup>2</sup> J. R. Morton,\* and K. F. Preston

Division of Chemistry, National Research Council of Canada, Ottawa, Canada K1A 0R9 (Received October 13, 1977)

Publication costs assisted by the National Research Council of Canada

Anisotropic EPR spectra detected at 30 K in  $\gamma$ -irradiated powdered  $\text{BaGeF}_6$ ,  $\text{K}_2\text{SnF}_6$ , and  $\text{BaPbF}_6$  have been assigned to the hexafluoride anion radicals  $\text{GeF}_6^{3-}$ ,  $\text{SnF}_6^{3-}$ , and  $\text{PbF}_6^{3-}$ , respectively. These species are members of a series of paramagnetic hexafluorides of the elements of groups 4–7 which constitutes one of the largest known groups of isoelectronic free radicals. The nature of the semiooccupied orbital in this type of radical is discussed in the light of unpaired electron spin densities computed from the measured hyperfine interactions for the hexafluorides.

### Introduction

We have, in recent years, studied the EPR spectra of various hexafluoride radicals. These have included the neutral halogen hexafluorides,<sup>3</sup> and the anionic hexafluorides of the group 6<sup>4</sup> and group 5 elements.<sup>5,6</sup> The purpose of the present article is to report and discuss data for the analogous radical anions of the group 4 elements:  $\text{GeF}_6^{3-}$ ,  $\text{SnF}_6^{3-}$ , and  $\text{PbF}_6^{3-}$ . In addition we shall try to correlate the data for this group of radicals with those for the other hexafluorides discovered earlier.

### Experimental Section

The radicals  $\text{GeF}_6^{3-}$ ,  $\text{SnF}_6^{3-}$ , and  $\text{PbF}_6^{3-}$  were prepared by  $\gamma$  irradiation at 77 K of powdered  $\text{BaGeF}_6$ ,  $\text{K}_2\text{SnF}_6$ , and  $\text{BaPbF}_6$ , respectively. Barium hexafluorogermanate was prepared by dissolving  $\text{GeO}_2$  in HF and adding  $\text{BaCl}_2$ , upon which  $\text{BaGeF}_6$  was precipitated.<sup>7</sup> Potassium hexafluorostannate was prepared by the action of  $\text{SF}_4$  on  $\text{SnO}_2$  in the presence of KCl in a Monel vessel.<sup>8</sup> Barium hexafluoroplumbate was prepared from  $\text{PbO}_2$  and  $\text{BaCO}_3$  heated to 600 °C in a stream of  $\text{N}_2$  to yield<sup>9</sup>  $\text{BaPbO}_3$ . The latter was fluorinated with elementary fluorine in a Monel vessel at 500 °C, yielding  $\text{BaPbF}_6$ .<sup>10</sup>

EPR spectra of the irradiated compounds were examined with a Varian E12 spectrometer previously described.<sup>3</sup> The spectrometer was equipped with an Oxford Instruments liquid helium cryostat (ESR 9).

### Results

The most abundant isotopes of all three elements germanium, tin, and lead have zero spin. Since an important feature of the EPR spectra of the hexafluoride

radicals is the central-atom hyperfine interaction it was necessary to obtain the satellite spectra of the magnetic isotopes  $^{73}\text{Ge}$ ,  $^{119}\text{Sn}$ , and  $^{207}\text{Pb}$ . In the latter case, the spectrum of  $^{207}\text{PbF}_6^{3-}$  was detected in natural abundance; the spectra of  $^{73}\text{GeF}_6^{3-}$  and  $^{119}\text{SnF}_6^{3-}$  were detected in isotopically enriched samples. The spectra of  $^{207}\text{PbF}_6^{3-}$  and  $^{73}\text{GeF}_6^{3-}$  possessed the characteristic anisotropic  $^{19}\text{F}$  hyperfine structure of the halogen hexafluorides,<sup>3</sup> indicative of an  $O_h$  ground-state symmetry. A successful analysis of the anisotropic  $^{19}\text{F}$  hyperfine structure of  $^{119}\text{SnF}_6^{3-}$  has not yet been achieved because of considerable deviation from  $O_h$  symmetry.

The  $^{73}\text{Ge}$  nucleus has spin  $9/2$ , and a negative magnetic moment. The  $^{73}\text{Ge}$  hyperfine interaction in  $\text{GeF}_6^{3-}$  is approximately -1780 MHz, a magnitude so large that only transitions having positive values of  $m_l$  were available.<sup>11</sup> In the case of  $^{119}\text{Sn}$  and  $^{207}\text{Pb}$  (both of which have spin  $I = 1/2$ ) the hyperfine interactions exceeded the microwave frequency, so that only one "normal" EPR transition was detectable, although a "forbidden" transition at higher field enabled the magnetic parameters to be determined.<sup>11</sup> The strong central features in the observed transitions of  $^{119}\text{SnF}_6^{3-}$  and  $^{207}\text{PbF}_6^{3-}$  were analyzed for  $^{119}\text{Sn}$  and  $^{207}\text{Pb}$  hyperfine interactions with a computerized solution of the Breit-Rabi<sup>12</sup> and Nafe-Nelson<sup>13</sup> equations.

The  $^{19}\text{F}$  hyperfine interactions in  $^{73}\text{GeF}_6^{3-}$  and  $^{207}\text{PbF}_6^{3-}$  were analyzed by the same methods which we employed for the halogen hexafluorides.<sup>3</sup> Although having considerably larger line widths than  $\text{ClF}_6$ , the  $^{19}\text{F}$  manifolds of the spectra of  $\text{GeF}_6^{3-}$  and  $^{207}\text{PbF}_6^{3-}$  were characteristic of an octahedral arrangement of six  $^{19}\text{F}$  nuclei about the central atom. In the case of  $\text{SnF}_6^{3-}$  in  $\text{K}_2\text{SnF}_6$  the  $^{19}\text{F}$



TABLE I: Spectral Parameters for the Group 4 Hexafluoride Anion Radicals at 30 K

Radical	Transition	Magn field, G (microwave freq, MHz)	<i>g</i>	A (central), MHz	<sup>19</sup> F hfsc, MHz
<sup>73</sup> GeF <sub>6</sub> <sup>3-</sup>	<i>m<sub>I</sub></i> = 0.5 <sup>a</sup>	828.28 (8969.91)	2.0038 ± 0.0010 <sup>b</sup>	-1779 ± 50	950 ± 20 620 620
	<i>m<sub>I</sub></i> = 1.5	2031.30 (8969.59)			
	<i>m<sub>I</sub></i> = 3.5	4519.48 (8970.81)			
	<i>m<sub>I</sub></i> = 4.5	5799.44 (8970.36)			
<sup>119</sup> SnF <sub>6</sub> <sup>3-</sup>	1,1⟩ ←  1,0⟩ <sup>c</sup>	5201.18 (8973.75)	2.0011 ± 0.0005	-29745 ± 50	Not resolved
	1,0⟩ ←  1,-1⟩	11241.25 (8973.78)			
<sup>207</sup> PbF <sub>6</sub> <sup>3-</sup>	1,0⟩ ←  1,-1⟩	5527.56 (8965.61)	2.0023 ± 0.0005	47868 ± 50	700 ± 20 310 310
	1,1⟩ ←  1,0⟩	8321.42 (8965.60)			

<sup>a</sup> High-field designation nuclear magnetic quantum number. <sup>b</sup> All errors are one standard error. <sup>c</sup> Low-field (*F*, *m<sub>F</sub>*) designation of quantum states.

TABLE II: Central-Atom Hyperfine Interactions<sup>a</sup> and *ns* Spin Densities for Various Hexafluoride Radicals

	MF <sub>6</sub> <sup>4-</sup>	MF <sub>6</sub> <sup>3-</sup>	MF <sub>6</sub> <sup>2-</sup>	MF <sub>6</sub> <sup>-</sup>	MF <sub>6</sub>
M	<sup>27</sup> Al	<sup>29</sup> Si	<sup>31</sup> P	<sup>33</sup> S	<sup>35</sup> Cl
<i>a<sub>M</sub></i>			1807	2211	
<i>M</i> (3s)			0.52	0.39	
<i>F</i> (2p)		0.055 <sup>b</sup>		0.16	
M	<sup>69</sup> Ga	<sup>73</sup> Ge	<sup>75</sup> As	<sup>77</sup> Se	<sup>79</sup> Br
<i>a<sub>M</sub></i>		-1779	9403	10222	11773
<i>M</i> (4s)		0.75	0.64	0.51	0.37
<i>F</i> (2p)		0.063	0.091	0.14	0.17
M	<sup>113</sup> In	<sup>115</sup> Sn	<sup>121</sup> Sb	<sup>125</sup> Te	<sup>127</sup> I
<i>a<sub>M</sub></i>		-29745	21390	-28318	17550
<i>M</i> (5s)		0.68	0.61	0.51	0.42
<i>F</i> (2p)			0.088	0.11	0.16
M	<sup>205</sup> Tl	<sup>207</sup> Pb	<sup>209</sup> Bi	Po	At
<i>a<sub>M</sub></i>	125010	47868	36020		
<i>M</i> (6s)	0.68	0.59	0.46		
<i>F</i> (2p)	0.050	0.074	0.094		

<sup>a</sup> Hyperfine interactions in MHz. <sup>b</sup> Reference 21.

manifolds were asymmetric, and the individual components poorly resolved. We conclude that SnF<sub>6</sub><sup>3-</sup> in this matrix is not octahedral, and offer no analysis of the <sup>19</sup>F hyperfine structure.

In Table I we collect the experimental data, together with the derived values of the *g* factor and hyperfine interactions.

## Discussion

In Table II we collect together the central-atom hyperfine interactions of all known hexafluoride radicals. These hyperfine interactions tend to be rather large, which reflects the dominant contribution of the valence *s* atomic orbital to the semioccupied orbital of the free radical. The semioccupied molecular orbital (SOMO) is doubtless of a totally symmetric representation, in most cases of the point group *O<sub>h</sub>* (octahedral). This is confirmed by the equivalence of the six fluorine nuclei, whose hyperfine interactions have axial symmetry (except SnF<sub>6</sub><sup>3-</sup>) with the principal directions pointing toward the central atom.

We have estimated the central atom (*M*) valence *s* and the *F*(2p) contributions to the SOMO with the atomic parameters recently obtained<sup>14</sup> from Herman and Skillman's<sup>15</sup> Hartree-Fock-Slater wavefunction. The parameters incorporate a relativistic correction of the

Mackey-Wood<sup>16</sup> type. After much deliberation, we have come to the conclusion that Mackey-Wood corrected Herman-Skillman (MWSH) parameters are the most useful for the interpretation of EPR data.<sup>14</sup>

We will discuss the matrix of radicals in Table II according to the horizontal grouping. Conclusions drawn from a comparison of spin densities for radicals within a given row (e.g., GeF<sub>6</sub><sup>3-</sup>, AsF<sub>6</sub><sup>2-</sup>, SeF<sub>6</sub><sup>-</sup>, and BrF<sub>6</sub>) are more likely to be valid than those deduced from a vertical comparison. This is because radicals in a row are genuinely isoelectronic; columns, on the other hand contain radicals which are only "pseudo" isoelectronic.

In each row of Table II we note (a) the *M*(*ns*) character of the SOMO decreases left to right, and (b) the *F*(2p) character increases concomitantly. Since electronegativity in *M* also increases left to right, we can legitimately assume a relationship between *M*(*ns*) character and the electronegativity of *M*. The "inverse" nature of this relationship arises from the antibonding nature of the SOMO, which is composed primarily of an antibonding combination of *M*(*ns*) and the six *F*(2p) atomic orbitals (we neglect here the very small *F*(2s) contribution). As electronegativity in *M* increases, *M* character in the bonding orbitals increases, whereas *M* character in the SOMO and other antibonding orbitals decreases. Of course, this is not a new effect;<sup>17</sup> but it is gratifying to see it in such a large array of radicals, and its observation lends credence to the MWSH parameters on which it is based.

Table II also demonstrates a discrepancy in the total spin count, which is everywhere in excess of unity. The excess varies from 0.02 for BiF<sub>6</sub><sup>2-</sup> to 0.39 for BrF<sub>6</sub>. In fact it is 0.35 or more for all three halogen hexafluorides. Rather than associate this discrepancy with errors in the MWSH parameters, we have suggested elsewhere<sup>3</sup> that it is due to negative spin density in *M*(*np*) atomic orbitals. INDO calculations which we carried out for SF<sub>6</sub><sup>-</sup> and ClF<sub>6</sub> yielded<sup>3</sup> estimates of 0.077 and 0.092 for the negative spin density in each 3p<sub>x</sub>, 3p<sub>y</sub>, and 3p<sub>z</sub> atomic orbital of sulfur and chlorine, respectively. These values are of the correct order of magnitude to account for the excess positive spin density in ClF<sub>6</sub>, and also suggest lower negative spin densities in *M*(*np*) orbitals on the left-hand side of Table II. This would explain (positive) spin counts closer to unity on that side of the table.

Elsewhere,<sup>18</sup> we have drawn a comparison between TlF<sub>6</sub><sup>4-</sup>, PbF<sub>6</sub><sup>3-</sup> and the impurity centers Tl<sup>2+</sup>, Pb<sup>3+</sup> in alkali

halide crystals.<sup>19,20</sup> The comparison shows that, from the point of view of their central-atom hyperfine interactions, which are isotropic and of magnitudes comparable to those of  $\text{TlF}_6^{4-}$  and  $\text{PbF}_6^{3-}$ , a molecular description is entirely appropriate. The anisotropy in the "ligand" hyperfine interaction also favors a molecular description. For this reason we have included in Table II data for  $\text{Si}^{3+}$  in  $\text{LiF}$ .<sup>21</sup> Its  $^{19}\text{F}$  hyperfine anisotropy is quite compatible with the other data when converted to a  $\text{F}(2p)$  contribution to the SOMO, although it is regrettable that no  $^{29}\text{Si}$  hyperfine satellites could be detected for this species. A prediction of the  $^{29}\text{Si}$  hyperfine interaction can be made from Table II and the MWS atomic parameters:<sup>14</sup>  $-3700 \pm 300$  MHz. The failure<sup>21</sup> to detect  $^{29}\text{Si}$  signals in samples where the signal/noise ratio for the main spectrum was  $\sim 100:1$  casts doubt on the identification of silicon as the impurity element.

## References and Notes

- (1) NRCC No. 16514.
- (2) NRCC Research Associate 1975-1977.
- (3) A. R. Boate, J. R. Morton, and K. F. Preston, *J. Phys. Chem.*, **80**, 2954 (1976).
- (4) J. R. Morton, K. F. Preston, and J. C. Tait, *J. Chem. Phys.*, **62**, 2029 (1975).
- (5) A. R. Boate, J. R. Morton, and K. F. Preston, *Chem. Phys. Lett.*, **50**, 65 (1977).
- (6) A. R. Boate, J. R. Morton, and K. F. Preston, *J. Chem. Phys.*, **67**, 4302 (1977).
- (7) R. P. Graham, J. Macnamara, I. H. Crocker, and R. B. MacFarlane, *Can. J. Chem.*, **29**, 89 (1951).
- (8) D. H. Brown, K. R. Dixon, R. D. W. Kemmitt, and D. W. A. Sharp, *J. Chem. Soc.*, 1559 (1965).
- (9) G. Wagner and H. Binder, *Z. Anorg. Allg. Chem.*, **297**, 328 (1958).
- (10) R. Hoppe and K. Blinne, *Z. Anorg. Allg. Chem.*, **293**, 251 (1958).
- (11) A. R. Boate, J. R. Morton, and K. F. Preston, *J. Magn. Reson.*, **23**, 259 (1976).
- (12) G. Breit and I. I. Rabi, *Phys. Rev.*, **38**, 2082 (1931).
- (13) J. E. Nafe and E. B. Nelson, *Phys. Rev.*, **73**, 718 (1948).
- (14) J. R. Morton and K. F. Preston, *J. Magn. Reson.*, in press.
- (15) F. Herman and S. Skillman, "Atomic Structure Calculations", Prentice-Hall, Englewood Cliffs, N.J., 1963.
- (16) J. H. Mackey and D. E. Wood, *J. Chem. Phys.*, **52**, 4914 (1970).
- (17) P. W. Atkins and M. C. R. Symons, "The Structure of Inorganic Radicals", Elsevier, Amsterdam, 1967, p 103.
- (18) A. R. Boate, J. R. Morton, and K. F. Preston, Proceedings of the VI International Symposium on Magnetic Resonance, Banff, Canada (*J. Magn. Reson.*, in press).
- (19) W. Dreybrodt and D. Silber, *Phys. Status Solidi*, **20**, 337 (1967).
- (20) D. Schoemaker and J. S. Kolopus, *Solid State Commun.*, **8**, 435 (1970).
- (21) J. Dugas, D.Sc. Thesis, University of Toulouse, 1970.

## Electron Paramagnetic Resonance Parameters of Copper(II) Y Zeolites

Richard G. Herman<sup>a</sup> and Dennis R. Flentge<sup>b</sup>

Department of Chemistry, Texas A&M University, College Station, Texas 77843 (Received July 25, 1977)

The number of electron paramagnetic resonance (EPR) parameters for copper(II) ions held in lattice positions in dehydrated low exchanged sodium Y zeolites, as well as the relative intensity of each set of  $g$  values observed in the spectrum, was found to vary as a function of evacuation time at ambient temperature prior to activation. The usual procedure of evacuating the sample for 15-60 min before beginning the thermal treatment in hourly increments resulted in the following parameters for low Cu(II) exchanged Y zeolites:  $g_{\parallel}^1 = 2.38(110)$ ,  $g_{\perp}^1 = 2.06(20)$ ,  $g_{\parallel}^2 = 2.30(175)$ ,  $g_{\perp}^2 = 2.03$ , and in some cases  $g_{\parallel}^3 = 2.36(125)$ , where the numbers in parentheses are the observed hyperfine splittings (in Gauss). Prolonged evacuation of the low Cu(II) ion exchanged Y zeolites yielded  $g_{\parallel}^1 = 2.37(125)$ ,  $g_{\perp}^1 = 2.06(20)$ ,  $g_{\parallel}^2 = 2.32(160)$ , and  $g_{\perp}^2 = 2.03$  following dehydration to 400-500 °C. Parameters similar to the latter values were obtained for highly ion exchanged Cu-Y zeolites following partial reduction with hydrogen or carbon monoxide, as well as upon partial reoxidation of the latter samples with oxygen or nitric oxide. The second set of EPR parameters is attributed to copper(II) ions located in sites in the small cages, while the  $g^1$  and  $g^2$  subsets of the first group are due to copper(II) ions localized in the zeolite supercages. Most of these sites provide a distorted trigonal environment for the divalent copper ions. By correlating the zeolite treatments reported in the literature to the present results, the disparity among previously given EPR parameters for Cu(II)-Y zeolites can be explained in most cases.

## Introduction

Metal cation exchanged zeolites are successful catalysts for a wide range of chemical reactions. The metal atoms or ions are the active sites, and many of those having unpaired electrons have been characterized by electron paramagnetic resonance (EPR). The resultant spectra have been used to interpret the oxidation states of the lattice-held ions and the degree of complexation by various ligands. Of current interest are the transition metal ion exchanged zeolites, and the systems consisting of the first row transition metal ions in Y zeolite, viz., chromium,<sup>2</sup> manganese,<sup>3,4</sup> iron,<sup>5,6</sup> cobalt,<sup>7-9</sup> nickel,<sup>2,10</sup> and copper,<sup>10-22</sup> have been the most intensively studied by EPR. Because of the numerous lattice sites that these ions can occupy, speculation as to the location of these cations in the

dehydrated Y zeolites, with the exception of Mn(II),<sup>3,4</sup> is not usually made. It is generally accepted that the cations in the hydrated zeolites exist as rather free aquo complexes located mainly in the supercages of the zeolite structure.

Unfortunately, little EPR data have been obtained for transition metal containing A zeolites. Due to the simplicity of the A zeolite structure, there are only three nonequivalent sites occupied by monovalent cations, but only one of these general sites (in or near the six rings) usually stabilizes divalent cations.<sup>23</sup> By using diffuse reflectance spectroscopic methods or single crystal x-ray structure determination techniques, the location of Cr(II),<sup>24</sup> Mn(II),<sup>25</sup> Co(II),<sup>26,27</sup> and Ni(II)<sup>28</sup> in dehydrated A zeolites has been asserted. The bare cations are found to be located near the center of the six-ring windows and to be

TABLE I: Experimental EPR Parameters Reported for Copper(II) in Dehydrated Low Ion Exchanged Y Zeolites<sup>a,b</sup>

% Cu(II) exchanged	$g_{\parallel}^1$	$g_{\perp}^1$	$g_{\parallel}^2$	$g_{\perp}^2$	Ref
1	2.377(129)	2.062(20.5)	2.325(160)		11
2			2.33(170) <sup>d</sup>	2.06	12
4	2.35(120)	2.058	2.31(175)	2.058	13
4	2.38(108)	<sup>c</sup>	2.30(175)		14
5	2.386(130)	2.084(16)	2.323(176)	2.048(24)	15
7	2.37(120)	2.07(22)	2.32(160)	2.06	16
10	2.38(107)	2.06	2.30(175)		17
11	2.26(130)	2.062(20)	2.32(154)		18
14	2.38(130)	2.06(13)	2.31(153)		19
14			2.346(160) <sup>d</sup>	2.071(16.4) <sup>d,e</sup>	20
14	2.382(137) <sup>d</sup>	2.077(15) <sup>d</sup>	2.328(171) <sup>d</sup>	2.06(26) <sup>d</sup>	21
14	2.38(126)	2.08	2.32(162)	2.05(22)	22
17	2.38(108)	<sup>c</sup>	2.30(175)	<sup>c</sup>	14

<sup>a</sup> The dehydration procedures used are as follows in order of reference numbers: (11) heat at 383 K in air for 8 h, increase temperature to 473 K for 8 h, and then heat in O<sub>2</sub> at 673 K for 72 h; (12) heat at 673 K; (13) heat at 423 K; (14) evacuate and then heat to 673 K stepwise under a dynamic vacuum; (15) evacuate at 343 K; (16) evacuate overnight and then heat to 773 K; (17) evacuate 1 h and then heat to 773 K stepwise under a dynamic vacuum; (18) evacuate at 373 K, add O<sub>2</sub>, and then evacuate stepwise to 773 K; (19) not given; (20) evacuate and then activate stepwise to 673 K under a dynamic vacuum; (21) heat to 623 K and evacuate 2 h; and (22) evacuate and heat to 472 K in 4-5-h under a dynamic vacuum. <sup>b</sup> Numbers in parentheses are the observed hyperfine splittings (in Gauss unless stated otherwise, 1 G = 1.070 × 10<sup>4</sup> (g<sub>e</sub>/g) cm<sup>-1</sup>). <sup>c</sup> Observed, but the g value was not given. <sup>d</sup> Hyperfine splitting is given in units of 10<sup>4</sup> cm<sup>-1</sup>. <sup>e</sup> A strong line at g ≈ 2.05 was also observed.

TABLE II: Chemical Composition (mequiv g<sup>-1</sup>) of the Hydrated Cu Y Zeolites

Sample	Cu(II)		Na <sup>+</sup>		% Cu(II)	Cu(II) ions per unit cell
	Found	Calcd <sup>a</sup>	Found	Calcd <sup>a</sup>		
CuY-0	0.000	0.000	3.21	3.21	0.0	0.0
CuY-1	0.033	0.032	3.16	3.18	1.0	0.3
CuY-2	0.068	0.070	3.07	3.13	2.2	0.6
CuY-4	0.136				4.3	1.2
CuY-10	0.316	0.314	2.90	2.89	9.8	2.7
CuY-17	0.555				17.4	4.9
CuY-32	1.028				32.0	9.0
CuY-60	1.932				60.2	16.9
CuY-68	2.167	2.170	1.03	1.03	67.8	19.0

<sup>a</sup> The values were calculated from the chemical composition of the parent NaY zeolite and the percent copper(II) (column 6). The degree of hydration was found to be approximately the same for all of the samples (≈ 260 H<sub>2</sub>O/unit cell).

coordinated to three oxygens in the ring. This results in the approximate  $D_{3h}$  ligand field symmetry around the cations.

This symmetry, as well as others, is also possible to attain in the Y zeolites. X-ray structure determinations have been carried out for a dehydrated Cu(II)-Y zeolite (from powder photographs)<sup>29</sup> and for hydrated and dehydrated Cu(II)-faujasite.<sup>30</sup> In both studies, it was found that the copper(II) ions strongly preferred site I' (site I'A in the latter work), which has approximately  $D_{3h}$  symmetry. No attempt has been made to correlate the structural data with EPR results. This might be due to the great variance (shown in Table I) between EPR parameters obtained by different research groups working with similar Cu(II)-Y zeolites. It should be noted that the structural studies made use of highly exchanged zeolites, while most EPR investigations used low exchange levels so that the paramagnetic ions were distributed widely enough to prevent the pairing of copper spins.

The present study was undertaken to correlate sample treatment with the resultant EPR parameters, to clarify the assignment of the parameters to the spectra, and to extend our knowledge of actual copper(II) ion locations in low exchanged Y zeolites.

### Experimental Section

**Materials.** CuNa-Y samples with various Cu(II) contents were prepared from a Linde Na-Y zeolite (lot no. 13544-76). This zeolite was ion exchanged with Cu(N<sub>2</sub>O)<sub>2</sub>·3H<sub>2</sub>O solutions of different concentrations in order

to obtain samples with different Cu(II) contents. The general procedure was to add the zeolite to the Cu(II) solution such that the ratio of solution to solid was 20 cm<sup>3</sup>/g, stir continuously for 4 h at ambient temperature, and then filter the solution and wash the collected zeolite 10 times using a total of 20 cm<sup>3</sup> of H<sub>2</sub>O/g of solid. The zeolite was subsequently dried at ambient temperature in an open vessel placed in a fume hood. The Cu(NO<sub>3</sub>)<sub>2</sub> content of the solution determined the final solution pH, as well as the amount of Cu(II) ion exchanged into the zeolite, e.g., 0.01 M Cu(II): pH 7.1 and CuY-10. The samples are denoted as CuY followed by a figure showing the exchange level of Cu(II) in percent of the total cation exchange capacity. The CuY-2 sample was prepared from a zeolite-0.01 M Cu(II) solution that was made alkaline by the addition of 0.1 M NaOH (final pH 9.0). CuY-68 was obtained by equilibrating the zeolite consecutively with two portions of 0.10 M Cu(II). The composition of the samples is given in Table II. The copper(II) concentrations were determined by atomic absorption measurements following back-exchange of the zeolites by Ag(I).

The sources and purification of the gases used have been previously reported.<sup>17</sup>

**Sample Treatments.** In the usual activation procedure, the zeolites were degassed to either 400 or 500 °C under vacuum (10<sup>-4</sup> Torr) in a conventional EPR batch cell (cell volume to zeolite mass ratio ≈ 200 cm<sup>3</sup>/g). The temperature was raised hourly in 100 °C increments after first evacuating the cell for 0.5-1 h at room temperature. Following this, oxidation was usually carried out at the

maximum dehydration temperature with 50–400 Torr of  $O_2$  for a short period of time. This treatment was usually applied to samples prepared as thin platelets,<sup>14</sup> but identical EPR parameters were obtained when the treated zeolites were in powder form.

Three of the Cu–Y zeolites were subjected to prolonged dynamic evacuation ( $10^{-4}$  Torr) at ambient temperature before being thermally dehydrated using the temperature programming given above. Following various periods of the initial evacuation, the samples were cooled to 77 K and EPR spectra were obtained. After warming to room temperature, the evacuation was continued. Water vapor was added to the samples in 20-Torr portions following the thermal activation. In this series of experiments, powdered zeolites were used.

In another set of experiments, the samples were subjected to various reduction and reoxidation treatments after dehydration. In the Results section, reference will be made to the following reduction procedures: (I) activate to 500 °C and reduce with 50 Torr of  $H_2$  at 500 °C for 3 h; (II) reduce with 300 Torr of  $H_2$  at 500 °C for 18 h; (III) dehydrate to 400 °C, oxidize with 50 Torr of  $O_2$  for 0.25 h at 400 °C, and reduce three times with 300 Torr of  $H_2$  for 1 h at 200 °C; (IV) dehydrate to 200 °C and reduce at 200 °C with 300 Torr of  $H_2$  for 2 h; (V) activate to 400 °C and reduce with 400 Torr of  $H_2$  at 200 °C for 0.25 h; (VI) dehydration to 500 °C, equilibration with 300 Torr of CO at 500 °C for 3 h, evacuate 2 h and equilibrate with 23 Torr of NO for 2 h, evacuate and add 265 Torr of CO at 500 °C, equilibrate for 2 h and then evacuate 0.5 h; (VII) dehydration at 400 °C and reduction by six treatments at 400 °C with 400 Torr of CO (total reduction time 66 h); and (VIII) oxidize with 500 Torr of  $O_2$ , evacuate, and then reduce with 300 Torr of CO at 500 °C for 3 h. The reoxidation treatments used were the following: (IX) heat for 3 h at 500 °C in the presence of 50 Torr of  $O_2$ ; (X) oxidize with 300 Torr of  $O_2$  at 500 °C for 18 h; (XI) equilibration with 20–22 Torr of NO at ambient temperature; (XII) add 43 Torr of NO and equilibrate at ambient temperature for 14 h; and (XIII) equilibration with 30 Torr of NO at 25 °C for 0.5 h.

**EPR Spectroscopy.** The EPR spectra were obtained at 77 K with a Varian E-6S spectrometer equipped with a TE<sub>102</sub> mode cavity as described previously.<sup>17</sup> The  $g$  values are reported relative to a 2,2-diphenyl-1-picrylhydrazil (DPPH) or phosphorus-doped silicon standard or to a sample of pitch in KCl. Usually the estimated error in the  $g$  values is  $\pm 0.005$  and in the hyperfine splittings is  $\pm 2$  G. However, the estimated errors in the parameters for CuY-1 and CuY-2 are approximately double these figures. Spin concentrations were determined by numerical double integration of the spectra and comparison to a reference spectrum obtained with a single crystal of copper(II) sulfate.

## Results

The preparation of Cu–Y zeolites by ion exchange in aqueous media is a rather straightforward procedure, but a diverse range of treatments can be used to prepare the materials for subsequent chemical, spectroscopic, and catalytic studies. In the present work, the influence on the resultant EPR parameters of CuO in or on a Cu–Y zeolite will be described. The changes in the EPR parameters, especially the parallel hyperfine splittings, obtained for activated Cu(II) ion exchanged Y zeolites for which the duration of evacuation at ambient temperature prior to dehydration was varied will be presented. These parameters will be compared with those obtained by partial reduction of the copper ions with hydrogen or

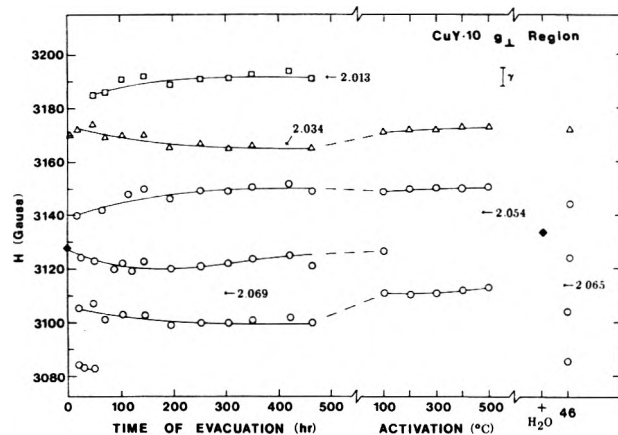


**Figure 1.** The variation of magnetic field position of the  $g_{\perp}$  hyperfine lines of CuY-10 as a function of sample treatment. The final treatment consisted of equilibration with water vapor for 1 h followed by evacuation at 295 K for 46 h.  $\gamma$  is the maximum estimated error (see the Experimental Section) in the  $g$  values, several of which are designated by arrows.

carbon monoxide and with those observed after partial reoxidation of the zeolites by oxygen or nitric oxide.

**Cu-2 Containing CuO.** The air-dried Cu–Y zeolites, except CuY-2, were all light blue with a gradation from nearly white (CuY-1) to a definite blue (CuY-68). CuY-2 was a light brown or tan in color. This sample had been prepared in a solution where the pH had been artificially adjusted to a value of 9, and this resulted in the precipitation of the copper that remained in solution following partial exchange of the zeolite. The initial color of the precipitate was light blue, but the color turned to light brown upon air drying at slightly higher than ambient temperature. The zeolite did not change color upon back-exchange overnight in the dark at approximately 70 °C with silver ions.

The tan color is assumed to be due to CuO, probably in a hydrated state, formed in or on the zeolite. The quantity of this oxide was calculated to be about 0.012 g/g of anhydrous zeolite, but an x-ray powder diffraction pattern of the hydrated sample failed to demonstrate the presence of any crystalline CuO. A portion of anhydrous Na–Y mixed with black 100% CuO (Baker Analyzed) in the proportions given above gave a diffraction pattern of CuO that could be seen only very faintly above the background. The appearance of the mixed sample was an off-white light grayish color. Upon activation of the ion exchanged zeolite sample, a dark grayish color resulted and a set of weak lines corresponding to CuO was detected in the x-ray diffraction pattern of the sample. The presence of CuO in or on the CuY-2 zeolite did not interfere with the EPR analysis of the lattice-held divalent copper ions.

**Evacuation and Thermal Treatments.** A wide variety of activation (dehydration) procedures had been previously employed for Cu–Y zeolites, as is evident from Table I. Some of those involved long periods of evacuation prior to heat treatment, while others used short evacuation or even no evacuation at all. Therefore, the effect of varying the duration of evacuation previous to the activation was studied. The air-dried low exchanged Cu–Y zeolites exhibited one set of  $g$  values with no hyperfine splitting (designated as |A|) observed in the  $g_{\perp}$  region. Upon evacuation at ambient temperature, a second set of EPR parameters arose, and following prolonged evacuation this became the dominant set. As indicated in Table III,  $g_{\perp}^2$  consisted of a single strong line. This line became more intense than the  $g_{\perp}^1$  signal by 6 h of evacuation for CuY-1 and by 18 h of evacuation for CuY-10. Figure 1 indicates

TABLE III: Experimental EPR Parameters<sup>a</sup> Obtained for Cu(II)-Y Zeolites upon Prolonged Evacuation

Treatment <sup>b</sup>	$g_{\parallel}^1$	$g_{\perp}^1$	$g_{\parallel}^2$	$g_{\perp}^2$ <sup>c</sup>	$g_{\perp}^3$ <sup>c</sup>
A. CuY-1					
1 min	2.371(120)	2.042 <sup>c</sup>			
2 h	2.373(122)	2.057(14)		2.029	
27 h	2.364(120)	2.057(16)	2.332(150)	2.025	
92 h		2.057(18)	2.324(150)	2.025	
100 °C, 1 h		2.059(17)	2.320(150)	2.023	
Activate <sup>d</sup>	2.342(138)	2.059(16)		2.021	
+ H <sub>2</sub> O <sup>e</sup>	2.377(122)	2.060(18)		2.022	
18 h		2.055 (18)	2.336(150)	2.024	
B. CuY-2					
1 min	2.360(136)	2.051 <sup>c</sup>			
0.75 h	2.369(122)	2.063(18)		2.033	
15 h	2.372(120)	2.065(18)	2.318(160)	2.030	
40 h	2.372(120)	2.067(19)	2.314(162)	2.030	
65 h	2.369(120)	2.064(19)	2.306(165)	2.028	
184 h	2.361(123)	2.060(19)	2.305(166)	2.025	
Activate <sup>f</sup>		2.065(16)	2.311(155)	2.025	
+ H <sub>2</sub> O <sup>e</sup>	2.36(135)	2.05 <sup>c</sup>			
16 h	2.364(120)	2.062(17)	2.314(160)	2.028	
40 h	2.363(123)	2.061(17)	2.307(168)	2.026	
C. CuY-10					
1 min	2.393(121)	2.053 <sup>c</sup>			
1.5 h	2.370(124)	2.055 <sup>c</sup>			
18 h	2.365(121)	2.063(18)	2.313(162)	2.026	
103 h	2.367(120)	2.064(20)	2.316(160)	2.026	2.011
219 h	2.369(121)	2.069(21)	2.320(159)	2.031	2.017
306 h	2.377(120)	2.074(23)	2.328(158)	2.034	2.013
465 h	2.376(118)	2.074(23)	2.325(158)	2.034	2.013
100 °C, 1 h	2.377(122)	2.061(20)	2.326(161)	2.028	
Activate <sup>f,g</sup>	2.378(124)	2.060(20)	2.325(164)	2.025	
+ H <sub>2</sub> O <sup>e</sup>	2.392(130)	2.056 <sup>c</sup>			
46 h	2.372(119)	2.056(20)	2.320(161)	2.027	

<sup>a</sup> Numbers in parentheses are the hyperfine splittings (given in Gauss). <sup>b</sup> Time listed is the total duration of evacuation at ambient temperature. <sup>c</sup> The given  $g$  value indicates the center of the perpendicular signal. <sup>d</sup> Heated to 673 K stepwise under a dynamic vacuum, oxidized at 673 K for 5 min with 400 Torr of O<sub>2</sub>, and then evacuated for 1 h at the same temperature. <sup>e</sup> Equilibrium water vapor pressure = 20–22 Torr; equilibrate for 1 h. <sup>f</sup> Heated to 773 K stepwise under a dynamic vacuum. <sup>g</sup> Oxidized for 2 h at 773 K with 50 Torr of O<sub>2</sub> and then evacuated for 68 h.

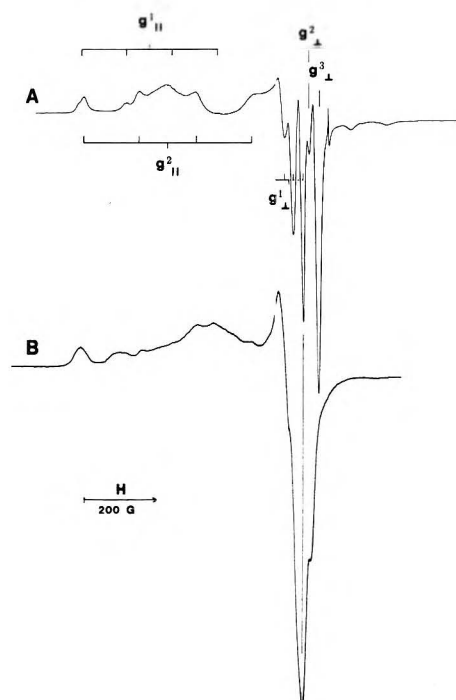


Figure 2. The EPR spectra obtained at 77 K for CuY-10 after being evacuated at ambient temperature for 465 h (A) and then subsequently being activated at 773 K (B) using the stepwise dehydration procedure. The sharp line at high field is due to the phosphorus-doped silicon that was used as a  $g$  value marker.

that for CuY-10 the  $g_{\perp}^2$  signal appeared (as a shoulder) before the  $g_{\perp}^1$  line was split by hyperfine interactions, which occurred after 18 h of evacuation.

From Table III, it is evident that the value of  $g_{\perp}^2$  decreased slightly for CuY-1 and CuY-2 as evacuation proceeded. However, it increased for CuY-10, and this increase was accompanied by the appearance of an additional line in the  $g_{\perp}$  region. This latter signal ( $g_{\perp}^2$ ) appeared after about 48 h of evacuation and grew from a shoulder to the most intense line within 15 h. After 200 h of evacuation,  $g_{\perp}^2$  was a weak signal that almost disappeared as is shown in Figure 2A.

In general, only a slight shifting of the EPR parameters occurred during the evacuation at 25 °C, but definite changes were noticed in the spectra upon activating the samples to 400–500 °C. The spectrum obtained upon activation of CuY-10 is given in Figure 2B, and the EPR parameters are listed in Table III C. Upon rehydration, the sets of  $g$  values collapsed into one set and the spectra resembled those of the starting hydrated zeolites. For CuY-1 and CuY-2, the Mn(II) that was present in the samples as an ion exchanged impurity produced a spectrum (in particular, the first line of the six-line spectrum) which was observable after the rehydration, while for the initial samples it was observable only with CuY-1.

The EPR parameters of the three activated samples (see Table III) were quite different. In contrast, Table IV shows that activation of low exchanged Cu-Y zeolites at 400–500 °C after a brief evacuation yielded  $g$  and  $|A|$  values

TABLE IV:  $g$  Values and Hyperfine Splittings<sup>a</sup> (in G) for Cu-Y Zeolites Dehydrated at 400–500 °C Following a Brief Period of Evacuation ( $\leq 1$  h)

Sample	$g_{\parallel}^1$	$g_{\parallel}^2$	$g_{\parallel}^3$	$g_{\perp}$	$g_{\perp}^1$	$g_{\perp}^2$ <sup>b</sup>
CuY-1	2.378(108)			2.044(21)	2.055(17)	2.027
CuY-2	2.380(110)			2.039(18)	2.051(15)	2.022
CuY-4	2.380(110)	2.300(175)		2.049(21)	2.060(18)	2.030
CuY-10	2.383(108)	2.308(174)	2.36(123)	2.060(20)	2.073(19)	2.040
CuY-17	2.386(108)	2.300(175)	2.36(125)	2.058(20)	2.059(20)	2.037

<sup>a</sup> The numbers in parentheses are hyperfine splitting values. <sup>b</sup> The  $g$  value is obtained from the center of the line.

that were nearly identical. In addition, the parallel hyperfine splittings belonging to the most intense lines ( $g_{\parallel}^1$  and  $g_{\parallel}^2$ ) were entirely different from the splittings listed in Table III. Magnifying the spectra by increasing the receiver gain of the spectrometer resulted in the detection of a third set of hyperfine splittings ( $A_{\parallel}^3$ ). The evacuation technique used was particularly important in determining the EPR parameters. For example, following the evacuation of CuY-10 for only 2 min and then allowing the sample to stand at ambient temperature for 23 h, EPR analysis yielded  $g_{\parallel} = 2.379(131)$  and  $g_{\perp} = 2.056$ , where the number in parentheses is the hyperfine splitting in units of Gauss. After activation to 500 °C, the spectral parallel components were  $g_{\parallel}^1 = 2.371(121)$  and  $g_{\parallel}^2 = 2.304(158)$ , which are approximately the same parameters as those obtained following prolonged evacuation and subsequent activation.

**Reductions with Hydrogen.** The above zeolite sample was reduced using reduction procedure I, and the resulting spectrum is shown in Figure 3A. The Cu(II) concentration was calculated from the spectrum to be approximately 0.15 Cu(II)/unit cell (corresponding to CuY-0.5), and the EPR parameters were observed to be  $g_{\parallel}^1 = 2.364(121)$ ,  $g_{\perp}^1 = 2.060(20)$ ,  $g_{\parallel}^2 = 2.324(160)$ , and  $g_{\perp}^2 = 2.025$ . The low-field ( $m_l = -3/2$ ) components of the two  $g$  values appeared to be resolved, and this agreed with the hyperfine splittings indicated. However, the resolution might be due to or enhanced by resolved hyperfine splittings for the <sup>65</sup>Cu isotope (31% abundance) that are approximately 7% larger than the splittings due to <sup>63</sup>Cu, although such resolution is not noted for the high-field parallel components. From the  $g_{\perp}$  lines, it is apparent that the  $g^1$  signal was more intense than the  $g^2$  line. Upon evacuation for 26 h at ambient temperature, the entire spectrum decreased in intensity. In addition, the  $g_{\perp}^2$  line decreased greatly in intensity while a signal ( $g_{\perp}^3$ ) at  $g = 2.017$  grew to be about as strong as  $g_{\perp}^1$ . No particular change in the  $g_{\parallel}$  region of the spectrum was evident. Reoxidation using procedure IX led to complete restoration of the activated Cu(II)-Y spectrum with EPR spectral components in the parallel region of  $A_{\parallel}^1 = 120$  G and  $A_{\parallel}^2 = 160$  G.

A fresh portion of CuY-10 was evacuated briefly and then activated at 500 °C, and the resultant spectrum yielded the EPR parameters given in Table IV. The sample was then reduced using reduction procedure II and reoxidized after evacuating for 0.25 h at the elevated temperature by using reoxidation procedure X. The reduced sample was bright reddish-pink (x-ray powder diffraction demonstrated the presence of metallic copper crystallites having diameters of at least 30 nm when another portion of CuY-10 was activated and reduced using the same procedure) and did not exhibit an EPR signal. The reoxidation converted 74% of the copper to divalent copper held in lattice sites, as determined from the intensity of the EPR spectrum, and the EPR parallel parameters of the reoxidized zeolite were  $g_{\parallel}^1 = 2.380(109)$  and  $g_{\parallel}^2 = 2.302(172)$ . After subjecting the sample to reoxidation procedure X for a second time, an EPR spectrum

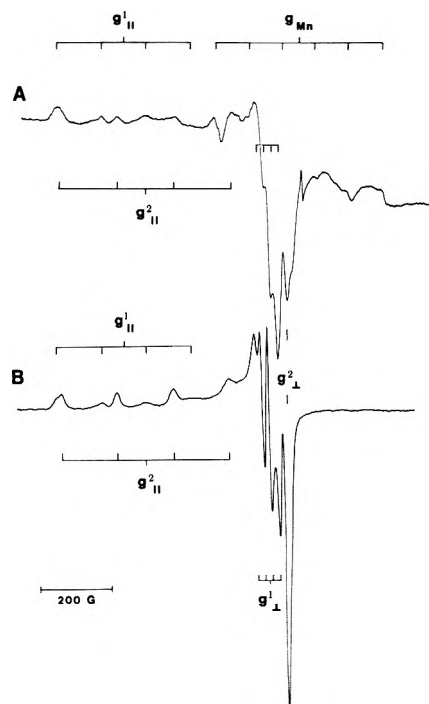


Figure 3. The EPR spectra of hydrogen reduced samples of (A) CuY-10 and (B) CuY-68 that were treated as follows: (A) reduction procedure I after equilibrating in vacuo for 23 h and (B) reduction procedure III.

with unchanged parameters was obtained with an intensity equivalent to 92% of that obtained with the initial activated sample. Although the sample appeared light gray, x-ray diffraction analysis failed to show the presence of CuO.

After evacuating for 1 h at room temperature, a sample of CuY-68 was reduced using reduction procedure III, and the H<sub>2</sub> was then evacuated at 200 °C for 0.25 h. The EPR spectrum shown in Figure 3B was obtained, where the calculated Cu(II) concentration was 0.4 Cu(II)/unit cell (equivalent to CuY-1.4), and the experimental parameters were  $g_{\parallel}^1 = 2.361(126)$ ,  $g_{\perp}^1 = 2.059(20)$ ,  $g_{\parallel}^2 = 2.315(155)$ , and  $g_{\perp}^2 = 2.023$ . The latter set of  $g$  values was the more intense set and no evidence of  $g_{\perp}^3 = 2.017$  was found. After recording the above spectrum, the sample was completely reduced at 400 °C with hydrogen and then reoxidized for 5 days according to procedure XI. The subsequent EPR spectrum indicated the Cu(II) content at lattice sites to be equivalent to CuY-1.5; the observed parameters were  $g_{\parallel}^1 = 2.371(125)$ ,  $g_{\perp}^1 = 2.066(19)$ ,  $g_{\parallel}^2 = 2.322(156)$ , and  $g_{\perp}^2 = 2.033$ . The same parameters were obtained by reduction of CuY-68 according to procedure IV following a 1-h evacuation.

A sample of CuY-60 was activated to 500 °C, completely reduced using reduction procedure II, and evacuated for 1 h at the elevated temperature. After adding oxygen at approximately 450 °C, reoxidation procedure IX was carried out. At the given pressure of oxidant, less than 50% of the copper was reoxidized to Cu(II). The resultant EPR spectrum indicated that approximately 50% of the

TABLE V: EPR Parameters<sup>a</sup> for the Spectra of CuY-10 Shown in Figure 4

Spectrum	$g_{\parallel}^1$	$g_{\perp}^1$	$g_{\parallel}^2$	$g_{\perp}^2$	$g_{\parallel}^3$
A	2.374(126)	2.083 <sup>b</sup>			
B	2.385(109)	2.054(13)			
C	2.385(109)	2.051(13)	2.305(172)	2.025 <sup>b</sup>	
D	2.380(110)	2.052(13)	2.304(170)	2.025 <sup>b</sup>	2.367(122)

<sup>a</sup> The numbers in parentheses are the hyperfine splittings (in Gauss). <sup>b</sup> The  $g$  value indicates the center of the perpendicular line.

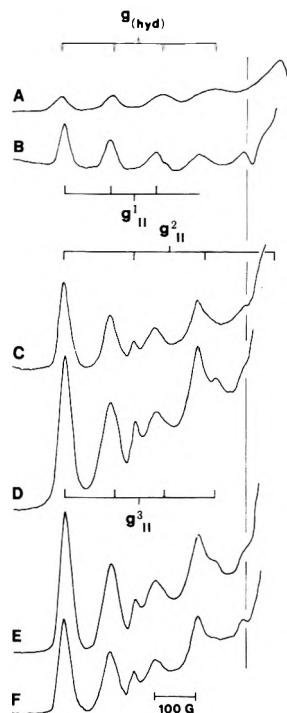


**Figure 4.** The EPR spectra of CuY-10 observed after the following consecutive treatments: (A) evacuation at 298 K for 0.5 h; (B) reduction procedure VI and reoxidation procedure XII; (C) heating at 473 K for 0.5 h; (D) evacuation for 0.5 h at 473 K and then 0.5 h at 573 K; (E) evacuation at 773 K for 16.5 h; and (F) reoxidation procedure XIII.

reoxidized copper existed as spin-paired copper ions with  $g_i = 2.16$  and with the remaining copper ions having spectral parallel components of 128 G ( $A_{\parallel}^1$ ) and 159 G ( $A_{\parallel}^2$ ). For comparison, CuY-32 was reduced to CuY-17 using reduction procedure V. The EPR parameters were  $g_{\parallel}^1 = 2.359(124)$ ,  $g_{\perp}^1 = 2.059(20)$ ,  $g_{\parallel}^2 = 2.306(157)$ , and  $g_{\perp}^2 = 2.022$ , where the  $g^1$  set was more intense than the  $g^2$  set. The  $g_{av}$  values corresponding to the  $g^1$  and  $g^2$  sets of parameters for the three partially hydrogen-reduced samples were  $2.160 \pm 0.001$  and  $2.121 \pm 0.004$ , respectively, where  $g_{av} = (g_{\parallel} + 2g_{\perp})/3$ .

**Reductions with Carbon Monoxide.** The partial reductions described above were carried out using hydrogen gas as the reducing agent, while the following reductions were carried out using carbon monoxide so that water could not be formed. After evacuating for 0.5 h, CuY-10 was reduced using procedure VI and reoxidized by procedure XII. The spectra obtained for the  $g_{\parallel}$  region are shown in Figure 4. No Cu(II) signal was observed after the reduction and, although the sample was white, the distinctive EPR spectrum of the Cu<sup>+</sup>-NO complex<sup>31</sup> was not apparent upon the addition of NO as the oxidant. The reasons for this have been discussed elsewhere.<sup>17</sup> The signal marked by the light vertical line in Figure 4 is the first line of the Mn(II) spectrum. The amplifications of spectra B and C and of spectra D, E, and F are approximately 64 and 51 times, respectively, that of spectrum A. The set of splittings corresponding to  $g_{\parallel}^3$  disappeared upon addition of NO but reappeared upon equilibration for 3

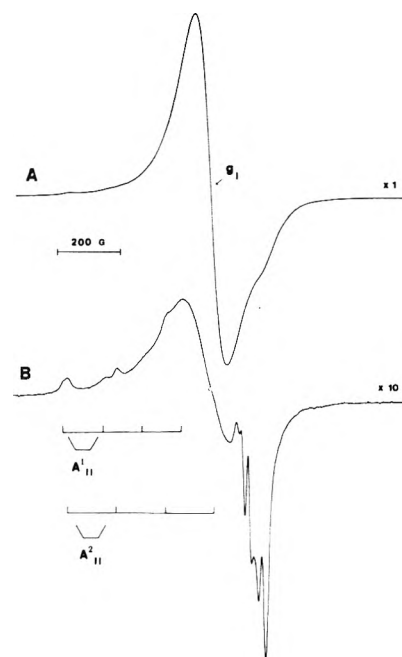


**Figure 5.** The EPR spectra of CuY-60 following stepwise activation to 773 K (A), oxidation with O<sub>2</sub>, and subsequent reduction with CO at 773 K for 3 h (B).

days. Following a 0.5-h heat treatment at 200 °C, mass spectrometric analysis showed that part of the NO had been converted into N<sub>2</sub> (along with a small quantity of N<sub>2</sub>O). After evacuation of these gases,  $g_{\parallel}^3$  was quite pronounced. The EPR parameters of the spectra in Figure 4 are listed in Table V, and it can be noted that two  $g_{\perp}$  values were observed, but a third could not be discerned.

Reducing a CuY-60 sample using reduction procedure VII, a sample corresponding to CuY-2.4 was obtained that exhibited the following EPR parameters:  $g_{\parallel}^1 = 2.378(123)$ ,  $g_{\perp}^1 = 2.073(20)$ ,  $g_{\parallel}^2 = 2.325(159)$ , and  $g_{\perp}^2 = 2.035$ . The intensities of the two sets of  $g$  values were approximately equal, and the spectrum indicated that no spin-paired copper was present. This sample was then completely reduced with CO at 500 °C and subsequently reoxidized using procedure XI. After 20 h, a Cu(II) EPR signal was barely visible above the very strong Cu<sup>+</sup>-NO spectrum. After standing for 68 h, an evacuation was carried out for 2 h, which destroyed the Cu<sup>+</sup>-NO complex and yielded a Cu(II) signal proportional to that of CuY-3. The two sets of parameters of similar intensity were  $g_{\parallel}^1 = 2.378(123)$ ,  $g_{\perp}^1 = 2.071(19)$ ,  $g_{\parallel}^2 = 2.320(155)$ , and  $g_{\perp}^2 = 2.038$ .

Beginning with a fresh sample of CuY-60, activation was carried out to 500 °C after a 1-h evacuation period. The resultant EPR spectrum was typical of Y zeolites highly exchanged with Cu(II) ( $g_i = 2.16$ ) and is shown in Figure 5A. Reduction procedure VIII was then carried out, and spectrum exhibited in Figure 5B was subsequently obtained. The indicated hyperfine splitting values were  $A_{\parallel}^1 = 128$  G and  $A_{\parallel}^2 = 154$  G, while the isotropic line demonstrated that spin-paired copper ions were still present. Analysis of the gas phase over the reduced zeolite by mass spectrometry showed that CO<sub>2</sub> had been formed during

the reduction. The remaining Cu(II) ions were reduced by two more CO treatments and then reoxidation procedure IX was applied. The intensity of the EPR spectrum that resulted was intermediate between those of the spectra in Figure 5, while the  $A$  values observed after the first CO reduction were regenerated. Spectrum 5B approximates those obtained by partial reduction and partial reoxidation of CuY-60 using hydrogen.

## Discussion

**Evacuation of Cu-Y Zeolites.** Upon evacuation of the low exchanged zeolites, e.g., CuY-1, CuY-4, and CuY-10, for 1 min to remove oxygen from the sample cell, a rather uniform set of EPR parameters were usually obtained, viz.,  $g_{\parallel} = 2.38 \pm 0.01$ ,  $g_{\perp} = 2.05 \pm 0.001$ , and  $A_{\parallel} = 122 \pm 3$  G. However, as observed in Table III, a hyperfine splitting of 136 G was found for CuY-2, but upon further evacuation the value decreased to approximately 120 G. Upon repeating the experiment with a fresh portion of CuY-2, identical results were obtained. Similar high initial splittings for CuY-10 and CuY-32 were obtained (135 G in each case) by evacuating the sample cell for only 0.25 min instead of 1 min. The latter hyperfine splitting value was also observed for these materials when the evacuation step was eliminated. Therefore, the presence of CuO in or on CuY-2 seemed to influence the hyperfine splitting value observed in the EPR spectrum after a brief evacuation, perhaps by hindering and delaying the removal of water from the supercages of the zeolite.

The set of parameters with values of  $g_{\parallel} \approx 2.38(135)$ ,  $g_{\perp} \approx 2.05$ , and  $g_{av} \approx 2.16$  is assigned to the hexaaquocopper(II) complex. For comparison,  $\text{Cu}(\text{H}_2\text{O})_6^{2+}$  in a 60% glycerine-40% water mixture at 253 K was found to have  $g_{av} = 2.199$  with  $g_{\parallel} = 2.400$  ( $\sim 137$ ) and  $g_{\perp} = 2.099$  ( $\sim 13$ ).<sup>32</sup> It is evident that the present experimental  $g_{av}$  value is lower than the frozen solution value,<sup>32</sup> and it is also lower than the  $g_{av}$  values of 2.192 and of 2.194 attributed to the hexaaquo complex exchanged into Dowex 50W.<sup>33,34</sup> Evacuation of the zeolites for 1-2 h resulted in the anisotropic spectrum with the approximate EPR parameters of  $g_{\parallel} = 2.37(122)$ ,  $g_{\perp} = 2.06(18)$ , and  $g_{av} = 2.16$ . This spectrum might be due to Cu(II) ions in a more-or-less square based penta-coordinated environment. Upon prolonged evacuation, a third set of parameters arose (see Table III) with  $g_{av} = 2.12$ -2.13. This set is attributed to the tetraaquocopper(II) complex, and the  $g_{av}$  value can be compared with that of  $g_{av} = 2.135$  for the square-planar  $\text{Cu}(\text{NH}_3)_4^{2+}$  complex in Y zeolites.<sup>14</sup> The aquo complexes were not observed to be in a solution-like environment in these zeolites insofar as dynamic Jahn-Teller distortions<sup>35</sup> and rapid tumbling<sup>36</sup> did not average the anisotropy nor appreciably broaden the spectra even at room temperature. It should be pointed out that  $g_{av}$  is the pseudoisotropic value of  $g_i$  that would be found at ambient temperature in solution when the viscosity is such as to allow the molecules to tumble freely. This assumes that no change in structure or bond lengths occurs upon freezing.

Addition of axial ligands to a square-planar copper(II) complex leads to an increase in the value of  $g$  and a decrease in  $A_{\parallel}$  (when the magnitude of  $A_{\parallel}$  is negative, as it is for most copper(II) complexes). Considering the parameters observed for the hexaaquo and tetraaquo complexes, values of  $g_{\parallel} = 2.35$ -2.38 and  $A_{\parallel} \leq 160$  G would be expected for a square-pyramidal-type of pentaquo-copper(II) complex. Considerable error might be involved in these estimates because the fifth ligand would tend to pull the copper ion out of the plane of the four equatorial ligands, and this should result in a decrease in the in-plane bonding strength, which would lead to an increase in the

$g$  values. The effect on the hyperfine splittings is less certain. Analogous to this treatment would be the situation where one of the weak axially coordinated water ligands would be replaced by a stronger ligand. This might be the case if the pentaquo complex were attracted to the zeolite skeletal wall in the sixth coordination site, such as might occur when much of the zeolitic water is removed by evacuation at ambient temperature for a short time. Thus, in fact, the Cu(II) ion is probably still six coordinate, but the interaction with the zeolite results in nonequivalent axial ligand fields and produces a pseudo-five-coordinate environment around the copper ions.

In addition to the EPR parameters attributed to the aquo complexes, a symmetric line at  $g = 2.27$  with a peak-to-peak width of  $\approx 100$  G appeared after evacuating CuY-2 for about 15 h. This line grew in intensity for the next 50 h, after which the intensity became constant. This  $g$  value is the same as that reported for CuO.<sup>37</sup> Upon activating the zeolite to 500 °C for 3 h under a dynamic vacuum, the signal disappeared but reappeared after rehydration of the sample with water vapor. These observations indicate that the symmetric line should probably be attributed to a disordered surface species such as  $[\text{Cu}(\text{OH})_n]^{2-n}$  or  $[\text{Cu}(\text{H}_2\text{O})_n]^{2+}$  rather than to CuO. A symmetric line such as this was not evident with CuY-1 nor with CuY-10.

**Activated and Reduced Cu-Y Zeolites.** Figures 1 and 2A indicate that upon prolonged evacuation of CuY-10, three  $g_{\perp}$  values were observed. Subsequent activation resulted in spectrum B of Figure 2, where the  $g_{\perp}$  portion of this spectrum is identical with the spectrum obtained by dehydration following a brief evacuation period (values given in Table IV), and an illustration of the latter spectrum is given elsewhere.<sup>17</sup> The  $g_{\perp}$  value is usually quoted to be  $\approx 2.06$  (see Table I), but in reference to Figure 1 and the spectra in Figure 2 it seems evident that two  $g_{\perp}$  values should be assigned instead, and these would correspond to the  $g_{\perp}$  values of the two strongest signals observed for the thermally activated samples. This would result in the  $g_{\perp}$  value given in Table IV to be converted from  $g_{\perp} = 2.05 \pm 0.01$  to  $g_{\perp}^1 = 2.06 \pm 0.01$  and  $g_{\perp}^2 = 2.03 \pm 0.01$ . The two weak high field lines in Figure 2, as well as a line near the third  $g_{\parallel}^1$  line ( $m_l = +1/2$ ) result from a monoquo- or diaquocopper(II) complex that will not be discussed here.

A strong  $g_{\perp}^3$  line is evident in Figure 2A, although a set of corresponding  $g_{\parallel}^3$  lines differing from  $g_{\parallel}^1$  and  $g_{\parallel}^2$  was not observed. Considering the data in Table III,  $g_{\parallel}^3$  and  $A_{\parallel}^3$  must approximate the  $g_{\parallel}^2$  parameters, e.g.,  $g_{\parallel}^3 = 2.32$  and  $A_{\parallel}^3 = 155$  G. Upon activation, the  $g_{\parallel}$  parameters changed very little but  $g_{\perp}^3$  disappeared and  $g_{\perp}^2$  showed a growth in intensity. In addition, there is a diminution in the overall EPR intensity. Since  $g_{\parallel}^1$ ,  $g_{\parallel}^2$ ,  $A_{\parallel}^1$ , and  $A_{\parallel}^2$  change very little in magnitude, especially for CuY-10, similar symmetries surrounding the Cu(II) ions are indicated for the evacuated and the activated zeolites. Upon rehydration, the copper(II)-hexaaquo complex was easily re-formed, and the loss in EPR intensity was regained.

Activation following a brief evacuation resulted in different EPR parameters, which were given in Table IV. Under these conditions, the zeolites proceed from a hydrated state to a dehydrated state rather quickly, and it might be expected that most of the Cu(II) ions would be rapidly stripped of their waters. The parameters of  $g_{\parallel}^1 = 2.38(110)$  and  $g_{\perp}^1 = 2.06(18)$  for the resultant zeolites demonstrate that the Cu(II) geometry is axial and is either (a) of a type between square-coplanar and tetrahedral, (b) a square-pyramidal configuration, or (c) a rhombically or



tetragonally elongated octahedral configuration with the complex having rather strong covalent bonding.<sup>38</sup> A Cu(II) ion in a square-coplanar environment would be expected to have a much greater  $|A_{\parallel}|$  value. In case (a),  $|A_{\parallel}|$  would indicate the symmetry to be analogous to compressed tetrahedral, such as that observed for copper-doped dichloro(1,10-phenanthroline)zinc<sup>39</sup> and dichloro(sparteine)zinc(II),<sup>40</sup> for which  $g_{\parallel} = g_z = 2.297(123)$  and  $2.299(90.4)$ , respectively, where the lower  $g$  values result from coordination through nitrogen rather than oxygen and where the unpaired electron is assigned to the  $d_{xy}$  orbital. Case (b) would not occur in a dehydrated copper(II)-Y zeolite, and case (c) would not be expected to make much of a contribution with copper(II) ion exchanged zeolites although site I in the hexagonal prism<sup>41</sup> could supply an octahedral environment. It is well known that divalent copper does not show an affinity for site I.<sup>29,30</sup> Most of the cation sites in Y zeolite have trigonal  $C_{3v}$  or  $D_{3h}$  symmetry. It is pertinent to note that Klier et al. have presented calculations<sup>42</sup> which indicate that the Cu(II) ions in these locations may lie off of the trigonal axis such that two O(3) (or O(2)) lattice atoms are closer to the cation than the third O(3) (or O(2)) atom. This would correspond to a distorted trigonal symmetry (possibly noncoplanar) with the unpaired electron in the  $d_{x^2-y^2}$  or  $d_{xy}$  orbital. Although  $g_{xx}$  and  $g_{yy}$  should then be different, it is expected that the difference would be too small to detect using powdered samples. It is of interest to note that  $g_{\parallel} = g_z = 2.252(181)$  for copper-doped tetrapyrizidinezinc(II) peroxydisulfate,<sup>43</sup> where the distortion is from a square configuration ( $d_{x^2-y^2}$  orbital) rather than a tetrahedral one.

Partial reduction of highly exchanged Cu(II)-Y zeolites which had been quickly dehydrated yielded the same EPR parameters as those observed for activated samples of low Cu(II) content that had been subjected to a prolonged evacuation treatment (hyperfine splittings of about 125 and 160 G, see Figures 2A and 3B). Since this is true when using either  $H_2$  or CO as the reducing agent, it appears that the EPR parameters derived from the extensively evacuated samples were not due to  $Cu(OH)_n$  species. Partial reoxidation of the reduced materials at either ambient temperature or at elevated temperatures using  $O_2$  or NO regenerated the same spectra, the EPR parameters of which are now attributed to divalent copper ions located in the small cages since these ions are the last ones to undergo reduction. However, the behavior of the lower Cu(II)-containing Y zeolites was somewhat different. Although the exhibited  $A_{\parallel}$  values for the latter samples that had been subjected to prolonged evacuation followed by activation, partial reduction, and reoxidation fit the pattern described above, e.g., see Figure 3A, the CuY  $\leq 17$  samples that were quickly dehydrated did not. These samples yielded hyperfine splittings of approximately 110 and 175 G as reported in Table IV. Upon reoxidation with NO (Figure 4) or  $O_2$  at ambient or elevated temperature, the latter  $A_{\parallel}$  values were regenerated. This suggests that the location of copper ions in Y zeolites is dependent upon the exchange level (that is, upon the number of sodium ions, which can block the 6-ring windows between the supercage and sodalite units, that remain in the unit cell), as well as the sample treatment.

*Consideration of the Redox Cycle and Cation Locations.* The above discussion demonstrates that the activation technique employed determines the location of the remaining copper(II) ions in partially reduced Cu-Y zeolites, where all of the zeolites under consideration were exchanged with the divalent cation from aqueous solutions using short equilibration times. Following complete re-

duction at high temperatures, reoxidation resulted in the observation that the first reoxidized copper(II) ions were located in the same type of sites as those occupied by the last Cu(II) ions to undergo reduction. This was demonstrated by the following events:

- prolonged evacuation of CuY-10 prior to thermal treatment resulted in the same EPR parameters [ $g_{\parallel}^1 = 2.37(125)$ ,  $g_{\perp}^1 = 2.06(20)$ ,  $g_{\parallel}^2 = 2.32(160)$ , and  $g_{\perp}^2 = 2.03$ ] after activation, after partial reduction by hydrogen, as well as after reoxidation by oxygen following complete reduction;
- "fast" evacuation of CuY-10 for 1 h prior to thermal treatment resulted in a different but constant set of EPR parameters [ $g_{\parallel}^1 = 2.38(110)$ ,  $g_{\perp}^1 = 2.06(20)$ ,  $g_{\parallel}^2 = 2.30(175)$ , and  $g_{\perp}^2 = 2.03$ ] following the same three treatments as in case (a);
- "fast" evacuation of CuY-10 prior to thermal treatment resulted in the same EPR parameters as those for case (b) when carbon monoxide rather than hydrogen was used as the reductant and nitric oxide was used as the oxidant instead of oxygen;
- "fast" evacuation of highly exchanged samples, e.g., CuY-32, 60, and 68, resulted in the EPR parameters given in case (a) upon partial reduction with hydrogen and after partial reoxidation by oxygen following complete reduction of Cu(II) ions;
- "fast" evacuation of CuY-60 resulted in the same EPR parameters as cases (a) and (d) following partial reduction by carbon monoxide and after partial reoxidation with nitric oxide at ambient temperature following complete reduction of the copper(II) ions.

Thus, these examples show that the zeolites exhibit a memory effect or that some of the copper ions were reduced in place and did not undergo migration even at 773 K during the reduction.

The possible mechanisms for the hydrogen reduction of Cu-Y zeolites have been previously discussed.<sup>17,44,45</sup> The quantity of hydrogen consumed during a mild reduction is approximately stoichiometrically equivalent to the number of copper ions reduced to the univalent state,<sup>17,46</sup> and the rate-limiting step has been suggested to be the migration of Cu(II) ions from the small cages to the supercages where reduction occurs.<sup>44</sup> This is expected to be true also when the larger CO molecule is used as the reductant. Support for this is provided by the general observations that the presence of water increases the rate of hydrogen reduction and the presence of ammonia increases the rate of carbon monoxide reduction of divalent copper. However, it would appear that the Cu(I) ions can easily migrate back into the small cages since the rate-determining step for further reduction and for reoxidation has been proposed to be the migration of the univalent cation from the small cages back into the supercages.<sup>44</sup> This might again suggest a memory effect of the Y zeolite lattice.

Hydrogen reduction of Cu-Y zeolites under more severe conditions results in a hydrogen consumption that can approach the quantity required for complete reduction of Cu(II) to Cu(0).<sup>44</sup> It has been shown for highly exchanged Cu-Y zeolites that at 673 K the reduction to metallic copper is incomplete<sup>17,45</sup> and some of the consumed hydrogen is held in a copper hydride moiety,<sup>45</sup> although large (on the order of 30 nm) copper crystallites are found. It has now been demonstrated that the reoxidation of Cu(0), as well as of the copper hydride species, resulted in the regeneration of the EPR spectra obtained after the initial activations. In the cases where a quantity of CuO was

formed upon reoxidation, an additional prolonged or more severe reoxidation converted at least part of the CuO into the desired lattice-held copper(II) ions. The memory effect might, at first thought, simply depend upon the localized formation of hydroxyl groups or oxygen vacancies created during the reduction process. Although hydroxyl groups and water have been shown by infrared and volumetric techniques to be qualitatively present after reduction of Cu-Y zeolites,<sup>17</sup> a study utilizing diffuse reflectance spectroscopy has failed to detect these moieties following prolonged reduction, where the method is estimated to be able to detect 0.01 water molecule and 0.1 hydroxyl group per copper atom.<sup>45</sup> In addition, it might be expected that simple oxidation of the Y zeolite by oxygen should destroy any hydroxyls or lattice oxygen vacancies present. Thus, the possible memory effect requires further investigation.

Figure 4 and Table V demonstrate that, upon reoxidation of a reduced CuY-10 sample that had been quickly evacuated initially, the first hyperfine splitting value observed was  $A_{\parallel}^1 = 109$  G. This was followed by the appearance of  $A_{\parallel}^2 = 172$  G and then by  $A_{\parallel}^3 = 122$  G. This was the same order observed for quickly evacuated activated samples as the copper(II) content was sequentially increased (Table IV). Upon prolonged evacuation of CuY-10,  $A_{\parallel}^2 \approx 160$  G was observed to be more intense than  $A_{\parallel}^1 \approx 120$  G (Figure 2A), which was the same ordering as those observed for partially reduced highly exchanged Cu-Y zeolites (Figures 3B and 5B). These observations show that a certain site in each case is energetically preferred over other sites. However, upon nearly complete reduction of divalent copper ions in these Y zeolites, the intensities of the two sets of lines become approximately equal, refer to Figure 3A. This might indicate that the copper(II) ions yielding  $A_{\parallel}^2 = 160$  G are slightly more exposed than are those that produce  $A_{\parallel}^1 = 120$  G. This is in contrast to the expectation when considering the sequential appearance of lines for quickly evacuated samples (Table IV) and for the slowly reoxidized samples (Table V and Figure 4), if the assumption is made that the  $A_{\parallel} \approx 120$  G hyperfine splitting is due in each case to Cu(II) ions in the same lattice site. Therefore, an unambiguous assignment of EPR parameters to copper(II) ions in specific lattice exchange sites cannot yet be made.

*Correlation with Other Studies.* A structure determination has been completed for dehydrated CuY-57 using powder diffraction data,<sup>29</sup> and the EPR spectrum of such a sample would consist of a single symmetric line, such as the one shown in Figure 5A, narrowed by spin exchange interactions between Cu(II) ions. A low ion exchanged Cu-Y sample dehydrated according to the procedure used for CuY-57 (heated in oxygen before evacuation) would exhibit  $g_{\parallel}^1 = 2.37(125)$ ,  $g_{\perp}^1 = 2.06(20)$ ,  $g_{\parallel}^2 = 2.32(160)$ , and  $g_{\perp}^2 = 2.03$ , e.g., see the first entry in Table I. This is also true of the activation treatment reported for the fully exchanged faujasite, for which the locations of the copper ions have been reported.<sup>30</sup> Even though the Si/Al ratios are the same within experimental error for the materials used in the structural studies, the distribution of aluminum atoms might not be the same in the synthetic Y zeolite as in the natural faujasite. However, the reported locations of the Cu(II) ions in the two structures are in good agreement, e.g., 11.1 Cu<sup>2+</sup> in site I'<sup>29</sup> vs. 11.4 and 2.8 Cu<sup>2+</sup> ions in I'A and I'B, respectively,<sup>30</sup> where I'A corresponds closely to site I'. This agreement shows that the distributions of aluminum atoms in the natural faujasite and synthetic Y zeolite samples must be very similar.

The structure determination of the highly exchanged hydrated Cu(II)-faujasite, prepared by equilibration in a

divalent copper solution for 3 weeks at ambient temperature, indicated the presence of 6.3 Cu(II) ion/unit cell in the sodalite cage in site I', while the remaining metal ions were not located.<sup>30</sup> From consideration of ion exchange data, it has been proposed that in low Cu(II) exchanged Y zeolite samples prepared by using equilibration times of 2 weeks, the aquocopper(II) complexes are preferentially held in the sodalite cages.<sup>47</sup> In contrast, an equilibration time of 16 h yielded Cu-Y samples in which the supercages contained all of the aquocopper(II) species.<sup>48</sup> Following activation, most of the divalent ions were located in the small cages.<sup>30,48</sup> This agrees with a recent study of the conductivity and dielectric dispersions of a few zeolites in which relaxation measurements on a dehydrated Cu(II)-Y zeolite indicated copper migration within the sodalite unit.<sup>49</sup> Since the Cu-Y zeolites in the present study were prepared by equilibration in the exchanging solutions for only 4 h, the proposal that the Cu(II)-aquo complexes are in the supercages is in agreement with the sitings previously reported. The copper(II) ion exchange process in Y zeolites appears to be analogous to the two steps (fast and slow) observed for the exchange of Ca<sup>2+</sup> into Na-X zeolite,<sup>50,51</sup> where the slow step is the migration of Ca<sup>2+</sup> into the small cages.

## Conclusions

When the ion exchange of Na-Y zeolites with low concentrations of copper(II) is carried out at ambient temperature with short equilibration times, e.g., 4 h, the exchanged hydrated copper(II) ions are located in the supercages. The free rotation of these complexes is hindered, probably by orientation through hydrogen bonding between the coordinated water and the negatively charged zeolite lattice. It appears that rapid dehydration tends to leave the divalent cations in the supercages, where the cations exhibit distinctive EPR parameters, but slow dehydration by prolonged evacuation allows the Cu(II) ions to migrate into the small cages. Following activation, cations in the latter positions exhibit a different distinctive set of EPR parameters and are the last divalent ions to undergo high temperature reduction. As the Cu(II) content of the zeolite increases and the Na<sup>+</sup> content decreases, rapid dehydration tends to yield copper(II) ions located in both supercage and small cage sites. The EPR parameters obtained upon partial reduction and reoxidation are the same as those exhibited by the particular sample following one of the dehydration procedures prior to reduction. Thus, the number of Na<sup>+</sup> ions remaining in the zeolite, the time of equilibration used for the Cu(II) ion exchange, and the dehydration procedure can influence the location of copper(II) ions in Y zeolites, and the diverse hyperfine splitting values exhibited in Table I are now understandable.

*Acknowledgment.* We sincerely thank Dr. Jack H. Lunsford for the use of his facilities, for constructive discussions, and for partial support of this research through National Science Foundation Grant No. CHE-74-08660. We appreciate the helpful and instructive discussions with Dr. Kamil Klier of Lehigh University. Portions of this paper were presented at the 7th Northeast Regional Meeting of the American Chemical Society, Albany, N.Y., August 1976, Abstract No. 252 and at the 9th Central Regional Meeting of the American Chemical Society, Charleston, W. Va., October 1977, Abstract No. INOR-35.

## References and Notes

- (1) Present addresses: (a) Center for Surface and Coatings Research, Sinclair Laboratory No. 7, Lehigh University, Bethlehem, Pa. 18015;

- (b) Tennessee Temple Schools, 1815 Union Avenue, Chattanooga, Tenn. 37404.
- (2) C. Naccache and Y. Ben Taarit, *J. Chem. Soc., Faraday Trans. 1*, **69**, 1475 (1973).
- (3) T. J. Barry and L. A. Lay, *J. Phys. Chem. Solids*, **29**, 1395 (1968).
- (4) N. N. Tkhomirova, I. V. Nikolaeva, V. V. Demkin, E. N. Rosolovskaya, and K. V. Topchieva, *J. Catal.*, **29**, 105, 500 (1973).
- (5) J. W. Jermyn, T. J. Johnson, E. F. Vansant, and J. H. Lunsford, *J. Phys. Chem.*, **77**, 2964 (1973).
- (6) E. G. Derouane, M. Mestdagh, and L. Vielvoye, *J. Catal.*, **33**, 169 (1974).
- (7) E. F. Vansant and J. H. Lunsford, *Adv. Chem. Ser.*, No. 121, 441 (1973).
- (8) K. A. Windhorst and J. H. Lunsford, *J. Am. Chem. Soc.*, **97**, 1407 (1975).
- (9) R. F. Howe and J. H. Lunsford, *J. Am. Chem. Soc.*, **97**, 5156 (1975).
- (10) P. H. Kasai and R. J. Bishop, Jr., *J. Phys. Chem.*, **77**, 2308 (1973).
- (11) H. B. Slot and J. L. Verbeek, *J. Catal.*, **12**, 216 (1969).
- (12) J. T. Richardson, *J. Catal.*, **9**, 178 (1967).
- (13) U. Krüerke and P. Jung, *Z. Phys. Chem. (Frankfurt am Main)*, **58**, 53 (1968).
- (14) D. R. Flentge, J. H. Lunsford, P. A. Jacobs, and J. B. Uytterhoeven, *J. Phys. Chem.*, **79**, 354 (1975).
- (15) J. Turkevich, Y. Ono, and J. Soria, *J. Catal.*, **25**, 44 (1972).
- (16) C. Naccache and Y. Ben Taarit, *Chem. Phys. Lett.*, **11**, 11 (1971).
- (17) R. G. Herman, J. H. Lunsford, H. Beyer, P. A. Jacobs, and J. B. Uytterhoeven, *J. Phys. Chem.*, **79**, 2388 (1975).
- (18) E. F. Vansant and J. H. Lunsford, *J. Phys. Chem.*, **76**, 2860 (1972).
- (19) I. E. Maxwell and E. Drent, *J. Catal.*, **41**, 412 (1976).
- (20) A. Nicula, D. Stamires, and J. Turkevich, *J. Chem. Phys.*, **42**, 3684 (1965).
- (21) N. G. Maksimov, U. F. Anufrienko, K. G. Ione, and N. A. Shestakova, *Zh. Strukt. Khim.*, **13**, 1020 (1972); Engl. Trans., p 953.
- (22) I. D. Mikheikin, V. A. Shvets, and V. B. Kazanskii, *Kinet. Katal.*, **11**, 747 (1970); Engl. Trans., p 609.
- (23) R. Kellerman and K. Klier in "Surface and Defect Properties of Solids", Vol. 4, M. W. Roberts and J. M. Thomas, Ed., Billing & Sons Ltd., London, 1975, pp 1-33.
- (24) R. Kellerman, P. J. Hutta, and K. Klier, *J. Am. Chem. Soc.*, **96**, 5946 (1974).
- (25) R. Y. Yanagida, T. B. Vance, Jr., and K. Seff, *Inorg. Chem.*, **13**, 723 (1974).
- (26) K. Klier, *Adv. Chem. Ser.*, No. 101, 480 (1971).
- (27) P. E. Riley and K. Seff, *Inorg. Chem.*, **13**, 1355 (1974).
- (28) K. Klier and M. Rálek, *J. Phys. Chem. Solids*, **29**, 951 (1968).
- (29) P. Gallezot, Y. Ben Taarit, and B. Imelik, *J. Catal.*, **26**, 295 (1972).
- (30) I. E. Maxwell and J. J. de Boer, *J. Phys. Chem.*, **79**, 1874 (1975).
- (31) C. C. Chao and J. H. Lunsford, *J. Phys. Chem.*, **76**, 1546 (1972).
- (32) W. B. Lewis, M. Alei, Jr., and L. O. Morgan, *J. Chem. Phys.*, **44**, 2409 (1966).
- (33) C. Heitner-Wirguin and R. Cohen, *J. Phys. Chem.*, **71**, 2556 (1967).
- (34) K. Umazarva and T. Yamabe, *Bull. Chem. Soc. Jpn.*, **45**, 56 (1972).
- (35) A. Hudson, *Mol. Phys.*, **10**, 575 (1966).
- (36) B. R. Mc Garvey in "Transition Metal Chemistry", Vol. 3, R. L. Carlin, Ed., Marcel Dekker, New York, N.Y., 1966, pp 89-201.
- (37) G. Vierke, *J. Chem. Soc., Faraday Trans. 1*, **69**, 1523 (1973).
- (38) B. J. Hathaway and D. E. Billing, *Coord. Chem. Rev.*, **5**, 143 (1970).
- (39) G. F. Kokoszka, C. W. Reimann, and H. C. Allen, Jr., *J. Phys. Chem.*, **71**, 121 (1967).
- (40) S. N. Choi, R. D. Bereman, and J. R. Wasson, *J. Inorg. Nucl. Chem.*, **37**, 2087 (1975).
- (41) For a discussion of the positions of and nomenclature used for lattice sites see J. V. Smith, *Adv. Chem. Ser.*, No. 101, 171 (1971).
- (42) K. Klier, P. J. Hutta, and R. Kellerman, *ACS Symp. Ser.*, **40**, 108 (1977).
- (43) H. G. Hecht and J. P. Frazier, III, *J. Chem. Phys.*, **44**, 1718 (1966).
- (44) P. A. Jacobs, M. Tielen, J.-P. Linart, J. B. Uytterhoeven, and H. Beyer, *J. Chem. Soc., Faraday Trans. 1*, **72**, 2793 (1976).
- (45) J. Texter, D. H. Strome, R. G. Herman, and K. Klier, *J. Phys. Chem.*, **81**, 333 (1977).
- (46) L. Riekert, *Ber. Bunsenges. Phys. Chem.*, **73**, 331 (1969).
- (47) A. Maes and A. Cremers, *J. Chem. Soc., Faraday Trans. 1*, **71**, 265 (1975).
- (48) P. P. Lai and L. V. C. Rees, *J. Chem. Soc., Faraday Trans. 1*, **72**, 1809 (1976).
- (49) R. A. Schoonheydt, W. De Wilde, and F. Velghe, *J. Phys. Chem.*, **80**, 511 (1976).
- (50) R. M. Barrer, J. A. Davies, and L. V. C. Rees, *J. Inorg. Nucl. Chem.*, **31**, 2599 (1969).
- (51) H. S. Sherry, *Adv. Chem. Ser.*, No. 101, 350 (1971).

## Metal-Ammonia Solutions. 10. Electron Spin Resonance. A Blue Solid Containing a Crown Ether Complexing Agent

R. L. Harris and J. J. Lagowski\*

Welch Chemical Laboratory, The University of Texas, Austin, Texas 78712 (Received October 27, 1977)

The results of ESR measurements on liquid and frozen solutions of potassium and 18-crown-6 in ammonia are reported. The results for the liquid state are similar to those previously reported for solutions without 18-crown-6. Three features are observed for frozen solutions which can be explained in terms of two different types of potassium metal species and an ion pair consisting of a "solvated" electron and the potassium cation complexed by the crown moiety. The implications of these results for liquid solution ESR spectra of metal-ammonia solutions are discussed.

### Introduction

During the course of extensive studies of metal-ammonia solutions<sup>1</sup> a number of unusual properties have been discovered. Among the more interesting magnetic properties of these solutions is the narrowness of the electron resonance absorption line. In the most widely accepted theory, the ESR results are explained in terms of motional narrowing of the hyperfine interaction with nitrogen nuclei.<sup>2</sup>

A better understanding of the solvated electron in liquid ammonia could be obtained if a detailed analysis were available on a similar species in the solid state. Many attempts<sup>3</sup> have been made to isolate the ammoniated

electron in the solid state. Various paramagnetic species can be isolated from ammonia and hexamethylphosphorous triamide as trapped paramagnetic centers, but the large number of such species that have been isolated bear little resemblance to those found in solution.

Dye and co-workers<sup>4</sup> have been successful in isolating the sodium anion, a species long presumed to exist in metal-amine solutions, by the judicious use of crown ether complexing agents in ethylamine solutions. Amorphous gold-colored and blue-colored solids have been obtained from a variety of solvents.<sup>5</sup>

In experiments preliminary to the work reported here we were able to obtain blue solids from liquid ammonia

solutions of calcium, sodium, and potassium containing crown ether by evaporating the solvent.<sup>6</sup> These solids behave both thermally and under partial ammonia pressure similarly to those obtained by Dye et al.<sup>5</sup> The most stable blue solid was obtained from potassium-ammonia solutions to which 18-crown-6 had been added. At no time was a bronze phase observed in either potassium- or sodium-ammonia solutions containing 18-crown-6, in spite of the fact that such solutions without 18-crown-6 easily can be made to yield a bronze phase.<sup>7</sup>

Several attempts were made to establish the composition of the blue solid by determining the ammonia-to-hydrogen ratio released upon decomposition. These experiments revealed no consistent composition as indicated by the ratios  $\text{NH}_3:\text{H}_2:\text{K}$  or  $\text{NH}_3:\text{H}_2:\text{crown}$ . The available data therefore suggests that this blue solid is not stoichiometric but is probably an ill-defined amorphous solid or a mixture of species.

The characterization of the blue solid by ESR spectroscopy was undertaken in an attempt to better understand metal ammonia solutions. In our early experiments we noticed that blue-colored ammonia matrices were formed upon freezing potassium-ammonia solutions containing 18-crown-6. The blue ammonia matrix was more resistant to decomposition than the amorphous blue solid obtained by evaporating ammonia from potassium, 18-crown-6 solutions as described above. Accordingly, we are concerned here exclusively with the characterization of the frozen 18-crown-6, potassium-ammonia solutions.

### Experimental Section

18-Crown-6 (1,4,7,10,13,16-hexaoxocyclooctadecane) either was obtained from PCR Inc. and used after sublimation, or made using published procedures. Both the melting point and IR spectra of the ether used in these experiments were identical with the reported data.<sup>8</sup>

Potassium was distilled once in vacuo and used without further purification.

Ammonia was distilled into a steel container and stored over sodium; then it was distilled from sodium prior to use.

The DPPH (2,2-diphenyl-1-picrylhydrazyl, Eastman Kodak certified at 93.9%) standard was powdered and mixed with KCl diluent.

After considerable experimentation the following procedure for determining the ESR spectrum of the blue solid evolved. A weighed amount of 18-crown-6 was placed in a 3-mm Pyrex tube which carried at stopcock and 12/5 glass socket joint. The tube was attached to a vacuum line, and both the tube and 18-crown-6 were well rinsed with anhydrous liquid ammonia. The tube was transferred to a helium atmosphere drybox without exposing the contents to the air. Within the drybox potassium was weighed and inserted into the tube, which was reattached to the vacuum line. Ammonia was condensed into the tube which was then sealed off. After the ESR measurements had been made, the tube was kept at room temperature until the contents had completely decolorized.

The ESR spectra were recorded either directly on a Varian E9 spectrometer using 100-kHz modulation and a resonance frequency of about 9.56 GHz, or were collected with a Nova computer. Spectra recorded with the computer were simultaneous sweeps of both the sample and reference cavities, each comprising 251 points which in turn consisted of 100 averages of the raw data. These spectra were then transferred to a CDC 6400-6600 computer for data analysis as described later.

An ESR tube with potassium iodide and 18-crown-6 dissolved in ammonia gave only the weak Pyrex absorption, detectable only at much higher microwave power than

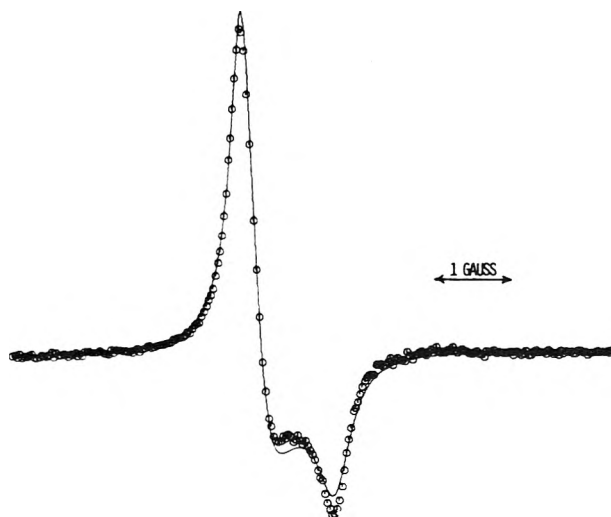


Figure 1a. ESR powder pattern fit (line) to 251 data points (circles) for a potassium, 18-crown-6 ammonia solution at  $-130^\circ\text{C}$ . The sample is 0.20 MPM in potassium and has a potassium/18-crown-6 ratio of 0.33.

that used with any of the other solutions.

The temperature in the ESR cavity was measured by a copper-constantan thermocouple that had been calibrated with slush baths of water ( $0.0^\circ\text{C}$ ), toluene ( $-95^\circ\text{C}$ ), and chloroform ( $-63.5^\circ\text{C}$ ).

The estimated accuracy of the field measurements is  $\pm 0.05\text{ G}$ , but the precision is much better. As a result of using a standard (DPPH) assumed to have the well-known value of 2.00360,<sup>9</sup> the errors we report are relative errors, and hence smaller than the actual accuracy of the  $g$  value measurements.

### Results and Analysis

Data analysis was conducted with a CDC 6400-6600 computer using the subroutines SIMPLEX and STEPIT.<sup>10</sup> Also used were IMSL subroutines for differentiation and integration, as needed.<sup>11</sup> Several of the spectra in which the type I feature dominated (see Figures 1a-d) were fit using these subroutines. These subroutines were also used to fit the liquid solution spectra to shapes<sup>12</sup> as described in the supplementary material (see paragraph at end of text regarding supplementary material). Goodness of fit was estimated using the Hamilton  $R$  factor.<sup>13</sup>

18-Crown-6 is only sparingly soluble in ammonia, but when 18-crown-6 is added to potassium-ammonia solutions, it is soluble to a much greater extent than a one-to-one K:18-crown-6 ratio. The solutions maintain their dark blue color. On cooling the solutions slowly a white precipitate forms; when the solutions are warmed to room temperature, the white precipitate redissolves.

The observed ESR spectra in the liquid state of solutions of 18-crown-6 and potassium in ammonia are narrow signals that approximate a Lorentzian shape. Tables I and II, which are available as supplementary material, contain some examples of the width of these signals at various concentrations.

Upon freezing these solutions, dramatic changes take place in the ESR spectrum. Three different types of features are observed, which for convenience here we arbitrarily designate type I, type II, and type III.

The type I feature dominates Figures 1a-d. The other types of spectra obtained for frozen solutions are shown in Figures 2a-3. The type II feature has the shape usually associated with conduction electron spin resonance (CESR) signals, and the type III feature has the shape and width that has been assigned<sup>14</sup> to a CESR signal in frozen po-

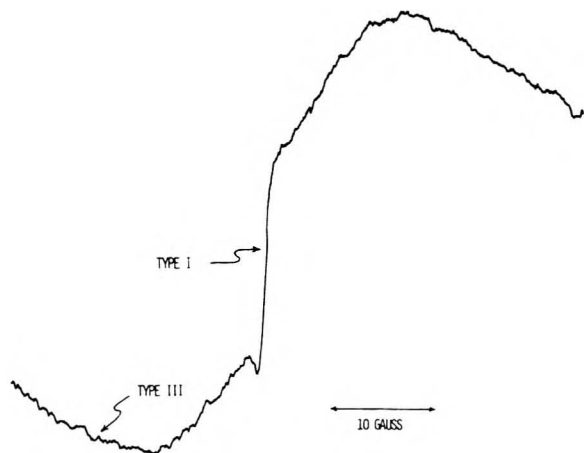


**Figure 2a.** Spectrum of a solution of 0.19 MPM potassium, 18-crown-6 in frozen ammonia at  $-135^{\circ}\text{C}$  taken at 15 mW power. The center portion (type I) is modulation broadened. The center portion is shown more clearly in the supplementary Figure 2b.

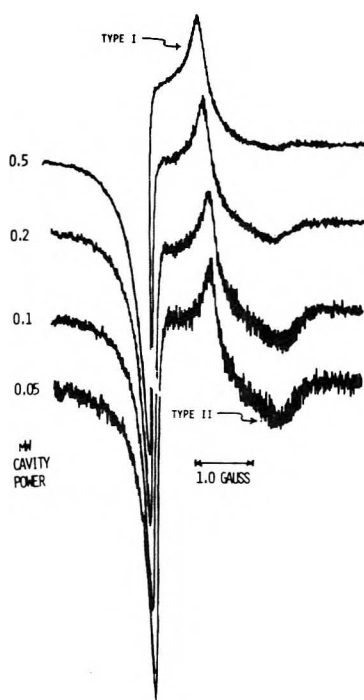


**Figure 3.** Saturation behavior of the type I and type II features in a slowly frozen potassium, 18-crown-6 solution at  $-140^{\circ}\text{C}$ . The sample is 0.20 MPM in potassium and has a potassium/18-crown-6 ratio of 0.33.

tassium-ammonia solutions.

The total electron spin in the frozen solutions was of the same order of magnitude as the number of spins in the liquid solutions. Exact paramagnetic spin densities were difficult to obtain because on freezing not all the sample remained in the radiation field.

**Liquid Solutions.** The results for liquid ammonia solutions containing 18-crown-6 and potassium show that the ESR line shape, width, and position<sup>15,16</sup> are essentially the same as measured for the solvated electron in ammonia solutions.

It has been shown,<sup>2</sup> that the long relaxation times in sodium-ammonia solutions can be explained in terms of motional narrowing as described by eq 1. In eq 1  $\tau_c$  is the

$$1/T_2 = (1.2 \times 10^{-31})(\tau_c + \tau_c/(\tau_c^2 \omega_0^2 + 1))P^2/N \quad (1)$$

electron-nitrogen correlation time,  $\omega_0$  is the angular frequency at resonance,  $P^2$  is the electron density at the

nucleus,  $N$  is the average number of molecules associated with the electron, and the constant is calculated from gyromagnetic ratios and spins.

**Type I Feature.** Attempts were made to fit the type I signal with (a) CESR shapes, (b) up to three separate Gaussian-Lorentzian shapes, (c) a combination of the CESR and up to two combination Gaussian-Lorentzian shapes, and (d) the powder pattern shape. CESR shapes, calculated using the derivative of eq 77 in ref 17 are totally unsatisfactory as an acceptable fit of the shape primarily because the ratio  $A/B$  (described previously<sup>18,19</sup>) must have a value in the range 2-19 except when the particle size is approximately less than the skin depth, for which case the shape becomes Lorentzian. The observed absorption signal can be fit well however by the CESR signal when used in conjunction with two combination Gaussian-Lorentzian bands, but there is no consistency in the diffusion time, relaxation time, or relative  $g$  values for the different signals from one sample to another or on changing temperature. The same problem occurs when the spectra are fit to three or more Gaussian-Lorentzian bands.

A closed form expression has been derived for ESR powder patterns, under the constraints that the intrinsic linewidth is Lorentzian and orientation independent, and that the  $g$  value symmetry must be axial.<sup>20</sup> The applicable equation in ref 20 was numerically integrated to fit the ESR spectra. The parameters involved were the Lorentzian half-width, the field at a perpendicular orientation of a crystallite, the field at a parallel orientation of a crystallite, and the intensity. This four-parameter equation fits the spectra much better than any eight-parameter equation (two Gaussian-Lorentzian or a CESR and a Gaussian-Lorentzian shape). The fit obtained when using 12-parameter equations (three Lorentzian-Gaussian shapes or a CESR shape and two Lorentzian-Gaussian shapes) was better than that obtained using the four-parameter powder pattern shape. However, the three parameters of half-width, position, and fraction Lorentzian from which the Gaussian-Lorentzian shapes were formed showed no regular variation with temperature, as explained above. In contrast to this, the two parameters of perpendicular and parallel crystallite orientation remained constant as a function of temperature in the powder pattern fits. Type I signals are therefore attributed to a single species that exhibit a powder pattern spectrum. Figure 3 shows that the saturation behavior across the entire part of the spectrum attributed to the powder pattern is uniform, thus giving further support to the single species hypothesis. Using the powder pattern shape, we were able to calculate an average  $g$  value of 2.00141 (10), a  $g_{\perp}$  of 2.00168 (10), and a  $g_{\parallel}$  value of 2.00096 (10) for the type I feature.

Figures 1a-d show examples of computer-collected data and the fit using the shape function for the axially symmetric powder pattern with Lorentzian broadening. The fits are good, and all deviations can be ascribed to a slight change of the intrinsic width as a function of the crystallite  $g$  value. The data for the fit of the type I signal are listed in Table III. There is no apparent temperature dependence and no apparent concentration dependence of the derived values of the spin-spin relaxation time. The intrinsic width becomes much broader with decomposition, i.e.,  $T_2$  becomes shorter, although the  $g$  values for both the perpendicular and parallel orientation remain the same.

**Type II Feature.** The type II feature is dependent on the rate of freezing of the sample. The variation of one type II spectrum with different freezing rates is shown in Figure 4. In all cases of rapid freezing only the type I

TABLE III: Spin-Spin Relaxation Times Calculated from the Type I Powder Pattern in Potassium, 18-Crown-6 Frozen Ammonia Solutions

Concentrations		Temp, °C	$T_2(10^7)^c$ s
K/NH <sub>3</sub> <sup>a</sup>	K/18-C-6 <sup>b</sup>		
2.46	0.45	-97 <sup>d</sup>	4.2
2.46	0.45	-106	6.1
2.46	0.45	-125	4.6
2.46	0.45	-150	2.3
1.41	1.59	-97	5.3
1.41	1.59	-106	4.3
1.41	1.59	-106	5.7
1.41	1.59	-117	4.4
1.41	1.59	-125	4.2
1.41	1.59	-134	3.5
1.41	1.59	-142	3.2
1.41	1.59	-150	5.1
0.38	0.83	-112.0 <sup>e</sup>	5.7
0.38	0.83	-120.9	8.2
0.38	0.83	-131.3	6.4
0.38	0.83	-141.0	6.9
0.38	0.83	-148.6	7.7
0.38	0.83	-156.6	6.9
0.20	0.33	-120.7	5.3
0.20	0.33	-127.2	5.9
0.20	0.33	-130.3	5.0
0.20	0.33	-136.4	3.9
0.20	0.33	-139.1	3.5
0.20	0.33	-140.0	3.4
0.20	0.33	-149.5	4.7
0.20	0.33	-157.3	4.0
0.20	0.33	-166.9	3.4

<sup>a</sup> MPM (mole fraction potassium times 100) (10% error).

<sup>b</sup> Mole ratio potassium to 18-crown-6 (<10% error).

<sup>c</sup> Calculated using  $T_2 = 2/(\gamma_e b)$ ,  $b$  obtained from computer fit using the equations developed by J. A. Ibers and J. D. Swalen, *Phys. Rev.*, 127, 1914 (1962). <sup>d</sup> ± 5.0. <sup>e</sup> ± 0.5.

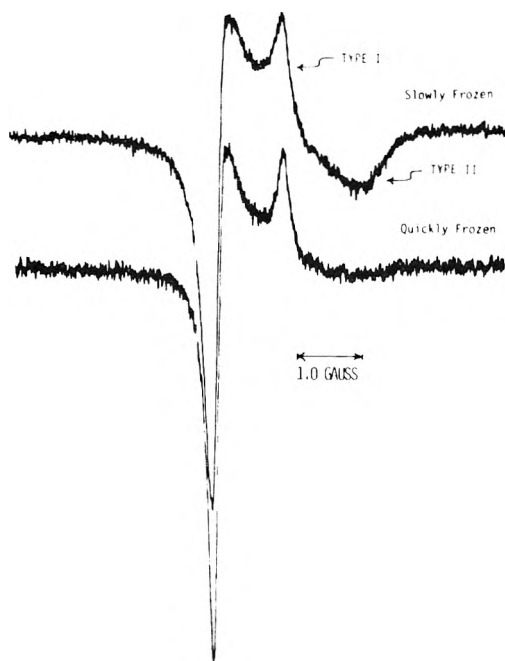


Figure 4. Effect of freezing rate on frozen potassium, 18-crown-6 ammonia solutions. Spectrum taken at 0.10 mW on a sample consisting of 0.38 MPM potassium and a potassium/18-crown-6 ratio of 0.83.

feature is observed. In all cases where a type II feature is observed a white precipitate appears in the frozen, sealed ESR tube. This white precipitate can be redissolved at room temperature, and then the tube quick frozen to give only the type I feature. The saturation behavior of these two types of signals, observed in the same sample, is shown in Figure 3.

The type II feature is always obscured by the type I feature. It does not appear practicable to attempt a fit of this signal, because the fit of the type II feature would be dependent on the "background" fit of the type I feature. Assignment of the type II feature as a CESR signal is based on its unusual shape. The shape is approximately that expected for a CESR signal in which the skin depth is less than the relaxation rate for a thick metal plate or a large sphere. The saturation behavior is reminiscent of the results observed in frozen potassium-ammonia solutions which were assigned to hyperfine coupling with the potassium nuclei<sup>21</sup> which lends credence to the assertion that the type II feature is strongly metal related. The type II feature has a  $g$  value at the peak of 2.000 (1), which is close to 1.9982 (6), the measured  $g$  value for potassium metal at 170 K.<sup>22</sup> If the type II feature is indeed that of a CESR signal, with  $T_d/T_2 \ll 1.0$ , then the actual  $g$  value should be somewhat less than the peak value.<sup>19</sup> The half-width would be given by

$$T_2 = 1.33/(\gamma_e \Delta H_{1/2}) \quad (2)$$

where  $\gamma_e$  is the electron gyromagnetic ratio,  $\Delta H_{1/2}$  is the width at half-height, and  $T_2$  is the transverse relaxation time.<sup>19</sup>

Since the width is approximately 1.0 G,  $T_2$  becomes  $7.6 \times 10^{-8}$ . For potassium in HMPA  $T_2$  has been measured at  $1.3 \times 10^{-9}$  at 150 K,<sup>22</sup> and as long as  $8. \times 10^{-7}$  in the pure metal.<sup>23</sup> The agreement is satisfactory and we may assign the type II absorption to a conduction electron where the skin depth is less than the relaxation rate, but where the size of the metal particles is greater than the skin depth.

**Type III Feature.** The type III feature as shown in Figure 2a exhibits both the shape and the line width observed in frozen potassium-ammonia solutions and this feature has been attributed to CESR with a particle size smaller than the skin depth.<sup>13,22</sup> The relaxation times calculated do not agree with values obtained for potassium metal in other solvents and they may indicate that potassium forms an ammoniate such as  $\text{Li} \cdot 4\text{NH}_3$ <sup>24</sup> or  $\text{Ba} \cdot 6\text{NH}_3$ .<sup>25</sup> No other evidence has been found to support this suggestion. The  $g$  value is in the range 2.0012 (5) and is significantly different than that for potassium (1.9982 (6))<sup>22</sup> or that which has been observed previously in frozen potassium-ammonia solutions.<sup>14,22</sup>

## Discussion

The type I feature is due to a species which has magnetic axial symmetry. Possible species are potassium metal, a potassium atom, a potassium species of the type  $\text{K}(\text{NH}_3)_n$ , an ammonia radical, or a frozen "solvated" electron. All of the isolated potassium species would require hyperfine coupling to the potassium nucleus, such as those species that have been observed previously.<sup>21,26</sup> A radical ammonia species would require hyperfine coupling to the nitrogen atom. The type II and type III species described above are of the CESR type and thus delocalized electrons are already well represented in these solutions. Furthermore, the powder pattern shape is a localized ESR signal, not one due to an extended state, such as a metal. Thus, of the possible species, only the "solvated" electron remains as a reasonable contender.

Current theories<sup>27</sup> of the structure of the solvated electron do not predict an asymmetric structure, but we can explain the observed asymmetry in the solid by postulating a "loose" ion pair. A representation of the proposed ion pair model is in Figure 5.

In Table III are listed values of  $T_2$  obtained for the type I feature. These relaxation times are of the same order of magnitude as those obtained in the liquid state for this

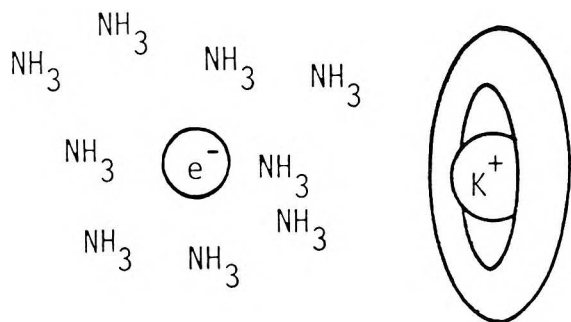


**Figure 5.** Representation of the proposed ion pair. The electron is in a cavity surrounded by ammonia molecules. The potassium cation is surrounded by an 18-crown-6 molecule.

system. Because these times are similar, we are tempted to explain the spin-spin relaxation times in the solid in the same manner as has been done<sup>2</sup> in the liquid. The correlation time expected in the solid state can be estimated using eq 1. The angular frequency of the Varian E9 spectrometer at resonance is about  $5.8 \times 10^{10}$ . If we use eq 1 with  $P^2$  estimated<sup>28</sup> at  $4.6 \times 10^{48}$  and  $N$  taken to be<sup>29</sup> about 10 we can calculate the expected correlation time  $\tau_c$  from the values of  $T_2$  in Table III. Using  $T_2 = 4 \times 10^{-7}$  we obtain  $2 \times 10^{-12}$  s for  $\tau_c$ . The self-diffusion in solid ammonia is much too slow to explain this correlation time, however, the molecular reorientation time of ammonia in the glassy solid at 170 K is  $1.2 \times 10^{-10}$  s.<sup>30</sup> On first consideration then,  $\tau_c$ , the correlation time, is nearly the same as the reorientation time of ammonia in these solutions, confirming the theory.<sup>31</sup>

Since the line width in this simple model is controlled by the reorientation of the ammonia molecules, and this reorientation is known to increase from  $1.2 \times 10^{-10}$  s at 170 K to  $1.4 \times 10^{-8}$  s at 100 K,<sup>30</sup> the width of the ESR signal would be expected to increase about two orders of magnitude as the temperature is lowered. Upon inspection of the data in Table III we are led to the conclusion that the motional narrowing mechanism by the movement of ammonia for an isolated species as determined by eq 1 does not describe the spectra. The line width does not appear to depend strongly on temperature. Further confirmation that the above interpretation may be faulty is obtained from the observed ESR line width of irradiated ammonia. At  $-150^\circ\text{C}$  a singlet was observed which was about 40 G wide.<sup>32</sup> This would correspond with a relaxation time,  $T_2$ , of  $1.6 \times 10^{-9}$  s, and a calculated  $\tau_c$  using eq 1, of  $6 \times 10^{-9}$  s. This number is in better agreement with the reorientation time of  $1.2 \times 10^{-10}$  s<sup>30,31</sup> than the correlation time of  $2 \times 10^{-12}$  s discussed above. Thus, a relaxation mechanism that is relatively insensitive to both temperature and metal concentration must be sought.

Previously, a mechanism of spin site exchange was proposed for metal-ammonia solutions that have some ion pairing present.<sup>33</sup> A splitting of the  $g$  value into perpendicular and parallel components gives a strong indication of asymmetry in the frozen electron cavity due to a perturbation by the metal cation. The spin site exchange model requires that some loose ion pairs must exist. In a frozen species there may be a great deal of spin pairing occurring, so that we postulate a species responsible for the type I feature as shown in Figure 5.

In ref 33  $\xi_K$  was calculated to be on the order of  $3.2 \times 10^7$ , from which can be derived for room temperature and 0.05 M a value of  $1.8 \times 10^{-8}$  s for  $\tau_{ex}$ , the exchange time. The diffusion time of liquid ammonia under the same conditions is  $1.6 \times 10^{-12}$  s,<sup>34</sup> which is much smaller than the exchange time. When freezing the solutions, however, the movement of the ammonia molecules slows drastically,

while the exchange time should become much faster, because all the cavities are "frozen" near cations in an ion paired state. We propose that as the exchange time becomes shorter than the self-diffusion time of ammonia, that the exchange time of the electron will dominate the motional narrowing.

In ref 33 we developed eq 3 for dilute solutions, where

$$1/T_2 = 1/T_{2c} + f_M(\Delta\omega_0)^2\tau_{ex}/(2\pi) \quad (3)$$

$f_M$  is the fraction of metal monomer and  $\Delta\omega_0$  is the difference in the peak positions of the cavity species and the metal monomer species;  $T_{2c}$  is the contribution to  $T_2$  by the cavity species. For  $\omega_0\tau_c \ll 1.0T_{1c}$ , the spin-lattice relaxation time for the cavity, and  $T_{2c}$ , the spin-spin relaxation time for the cavity, are given by eq 4. Since

$$1/T_{1c} = 1/T_{2c} = (2.4 \times 10^{-31})\tau_c P^2/N \quad (4)$$

the primary contribution to  $T_1$  is always  $T_{1c}$ ,  $T_1$  will be equal to  $T_2$  when the second term of eq 3 is negligible compared to the first term.<sup>33</sup> The correlation time for motional narrowing,  $\tau_c$ , consists of both the movement of ammonia molecules relative to the cavity,  $\tau_d$ , and the movement of the electron relative to the cavity,  $\tau_{ex}$ , as given by eq 5.

$$\tau_c = \tau_{ex} + \tau_d \quad (5)$$

For the type I species  $1/T_{2c}$  with  $\tau_{ex} \gg \tau_d$  dominates  $1/T_2$ . This predicts that  $T_1$  and  $T_2$  would be nearly equal for the species responsible for the type I pattern. Since  $\tau_{ex}$  is expected to be a function of the distance between the metal and the cavity, and not a function of temperature or concentration, part of the variation encountered in Table III is explained by slight variations in the frequency of resonance, and the rest of the variation is explained by the differences in distance between ion pairs expected as different freezing rates are applied.

As decomposition of the sample proceeds the spectra get broader. The currently preferred explanation for this behavior is that the term  $P^2/N$  becomes larger, due to both the association of fewer ammonia molecules ( $N$  becomes smaller) and to a larger density of the electron at the remaining nuclei ( $P$  becomes larger). Eventually the electron and ammonia react to give  $e^- + \text{NH}_3 \rightarrow \text{NH}_2^- + \frac{1}{2}\text{H}_2$ .

The ESR results for a wider range of concentrations and temperatures for metal-ammonia liquid solutions may be understood by considering the arguments developed for the frozen solutions. At very low concentrations of metal the ESR spectrum in the liquid is dominated by the motional narrowing of the electron hyperfine interaction with the nitrogen atoms of the ammonia. This relative motion is controlled by the diffusion of ammonia.<sup>2</sup> At higher, but still dilute concentrations, the spin site exchange process begins to operate as shown in eq 3. In this intermediate range, the relaxation times  $T_1$  and  $T_2$  are no longer equal.<sup>33</sup> At still higher concentrations the motional narrowing of the electron hyperfine interaction with nitrogen atoms again becomes important, although the relative motion is now  $\tau_{ex}$ , the exchange of the electron between the cavity and the metal sites. Eventually  $T_1$  will be equal to  $T_2$  and be controlled by the same type of motional narrowing found for the solid state "solvated" electron as described by eq 4 with  $\tau_{ex} \gg \tau_d$ . The only magnetic data that would require additional species is the observed spin pairing.<sup>15,25</sup> As has been suggested elsewhere,<sup>35</sup> two different situations could explain the spin pairing, both of which would be expected to occur at higher concentrations and temperatures. The first is formation

of alkali metal anions. The second is spin-paired electrons in two distinct cavities.

The spin site exchange mechanism explains why the hyperfine coupling of the metal is not observed in most metal ammonia solutions, although there is good reason to believe some monomers must be present.<sup>28</sup> The exchange of the electron from the cavity site to the metal site is so facile the hyperfine coupling is averaged out, as has been proposed elsewhere.<sup>35</sup>

The explanation of the ESR observations proposed here need not conflict with the corresponding explanations of the near IR spectrum observed in liquid metal-ammonia solutions. The value of  $\tau_{ex}$  is calculated from  $\xi_K = (\Delta\omega_0\tau_{ex}/2\pi)$  in ref 33 to be  $1.8 \times 10^{-8}$  s. Approximately 0.1% of the electrons in solution are associated with the cation,<sup>28</sup> so that the residence time of the electron on the metal becomes  $1.8 \times 10^{-11}$  s. This is probably long enough for collapse of the cavity to occur. However, cavities are formed at faster rates than  $5 \times 10^{-12}$  s in ammonia,<sup>36</sup> so that cavity collapse would not prevent formation of an alternate cavity to which the electron on the metal could move. Since the monomer is in very low concentration, the spectrum will be essentially the same as if there is no monomer. At concentrations where significant ion pairing occurs as proposed for this solid blue species, we predict an effect upon the near-IR spectrum which for  $-65^\circ\text{C}$  sodium-ammonia solutions should begin at  $10^{-3}$  M.<sup>37</sup>

## Conclusion

ESR signals have been observed for 18-crown-6, potassium-ammonia solutions in both the liquid and solid states. The liquid state has a single absorption that is nearly the same as that observed in potassium-ammonia solutions, and can be explained in the same way. This observation confirms the supposition that the potassium cation does not significantly participate in the paramagnetism exhibited by dilute solutions.

In the frozen state, three distinct features are observed. Type I can be described as an ion pair of a "frozen" cavity and a cation trapped by a crown complexing agent. The intrinsic powder pattern width can be explained by hyperfine motional narrowing with the nitrogen nuclei. The axially symmetric magnetic properties are explained by assuming a perturbation of the cavity by the cation. Type II and type III are both explained in terms of CESR absorptions of species previously observed.

*Acknowledgment.* We gratefully acknowledge the generous support of the Robert A. Welch Foundation as well as fruitful discussions with J. C. Thompson, L. O. Morgan, and C. G. Wade.

*Supplementary Material Available:* Type I signals and fits are in Figures 1b-d. Figure 2b shows the modulation broadened part of Figure 2a. Figure 6 shows a Lorentzian fit to a liquid potassium, 18-crown-6 solution spectrum. Figure 7 shows the saturation behavior of a typical sample with type I and type II features. Figure 8 shows a sodium, 18-crown-6 frozen solution signal with both type I and type III features. Details of the solution fits as well as an attempt to find a type I feature in frozen sodium, 18-crown-6 solutions are discussed (11 pages). Ordering

information is available on any current masthead page.

## References and Notes

- J. C. Thompson, "Electrons in Liquid Ammonia", Clarendon Press, Oxford, 1976; Colloque Weyl IV, *J. Phys. Chem.*, **79**, 2789-3081 (1975).
- D. E. O'Reilly, *J. Chem. Phys.*, **35**, 1856 (1961); D. Cutler and J. G. Powles, *Proc. Phys. Soc.*, **80**, 130 (1962).
- M. J. Blandamer, L. Shields, and M. C. R. Symons, *J. Chem. Soc.*, 4352 (1964).
- J. L. Dye, J. M. Ceraso, M. T. Lok, B. L. Barnett, and F. J. Tehan, *J. Am. Chem. Soc.*, **96**, 608 (1974); F. J. Tehan, B. L. Barnett, and J. L. Dye, *ibid.*, **96**, 7203 (1974).
- J. L. Dye, C. W. Andrews, and S. E. Mathews, *J. Phys. Chem.*, **79**, 3065 (1975).
- R. L. Harris and J. J. Lagowski, presented at the 173rd National Meeting of the American Chemical Society, New Orleans, La., March 20-25, 1977; INORG 206.
- M. J. Sienko, "Metal-Ammonia Solutions", Proceedings of Colloque Weyl I, G. Lepoutre and M. J. Sienko, Ed., W. A. Benjamin, New York, N.Y., 1964, pp 23-40.
- J. Dale and P. O. Kristiansen, *Acta Chem. Scand.*, **26**, 1471 (1972); G. W. Gokel, D. J. Cram, C. L. Liotta, H. P. Harris, and F. L. Cook, *J. Org. Chem.*, **39**, 2445 (1974).
- R. S. Alger, "Electron Paramagnetic Resonance: Techniques and Applications", Interscience, New York, N.Y., 1968, pp 203-204.
- STEPIT and SIMPLEX, J. P. Chandler, Quantum Chemistry Program Exchange, Department of Chemistry, Indiana University, Bloomington, Ind.
- IMSL, Inc., Houston, Tex. 77036.
- A. Carrington and A. D. McLachlan, "Introduction to Magnetic Resonance", Harper and Row, New York, N.Y., 1967.
- W. C. Hamilton, "Statistics in Physical Science", Ronald Press, New York, N.Y., 1964, p 158.
- R. A. Levy, *Phys. Rev.*, **102**, 31 (1956).
- C. A. Hutchison, Jr., and R. C. Pastor, *J. Chem. Phys.*, **21**, 1959 (1953).
- D. S. Thompson, E. E. Hazen, and J. S. Waugh, *J. Chem. Phys.*, **44**, 2954 (1966).
- F. J. Dyson, *Phys. Rev.*, **98**, 349 (1955).
- R. H. Webb, *Phys. Rev.*, **158**, 225 (1967).
- G. Feher and A. F. Kip, *Phys. Rev.*, **98**, 337 (1955).
- J. A. Ibers and J. D. Swalen, *Phys. Rev.*, **127**, 1914 (1962).
- R. Catterall, W. T. Cronenwett, R. J. Eglund, and M. C. R. Symons, *J. Chem. Soc. A*, 2396 (1971).
- R. Catterall and P. P. Edwards, *Adv. Mol. Relaxation Processes*, **7**, 87 (1975).
- W. M. Walsh, Jr., L. W. Rupp, Jr., and P. H. Schmidt, *Phys. Rev.*, **142**, 414 (1966).
- N. Mammano, "Metal Ammonia Solutions", Proceedings of Colloque Weyl II, J. J. Lagowski and M. J. Sienko, Ed., Butterworths, London, 1970, pp 367-393; W. S. Glaunsinger and M. J. Sienko, *J. Chem. Phys.*, **62**, 1873, 1883 (1975).
- M. T. Lok, Ph.D. Dissertation, Michigan State University, 1973; University Microfilms No. 74-19833.
- K. Bar-Eli and T. R. Tuttle, Jr., *J. Chem. Phys.*, **40**, 2508 (1964).
- D. E. O'Reilly, *J. Chem. Phys.*, **41**, 3736 (1964); B. C. Webster and G. Howat, *Radiat. Res.*, **4**, 259 (1972).
- D. E. O'Reilly, *J. Chem. Phys.*, **41**, 3729 (1964).
- R. Catterall, "Metal Ammonia Solutions", Proceedings of Colloque Weyl II, J. J. Lagowski and M. J. Sienko, Ed., Butterworths, London, 1970, pp 105-130.
- J. L. Carolan and T. A. Scott, *J. Magn. Reson.*, **2**, 243 (1970); D. E. O'Reilly, E. M. Pererson, and S. R. Lammert, *J. Chem. Phys.*, **52**, 1700 (1970); P. W. Atkins, A. Loewenstein, and Y. Margalit, *Mol. Phys.*, **17**, 329 (1969).
- Notice that the reorientation time of ammonia may not be the correct correlation time for motional narrowing since the reorientation time is primarily due to rotation of the ammonia and is thus probably poorly correlated with the movement of the nitrogen atoms.
- V. I. Tupikov and S. Ya. Pshchelskii, *Zh. Fiz. Khim.*, **37**, 1900 (1963) (*Russ. J. Phys. Chem.*, **37**, 65 (1963)).
- R. L. Harris and J. J. Lagowski, *J. Chem. Phys.*, **67**, 4782 (1977).
- D. E. O'Reilly, *J. Chem. Phys.*, **50**, 4743 (1969).
- J. L. Dye, *Pure Appl. Chem.*, **49**, 3 (1977).
- J. Balloni, M. Clerc, P. Goujon, and E. Saito, *J. Phys. Chem.*, **79**, 2848 (1975); W. J. Chase and J. W. Hunt, *ibid.*, **79**, 2835 (1975).
- G. Rubinstein, *J. Phys. Chem.*, **79**, 2963 (1975); J. J. Lagowski, "Electrons in Fluids", Proceedings of Colloque Weyl III, J. Jortner and N. R. Kestner, Ed., Springer-Verlag, Berlin, 1973, pp 29-38.



# The Role of Defects in the Thermal Decomposition of Barium Azide

V. R. Pal Verneker\* and M. P. Kannan

High-Energy Solids Laboratory, Department of Inorganic and Physical Chemistry, Indian Institute of Science, Bangalore 560 012, India  
(Received June 3, 1977)

New results on the thermal decomposition of barium azide are presented in this investigation. Thermal decomposition of pure and doped anhydrous single crystals of barium azide has been studied in the temperature range 120–190 °C. Diffusion of Ba<sup>2+</sup> interstitials is shown to be the rate-determining step in the thermal decomposition of barium azide, rather than an electron transfer process.

## Introduction

Thermal decomposition of barium azide has been extensively studied by many workers.<sup>1–14</sup> The earlier work was invariably carried out on dehydrated barium azide monohydrate in the temperature range 100–140 °C. The thermal decomposition studied in vacuo by manometric techniques is characterized by an activation energy whose value ranges from 21 to 29 kcal/mol (shown in Table I). In 1967, Torkar and Spath<sup>6,7,14</sup> studied the thermal decomposition of anhydrous barium azide single crystals. They obtained an activation energy of 26 kcal/mol. Based on the noncoincidence of the activation energy for ionic conductance<sup>15</sup> and that for thermal decomposition, they suggested an electron transfer mechanism for the thermal decomposition of barium azide. Recent electrical conductivity studies by Maycock<sup>16</sup> on pure and doped anhydrous barium azide single crystals have clearly shown that the region 100–140 °C in the log  $\sigma$  vs.  $1/T$  plot corresponds to extrinsic conduction with an activation energy of 19.6 kcal/mol. Conductance measurements in the temperature range above 140 °C could have gone a long way in proving the existence of an intrinsic conductance region in that temperature range. However, barium azide decomposes rather fast above 140 °C and the conductance experiments become difficult to interpret. As Torkar and Spath<sup>14</sup> have observed correlation between their conductance data and thermal decomposition results on NaN<sub>3</sub>, it might be worthwhile to study the thermal decomposition above 140 °C on pure and doped single crystals of anhydrous barium azide. Thermal decomposition of Ba(N<sub>3</sub>)<sub>2</sub> powder may not serve the objective since it contains large concentrations of gross imperfections which may obscure fine differences in the behavior pattern of thermal decomposition below and above the knee temperature.

The present work, therefore, deals with the thermal decomposition of pure and doped single crystals of anhydrous barium azide in the temperature range 120–190 °C. Some data on the effects of precompression on the subsequent thermal decomposition of powdered anhydrous barium azide are also reported.

## Experimental Section

**Materials.** Barium azide was prepared from barium carbonate (BDH, Analar grade) by reaction with hydrazoic acid. An aqueous solution of hydrazoic acid was obtained by passing a 10% solution of sodium azide through an ion-exchange column made up of Dowex 50-x8(H<sup>+</sup>). A water suspension of barium carbonate was slowly added to the acid solution to obtain an aqueous solution of barium azide. Care was taken to see that there was always excess acid in the system (tested by means of litmus). Barium azide was then precipitated from this aqueous solution by diluting it with Analar acetone. The barium

azide powder thus obtained was redissolved in a minimum amount of water and reprecipitated by adding acetone. The powder thus obtained served as the stock sample.

**Preparation of Single Crystals of Anhydrous Barium Azide.** A dilute aqueous solution of barium azide was prepared using the above stock sample. The solution was then allowed to evaporate slowly on a hot plate maintained at a temperature of ca. 60 °C. Single crystals formed were separated, dried in the folds of filter paper, and kept over P<sub>2</sub>O<sub>5</sub> in a vacuum desiccator.

The anticipated anhydrous state of these crystals was checked by gravimetric analysis which showed the crystals to be water free.

Single crystals of doped anhydrous barium azide were grown in a similar manner by slowly evaporating an aqueous solution of barium azide containing the desired concentration of the dopant, at a temperature of ca. 60 °C on a hot plate. The dopant materials used were NaN<sub>3</sub>, AlCl<sub>3</sub>, BaCl<sub>2</sub>, and BaCO<sub>3</sub> (Analar grade, BDH).

Anhydrous barium azide powder used in the present study was prepared by grinding the single crystals to the desired particle size (150–180  $\mu$ m). All powder samples used in the present study had a particle size of 150–180  $\mu$ m. The actual concentrations of the dopants present in doped anhydrous barium azide single crystals were not determined, and hence the concentrations referred to are those in solution.

**Method.** The kinetics of the thermal decomposition of barium azide (crystals and powder) were followed in a conventional constant volume vacuum system. A crystal weighing around 2 mg was used in each run. In the case of the powder, the amount of sample used in each run was 2 mg. The initial pressure employed before starting each run was  $1 \times 10^{-5}$  Torr.

## Results and Discussion

**Thermal Decomposition of Anhydrous Barium Azide Single Crystals.** Typical plots of  $\alpha$ , the fraction of the salt decomposed, vs.  $t$ , the time of heating single crystals of barium azide, are shown in Figure 1. The data have been fitted to the Avrami–Erofevey equation

$$(-\ln(1 - \alpha))^{1/n} = kt \quad \text{with } n = 3$$

(The best value of  $n$  was found to be 3 by least-squares fit). This is shown in Figure 2. It can be seen that the data give a very good fit in the range of  $\alpha = 0.05$  to  $\alpha = 0.90$ . The rate constants ( $k$ ) were calculated from these fits. Thermal decomposition of anhydrous barium azide single crystals doped with  $10^{-4}$  mol % Na<sup>+</sup>,  $10^{-1}$  mol % Na<sup>+</sup>,  $10^{-2}$  mol % Al<sup>3+</sup>,  $10^{-2}$  mol % Cl<sup>-</sup>, and  $10^{-2}$  mol % CO<sub>3</sub><sup>2-</sup> were also studied and the thermal decomposition data could also be fitted well to the Avrami–Erofevey equation ( $n = 3$ ) in the range  $\alpha = 0.05$  to  $\alpha = 0.90$ .

TABLE I: Summary of the Thermal Decomposition Data of Barium Azide<sup>a</sup>

Ref	Material	Exptl method <sup>b</sup> and temp range, °C	Kinetic analysis	Activation energy, kcal/mol
1	Dehydrated monohydrate	P(in vacuo) 100-130	Exponential expression	21.0
2	Dehydrated monohydrate	M 100-123.5	$r = kt$	23.5
3	Dehydrated monohydrate	P(in vacuo) 102.2-123.4	$p = C(t - y)^6$	29.0 (slow growth)
4	Dehydrated monohydrate	M 120-145		23.0
5	Dehydrated monohydrate	P(in vacuo) 110-140	AE, $n = 4$	26.8
6, 7	Anhydrous single crystals	P(in vacuo) M 120-145	$\alpha = Kt^4$	26.0

<sup>a</sup> A complete listing of the thermal decomposition data is available as supplementary material. See paragraph at end of text regarding supplementary material. <sup>b</sup> P, pressure increase; M, microscopic study;  $r$ , radius;  $t$ , time;  $p$ , pressure of  $N_2$ ;  $y$  slow growth correction; AE, Avrami-Erofev equation;  $\alpha$ , fraction decomposition.

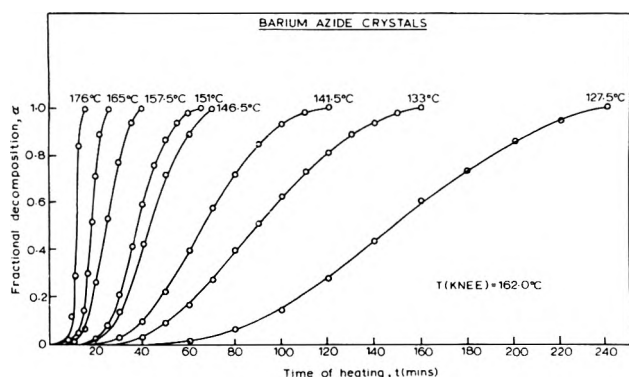


Figure 1. Plots of the fractional decomposition,  $\alpha$ , vs. the time,  $t$  (in min), of heating of anhydrous barium azide single crystals at various temperatures.

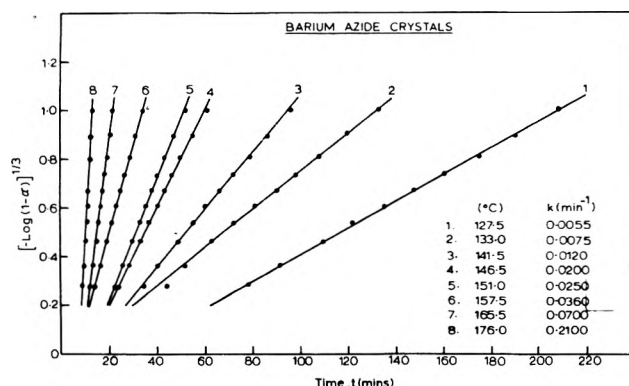


Figure 2. Typical fits of the  $\alpha$ - $t$  curves for the thermal decomposition of anhydrous barium azide single crystals to the Avrami-Erofev equation ( $n = 3$ ).

Subsequently the rate constants for the thermal decomposition of doped samples were calculated from these fits. Figure 3 shows an Arrhenius plot in the temperature range 120-190 °C for the thermal decomposition of single crystals of anhydrous barium azide, both pure and doped with respective impurities. It can be seen that in every case a break is apparent, and the activation energy in the low temperature range is  $23 \pm 1$  kcal/mol and in the high temperature range the activation energy value is  $36.8 \pm 1$  kcal/mol. The break or knee temperature is further seen to depend on the type of the dopant and its concentration (presented in Table II). Whereas  $\text{Cl}^-$  ion impurity affects neither the rate of decomposition of pure  $\text{Ba}(\text{N}_3)_2$  nor its knee temperature, an  $\text{Na}^+$  ion or  $\text{CO}_3^{2-}$  ion impurity is seen to shift the knee to higher temperature and sensitize the

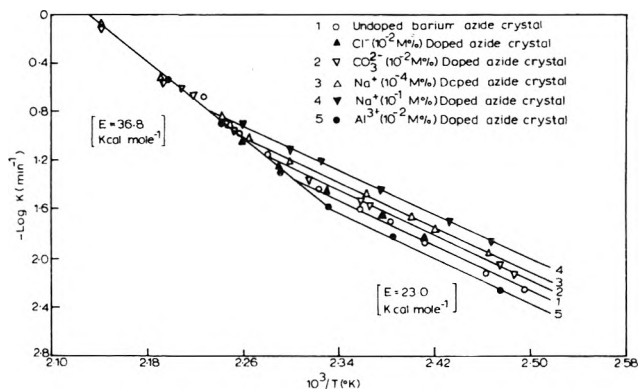


Figure 3. Arrhenius plots for the thermal decomposition of pure and doped anhydrous barium azide single crystals.

TABLE II: Effect of the Dopant Ion and Its Concentration on the Knee Temperature in the Thermal Decomposition of Barium Azide Crystals

Dopant ion	Dopant ion concn, mol %	Knee temp, °C	Rate constant <sup>a</sup> $k$ , $\text{min}^{-1}$	
			Below knee temp (at 141.5 °C)	Above knee temp (at 178.0 °C)
None	None	162.0	0.01200	0.2188
$\text{Cl}^-$	$10^{-2}$	162.0	0.01200	0.2188
$\text{Na}^+$	$10^{-4}$	169.0	0.01905	0.2188
$\text{Na}^+$	$10^{-1}$	175.5	0.02512	0.2188
$\text{CO}_3^{2-}$	$10^{-2}$	166.0	0.01660	0.2188
$\text{Al}^{3+}$	$10^{-2}$	156.0	0.01096	0.2188

<sup>a</sup> In all cases the activation energy below the knee temperature was  $23 \pm 1$  kcal/mol and above the knee temperature the activation energy was  $36.8 \pm 1$  kcal/mol.

decomposition rate and an  $\text{Al}^{3+}$  ion impurity lowers the knee temperature and desensitizes the decomposition rate.

The shift of knee temperature with the type of the impurity and its concentration is a common phenomenon in the usual conductance plot of  $\log \sigma$  vs.  $1/T$  for well-known solids showing ionic conductivity. In barium azide, Maycock<sup>16</sup> has shown that an  $\text{Na}^+$  impurity increases the conductance of barium azide. He explained his result assuming that barium azide, in analogy with barium chloride, is an anionic conductor. However the later work of Pai Verneker et al.<sup>17</sup> has shown that in barium azide the current carrying species is the barium ion and not the azide ion. The results of Maycock on  $\text{Na}^+$  doped  $\text{Ba}(\text{N}_3)_2$ <sup>16</sup> are equally well explained on the model that  $\text{Ba}(\text{N}_3)_2$  has a Frenkel defect structure and that the current carrying species is the interstitial barium ion. Doping barium azide with  $\text{Na}^+$  results in a decrease in the concentration of the

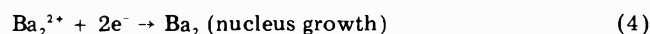
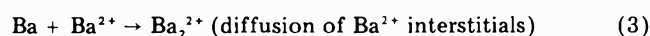
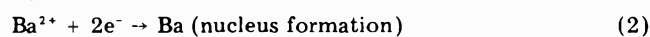
cation vacancies according to the equation

$$(+)(-) = \text{constant}$$

where (+) and (-) represent the concentrations of the cation and anion vacancies. Further, it is evident from the expression

$$(+)(I^+) = \text{constant}$$

where ( $I^+$ ) represents the concentration of positive ion interstitials, that a decrease in the concentration of cation vacancies in a crystal lattice should lead to an increase in the concentration of the positive ion interstitials. In the light of this, one can argue that the concentration of barium ion interstitials increases when doped with  $\text{Na}^+$  or  $\text{CO}_3^{2-}$  ions, decreases when doped with  $\text{Al}^{3+}$  ions, and remains unchanged when doped with  $\text{Cl}^-$  ions. Undoubtedly, conductance experiments on doped barium azide crystals could prove this point unambiguously. In the absence of conductance data, one can speculate that the sensitization of the thermal decomposition by impurities such as  $\text{Na}^+$  and  $\text{CO}_3^{2-}$  and desensitization by the  $\text{Al}^{3+}$  ion are related to the concentration of the barium ion interstitials in the barium azide crystals. This speculation derives weight from the fact that, in the high temperature region, the intrinsic region where the barium ion interstitials are self-generated due to the thermal effects, the impurities do not affect the rate of thermal decomposition. The present data on pure and doped barium azide, therefore, suggest that the rate-determining step in the thermal decomposition of barium azide is the diffusion of the barium ion interstitials rather than an electron transfer process as suggested by earlier workers.<sup>3,11,14,18</sup>  $\text{Ba}^{2+}$  ions arriving at the metal-salt interface lower the Fermi level of Ba and thus facilitate subsequent electron transfer to the metal.  $\text{N}_3^-$  radicals formed simultaneously decompose to form  $\text{N}_2$  gas. Repetition of these processes represents the nucleus growth, diffusion of  $\text{Ba}^+$  interstitials being the rate-determining step. The mechanism of thermal decomposition of barium azide can be schematically represented as follows:



Reaction 3 is the slowest step. The activation energy in the low-temperature region, viz. 23 kcal/mol, then corresponds to the energy of diffusion of  $\text{Ba}^{2+}$  interstitials. It is worthwhile to mention here that, according to Thomas and Tompkins,<sup>19</sup> the activation energy for the mobility of barium ions in  $\text{Ba}(\text{N}_3)_2$  is expected to be similar to that of lead ions in lead halides, which is ca. 20 kcal/mol.<sup>20</sup>

The diffusion-controlled mechanism proposed above for the thermal decomposition of barium azide is supported by the correlation found between the activation energy value for extrinsic conduction in  $\text{Ba}(\text{N}_3)_2$  (19.6 kcal/mol) obtained by Maycock<sup>16</sup> and the activation energy we obtained for the low temperature thermal decomposition of barium azide (23 kcal/mol).

The high temperature region (activation energy  $36.8 \pm 1$  kcal/mol) probably corresponds to the intrinsic region where the  $\text{Ba}^{2+}$  interstitials are self-generated due to thermal effects. This conjecture derives weight from the fact that dopants do not affect the rate of decomposition in this temperature range. Conductance studies would have helped in confirming this fact. Unfortunately, no

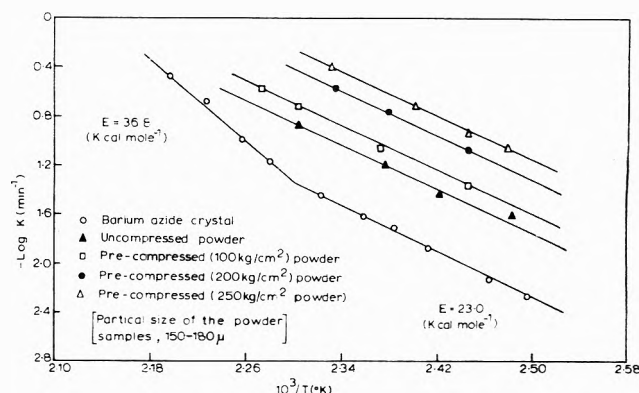


Figure 4. Arrhenius plots for the thermal decomposition of anhydrous barium azide crystals and uncompressed and precompressed powders (particle size, 150–180  $\mu\text{m}$ ).

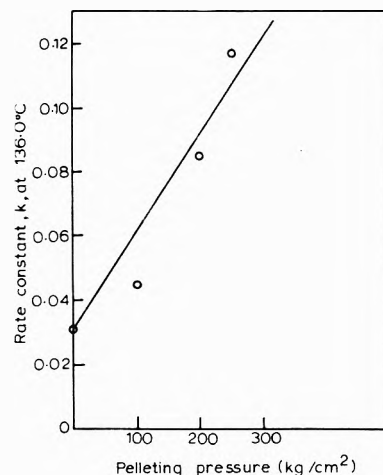


Figure 5. Effect of pelleting pressure on the rate of thermal decomposition of anhydrous barium azide (powder size, 150–180  $\mu\text{m}$ ) at 136  $^{\circ}\text{C}$ .

conductance measurements have been, so far, carried out in this high temperature range because of the relatively faster decomposition of barium azide.

*Thermal Decomposition of Anhydrous Barium Azide Powder.* The thermal decomposition of barium azide is envisaged to occur by the diffusion of the barium ion interstitials to selective sites where the decomposition is favored. Hence a change in the concentration of the selective sites should also alter the rate of thermal decomposition of barium azide. With this view, therefore, the thermal decomposition of barium azide powder (uncompressed and precompressed) was investigated.

Anhydrous barium azide powder was prepared by grinding anhydrous barium azide single crystals to the desired particle size (150–180  $\mu\text{m}$ ).  $\alpha$ - $t$  plots and Avrami-Erofeyev fits for the thermal decomposition of the powder samples at all temperatures studied were similar to those shown in Figures 1 and 2, respectively. Thermal decomposition of powder precompressed to 100, 200, and 250  $\text{kg}/\text{cm}^2$  was also studied. Following the precompression, the pellet has been dismantled and ground to the same particle size fraction (150–180  $\mu\text{m}$ ) in all cases.  $\alpha$ - $t$  plots and the fits to the Avrami-Erofeyev equations were used to calculate the rate constants for the thermal decomposition of precompressed powder at various temperatures. Figure 4 presents an Arrhenius plot for the thermal decomposition of barium azide crystal and powder. It is evident that the activation energy remains unchanged but the rate of thermal decomposition is drastically enhanced by powdering the crystal. Figure 4 also shows the effect of precompression on decomposition rate. It can be

seen that the rate of thermal decomposition is a function of the precompression pressure (shown in Figure 5). Earlier works by Pai Verneker and Rajeshwar<sup>21,22</sup> on ammonium and potassium perchlorates and Pai Verneker and Nair<sup>23</sup> on ammonium oxalate by x-ray diffraction and IR techniques have revealed that (i) precompression increases the concentration of gross imperfections such as dislocations in these crystals, (ii) the concentration of these defects is linearly proportional to the applied pressure, and (iii) the thermal decomposition of these crystals is proportional to the applied pelleting pressure. In light of this, one can say that gross imperfections produced by precompression enhance the thermal decomposition of barium azide in a systematic manner. This is in accordance with the fact that an increase in the concentration of the selective sites where decomposition takes place should enhance the diffusion of barium ion interstitials.

### Conclusions

The thermal decomposition of anhydrous barium azide single crystals and powder has been studied in detail over a wide temperature range. The results of the present investigation reveal that (i) doping  $\text{Ba}(\text{N}_3)_2$  with impurity ions such as  $\text{Na}^+$  and  $\text{CO}_3^{2-}$  results in a sensitization of the thermal decomposition, whereas an  $\text{Al}^{3+}$  impurity slows down the decomposition rate; (ii) precompression causes a drastic increase in the decomposition rate. These effects clearly exhibit the role of crystal imperfections in the reactivity of solids. Whereas doping results in the creation of point defects, precompression leads to the production of gross imperfections such as dislocations.

The break (knee) observed in the Arrhenius plot for the thermal decomposition of pure and doped barium azide and the shift in the knee temperature depending upon the type and concentration of the dopant, clearly speak in favor of a diffusion-controlled mechanism,  $\text{Ba}^{2+}$  interstitials being the diffusing species. A mechanism involving electron transfer as the rate-determining step seems to be very unlikely. Torkar et al.<sup>14</sup> have shown that it is the diffusion of  $\text{Na}^+$  ions that controls the rate in the thermal decomposition of  $\text{NaN}_3$ . Recent investigations by

Maycock<sup>16</sup> support a diffusion-controlled mechanism for the thermal decomposition of  $\text{KN}_3$ , the migrating species being  $\text{K}^+$  ions. Our results combined with the results of earlier workers<sup>14,16</sup> lead to the conclusion that, in the thermal decomposition of metallic azides in general, diffusion of metal ions does play an important role in controlling their reactivity.

*Supplementary Material Available:* Thermal decomposition data of doped, undoped, precompressed, and uncompressed barium azide crystals (Figures 1–9 and Tables I–X) (14 pages). Ordering information is available on any current masthead information.

### References and Notes

- (1) F. E. Harvey, *Trans. Faraday Soc.*, **29**, 653 (1933).
- (2) A. Wischin, *Proc. R. Soc. London, Ser. A*, **172**, 314 (1939).
- (3) J. M. Thomas and F. C. Tompkins, *Proc. R. Soc. London, Ser. A*, **210**, 111 (1951).
- (4) B. E. Bartlett, F. C. Tompkins, and D. A. Young, *Nature (London)*, **179**, 365 (1957).
- (5) E. G. Prout and D. J. Moore, *Nature (London)*, **203**, 860 (1964).
- (6) K. Torkar and H. T. Spath, *Monatsh. Chem.*, **98**(5), 1696 (1967).
- (7) K. Torkar and H. T. Spath, *Monatsh. Chem.*, **98**(5), 1712 (1967).
- (8) K. Torkar and H. T. Spath, *Monatsh. Chem.*, **98**(5), 1733 (1967).
- (9) K. Torkar and H. T. Spath, *Monatsh. Chem.*, **98**(5), 2020 (1967).
- (10) K. Torkar, H. T. Spath, and K. Mayer, *Monatsh. Chem.*, **98**(6), 2362 (1967).
- (11) K. Torkar and H. T. Spath, *Monatsh. Chem.*, **99**(1), 118 (1968).
- (12) K. Torkar and H. T. Spath, *Monatsh. Chem.*, **99**(2), 773 (1968).
- (13) K. Torkar, U.S. Clearing House of Federal Scientific Technical Information, AD 1967, AD-818356, 190 (Eng).
- (14) K. Torkar, H. T. Spath, and G. W. Herzog, *React. Solids, Proc. Int. Symp.*, **6th**, 1968, 287 (1968).
- (15) K. Torkar and H. T. Spath, *Monatsh. Chem.*, **98**(6), 2382 (1967).
- (16) J. N. Maycock, "Lattice Defects in Meta-stable Solids", RIAS, Martin Marietta Corp. Md., Feb 1972.
- (17) V. R. Pai Verneker, R. K. Sood, and V. Krishna Mohan, *Indian J. Chem.*, **13**, 908 (1975).
- (18) N. F. Mott, *Proc. R. Soc. London, Ser. A*, **172**, 325 (1939).
- (19) J. M. Thomas and F. C. Tompkins, *J. Chem. Phys.*, **20**, 662 (1952).
- (20) Von G. V. Hevesey and W. Seith, *Z. Phys.*, **56** 790 (1929); **57**, 869 (1929).
- (21) V. R. Pai Verneker and K. Rajeshwar, *J. Phys. Chem. Solids*, **37**, 63 (1976).
- (22) V. R. Pai Verneker and K. Rajeshwar, *J. Phys. Chem. Solids*, **37**, 67 (1976).
- (23) V. R. Pai Verneker and M. N. Radhakrishnan Nair, *Combust. Flame*, **25**, 301 (1975).

## Size and Geometric Effects in Copper and Palladium Metal Clusters

R. C. Baetzold

Research Laboratories, Eastman Kodak Company, Rochester, New York 14650 (Received September 6, 1977)

Publication costs assisted by Eastman Kodak Company

Self-consistent extended Hückel calculations for cluster and bulk Cu and Pd are reported. The density of states function of clusters up to 40 atoms takes on the shape but not the width of the bulk function. Vacant d orbitals are observed on Pd atoms which have coordination numbers 5–7 in irregularly shaped clusters. This effect correlates with a greater projected density of states at the Fermi energy. This effect is not present in Cu clusters. These effects and their implications for catalysis are discussed.

### 1. Introduction

Catalysis involving small metal particles is of great commercial importance. While a vast background of experimental work exists classifying catalytic properties of small metal particles, little understanding of their microscopic role in catalysis exists. Attempts<sup>1–3</sup> to correlate catalytic activity with particular properties such as percent

and character of the metal bond, heats of adsorption or sublimation, metallic radius, densities of states at the Fermi level, or surface d electrons<sup>4</sup> are useful to provide understanding within a particular class of reactions, but often do not apply to more general reactions.

Outstanding questions include the matter of determining catalyst electronic effects with size and its influence upon

catalytic reactions. Boudart<sup>5</sup> has classified reactions into structure sensitive and insensitive based upon this size effect. Some reactions show pronounced effects of catalyst particle size while others are independent<sup>6</sup> of the catalyst size. A critical size exists for some reactions, where 8–20 atoms of Pd, Ag<sub>4</sub>, and Au<sub>2</sub> represent this size for metal deposition from solution.<sup>7</sup> Thus experimental evidence suggests that important catalytic effects take place as metal particle size changes. The role of the catalyst support in influencing electronic properties of the catalyst may also be important. The question of whether support effects are dominant in determining catalytic properties of the small particles depends in part upon how the electronic properties of the catalyst particle compare with those of the bulk metal.

The role of catalyst structure involving special arrangements of atoms remains open. Significant in this regard have been the stepped surface studies which define an active catalyst site for some reactions.<sup>8</sup> These active sites on metal crystals involving atoms with low coordination number are comparable to small metal particles in catalytic activity for some reactions.<sup>8</sup> The possible relationship between electronic properties and structure of these sites is now actively under investigation.<sup>9,10</sup>

Theoretical studies of small metal particles using semiempirical molecular orbital theory have focused on their electronic<sup>11</sup> and chemisorptive properties.<sup>12–14</sup> The approach of binding energies, ionization potential, and energy level spacing to bulk values has been deduced to generally require particles larger than 10 Å diameter for close correspondence.<sup>11</sup> Clusters of Ag having 55 atoms were calculated to possess 1/3 to 1/2 of the bulk binding energy per atom. Ionization potentials of large clusters of Cu, Ag, and Au containing up to 135 atoms have been studied.<sup>15</sup> Changes are found in this property upon progressing from 79 to 135 atoms. In contrast to this behavior, chemisorptive studies have generally shown that a localized model is sufficient to describe the interaction between adsorbate and metal surface.<sup>12,14,16</sup> The primary surfaces studied here have been Ni and W where 9- to 10-atom surface models have been employed.

The present work is aimed at principally studying the valence density of states (DOS) for Cu and Pd clusters in both highly symmetric and asymmetric geometries. These two metals differ significantly in electronic and catalytic properties. We wish to examine the behavior of the DOS as particle size changes and make direct comparisons with the calculated bulk value. In addition, some special sites, analogous to steps in that they possess atoms with low coordination, will be examined. These calculations have been performed using extended Hückel theory<sup>16</sup> within the framework of the self-consistent procedure for metal complexes.<sup>17</sup> Thus, excessive charge buildups sometimes observed in extended Hückel calculations are avoided.

## 2. Method

The extended Hückel procedure developed by Hoffmann requires diagonalization of a secular determinant:

$$|H - ES| = 0 \quad (1)$$

The overlap elements ( $S_{ij}$ ) are calculated using Slater orbitals involving two functions for the d orbital and one function for the s and p orbitals. Thus 4d, 5s, and 5p orbitals for Pd and 3d, 4s, and 4p orbitals for Cu are treated. The Hamiltonian matrix elements ( $H_{ij}$ ) were taken from the Wolfsberg–Helmholtz formula<sup>19</sup>

$$H_{ij} = K(H_{ii} + H_{jj})S_{ij}/2 \quad K = 1.75 \quad (2)$$

and the atomic ionization potential provided values for the

TABLE I: Parameters of the Calculation

		Cu		Pd	
		Slater exponents			
3d	5.950 (0.5933), 2.300 (0.5744)	4d	5.983 (0.5264), 2.613 (0.6372)		
4s	1.550	5s	1.568		
4p	1.550	5p	2.190		
		Cu		Pd	
Electron ionized	Configuration <sup>b</sup>	A, eV	B, eV	A, eV	B, eV
s	d <sup>N</sup> <sub>s</sub>	7.72	9.91	7.43	8.65
s	d <sup>N-1</sup> <sub>s</sub> <sup>2</sup>	9.17	10.63	8.28	8.65
s	d <sup>N-1</sup> <sub>sp</sub>	10.86	10.90	11.21	8.65
p	d <sup>N</sup> <sub>p</sub>	3.98	7.69	3.85	7.36
p	d <sup>N-1</sup> <sub>p</sub> <sup>2</sup>	5.28	7.91	7.73	7.36
p	d <sup>N-1</sup> <sub>sp</sub>	5.03	8.13	6.44	7.36
d	d <sup>N+1</sup> <sub>c</sub>	2.50	17.87	8.51	11.82
d	d <sup>N</sup> <sub>s</sub>	10.66	16.08	11.68	11.82
d	d <sup>N</sup> <sub>p</sub>	12.86	15.47	12.97	11.82

<sup>a</sup> Two exponents with coefficients in parentheses. <sup>b</sup>  $N = 10$  for Cu, 9 for Pd. <sup>c</sup> Extrapolated for Cu.

$H_{ii}$  elements. The  $H_{ii}$  values were expressed in terms of valence state ionization energy ( $H_{ii}'$ ) using the procedure of Basch, Viste, and Gray<sup>17</sup>

$$-H_{ii}' = A + BQ \quad (3)$$

where  $Q$  is the charge on the atom and  $A$  and  $B$  are obtained by fitting to average electron configuration energy for the atom or ion. Nine configurations were employed for Cu,<sup>17</sup> while spectroscopic data<sup>20</sup> were employed to obtain average energies in order to determine the  $A$  and  $B$  values of Pd. These values as well as other input data are listed in Table I. The calculations went through 10–15 iterations generally, giving a Mulliken charge distribution varying less than 0.01 on each atom between successive cycles. Clusters larger than 19 atoms were calculated using the self-consistent  $H_{ii}$  values appropriate to the 19-atom cluster in a noniterative manner. Some of the calculations for Pd clusters in asymmetric geometries required 30 cycles.

The use of extended Hückel theory for bulk crystals is very similar to that employed recently for Ni bulk and surfaces.<sup>21</sup> Slater orbitals representing valence d, s, and p orbitals were employed with the exponents of Table I and  $H_{ii}$  values appropriate to d<sup>10</sup><sub>s</sub><sup>1</sup> for Cu and d<sup>9</sup><sub>s</sub><sup>0.6</sup> for Pd. Lattice constants were determined by bulk experimental values. Bloch functions are the basis functions which convert the secular equations to a function of  $\bar{k}$ , the reciprocal lattice vector. Overlap elements were determined from

$$S_{\mu\nu}(\bar{k}) = \sum_l S_{\mu\nu}^{0,l}(k) e^{i\bar{k} \cdot \bar{R}_l} \quad (4)$$

where  $\bar{R}_l$  is the translation vector, and the superscripts 0, $l$  define the unit cells where  $\mu$  and  $\nu$  have their origin. The sum includes terms up to the fourth nearest neighbor. Hamiltonian elements were constructed in a similar fashion. The secular equation is solved at an equivalent of 2048 points in  $\bar{k}$  space. The resulting eigenvalues were averaged over these points to obtain a DOS histogram. The histogram was further smoothed by centering a Gaussian function of 0.1 eV width upon each energy level. This procedure employing Gaussian functions was also used for the finite clusters and for preparing all of the figures shown here. The smoothing procedure employing Gaussian functions groups the discrete energy levels within a small energy interval. This effect occurs in any experimental measurement of DOS due to finite instrumental

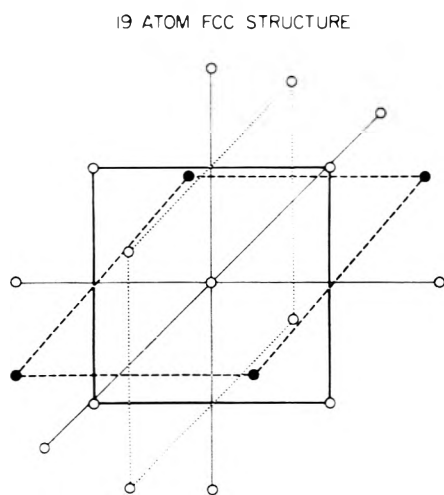


Figure 1. Fccub model for 19-atom cluster.

resolution. Gaussian functions are often employed to express the instrumental line width.

The projection of the DOS upon particular atoms was obtained from the coefficients  $C_{ij}$ . The relation

$$\rho_i = \sum_j (2C_{ji}^2 + \sum_{j \neq k} C_{ji} C_{ki} S_{jk}) \quad (5)$$

provides the projection of a given molecular orbital  $i$  upon a particular atom when the sum over  $j$  only runs over orbitals on the atom in question. Analysis of each molecular orbital provides the projection which is plotted vs. energy. This value is multiplied by a Gaussian function as described earlier to determine the projected DOS.

### 3. Results

**3.1. Model.** Calculations have been performed for three-dimensional symmetric geometries up to 8 atoms (triangles, tetrahedrons, bipyramids, bicapped pentagons, cubes) and face-centered-cubic geometries (fccub) at larger sizes. The model for a 19-atom fccub cluster depicts this geometry in Figure 1. The center atom is surrounded by shells of nearest neighbors containing 12, 6, and 24 atoms successively in complete shells. We consider highly symmetric clusters containing 13, 19, and 43 atoms as well as less symmetric clusters containing incomplete shells of nearest neighbors. All nearest neighbor distances are equal in these calculations and taken as 2.50 and 2.74 Å for Cu and Pd, respectively. These values correspond closely to the experimental bulk distances. Calculated equilibrium distances for the large clusters are 2.5 and 2.3 Å, respectively, for Cu and Pd for noniterative calculation. The results of the non-self-consistent calculation for bond length agrees better with bulk experiment for Cu than Pd. This is due to the greater calculational difficulty in properly describing the partially filled d band which exists for Pd, but not for Cu.

**3.2. Cu Cluster DOS.** The bonding in Cu clusters is due primarily to overlap of 4s orbitals. The density of states function (DOS) for various sized clusters is shown in Figure 2. The DOS profiles were obtained using the Gaussian procedure described earlier. The most intense peaks in Figure 2 are due primarily to d molecular orbitals, with less intense peaks due to s molecular orbitals appearing on both sides of the d states. The filling of the s band with size is particularly apparent in this figure. Multiple peak structure appears in the DOS for small sizes, yet changes are apparent in all clusters in this size range. In addition to these effects the highest occupied molecular orbital (HOMO) shifts toward the vacuum level by 2.66 eV from Cu<sub>2</sub> to Cu<sub>43</sub> as seen in Table II. The top of the d band

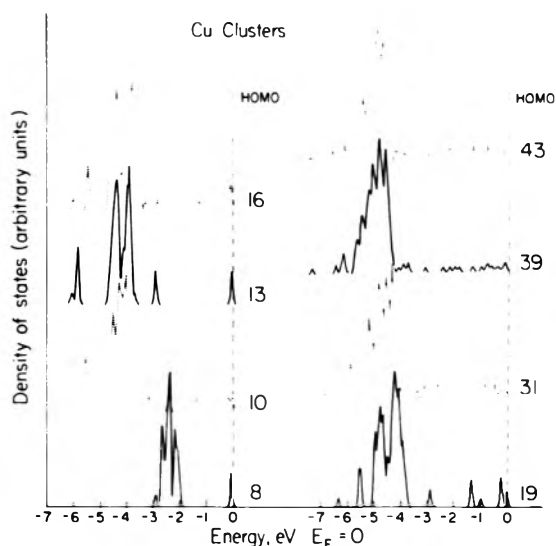


Figure 2. Valence density of states for Cu clusters containing 8-43 atoms vs. energy measured relative to the Fermi energy,  $E_F$ .

TABLE II: Properties of the Clusters

No. of atoms	Copper		Palladium	
	HOMO, eV	$\Delta$ , <sup>b</sup> eV	HOMO, eV	$\Delta$ , eV
2	9.36	2.33		
8 <sup>a</sup>	8.91	2.66	9.09	0.01
10	7.17	0.14	9.12	0.03
13	7.32	0.94	9.27	0.12
16	7.44	0.05	9.49	0.01
19	7.16	0.72	9.21	0.01
31	7.11	0.23	9.17	0.01
39	6.81	0.17	9.15	0.01
43	6.70	0.01		
<sup>a</sup>	6.01			

<sup>a</sup> Cubic geometry. <sup>b</sup>  $\Delta$  is the energy gap between highest occupied and lowest unoccupied molecular orbitals.

is located closer to the HOMO for the small clusters. The energy level spacing at HOMO decreases with increasing size. The general features of ESCA spectra of the bulk can be observed in the largest clusters where an intense peak in the d band is found nearer the vacuum level and a less intense shoulder appears at more negative energy. This feature is less pronounced in the smaller clusters.

The calculated DOS may be compared for the finite clusters and bulk solid. Figure 3 shows that the DOS is different for the bulk than for the small clusters. The comparison between symmetric clusters in the figure shows a much larger bandwidth for the bulk and a different shape. The calculated bulk d bandwidth of 2 eV is about 1/3 greater than observed for the finite clusters. While a general convergence toward the bulk calculated structure is occurring with cluster size, the transition is by no means complete at 43 atoms.

**3.3. Bulk Bands of Cu.** The energy bands calculated for Cu are shown in Figure 4. Only the five d and one s-p band are shown. The shape of the bands in the Brillouin zone is similar to that observed in augmented plane wave calculations.<sup>22</sup> The  $e_g$  bands lie 0.47 eV closer to the vacuum than the  $t_{2g}$  bands at  $\vec{k} = (000)$ . The d bands are narrower in the present work and located further from the Fermi energy than those calculated by the augmented plane wave method. While a better choice of parameters might be expected to remedy this discrepancy, the primary purpose in the work is to make relative comparisons of DOS vs. size using the same parameters. The present calculation gives a d bandwidth of 1.63 eV and top d band

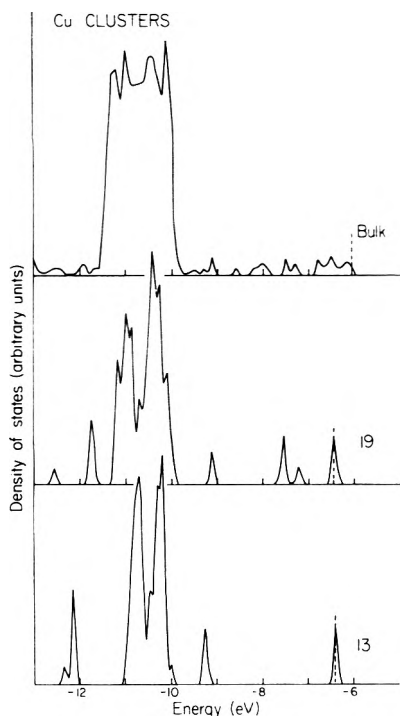


Figure 3. Comparison of density of states calculated for Cu<sub>13</sub> and Cu<sub>19</sub> clusters and Cu bulk using the parameters of Table I.

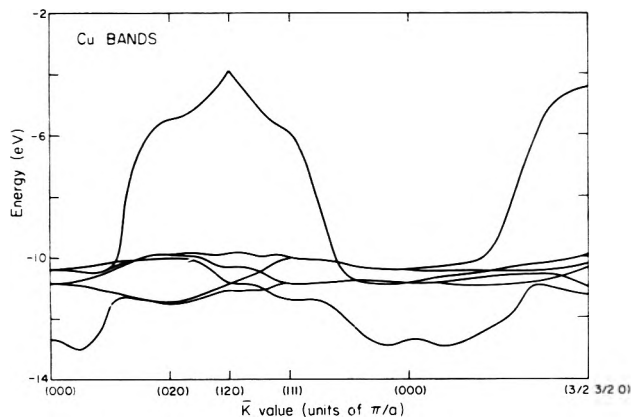


Figure 4. Display of the lowest energy bands calculated for Cu bulk vs. the Brillouin zone value,  $\bar{k}$ . The Fermi level is  $-6.01$  eV.

edge below the Fermi energy of  $3.87$  eV.

3.4. *Projected DOS of Cu.* The projection of the DOS upon particular atoms in the Cu cluster shows the effect of the self-consistent potential. This is illustrated in Figure 5 for the occupied energy levels in the 19-atom Cu model. The molecular orbitals of the center atom are significantly shifted to lower energy relative to the other orbitals. These energy levels appear more pronounced near the bottom of the DOS profile, while the energy levels associated with atoms having fewer nearest neighbors appear near the top. The charges of each atom in this model are shown in Table III and indicate only a minor degree of charge transfer. The shifts in potential relative to the center atom are also tabulated. These values indicate that the density of states profile associated with a given atom is strongly dependent upon the number of nearest neighbors of the atom.

The charge separation calculated in metal clusters is greatly reduced by the self-consistent procedure. Data in Table III refer to the 19-atom cluster of Figure 1 and the 16-atom cluster formed by removing two atoms along the same axis. The d orbital occupation of Cu clusters is unaffected by shape, position, or self-consistency and remains essentially completely full.

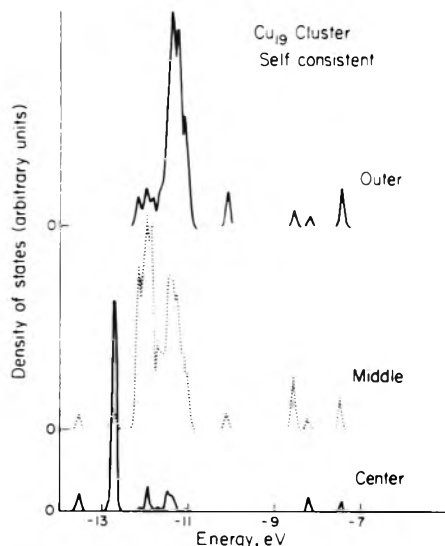


Figure 5. A projection of the density of states upon center, middle, and outer atoms in the 19-atom fccub Cu cluster.

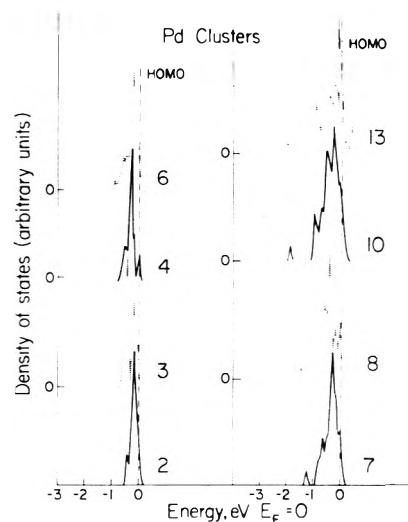


Figure 6. The dependence of the Pd valence density of states is shown for 2-13 atom clusters. The HOMO is indicated by the dashed line.

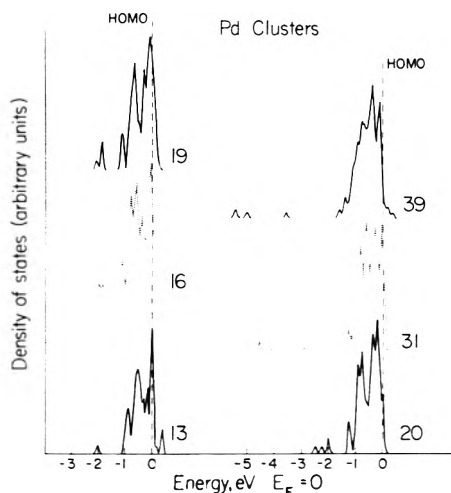


Figure 7. The dependence of the Pd valence density of states is shown for 13-39 atom clusters. The HOMO is indicated by the dashed line.

3.5. *Pd Cluster DOS.* Clusters of Pd have a high DOS at the Fermi level, unlike the Cu clusters just discussed. The changes in DOS from Pd<sub>2</sub> to Pd<sub>39</sub> are shown in Figures 6 and 7. It is clear that drastic changes take place in the bandwidth, shape, and density of states at the Fermi level.

TABLE III: Properties of Cu and Pd 16- and 19-Atom Clusters: Charges, d Occupation, and Self-Consistent Potential

Atom type <sup>a</sup>	Non-self-consistent		Self-consistent				
	Charge	d occupation	Charge	d occupation	-H <sub>ii</sub> potential, eV		
					s	p	d
M <sub>16</sub>							
Cu center	+0.48	9.9	+0.09	10.0	9.01	4.58	12.45
Cu middle	-0.04	9.9	-0.01	9.9	8.14	3.80	11.67
Cu outer	+0.003	10.0	+0.001	10.0	8.09	3.83	11.39
Pd center	+2.11	8.1	-0.03	9.7	6.77	1.87	10.12
Pd middle	-0.04	9.5	-0.11 (4) <sup>b</sup>	9.7	6.34	0.88	9.77
			-0.28 (4) <sup>b</sup>				
			-0.23 (4) <sup>b</sup>				
Pd outer	-0.28	9.8	+0.48 (2) <sup>b</sup>	9.6	6.52	0.92	9.59
			+0.01 (2) <sup>b</sup>				
			+0.14 (2) <sup>b</sup>				
M <sub>19</sub>							
Cu center	+0.50	9.9	+0.05	9.9	9.11	4.52	12.67
Cu middle	-0.04	9.9	-0.02	9.9	8.06	3.75	11.51
Cu outer	-0.14	9.9	-0.10	10.0	7.84	3.69	11.15
Pd center	+1.58	8.2	+0.29	9.8	6.76	1.22	10.33
Pd middle	+0.09	9.4	-0.05	9.5	6.48	1.02	9.85
Pd outer	-0.45	9.8	-0.07	9.5	6.45	1.23	9.76

<sup>a</sup> Center atoms have 12 nearest neighbors, middle atoms have 7 nearest neighbors, and outer atoms have 4 nearest neighbors. <sup>b</sup> Differing charges on atoms in single shell, number of atoms in parentheses.

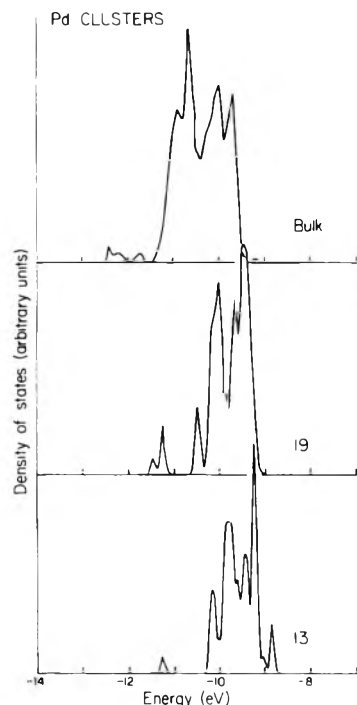


Figure 8. The valence density of states is compared for Pd<sub>13</sub> and Pd<sub>19</sub> clusters and bulk Pd.

There are particular effects due to irregularly shaped structures. The band broadens and the density of states at the Fermi level increases as the clusters increase in size. Molecular orbitals composed of s orbitals overlap the d band and are responsible for the less intense peaks appearing lower in energy than the d levels. The comparison of these profiles with the calculated profile for bulk Pd in Figure 8 shows that bulk behavior is not attained for these cluster sizes even though there is a general similarity with the bulk DOS. The d band calculated here is more narrow for the bulk than is observed experimentally. Calculations using the bond length of 2.5 Å give a broader bulk d bandwidth of 2.9 eV, but the main features of the DOS are unchanged.

3.6. *Projected DOS of Pd Clusters.* The projected DOS is strongly dependent upon the number of nearest

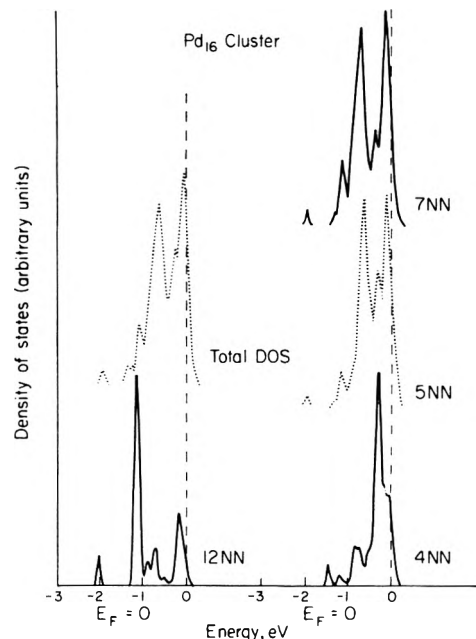


Figure 9. Projected density of states for various atoms in Pd<sub>16</sub> cluster containing different numbers of nearest neighbors (NN).

neighbors an atom possesses. The behavior of this function for Pd<sub>13</sub> and Pd<sub>19</sub> is very similar to the results reported for Cu<sub>19</sub> in Figure 5. Outer atoms with the fewest nearest neighbors possess the greatest component near the top of the bands and also the greatest density of states at the Fermi energy. In the case of Pd clusters with incomplete shells of nearest neighbors, such as Pd<sub>16</sub> shown in Figure 9, the largest density of states at the Fermi energy occurs for atoms with five or seven nearest neighbors. In this particular cluster there are three atoms in an incomplete shell, two of which are located on the same axis. Similar behavior is found for the Pd<sub>20</sub> cluster in Figure 10. Here the atom with five nearest neighbors has the largest projected density of states at the Fermi energy. Apparently, atoms with intermediate coordination numbers tend to maximize this function on small clusters.

The average electron configuration of Pd clusters does not vary strongly with size. It is, however, more dependent upon the atom's position. Data for the self-consistent



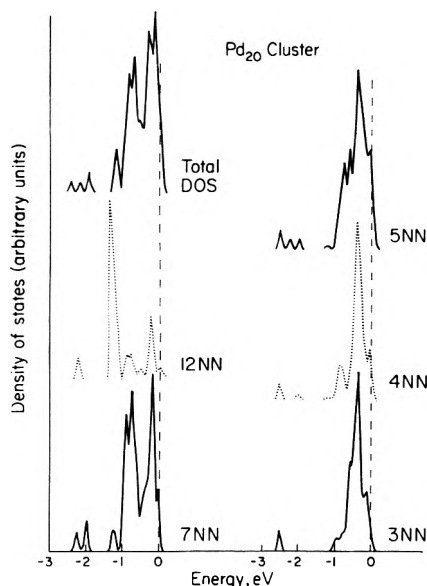


Figure 10. Projected density of states for various atoms in  $\text{Pd}_{20}$  cluster containing different numbers of nearest neighbors (NN).

calculation in Table III show that d orbital occupancy differs for the outer atom in  $\text{Pd}_{16}$  and  $\text{Pd}_{19}$  clusters. This type of effect is also observed for other irregularly shaped clusters. The charge distribution in Pd clusters shows minor charge buildups, although largest values usually appear on atoms in incomplete shells.

The effects of the charge self-consistent calculations are clearly shown for Pd clusters in Table III. A large positive charge with a depletion of d electrons is observed on the center atom in the non-self-consistent calculation. This is because this calculation predominately puts orbitals on atoms with the largest number of nearest neighbors near the top and bottom of bands. Thus, in Pd with an incompletely filled d band, a positive charge results on the center atom. Doing the self-consistent calculation lowers these orbitals resulting in more complete electron filling of the d levels associated with this atom. This results in a depletion of electrons in d levels associated with atoms on the surface and is responsible for the effects shown in Table III.

#### 4. Discussion

The extended Hückel procedure employed here for clusters and bulk crystals is very similar to the tight-binding method of solid state physics. All overlap and energy interactions between orbitals are retained permitting hybridization effects. Inclusion of nondiagonal terms between nonnearest neighbors results in greater destabilization of antibonding orbitals than would be obtained otherwise. The self-consistency procedure included here also leads to a more realistic charge distribution. Thus, the present procedure is thought to provide a reasonably accurate description of the DOS of transition metal clusters and bulk just as the tight-binding method has provided.<sup>23</sup>

There are close parallels observed between the calculated properties of thin films and clusters. Other calculations treating a monolayer of copper using a Green's function method have shown a more narrow d band for the monolayer vs. bulk and a Fermi energy shifted closer to the d band.<sup>24</sup> Both of these effects are apparent in Figures 2 and 3. Of course the narrowing of the rms width of bands near the surface has been observed in tight-binding calculations.<sup>25</sup> Other cluster calculations using multiple scattering methods have reported narrowing of d bands

for transition metal clusters<sup>10</sup> which is consistent with the behavior observed here. The DOS behavior of small metal particles deviates significantly from the corresponding bulk quantity as determined from our calculations. The bandwidth and shape of the DOS change significantly up to 40 atoms of Cu and Pd in various shaped fccub clusters.

There is an intermediate coordination number for Pd atoms in the unsymmetrical clusters which facilitates the greatest density of states at the Fermi energy and greatest hole population in the d levels. In asymmetric clusters the self-consistent calculation provides this result at coordination numbers of 5 or 7. These data are observed in Figures 9 and 10 as well as Table III. Included in this behavior are 18- and 20-atom clusters related to the model of Figure 1 by addition or removal of one atom. Atoms in the copper clusters do not show this effect. The vacant d levels in the Pd clusters would be suitable for accepting electrons from a chemisorbing species. Such a partial or complete electron transfer could have significant effect on the bonding in the chemisorbed species and thus account for the catalytic effect. In this proposed mechanism of catalytic effect by very small metal particles, only some clusters with particular shapes would be the active catalysts. In larger particles several active sites could exist on the same particle.

The larger projected density of states at the Fermi level observed for Pd atoms of intermediate coordination is due in part to the self-consistent potential. This potential arises from the negative charges calculated for surface atoms. The potential shifts d orbitals on atoms with incomplete coordination toward the top of the d band where the Fermi level is located. The molecular orbitals are spread apart in energy to a degree which increases with increasing number of nearest neighbors. These effects position d orbitals on atoms with intermediate coordination near the Fermi level. In this position, these orbitals can interact with chemisorbed species through electron donation and reception.

These results may be compared with recent SCF- $X\alpha$ -SW calculations for transition metal clusters.<sup>26</sup> A similarity exists in the ionization potential and its dependence upon size. Values of the IP greater than for the bulk are observed in both calculations and 13-atom clusters of Cu have values of 1.3 eV larger than calculated bulk in this work vs. the value 2 eV reported in the SCF- $X\alpha$ -SW work. Values of the electron affinity greater than the bulk work function are not observed in this work. A significant difference also exists in the interpretation of DOS behavior. The shape of the DOS deviates significantly from the bulk for the asymmetric clusters considered in this work. Symmetric 13- and 19-atom clusters have a d bandwidth less than the bulk calculated value. This effect is true apart from the choice of parameters which is the same for bulk and cluster.

Single  $\zeta$  Slater orbitals used in prior work<sup>11</sup> generate too narrow d bands when exponents of Clementi<sup>27</sup> are employed. However, as the prior work has shown, the more diffuse matching overlap orbitals of Cusachs<sup>28</sup> give a much wider d band for clusters such as  $\text{Pd}_{19}$ . It should also be pointed out that no experiments have been reported on the DOS of monodisperse distributions of metal clusters. This type of data would be required to determine when the DOS of the cluster becomes bulklike.

We have observed significant effects on the d orbital population of Pd but not Cu irregularly shaped clusters. This effect is in accord with a model derived by using an appropriate solution to the Schrödinger-Poisson-Hartree calculation.<sup>29</sup> There it was concluded that on stepped

surfaces significant changes were expected in the population of d orbitals when the density of states at the Fermi energy is large, as in the case of Pd, but not for Cu.

We have employed a relatively simple method to examine properties of metal clusters. The thrust of this work is to uncover the trends rather than absolute numbers. The latter task is left to more exact procedures when they become applicable to the shapes and sizes of clusters examined here. The density of states at the Fermi level for Pd clusters shows an interesting dependence on size. This quantity may be obtained from the data plotted in Figures 6 and 7. This property increases with size for more than four atoms and may be important in explaining critical catalytic size observed for Pd clusters.<sup>8</sup>

## References and Notes

- (1) G. C. Bond, *Surface Sci.*, **18**, 77 (1969).
- (2) V. Ponec, "Heterogeneous Catalysis. Some Selected Problems", in "Dynamic Aspects of Surface Physics", LVIII Corso, Bologna, Italy, 1974.
- (3) H. Wise, *J. Catal.*, **10**, 69 (1968).
- (4) O. Johnson, *J. Catal.*, **29**, 508 (1973).
- (5) M. Boudart, *Adv. Catal.*, **20**, 153 (1969).
- (6) T. A. Dorling, M. J. Eastlake, and R. L. Moss, *J. Catal.*, **14**, 23 (1969).
- (7) J. F. Hamilton and P. C. Logel, *Photogr. Sci. Eng.*, **18**, 507 (1974); *J. Catal.*, **29**, 253 (1973).
- (8) G. A. Somorjai, *Acc. Chem. Res.*, **9**, 248 (1976).
- (9) M. C. Desjonqueres and F. Cyrot-Lackman, *J. Phys. F: Metal Phys.*, **5**, 1368 (1975); *Solid State Commun.*, **18**, 1127 (1976).
- (10) R. O. Jones, P. J. Jennings, and G. S. Painter, *Surface Sci.*, **53**, 409 (1975).
- (11) R. C. Baetzold, *J. Chem. Phys.*, **55**, 4363 (1971); R. C. Baetzold and R. E. Mack, *ibid.*, **62**, 1513 (1975).
- (12) G. Blyholder, *Surface Sci.*, **42**, 249 (1974); *J. Chem. Phys.*, **62**, 3193 (1975); *J. Phys. Chem.*, **79**, 756 (1975).
- (13) P. Politzer and S. D. Kasten, *J. Phys. Chem.*, **80**, 385 (1976).
- (14) L. A. Anders, R. S. Hansen, and L. S. Bartell, *J. Chem. Phys.*, **62**, 1641 (1975).
- (15) E. R. Davidson and S. C. Fain, *J. Vac. Sci. Technol.*, **13**, 209 (1976).
- (16) D. J. M. Fassaert, H. Verbeek, and A. van der Avoird, *Surface Sci.*, **29**, 501 (1972); D. J. M. Fassaert and A. van der Avoird, *ibid.*, **55**, 313 (1976).
- (17) R. Hoffmann, *J. Chem. Phys.*, **39**, 1397 (1963).
- (18) H. Basch, A. Viste, and H. B. Gray, *J. Chem. Phys.*, **44**, 10 (1966).
- (19) M. Wolfsberg and L. Helmholz, *J. Chem. Phys.*, **20**, 857 (1953).
- (20) C. E. Moore, *Natl. Bur. Stand. (U.S.), Circ.*, No. 467, Vol. 1-3 (1949).
- (21) D. J. M. Fassaert and A. van der Avoird, *Surface Sci.*, **55**, 291 (1976).
- (22) G. A. Burdick, *Phys. Rev.*, **129**, 138 (1963).
- (23) N. V. Smith and L. F. Mattheiss, *Phys. Rev. B*, **9**, 1341 (1974).
- (24) B. R. Cooper, *J. Vac. Sci. Technol.*, **10**, 713 (1973).
- (25) R. Haydock and M. J. Kelly, *Surface Sci.*, **38**, 139 (1973).
- (26) R. P. Messmer, S. K. Knudson, K. H. Johnson, J. B. Diamond, and C. Y. Yang, *Phys. Rev. B*, **13**, 1396 (1976).
- (27) E. Clementi and D. L. Raimondi, *J. Chem. Phys.*, **38**, 2686 (1963).
- (28) L. C. Cusachs and J. H. Corrington in "Sigma M.O. Theory", O. Sinanoglu and K. Widberg, Ed., Yale University Press, New Haven, Conn., 1970.
- (29) L. L. Kesmodel and L. M. Falicov, *Solid State Commun.*, **16**, 1201 (1975).

## Vortical Flow as a Source of Optical Activity in J Aggregates of Cyanine Dyes?

Bengt Nordén

Department of Inorganic Chemistry 1, Chemical Center, University of Lund, S-220 07 Lund, Sweden (Received September 7, 1977)

An examination was made of the reported swirl-induced optical activity of J aggregates (Scheibe polymer) of 1,1'-diethyl-2,2'-cyanine chloride. The vortex strain in a model swirl was found to be theoretically capable of degrading this polymer. However, experiments did not lead to any significant intrinsic optical activity. Circular dichroism deflections were due to macroscopic linear dichroism from accidentally oriented material.

A new mechanism for producing asymmetric species has recently been suggested by Honda and Hada.<sup>1</sup> They reported that opposite enantiomorphs of the optically active Scheibe polymer (aggregated 1,1'-diethyl-2,2'-cyanine chloride) could be preferentially formed during synthesis by right- and left-handed swirling of the solution.

In earlier trials we did not succeed in reproducing their results in the preparation of polymeric 1,1'-diethyl-2,2'-cyanine in a conical swirl and suggested that their observation could have been an artifact due to linear dichroism from accidentally oriented material.<sup>2</sup> A recent study by Saeva and Olin supported this concept.<sup>3</sup> However, since neither the structure of the Scheibe polymer nor the hydrodynamic conditions can be uniquely defined very easily we cannot eliminate the possibility that Honda and Hada really obtained optical activity by application of dissymmetric flow, which they continue to claim in repeated studies.<sup>4</sup> In view of its general importance we give the question some further consideration here.

No example has previously been reported on specific interactions between dissymmetric matter and dissymmetric flow on the molecular level but this possibility has been tentatively referred to in various macroscopic connections (the relative proportions of right- and left-handed

shells on some ocean beaches have been ascribed to hydrodynamic effects;<sup>5</sup> a rotating drum apparatus has been suggested for separation of enantiomeric crystals<sup>6</sup>). In macroscopic systems gravitation usually provides a physical reference axis with which even a two-dimensional swirl defines a dissymmetric system. However, on a molecular level it seems necessary to require intrinsic (three-dimensional) dissymmetry. As a measure of the "vortex strain" we may define

$$S = \int \langle v \rangle \cdot \text{curl } v \, d\tau = \int \langle v \rangle \cdot \left( \frac{\partial v_z}{\partial y} - \frac{\partial v_y}{\partial z}, \frac{\partial v_x}{\partial z} - \frac{\partial v_z}{\partial x}, \frac{\partial v_y}{\partial x} - \frac{\partial v_x}{\partial y} \right) d\tau \quad (1)$$

where  $\text{curl } v(x, y, z)$ , the vorticity, is proportional to the instantaneous angular momentum of a spherical particle of fluid, centered in the point  $(x, y, z)$ , and  $\langle v \rangle$  is the average flow vector of the system considered. The signs of the terms in eq 1 take into account that a rotation about the direction of  $\langle v \rangle$  results in a positive  $S$  (right-handed coordinate system) if it is in the direction of turning of a right-handed screw moving along  $\langle v \rangle$ , and so on.

Diffusion differences in an asymmetric flow would in principle provide a way to separate optical isomers.

TABLE I: Approximate Components of Shear Stress<sup>a</sup>

$10^2 x/m$	$(A/r_0)/m\ s^{-1}$	$E$	$10^4 \delta/m$	$p_{zx}/m^{-1}\ kg\ s^{-2}$						$p_{zy}/m^{-1}\ kg\ s^{-2}$		
				$z =$								
				$\delta/2$	$10^{-5}\ m$	$10^{-6}\ m$	$\delta/2$	$10^{-5}\ m$	$10^{-6}\ m$	$\delta/2$	$10^{-5}\ m$	$10^{-6}\ m$
I 0.05	1	6.81	1	(-17)	(43)	(65)	(10)	(18)	(20)			
				(-16)	(41)	(62)	(10)	(18)	(19)			
				(-15)	(38)	(58)	(9)	(16)	(18)			
II 0.80	0.1	2.11	23	-0.023	0.092	0.092	0.043	0.086	0.086			
				-0.021	0.086	0.086	0.043	0.086	0.086			
				-0.020	0.065	0.065	0.043	0.086	0.086			
III 0.985	0.1	0.533	4.0	-0.33	0.12	0.13	0.25	0.48	0.48			
				-0.028	0.10	0.11	0.25	0.48	0.48			
				-0.019	0.07	0.08	0.25	0.48	0.48			

<sup>a</sup> (I) Close to orifice. (II) Skin friction ca. 45° to the  $x$  axis, i.e.,  $p_{zx} \approx p_{zy}$  at  $z = 0$ . (III) Close to top ( $x \approx c$ ).

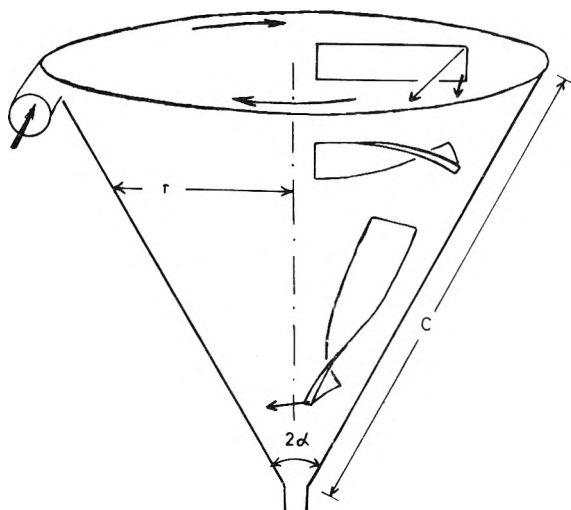


Figure 1. Swirl with positive vortex strain. Configuration of flow cell employed in the experiment is as follows:  $c = 1\ cm$ ,  $r_{top} = 0.75\ cm$ ,  $r_{orifice} = 0.015\ cm$ ,  $2\alpha = 90^\circ$ ; flow rate  $A/r_{top} = 10\ cm\ s^{-1}$ . Deformation expected intuitively for a band-shaped object due to asymmetric force fields.

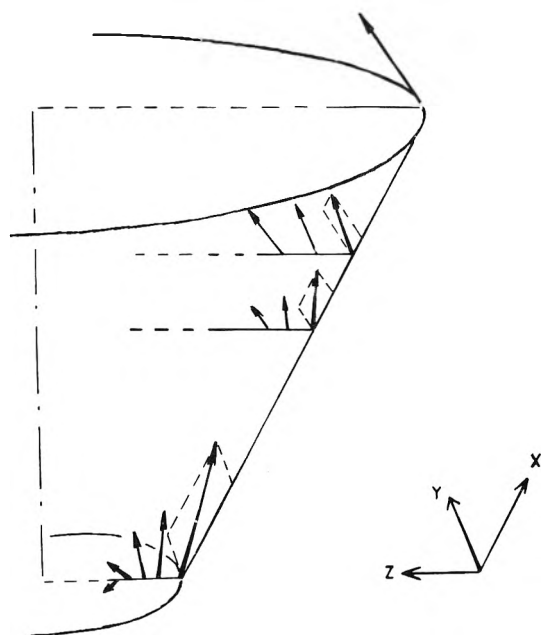


Figure 2. Expected friction forces in a swirl with positive vortex strain.

Asymmetric strain (twisting in one direction) could theoretically perturb conformer equilibria asymmetrically to give optical activity. Preferential degradation could also theoretically give rise to optical activity. Figure 1 illus-

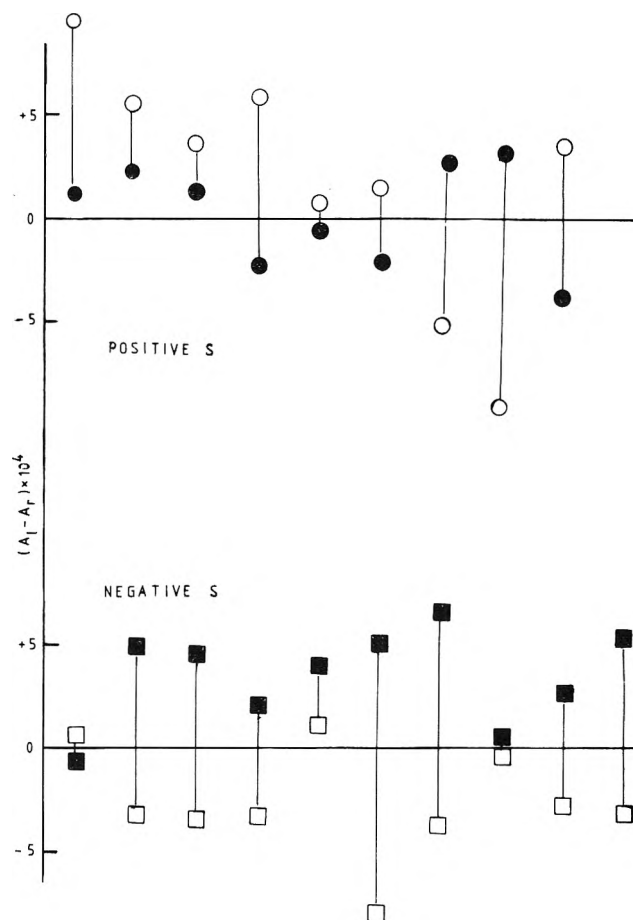


Figure 3. Observed CD at the J band (572 nm) for 19 solutions of  $7.5 \times 10^{-4}\ M$  1,1'-diethyl-2,2'-cyanine iodide in 0.25 M NaCl after swirling. Each solution was allowed to cool slowly from 70 °C (monomeric solution) to 25 °C (Scheibe polymer) in a swirl cell of the geometry given in Figure 1. Each sample (5 mL) was circulated for 4 min through the cell. CD was measured in a rectangular cell (1 × 2 cm; pathlength 0.2 cm) filled in vertical position ( $\phi = 0$ , unfilled symbols) but also measured in horizontal position ( $\phi = 90^\circ$ , filled symbols). These positions corresponded to extreme deflections of opposite directions, so the true CD is approximately the mean value.<sup>10</sup>

trates a population of predominantly right-handed band-shaped helices (Scheibe polymers with positive J-band CD), possible in a right-handed (positive  $S$ ) swirl.

A steady flow with swirl, of the geometry defined in Figure 2, was applied to an aqueous solution of polymerizing 1,1'-diethyl-2,2'-cyanine iodide (Figure 3). Such a swirl provides a rotationally symmetric boundary layer (of thickness  $\delta$ ) for which the momentum equations have been described.<sup>7</sup> The tangential velocity components in the layer are

$$\begin{aligned} u_x &= (A/r_0)E(\eta - 2\eta^2 + \eta^3) \\ u_y &= (A/r_0)(2\eta - \eta^2) \end{aligned} \quad (2)$$

where  $\eta = z/\delta$  and  $A/r_0$  is the flow rate ( $E$  according to ref 7). The orientation and possible deformation and degradation of the polymer is governed by the shear force field. The shear stress can be approximated (neglecting radial components) by

$$p_{zx} = \mu(\partial u_x/\partial z), \quad p_{zy} = \mu(\partial u_y/\partial z) \quad (3)$$

where  $\mu$  is the viscosity. Table I shows roughly how the shear varies within a swirl of the geometry used. The shear forces near the orifice are clearly large enough to disintegrate polymer strands (cf. the observation<sup>2</sup> of a degradation at velocity gradients less than  $10^3 \text{ s}^{-1}$ , i.e.,  $1 \text{ m}^{-1} \text{ kg s}^{-2}$ ).

The observed circular dichroism in a number of experiments (Figure 3) does not suggest any correlation between the sense of swirl and the optical activity. The natural optical activity is in the present performance small compared to linear dichroism arising from accidental orientations of aggregates in the optical cell. An extensive study of how linear and circular dichroism affect the signals

in a circular dichroism spectrometer has been performed in our laboratory<sup>8,9</sup> (technique of measuring circular dichroism on oriented films;<sup>10</sup> general optical formalism<sup>11</sup>).

The present results are in accord with our previous concept of macroscopic linear dichroism as the only significant source of the observed "circular dichroism". However an explanation, which cannot definitely be dismissed, of the difference between these results and those of Honda and Hada, could be a greater turbulence in the boundary layer and the present apparatus, designed to promote laminar flow, may have suppressed some "microvorticity" responsible of their observations.

## References and Notes

- (1) C. Honda and H. Hada, *Tetrahedron Lett.*, **3**, 177 (1976).
- (2) B. Nordén, *J. Phys. Chem.*, **81**, 151 (1977).
- (3) F. D. Saeva and G. R. Olin, *J. Am. Chem. Soc.*, **99** 4848 (1977).
- (4) C. Honda and H. Hada, private communication.
- (5) J. S. Nagle, *J. Sediment. Petrol.*, **37**, 1124 (1967).
- (6) D. W. Howard, E. N. Lightfoot, and J. O. Hirschfelder, *AIChE J.*, **22**, 794 (1976).
- (7) L. F. Crabtree, D. Kuchemann, and L. Sowerby in "Laminar Boundary Layers", L. Rosenheard, Ed., Clarendon Press, Oxford, 1963, p 432.
- (8) Å. Davidsson and B. Nordén, *Spectrochim. Acta*, **32**, 717 (1976).
- (9) Å. Davidsson and B. Nordén, *Chem. Scr.*, **9**, 49 (1976).
- (10) B. Nordén, *Acta Chem. Scand.*, **26**, 1763 (1972).
- (11) H. P. Jensen, *Spectrosc. Lett.*, **10**, 471 (1977).

## Influence of Dynamic Quenching on the Thermal Dependence of Fluorescence in Solution. Study of Indole and Phenol in Water and Dioxane

Gilbert Laustriat\* and Dominique Gerard

Laboratoire de Physique, Faculté de Pharmacie de l'Université Louis Pasteur, Equipe Associée au CNRS (ERA 551), 67083 Strasbourg Cedex, France (Received November 21, 1977)

Publication costs assisted by Institut National de la Santé et de la Recherche Médicale

The thermal dependence of fluorescence quantum yield  $\phi$  and lifetime  $\tau$  is modified in the presence of diffusion-controlled quenching because of temperature effects on the fluorophore lifetime and on molecular mobilities. This phenomenon can be evaluated and studied by means of the temperature coefficient  $C$  (relative variation of  $\phi$  and  $\tau$  per degree). Expressions of  $C$  in the absence and the presence of quencher show that  $C$  is temperature dependent, may increase or decrease upon addition of quencher, and tends at high quencher concentration to a limiting value which essentially depends on the activation energy for diffusion in the solvent. These properties were experimentally studied on solutions of indole and phenol in water and dioxane that are model systems of protein residues.

## Introduction

It is well known that increased temperature reduces the fluorescence quantum yield and lifetime of excited molecules by increasing the efficiency of radiationless deactivation.<sup>1</sup> In solution, the magnitude of this effect generally depends on the solvent since solvent-solute interactions may modify the thermal dependence of radiationless transitions. For instance, the effect of temperature on indole fluorescence has been shown to be much greater in water than in nonpolar solvents.<sup>2-4</sup>

In the presence of an external "dynamic" quencher, there is additional deactivation resulting from a diffusion-controlled bimolecular reaction. How this process influences the thermal dependence of fluorescence is not obvious. As a matter of fact, an increase in temperature induces opposite changes in two important parameters of the quenching mechanism: the fluorophore lifetime decreases, thus reducing the probability of an encounter with the quencher, but molecular mobilities increase, thus

enhancing this probability. According to which effect is predominant, the quenching efficiency, and therefore the fluorescence quantum yield, may be more temperature dependent or less so in the presence than in the absence of quencher.

To our knowledge, such a phenomenon has not yet been analyzed. Besides its general interest for fluorescence studies, it is particularly important in the case of complex systems such as proteins, where it accounts for the variety of thermal variations of fluorescence observed.<sup>5</sup> We therefore studied it in some detail in solutions that are model systems for aromatic residues of proteins: phenol and indole in water and dioxane.<sup>6</sup> These solutions had the additional advantage that the spectroscopic behaviors of the solutes and the molecular properties of the solvents were quite different.

In this study, the magnitude of the temperature effect was evaluated by means of the "temperature coefficient", giving the relative change in quantum yield and lifetime

per unit temperature increment. This parameter has the double advantage of being a convenient index in comparative studies and, as we shall see, of being related to molecular parameters, about which it may give interesting information. In the following, we shall establish the expressions of this coefficient in the absence and the presence of quencher, and show that its predicted properties are experimentally verified, thus giving a consistent interpretation of the observed phenomena.

### Experimental Section

Solutions were prepared in twice-distilled water or spectroquality dioxane. They were used in equilibrium with air since fluorescence quenching by oxygen is nil in water and very small ( $\approx 5\%$  at ambient temperature) in dioxane.

Indole (Prolabo or Sigma) was twice recrystallized in twice-distilled water. Phenol and carbon tetrachloride (Merck) and L-histidine (Sigma,  $\Sigma$  grade) were used without further purification.

Absorption spectra were recorded with a Cary 15 spectrophotometer and fluorescence spectra with an absolute spectrofluorimeter (Fica 55 M KII). Indole derivatives were excited at 295 nm and phenol derivatives at 275 nm (band width 2.5 nm). Relative fluorescence quantum yields were determined from the areas under corrected emission spectra of solutions of equal optical densities; absolute yields were obtained using the reported value of 0.14 for L-tryptophan in water at 25 °C.<sup>7,8</sup>

Lifetimes were measured by the single photoelectron technique with a laboratory-built apparatus previously described.<sup>9</sup>

Quartz cells (1 cm  $\times$  1 cm) containing solutions were placed in a metal sample holder whose temperature was regulated by circulation of liquid. The temperature of solutions was measured by a thermocouple and maintained within 0.5 °C during measurements. The ranges investigated were 10–75 °C in water, and 10–60 °C in dioxane.

The temperature coefficient  $c(T)$  at a given temperature  $T$  (eq 1) was determined from plots of quantum yield  $\phi$

$$c(T) = \frac{1}{\phi(T)} \left( \frac{d\phi}{dT} \right)_T = \frac{1}{\tau(T)} \left( \frac{d\tau}{dT} \right)_T \quad (1)$$

or lifetime  $\tau$  vs. temperature. Such plots often being linear or only slightly curved (Figure 1), we did not attempt to draw the tangent to the curve; we evaluated  $c$  from the changes in  $\phi$  (or  $\tau$ ) for a temperature increment of 15° around  $T$ :

$$c(T) \approx \frac{1}{15} \frac{\phi(T + 7.5) - \phi(T - 7.5)}{\phi(T)}$$

In most cases we used for convenience (ambient temperatures) the value of  $c$  corresponding to  $T = 30$  °C.

### Results and Discussion

#### I. Temperature Coefficient in the Absence of Quencher.

(1) *Expression.* In a solution containing only one solute, the fluorescence quantum yield and lifetime are given by

$$\phi_0 = k_f \tau_0 \quad (2)$$

$$\tau_0 = (k_f + k_{nr})^{-1} \quad (3)$$

where  $k_f$  and  $k_{nr}$  are the rate constants of emission and of nonradiative deactivation, respectively. Extensive studies, recently reviewed by Birks,<sup>1</sup> have shown that temperature has practically no influence on the emission rate but affects the efficiencies of intersystem crossing to the triplet state and/or internal conversion to the ground state. Since one

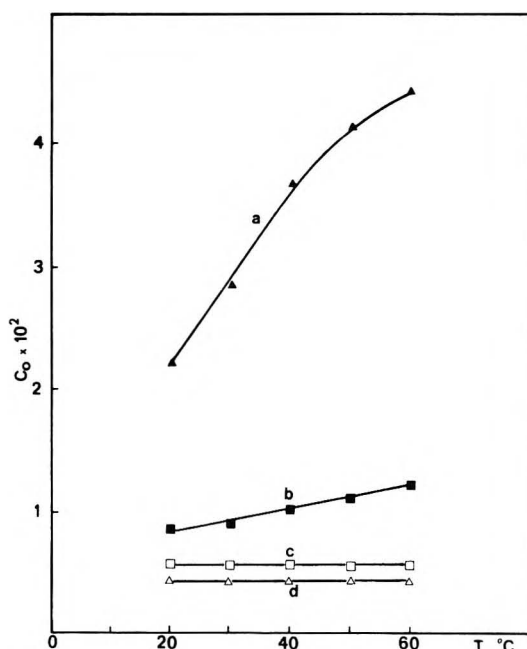


Figure 1. Thermal dependence of the temperature coefficient ( $C_0$ ) of fluorescence in the absence of dynamic quenching for (a) indole/water; (b) phenol/water; (c) indole/dioxane; (d) phenol/dioxane.

of these thermal effects is generally predominant, the rate constant of radiationless transitions may be expressed as<sup>1</sup>

$$k_{nr}(T) = k_{nr}^0 + k_{nr}' \exp(-W_{nr}/kT)$$

where  $k_{nr}^0$  is a constant,  $k_{nr}'$  and  $W_{nr}$  are respectively the frequency factor and the activation energy of the main temperature-dependent process, and  $k$  is the Boltzmann constant.

Using this expression of  $k_{nr}$  in eq 3 and differentiating the latter with respect to temperature leads to (see eq 1)

$$c_0 = -\tau_0 \left[ \frac{k_{nr}' W_{nr}}{kT^2} \exp(-W_{nr}/kT) \right] \quad (4)$$

The temperature coefficient is negative; in the following we shall consider its absolute (positive) value, which will be denoted by  $C_0$ .

(2) *Properties.* Equation 4 shows that  $c_0$  is temperature dependent, but in a nonobvious manner as the terms ( $\tau_0 T^{-2}$ ) and  $\exp(-W_{nr}/kT)$  display opposite thermal variations. Differentiation of (4) shows that  $C_0$  increases with temperature ( $dc_0/dT < 0$ , i.e.,  $dC_0/dT > 0$ ) if

$$W_{nr} > 2kT + C_0 kT^2 \quad (5)$$

Figure 1, where experimental values of  $C_0$  for indole and phenol in water and dioxane are plotted, shows that  $C_0$  does increase with temperature for both solutes in water (curves a and b). This is in agreement with (5) since for both systems reported values of  $W_{nr}$  are greater than values  $w$  of the right-hand side of (5) in the temperature range explored (20–60 °C): (indole/water)  $W_{nr} = 0.52$  eV,<sup>4</sup>  $0.53$  eV,<sup>10</sup>  $0.12 < w < 0.48$  eV; (phenol/water)  $W_{nr} = 0.27$  eV,<sup>11</sup>  $0.11 < w < 0.17$  eV.

In dioxane, however, both coefficients are almost invariant (Figure 1, curves c and d), indicating that  $dC_0/dT \approx 0$ , i.e.,  $W_{nr} \approx w$ . Since  $W_{nr}$  is a constant, this condition first implies that  $w$  varies only slightly, in the temperature range considered, which is effectively the case, because of the low values of  $C_0$ :  $0.075 < w < 0.095$  for indole;  $0.08 < w < 0.11$  for phenol. Furthermore, the predicted proximity of  $W_{nr}$  to  $w$  is verified for indole, whose the activation energy in dioxane has been reported to be 0.065

TABLE I: Absolute Values ( $\times 10^2$ ) of Fluorescence Temperature Coefficients (Relative Variation per Degree of Quantum Yield at 30 °C)

Solute	Water	Dioxane
Indole	3.0 $\pm$ 0.2	0.45 $\pm$ 0.1
Phenol	0.85 $\pm$ 0.1	0.55 $\pm$ 0.1

eV.<sup>4</sup> For phenol the value of  $W_{nr}$  is not known; our results indicate that it should be about 0.09 eV.

The thermal dependence of the temperature coefficient in the absence of quencher is thus consistently explained and may be useful in fluorescence studies. However, when this parameter is used in comparative studies of different systems, this phenomenon requires that coefficients be determined at the same temperature. As already mentioned, we choose 30  $\pm$  7.5 °C. Values of  $C_0$  (30 °C) are indicated in Table I for the four systems studied. For indole they agree with those deduced from data in the literature:  $2.8 \times 10^{-2}$  and  $3.2 \times 10^{-2}$  in water,<sup>3,4</sup> and  $0.45 \times 10^{-2}$  in dioxane.<sup>4</sup> For phenol in water our value is somewhat higher than that calculated from Turoverov's results<sup>11</sup> ( $0.7 \times 10^{-2}$ ); no literature data are available for this compound in dioxane.

II. *Temperature Coefficient in the Presence of Quencher.* (1) *Expression.* A quencher Q at molar concentration [Q] deactivates the excited fluorophore with a probability  $k_q[Q]$  per unit time. The rate constant  $k_q$  of the bimolecular reaction may be expressed as<sup>12</sup>

$$k_q = \frac{4\pi N}{1000} (D_F + D_Q) R_{FQ} p (1 + A_{FQ})$$

where  $N$  is the Avogadro number,  $D_F$  and  $D_Q$  are the diffusion constants of the two molecules,  $R_{FQ}$  is their interaction distance, and  $p$  is the probability of deactivation per encounter.

In the present study, the "transient term"  $A_{FQ} = R_{FQ}[(D_F + D_Q)\tau_0]^{-1/2}$  can be neglected; its value is small ( $<0.15$ ) and almost temperature independent because ( $D_F + D_Q$ ) and  $\tau_0$  have opposite thermal dependences. One can also neglect the very small changes in [Q] due to thermal expansion of the solvent. The temperature effect on  $k_q$  is thus mainly attributable to variations in the diffusion constants. Like changes in viscosity, these variations are described by an Arrhenius law<sup>13</sup>

$$D = D' \exp(-W_d/kT)$$

where the activation energy  $W_d$  may be considered to be the energy required for the formation of a hole in the solvent and for a solute molecule to jump into the hole.<sup>14</sup> Values of  $W_d$  thus depend on both solvent and solute, but as fluorophores used in this work have similar sizes we shall assume that thermal effects on ( $D_F + D_Q$ ) essentially depend on the solvent. The rate constant  $k_q$  is therefore written as

$$k_q = k_q' \exp(-W_d/kT)$$

where  $k_q'$  is a temperature-independent constant.

The temperature coefficient in the presence of dynamic quenching

$$c_q = \frac{1}{\phi_q} \frac{d\phi_q}{dT} = \frac{1}{\tau_q} \frac{d\tau_q}{dT}$$

where  $\phi_q = k_f\tau_q$

$$\phi_q = k_f\tau_q$$

$$\tau_q = (k_f + k_{nr} + k_q[Q])^{-1}$$

is then

$$c_q = -\tau_q \left[ \frac{k_{nr}' W_{nr}}{kT^2} \exp\left(-\frac{W_{nr}}{kT}\right) + k_q[Q] \frac{W_d}{kT^2} \right]$$

and may be rewritten as

$$c_q = \frac{\tau_q}{\tau_0} \left[ -C_0 + k_q\tau_0[Q] \frac{W_d}{kT^2} \right]$$

Noting that

$$\tau_q/\tau_0 = 1 + K[Q]$$

where  $K = k_q\tau_0$  is the Stern-Volmer constant, and using absolute values  $C$  of temperature coefficients, one finally obtains

$$C_q = C_0 \frac{1 + K[Q] (W_d/C_0 kT^2)}{1 + K[Q]} \quad (6)$$

(2) *Properties.* Equation 6, which reduces to  $C_q = C_0$  if [Q] = 0, shows that addition of a quencher to a fluorescent solution may increase or decrease the temperature coefficient according to the respective values of  $C_0$  and  $W_d$ . As a matter of fact, differentiation of (6) with respect to [Q] at constant temperature leads to

$$\left( \frac{\delta C_q}{\delta [Q]} \right)_T = \frac{C_0 K}{(1 + K[Q])^2} \left( \frac{W_d}{C_0 kT^2} - 1 \right)$$

which indicates that  $C_q$  is an *increasing* function of the quencher concentration (i.e.,  $C_q > C_0$ ) if

$$W_d/kT^2 > C_0 \quad (7)$$

and is a *decreasing* function of [Q] ( $C_q < C_0$ ) in the opposite case ( $W_d/kT^2 < C_0$ ).

Inequality 7 brings out the respective influences of the two main thermal effects (on lifetime and quenching efficiency) involved in the phenomenon. Indeed a low value of  $C_0$ , satisfying (7), implies a small temperature dependence of the fluorescent lifetime  $\tau_0$ , in which case the predominant effect of temperature is to modify molecular mobilities and therefore to increase the quenching efficiency; the thermal dependence of the fluorescence yield is then greater in the presence than in the absence of quencher (i.e.,  $C_q > C_0$ ). Conversely, a high value of  $C_0$ , such that  $W_d/kT^2 < C_0$ , implies that an increase in temperature greatly shortens the fluorophore lifetime and therefore reduces the quenching efficiency; this thermal reduction of quenching attenuates the decrease of the fluorescence yield due to the fluorophore itself (i.e.,  $C_q < C_0$ ). In the particular case where  $W_d/kT^2 = C_0$ , the two effects (lifetime decrease and quenching increase) cancel each other, and  $C_q = C_0$ .

Finally, eq 6 also shows that in every case  $C_q$  at *high quencher concentration* tends toward a single limiting value, which essentially depends on the solvent

$$\lim (C_q)_{[Q] \rightarrow \infty} = (C_q)_\infty = W_d/kT^2$$

Determination of this value thus allows evaluation of the activation energy for diffusion  $W_d$ .

(3) *Experimental Verification.* (a) *Aqueous Solutions.* The influence of protonated histidine, an efficient quencher of indole<sup>15</sup> and phenol,<sup>16</sup> on the temperature coefficient (at 30 °C) of these solutes in aqueous solutions was investigated at concentrations up to 1 M.

Two concordant estimations of  $W_d$  in water were possible a priori: (i) from the activation energy for viscosity,  $W_d \approx W_\eta = 0.165$  eV;<sup>17</sup> and (ii) from Eyring's relation  $W_d$

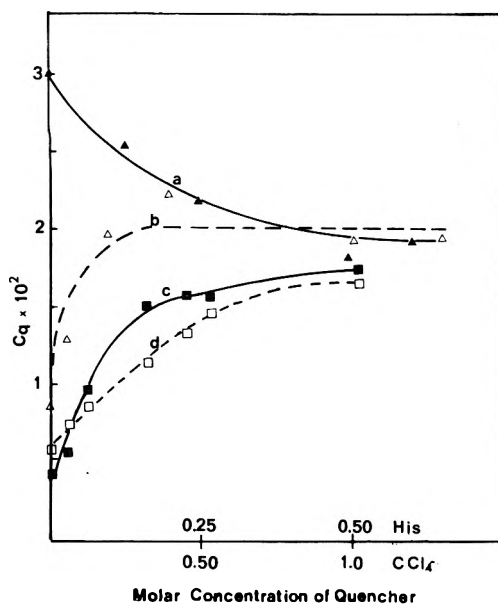


**Figure 2.** Influence of the quencher concentration on the fluorescence temperature coefficient ( $C_q$ ) for (a) indole + histidine/water, pH 5; (b) phenol + histidine/water, pH 5; (c) indole +  $\text{CCl}_4$ /dioxane; (d) phenol +  $\text{CCl}_4$ /dioxane.

$\approx \Delta H_v/n$ ,<sup>14</sup> where  $\Delta H_v$  is the heat of vaporization (10 kcal/mol for water<sup>18</sup>) and  $n \approx 2.4$  for associated liquids:  $W_d \approx 0.17$  eV.

At 30 °C ( $kT^2 = 8$  eV deg), one then has  $W_d/kT^2 \approx 2.1 \times 10^{-2}$  deg<sup>-1</sup> a value greater than that of  $C_0$  for phenol ( $0.85 \times 10^{-2}$ ) but smaller than that of  $C_0$  for indole ( $3.0 \times 10^{-2}$ ). Addition of the quencher was therefore expected to increase the temperature coefficient of the phenol solution and to decrease that of the indole solution. Results presented in Figure 2 (curves a and b) show that both effects were observed, and that the two experimental curves have the predicted common asymptote at high quencher concentrations ( $[Q] > 0.4$  M), whose ordinate  $[(C_q)_\infty \approx 2 \times 10^{-2}$  deg<sup>-1</sup>] is furthermore in excellent agreement with the estimated value of  $W_d/kT^2$ .

(b) *Dioxane Solutions.* Using  $\text{CCl}_4$  as the quencher, similar experiments were performed in dioxane, where the estimated values of  $W_d$  are 0.125 eV from the thermal dependence of viscosity<sup>17</sup> and 0.138 eV from Eyring's

relation ( $n = 2.4$ ,  $\Delta H_v = 7.6$  kcal/mol<sup>18</sup>). Taking, thus,  $W_d = 0.13$  eV yields  $W_d/kT^2 = 1.6 \times 10^{-2}$  deg<sup>-1</sup>, a value higher than those of both coefficients  $C_0$  ( $0.4 \times 10^{-2}$  for indole and  $0.55 \times 10^{-2}$  for phenol).

Addition of the quencher was then expected to increase the temperature coefficients in both cases, and the increase was indeed observed experimentally (Figure 2, curves c and d). Again a common asymptotic value was reached by both coefficients at higher quencher concentration, whose value  $[(C_q)_\infty \approx 1.7 \times 10^{-2}$  deg<sup>-1</sup>] agrees with that of  $W_d/kT^2$  estimated above.

### Conclusion

This study shows that dynamic quenching may either increase or decrease the thermal dependence of fluorescence in solution, according to the properties of both solvent and solute. It also shows that the temperature coefficient is a useful parameter that permits quantification of this phenomenon and may also give information on the activation energy for diffusion.

### References and Notes

- (1) J. B. Birks in "Organic Molecular Photophysics", Vol. 1, J. B. Birks, Ed., Wiley, London, 1973, pp 32-41.
- (2) M. S. Walker, T. W. Bednar, and R. Lumry in "Molecular Luminescence", E. C. Lim, Ed., W. A. Benjamin, New York, N.Y., 1969, pp 135-152.
- (3) M. S. Walker, T. W. Bednar, R. Lumry, and F. Humphries, *Photochem. Photobiol.*, **14**, 147 (1971).
- (4) E. P. Kirby and R. F. Steiner, *J. Phys. Chem.*, **74**, 4480 (1970).
- (5) G. Laustriat and D. Gerard in "Excited States of Biological Molecules", J. B. Birks, Ed., Wiley, London, 1976, pp 388-399.
- (6) D. Gerard, G. Laustriat, and H. Lami, *Biochim. Biophys. Acta*, **263**, 482 (1972).
- (7) C. F. Chen, *Anal. Lett.*, **1**, 35 (1967).
- (8) J. Eisinger and G. Navon, *J. Chem. Phys.*, **50**, 2069 (1969).
- (9) G. Pfeffer, H. Lami, G. Laustriat, and A. Coche, Colloque International d'Electronique Nucléaire, OCDE, Paris, 1963.
- (10) N. Glasser, private communication.
- (11) K. K. Turoverov and B. V. Shchelchokov, *Biofizika*, **15**, 800 (1970).
- (12) R. Voltz, J. Klein, F. Heisel, H. Lami, G. Laustriat, and A. Coche, *J. Chim. Phys.*, **53**, 1259 (1966).
- (13) A. M. North, "The Collision Theory of Chemical Reactions in Liquids", Wiley, New York, N.Y., 1964, pp 19-36.
- (14) S. Glasstone, K. Laidler, and H. Eyring, "Theory of Rate Processes", McGraw-Hill, New York, N.Y., 1941, Chapter 9.
- (15) M. Shinitzky and R. Goldman, *Eur. J. Biochem.*, **3**, 139 (1967).
- (16) D. Gerard, Thesis, University of Strasbourg, 1975.
- (17) "American Institute of Physics Handbook", 2nd ed, McGraw-Hill, New York, N.Y., 1963, p II-181.
- (18) "Physikalisch-Chemische Tabellen", 5th ed, W. A. Roth and K. Scheel, Ed., Berlin, 1931, pp 1483-1490.

## COMMUNICATIONS TO THE EDITOR

### Pulse Radiolysis and Electron Spin Resonance Studies Concerning the Reaction of $\text{SO}_4^{\cdot-}$ with Alcohols and Ethers in Aqueous Solution

Publication cost assisted by the Institut für Strahlenchemie

Sir: The  $\text{SO}_4^{\cdot-}$  radical has been shown to react with benzene derivatives by electron transfer.<sup>1-6</sup> A similar mechanism has also been proposed for the reaction of  $\text{SO}_4^{\cdot-}$  with alcohols.<sup>7</sup> However, it has recently been suggested<sup>8,9</sup> that this reaction involves H abstraction. In order to elucidate the reaction mechanism, the rate constants for the reaction of  $\text{SO}_4^{\cdot-}$  in aqueous solution which unde-

terated and deuterated alcohols (and with some ethers) were determined by a competition method which utilizes the reaction<sup>3</sup> of  $\text{SO}_4^{\cdot-}$  with 1,3,5-trimethoxybenzene (TMB) to yield  $\text{TMB}^{\cdot+}$  ( $\lambda_{\text{max}} 580$  nm,  $\epsilon 5700$  M<sup>-1</sup> cm<sup>-1</sup>). Since the rate constant for reaction of  $\text{SO}_4^{\cdot-}$  with TMB is used as a standard, this rate constant was redetermined by pulse irradiating, with 2.8-MeV electrons, argon-saturated aqueous solutions at pH 7-8 containing 1 mM  $\text{K}_2\text{S}_2\text{O}_8$  and 0.01-0.1 mM TMB and monitoring the buildup of  $\text{TMB}^{\cdot+}$  at 580 nm.  $k(\text{SO}_4^{\cdot-} + \text{TMB})$  was found to be  $(2.4 \pm 0.5) \times 10^9$  M<sup>-1</sup> s<sup>-1</sup>, which is slightly higher than the value<sup>3</sup> reported previously. For determination of the  $k(\text{SO}_4^{\cdot-} + \text{alcohol})$  values, the solutions pulse-irradiated typically

TABLE I: Rate Constants for the Reaction  $\text{SO}_4^{\cdot-}$  with Alcohols and Ethers Determined at  $20 \pm 2^\circ\text{C}^a$ 

Substrate	$k_{\text{H}},^b \text{ M}^{-1} \text{ s}^{-1}$	$k_{\text{D}}^b \text{ M}^{-1} \text{ s}^{-1}$	$k_{\text{H}}/k_{\text{D}}$	$k_{\alpha},^c \text{ M}^{-1} \text{ s}^{-1}$	$k(\text{OH} + \text{substrate}),^e \text{ M}^{-1} \text{ s}^{-1}$
Methanol	$3.2 \times 10^6$	$1.2 \times 10^6$	2.7	$1.1 \times 10^6$	$9 \times 10^8$
Ethanol	$1.6 \times 10^7$	$6.7 \times 10^6$	2.4	$7.9 \times 10^6$	$1.7 \times 10^9$
2-Propanol	$3.2 \times 10^7$	$1.2 \times 10^7$	2.7	$3.2 \times 10^7$	$2.0 \times 10^9$
2-Methyl-2-propanol	$4.0 \times 10^5$			$4.4 \times 10^4 d$	$4.5 \times 10^8$
1,4-Dioxane	$1.6 \times 10^7$	$9.2 \times 10^6$	1.7		$1.8 \times 10^9$
Tetrahydrofuran	$1.0 \times 10^8$	$5.1 \times 10^7$	2.0		$2.7 \times 10^9$

<sup>a</sup> Rate constants for reaction of  $\text{OH}$  with the substrates are included for comparison. <sup>b</sup>  $k_{\text{H}}(k_{\text{D}})$  are the rate constants for reaction of  $\text{SO}_4^{\cdot-}$  with undeuterated (deuterated) substrates. <sup>c</sup>  $k_{\alpha} = (k_{\text{H}} - n_{\beta}k_{\beta})/n_{\alpha}$ , where  $n_{\alpha}(n_{\beta})$  is the number of H atoms at  $\text{C}_{\alpha}(\text{C}_{\beta})$ .  $k_{\beta}$  is the rate constant for abstraction of one H atom from  $\text{C}_{\beta}$ .  $k_{\beta} \equiv 1/9 k(\text{SO}_4^{\cdot-} + 2\text{-methyl-2-propanol})$ . <sup>d</sup>  $k_{\beta}$ . <sup>e</sup> Averaged values, taken from ref 20.

contained 0.01–0.5 M alcohol, 1 mM  $\text{K}_2\text{S}_2\text{O}_8$ , and 0.1–0.2 mM TMB.

As seen in Table I, the rate constants for reaction of  $\text{SO}_4^{\cdot-}$  with the alcohols and ethers containing C–H bonds are a factor of 2–3 larger than those for reaction of  $\text{SO}_4^{\cdot-}$  with corresponding C-deuterated substrates. The reaction of  $\text{SO}_4^{\cdot-}$  with alcohols and ethers is thus seen to involve the breaking of a C–H (C–D) bond. The  $k_{\text{H}}/k_{\text{D}}$  values for the reaction of  $\text{SO}_4^{\cdot-}$  are slightly larger than those<sup>10</sup> determined for the reaction of  $\text{OH}$  with alcohols which also proceeds by H abstraction.

Except for the case of 2-propanol, the  $k(\text{SO}_4^{\cdot-} + \text{alcohol})$  values determined in the present study are lower than those<sup>11–13</sup> reported previously. The latter values were measured by monitoring the decay of  $\text{SO}_4^{\cdot-}$ . As pointed out by Henglein,<sup>11</sup> this method is likely to yield values which are too high, due to contribution of second-order decay of  $\text{SO}_4^{\cdot-}$ .

Column 5 of Table I contains the partial rate constants  $k_{\alpha}$  (rate constant for abstraction of one H atom from  $\text{C}_{\alpha}$ ) for  $\text{SO}_4^{\cdot-}$  attack on the alcohols. In calculating these values it was assumed that the partial rate constant  $k_{\beta}$  (rate constant for abstraction of one H atom from  $\text{C}_{\beta}$ ) is equal to  $1/9 k(\text{SO}_4^{\cdot-} + 2\text{-methyl-2-propanol})$  for all alcohols and that the contribution of H abstraction from the alcoholic OH group is negligible (see ESR data). The partial rate constants  $k_{\alpha}$  increase strongly with increasing alkylation at  $\text{C}_{\alpha}$ . This effect is suggested to reflect the electrophilicity<sup>6</sup> of  $\text{SO}_4^{\cdot-}$  which is larger than that<sup>10,14</sup> of  $\text{OH}$ . A plot of  $\log(k(\text{SO}_4^{\cdot-} + \text{substrate})/k(\text{SO}_4^{\cdot-} + \text{methanol}))$  vs.  $\log(k(\text{OH} + \text{substrate})/k(\text{OH} + \text{methanol}))$  yields a straight line with a slope corresponding to 3, which demonstrates that  $\text{SO}_4^{\cdot-}$  is more sensitive than  $\text{OH}$  with respect to the changes at  $\text{C}_{\alpha}$  induced by  $\alpha$ -alkylation.<sup>15</sup> This leads to an increased selectivity of  $\text{SO}_4^{\cdot-}$  as compared to that<sup>10,16</sup> of  $\text{OH}$  with respect to H abstraction from  $\text{C}_{\alpha}$  vs  $\text{C}_{\beta}$ . On the basis of the  $k_{\alpha}$  and  $k_{\beta}$  values, in the reaction of  $\text{SO}_4^{\cdot-}$  with ethanol and 2-propanol the yield of H abstraction from  $\text{C}_{\alpha}$  is >99%.

In order to further test the mechanisms of reaction of  $\text{SO}_4^{\cdot-}$  with alcohols, ESR experiments were carried out. If  $\text{SO}_4^{\cdot-}$  reacts with alcohols by electron transfer, alkoxy radicals should be formed via deprotonation of the initially produced radical cations. It has been demonstrated<sup>17,18</sup> that alkoxy radicals can be scavenged by the aci anion of  $\text{CH}_3\text{NO}_2$ . On photolysis of 50 mM  $\text{K}_2\text{S}_2\text{O}_8$  solutions at pH 10–11 containing 1–2 M methanol, ethanol, 1- or 2-propanol, and 10–100 mM  $\text{CH}_3\text{NO}_2$  no spin adducts of the type  $\text{ROCH}_2\text{NO}_3^{\cdot-}$  were detected. In all cases the radicals detected were of or derived from the  $\alpha$ -hydroxyalkyl type and  $\beta$ -hydroxyalkyl radicals were not observed, with the exception of the 2-methyl-2-propanol system where the radical  $\dot{\text{C}}\text{H}_2(\text{CH}_3)_2\text{C}(\text{OH})$  was found to be produced. The

2-methyl-2-propoxy radical is known to undergo  $\beta$  fragmentation to yield methyl radical which subsequently adds to  $\text{CH}_2\text{NO}_2^{\cdot-}$  to yield  $\text{CH}_3\text{CH}_2\text{HO}_2^{\cdot-}$ .<sup>17</sup> On reaction of  $\text{SO}_4^{\cdot-}$  with 2-methyl-2-propanol in the presence of  $\text{CH}_2\text{NO}_2^{\cdot-}$ , the radical  $\text{HOC}(\text{CH}_3)_2\text{CH}_2\text{CH}_2\text{NO}_2^{\cdot-}$  was the only species observed which was derived from 2-methyl-2-propanol.<sup>19</sup> For comparison, on production of 2-methyl-2-propoxy radicals by photolysis of di-*tert*-butyl peroxide in the presence of  $\text{CH}_2\text{NO}_2^{\cdot-}$  intense lines from  $\text{CH}_3\text{CH}_2\text{NO}_2^{\cdot-}$  were seen. From the signal-to-noise ratio observed for  $\text{HOC}(\text{CH}_3)_2\text{CH}_2\text{CH}_2\text{NO}_2^{\cdot-}$  in the 2-methyl-2-propanol– $\text{K}_2\text{S}_2\text{O}_8$ – $\text{CH}_2\text{NO}_2^{\cdot-}$  system and assuming equal lifetimes for this radical and  $\text{CH}_3\text{CH}_2\text{NO}_2^{\cdot-}$  it is concluded that the rate constant for H abstraction from the OH group by  $\text{SO}_4^{\cdot-}$  is a factor  $\geq 4$  smaller than the measured rate constant for reaction of  $\text{SO}_4^{\cdot-}$  with 2-methyl-2-propanol.

The results of the ESR experiments are therefore in support of the results of the kinetic studies described above further demonstrating that the reaction of  $\text{SO}_4^{\cdot-}$  with alcohols proceeds by H abstraction from a C–H bond and not by electron transfer.

## References and Notes

- O. P. Chawla and R. W. Fessenden, *J. Phys. Chem.*, **79**, 2693 (1975).
- H. Zemel and R. W. Fessenden, *J. Phys. Chem.*, **79**, 1419 (1975).
- P. O'Neill, S. Steenken, and D. Schulte-Frohlinde, *J. Phys. Chem.*, **79**, 2773 (1975).
- S. Steenken, P. O'Neill, and D. Schulte-Frohlinde, *J. Phys. Chem.*, **81**, 26 (1977).
- K. Sehested, J. Holcman, and E. J. Hart, *J. Phys. Chem.*, **81**, 1363 (1977).
- P. Neta, V. Madhavan, H. Zemel, and R. W. Fessenden, *J. Am. Chem. Soc.*, **99**, 163 (1977).
- A. Ledwith, P. J. Russell, and L. H. Sutcliffe, *Chem. Commun.*, 964 (1971).
- K. M. Bansal and R. W. Fessenden, *Radiat. Res.*, **67**, 1 (1976).
- P. Maruthamuthu and P. Neta, *J. Phys. Chem.*, **81**, 1622 (1977).
- M. Anbar, D. Meyerstein, and P. Neta, *J. Chem. Soc. B*, 742 (1966).
- E. Heckel, A. Henglein, and G. Beck, *Ber. Bunsenges. Phys. Chem.*, **70**, 149 (1966).
- E. Hayon, A. Treinin, and J. Wilf, *J. Am. Chem. Soc.*, **94**, 47 (1972).
- J. L. Redpath and R. L. Willson, *Int. J. Radiat. Biol.*, **27**, 389 (1975).
- M. Anbar, D. Meyerstein, and P. Neta, *J. Phys. Chem.*, **70**, 2660 (1966).
- A similar effect is shown by the  $\text{H}_2\text{PO}_4^{\cdot-}$  radical (see ref 9).
- K.-D. Asmus, H. Möckel, and A. Henglein, *J. Phys. Chem.*, **77**, 1218 (1973).
- B. C. Gilbert, R. G. G. Holmes, H. A. H. Laue, and R. O. C. Norman, *J. Chem. Soc., Perkin Trans. 2*, 1047 (1976).
- Y. Kirino and R. W. Fessenden, Mellon Institute of Science, Radiation Research Laboratories, Quarterly Report, July 1–Sept 30, 1974, p 10.
- In addition, radicals derived from reaction of  $\text{SO}_4^{\cdot-}$  with  $\text{CH}_2\text{NO}_2^{\cdot-}$  were seen (see ref 1 for information on the  $\text{S}_2\text{O}_8^{2-}$ – $\text{CH}_2\text{NO}_2^{\cdot-}$  system).
- L. M. Dorfman and G. E. Adams, *Natl. Stand. Ref. Data Ser., Natl. Bur. Stand.*, No. 46 (1973).

Institut für Strahlenchemie  
im Max-Planck-Institut für Kohlenforschung  
D-4330 Mülheim, West Germany

H. Eibenberger  
S. Steenken\*  
P. O'Neill  
D. Schulte-Frohlinde

Received December 27, 1977



## Infrared Study of Hydrogen Sulfide and Carbon Monoxide Adsorption in the Presence of Hydrogen on Alumina-Supported Nickel Catalysts

Publication costs assisted by SRI International

Sir: The adsorption of CO on Ni catalysts studied by infrared (IR) absorption spectroscopy has been the subject of several investigations.<sup>1,2</sup> The results have been interpreted in terms of two predominant surface configurations<sup>3</sup> for CO bonding to Ni: single site attachment ( $\alpha$ -CO) with IR bands at frequencies above 2000  $\text{cm}^{-1}$  and multisite attachment ( $\beta$ -CO) at frequencies below 2000  $\text{cm}^{-1}$ . In the presence of  $\text{H}_2$ , the IR band associated with  $\alpha$ -CO on group 8 metals shift to higher frequencies,<sup>4,5</sup> with little change in the position of the  $\beta$ -CO frequency. In the following study we examine the effect of hydrogen sulfide on the IR bands of carbon monoxide in the presence of hydrogen.

For IR absorption measurement the 7-cm Pyrex IR cell, in the form of an inverted T, was designed to allow heating of the catalyst disk ( $\text{Ni}/\text{Al}_2\text{O}_3$ ) by raising it into the vertical section which was wrapped with resistance wire and provided with a thermocouple well. Absorption studies were carried out after lowering the catalyst disk into the horizontal section equipped with NaCl windows. The catalyst disk was held in position for IR study while the gaseous reactants and the inert carrier gas (He) were introduced into the cell. Spectra were obtained under flow conditions at 1 atm total pressure with a Perkin-Elmer Model 457 spectrometer. With the catalyst samples under study, we achieved good spectral transmission in the frequency range from 2500 to 1800  $\text{cm}^{-1}$ .

The  $\text{Ni}/\text{Al}_2\text{O}_3$  catalyst was prepared by adding an aqueous solution of  $\text{Ni}(\text{NO}_3)_2 \cdot 6\text{H}_2\text{O}$  to a slurry of sieved Kaiser  $\text{Al}_2\text{O}_3$ <sup>11</sup> (<41  $\mu\text{m}$ ) to give a product containing 4.8 wt % Ni on a dried and reduced basis. An aliquot of this powdered sample (100 mg), pressed into a 0.36-mm thick disk (using a 1.25-cm die and a pressure of about 5900 psi), was converted inside the IR cell to the oxide by heating for 1 h at 573 K in flowing helium, and then reduced by exposure to 10  $\text{H}_2/90$  He (vol %) for 15 h at 623 K.

All infrared measurements, except when indicated, were made at room temperature in the presence of 10  $\text{H}_2/90$  He (vol %) carrier gas to which we added CO (<2 Torr) and  $\text{H}_2\text{S}$  (100 ppm). The band intensities reported in these studies are semiquantitative, since small peak overlap corrections have not been made. Of greatest interest are the peak intensity changes for  $\alpha$ -CO and  $\beta$ -CO. In this study the molar extinction coefficients ( $\epsilon$ ) for the  $\alpha$ - and  $\beta$ -CO stretching frequencies are taken to be equal. However, a correlation of IR intensity measurements with data obtained from temperature-programmed desorption studies<sup>6</sup> suggest that  $\epsilon$  for  $\alpha$ -CO may be two to three times greater than for  $\beta$ -CO.

The infrared bands observed during CO/ $\text{H}_2$  exposure exhibit two strong asymmetric bands assigned to the CO stretching vibrations<sup>3</sup> at 2085 and 1946  $\text{cm}^{-1}$  of  $\alpha$ -CO and  $\beta$ -CO (Figure 1). Exposure of an  $\text{Al}_2\text{O}_3$  blank to CO did not yield any observable IR absorption in the wavelength region studied. Of interest to our study was (1) the influence of progressive surface coverage with sulfur ad-species on CO adsorption, and (2), the displacement of adsorbed CO from  $\alpha$  and  $\beta$  sites by exposure to  $\text{H}_2\text{S}$  in the presence of  $\text{H}_2$ .

Preexposure of  $\text{Ni}/\text{Al}_2\text{O}_3$  to  $\text{H}_2\text{S}$  had a pronounced effect on the subsequent absorption spectrum of CO. In this study, the surface was exposed to progressively larger doses of  $\text{H}_2\text{S}$  followed by a fixed exposure to CO/ $\text{H}_2$ . The sequence was repeated at progressively higher  $\text{H}_2\text{S}$  levels

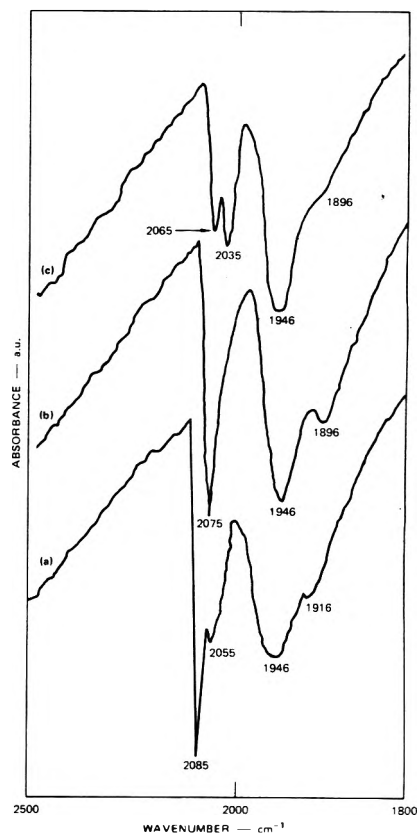


Figure 1. Infrared spectra of CO adsorbed on  $\text{Ni}/\text{Al}_2\text{O}_3$  catalyst: (a) after exposure to CO- $\text{H}_2$ -He; (b) spectrum a after exposure to  $\text{H}_2$ -He; (c) spectrum b after exposure to He.

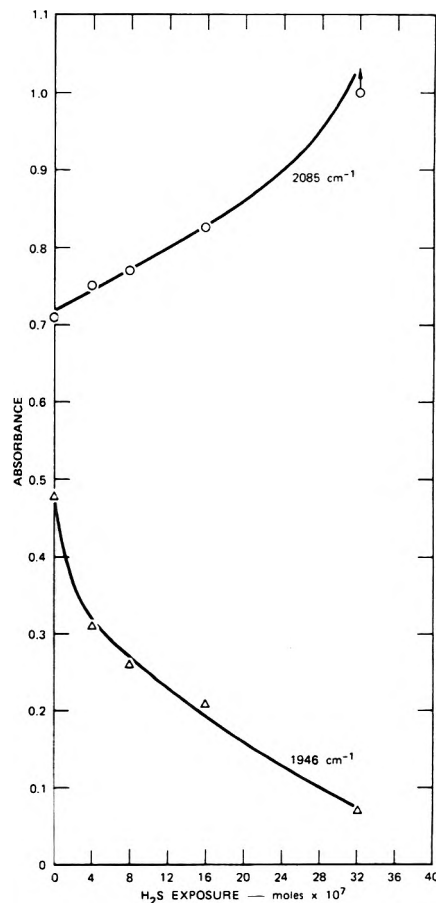
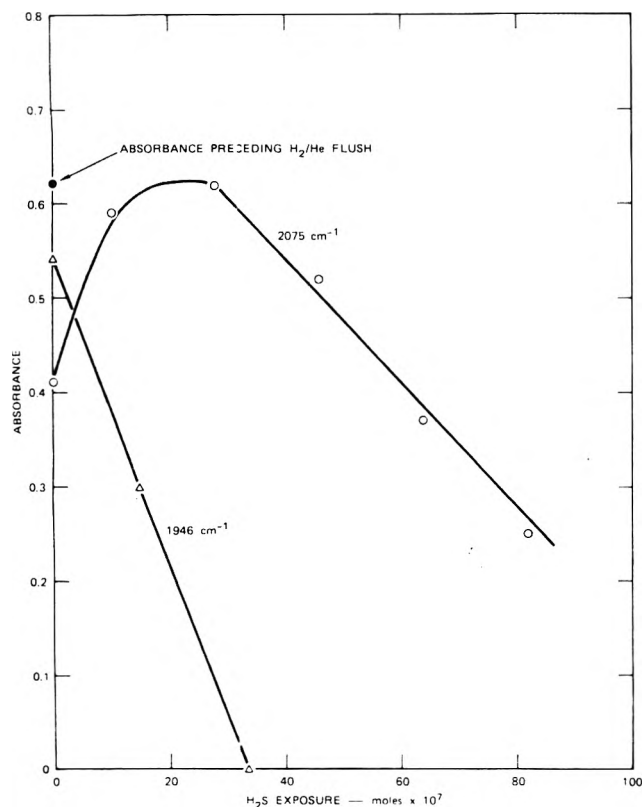


Figure 2. CO/ $\text{H}_2$  adsorption on  $\text{Ni}/\text{Al}_2\text{O}_3$  catalyst exposed to  $\text{H}_2\text{S}$  (CO exposure =  $7.4 \times 10^{-5}$  mol).

after removal of CO previously adsorbed in a stream of 10  $\text{H}_2/90$  He (vol %) at 573 K. The results (Figure 2)



**Figure 3.** Effect of  $\text{H}_2\text{S}/\text{H}_2$  on CO preadsorbed on  $\text{Ni}/\text{Al}_2\text{O}_3$  catalyst (CO exposure =  $7.1 \times 10^{-4}$  mol).

demonstrate that the S adspecies preempt the  $\beta$ -CO binding sites ( $1946\text{ cm}^{-1}$ ). At the same time, the absorbance due to the band frequency at  $2085\text{ cm}^{-1}$  grows, indicative of new surface sites that can adsorb CO in the presence of S adspecies. However, the binding energy of the CO adspecies formed is quite low, since a large fraction can be desorbed in  $\text{H}_2/\text{He}$  at room temperature.

The displacement of CO adspecies by  $\text{H}_2\text{S}$  was studied by contacting the catalyst sample with  $\text{H}_2\text{S}$  (100 ppm) in 10  $\text{H}_2/90\text{ He}$  (vol %) carrier gas after it had acquired CO saturation coverage (Figure 1, curve a). Preceding the exposure to  $\text{H}_2\text{S}/\text{H}_2/\text{He}$ , the sample was flushed in 10  $\text{H}_2/90\text{ He}$  (vol %) for 1 h at room temperature, which

treatment caused a reduction in the intensity of the  $\alpha$ -CO band and a frequency shift of  $\alpha$ -CO from a wavenumber of  $2085$  to  $2075\text{ cm}^{-1}$  (Figure 1, curve b). The admission of  $\text{H}_2\text{S}$  causes preferential displacement of  $\beta$ -CO as manifested by the considerable reduction in the intensity of the  $1946\text{-cm}^{-1}$  band (Figure 3). However, the band at  $2075\text{ cm}^{-1}$  exhibits entirely different characteristics on admission of  $\text{H}_2\text{S}$ ; the band intensity goes through a maximum. The data suggest that sites vacated by very weakly bound  $\alpha$ -CO, i.e., the CO ad molecules removable by pretreatment in  $\text{H}_2/\text{He}$ , become occupied by the CO ad molecules originally bound in  $\beta$ -CO sites and displaced by the adsorption of  $\text{H}_2\text{S}$ . Only after these sites have been filled and  $\beta$ -CO nearly removed does the band at  $2075\text{ cm}^{-1}$  begin to diminish in intensity.

Our studies show that S adspecies favor high coordination sites irrespective of the presence or absence of adlayers of carbon monoxide and hydrogen. These results parallel previous studies<sup>7-10</sup> on the interference of S adatoms on CO adsorption in the absence of hydrogen.

*Acknowledgment.* This study was carried out under the sponsorship of the American Gas Association, whose support is gratefully acknowledged.

#### References and Notes

- (1) R. R. Ford, *Adv. Catal.*, **21**, 51 (1970).
- (2) L. H. Little, "Infrared Spectra of Adsorbed Species", Academic Press, New York, N.Y., 1966.
- (3) R. P. Eischens, S. A. Francis, and W. A. Pliskin, *J. Phys. Chem.*, **60**, 194 (1956).
- (4) M. Primet and N. Sheppard, *J. Catal.*, **41**, 258 (1976).
- (5) J. F. Harrod, R. W. Roberts, and E. F. Rissmann, *J. Phys. Chem.*, **71**, 343 (1967).
- (6) J. Falconer and H. Wise, to be submitted for publication.
- (7) C. W. Garland, *J. Phys. Chem.*, **63**, 1423 (1959).
- (8) W. Crell, H. Hobert, and B. Knappe, *Z. Chem.*, **8**, 396 (1968).
- (9) C. H. Rochester and R. J. Terrell, *J. Chem. Soc., Faraday Trans. 1*, 609 (1977).
- (10) G. Marx, H. Hobert, V. Hopfe, B. Knappe, W. Vogelsberger, P. Mackrodt, and K. Meyer, *Z. Chem.*, **12**, 444 (1972).
- (11) 65%  $\alpha$  alumina, surface area  $20\text{ m}^2/\text{g}$ .

Solid State Catalysis Laboratory  
SRI International  
Menlo Park, California 94025

R. T. Rewick\*  
H. Wise

Received November 30, 1977

# Special Centennial Tapes

4 Historic Symposia! 24 Speakers! Custom Packaging! Special Prices!

## Milestones in Physical Chemistry

8 Speakers — 315 Figures  
Length: 5 Cassettes — 8 Hours  
PRICE: \$45 (postpaid)

The Speakers:

- G. T. Seaborg — 40 Years of Transuranium Elements
- D. Hodgkin — Structure of Molecules in Crystals
- G. Porter — Chemistry in Microtime
- P. J. Flory — Thermodynamics of Polymer Solutions
- W. O. Baker — Chemistry of the Solid State
- L. C. Pauling — Perspectives in Chemical Bonding & Structure
- H. Eyring — Reaction Rate Theory
- J. H. Van Vleck — Evolution of Theoretical Chemistry in America

## Structure and Quantum Chemistry + Evolution of Magnetic Resonance

8 Speakers — 210 Figures  
Length: 4 Cassettes — 6 Hours  
PRICE: \$35 (postpaid)

The Speakers:

- J. A. Pople — Orbital Studies of Molecular Structure & Stability
- H. G. Drickamer — Pressure & Electronic Structure
- F. H. Stillinger — Quantum Chemistry & Eccentric Behavior of Liquid Water
- R. Zwanzig — Molecular Hydrodynamics
- H. S. Gutowsky — 30 Years of Relaxation
- J. S. Waugh — Alchemy of Nuclear Spins
- H. M. McConnell — Spin Labels
- F. A. Bovey — NMR of Macromolecules

## Evolution of Kinetics

8 Speakers — 140 Figures  
Length: 4 Cassettes — 6 Hours  
PRICE: \$35 (postpaid)

The Speakers:

- B. S. Rabinovitch — Perspectives on Vibration Energy Relaxation in Unimolecular Reactions
- W. A. Noyes, Jr. — Photochemical Kinetics
- R. A. Marcus — Trends in Theoretical Chemical Kinetics
- K. F. Freed — Radiationless Processes in Polyatomic Molecules
- G. B. Kistiakowski — Early Years of Gas Phase Chemical Kinetics
- J. C. Polanyi — Recent Studies of Infrared Chemiluminescence & Fluorescence
- S. Claesson — Diffusion Rates & Chemical Reaction Kinetics
- J. Jortner — Intramolecular Dynamics in Excited Molecular States

— SPECIAL PRICE —

BUY ALL THREE SETS —  
ONLY \$85 (postpaid)

SAVE \$30!

ORDER FROM:  
American Chemical Society  
1155 Sixteenth St., N.W.  
Washington, D.C. 20036  
ATTN: DEPT. AP

Name \_\_\_\_\_

Address \_\_\_\_\_

City \_\_\_\_\_

State \_\_\_\_\_

Zip \_\_\_\_\_

(allow 4 to 6 weeks for delivery)



## BETTER BET ON THE RABBIT.

In the fable, the tortoise wins.  
Of course, everybody knows it didn't really happen that way.  
That's why they call it a fable.  
No two ways about it. . .  
**THE RACE IS TO THE SWIFT.**

To keep current on developments in the fast-moving discipline of physical chemistry, you need a journal that publishes up-to-date articles, communications, and symposia. Biweekly—now *that's* up to date. And you'll get biweekly information in. . .

### THE JOURNAL OF PHYSICAL CHEMISTRY.

Swift is fine, but it's not nearly enough for an authoritative publication of ACS. You'll find more than 20 papers in every issue, covering spectroscopy, thermodynamics, reaction kinetics, and other areas of experimental and theoretical physical chemistry.

Would you like to be a little bit ahead of the rest of your field—the people who don't use the Journal? Then, just . . .  
*Complete, clip, and mail the coupon below. Now?*

Available in Hard Copy or Microfiche

- new concepts
- new techniques
- new interpretations  
... plus reports on classical areas

The editors of the Journal of Physical Chemistry strive to select material that is useful in the classical areas of chemistry as well as in modern structural quantum mechanical areas. Start your subscription now. We'll do the rest.



Another service of ACS

#### The Journal of Physical Chemistry

American Chemical Society

1978

1155 Sixteenth Street, N.W.

Washington, D.C. 20036

Yes, I would like to receive the JOURNAL OF PHYSICAL CHEMISTRY at the one-year rate checked below:

		U.S.	All Other Countries
ACS Member*	<input type="checkbox"/>	\$24.00	<input type="checkbox"/> \$34.00
Nonmember	<input type="checkbox"/>	\$96.00	<input type="checkbox"/> \$106.00

Bill me  Bill company  Payment enclosed

Air freight rates are available on request.

Name \_\_\_\_\_

Street \_\_\_\_\_

Home   
Business

City \_\_\_\_\_

State \_\_\_\_\_

Zip \_\_\_\_\_

Journal subscriptions start in January '78.

Allow 60 days for your first copy to be mailed.

\* NOTE: Subscriptions at ACS member rates are for personal use only.

31. W.P. 2521